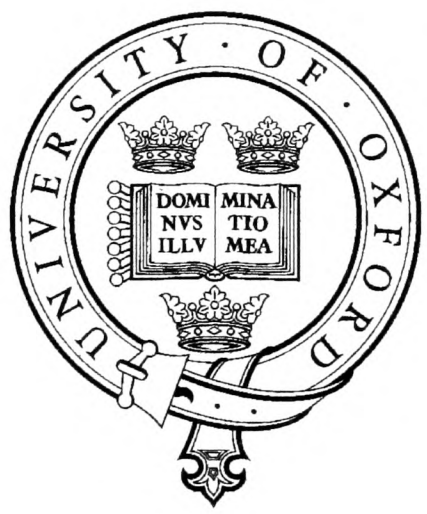
Chemical, Electronic and Electrochemical Properties *of* Diamond Thin Films



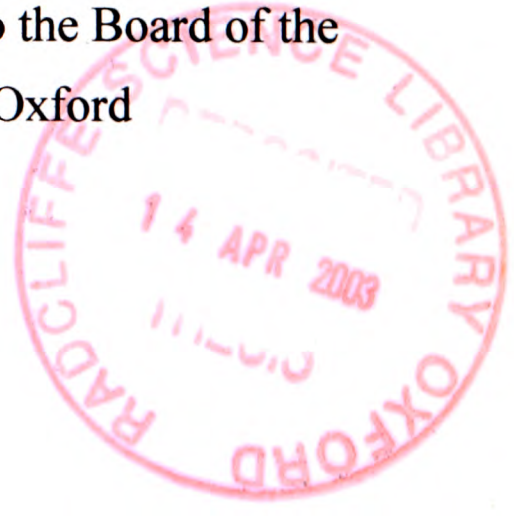
by

Chi Hian, Lau

St. Catherine's College, Oxford

A thesis submitted for the degree of Doctor of Philosophy to the Board of the Faculty of Physical Sciences at the University of Oxford

Trinity 2002



Acknowledgement

I would like to give massive thank to my project supervisor and thesis advisor Prof John S. Foord for his continuous and unfailing guidance over the last three years. Without your help, I won't have achieved this far. Thanks John! I hope I can make good use of the knowledge that I learnt from you.

I am indebted to Dr Mineo Hiramatsu for his support and help, for the time we shared together in the lab and in the conference.

I thank Dr Frank Marken for his endurance of teaching me about electrochemistry and his valuable comments.

I thank Dr Christiaan and Dr Simon for teaching me the experimental techniques. Special thank to the first for his guidance on my nanodiamond project, and the latter for guiding me through my experimental works in my first year.

I thank Dr Jun and Dr Alun for being good friends in the lab. Thanks also to Dr Katherine and Arnab, who have given me motivation and valuable electrochemical key points. "Thank" to Andy and Kieron for willingly being my instruct-ee-s and sharing the up-and-down of doing projects together! To Wolfgang, Jana, Tak, Rumi and Mike, it has been great fun joining the trips together with you all and I would miss the good moments a lot. Also to Chris, Kim, Chun-Te and Kaori, thanks for your friendships. Thanks also to Leesia, Phung, Kok Sieng, Siew Siew, Belinda for your support back home. All of you have been my good companions throughout my staying in Oxford, making the very precious memory for me. Thanks very much.

I sincerely thank all PTCL and CCL technical staffs, particularly Mervyn, John and Nigel.

Finally, I thank my parents and family for their unconditional love and support. This thesis is for you, pa and ma.

Sincerely,
July, 2002
Chi Hian, Lau

Chemical, Electronic and Electrochemical Properties *of* Diamond Thin Films

Chi Hian, Lau
St. Catherine's College, Oxford

Doctor of Philosophy
July, 2002

Abstract

Diamond is of interest as an advanced functional material, since the extreme physical properties of diamond, suggests it is ideally suited to a range of new demanding applications. In this context, the thesis explores basic surface chemical properties of diamond thin films, along with electrochemical, electronic and electron emission processes involving this material.

New experiments are reported concerning the nature of surface conductivity on diamond. Measurements clearly show that the conductivity only arises if a hydrogenated diamond surface is exposed to water vapour, in the presence of chemical species capable of acting as electron acceptors. The conduction properties of surface conductive diamond in aqueous solution are also studied, and the first detailed electrochemical investigations of this material are described.

Comparative electrochemical studies of nanocrystalline and boron-doped diamond have been performed. Investigations of electrode stability, and the accessible "potential window" are described, as well as the behaviour of a range of 'redox' systems, including transition metal complexes, metal deposition/stripping, and bio-related organic species. Significant differences between the behaviour of nanodiamond and microcrystalline boron-doped material are observed.

A range of surface chemical and threshold photoemission studies of diamond thin films are reported. The results indicate that quantum photoyields (QPYs) are insensitive to the diamond "quality", although the wavelength selectivity is dependent on it. The adsorption of oxygen strongly reduces the QPY, although this only occurs slowly in the presence of O_2 because of a low reactive sticking probability. Much more rapid uptake of oxygen and consequent reduction of photoyield is observed in the presence of atomic O or electronically excited dioxygen O_2*. The presence of alkali metals on the diamond surface increases the QPY, and reduces the sensitivity of the QPY to surface oxygen. Significant differences between the surface chemical properties of Li, and other adsorbed akali metals (K and Cs) are observed.

Content

Chapter 1 Diamond – Introduction 1

1.1 Introduction and History of Diamond 1
1.2 Varieties of Diamond 3
1.3 Physics and Chemistry of Diamond 5
1.4 Properties of Diamond 8
1.5 Application of Diamond 9
1.6 Aims of Project 11
1.7 References for Chapter 1 12-12

Chapter 2 Experimental Theories and Techniques 13

2.1 Surfaces 13
2.2 Adsorption 14
2.3 Ultra High Vacuum 16
2.3.1 Gas Kinetics in UHV 16
2.3.2 UHV Apparatus 18
2.4 Sample Mounting and Preparation 19
2.5 Mass Spectrometry 20
2.5.1 Quadrupole Mass Spectrometer 20
2.5.2 Temperature Programmed Desorption 21
2.6 Microwave Plasma Discharge Beam Source 23
2.7 Electron Affinity 23
2.8 Threshold Photoemission 26
2.8.1 Reflective Emission of Electrons 26
2.8.2 Transmissive Emission of Electrons 30
2.9 X-ray Photoelectron Spectroscopy 32
2.10 Electrochemistry 38
2.10.1 Electrode Dynamics 38
2.10.2 Cyclic Voltammetry 41
2.10.3 Rotating Disc Assisted Electrochemistry 42
2.11 Scanning Electron Microscopy 44
2.12 Atomic Force Microscopy 45

2.13 Raman Spectroscopy 47
2.14 Field Emission 49
2.15 Growth of CVD Diamond by MWPECVD 52
2.15.1 Surface Chemistry of CVD Diamond Growth 52
2.15.2 Growth of CVD Diamond 59
2.15.3 Characterization of CVD Diamond 63
2.15.4 Summary 69
2.16 References for Chapter 2 70-73

Chapter 3 Diamond Surface Conductivity 74

3.1 Introduction 74
3.2 Gaseous Environment Studies 77
3.2.1 Experimental 77
3.2.2 Results 79
3.2.2.1 Gas Adsorbates 79
3.2.2.2 Thermal Stability 85
3.2.3 Discussion 88
3.2.3.1 Surface Adsorbates 88
3.2.3.2 Temperature 94
3.2.4 Conclusion 96
3.3 Solution Phase Effect and Electrochemical Studies 97
3.3.1 Experimental 97
3.3.2 Results 99
3.3.2.1 pH and Temperature 99
3.3.2.2 Electrochemistry 102
3.3.2.3 Metal Deposition and Stripping 103
3.3.2.4 SEM Investigation 109
3.3.2.5 Potential Pretreatment Modification 110
3.3.2.6 Conductance *vs* Metal Deposition 114
3.3.3 Discussion 116
3.3.3.1 Changes of Conductivity 117
3.3.3.2 Electrochemical Properties 120
3.3.4 Conclusion 129
3.4 References for Chapter 3 130-131

Chapter 4 Nanodiamond and Electrochemistry 132

4.1 Introduction 132
4.2 Experimental 136
4.3 Characterization 137
4.4 Results and Discussion 143
4.4.1 Growth 143
4.4.2 Solvent Window and Stability in Aqueous Media 145
4.4.3 Electrochemical Characterization 149
4.4.3.1 The Reduction of $Ru(NH_3)_6^{3+}$ 149
4.4.3.2 The Oxidation of $Fe(CN)_6^{4-}$ 152
4.4.4 The Redox System of Organic Compounds 155
4.4.4.1 Ascorbic Acid 155
4.4.4.2 Hydroquinone 158
4.4.4.3 NADH 162
4.4.4.4 Cytochrome *c* 165
4.4.4.5 Deactivation Test 167
4.4.5 $Ce^{4+/3+}$ Redox System 168
4.4.6 The Deposition and Stripping of Metals 170
4.4.6.1 Gold 170
4.4.6.2 Copper 175
4.4.7 Summary 179
4.4.8 Surface Modification 180
4.4.8.1 Surface Treatments 180
4.4.8.2 Effect of Thermal Annealing 182
4.4.8.3 Abrasive and Adhesiveness Test 184
4.4.8.4 Solvent Test 186
4.5 Conclusion 187
4.6 References for Chapter 4 188-190

Chapter 5 Diamond Adsorption Chemistry 191

5.1 Introduction 191
5.2 Experimental 193
5.3 Oxygen Adsorption Chemistry 195
5.3.1 Previous Work 195
5.3.2 Results 197
5.3.2.1 Effect of pre-Hydrogenation on Oxygen Adsorption 197
5.3.2.2 Effect of Substrate Temperatures on Oxygen Adsorption 205
5.3.2.3 Hydrogen Etching on Oxygenated Surfaces 210
5.3.2.4 Effect of Thermal Annealing on Oxygenated Surfaces 212

5.3.3 Discussion 213
5.3.4 Conclusion 220
5.4 Lithium Adsorption Chemistry 222
5.4.1 Previous Work 222
5.4.2 Results 223
5.4.2.1 Adsorption of Li on Diamond Surface 223
5.4.2.2 Depth Profiling of Li Adsorption 225
5.4.2.3 XPS Investigation 227
5.4.2.4 Lithium and Hydrogen 230
5.4.2.5 Lithium and Oxygen 233
5.4.2.6 Lithium and Ammonia 237
5.4.3 Discussion 241
5.4.4 Conclusion 247
5.5 References for Chapter 5 248-250

Chapter 6 Diamond Photocathode 251

6.1 Introduction 251
6.2 Experimental 254
6.3 Results 257
6.3.1 Growth and Quality Mode of Photoemission 257
6.3.2 Reflective Photoemission Mode 263
6.3.2.1 Photoyield Studies of Gas Hydrogen and Gas Oxygen on Diamond 263
6.3.2.2 Photoyield Study of K on Diamond 268
6.3.2.3 Photoyield Study of Cs on Diamond 273
6.3.2.4 Photoyield Studies on Thermal Stability of Alkali Metals 279
6.3.3 Transmissive Photoemission Mode 280
6.3.3.1 Surface Characterization 280
6.3.3.2 Photoyield Studies 283
6.3.4 Analysis of the Filters 288
6.4 Discussion 291
6.4.1 Growth and Comparison 291
6.4.2 Reflective Mode 296
6.4.2.1 Photoyield Studies 296
6.4.2.2 X-ray Photoemission Studies 301
6.4.3 Transmissive Mode 304
6.5 Conclusion 307
6.6 References for Chapter 6 309-310

Abbreviation

amu	atomic mass unit
ASV	anodic stripping voltammetry
AbSV	abrasive stripping voltammetry
AFM	atomic force microscopy
BDD	boron-doped diamond
BEN	bias enhanced nucleation
CBM	conduction band minimum
CV	cyclic voltammetry
CVD	chemical vapour deposition
DLC	diamond-like carbon
DOS	density of states
E_B	binding energy
E_d	desorption energy
EDX	energy dispersive X-ray spectroscopy
E_F	energy at fermi level
E_k	kinetic energy
Ep	potential *vs* SCE corresponds to peak current
eqn	equation
eV	electron volt
E_V	vacuum level energy
FWHM	full width at half maximum
HPHT	high-pressure high temperature
HFACVD	hot-filament-assisted chemical vapour deposition
IMFP, λ	inelastic mean free path
Ip	peak current
J or j	current density
L	electron diffusion length or Langmuirs
ML	monolayer

MWPECVD	microwave plasma enhanced chemical vapour deposition
NCD	nanodiamond or nanocrystalline diamond
NEA	negative electron affinity
PEA	positive electron affinity
QMS	quadrupole mass spectrometry
QPY	quantum photoyield
$Q_{stripping}$, Q+/Q-	stripping efficiency
r^2, R^2	regression coefficient
r.f., RF	radio frequency
rms	root mean square
rpm	revolutions per minute
RT	room temperature
SC	surface conductivity
SCE	saturated calomel electrode
sccm	standard cubic centimeter per minute, $cm^3\ min^{-1}$
SEM	scanning electron microscopy
SIMS	secondary ion mass spectrometry
SS	surface states
T_d	desorption temperature
TD	thermal desorption
TDS	thermal desorption spectrometry
TPD	thermal programmed desorption
UHV	ultra high vacuum
VB	valence band
χ	electron affinity
XPS	X-ray photoelectron spectroscopy

Chapter 1

Diamond – Introduction

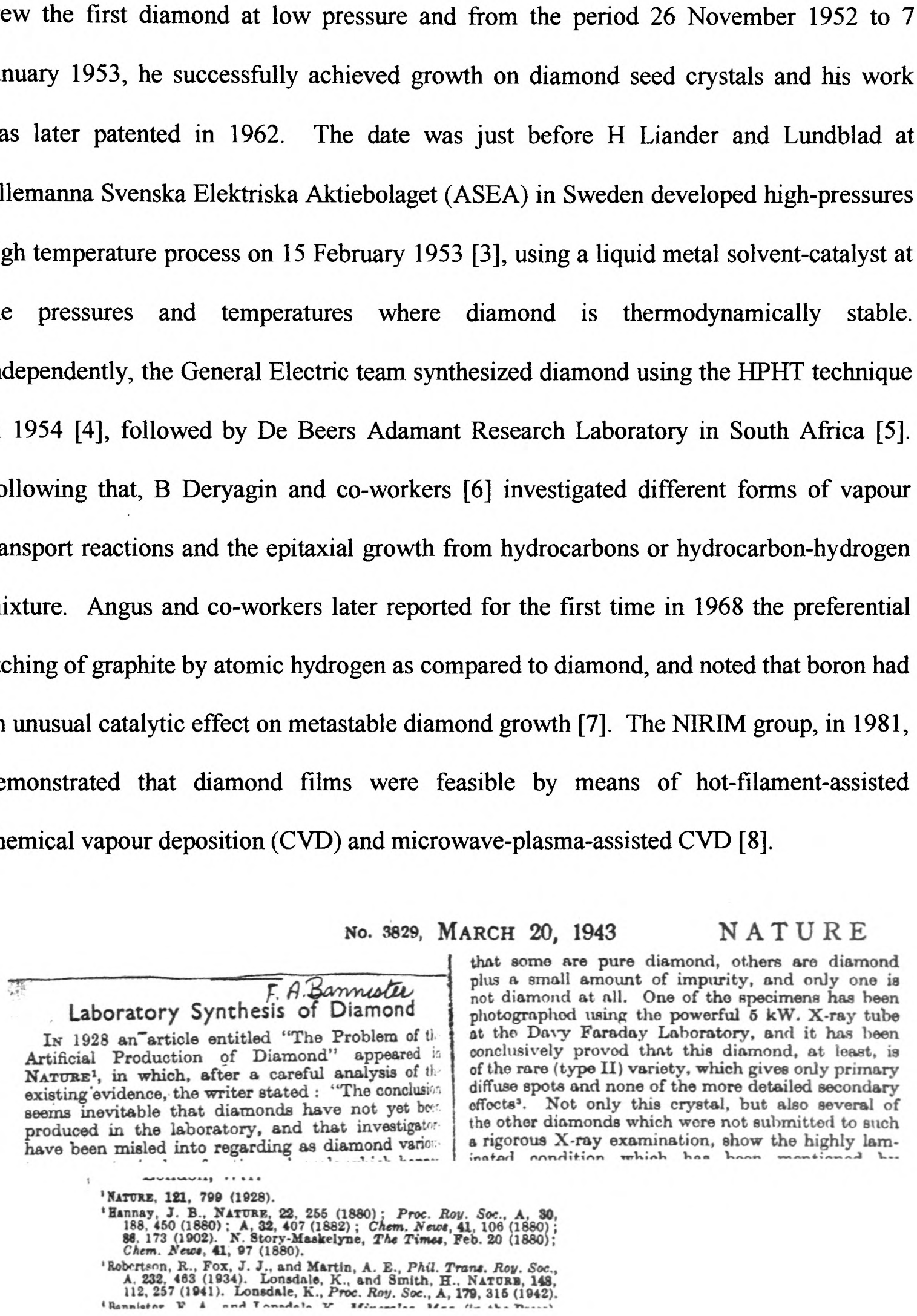
1.1 Introduction and History of Diamond
1.2 Varieties of Diamond
1.3 Physics and Chemistry of Diamond
1.4 Properties of Diamond
1.5 Application of Diamond
1.6 Aims of Project

1.1 Introduction and History of Diamond

Diamond derived from the Greek *adamas*, meaning "unconquerable, invincible" – was traditionally the emblem of fearlessness. Diamond has long held a special place in the hearts and minds both of the scientists and the public. Under the "4 C" characterisation (Clarity, Colour, Cut and Carat), the diamond has been the most glamorous precious gemstone for centuries. As diamond has a crystal structure, it can be cleaved to bring out the brilliance and fire created by its high refractive index and optical transparency. To scientists, diamond could be the most interesting material owing to its extreme properties and potential in the wide range of applications. Many of the new potential opportunities stem not from the bulk properties, but from the surface chemistry and surface properties of diamond.

Whilst Sir Issac Newton was the first to characterize diamond as containing carbon, the French chemist Antoine L Lavoisier was the first to determine that its product of combustion was limited to carbon dioxide [1]. Later, the power of x-rays enabled Sir William Henry Bragg and his son Sir William Lawrence Bragg to determine that the thermodynamically stable carbon allotropes were cubic (diamond), hexagonal (graphite) and amorphous. With this information, early attempts to synthesize diamond began in France in 1832 with C. Cagniard and later in England by J B Hanney and Henry Moisson.

In 1943, an early report on the synthesis of diamond in the laboratory was documented in Nature (see figure 1). In 1949, W G Eversole from the Union Carbide Corporation [2] grew the first diamond at low pressure and from the period 26 November 1952 to 7 January 1953, he successfully achieved growth on diamond seed crystals and his work was later patented in 1962. The date was just before H Liander and Lundblad at Allemanna Svenska Elektriska Aktiebolaget (ASEA) in Sweden developed high-pressures high temperature process on 15 February 1953 [3], using a liquid metal solvent-catalyst at the pressures and temperatures where diamond is thermodynamically stable. Independently, the General Electric team synthesized diamond using the HPHT technique in 1954 [4], followed by De Beers Adamant Research Laboratory in South Africa [5]. Following that, B Deryagin and co-workers [6] investigated different forms of vapour transport reactions and the epitaxial growth from hydrocarbons or hydrocarbon-hydrogen mixture. Angus and co-workers later reported for the first time in 1968 the preferential etching of graphite by atomic hydrogen as compared to diamond, and noted that boron had an unusual catalytic effect on metastable diamond growth [7]. The NIRIM group, in 1981, demonstrated that diamond films were feasible by means of hot-filament-assisted chemical vapour deposition (CVD) and microwave-plasma-assisted CVD [8].



No. 3829, MARCH 20, 1943 NATURE

F. A. Bannister

Laboratory Synthesis of Diamond

IN 1928 an article entitled "The Problem of the Artificial Production of Diamond" appeared in NATURE[1], in which, after a careful analysis of the existing evidence, the writer stated: "The conclusion seems inevitable that diamonds have not yet been produced in the laboratory, and that investigators have been misled into regarding as diamond various

that some are pure diamond, others are diamond plus a small amount of impurity, and only one is not diamond at all. One of the specimens has been photographed using the powerful 5 kW. X-ray tube at the Davy Faraday Laboratory, and it has been conclusively proved that this diamond, at least, is of the rare (type II) variety, which gives only primary diffuse spots and none of the more detailed secondary effects[3]. Not only this crystal, but also several of the other diamonds which were not submitted to such a rigorous X-ray examination, show the highly lam-

[1] NATURE, 121, 799 (1928).

[2] Hannay, J. B., NATURE, 22, 255 (1880); *Proc. Roy. Soc.*, A, 30, 188, 450 (1880); A, 32, 407 (1882); *Chem. News*, 41, 106 (1880); 86, 173 (1902). N. Story-Maskelyne, *The Times*, Feb. 20 (1880); *Chem. News*, 41, 97 (1880).

[3] Robertson, R., Fox, J. J., and Martin, A. E., *Phil. Trans. Roy. Soc.*, A, 232, 463 (1934). Lonsdale, K., and Smith, H., NATURE, 148, 112, 257 (1941). Lonsdale, K., *Proc. Roy. Soc.*, A, 179, 315 (1942).

Figure 1. An early article by F.A. Bannister of Mineral Department in British Museum and K. Lonsdale of Royal Institution reporting the diamond synthesis under laboratory scaled conditions

1.2 Varieties of Diamond

Natural diamond consists of 98.9 % ^{12}C and 1.1 % ^{13}C. Conventional models have diamond growing over geological eons, 200 or more kilometers below the surface of the earth under high temperatures and pressures, and subsequently being transported to the surface by primary volcanic intrusions. Volcanic rock associated with diamonds is called kimberlite in South Africa and lamproite in Australia [9]. Natural diamond is classified into four main types: Ia; Ib; IIa; IIb, accordingly to the presence and form of incorporation of nitrogen and boron as atomic-scale impurities found in diamond. Most natural diamonds are of type Ia, which contains nitrogen as an aggregated impurity in fairly substantial amounts (of the order of 0.3 %) [10], whereas the other three types are very rare in nature. Therefore, natural diamond does not give promise as an advanced material in electronics due to its rarity and the inconsistency of impurities.

Under high-pressure high temperature (HPHT) techniques, **HPHT diamond** can be crystallised from metal solvated carbon at P ~ 5-10 GPa and T ~ 1800-2300 K (refer to catalytic HPHT synthesis in figure 3) [11]. However, the synthetic diamond is always contaminated with metal catalysts trapped in the diamond lattice as it forms, which produce diamond with colours. For example, type Ib yellow diamonds are grown from an iron/cobalt solvent/catalyst (the most produced synthetic diamond in the world) and type IIa diamonds are grown from a cobalt/titanium solvent/catalyst and an iron/aluminium solvent/catalyst (with the varied percentage of aluminium or titanium getter). The metal impurities that create slight imperfections in the crystal lattice would cause too many flaws for electronic circuitry and many other applications.

Growth of **chemical vapour deposition** (CVD) **diamond** is driven by the chemistry and kinetics of gas phase and surface reactions, rather than their thermodynamics. This has to be carried out at high degrees of supersaturation, at which the probability of the formation of a critical diamond seed crystal is comparable to that of

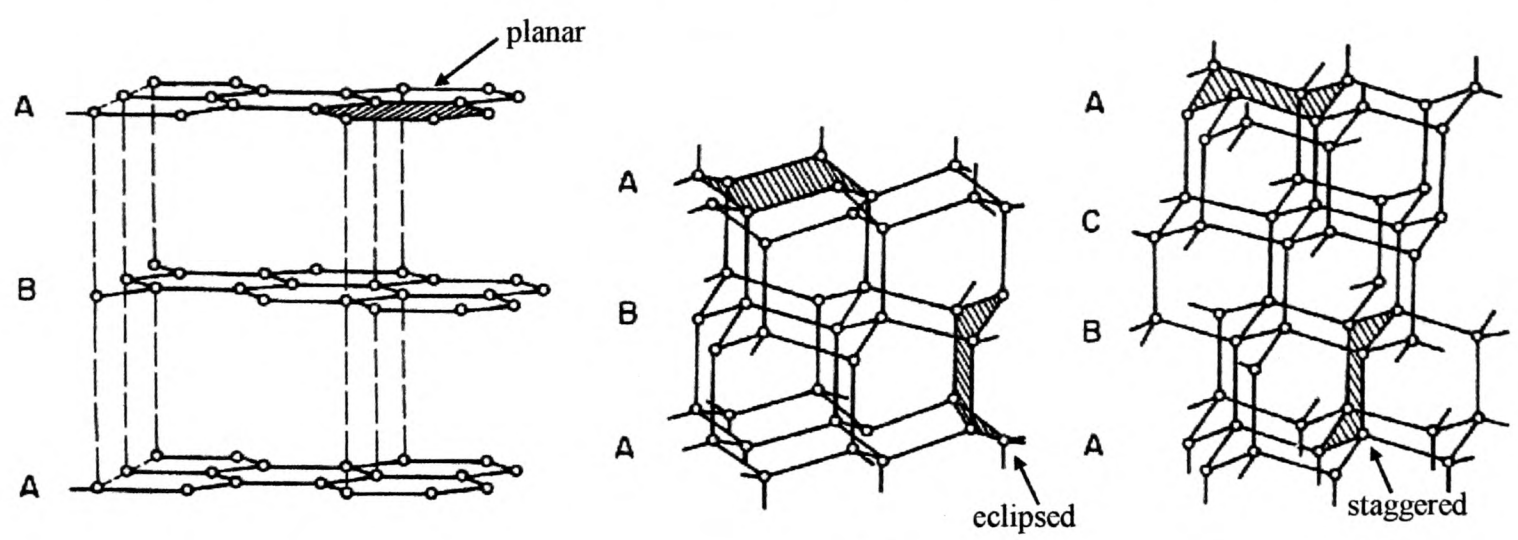
the formation of a critical graphite seed and at a temperature where the transformation of diamond to graphite is inhibited [1]. Non-diamond carbon phases, deposited on the growing diamond are removed through gasification of graphite by atomic hydrogen, or oxygen species and by ion impact. CVD diamond possesses the advantageous properties over the weaknesses of the synthetic and natural diamonds. Diamond can be grown easily as coatings over different substrates, provided that the substrates have higher melting point than the working temperature window for diamond growth 1000 – 1400 K. With its excellent hardness, diamond can be fabricated for multiple cutting edges on a single tool, and thus the need for polishing diamond edges could be eliminated. Since doping is possible within the controllable growth system, research or technological application demands can be met. With the comparative lower costs of gases and facilities, the production of CVD diamond could be one of the most economical alternatives.

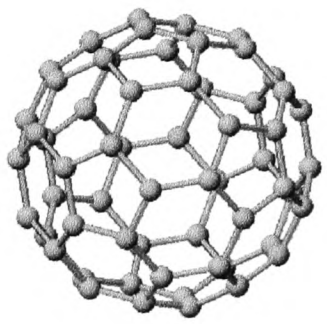
Nanocrystalline diamond is a new diamond type that can be grown by a relatively unexplored mechanism involving the C_2 molecule as the primary growth species. It consists of nanometer-sized crystals of phase-pure diamond with sp^2-bonded grain boundary carbon atoms. They are smooth (20 to 50 nm rms surface roughness), electrically conductive and highly reflective [12].

Diamond-like carbon (DLC) is a metastable amorphous material, containing a mixture of sp^3, sp^2, and sp^1 hybridized carbon, along with hydrogen [1]. Although DLC films may crystallize under high-energy ions bombardment at substrate temperatures below 325 °C and with some degree of crystallinity at high substrate temperature, DLC films are essentially amorphous materials without any long-range order, but with short- or medium-range order. While diamond is a well-defined material with fixed properties, the properties of DLC cover a wide range of values between those of diamond, graphite, and hydrocarbon polymers.

1.3 Physics and Chemistry of Diamond

Diamond belongs to the space group $O_h^{\ 7}$ with eight atoms per primitive (Bravais) cell. Each carbon atom has a tetrahedral configuration consisting of sp^3 hybrid atomic orbitals. The lattice constant is 3.56 Å and the bond length is 1.54 Å. The atomic density of diamond is the highest of any terrestrial material, and this is coupled with its strong, directional covalent bonding. The diamond-cubic lattice consists of two interpenetrating face-centered cubic lattices, displaced by one quarter of the cube diagonal [13,14,15].





(iv)

Figure 2. Schematic illustrations of the atomic arrangements in (i) hexagonal graphite, (ii) hexagonal lonsdaleite (iii) cubic diamond and (iv) fullerene C60. The letters depict the stacking sequence of carbon layers: planar layers for graphite, puckered for lonsdaleite and diamond

Carbon has three more isomers; lonsdaleite (found in meteorites), graphite and fullerene. The graphitic sp^2 bonding creates strongly bonded two-dimensional planes, but weak bonding between the planes. The four equivalent tetrahedral sp^3 bonds in lonsdaleite and diamond form strong, uniform three-dimensional framework structures, but differ in the stacking sequence. In diamond, the C_3C-CC_3 connected to the C-C bonded carbons are staggered, while in lonsdaleite they are eclipsed. All of the puckered hexagonal rings in diamond (see figure 2) exhibit the "chair" form whereas the hexagonal rings of lonsdaleite are in a "boat" configuration. Fullerene is a family of molecular, geodesic

structures in the form of cage-like spheroids, consisting of a network of five-membered rings (pentagons) and six-membered rings (hexagons) and involves the hybridisation of sp^3 and sp^2 bonding with no unpaired electron [16].

Table 1. Comparison of physical properties of diamond, lonsdaleite and graphite [10]

Property Field	Cubic diamond	Hexagonal lonsdaleite	Planar graphite
Point group of atoms	T_d	T_d	-
Space group	O_h^7; Fd3 m	D_{6h}^4; P63/ mmc	D_{6h}^4; P63/ mmc
Unit cell constants/ nm	a = 0.357	a = 0.252; c = 0.412	a = 0.246; c = 0.671
C-C nearest neighbour distance/ nm	0.154	0.152	0.142
Bonding	sp^3	sp^3	sp^2
Atoms located at	(000)(½½0) (0½½)(½0½) (¼¼¼)(¾¾¼) (¼¾¾)(¾¼¾)	(000)(00$^3/_8$) ($^1/_3$$^2/_3$½)($^1/_3$$^2/_3$$^7/_8$)	($^1/_3$$^2/_3$0)($^2/_3$$^1/_3$0) ($^1/_3$$^2/_3$$^1/_3$)(00½)
General crystal	Zinc blend type	2H-wutztite	-
Density/ kg m^{-3}	3.52 x 10^3	3.52 x 10^3	2.3 x 10^3
Refractive index	2.417	2.41-2.42; birefringent	-

According to equilibrium thermodynamics, graphite has an even more favourable free energy of formation than diamond under normal ambient pressures and temperatures. The Gibbs free energy of formation at room temperature and pressure is 2.9 kJ/mol more negative for graphite than for diamond. However, graphite can be transformed into diamond upon the application of pressure P (in atm) and temperature T (K) particularly in the high-pressure high temperature system (HPHT), by which this relationship is expressed by equation 1 [17] (see figure 3).

$$P_{\text{equilibrium}}\,(\text{atm}) = 7000 + 27\ \text{T (K)}\ (\text{for T} > 1200\ \text{K}) \qquad \text{(eqn 1)}$$

At higher temperatures the pressure stability region of graphite expands even further, and thus even higher pressures are required to favour the growth of diamond. Equation 1 was determined from extensive thermodynamic data (listed in Table 2), which includes the

heat of formation of graphite-diamond, the heat capacity of graphite as a function of temperature, and the atomic volume and coefficient of thermal expansion of diamond. Under the low pressure of the CVD process, diamond is a metastable phase of carbon while graphite is a stable phase. Therefore, a real diamond CVD process would have taken place under highly non-equilibrium conditions and should be treated by non-equilibrium thermodynamics [18]. High concentrations of hydrogen atoms and other activated particles provide the driving force for diamond synthesis from the gas phase or even from graphite *via* gaseous intermediates through a set of coupled reactions [19].

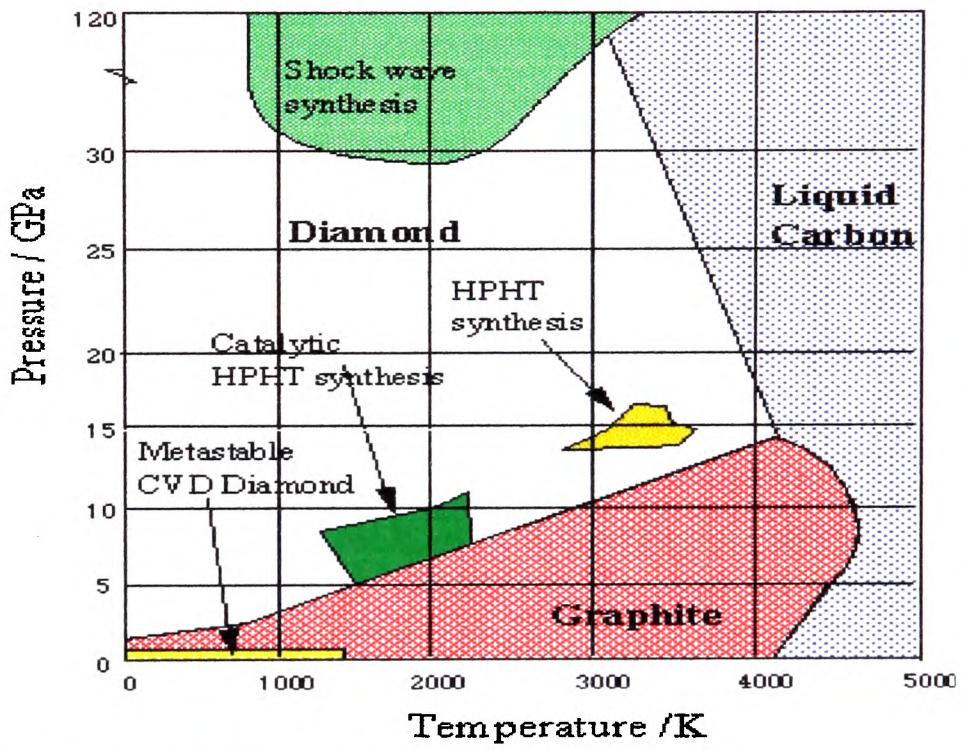


Figure 3. Schematic illustration of the carbon phase diagram [20]

Table 2. Characteristics of the transition reaction of graphite-diamond [21]

$\Delta H°_{298\ K}$, J/mol	1872 ± 75
$\Delta S°_{298\ K}$, J/mol.K	-3.22
ΔC_p above 1100 K, J/mol.K	0
Equilibrium pressure at 2000 K, Pa	64×10^8
Volume change at 2000 K transition, cm^3/mol	1.4
Atomic volume, cm^3/mol	
V graphite	5.34
V diamond	3.41
ΔV	-1.93

Although diamonds convert to graphite exothermically, the reaction is slow due to the high activation energy, which explains why diamonds stored at ambient temperatures do not crumble into black graphite.

1.4 Properties of Diamond

The compact structure and surface chemical composition of diamond are important in determining a uniquely wide range of physical and chemical properties. Even though diamond is obtained as a polycrystalline material by CVD, its properties are similar to those of natural diamond [22]. The properties of CVD diamond are listed in the table 3.

Table 3. The properties of CVD diamond [10, 23]

Properties	Value
General	The highest molar density (0.293 g atom cm^{-3}), high specific mass density (3.52 g cm^{-3}), highest sound propagation velocity (18.2 km s^{-1})
Mechanical	The lowest compressibility (8.3 x 10^{-13} m^2/N), the largest Young modulus (1.2 x 10^{12} N/m^2) with large elastic constant, 107.6 x 10^{11} dyn/cm^2, the highest mechanical hardness (~ 90 GPa and scaled 10 °Mohs) with low coefficient of friction, the lowest loss tangent (applications in microwave and millimeter wave), low Poisson's ratio (0.10 – 0.16), low coefficient of friction (0.05 – 0.1 in air; near 1 in vacuum)
Optical	Appropriate refraction index (2.417 at 589.29 nm - D line) and broad optical transparency (0.22 – 2.5 & > 0.6 μm) from the deep *uv* to the far IR region (6 - 13 μm) of the electromagnetic spectrum (small absorption coefficient); potential for both passive and active optical application; negative electron affinity
Chemical & Biological	Inert to common acids, corrosive with molten hydroxides, the salts of oxy-acids, and some metals; can oxidize (graphitize) readily at high temperatures in an oxygen atmosphere, air, water vapor and CO_2; resistant to X-ray-radiation, γ-radiation, ultraviolet light, and nuclear particles. Biologically compatible
Electrochemical	Large potential window for water stability (-1.25 V to +2.30 V), low background current densities (~ 1 $\mu A/cm^{-2}$), good response to redox system
Electrical	Low dielectric constant (n = 5.58); high breakdown voltage (10^7 V cm^{-1}); high carrier mobility (high electron/hole mobility with 1900/1600 $cm^2V^{-1}s^{-1}$); high saturation electron velocity (250 μm/ns); good electrical insulator (room temperature resistivity is ~ 10^{16} Ωcm); can also be doped to change its resistivity over the range 10-10^6 Ωcm, so becoming a semiconductor with a wide band gap of 5.4 eV
Thermal	Excellent conductors of heat with thermal conductivity (2 x 10^3 W/m/K), small thermal expansion coefficient (4.50 x 10^{-6} K^{-1} at 750 °C), effective Debye temperature (1860 K at 273-1100 K)

1.5 Application of Diamond

With such extensive and excellent natural properties, there are some emerging commercial potential applications of CVD diamond. The application of diamond in electronics is one of the promising aspects, as diamond possesses a unique combination of desirable properties. Two recognised figures of merit exist for evaluating the relative usefulness of semiconductor materials [24] (see equation 2 and 3), and from these diamond has rated highest according to both Johnson's figure of merit (JFM) and Keyes' figure of merit (KFM), with respect to other semiconductors, such as Si, GaAs, InP, GaN and β-SiC (see table 3).

$$JFM = \left(\frac{E_B \upsilon_S}{\pi} \right)^2 \qquad \text{(eqn 2)}$$

$$KFM = \sigma_T \sqrt{\frac{c\upsilon_S}{4\pi\varepsilon_r}} \qquad \text{(eqn 3)}$$

where E_B = electrical breakdown strength, υ_S = saturation carrier velocity, σ_T = thermal conductivity, c = velocity of light (in vacuum), ε_r = dielectric constant.

JFM is usually invoked to evaluate materials for high-frequency, high-power applications such as microwave and millimetre wave amplifiers. Thus, a high JFM comes from high dielectric breakdown strength and a high value for the saturated carrier velocity. The KFM aims to reflect the suitability of a material for use in very densely packed integrated circuit application. With high KFM, more heat can be dissipated from the device per unit area, and a low dielectric constant is valued as this could minimise device's impedance.

Table 4. Relative figures of merit for electronic device materials

Material	E_B (V cm^{-1})	υ_S (cm s^{-1})	σ_T (W cm^{-1})	ε_r	Ratio to Silicon	
					Johnson	Keyes
Si	3×10^5	1.0×10^7	1.5	11.8	1.0	1.0
GaAs	4×10^5	2.0×10^7	0.5	12.5	6.9	0.5
InP	6×10^5	2.0×10^7	0.7	14.0	16.0	0.6
GaN	20×10^5	2.5×10^7	1.5	9.5	281.6	1.8
β-SiC	40×10^5	2.5×10^7	5.0	9.7	1137.8	5.8
Diamond	100×10^5	2.7×10^7	20.0	5.5	8206.0	32.2

Table 5 shows that each of the potential application requires the properties of diamond to be optimized to fulfill a different function.

Table 5. The potential application of CVD diamond [10, 23]

Properties	Applications
General	Excimer laser patterning, millimeter-wave traveling wave amplifiers, backward wave oscillators, speaker diaphragms
Mechanical	Tribological and wear resistant coating for cutting tool inserts, conformal coatings for microelectromechanical system *e.g.* CVD diamond-coated drill bits, reamers, countersinks, gearboxes, engines for machining non-ferrous metals and composite materials, with reduced lubrication and longer lifetimes, medical implants, circuit-board drills, abrasive pump seals, extrusion dies, jet-nozzle coating
Optical	*uv* detectors for solar physics missions, infrared optics and emission sensor in harsh environments, laser protection, X-ray window, cold-cathode emitters, antireflection and bearing surfaces, picosecond high-voltage electro-optic switches, fiber optics, radomes, laser and x-ray windows
Chemical & Biological	Electrode for electrochemical waste treatment; corrosion and erosion resistant coatings; hazardous bio-agents and gases sensors, reaction vessels, ion barriers, crucibles, fiber coatings
Electrochemical	Electrosynthesis; electrocatalysis; electroanalysis; electrochemical detector for flow injection analysis, liquid chromatography, electrodestructive application for waste water treatment and pollution control
Electrical	Flat panel display, field effect transistor, thermistors, varistors and negative resistance devices; charged particles detectors, high-power transistors, high-power microwave, photovoltaic elements
Thermal	Electrically insulating thermal conductor and heat sinks for various electronics applications, e.g. laser diodes, small microwave integrated circuits, multi-chip modules, surface acoustic wave devices, and high power GaAs-based circuits

1.6 Aims of the Project

The aim of this project is to gain clear insight into the manipulation of surface electronic states of diamond by controlling the surface adsorbate termination and by changing the environment chemically or physically.

- To grow diamond in the scale of microscopic and nanoscopic size, perform extensive surface characterization and maximize the quality of the grown diamond (Chapter 2, 4 and 6)
- To monitor and analyse the surface conductive layer for undoped diamond in *vacuo* and solution. Various gases, solution pH and temperature were amongst the parameters of investigation. Electrochemical response was also made possible for analysis (Chapter 3)
- To investigate the electrochemical properties of nanodiamond as compared to microscopic boron-doped diamond, in response to standard buffer solutions, organic compounds and metal deposition. Various surface manipulations were also carried out (Chapter 4)
- To investigate the oxygen adsorption chemistry on diamond with regard to differing oxygen dosage methods, such as molecular, excited and atomic oxygen. The effect of hydrogen pre-adsorption and substrate temperature platen are also examined on oxygen adsorbability. And the manipulation of the gaseous adsorption-and-desorption by using Li was also studied (Chapter 5)
- To study the photoemission property of diamond for a possible cold photocathode application in correlation to photoyield *vs* adsorption of gases and deposition of alkali metals. The dependence of photoyield on growth, quality, reflective and transmissive modes were investigated (Chapter 6)

1.7 References for Chapter 1

[1] H.E. Spear and J.P. Dismukes (*eds.*), Synthetic Diamond – Emerging CVD Science and Technology, John Wiley & Sons, Inc., New York, 1988

[2] W.G. Eversole, Synthesis of diamond (1962) US Patents 3,030,187 and 3,003,188

[3] H. Liander, *ASEA JI* **28** (1955) 97

[4] F.P. Bundy, H.T. Hall, H.M Strong and R.H. Wentorf, *Nature* **176** (1955) 51

[5] H.B. Dyer, F.A. Raal, L. du Preez and J.H.N. Loubser, *Phil. Mag.* **11** (1965) 763

[6] B.V. Deryagin, D.V. Fedoseev, V.M. Lukyanovich, B.V. Spitsyn, A.V. Ryanov and A.V. Lavrentyev, *J. Crystal Growth* **2** (1968) 380

[7] J.C. Angus, H.A. Will and W.S. Stanko, *J. Appl. Phys.* **39** (1968) 2915; D.J. Poferl, N.C. Gardner and J. C. Angus, *ibid.* **44** (1973) 1418

[8] S. Matsumoto and N. Setaka, 8th Japan Carbon Soc. Fall Meeting (1981)

[9] H.O.A. Meyer, M. Seal, Natural diamond, in: M.A. Prelas, G. Popoovici and L.K. Bigelow (*eds.*), Handbook of Industrial Diamonds and Diamond Films, Marcel Dekker, New York, 1998

[10] J.E. Field, The properties of natural and synthetic diamond, Academic Press Limited, London, 1992

[11] P.W. May, *Endeavour Magazine* **19**(3) (1995) 101

[12] Q.Y. Chen, D.M. Gruen, A.R. Krauss, T.D. Corrigan, M. Witek and G.M. Swain, *J. Electrochem. Soc.* **148**(1) (2001) E44

[13] S.T. Lee, Z.D. Lin and X. Jiang, *Mater. Sci. Eng. Reports* **25** (1999) 123

[14] J.C. Angus and C.C. Hayman, *Science* **241** (1988) 913

[15] J.C. Angus and Alan T. Collins, *Nature* **370** (1994) 601

[16] H.W. Kroto, J.R Heath, O.B. SC., R.F. Curl and R.E. Smalley, *Nature* **318** (1985) 162

[17] F.P. Bunday, H.M. Strong and R.H. Wentorf, Chemistry and Physics of Carbon, Vol. 10 (P.L. Walker, *Jr.* and P.A. Thrower, *eds.*), Marcel Dekker Inc, London, 1973

[18] J.T. Wang, Y.Z. Wan, Z.J. Liu, H. Wang, D.W. Zhang and Z.Q. Huang, *Mater. Lett.* **33** (1998) 311

[19] Z.J. Liu, W. Zhang, P.F. Wang, S.J. Ding, J.Y. Zhang, J.T. Wang and K. Kohse-Hoinghaus, *Thin Solid Films* **368** (2000) 253

[20] P.K. Bachmann and R. Messier, *Chem. Eng. News* **15** (1989) 24

[21] L. Peterman, Proc. SPI/RP-Ci, 41st. Annual Conf., Jan 1986

[22] H.O. Pierson, Handbook of Carbon, Graphite, Diamond and Fullerences, Noyes Publications, Park Ridge, New Jersey, 1993

[23] K. Kobashi, K. Nishimura, Y. Kawate and T. Horiuchi, *Phys. Rev. B* **38**(6) (1988) 4067

[24] G. Sh. Gildenbalt, S.A. Grot and A. Badzian, *Proc. IEEE* **79** (1991) 647

Chapter 2

Experimental Theories and Techniques

2.1 Surfaces
2.2 Adsorption
2.3 Ultra High Vacuum
  2.3.1 Gas Kinetics in UHV
  2.3.2 UHV Apparatus
2.4 Sample Mounting and Preparation
2.5 Mass Spectrometry
  2.5.1 Quadrupole Mass Spectrometer
  2.5.2 Temperature Programmed Desorption
2.6 Microwave Plasma Discharge Beam Source
2.7 Electron Affinity
2.8 Threshold Photoemission
  2.8.1 Reflective Emission of Electrons
  2.8.2 Transmissive Emission of Electrons
2.9 X-ray Photoelectron Spectroscopy
2.10 Electrochemistry
  2.10.1 Electrode Dynamics
  2.10.2 Cyclic Voltammetry
  2.10.3 Rotating Disc Assisted Electrochemistry
2.11 Scanning Electron Microscopy
2.12 Atomic Force Microscopy
2.13 Raman Spectroscopy
2.14 Field Emission
2.15 Growth of CVD Diamond by MWPECVD
  2.15.1 Surface Chemistry of CVD Diamond Growth
  2.15.2 Growth of CVD Diamond
  2.15.3 Characterization of CVD Diamond
  2.15.4 Summary

2.1 Surfaces

The importance of the surface composition and properties of solid materials has gained recognition and attention for a long time ago. The earliest documented references written in 1250 AD from the manuscript of *De Proprietatibus Rerum* (The properties of things) [1], stating the importance and problems faced in bondability:

When a plate of gold shall be bonded with a plate of silver or joined thereto, it is necessary to beware of three things, of dust, of wind and of moisture: for if any come between the gold and silver they may not be joined together ...

Compared to the bulk composition, the topmost atomic layers of materials are always more difficult to be controlled as the nature of the surface is influenced more by its environmental parameters. Interfaces and thin films display a myriad of fascinating fundamental structural, electronic and chemical properties. These lie at the heart of a diverse range of modern technologies encompassing such areas as colloids, detergents, biological systems, electrochemistry, catalysis, nanotechnology, chemical sensors, organic electronics and most other modern semiconductor devices.

What is the microscopic structure of the interface or thin film, and how is this related to the molecular forces involved? How can the macroscopic properties and function of the system be controlled by the nature of the atomic and molecular constituents at the interface? These are unifying questions, which run across a very significant range of research activities, concerned with interfaces and thin films. Answers to the basic questions noted above, which are the focus of academic study today, should underpin new industries and technologies in the future, since it is increasingly the trend that the successful applications of new materials rest critically on the molecular control of surface properties.

2.2 Adsorption

Langmuir first developed a simple theory of surface adsorption, which assumes that there are a specific and fixed number of adsorption sites per unit area available on a surface [2]. The probability that an incident particle will adsorb is known as the sticking probability, S_θ, which is dependent upon the fractional surface coverage, θ, given as

$$S_\theta = S_0 (1 - \theta) \qquad \text{(eqn 1)}$$

where S_0 is the initial sticking probability on a clean surface. However, some doubtful assumptions of this model were made, including the presence of one adsorption monolayer, negligence for the lateral interactions between adsorbate species and also the omission of the consideration for precursor states.

Lennard-Jones model [3] was later proposed (illustrated in figure 1), considering the roles of precursor states, and conceptualising the binding of an adsorbate in a 1 D potential *via* four main channels (hypothetical trajectories). The channels are elastic scattering (no energy is exchanged), direct inelastic scattering (energy exchanges and the molecule is reflected from the repulsive wall with more kinetic energy at a broader angular distribution) and sticking either due to chemisorption or physisorption. Chemisorption involves a total energy drops below the zero potential energy curve after a sufficient energy loss on the first encounter with the repulsive wall. The molecule will lose further energy and drops to the bottom of the chemisorption well. Molecule involving physisorption, however will fall into the physisorption well, and is required to overcome a barrier in order to enter the chemisorbed state.

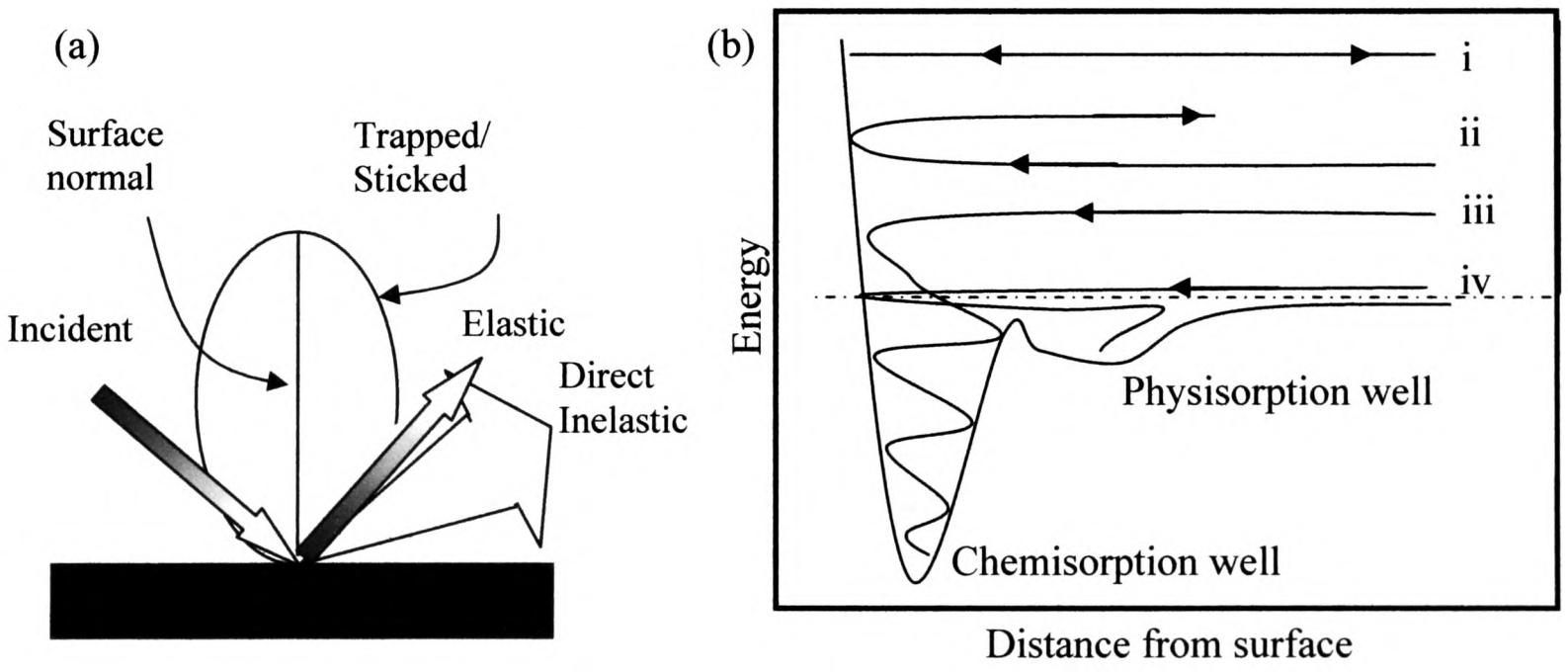


Figure 1. (a) Schematic diagram of scattering channels for a molecule incident on a surface; and (b) an one-dimensional representation of non-activated adsorption (i = elastic scattering trajectory, ii = direct inelastic scattering trajectory, iii = sticking event of chemisorption, iv = sticking event of physisorption)

Therefore, the initial sticking probability according to this model is

$$S_0 = \lim_{\theta \to 0} \frac{Nstick}{Ninc} = \lim_{\theta \to 0} \frac{Nstick}{Nel + Nin + Nstick} \qquad \text{(eqn 2)}$$

where *Nstick* is the number of particles that stick to the surface, *Ninc* is the total number incident on the surface, *Nel* is the number scattered elastically and *Nin* is the number scattered inelastically.

And the modified sticking probability for equation 1 will then become

$$S_\Theta = \frac{S_0 (1 + K\Theta)}{(1 - \Theta)} \qquad \text{(eqn 3)}$$

where K is a system constant, dependent upon the statistical probabilities of each possible post-precursor states.

A chemisorption is *non-activated* (as shown in figure 1b) if the chemisorption energy is equal to the desorption energy and the sticking probability will often decrease with the increasing of temperature. Whereas, for *activated* chemisorption, by which the chemisorption energy is less than the desorption energy, the sticking probability will increase with the increasing of temperature. A barrier separating the chemisorption well from the gas phase will distinguish activated adsorption from non-activated adsorption.

2.3 Ultra High Vacuum

2.3.1 Gas Kinetics in UHV

Ultra high vacuum (UHV) was born in 1950 with the invention of the Bayard-Alpert gauge [4], which made possible for the first time measurement of pressure below 10^{-8} Torr. Such ultra low pressure is essential as the fundamental environment for surface analysis studies in order to minimise the collision frequencies of unwanted gas particles from bombarding (contaminating) the surface of interest. The particles under UHV can move freely without any mutual hindrance and is the type of molecular flow, by which its

mean free path is greater than the diameter of the conducting tube, *i.e.* $\lambda > d$ [5]. The rate of flow is therefore determined by the collisions of molecules with the tube walls rather than molecule-molecule collisions.

From the kinetic theory of gases, the arrival rate of Z molecules $cm^{-2}s^{-1}$ of molecular weight M g $mole^{-1}$ at a temperature T K and at a pressure of P Torr (1 Torr = 1.33×10^{-2} Ncm^{-2}) is given by the Hertz-Knudsen equation (equation 4) [6]

$$Z = P/(2\pi MkT)^{1/2} \text{ molecules } cm^{-2}s^{-1} \qquad \text{(eqn 4)}$$

with k = Boltzmann constant of 1.38066×10^{-23} JK^{-1}, and can later be simplified as

$$Z = 3.51 \times 10^{22} P/(MT)^{1/2} \text{ molecules } cm^{-2}s^{-1} \qquad \text{(eqn 5)}$$

Hence at pressures below 10^{-9} Torr at room temperature, the arrival rate of molecules would take up several hours to form a monolayer compared to several seconds at a pressure of 10^{-6} Torr.

To obtain the equilibrium pressure, p_u (see equation 6) set under UHV, the consideration of many factors as follows would be crucial;

$$p_u = \frac{Q_B + Q_L + Q_W}{S'_p} \qquad \text{(eqn 6)}$$

The parameters involved are the gas that backstreams from the pump (Q_B), the gas that permeates or 'real leaks' through the fabric of the vacuum chamber (Q_L) and the gas desorbs from the walls and materials of the vacuum chamber (Q_W). From the equation 6, P_u can be minimized by simply decreasing the gas influx (Q_B, Q_L and Q_W) or by increasing pumping speed (S_p). For efficient pumps and leak tight apparatus, Q_W represents the most important barrier to the attainment of UHV as the gases tend to chemisorb on the metal components of the vacuum chamber or glass surfaces of viewing ports, which would not be obtained without proper bake-out [7].

2.3.2 UHV Apparatus

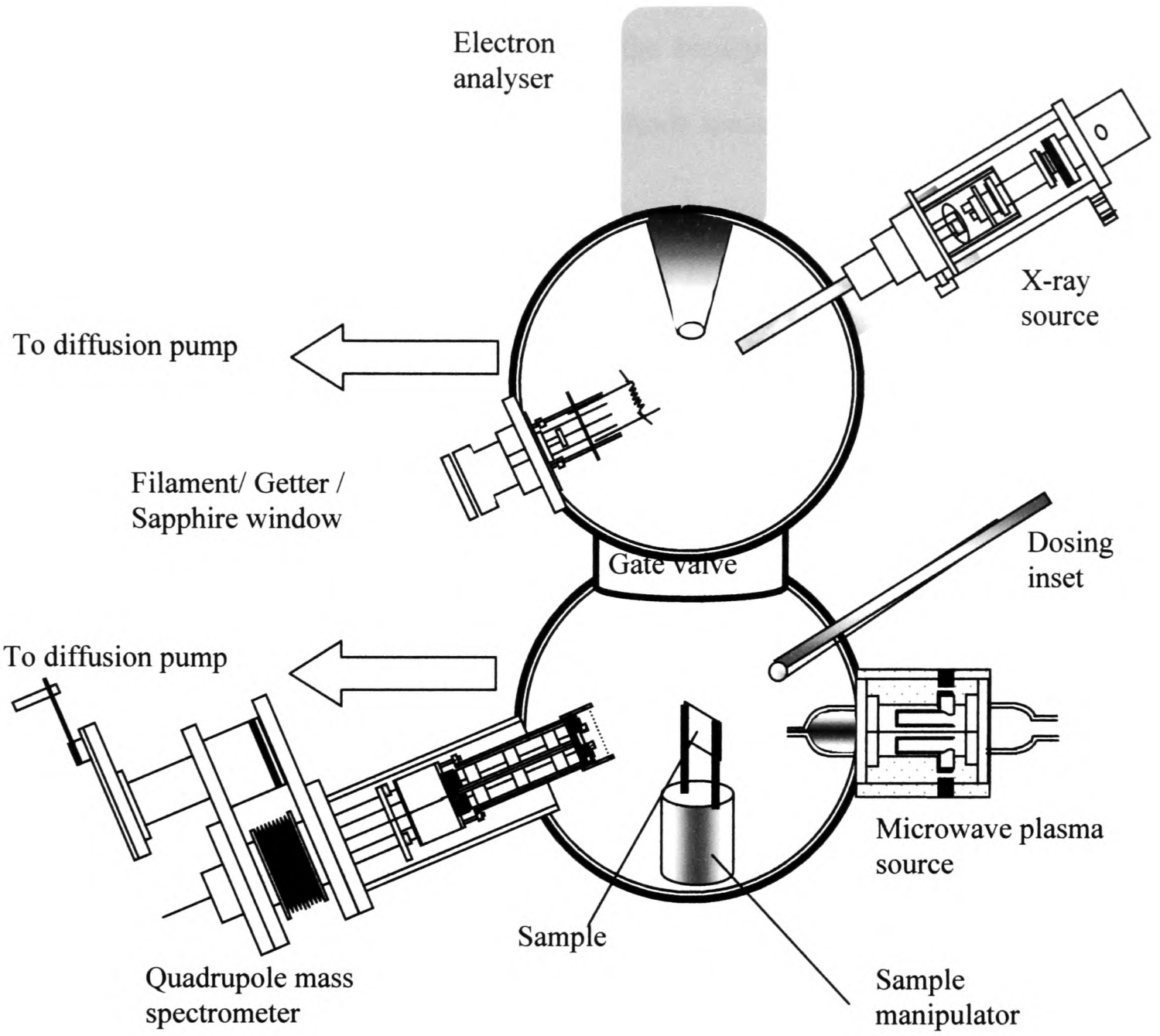


Figure 2. Pictorial diagram of UHV chamber for surface science studies

The UHV system illustrated in figure 2 employing suitable experimental procedures will give the base pressure of 2 x 10^{-10} mbar after bake-out. The system is divided into two separate chambers by a gate valve. The upper chamber was pumped by a 150 l s^{-1} oil vapour diffusion pump and equipped with a 100 mm VG Microtech CLAM 2 hemispherical sector analyser and a PSP dual Mg-Al anoded X-ray source for XPS studies. The lower chamber was pumped by a 1350 l s^{-1} oil vapour diffusion pump and equipped with a Hiden Analytical HAL EPIC 1-300 *amu* quadrupole mass spectrometer for temperature programmed desorption (TPD) and residual gas analysis. The lower

chamber was also equipped with an *in*-house built microwave discharge source (without magnetic field) for generating atomised gas beams. The diffusion pumps were backed by a two-stage high vacuum rotary pump, and the background pressure of both chambers were monitored by two Bayard-Alpert hot cathode ionisation gauges to allow the system pressure to be constantly monitored.

Ir-filaments were fitted at upper chamber to activate or dissociate gases, as used for the experiment set up in Chapter 5. A sapphire window was housed at the same port for *uv* excitation for the photoemission project as stated in Chapter 6. Other dosing gases were introduced into the chamber by *ex-situ* stainless steel gas lines fitted with precise leak valves.

2.4 Sample Mounting and Preparation

Diamond samples were cleaned in acetone by 15 min sonication in an ultrasonic bath, followed by 10 min in ethanol and was later dried. The sample was mounted on two tantalum (Ta) foil support clips (shown in figure 3), which were previously spot-welded to stainless steel holders on top of the sample manipulator. Good mounting of sample on the clips is crucial to allow adequate provision for 3 dimensional movements in order to enable its access to all experimental probes and gas sources within the chamber. Apart from that, this could also enable good thermal contact, which is essential to achieve uniform heating across the sample. Tantalum was chosen as it has a very high melting point (3269 K) and retains much of its Young's Modulus at high temperatures. The sample temperature was monitored by using a chromel-alumel thermocouple spot-welded to another tantalum foil clip, in full contact with the back of the sample. The heating of samples was controlled by computer with Labtech Notebook software for the purposes of constant, manual and linear-ramped heating. The sample was annealed gradually to 1000 °C after proper system bake-out to remove residual carbon, hydrogen and oxygen species

from the sample. This step was followed by more repeated cycles of flashing to high temperatures and cooling to room temperature until a clean surface was obtained under the examination of XPS.

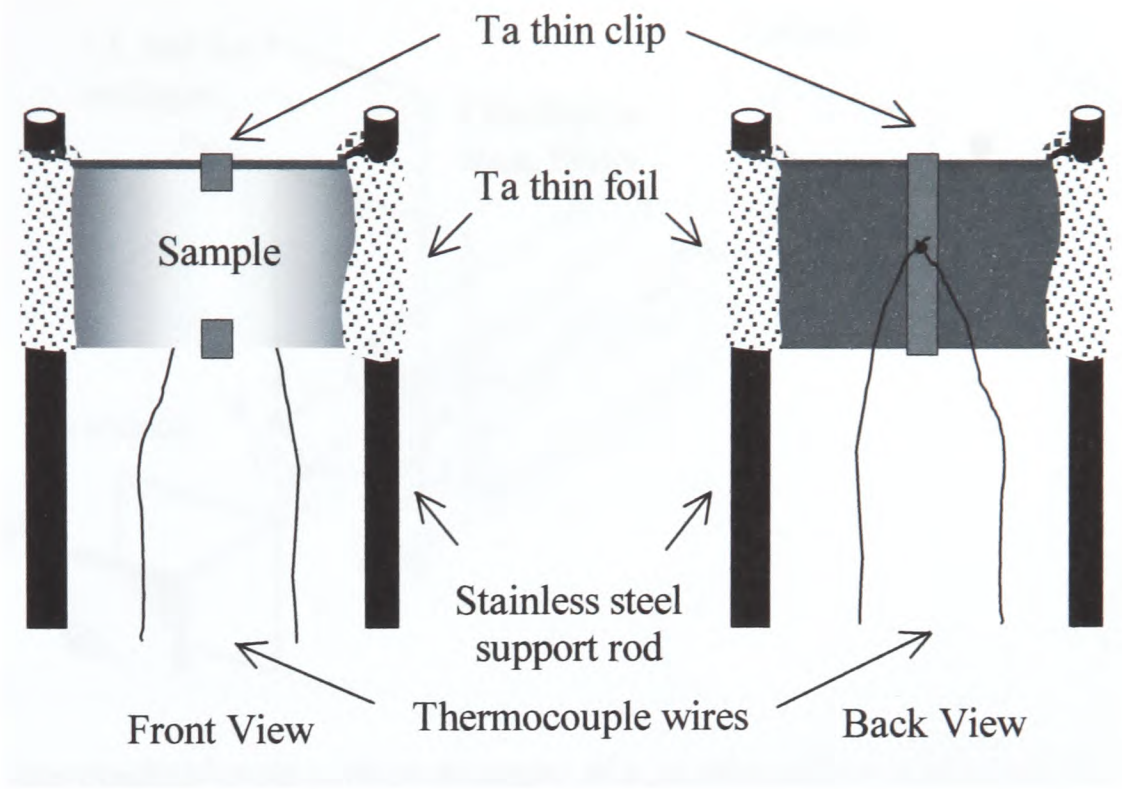


Figure 3. The schematic picture of sample mounting

2.5 Mass Spectrometry

2.5.1 Quadrupole Mass Spectrometer

The quadrupole mass filter was first proposed by Paul in 1953 [8], and figure 4 shows the instrument schematically. A quadrupole mass spectrometer is a mass analyser with a combination of a d.c. and a radio frequency (r.f.) electric field applied to four parallel rods, in order to separate ions according to their mass-to-charge ratio [5,7]. A potential consisting of a constant d.c. (U) component plus an oscillating r.f. component (V cos ωt) is applied to one pair of rods whilst an equal but opposite voltage is applied to the other pair. At a given set of voltage conditions, only ions with a certain mass to charge ratio (m/z) could manage to follow a stable periodic trajectory of limited amplitude and are transmitted to the detector or an electron multiplier. A simple pulse height reading circuit is used to convert the periodic pulses from the electron multiplier to a d.c. signal suitable for driving an X-Y recorder. By increasing the d.c. and a.c. fields whilst keeping a

constant ratio between them, this resonant condition is satisfied for ions of each ascending m/z ration in turn.

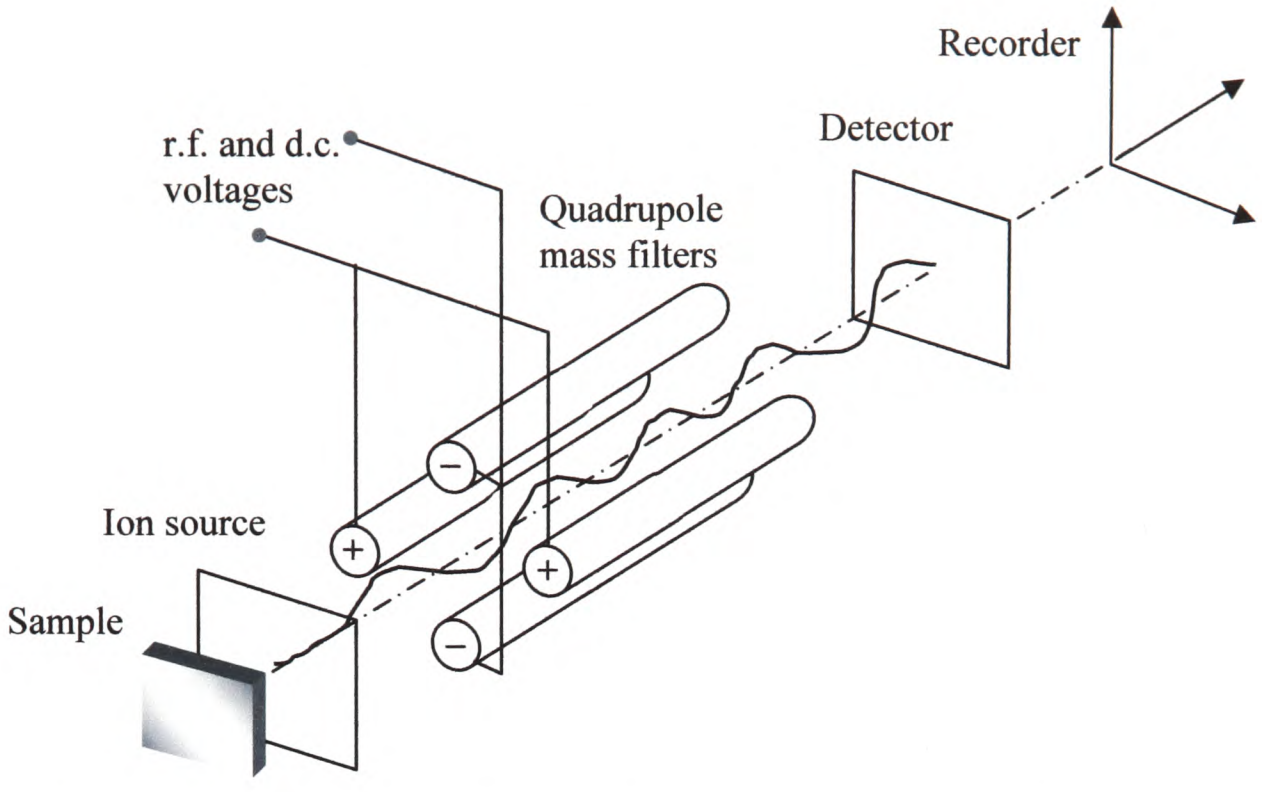


Figure 4. The longtitudinal cross-section structure of a quadrupole mass filter, showing a stable trajectories

2.5.2 Temperature Programmed Desorption

Thermal desorption of an adsorbed molecule occurs when a surface is heated, as a result of a species being thermally promoted to higher bound and eventually unbound states in the shallow potential energy well, representing the surface-particle interaction [9]. It is a process that is heavily dependent on activation energy and temperature according to the Arrhenius equation:

$$-\frac{dn}{dt} = n^X v_X \exp\left(\frac{-E_d}{RT}\right) \qquad \text{(eqn 7)}$$

where, x = order of reaction, n = surface concentration, v_X = frequency factor and E_d = desorption energy. When the surface is being heated up by a linear temperature ramp, the gas will evolve from the surface on assumption that the heat applied and temperature rises are homogenised on the surface. At the same time, masses of interest are monitored by a mass spectrometer to record the pressure versus temperature spectrum. The desorption of

a particular binding state results in a transient mass spectrometer signal and a peak in the pressure-temperature curve. The desorption peak height is proportional to the desorption rate as long as the pumping speed is sufficient for re-adsorption to be negligible.

According to the analysis of Redhead [10], the temperature at which the peak is maximum (desorption peak) corresponds to the maximum rate of desorption when $d^2n/dT^2 = 0$ and $T = T_d$, which later yields the first-order desorption (x = 1);

$$\frac{E_d}{RT_d^2} = \nu_1 \frac{dt}{dT} \exp\left(\frac{-E_d}{RT_d}\right) \qquad \text{(eqn 8)}$$

The peak is asymmetrical and T_d is independent of surface concentration, n.

For a second order desorption (x = 2), a series of desorption peaks would shift to lower temperatures at increasing coverage, thus the process is surface concentration dependent. However, the T_d peak is symmetrical with bell-shaped profile.

$$\frac{E_d}{RT_d^2} = 2n_d\nu_2 \frac{dt}{dT} \exp\left(\frac{-E_d}{RT_d}\right) \qquad \text{(eqn 9)}$$

Due to highly linearity for the relation in between E_d and T_d within $10^8 < \nu/\beta < 10^{13}$ (K^{-1}), Redhead made an approximation of equation 8 of a first order reaction into

$$\frac{E_d}{RT_d} = \ln\left(\frac{\nu T_d}{\beta}\right) - 3.64 \qquad \text{(eqn 10)}$$

In brief, temperature programmed desorption (TPD) spectra can provide information of adsorbed species and desorption reaction products according to their atomic mass units (*amu*); the temperature regimes where desorption occurs; the extent of surface coverage by the adsorbate and some other important kinetic parameters, such as the order of reaction, the pre-exponential frequency factor, ν_x and the activation energy of desorption, E_d as a function of surface coverage.

Desorption from a CVD diamond surface encompasses desorption from all of the exposed facets, as well as from grain boundaries and defects. Although desorption spectra

from polycrystalline surfaces are expected to be far more complex than those from single crystals, it is instructive to compare kinetic parameters obtained from CVD diamond surfaces with those of the low-index planes of natural diamond single crystals [11]. This may help to determine which sites are most active for diamond growth. The areal densities of carbon atoms on the low-index planes of the diamond lattice vary from 1.57 x 10^{15} atoms/cm^2 for the (100) to 1.81 x 10^{15} atoms/cm^2 for the (111) to 2.22 x 10^{15} atoms/cm^2 for the (110). Since the CVD diamond surface is composed of a combination of these and other higher index planes, an average of these values is used; however, this introduces an uncertainty of up to 20 % [11].

2.6 Microwave Plasma Discharge Beam source

A microwave discharge source without magnetic field has been employed inside the UHV system (see figure 2), to produce high purity and highly dissociated atomic beams of hydrogen and oxygen. The source consisted of a compressed-liquid nitrogen-cooled Pyrex cavity with the pressure inside being monitored by a pirani gauge. The discharge was excited by feeding about 150 W of microwave input power into a coaxial cavity resonant at 2.45 GHz (Sairem). Atomic gases diffused into the reaction chamber via a 1 mm diameter capillary through 20 mm long of exit canal [12,13].

2.7 Electron Affinity

The electron affinity of a semiconductor, χ is the difference between the vacuum level and the conduction band edge/ minimum, *i.e.* $\chi = \phi + (E_F - E_V) - Eg$

$$= (E_{Vac} - E_F) + (E_F - E_V) - Eg$$

$$= E_{Vac} - E_{CBM} \qquad \text{(eqn 11)}$$

where ϕ (work function), E_F (Fermi level), E_V (valence band maximum), E_{Vac} (vacuum level), E_{CBM} (conduction band minimum), Eg (band gap). A typical band scheme of a

semiconductor surface is shown in figure 5. For a typical surface with a positive electron affinity (figure 5a), the vacuum level lies above the conduction band minimum (CBM) creating an energy barrier of positive electron affinity ($\chi > 0$), which prevents low energy electrons in the conduction band to escape into the vacuum [14]. If the vacuum level lies below the CBM (figure 5b), a *true* negative electron affinity (NEA) surface is produced with $\chi < 0$. In most cases, instead of true NEA, the vacuum level lies below the CBM only for bulk generated electrons and not for surface excited electrons (figure 5c), producing an *effective* NEA. This is due to the reduction in electron affinity and downward band bending in a short characteristic length at the surface as a result of positive charge at the dipole induced-surfaces, such as in the presence of electropositive adsorbates.

The magnitude of the effective NEA (see figure 5(c)) is determined as

$$\chi_{eff} = \varphi_{BB} - \chi \qquad \text{(eqn 12)}$$

where φ_{BB} is band bending and χ is positive electron affinity. Therefore, the surface modification by electropositive species is required for promoting effective NEA (increase band bending) that could increase the probability of photoelectron escape into vacuum. An effective NEA gives most efficient emission of electrons if the depletion (bending) region is thin since this allows little time for electrons to lose energy to a point where cannot escape. Electrons can even tunnel from bulk to vacuum if the depletion region is suitably thin, which can avoid surface charging effect due to electrons trapping in the surface region.

In general, excitation of electron into the conduction band can be accomplished using light (photoemission), particle bombardment (secondary emission), a forward-biased *n*-contact (cold emission), applied field (field emission) or a rise in temperature (thermionic emission).

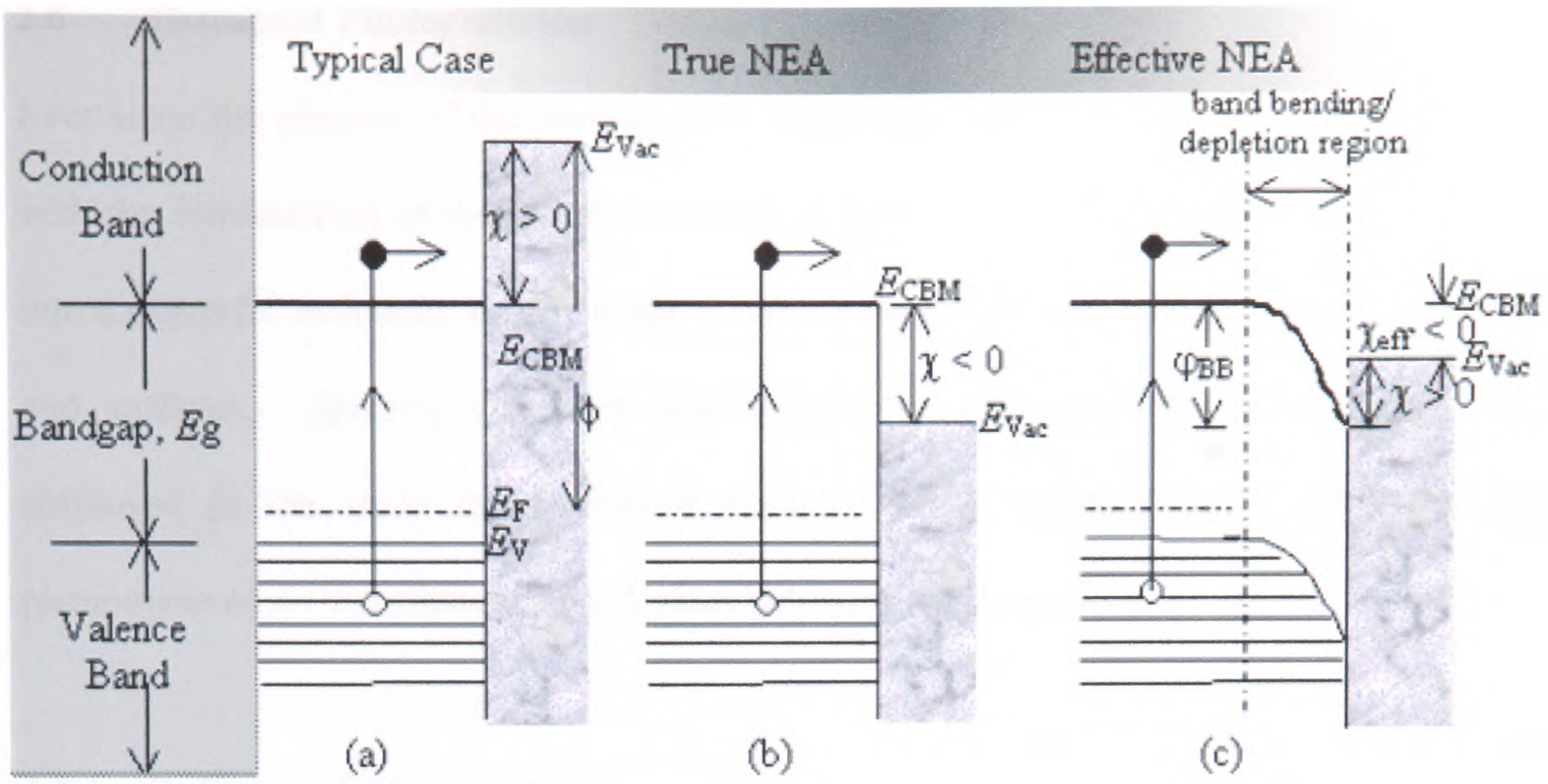


Figure 5. Band schemes of semiconductor surface: (a) Positive electron affinity, (b) true negative electron affinity, and (c) effective negative electron affinity

The presence of NEA can be determined experimentally by measuring the energy distribution curves of the photoexcited electrons and observing whether the low kinetic energy threshold coincides with the CBM [15,16]. In practice, NEA can be obtained for many conventional semiconductor materials by heavy *p*-doping of the semiconductor (to encourage downward band bending the surface) and by adding a thin film (several atomic layers) of caesium rich-caesium oxide on the clean semiconductor surface.

A lot of interest exists concerning diamond since NEA can be induced by H-termination as a result of the dipole present in the chemisorption bond. Hydrogen-induced NEA on diamond surface can be achieved by a variety of means including mechanical polishing in olive oil followed by solvent degreasing, exposure of the clean surface at room temperature to atomic hydrogen, cleavage in molecular hydrogen at atmospheric pressure and exposure of the surface to hydrogen plasmas [14].

2.8 Threshold Photoemission

Ever since the physics of the photoelectric effect was resolved by Einstein in 1905 [17] with the introduction of the quantum nature of light, photoelectric emission has evolved into a powerful technique for the study of the electronic and geometric structure of solids and surfaces. Spicer's three-step model [18] for photoelectric emission was first employed to the study the excitation, bulk-to-surface transport and electron escape phenomena of 3 - 5 compounds NEA photocathodes since late 70's.

2.8.1 Reflective Emission of Electrons

The Spicer equation for quantum photo-yield (QPY) [18] is derived from the product of all probabilities of each step, which give overall probability of photoemission (see figure 6)

$$QPY(h\nu) = [\boldsymbol{P}_{electron\ excitation}] \times [\boldsymbol{P}_{electron\ transport}] \times [\boldsymbol{P}_{electron\ escape}] \quad \text{(eqn 13)}$$

$$QPY(h\nu) = \left[(1-R)\frac{\beta(h\nu)}{\alpha(h\nu)}\right] \; x \; \left[\frac{1}{1+1/\alpha(h\nu)\,L}\right] \; x \; P, \quad \text{(eqn 14)}$$

where $\beta(h\nu)/\alpha(h\nu)$ is the fraction of the absorption events to generate 'useful' electrons. $\alpha(h\nu) = \beta(h\nu) + \alpha_n(h\nu)$, by which $\beta(h\nu)$ and $\alpha_n(h\nu)$ are the optical absorption coefficient for excitation into states above and below the vacuum level, respectively. $R(h\nu)$ is the optical reflectivity of the material, and $\boldsymbol{P}$ is the surface escape probability for electrons. L is the electron diffusion length in the bulk and is a function of the kinetic energy of the photoexcited electrons, which is dependent on the photon energy.

The β/α ratio will approach unity as electron affinity (χ) is reduced to zero. As χ is decreased, $L(h\nu)$ will be increased since each electron is able to lose more energy to inelastic scattering and can still escape [19].

Thus, the simplified quantum photo-yield for reflective emission is

$$QPY(h\nu) = \frac{(1-R)}{1+1/\alpha(h\nu)\,L} P \qquad \text{(eqn 15)}$$

Qualitatively - large values of $\alpha(h\nu)L$ will result in high electron yields, since the electrons are created in a region near the surface, short compared to their transport length. For semi-transparent films, the situation is more complicated since carriers need to be created within their transport length of the back surface; if α or the film thickness is too large, the light does not reach this region, whilst if these parameters are too small insufficient absorption takes place. Models show that high electron yields are expected when the transport length and the thickness of the absorbing film are comparable, and are greater than the absorption length [20]. Electron escape depths, while only up to about 10 nm in PEA devices (CsI for example has low values of L due to electron-phonon collisions [21,22] can be as high as 5 μm in NEA devices. For high L, crystal with excellent quality is required as the existence of defect states in band gaps can act as traps for electrons travelling at conduction band minimum.

- As for the case of diamond, L varies from 10 to 50 nm for photon energies of ≥ 7.3 eV (170 nm) to more than 1 μm for photons with energies close to the indirect band gap of 5.5 eV [23]
- For high α, direct bandgap materials are needed – obviously diamond is not ideal for this until very high energy radiation is applied
- $\boldsymbol{P}$ as the surface escape probability for electrons, would be a function of the surface treatment and condition. For high $\boldsymbol{P}$, the diamond should possess surface NEA properties

The fundamental aspects of photoemission from solids are normally understood in terms of a three-step model developed by Spicer [18,19] with the assumption that photoemission was a bulk rather than purely surface event (see figure 6).

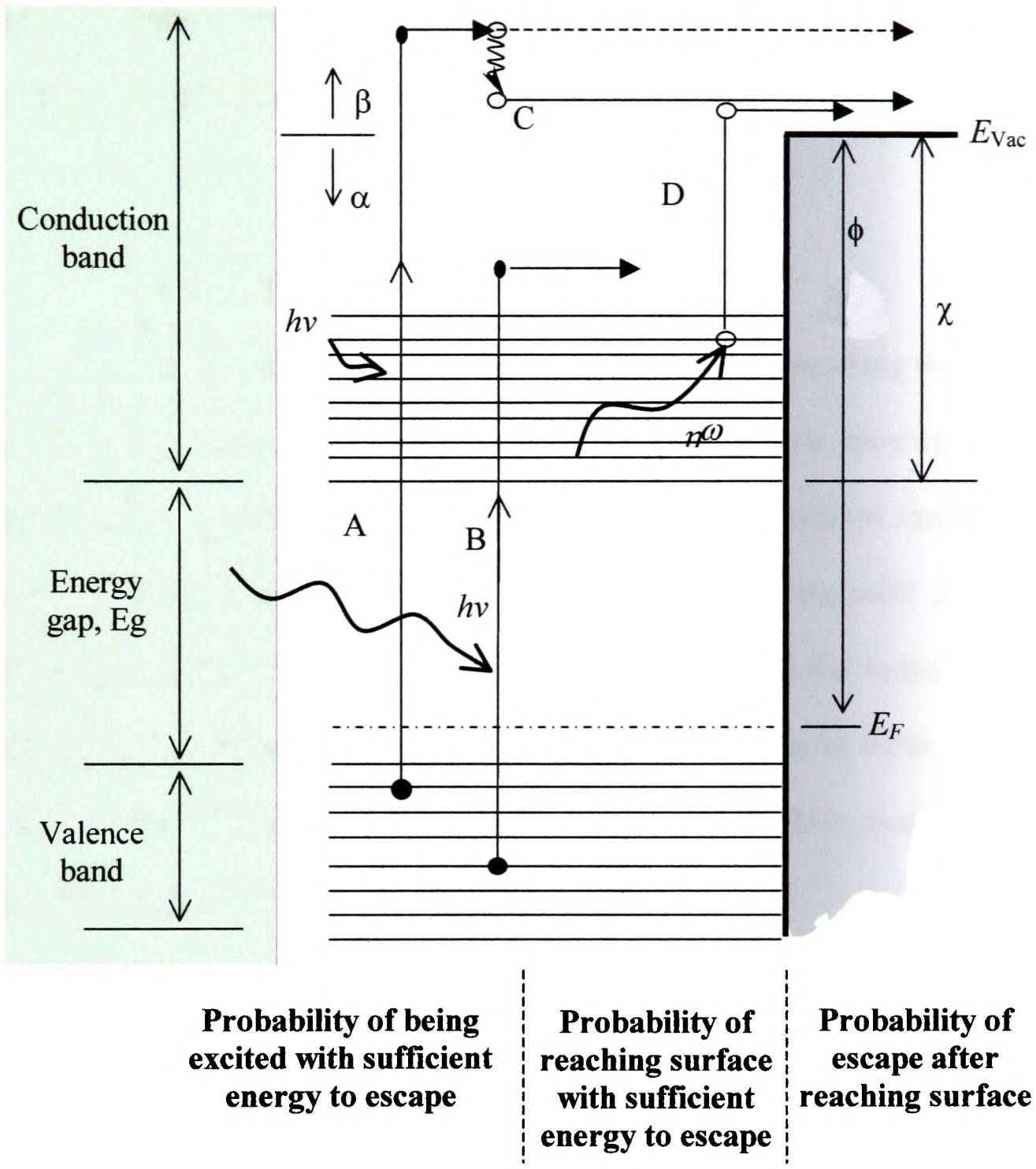


Figure 6. The three-step model of photoemission drawn for a conventional cathode. A is the successful excitation of electron high into conduction band, whereas B is not; C is the thermalization process (losing energy) during electron transport due to collision, with lattice or with other electrons; D is due to the thermodynamic temperature excitation, obtained as dark current when semiconductor was shielded from all incoming radiation. The electron affinity, χ should be low to increase the number of electrons able to escape. The work function, ϕ should be high to reduce the thermal excitation, D

Step 1. Absorption of light or Excitation of electrons

The optical absorption coefficient should be high in order that the incoming photons can be absorbed at appreciable distances from the surface and excite the electrons high into the conduction band, well above the vacuum level (A rather than B in figure 6), so that they can escape even after losing energy in collision. In the case of diamond photoemission, light is needed with energy above the indirect diamond band gap (5.5 eV), or in order to induce better absorption, energy above the direct band gap of 7.2 eV is needed.

Step 2. Electron Transport

Energetic electrons have short mean free path and little hope of reaching the surface with their kinetic energy intact. With a positive electron affinity surface, most electrons would therefore be trapped. For the case of negative affinity, the electrons energies are first moderated by collisions with lattice phonons, on a time scale of the order of 10^{-12} s. The electrons may then diffuse through the conduction band towards the surface as 'minority carriers', occupying states near the bottom of the conduction band before falling to an empty state in the valence band ('recombining' with a hole). This recombination takes place in a time scale of the order of 10^{-9} s to 10^{-7} s [20].

Step 3. Emission or Electron escape

Electrons, which reach the surface before recombining will be emitted as photoelectrons. However, not every electron that reaches the surface will be emitted, even for NEA semiconductors. This is because there is a finite probability for quantum mechanical reflection at the vacuum-solid interface and only the component of momentum perpendicular to the surface could overcome the potential barrier at the surface [14,24].

2.8.2 Transmissive Emission of Electrons

Incident of light on the near surface will generate the photoexcited electrons, which will diffuse through the thickness of the film and emitted from the backside of film. The term for this type of emission from the far face is called *transmission mode* photoemission. The system with emission from either the same face or far face can be treated by use of planar-diffusion models [20]. The theory has been studied in some depth by Antypas *et al.* [25], Symn [26] and Lui *et al* [27]. The calculation is not dissimilar to the calculation in equation 15, although a different excitation function is used, with the main extra emphasis for the calculation of flux of electrons reaching the far face. If the thickness of the film is larger than one electron diffusion length, L, the transport of the photoexcited electrons at photon energies near the band gap can be described by the continuity equation

$$\frac{d^2n}{dx^2} - \frac{n}{L^2} = -\frac{g(x)}{D_n} \qquad \text{(eqn 16)}$$

where n is the excess electron density, D_n is the electron diffusion constant, and $g(x)$ is the generation rate of electrons.

The photoelectrons generated by the *uv* photons, however may suffer from many elastic or inelastic collisions, before they could finally approach the surface and escape. The probability for a photoelectron produced at thin layer with a distance dx from the surface of a thick photocathode is

$$\frac{Q\,dx}{\lambda} e^{-x/\lambda} \qquad \text{(eqn 17)}$$

which is termed as conventional *reflective mode* of photoemission. x is measured from the surface through which the photon entered. The situation would obviously be more difficult for the transmissive mode than the reflective. For *transmissive mode*, the thickness d of which the photon enters, transports through and escapes from the surface must be considered.

If x is measured from the surface across which the electron escapes, the probability that a photoelectron is produced at x is

$$\frac{Q\,dx}{\lambda}\, e^{-(d-x)/\lambda} \qquad \text{(eqn 18)}$$

The *escape probability* $G(x)$ is assumed as

$$G(x) = T\, e^{-x/L} \qquad \text{(eqn 19)}$$

where L is the escape length and $T \leq 1$ is the probability that an electron can reach the surface from bulk and escape. By the multiplication of equation 18 and 19, a model for the observed quantum efficiency of a transmissive mode of photocathode [21] can be obtained

$$QE_{obs} = \frac{QT}{\lambda}\int_0^d e^{-(d-x)/\lambda} e^{-x/L}\, dx \quad ,$$

$$= QT\,\frac{L}{L-\lambda}\left(e^{-d/L} - e^{-d/\lambda}\right) \qquad \text{(eqn 20)}$$

Figure 7 shows the predicted results in term of the variation in photoyield with the sample thickness. The plot shows that both transmissive and reflective emissions increase with the absorption on the surface of a photocathode. This is due to the excitation of electrons to the conduction band. For reflective emission – once absorption becomes high enough and the incident light is absorbed within 'reach' of the surface, the reflective photoyield would tend to be saturated which is in compromise in between the parameters of absorption depth and electron diffusion length. This reflects the behaviour of the Spicer model.

For transmissive emission (depending on recombination rate), the yield reaches a maximum before the absorption becomes so high that most light is absorbed near the front surface and electrons do not reach the far surface. The photoyield will then decrease towards zero as less and less light can penetrate far enough into the film to produce

electrons within their diffusion length of the far surface. If the film becomes thicker than the sum of the maximum absorption depth and maximum diffusion length, then no transmissive electron emission should take place.

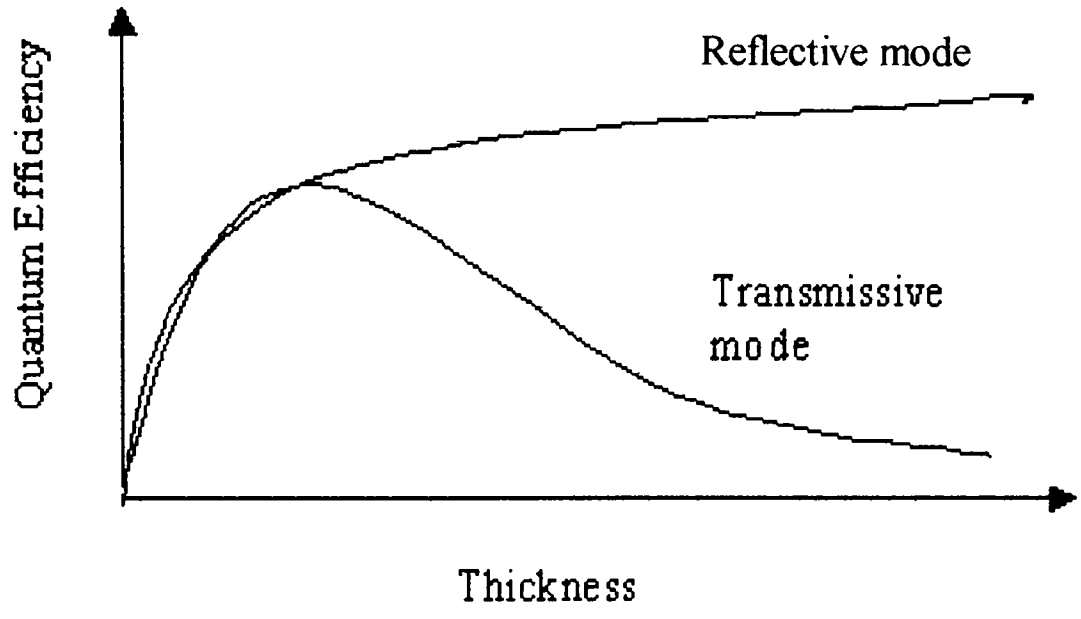


Figure 7. Dependence of photoemission on sample thickness, including reflective and transmissive mode

While the changes of emission with thickness is shown in plot figure 7, the subsequence change in absorption coefficient or carrier transport length will also lead to a change in emission. A similar plot with αL on the x-axis instead of thickness would look very similar.

2.9 X-ray Photoelectron Spectroscopy

The revolutionary development of the photoelectric effect was initiated on the basic of Planck's quantization of energy concept in 1900 [28] and Einstein's photoelectric effect in 1905 [17]. Both of the ideas have laid the foundation for the theoretical understanding of X-ray photoelectron spectroscopy (XPS) or electron spectroscopy for chemical analysis (ESCA), which explain the direct transfer of a photon's energy to electrons within an

atom, resulting in the emission of the electrons without energy loss [29]. Throughout the 1950's and 1960's, Siegbahn and co-workers in Uppsala of Sweden have further developed the instrumentation and theory of ESCA [5,30], which have provided the method we use today.

XPS provides a compositional analysis of a surface with both qualitative and quantitative information on binding energy as the indicators for *chemical states* of particular elemental species and *chemical shifts* of bonding environments or functional groups.

In photoelectron spectroscopy of solids, the kinetic energy of electrons is ejected when a solid is irradiated with monoenergetic photons of energy $h\nu$. The relevant energy conservation equation is

$$h\nu + E^{i}_{tot} = E_{kin} + E^{f}_{tot}(k) \qquad \text{(eqn 21)}$$

where E^{i}_{tot} is the total energy of the initial state, E_{kin} is the kinetic energy of the photoelectron, and $E^{f}_{tot}(k)$ is the total final energy of the system after ejection of the photoelectron from the k th level. The *binding energy* of the photoelectron is defined as the energy required to remove an electron to infinity with a zero kinetic energy [31]. In XPS measurements $E_B(k)$, the binding energy of an electron in the k th level referred to the local fermi level is given by,

$$E_B(k) = E^{f}_{tot} - E^{i}_{tot} \qquad \text{(eqn 22)}$$

Thus, the resultant photoelectric equation is

$$h\nu = E_{kin} + E_B(k) \qquad \text{(eqn 23)}$$

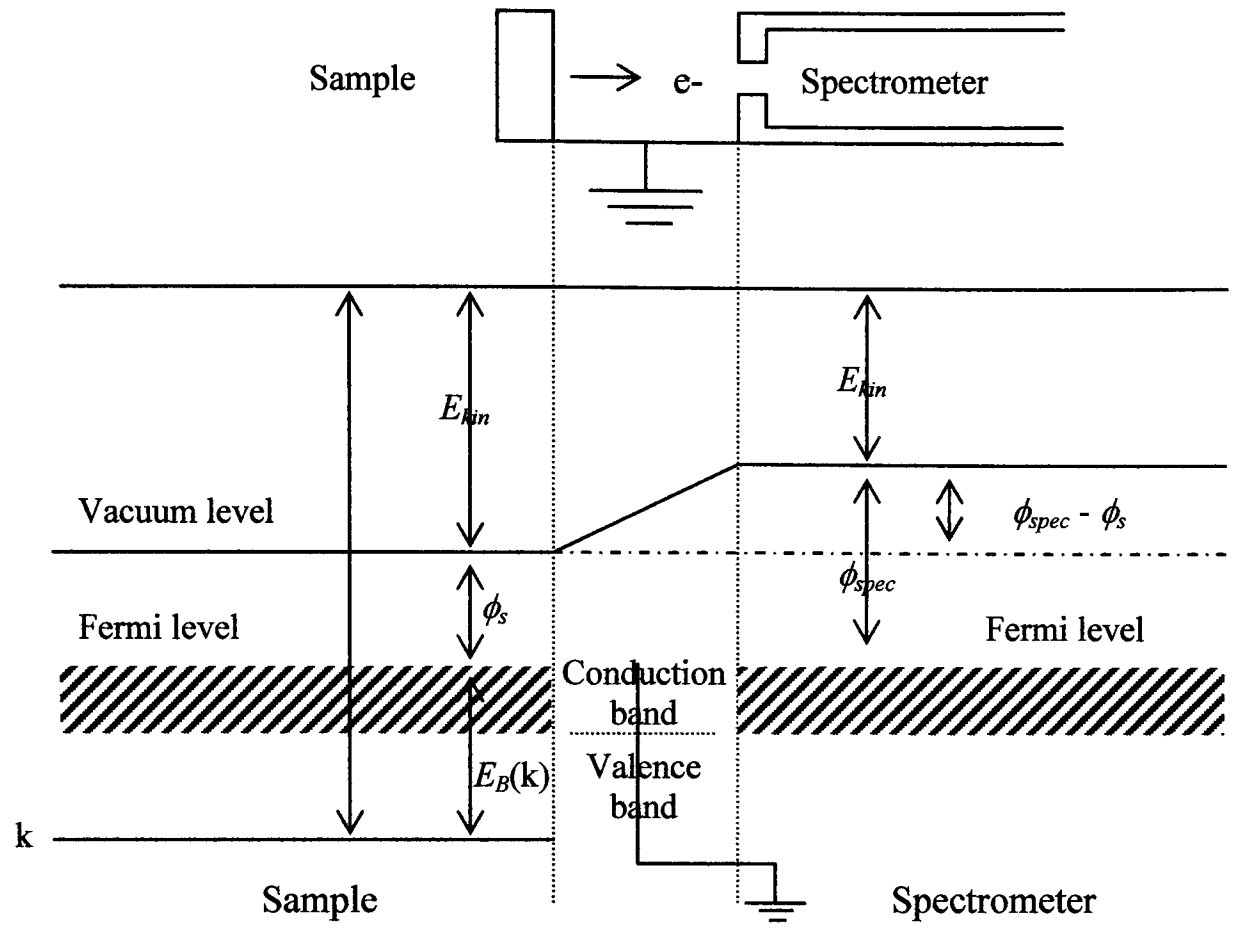


Figure 8. Schematic diagram of the relevant energy levels for binding energy measurements. The incoming photons, energy hv, create an electron of kinetic energy E_{kin} relative to the vacuum level of the sample. The electron is detected by a spectrometer with a work function ϕ_{spec}, so that the measured energy $E_{kin} = E_{kin} - (\phi_{spec} - \phi_s)$

By grounding the sample and the spectrometer, a good electrical contact will be made between them, putting both of the Fermi levels (E_F) at the same energy level (figure 8). However, the E_{Kin} and E_B of the spectrometer do not exactly equal the X-ray energy of Einstein equation. The difference is the work function of the spectrometer (ϕ_{spec}). Since the work function, ϕ is related to the E_F and vacuum level (E_{Vac}) (see equation 24),

$$\phi = E_{Vac} - E_F \qquad \text{(eqn 24)}$$

and is the minimum energy required to eject an electron from the highest occupied level (E_F) into vacuum and, and the Einstein equation now becomes;

$$E_B(k) = hv - E_{kin} - \phi_{sp} \qquad \text{(eqn 25)}$$

The assumption for the equation is that the binding energy and the spatial distribution of the remaining electrons after photoemission is exactly the same as in the initial state. This approximation is called *Koopman's theorem*, assuming that the photoemission process is fast relative to rearrangement of other electrons in the atom [32], and the binding energy equates with the negative orbital energy of the emitted electron;

$$E_B = -\varepsilon \quad (\varepsilon = \text{orbital energy}) \qquad \text{(eqn 26)}$$

However, this theorem does not occur in reality as the photoionisation and photoemission happens in such a way to permit modification to the states and energies of other electrons in order to reach a stable equilibrium with the involvement of *intra-atomic relaxation*;

$$E_{kin} = h\nu - E_B(k) + E_{intra} \qquad \text{(eqn 27)}$$

where E_{intra} is energy for intra-atomic relaxation shift. In the case of metal, in particular, the valence electrons are weakly bound and very mobile and so will screen the core hole efficiently which leads to an additional *inter-atomic relaxation* shift and to an emitted kinetic energy which is higher than from the atom in its free state,

$$E_{kin} = h\nu - E_B(k) + E_{intra} + E_{inter} \qquad \text{(eqn 28)}$$

where E_{inter} is energy for inter-atomic relaxation shift. Both relaxation shift energies are only of the order of a few eV or less, as compared to $E^V_B(k)$ of several hundred eV and are thus intentionally ignored in a simple treatment.

As well as the generation of core photoelectron lines in XPS, certain outgoing photoelectrons undergo characteristic energy losses as they are ejected from the atom. The consequential loss of kinetic energy by the photoelectron is observed in the XPS spectrum as a minor peak to the higher binding energy side of the characteristic core level. So-called *shake-up satellites* occur when the emergent electron promotes a valence band

electron to a higher energy level, and *plasmon loss* peaks arise from emitted electrons losing energy to collective oscillations of electrons in the valence or conduction band. The *auger* process is the another phenomena which is due to an outer electron falling to populate an inner unfilled orbital, causing the transfer of excess energy to another outer orbital electron which will result in the emission of that outer electron.

From the core electron binding energies, important information about the chemical elements can be obtained. However, the presence of the atoms bound to particular chemical configurations will change the electron binding energies. Such dependence on atomic environment causing the difference energy shifts from the characteristic peak is known as *chemical shifts*. The size and direction of these chemical shifts will provide the information of the related chemical states on the bonding environment.

The *average depth* from which electrons of a given energy can be emitted is given

$$\text{Emission depth, } d = \lambda(E')\cos\theta \qquad \text{(eqn 29)}$$

where $\lambda(E')$ is the average distance within the substrate between inelastic collisions of electrons with energy E', and θ is the angle of motion with respect to the surface normal. The λ value is predicted by Seah and Briggs [33] by following an empirical relationship in equation 30. This assumption is based on the E_{kin} of certain material and its atomic diameter, with a range within 2 - 10 atom layers.

$$\frac{\lambda}{nm} = \frac{538a}{E^2} + 0.41a^{3/2}\left(E_{kin}\right)^{1/2} \qquad \text{(eqn 30)}$$

where E' is the kinetic energy of the electrons (eV) and a is the mean atomic diameter of the element (nm). Despite the fact that the incident x-ray photons can penetrate significant distances into the substrate bulk, the stimulated electrons are subject to inelastic collisions which prevent them from reaching the surface, so that the value of λ is actually a couple of orders of magnitude lower than the photon penetration depth. It is found that the

maximum surface sensitivity is achieved when $5 < E' < 2000$ eV, which corresponds typically to values of λ of around 3 atomic layers [33].

The *line intensities* or *areas* of the photoelectron peaks are of interest for quantitative analysis. The intensity of a given line depends on a number of factors including the photoelectric cross section σ, the electron escape depth λ, the spectrometric transmission, surface roughness or inhomogenities as well as the presence of satellite structure. For XPS peaks of elements A and B with similar energy $\lambda_A = \lambda_B$ presuming the instrumental factors for both elements are the same, then relative composition ratio can be obtained as given in equation 31 if they are distributed homogenously throughout the sampling depth,

$$\frac{C_A}{C_B} = \frac{I_A}{I_B} x \frac{\sigma_B}{\sigma_A} \qquad \text{(eqn 31)}$$

where C = atomic concentration, I = XPS peak area of core level, σ = photoemission cross-section of core level for atomic A or B.

The XPS of core level C 1*s* peak at 284.75 eV (referenced to clean Ni(100) Fermi edge [34]) is fairly independent of carbon hybridisation, which is insensitive to differentiate between graphite, diamond and amorphous carbon. However, at the low binding energy end between 0 - 30 eV, the XPS valence band spectra can be used for various carbon phase characterisation as a result of contributions from *s*, *p*-σ and *p*-π valence electrons. At around 285 - 320 eV, the information about the plasmon loss structure region can also be used to differentiate the differing forms of carbon phases. The bulk diamond plasmon peak occurs at + 35 eV relative to the carbon C 1*s* peak, and a smaller peak due to the surface plasmon excitation occurs at + 23 eV. In contrast, the main plasmon band for graphite gives a broader π + σ peak at + 26.8 eV plus a small fingerprint peak at + 6 eV [35], whereas the plasmon peak for the amorphous carbon occurs at 25 eV [36].

2.10 Electrochemistry

2.10.1 Electrode Dynamics

The work of Faraday in 1834 and the laws of diffusion proposed by A. Fick in 1855 have laid the foundations for dynamic electrochemistry [37], which is concerning the study of electron transfer reactions between electrode and reactant molecules in a solution phase. With the fundamental measurements of potential, current and time, many electroanalytical techniques have been developed and more parameters to be considered responsible for controlling the rate of the charge transfer process, such as the electrode potential, transport of material between the electrode and bulk solution, the reactivity (ease of oxidation or reduction) of the solution species, the nature of the electrode surface and the structure of the interfacial region over which the electron transfer occurs [38].

The *Nernst equation* is named after the German physical chemist Walther H. Nernst who first formulated it. A general charge transfer reaction proceeds as in equation 32, with oxidant *O* being reduced to reductant *R* or *vice verse* for oxidation

$$v_i O_i\,(\mathrm{aq}) + \ldots + n\mathrm{e}^- \leftrightarrow v_j R_j\,(\mathrm{aq}) + \ldots \qquad \text{(eqn 32)}$$

From the relation of the reaction Gibbs function, ΔG_r with the composition of

$$\Delta G_r = \Delta G^{\ominus} + RT \ln K \qquad K = \frac{\prod_j [R]_j^{Vj}}{\prod_i [O]_i^{V_i}} \qquad \text{(eqn 33)}$$

where K corresponds to the equilibrium constant for the electron-transfer reaction given. Therefore,

$$E_{eq} = -\frac{\Delta G^{\ominus}}{nF} - \frac{RT}{nF} \ln K \qquad \text{(eqn 34)}$$

the first term on the right of this equation is called the standard cell potential and denoted E^{θ} is given as,

$$-nFE^{\ominus} = \Delta G^{\ominus} \qquad \text{(eqn 35)}$$

which E^{θ} is the standard reaction Gibbs function of the reaction expressed as a potential (in volts). It follows that

$$E_{eq} = E^{\ominus} - \frac{RT}{nF} \ln K$$

$$E_{eq} = E^{\ominus} + \frac{RT}{nF} \ln \frac{\prod_i [O]_i^{V_i}}{\prod_j [R]_j^{Vj}} \qquad \text{(eqn 36)}$$

where R is the universal gas constant, T is the absolute temperature (K), n is the charge number of the electrode reaction, and F is the Faraday constant (96485.3415 C mole^{-1}). The equation 36 is the *Nernst equation*, which describes the variation of electrode potential for each electrochemical reaction with the activities (concentration) of oxidised and reduced species under conditions of equilibrium at the electrode surface.

For an electron to transfer from one form to the other, *i.e.*, from the reduced to oxidized form or *vice versa*, an energy barrier of height ΔG_r (activation Gibbs function) must be surmounted. Although the current is zero for the net rate of passage of electrons, the passage of current called *exchange current*, i_0 in a single direction is not zero in the dynamic equilibrium.

$$i_0 = nFAj, \qquad \text{(eqn 37)}$$

where, A is the electrode area/ cm^2 and j is the flux of oxidant or reductant reaching the electrode surface/mol cm^{-2} s^{-1}. A rate law can describe the flux:

$$j = k_0 [R]_0 \quad \text{or} \quad j = k_0 [O]_0 \qquad \text{(eqn 38)}$$

where k_0 is the heterogeneous rate constant for the electron transfer reaction and $[R]_0$ the concentration of the reductant (or oxidant $[O]_0$) at the electrode surface. Unlike in the equilibrium situation, the concentration of the reductant or oxidant at the electrode surface is not equal to that in bulk solution, because the rate of depletion of the species by

electrolysis is usually greater than the rate of diffusion from the bulk solution to the interfacial region.

From $$O(aq) + e^{-} \underset{k_{ox}}{\overset{k_{red}}{\rightleftharpoons}} R(aq) \qquad \text{(eqn 39)}$$

the currents from reductive and oxidative components are:

$$i_c = nFAk_{red}\,[O]_0 \text{ and } i_a = nFAk_{ox}\,[R]_0 \qquad \text{(eqn 40)}$$

thus the total current flowing,

$$i = i_a - i_c = nFA(k_{ox}[R]_0 - k_{red}[O]_0) \qquad \text{(eqn 41)}$$

The rate constant for a heterogeneous electron transfer process is dependent on the potential field close to the surface driving the movement of electrons, hence on the applied electrode potential E. As found experimentally, the dependence of constants is of the form

$$k_{red} = k^0_{red} \exp\left[-\frac{\alpha\eta F}{RT}\right] \qquad k_{ox} = k^0_{ox} \exp\left[\frac{(1-\alpha)\eta F}{RT}\right] \qquad \text{(eqn 42)}$$

where α is transfer coefficient - a measure of the symmetry of the energy barrier and a constant over a reasonable range of potential, with value commonly close to 0.5 ($0 \le \alpha \le 1$). $\eta = E - E_e$ is overpotential - a measure of reversibility of the redox process.

From both equations of 41 and 42, these give the *Butler-Volmer equation*, relating the net current flowing at the working electrode to the overpotential, which is fundamental to electrode kinetics:

$$i = i_0 \left(\exp\left[\frac{(1-\alpha)\eta F}{RT}\right] - \exp\left[-\frac{\alpha\eta F}{RT}\right]\right) \qquad \text{(eqn 43)}$$

If the overpotential is oxidative (anodic) process driven, then the corresponding reductive component is vanishingly small

$$i = i_0 \exp\left[\frac{(1-\alpha)\eta F}{RT}\right] \qquad \text{(eqn 44)}$$

At overpotentials that drive the reductive (cathodic) process, negligible oxidation currents flow; thus equation 43 simplifies to

$$i = i_0 \exp[-\frac{\alpha \eta F}{RT}] \qquad \text{(eqn 45)}$$

2.10.2 Cyclic Voltammetry

Cyclic voltammetry (CV) yields information on the kinetics and the mechanism of the electrode dynamic process by sweeping the working electrode potential back and forth across the formal potential of the analyte. In the cases of electrochemical processes at metal electrodes in which both the oxidizing and the reducing agent are soluble, the following equations (46-51) hold:

For diffusion-controlled, reversible simple electron transfer reactions, the peak current is given by the *Randles-Sevcik* equation (at 25 °C) [39,40],

$$i_p = 2.69 \times 10^5 n^{3/2} D^{1/2} v^{1/2} c_0 \qquad \text{(eqn 46)}$$

$$d\,Ep/d\,v = 0 \qquad \text{(eqn 47)}$$

$$|\Delta Ep| = 0.059/n \qquad \text{(eqn 48)}$$

and for diffusion-controlled, irreversible simple electron transfer reactions,

$$i_p = 2.99 \times 10^5 n \alpha^{1/2} D^{1/2} v^{1/2} c_0 \qquad \text{(eqn 49)}$$

$$d\,Ep/d\log v = -0.030/\alpha \qquad \text{(eqn 50)}$$

$$|\Delta Ep| = 0.048/\alpha n \qquad \text{(eqn 51)}$$

In these equations, i_p represents the peak current density, n the number of electrons being transferred per substrate molecule, D the diffusion coefficient, v the potential scan rate, c_0 the bulk concentration, α the transfer coefficient, Ep the peak potential, ΔEp is the separation between the peak potentials = $Ep,a - Ep,c$. ΔEp is a measure of reversibility of

which the heterogeneous transfer rate constant can be calculated, using the reduced expression in equation 52, where Ψ is obtained from ΔEp *vs* Ψ calibration curve [41,42].

$$k^0 = \Psi\,[\pi D\, v\, (nF/RT)]^{1/2} \qquad \text{(eqn 52)}$$

For quasi-reversible systems (with $10^{-5} < k^0 < 10^{-1}$ cm s^{-1}), the current is controlled by both the charge transfer and mass transport. The shape of the cyclic voltammogram is a function of $k^0/(\pi Da)^{1/2}$ (where $a = nFv/RT$). As $k^0/(\pi Da)^{1/2}$ increases, the process approaches the reversible case. For small values of $k^0/(\pi Da)^{1/2}$ (*i.e.*, at very fast v) the system exhibits an irreversible behaviour.

The current response is limited by the rate at which reactants can be transported to the electrode surface. By using Ficks Laws and Nernst's diffusion layer model, the expression for the transport limiting current can be formulated

$$i_{lim} = n\,F\,A\,D\,c_0/\,\delta \qquad \text{(eqn 53)}$$

where i_{lim} is the limiting current related to the diffusion layer thickness (δ).

2.10.3 Rotating Disc Assisted Electrochemistry

On rotating disc-assisted electrochemistry, the electrode is embedded centrally within a large cylinder composed of an insulating material such as Teflon™ (figure 9), and rotated at a constant speed. The rotation spins the solution out from the cylinder surface in a radial direction, drawing out the fresh material up towards the disc and a sustainable steady supply of electroactive material to the electrode is achieved. At higher rotation speeds, the velocity of the solution towards the electrode is greater.

$$i_{lim} = 0.62\,n\,F\,A\,c_0\,D^{2/3}\,v^{-1/6}\,\omega^{1/2} \qquad \text{(eqn 54)}$$

Equation 54 is the Levich equation for the rotating disc-assisted electrochemistry and predicts the variation in the transport limited current, i_{lim} as a function of the rotation speed, ω. v is the kinematic viscosity of the bulk solution, $cm^2\ s^{-1}$ (viscosity/density). Ideally, a plot of the transport-limited current against the square root of rotation speed should yield a straight line, which passes through the origin. A deviation from linearity of the Levich plot suggests some kinetic limitations.

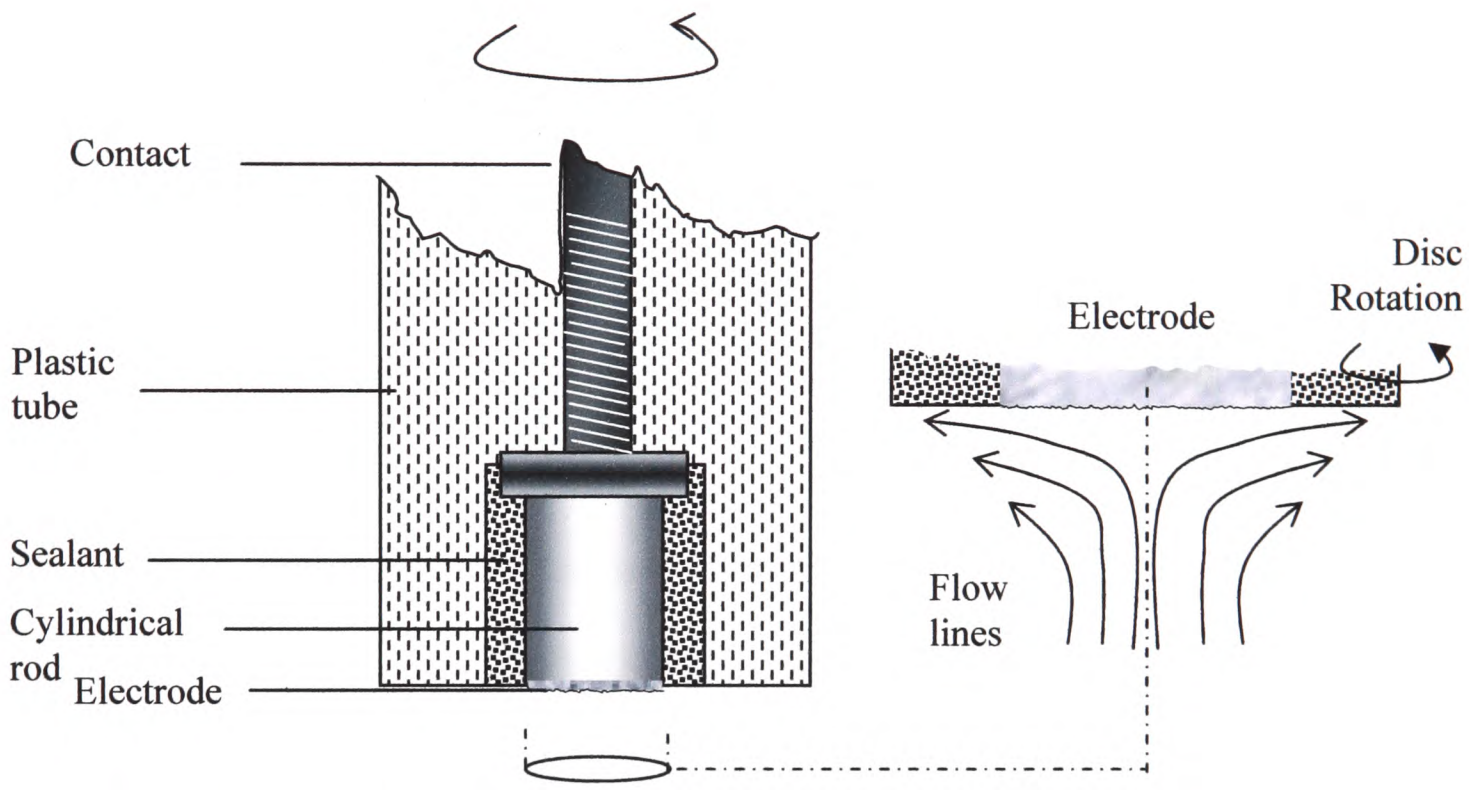


Figure 9. (a) The typical construction mounting of a disk electrode; (b) laminar flow lines at the rotating disc

From the equation 53 and 54,

$$n F A D c_0 / \delta = 0.62\, n F A c_0 D^{2/3} v^{-1/6} \omega^{1/2}$$

$$\delta = 1.613\, D^{1/3} \omega^{-1/2} v^{1/6} \qquad \text{(eqn 55)}$$

As noted in the equation 55, the diffusion layer thickness δ has shown to be proportional to $D^{1/3}$ and the enhanced convective transport of the electroactive material (with the increasing electrode angular velocity, ω) will subsequently results in concomitant

shrinking of the diffusion layer thickness. Rotation speeds of 100 - 4000 rpm thus correspond to δ value in the 5 - 50 μm range.

For voltammetric studies an Autolab PGSTAT 30 potentiostat system (EcoChemie, Netherlands) was employed with a Pt mesh counter electrode, a saturated Calomel (SCE) reference electrode (Radiometer, Copenhagen). Demineralised and filtered water was taken from an Elgastat water purification system (Elga, High Wycombe, Bucks) with a resistivity of not less than 18 MOhm cm.

Ever since the first mentioned of diamond used as electrochemical electrode [43], the electrochemistry of diamond has been studied intensely over the recent years and proposed for demanding applications such as wastewater treatment [44], electroanalysis [45], electrosynthesis [46], sonoelectrochemistry [47] and post column detection [48]. Most work to date has been carried out with boron-doped diamond electrodes, which can be obtained with different doping levels and properties [49].

Accurate control and reproducibility of the doping level are, however, problematic and therefore alternative procedures for the formation of electrically conductive diamond films are still in demand. In this project, surface conductive diamond (Chapter 3) and nanodiamond (Chapter 4) were compared to boron-doped diamond in the aspect of electrochemical characterization and electroanalysis.

2.11 Secondary Electron Microscopy

Secondary electron microscopy (SEM) is a useful qualitative imaging technique, giving the information of topography (the texture), morphology (the shape, size and arrangement of the particles making up the object) and composition (the elements and compounds the sample is composed of and their relative ratios).

SEM may utilise a number of different types of signal to produce an image from a sample. All of the images taken under SEM throughout this project are based on emissive

mode, which collects secondary emitted electrons or back-scattered electrons with high sensitivity to variations in atomic number (hence composition) and topography [50].

The secondary electrons, with low kinetic energies can be obtained as an ionization product at very shallow depths (~ 0.1 μm) from a wide range of trajectories. The reflected primaries or back-scattered electrons are scattered from atoms within a shallow depth (~ 1 μm) in the sample, and the heavier atoms can scatter electron beam to higher extent than lighter atoms. X-ray fluorescence will also be generated simultaneously from the atoms in its path, with each X-ray photon energy is the characteristic of an element. The Energy Dispersive X-ray Spectroscopy (EDX) microanalysis system collects the X-rays, sorts and plots them by energy, and automatically identifies and labels the elements responsible for the peaks in this energy distribution.

Two major SEM systems were used for projects, a Jeol JSM-5200 system operating at 25 kV with a beam current of ~ 130 μA for surface topographic studies and SEM Cambridge Stereoscan 360 system with EDX for compositional elementals analysis and higher resolution images.

The SEMs were used for surface characterization of CVD polycrystalline diamond at varying growth times, nanocrystalline diamond and metal deposits.

2.12 Atomic Force Microscopy

Unlike Scanning Tunneling Microscopy (STM), the Atomic Force Microscope (AFM), designed by Binnig, Quate, and Gerber in 1986 [51], is capable of resolving individual atoms on insulating surface as well as conducting materials. The AFM is a combination principle of the STM and stylus profilometer (SP), respectively to resolve the atomic surface structure of conductors and to record three-dimensional images of the surfaces with high lateral and vertical resolutions. The images are obtained by measurement of the force on a sharp tip created by the proximity to the surface of the sample. When the tip is

moved sideways, it will follow the surface contours. This force is kept small at a constant level with a feed back mechanism.

AFM has two important modes of operation, the contact mode and non-contact mode. In the static or contact (repulsive-force) mode, the tip is in contact with the surface. At the front of the cantilever spring, a tip, typically the V-shaped Si_3N_4 cantilever (120 mm long) is mounted and the force sensor is integrated on the base.

$$D \sim F \sim \Delta h \qquad \text{(eqn 56)}$$

where D = deflection of the cantilever, F = interaction force, Δh = vertical tip motion. The force applied is of the order of 1 – 10 eV/ Å, or 10^{-9} – 10^{-8} N, and the individual atoms can be imaged. In AFM non-contact (attraction-force/ tapping or dynamic) mode, the tip is not in contact with the surface. The cantilever spring is oscillated at its resonance frequency, which is influenced by changing forces from the sample. The frequency deviation is used to make an image of the sample.

$$\Delta f \sim F \sim h \qquad \text{(eqn 57)}$$

where Δf = shift in resonance frequency of vibrating cantilever, F = interaction force, h = tip-surface distance. The tip is usually a bar-shaped single crystal Si cantilever (125 mm long, f = 265 kHz). Different interactions due to a range of forces can be monitored and detected, including Van der Waals, electrostatic and magnetic forces. Though the atomic resolution is difficult to be achieved in non-contact mode, the important information about the surface is obtainable [52].

Root mean square (RMS) roughness in AFM describes the variation in surface elevation. It is also known as the standard deviation of the surface height within a given area. In this project, a Digital Instruments Multimode Scanning Probe Microscope is used to obtain the AFM images for diamond thin films and nanocrystalline diamond. Most of

the time, the contact mode is applied for imaging, unless if the diamond surface has too rough contour, the non-contact mode is utilised instead.

2.13 Raman Spectroscopy

In 1928, Sir Chandrasekhra Raman discovered the phenomenon that bears his name [53]. In Raman spectroscopy, the sample is normally irradiated by intense laser beams in the *uv*-visible region (at a frequency of v_0), and the scattered light is usually observed in the direction at 90° (right angle scattering) and 180 ° (backscattering) of the incident beam [54,55]. The scattered light consists of *Rayleigh scattering*, which is strong and has the same frequency as the incident beam, and the other is *Raman scattering*, which is very weak (~ 10^{-7} of the incident beam) and has frequencies $v_0 \pm v_m$, where v_m is a vibrational frequency of a molecule in the case of vibrational Raman spectroscopy.

An electric dipole moment P is induced when a substance is irradiated by laser where α is a proportionality constant, called *polarizability*, E is electric field strength of the electromagnetic wave, t is time.

$$P = \alpha E = \alpha E_0 \cos 2\pi v_0 t \qquad \text{(eqn 58)}$$

If the sample material is Raman active, the laser photons are scattered after having lost or gained energy, depending whether they have excited (v_o - v_m: Stokes Raman line) or de-excited ($v_0 + v_m$ anti-stokes Raman line) of a lattice vibration in the sample.

The anti-Stokes line is much weaker than the Stokes line, and it is the latter which is normally observed and used. Thus, Raman spectroscopy is a measurement of the vibrational frequency of a molecule, v_m as a shift from the incident beam frequency, v_o. Since

$$\alpha = \alpha_0 + \left(\frac{\partial \alpha}{\partial q}\right)_0 q + \mathrm{K} \qquad \text{(eqn 59)}$$

$$q = q_0 \cos 2\pi v_m t \qquad \text{(eqn 60)}$$

where q_0 is the vibrational amplitude, α_0 is the polarizability at the equilibrium position, thus

$$P = \alpha_0 E_0 \cos 2\pi v_0 t + \left(\frac{\partial \alpha}{\partial q}\right)_0 q\, E_0 \cos 2\pi v_0 t$$

$$P = \alpha_0 E_0 \cos 2\pi v_0 t + \left(\frac{\partial \alpha}{\partial q}\right)_0 q_0 E_0 \cos 2\pi v_0 t\ \cos 2\pi v_m t$$

$$P = \alpha_0 E_0 \cos 2\pi v_0 t + \frac{1}{2}\left(\frac{\partial \alpha}{\partial q}\right)_0 q_0 E_0\, [\cos\{2\pi(v_0 - v_m)t\} + \cos\{2\pi(v_0 + v_m)t\}] \quad \text{(eqn 61)}$$

The first term represents the Rayleigh scattering effects, and the second term corresponds to the Raman scattering of frequency Stokes and anti-Stokes respectively. If the rate of change of polarizability $(\partial\alpha/\partial q)_0$ is zero, then the vibration is not Raman-active.

As based on the diamond's face-centred cubic lattice with space group Fd3m, it was predicted that singly degenerate first order phonon of symmetry T_{2g} is raman active and appears at 1333 cm^{-1} with a full width at half maximum (FWHM) of 2 cm^{-1} for natural diamond [56]. Lattice strain, particle size and impurity inclusion may cause broadening and shifting of this peak [57]. In CVD diamond, there is often disorder graphitic and/or glassy carbon and amorphous sp^2/ sp^3 carbon mixture present in the lattice, which manifests itself as a weak signal at 1357 cm^{-1} (the "D" band, as attributed to a shear mode of adjacent sheets) and a stronger broad peak at 1580 cm^{-1} (the "G" band, as attributed to stretching of individual sheets). Group theory predicts these two Raman active modes of graphite with space group P63/mmc, both of E_{2g} symmetry.

The scattering cross section and penetration depth of laser light are very different for diamond and non-diamond species, which makes Raman spectroscopy a bulk characterisation tool for diamond (*eg.* sampling depth around 10 micron), but a much more surface sensitive characterisation tool for graphite. For example, an argon ion (Ar^+) 514.5 nm laser has lower sensitivity to non-diamond carbon than a helium-neon laser (HeNe) 633.8 nm laser. Therefore, the measure factors that can be used for the diamond

quality are (a) the ratio of diamond line to non-diamond broad peak height I_D/I_G, and (b) spectral features such as band widths and peak shifts [58]. It is also worth to note that the appearance of a Raman peak near 1150 cm^{-1} has always been an indicator for poor quality CVD diamond or even a coexisting sp^2 phase of transpolyacetylene [59], though the peak has been assigned widely as the signature of nanocrystalline diamond [60].

A Dilor Labram spectrometer was employed for all Raman studies. A X100 objective was used, resulting in a laser spot size of a few μm in diameter. The spectra were referenced against the silicon Raman line at 520.7 cm^{-1}.

2.14 Field Emission

Field emission was arguably first studied by Winkler in the 18th century [61], but Wood was apparently the first who reported the phenomenon in 1897 [62]. However, all of the classical theories had failed completely to describe the occurrence. Only when Fowler and Nordheim proposed the phenomenon in 1928 [63], the puzzle was solved. They were the first who applied quantum mechanics to explain the field emission of electrons from a metal.

Field emission is the process of electrons tunnelling through the potential barrier at a solid-vacuum interface in the presence of a large surface electrical field. This is in contrast to thermionic emission and photoemission. The thermionic emission is intrinsically temperature-dependent which requires high operating temperatures. It also contributes to the background noise as dark current. For photoemission, it is dependent on the intensity of incident photon energy to excite the electrons in the valence band.

According to Fowler and Nordheim, the current density I varied with the applied voltage V (in equation 62), where ϕ is the work function, A is a function of ϕ, B is a constant, and β is a geometrical factor dependent on the electrode configuration, $F = \beta V$, with F is the magnitude of the applied electric field (V/μm)

$$I = A\,(\beta V)^2\, exp\,(-B\phi^{3/2}/\,\beta V) \qquad \text{(eqn 62)}$$

Thus, a plot of $\ln(I/V^2)$ *vs* $1/V$ should be linear and have a slope proportional to $\phi^{3/2}$.

Some other models for this charge transport were also been proposed to yield linear correlations of their respective parameters, such as the Schottky emission model for ejection over a surface barrier (a current-voltage relation of $I \sim exp(aV^{1/2}/kT)$), the space-charge-limited current (SCLC) model for transport through the bulk ($I \sim V$ for low fields, $I \sim V^n$ for high field with $n > 1$) and the Poole Frenkel (PF) hopping model modified by SCLC ($I \sim V^2\, exp(aV^{1/2}/kT)$ [64].

In the absence of an external field, electrons in the highest filled energy level are confronted by a wide potential barrier, which prevent the electrons from escaping into vacuum. The height of such barrier is known as work function ϕ for metals. By applying electric field, the barrier height can be reduced and electrons in the vicinity of the surface will experience a finite potential barrier, enabling the quantum mechanical tunnelling of electron to take place through the sufficiently low and thin barriers (figure 10 a).

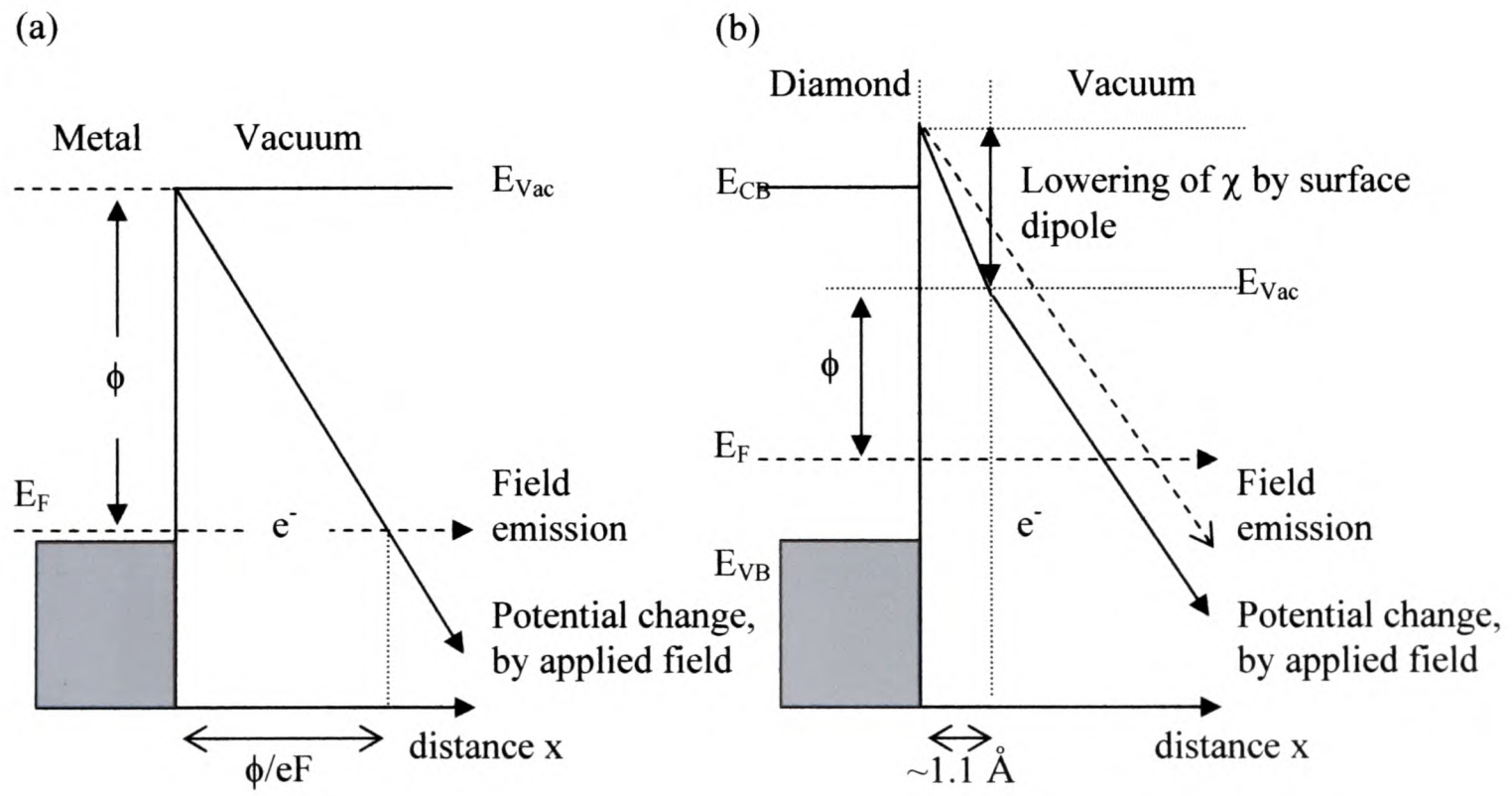


Figure 10. A schematic drawing of the energy level representation for the field emission process. (a) Field emission from a metal and, (b) from boron-doped diamond, showing the lowering of χ by surface dipole

For diamond, the barrier height (or electron affinity) can be altered by surface modification with adsorbates. The treated surface with electropositive species, such as hydrogen and alkali metals are well known for enhancing better emission properties [65,66], both in terms of low threshold voltage and high emission currents. Positive electron affinity of as-grown diamond was converted to negative electron affinity (NEA) with the vacuum level lies beneath the conduction band minimum, which will ease the emission of electron without barrier (figure 10 b). In contrast, the oxidised and halogenated films will induce the opposite effects.

The emission properties could also be crucially dependent on the total emission sites and graphite contents. Higher defective density or poor diamond [67,68], fibrous diamond-like material [69] or discontinuous diamond [70] and nanocrystalline diamond [71,72] has shown to be much better field emitters than high quality, well-faceted, continuous and microcrystalline diamond. The surface morphological effect is illustrated as in figure 11. Electrons are believed to preferably transport through the conducting medium along grain boundaries and defective sites of higher graphitic contents, and thus would increase the total emission in the vicinity of the diamond-graphite-vacuum triple junction.

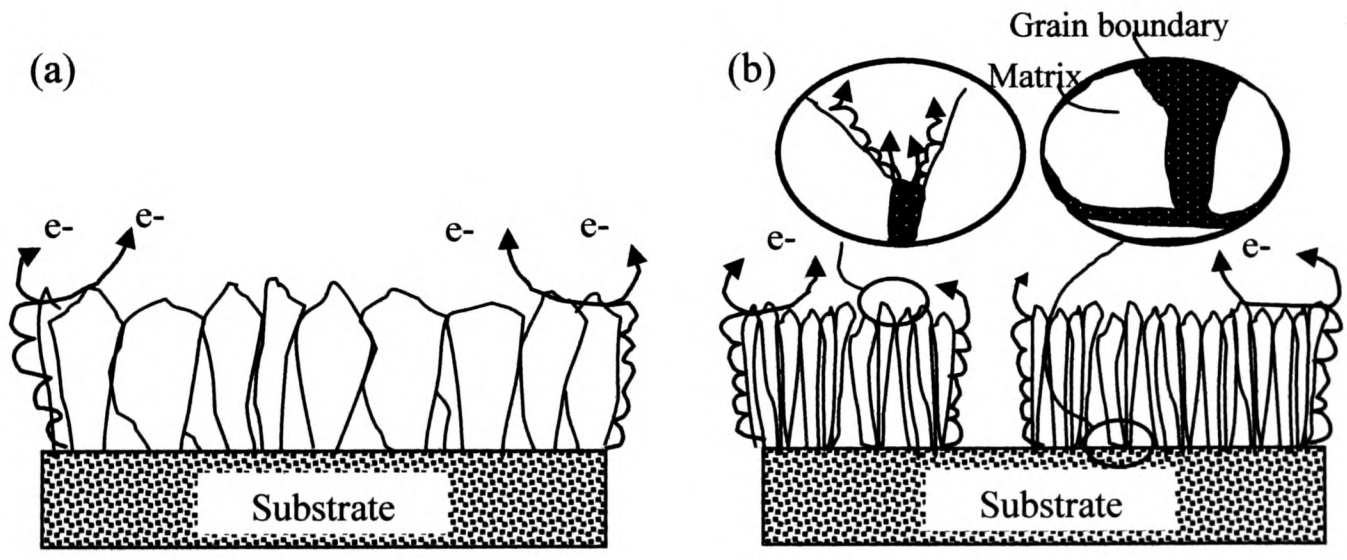


Figure 11. A microstructure model for describing the electron transport path and the resulting field emission mechanism of the CVD diamond with different structural properties; (a) Structure of well-faceted, continuous film with high quality, large grain size and minimal nondiamond carbon content, and (b) structure of non-faceted, discontinuous film with poor quality, small grain size and large nondiamond carbon content

2.15 Growth of CVD Diamond by MWPECVD

2.15.1 Surface Chemistry of CVD Diamond Growth

Chemical vapour deposition (CVD) [73] is the process of thin film formation on a solid surface by the heterogeneous reaction between a reacting gas and a hot surface. Under the operating gas phase mixture of H_2 and CH_4 at optimal surface temperature, diamond growth can take place from the (100)-2 x 1: H and (111)-1 x 1: H surface structures, by employing methyl radicals, acetylene or both as the assumed growth precursors, governing the growth rate and quality [74]. On the basic of growth, the incident hydrogen atoms abstract hydrogen from surface C-H bonds *via* an Eley-Rideal mechanism (with products escape directly into the gas phase), creating dangling-bond sites at which hydrocarbons can adsorb. Further surface H-abstraction and rearrangement reactions will form new C-C bonds and remove the remaining H atoms, incorporating the adsorbed species into the diamond lattice. The main growth process of diamond proceeds through (i) nucleation, (ii) growth and (iii) formation of surface morphology.

(a) Nucleation

A surface nucleation process is initiated by the impingement of atoms upon the deposition substrate from the gas phase and become adsorbed onto the surface. The adatoms may re-evaporate, diffuse over the surface, diffuse into the substrate or bond to other surface atoms. With the increasing of time, the surface concentration of the adatoms increases at the substrate surface and clusters will be formed *via* the free growth of the individual seed crystals. Diamond was also suggested to have nucleated in the vapor phase [75] or even with the possible embryos formation of several hydrocarbon cage compounds [76] *e.g.* adamantane, tetracyclopentadecane and hexacyclopentadecane or ring compounds [77] *e.g. cis* boat-boat bicyclodecane and *trans* boat-boat bicyclodecane. Defects induced phenomena, such as mechanical scratches, grain boundaries, dislocation outcrops, bias

enhancement, ion implantation, *etc* can also mediate further growth of the crystal *via* the arising re-entrants from the intersection of twin bands or stacking faults with the surface, acting as favourable sites for nucleation of new layers [78].

The presence of additional gaseous impurities can also increase nucleation densities, inducing rapid decomposition of gases and nucleation of small clusters which serve as seeds for the subsequent deposition of carbon on their surface [79], such as in the presence of halogen/hydrogen mixtures [80], oxygen [81], SiH_4 [75], B_2H_6 [75] and CO_2 [82]. The nucleation density critically influences the thickness, crystallite size, homogeneity, morphology, adhesion and surface roughness of deposited diamond films. A high nucleation density allows a complete film of smaller grains to form within a relatively short time, and leads to a smoother film surface than those grown at lower nucleation densities [83]. A low nucleation density may give rise to large crystallites and a discontinuous film within a limited time.

(b) Growth

The reactants, products and reactive species are transported throughout the reactor by diffusion and convection (figure 12). The stable clusters formed in nucleation stage will provide suitable sites for growth either from the continued migration of single adatoms or from the direct impingement of atoms from the gas phase, causing the sizes of clusters to increase almost uniformly until the crystals approach each other. For processes at higher pressure, a stagnation layer is formed just above the deposition surface through which the reacting species must diffuse. But at low pressure, the near surface chemical environment may proceed *via* adsorption, diffusion, reaction and desorption of various species, leading to the nucleation of diamond particles, suppression of graphitic (or sp^2) carbon, and ultimately the growth of a continuous diamond film.

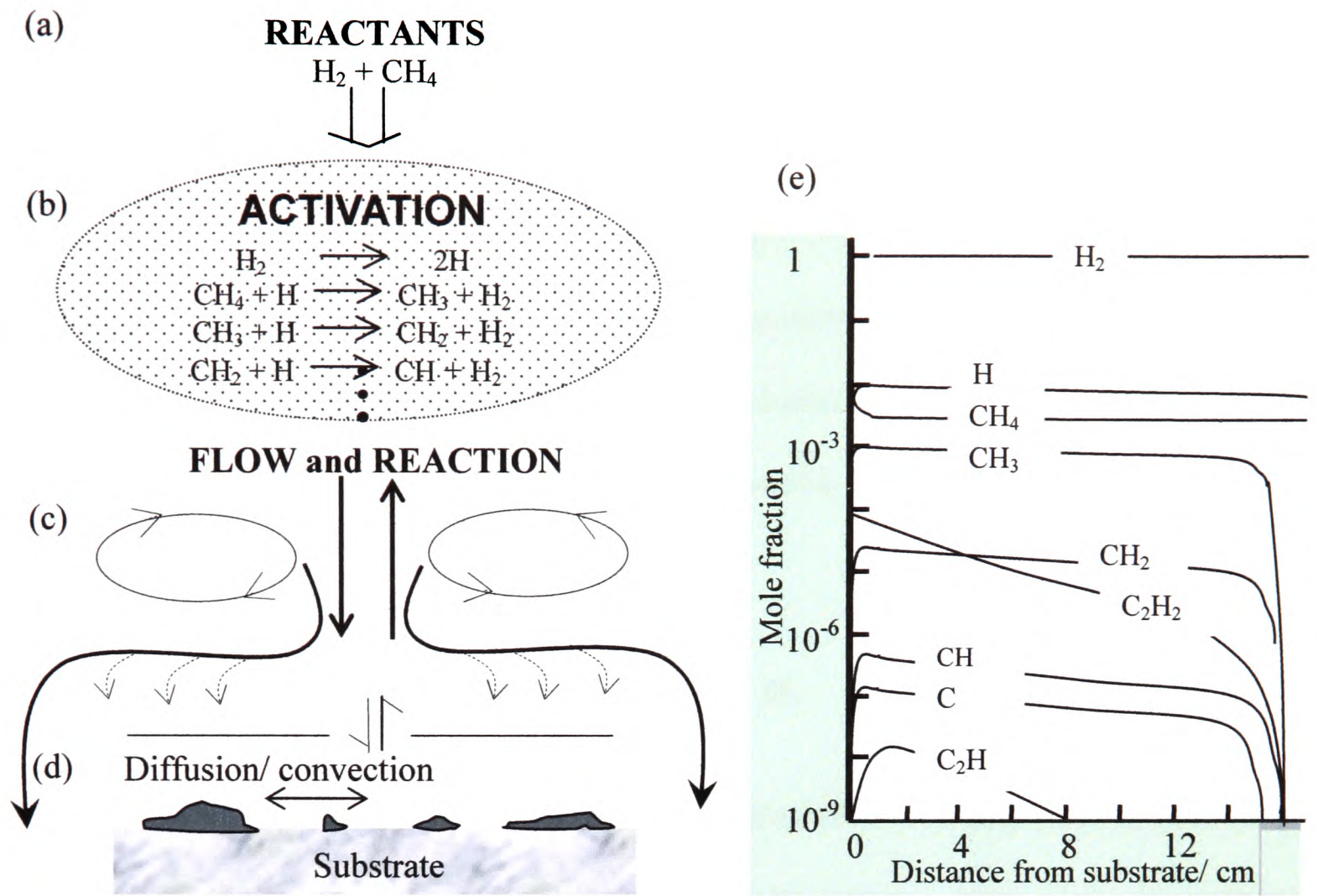


Figure 12. Schematic diagram of the principal elements in the complex diamond CVD process; (a) flow of reactants in to the reactor, (b) activation of the reactants by thermal and plasma processes, (c) reaction and transport of the species to the growing surface, and (d) surface chemical processes depositing diamond and other forms of carbon; (e) the gas phase species mole fraction profiles for CH_4 (0.5 %) in a H_2 flow containing 1 % atomic hydrogen, after [78]

The gaseous chemistry in CVD diamond is driven by the reactions of atomic hydrogen with hydrocarbon species and reactions among the hydrocarbon species. The hydrocarbon reactants would be coupled by hydrogen transfer reactions and rapidly equilibrate on the surface with their distribution depends directly on the atomic to molecular hydrogen ratio. Subsequent reactions among hydrocarbon species may be near or far from equilibrium depending upon pressure and residence time since hydrocarbon concentrations are quite low (figure 12 e). The chemical composition for the flux of species arriving at the deposition surface may differ from the bulk gas well away from the surface due to chemical reactions caused by the temperature and concentration gradients in the boundary layer. Other important roles that played by atomic hydrogen are (i) etching

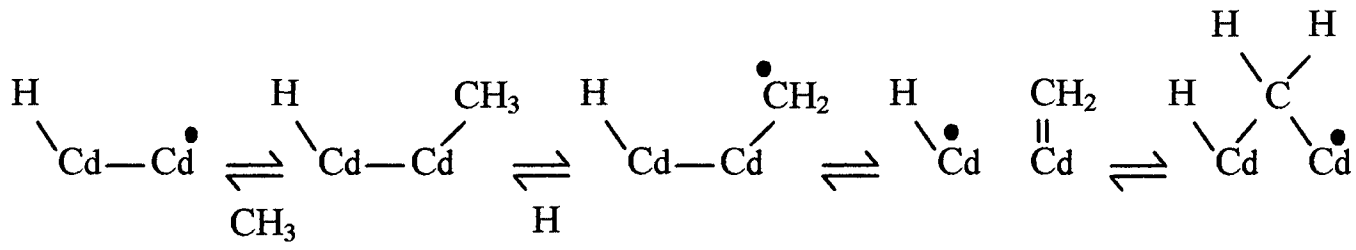
non-diamond phases that can be formed simultaneously with the diamond phase, (ii) stabilizing the surface by saturating the surface dangling bonds (sp^3 configuration of the growth sites instead of a sp^2 configuration), (iii) reducing the dimension of the critical seeds, leading to a reduction in their surface energy, (iv) generating growth sites at the surface by H-atom surface abstraction, and (v) prohibiting the formation of aromatic hydrocarbons such benzene, which can lead to non-diamond phase formation.

The first initiation step involves the activation of a surface carbon by the H abstraction is shown in equation 63;

$$C_dH + H \rightarrow C_d\bullet + H_2 \qquad \text{(eqn 63)}$$

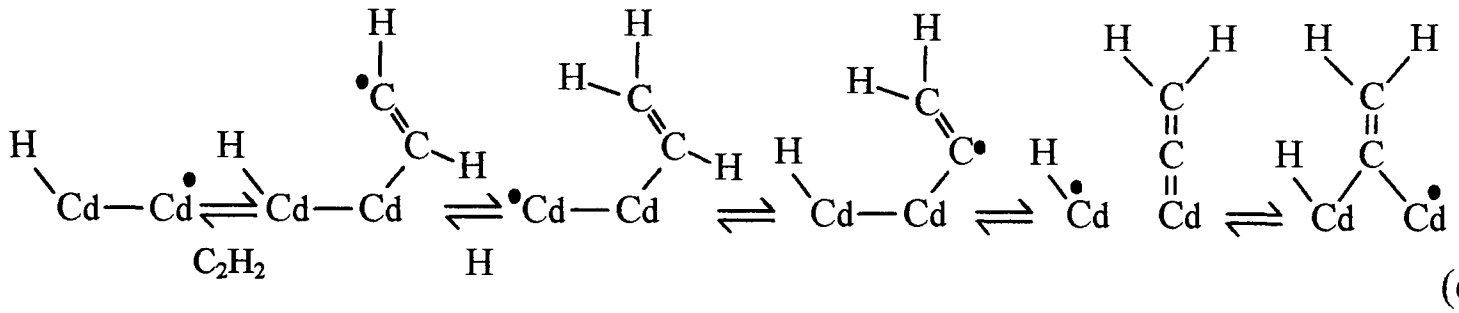
This step is followed by the addition of methyl or acetylene molecules [84,85], and is later activated by the H abstraction for further propagation process. Most of the propagation steps would involve the facile hydrogen abstraction and re-attachment, the occasional chemisorption of the hydrocarbon species at a radical site, unimolecular desorption of hydrocarbon species singly bonded to the surface at higher temperatures, and facile radical-radical reactions on the surface.

(i) methyl addition, through the successive attachments of CH_x ($x < 4$) species (methyl radicals) at radical sites and reactivated by H abstraction (equation 64).



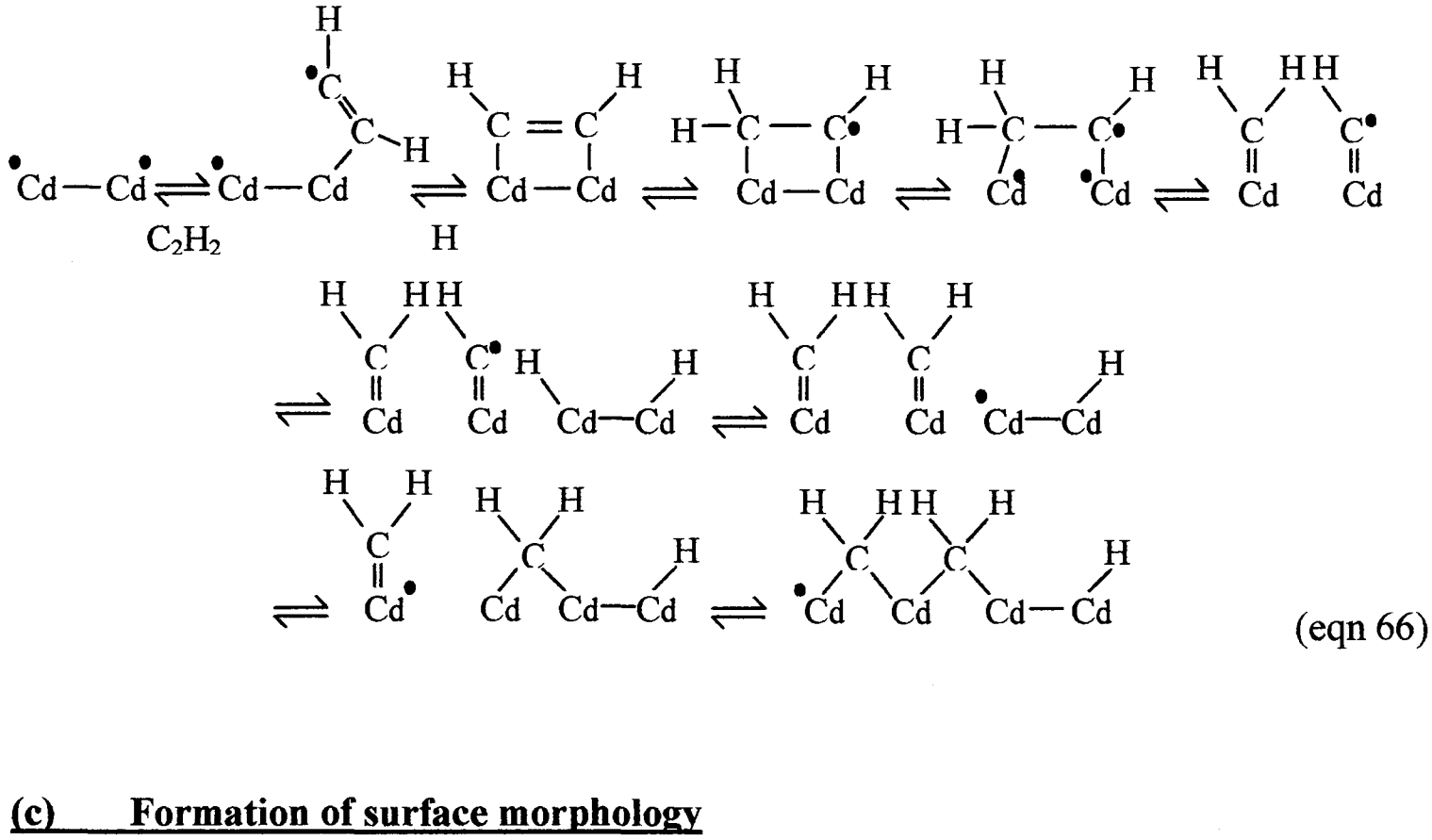
(eqn 64)

(ii) acetylene addition, with C_2H_2 acts as the principal precursor for adventitious sp^2-bonded carbon, producing more defective diamond than CH_3 in the form of point defect and dislocations which are likely to cause cracking or graphitisation [86].



(eqn 65)

or proceed *via*



(eqn 66)

(c) Formation of surface morphology

A secondary growth involves the growth on primary grain faces and the evolution of secondary particles, with the fusion and absorption on their particle faces. With the increasing of growth time, the average crystal size increases as the films grow and at the same time, the size distribution broadens. The feasibility of specific transformations of diamond surface could critically depend on the change in entropy due to factors such as adsorption or desorption, steric hindrances, and transition-state configurations. Various classes of morphological structures are determined by the concentration of hydrocarbon gas in the reaction gas and substrate temperature. Normally, as refer to figure 13, at low temperature (high hydrocarbon supersaturation) with high methane concentration, crystals with {111} faces are favoured and at high substrate temperature (low supersaturation) with low methane concentration, cube faces are dominant [87,88].

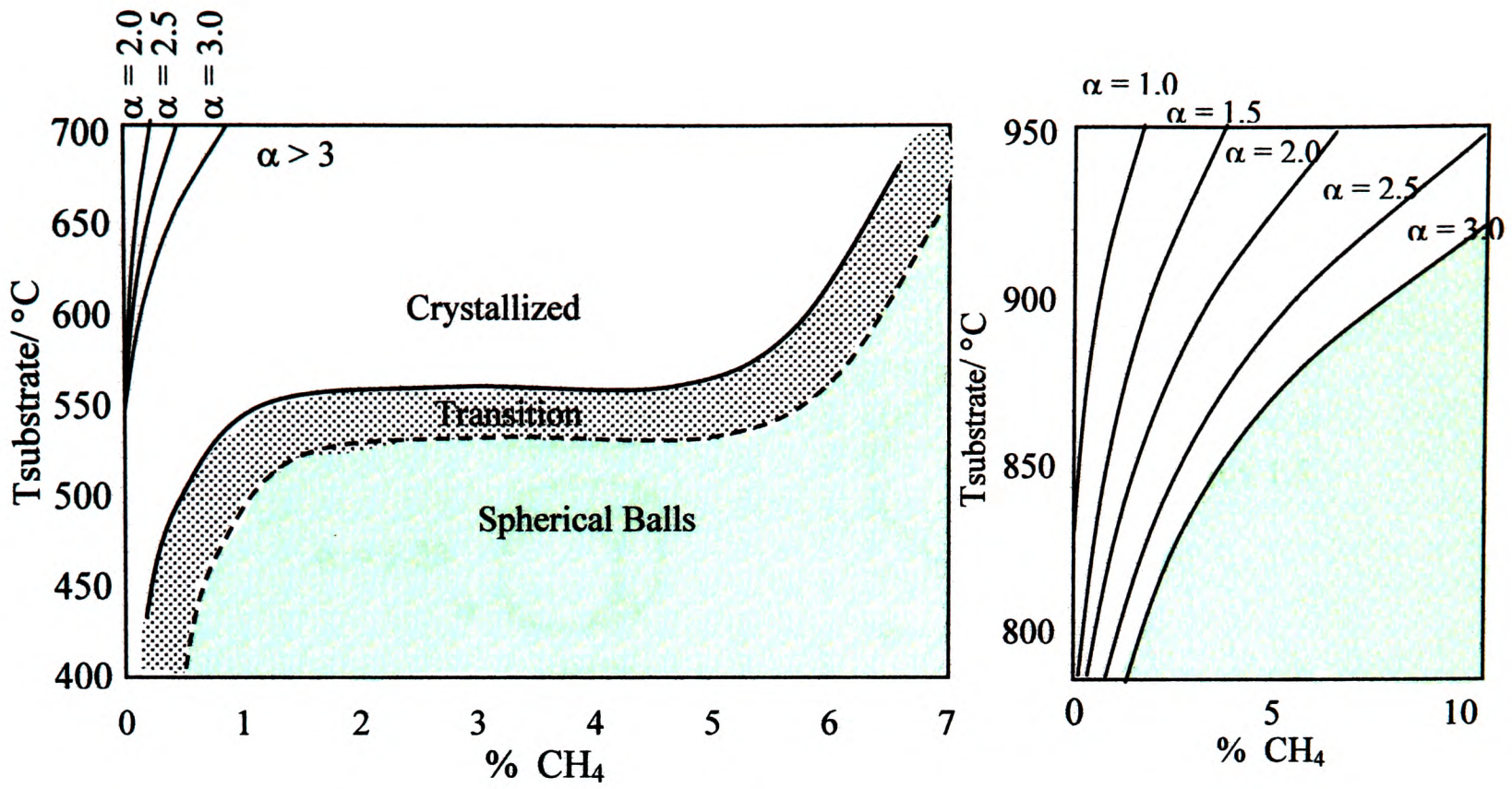


Figure 13. Evolution of the diamond films morphology as function of % CH_4 and substrate temperature, with the figure on the right showing the expanded region of higher substrate temperature

The evolution of the morphology and texture of diamond is illustrated by van der Drift's model [89], which is based on the principle of "survival of the fastest" or the model of "evolutionary selection", stating that only those crystals with a rapid growth direction perpendicular to the substrate surface will survive, whereas crystals with all other orientations will be gradually buried. According to the model as shown in figure 14, a continuous transition is expected in its vertical growth rate from a <100> texture for cubic crystals with $\alpha = 1$, a <110> texture for cubo-octahedral crystals with $\alpha = 1.5$, and to a <111> texture for octahedral diamond crystals $\alpha = 3$. However, the <110> textures could develop for $1.5 \leq \alpha \leq 3$ due to the modification by twin formation [90,91]. In a theoretical study, Wild *et al.* [92] have defined α factor as $\alpha = 3^{1/2}$ (V{100}/V{111}), where V{100} and V{111} are the growth rates of the <100> and <111> directions, respectively. The calculated [93] and experimental [90,93] results show that <110> is the direction of fastest growth with the film surface consisting of {111} planes. However, the film texture and

surface morphology are critically dependent on the growth conditions. Under conditions where {100} or both {100} and {111} planes develop, the preferred orientations that different from the (110) fiber texture may form.

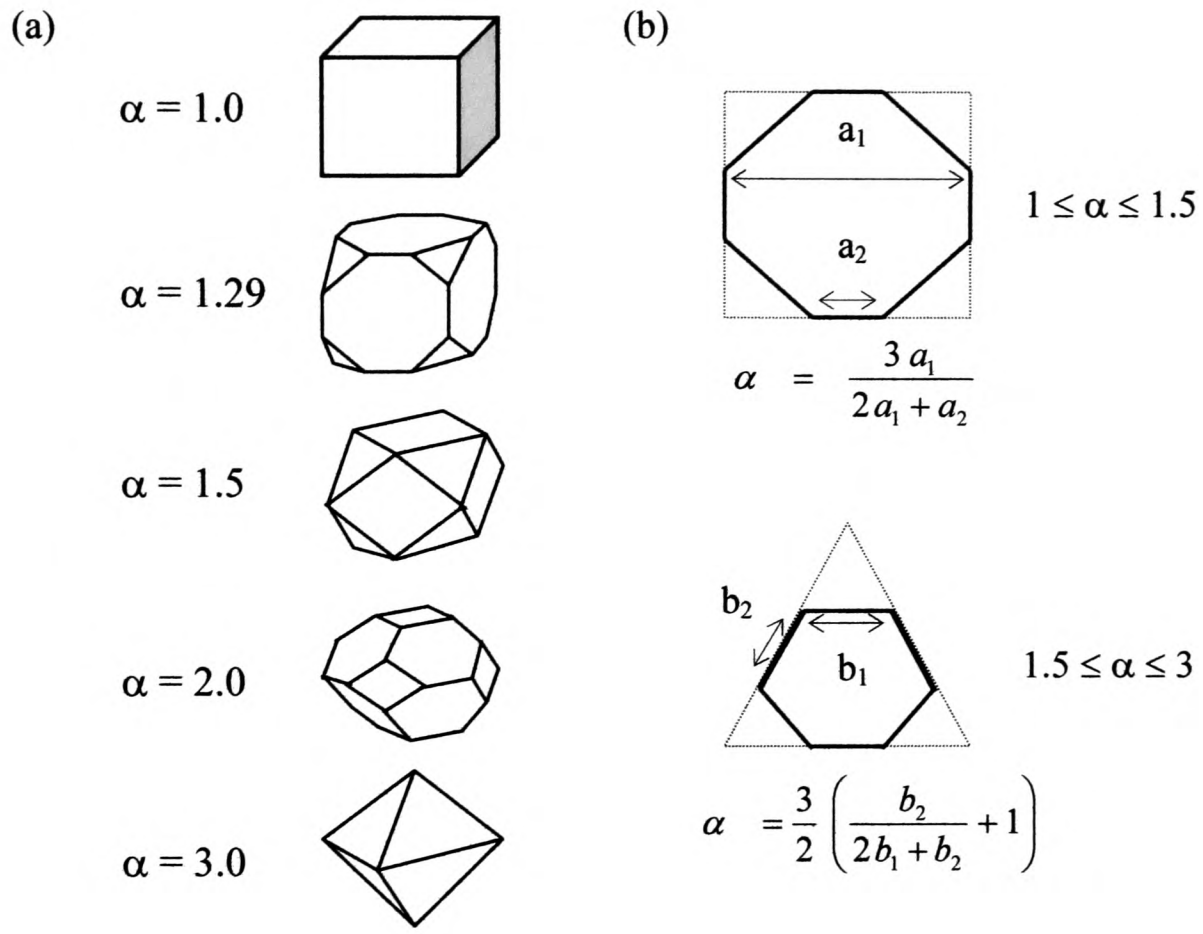


Figure 14. (a) Growth forms of diamond crystals for growth parameters α = 1.0, 1.29, 1.5, 2.0 and 3.0 (b) A (100) facet for 1 ≤ α ≤ 1.5 and a (111) facet for 1.5 ≤ α ≤ 3, which can be used to determine α, after [94]

According to the principle of *evolutionary selection* [95], the development of fiber textures is a result of the growth competition between randomly oriented diamond crystals, and the resultant direction of fiber axis coincides with the direction of fastest growth. With the increasing of film thickness, both crystal size and size distribution increase, and the degree of texture improve with the concomitant reduction of overall misorientation. However, due to the lack of surface diffusion and re-evaporation at the diamond film, *morphological instabilities* occur in high rate CVD of thick diamond films (typically > 20 μm) [96]. The morphological instabilities are magnified during sustained growth as a result of competitive shadowing, nutrient starvation/ overfeeding, orientation

effect and anisotropic growth of crystals as well as surface chemical reactions between the growing diamond surface and oxidizing species, causing not only extreme variation in crystal size, but also incorporation of voids and non-crystalline phases in diamond films. Two approaches have been suggested to overcome the morphological instabilities by increasing the nucleation density and by introducing periodic interruption of a growth process for each 20 μm. This is done by deliberately depositing very thin diamond-like carbon films on the surface in order to stimulate the re-nucleation on diamond for recommencing further growth.

2.15.2 Growth of CVD Diamond

Microwave is an electromagnetic wave having a wavelength from 300 mm to 10 mm (1 GHz to 30 GHz), generated in a high frequency generator (magnetron) which is tuned at a fixed oscillating frequency whereas a **plasma** is a gas containing charged and neutral species, including some or all of the electrons, positive ions, negative ions, atoms and molecules at very high temperature [97]. Plasma is often referred as the *fourth state of matter*, since it occurs by transmitting energy (electric or heat) to a gas *via* an electric field. Under plasma discharge at low pressures (low collision frequencies), the electrons can accumulate sufficient kinetic energy thus having a higher probability of producing excitation or ionization during collisions with heavy particles. Thus, higher dissociation of gas can be promoted, increasing the concentration of atomic gases.

Ever since 1970s, microwave plasma had been applied as another alternative to other low pressure diamond growth methods, such as hot filament, DC discharge, DC plasma jet combustion flame and RF-assisted CVD [78]. Microwave plasma-assisted CVD has proved to enhance significantly the dissociation of molecular hydrogen into atomic hydrogen and to activate hydrocarbon radicals into promoting diamond formation. The excitation frequency of typically 2.45 GHz for microwave plasma CVD is used to

oscillate and to accelerate electrons or ions to energies of 50 – 1000 eV in the vicinity of the deposition or etching substrate, and the collision between electrons with gas atoms or molecules could further generate higher ionization fractions [97,98]. The evolution of MPACVD accordingly to the excitation frequency is shown in table 1.

Table 1. The time evolution of MPACVD according to the excitation frequency of the plasma

Method	**Reference** *after* [78]
915 MHz plasma	Miyake *et al.* (1988)
2.45 GHz low pressure plasma	Kamo *et al.* (1983, 1990); Badzian *et al.* (1986); Bachmann *et al.* (1988a, b); Smith *et al.* (1992); Ishibori & Ohira (1990); Jiang & Klages (1993); Liou *et al.* (1988); Chang *et al.* (1988)
2.45 GHz thermal plasma torch	Mitsuda *et al.* (1989)
2.45 GHz magnetized (ECR) plasma	Kawarada *et al.* (1987); Suzuki (1989); Yuasa *et al.* (1991)
8.2 GHz plasma	Aklufi & Brock (1989)

Compared to other low pressures growth methods, diamond can be grown at linearly controllable growth rates with good stability of the deposition parameters under microwave plasma assisted CVD. The MPACVD also allows feasible mixtures of different reactants, and a wide area of deposition can be achieved on a wide variety of substrates. With a higher power input, higher gas temperatures of plasma can result in higher deposition rates [78]. However, the difficulty to deposit diamond on three-dimensional substrates is the main drawback of this growth method.

Diamond films are grown on different substrates, using microwave plasma reactor (2.45 GHz; Penta Science & Technology Ltd PD01A) with a 2 kW microwave generator as shown in figure 15. The chamber is equipped with three channels of mass flow gas controllers to accurately control and to measure process gas flow, *i.e.* hydrogen (0 - 200 sccm), methane (0 - 100 sccm) and other gases (0 - 20 sccm). Vacuum pressure is

controlled accurately from 1 – 100 Torr by throttle valve and is measured by capacitance manometer gauge.

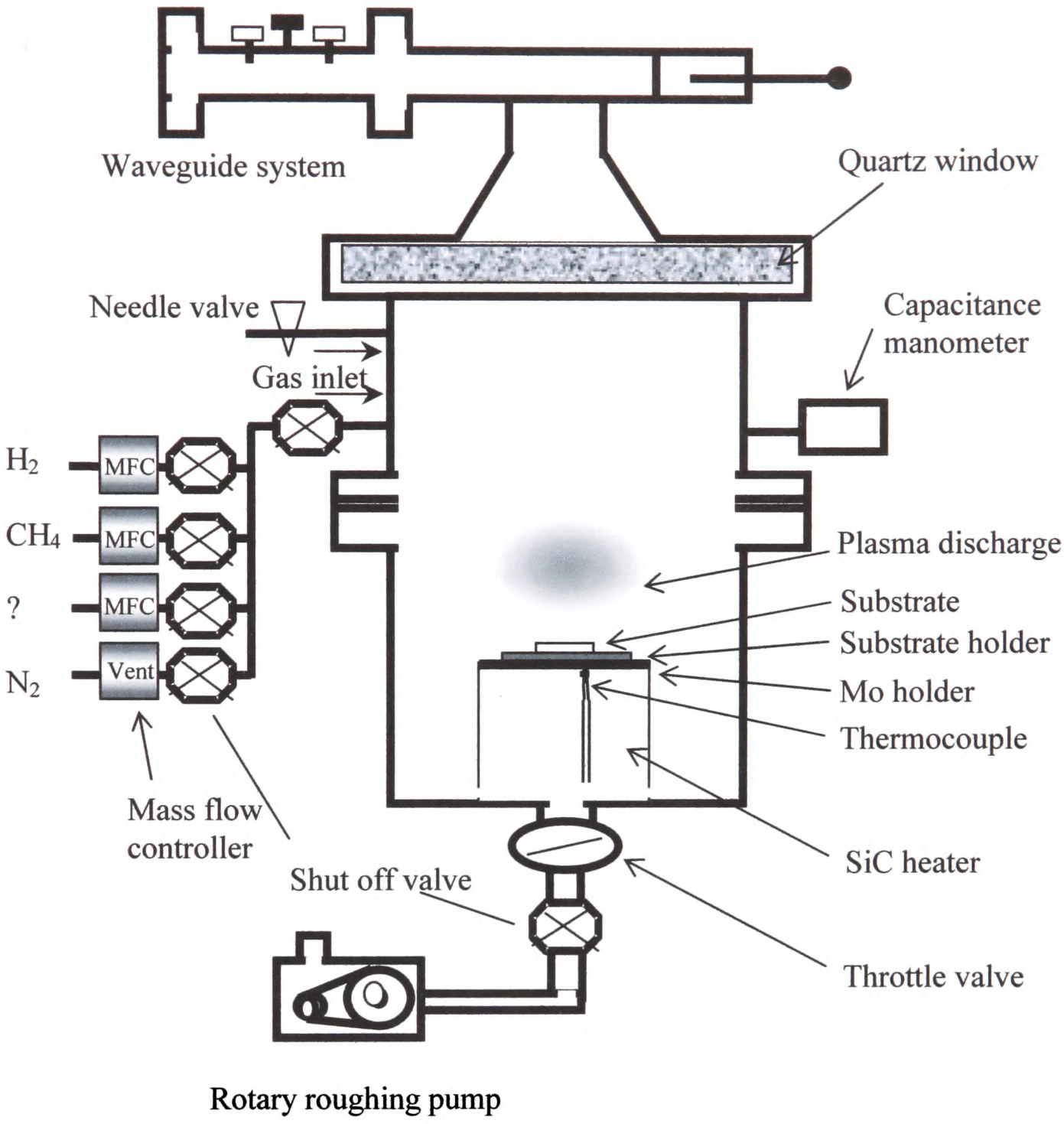


Figure 15. Schematic diagram of microwave vacuum system and associated components

The reactor consists of a cylindrical stainless steel chamber of 20 cm inner diameter. The microwave is coupled from the magnetron waveguide (WG9A waveguide and UDR26 flange output) into the cavity *via* an axial antenna, fitted with the incident and reflected power measurement and controllers. A discharge "plasma ball" is generated above the substrate. Mo block of 30 x 30 x 4 mm size or graphite block of 50 x 50 x 5 mm size was used as a substrate holder, which was attached on the Mo circular platen of

10 cm diameter placed on the SiC heater. These substrate holders were cleaned prior to new growth experiment. During the growth process, substrate temperature was monitored by a thermocouple in contact with the backside of the Mo platen. The Mo platen and also the substrates were grounded all through the diamond film deposition.

Film deposition was carried out for 20 - 40 hours where the total deposition was divided into initial and growth stages. The initial and growth stages are the period up to 1 hour and the period from 1 hour to the end of the deposition, respectively. The samples were deposited in a mixture of CH_4 and H_2 at a total pressure of 45 Torr with a substrate temperature of 700 °C. The H_2 flow rate was kept constant at 200 sccm during deposition in both initial and growth stages. As a result of preliminary experiment, optimum CH_4 flow rate in the initial and growth stages was found to be 6 sccm and 3 - 4 sccm, respectively, for the growth of textured diamond films on the scratched Si substrate placed on the Mo block. In the present work, therefore, all experiments were carried out under the same condition as for the CH_4 flow rate in the initial and growth stages in order to compare the results with the textured diamond film grown on scratched Si substrate placed on the Mo block. The input microwave power was kept constant at 1.5 kW.

In this work, undoped diamond was successfully grown on various substrate materials of different sizes and shapes, including tungsten (15 x 15 mm size), molybdenum (15 x 15 mm size), *n*-type Si (100) (10 x 12 mm size), nickel (10 x 15 mm size), tantalum (15 x 15 mm size) and sapphire (20 x 20 mm size). All of the substrates were pre-scratched by mechanical polishing with diamond particles (1-3 μm Grade 1-KD-C1, otherwise stated) in order to enhance nucleation. The substrates were placed on the substrate holder made of Mo or graphite. The overall growth rate was ~1 micron per hour.

2.15.3 Characterization of CVD Diamond

Typical SEM images of diamond films grown under various conditions are shown in figure 16. Figure 16(a) and 16(b) show the surface morphologies of diamond films grown for 15 hours and 30 hours respectively, on the well scratched Si (100) substrates placed on the Mo holder at CH_4 flow rate in the growth stage 4 sccm, revealing that the surface consists almost exclusively of diamond crystallites with smooth crystalline facets. Higher surface coverage and bigger size of crystalline were obtained with the increase of growth period. Twinned crystals, multiple twins, and minimal secondary nucleation growth were also being observed in these films. Smaller (100) diamond crystals were observed for the growth stage set at CH_4 flow rate of 3 sccm, figure 16(c). On the other hand, figure 16(d) and 16(e) show the surface images of diamond films grown for 20 hours respectively on the Si (100) and W substrates placed on the graphite holder, with CH_4 flow rate in the growth stage of 4 sccm. The well faceted morphology disappeared and the particle size of the film decreased, as shown in figure 16(d), by which its morphology is almost identical to the films reported as nanocrystalline diamond [99,100]. The average grain size was about 400 nm for the film grown on the Si (100) substrate placed on the graphite block.

It has been reported recently that the bias enhanced nucleation (BEN) technique is effective for the film formation on the W substrate [101]. The W substrate used here was not pretreated by scratching with diamond paste. Without utilizing BEN technique, deposits were localized on the W substrate placed on both Mo and graphite holders. On the W substrate placed on the graphite, the surface consists of ragged deposits with small facets, as shown in figure 16(d). SEM in figure 16(f) shows the diamond grown on negatively bias treated Si (100) for 2 hours with an applied voltage of – 120 V. The Si substrate has clearly shown that the rough surface is randomly deposited with ball-shaped diamond particles range in between 10 - 30 μm. The BEN is believed to enhance the nucleation and deposition of diamond by the combination of forming

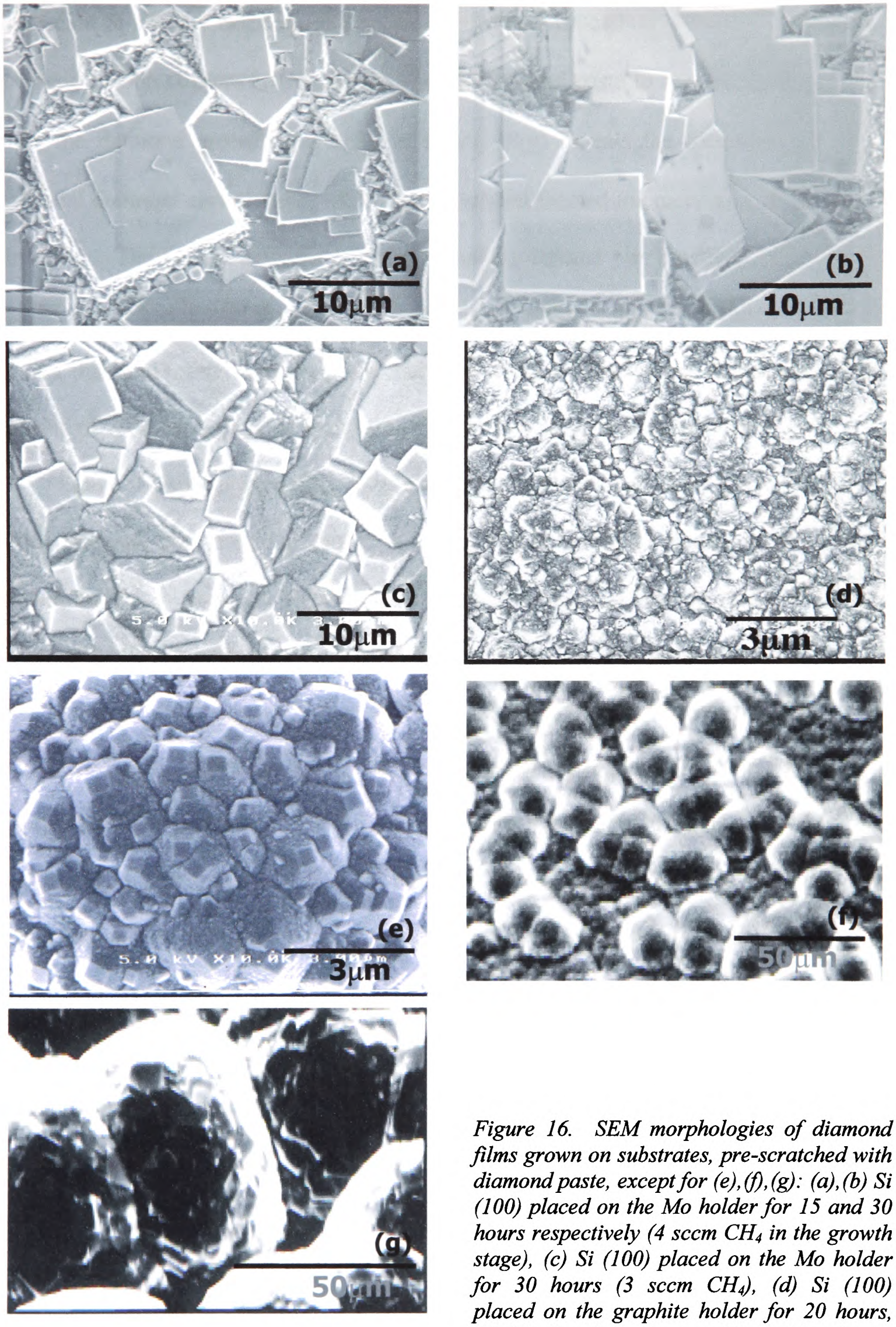


Figure 16. SEM morphologies of diamond films grown on substrates, pre-scratched with diamond paste, except for (e),(f),(g): (a),(b) Si (100) placed on the Mo holder for 15 and 30 hours respectively (4 sccm CH_4 in the growth stage), (c) Si (100) placed on the Mo holder for 30 hours (3 sccm CH_4), (d) Si (100) placed on the graphite holder for 20 hours, (e) W placed on the graphite holder for 20 hours, (f) Si (100) placed on the Mo holder under BEN for 2 hours and (g) Si (100) placed on the Mo holder for 30 hours (4 sccm CH_4)

heteroepitaxial SiC on the Si substrate, selective etching of Si in the SiC network, filling the vacant Si sites by carbonaceous ions and adding hydrocarbon radicals to the oriented sp^3 bond carbon clusters [102]. Without using diamond paste to scratch the Si substrate prior the diamond growth, the SEM in figure 16(g) reveals the formation of 50-μm spherical diamond crystal balls, with {100} diamond faceted microcrystals, wrapping the structures. The lack of smooth surface morphology formed was mostly attributed to the insufficient nucleation of diamond on Si with large effect of lattice mismatch in between Si and diamond. The nucleation was believed to have started from the nanostructured seeding of very fine carbon or even SiC with very low nucleation densities [103].

Figure 17 shows examples of Raman spectra of diamond films grown on: (a) Si (100) substrate placed on the Mo holder, (b) Si (100) substrate placed on the graphite holder, and (c) W substrate placed on the graphite holder. As was expected, in the case using the Mo block as a substrate holder, a sharp 1332 cm^{-1} peak is apparent, indicative of good-quality CVD diamond [Raman spectrum (a)]. Raman spectra from the films grown on the W and Mo substrates placed on the Mo holder were similar to the typical Raman spectrum (a) for undoped diamond film. The diamond grown on Si(100) without being pre-scratched with diamond paste and diamond grown on Si(100) under BEN show the same Raman feature for diamond (Raman not shown), except for wider FWHM at 1332 cm^{-1} peaks and smaller I_D/I_G ratio (see Table 2). On the other hand, in the case using the graphite block as a substrate holder, the Raman spectrum was drastically changed. The most prominent features exhibited by the Raman spectrum (b) are the weak 1332 cm^{-1} diamond peak and broad bands centered near 1350 and 1550 cm^{-1} attributable to sp^2-bonded carbon present at the grain boundaries. Special attention should be paid to the additional peak at approximately 1140 cm^{-1}, which is caused by size effect of the nanoscale diamond grains [59], and provides more evidence for the nanocrystalline nature of the film grown using the graphite holder. The Raman spectrum (c) from the film grown

on the W substrate placed on the graphite holder was similar to the Raman spectrum (b) for the nanocrystalline diamond film.

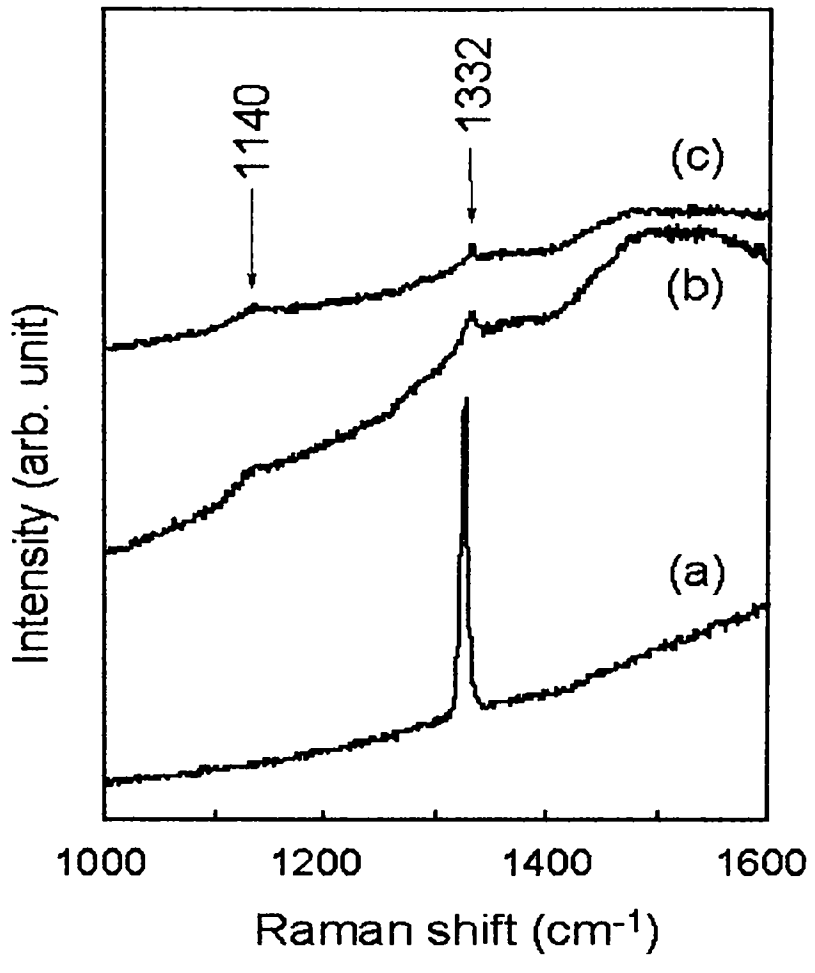
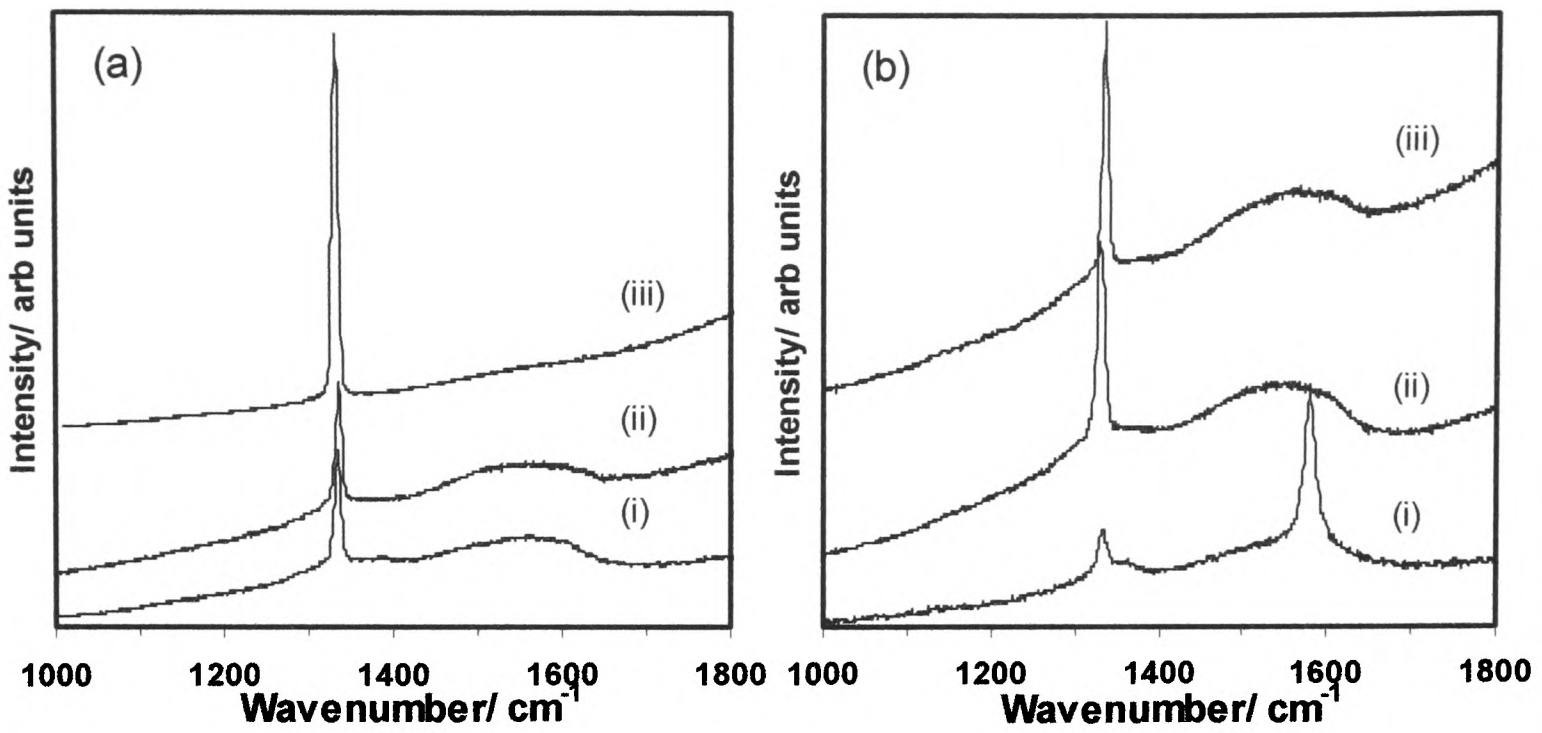


Figure 17. Typical Raman spectra from the diamond films grown on: (a) Si (100) placed on the Mo holder, (b) Si (100) placed on the graphite holder, and (c) W placed on the graphite holder. All spectra were excited with 514.5 nm light

Raman spectra in figure 18(a) and 18(b) show the different diamond growth stage on Mo and Ni substrate under the typical growth condition; on top of the Mo substrate holder and at a flow rate of CH_4 of 4 sccm. The growth on Mo substrate shows very well growth manner of diamond as the growth period increases, with an increase in the intensity of 1333 cm^{-1} diamond peak and a decrease in the broad peak around 1500 cm^{-1}. During the early period of diamond growth on Ni, Raman (figure 18 b) shows the graphitic type of atomic structure, very similar to carbon nanotubes. The characteristic features are: a high intensity of "G" graphite peak at 1582 cm^{-1}, a low contribution of a disorder-induced "D" peak at 1350 cm^{-1}; and intense narrow band of two-phonon scattering at 2714 cm^{-1}. SEM (c) shows the image of the nanostructured material. It is believed that the high content of CH_4 in the nucleation stage, coupled with the presence of

Ni as a good catalyst, enhances the growth of such well-structured nanomaterial [104,105]. However, with increasing growth period, the non-diamond will be etched away by atomic hydrogen and favour the diamond growth, though non-diamond properties could still be embedded in the diamond lattice, as revealed with low I_D/I_G of 0.33.



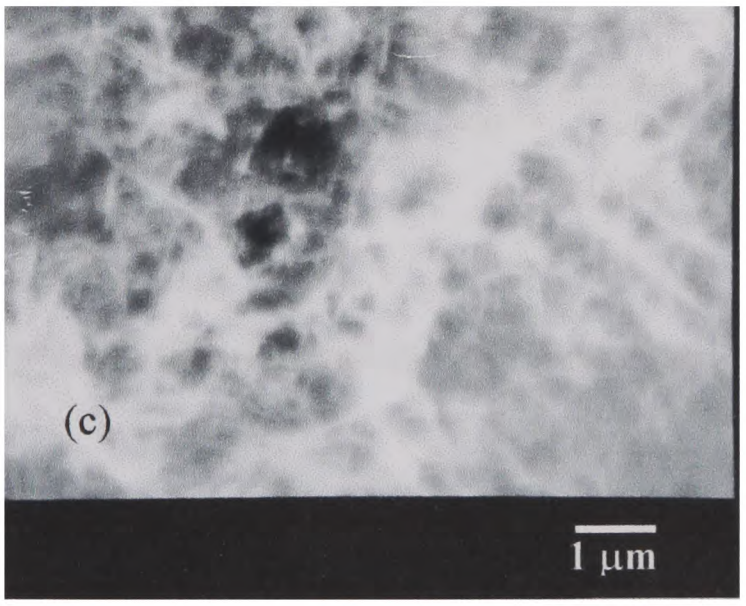


Figure 18. Raman spectrum at varying deposition period of diamond on (a) molybdenum plate and (b) nickel foil; (i) 8 hrs, (ii) 20 hrs, and (iii) 30 hrs; (c) SEM shows the image of sample grown on Ni substrate for 2 hrs

Table 2. Raman parameters of diamond films on various substrates

Substrate	FWHM/ cm^{-1}	I_D/I_G	Adhesiveness to substrate
Single crystal	3	∞	-
Si (with scratched)	5.89	6.59	Good
Si (non-scratched)	8.67	4.64	Good
Si (BEN)	10.31	2.3	Good
Mo	8.35	86.3	Good
W	7.66	1.68	Good
Ni	11.61	0.33	Poor
Ta	8.16	1.13	Poor
Sapphire	7.93	3.52	Poor

Most of the diamond growths show continuous and dense films on different substrates except for Ni, Ta and sapphire. The fracture might occur during the cooling process because of the difference in thermal expansion between diamond and the substrates. Table 2 shows the FWHM of the peak at 1332 cm^{-1} and the intensity ratio of the peaks that are indicative of sp^3 and sp^2 bonding (I_D/I_G). The adhesiveness of diamond bonded to the substrates was tested by scratching the grown surface with diamond-coated pen.

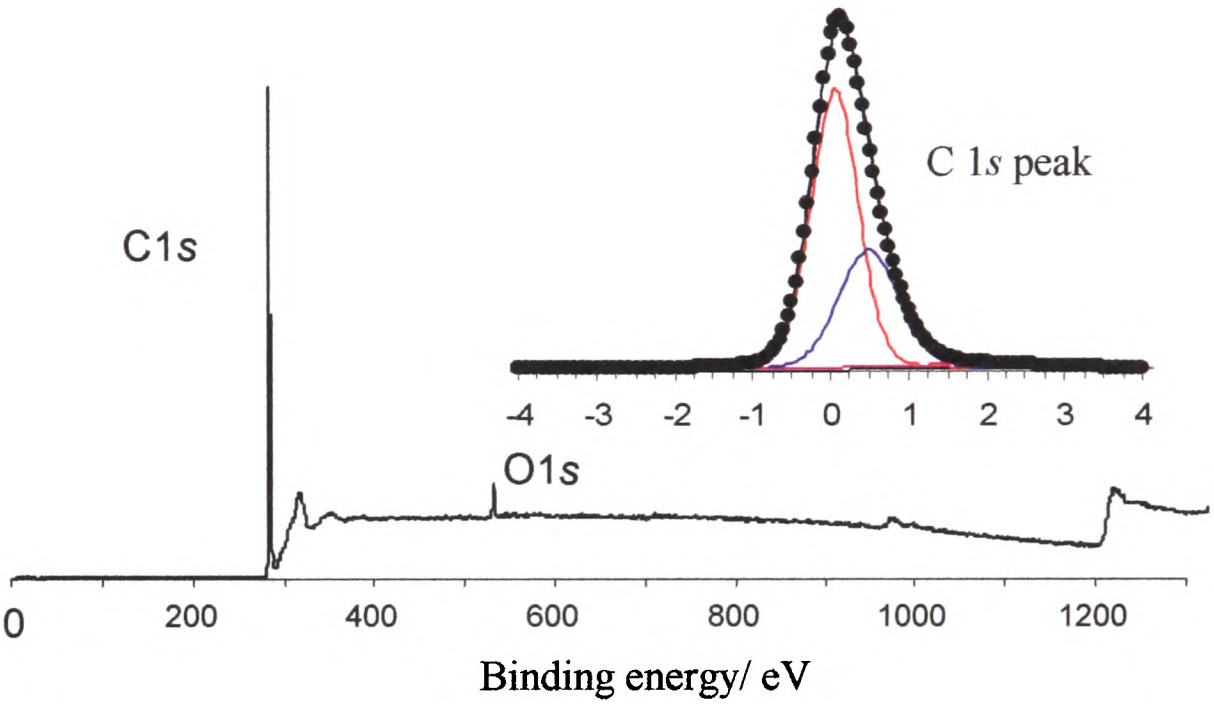


Figure 19. XPS wide scan spectra, with inset showing the deconvoluted C 1s core-level

Figure 19 shows a XPS wide scan spectrum of a typical as-grown diamond film. The bulk C 1*s* peak for the as-grown sample is positioned approximately at 284.0 eV, with a deconvoluted peak at + 0.5 eV being attributed to polyhydride configuration bonded (-CH_x, $x \geq 2$) to carbon [106]. Apart from a small amount of oxygen, the diamond surface is clean of metal or inorganic impurities, indicative of good quality diamond. The shoulder on the higher binding energy side of the C 1*s* peak can be attributed to adsorbed hydrocarbon species.

2.15.4 Summary

The surface condition of chamber wall has shown to influence on the diamond growth, especially on the growth rate. In the case that the surface of chamber wall was clean, diamond growth rate was as low as 0.4 μm/hour and an amount of non-diamond phase was included even in the film grown on the Si substrate placed on Mo holder from the Raman spectrum. In this work, therefore, the surface of chamber wall was well passivated by repeating growth runs for 50 hours totally in advance. As a result of passivation of chamber wall with amorphous carbon [107], films were obtained reproducibly and the typical diamond growth rate for the film on the Si substrate placed on the Mo holder was about 1 μm/hour.

Results in figures 16 and 17 indicate that the behaviour of diamond precursors would be influenced by the substrate holder materials, even if the external parameters for diamond growth (process gases, substrate temperature, input power, bias, and so on) are unchanged. Typical way to obtain nanocrystalline diamond films from MWPECVD employing conventional CH_4 and H_2 mixtures is simply to increase the CH_4 flow rate ratio more than 10% during deposition [108,109]. In this case the incident flux of C_2 radicals, which are reported to be important species for nanocrystalline diamond growth [8], would increase on the growing surface to enhance the secondary nucleation. Another way reported recently to fabricate nanocrystalline diamond films is to apply positive or negative bias to the substrate during deposition [110,111]. Applying bias to the substrate will change the flux of charged particles arriving at the growing surface, increase the substrate temperature by electron or ion bombardment, or increase the defects and secondary nucleation sites on the growing surface. In our case, both substrates and substrate holders were grounded through the experiments in order to make the influence of ions incident on the substrate common in all cases. On one hand, secondary products such

as C_2 and CH_n radicals from the graphite surface will possibly influence on the diamond growth.

2.16 References for Chapter 2

[1] J.M. Walls (*ed.*), Methods of Surface Analysis, Cambridge University Press, Cambridge, 1989

[2] I. Langmuir, *J. Am. Chem. Soc.* **40** (1918) 1361

[3] J.E. Lennard-Jones, *Trans. Farad. Soc.* **28** (1932) 333

[4] R.T. Bayard and D. Alpert, *Rev. Sci. Instrum.* **21** (1950) 571

[5] J.C. Vickerman (*ed.*), Surface Analysis – The principal techniques, Sussex, John Wiley & Sons, New York, 1997

[6] S. Glasstone, K.T. Laidler and H.E. Ehring, The Theory of Rate Processess, McGraw, 1941

[7] T.A. Delchar, Vacuum Physics and Techniques, Chapman & Hall, London, 1993

[8] W. Paul and H. Steinwedel, *Z. Naturforsch. Teil. A* **8** (1953) 448

[9] P.W. Atkins, Physical Chemistry 4th edition, Oxford University Press, Oxford, 1990

[10] P.A. Redhead, *Vacuum* **12** (1962) 203

[11] M.T. Schulberg, C.A. Fox, G.D. Kubiak and R.H. Stulen, *J. Appl. Phys.* **77** (1997) 3484

[12] D.P. Higgins, R.W. McCullough, J. Geddes, J.M. Woolsey, M. Schlapp and H.B. Gilbody, *Key Eng. Mater.* **99-100** (1995) 177

[13] R.W. McCullough, J. Geddes, A. Donnelly, M. Liehr, H.B. Gilbody, *Nucl. Inst. Meth. Phys. Res. B* **79** (1993) 708

[14] C. Bandis and B.B. Pate, *Phys. Rev. B* **52**(16) (1995) 12056

[15] J. van der Weide and R.J. Nemanich, *J. Vac. Sci. Technol. B* **12** (1994) 2475

[16] W. Monch, *Europhys. Lett.* **27** (1994) 479

[17] A. Einstein, *Ann. Physik* **17** (1905) 132; A. Einstein, *Ann. Physik* **18** (1905) 639; A. Einstein, *Ann. Physik* **20** (1906) 199

[18] W.E. Spicer, *Phys Rev.* **112** (1958) 114

[19] W.E. Spicer, *Appl. Phys.* **12** (1977) 115

[20] R.L. Bell, Negative electron affinity devices, Oxford University Press, London, 1973

[21] C. Lu and K.T. McDonald, *Nucl. Inst. Meth. Phys. Res. A* **343** (1994) 135

[22] A. Breskin, *Nucl. Instrum. Method Phys. Res. A* **371** (1996) 116

[23] J. Ristein, W. Stein and L. Ley, *Phys. Rev. Lett.* **78** (1997) 1803

[24] C.N. Berglund and W.E. Spicer, *Phys. Rev.* **136** (1964) A1030

[25] G.A. Antypas, *et al.*, *J. Appl. Phys.* **42** (1970) 3201

[26] C.H.A. Syms, *Adv. Electronics Elec. Phys.* **28** A (1969) 399

[27] Liu *et al.*, *Appl. Phys. Lett.* **17** (1970) 60

[28] M. Planck, *Annalen der Physik* (1900); M. Planck, *Thermodynamik* (1897); M. Planck, Theorie der Wärmestrahlung (1906); M. Planck, *Nature* **106** (1920) 508

[29] G. Attard and C. Barnes, Surfaces, Oxford Chemistry Primers (**59**), Oxford University Press, Oxford, 1998
[30] C. Nordling, E. Sokolowski and K. Siegbahn, *Phys. Rev.* **105** (1957) 1676; A. Fahlman, K. Hamrin, J. Hedman, R. Nordberg, C. Nordling and K. Siegbahn, *Nature* **210** (1966) 4; C. Nordling, S. Hagstrom and K. Siegbahn, *Z. Physik* **178**(5) (1964) 433
[31] L.C. Feldman and J.W. Mayer, Fundamentals of Surface and Thin Film Analysis, Elservier Science Publishing Co. Inc., Holland, 1986
[32] D.P. Woodruff and TA Delchar, Modern Techniques of Surface Science, Cambridge University Press, Cambridge, 1994
[33] M.P. Seah and D. Briggs, Auger and X-ray Photoelectron Spectroscopy, John Wiley & Sons, UK, 1994
[34] D.N. Belton and S.J. Schmieg, *J. Vac. Sci. Technol. A* **8**(3) (1990) 2353
[35] A.R. Chourasia, D.R. Chopra, S.C. Sharma, M. Green, C.A. Dark and R.C. Hyer, *Thin Solid Films* **193**(1-2) (1990) 1079
[36] P. Kovarik, E.B.D. Bourdon and R.H. Prince, *Phys. Rev. B* **48**(16) (1993) 12123
[37] A. Fick, *Pogg. Ann.* **94** (1855) 59
[38] A.C. Fisher, Electrode Dynamics, Oxford Chemistry Primers (**34**), Oxford, 1996
[39] J. Wong, Analytical Electrochemistry (2nd edition), Wiley-VCH, New York, 2000
[40] Southampton electrochemistry Group: Instrumental Methods in electrochemistry, Ellis Horwood Ltd., UK, 1985
[41] R.S. Nicholson, *Anal. Chem.* **37** (1965) 1351
[42] A.J. Bard and L.R. Faulkner, Electrochemical Methods, Fundamentals and Applications, Wiley, New Work, 1980
[43] Y.V. Pleskov, A.Y. Sakharova, M.D. Krotova, L.L. Bouilov and B.V. Spitsyn, *J. Electroanal. Chem.* **228** (1987) 19
[44] M. Fryda, D. Herrmann, L. Schafer, C.P. Klages, A. Perret, W. Haenni, C. Comninellis and D. Gandini, *New Diamond Front. Carbon Technol.* **9** (1999) 229
[45] B.V. Sarada, T.N. Rao, D.A. Tryk and A. Fujishima, *New Diam. Front. Carbon Technol.* **9** (1999) 365
[46] F. Okino, H. Shibata, S. Kawasaki, H. Touhara, K. Momota, M. Nishitani-Gamo, I. Sakaguchi and T. Ando, *Electrochem. Solid State Lett.* **2** (1999) 382
[47] C.H. Goeting, F. Marken, A. Gutierrez-Sosa, R.G. Compton and J.S. Foord, *New Diamond Front. Carbon Technol.* **9** (1999) 207
[48] M.C. Granger, J.S. Xu, J.W. Strojek and G.M. Swain, *Anal. Chim. Acta.* **397** (1999) 145
[49] C. Levy-Clement, F. Zenia, N.A. Ndao and A. Deneuville, *New Diamond Front. Carbon Technol.* **9** (1999) 189
[50] P.J. Grundy and G.A. Jones, Electron Microscopy in the Study of Materials - The Structure and Properties of Solids 7, Edward Arnold, London, 1976
[51] G. Binnig, C.F. Quate, and C.H. Gerber, *Phys. Rev. Lett.* **56** (1986) 930
[52] C. Julian Chen, Introduction to Scanning Tunneling Microscopy, Oxford University Press, Oxford, 1993
[53] C.V. Raman and K.S. Krishnan, *Nature* **121** (1928) 501
[54] J.R. Ferraro and K. Nakamoto, Introductory Raman Spectroscopy, Academic Press, Inc., London, 1994
[55] M.J. Pelletier (*ed.*), Analytical Applications of Raman Spectroscopy, Blackwell Science Ltd, Oxford, 1999
[56] D.S. Knight and W.B. White, *J. Mater. Res.* **4** (1989) 385
[57] M.S. Haque, H.A. Naseem, J.L. Shultz, W.D. Brown, S. Lal and S. Gangopadhyay, *J. Appl. Phys.* **83**(8) (1998) 4421

[58] W.D. Cassidy, P.W. Morrison, *Jr.* and J.C. Angus in *Proceedings of the 4th International Symposium on Diamond Materials*, K.V. Ravi and J.P. Dismukes (*eds.*), ECS, Pennington, 1995, pg 85
[59] A.C. Ferrari and J. Robertson, *Phys. Rev. B* **63** (2001) 121405(R)
[60] W.A. Yarbrough and R. Messier, *Science* **247** (1990) 3842
[61] C. Kleint, *Prog. Surf. Sci.* **42** (1993) 101
[62] R.W. Wood, *Phys. Rev.* **5** (1897) 1
[63] R.H. Fowler and L.W. Nordheim, *Proc. R. Soc. London Ser. A* **119** (1928) 173
[64] P.W. May, M.T. Kuo and M.N.R. Ashfold, *Diamond Relat. Mater.* **8** (1999) 1490
[65] P.W. May, J.C. Stone, M.N.R. Ashfold, M.R. Hallam, W.N. Wang and N.A. Fox, *Diamond Relat. Mater.* **7** (1998) 671
[66] M.W. Geis, J.C. Twichell, J. Macaulay and K. Okano, *Appl. Phys. Lett.* **67**(9) (1995) 1328
[67] W. Zhu, G.P. Kochanski and S. Jin, *Mater. Res. Soc. Symp. Proc.* **416** (1996) 443
[68] J.Y. Shim, H.K. Baik and K.M. Song, *J. Appl. Phys.* **87**(10) (2000) 7508
[69] J.W. Glesener, H.B. Lin and A.A. Morrish, *Thin Solid Films* **308-309** (1997) 204
[70] X.L. Peng, *Thin Solid Films* **370** (2000) 63
[71] O.M. Kuttel, O. Groning, Ch. Emmenegger, L. Nilsson, E. Maillard, L. Diederich and L. Schlapbach, *Carbon* **37** (1999) 745
[72] J.B. Cui, M. Stammler, J. Ristein and L. Ley, *J. Appl. Phys.* **88**(6) (2000) 3667
[73] A. Sherman, Chem. Vapor Deposition for Microelectronics, Noyes Publications, Park Ridge, NJ, 1987
[74] J. Harris and A.M. Weiner, *J. Appl. Phys.* **74** (1993) 1022; M. Frenklach and H. Wang, *Phys. Rev. B* **43** (1991) 1520; L.L. Connell, J.W. Fleming, H.N. Chu, D.J. Vestyck and J.E. Butler, *J. Appl. Phys.* **78**(6) (1995) 1; D.G. Goodwin, *J. Appl. Phys.* **74**(11) (1993) 6888
[75] M. Frenklach, W. Howard, D. Huang, J. Yuan, K.E. Spear and R. Koba, *Appl. Phys. Lett.* **59**(5) (1991) 546
[76] S. Matsumoto and Y. Matsui, *J. Mater. Sci.* **18** (1983) 1785
[77] J.C. Angus, J.A. Mann, Y. Wang, M. Sunkara, P.A. Washlock, M. Kuczmarski and Z. Li, Progress Report, DARPA University Research Initiation Grant, Contract #N00014-89J-3167 (Jan. 31, 1991)
[78] A. Lettington and J.W. Steeds, Thin Film Diamond, Chapman & Hall, UK, 1994
[79] S.A. Godleski, P.V. Schleyer, E. Osawa and W.T. Wipke, *Prog. Phys. Org. Chem.* **13** (1981) 63
[80] G. Popovici and M.A. Prelas, *Phys. Stat. Sol. (a)* **132**(2) (1992) 233
[81] M. Frenklach, R. Kematick, D. Huang, W. Howard, K.E. Spear, A.W. Phelps and R. Koba, *J. Appl. Phys.* **66**(1) (1989) 395
[82] P.R. Buerki and S. Leutwyler, *J. Appl. Phys.* **69**(6) (1991) 3739
[83] B.R. Stoner, B.E. Williams, S.D. Wolter, K. Nishimura and J.T. Glass, *J. Mater. Res.* **7**(2) (1992) 257
[84] M. Okkerse, M.H.J.M. de Croon, C.R. Kleijn, H.E.A. van den Akker and G.B. Marin, *J. Appl. Phys.* **84**(11) (1998) 6387
[85] M. Frenklach and K.E. Spear, *J. Mater. Res.* **3**(1) (1988) 133
[86] M.P. D'Evelyn, J.D. Graham and L.R. Martin, *J. Crys. Growth* **231** (2001) 506
[87] H. Nakazawa, Y. Kanazawa, M. Kamo and K. Osumi, *Thin Solid Films* **151** (1987) 199
[88] K. Kobashi, K. Nishimura, Y. Kawate and T. Horiuchi, *Phys. Rev. B.* **38**(6) (1988) 4067
[89] A.van der Drift, *Philips Res. Report* **22** (1967) 267

[90] C. Wild, P. Koidl, N. Herress, W. Muller-Sebert and T. Eckermann, *Electrochem. Soc. Proc.* **91**(8) (1991) 224
[91] R.E. Clausing, L. Heatherly, L.L. Horton, E.D. Specht, G.M. Begun and Z.L. Wang, *Diamond Relat. Mater.* **1** (1992) 411
[92] C. Wild, P. Koidl, W. Muller-Sebert, H. Walcher, R. Kohl, N. Herres, R. Locher, R. Samlenski and R. Brenn, *Diamond Relat. Mater.* **2** (1993) 158
[93] C. Wild, N. Herres and P. Koidl, *J. Appl. Phys.* **68**(3) (1990) 973
[94] H.G. Busmann and I.V. Hertel, *Carbon* **36**(4) (1998) 391
[95] H.M. Liu and D.S. Dandy, Diamond Chemical Vapor Deposition – Nucleation and Early Growth Stages, Noyes Publications, Park Ridge, NJ, 1995
[96] K.V. Ravi, *J. Mater. Res.* **7**(2) (1992) 384
[97] S.M Rossnagel, J.J. Cuomo and W.D. Westwood (*eds.*) Fundamentals, Etching, Deposition, and Surface Interactions, Noyes Publication, Park Ridge, NJ, 1990
[98] S.T. Lee and Z.D. Lin, *Mater. Sci. Eng.* **25** (1999) 123
[99] K. Wu, E.G. Wang, Z.X. Cao, Z.L. Wang and X. Jiang, *Appl. Phys. Lett.* **88** (2000) 2967
[100] J.Y. Shim, E.J. Chi, H.K. Baik, K.M. Song and S-.J. Lee, *J. Vac. Sci. Technol. B* **18** (2000) 1040
[101] M.D. Whitfield, J.A. Savage and R.B. Jackman, *Diamond Relat. Mater.* **9** (2000) 262
[102] Y.K. Kim, Y.S. Han and J.Y. Lee, *Diamond Relat. Mater.* **7** (1998) 96
[103] Z. Feng, S. Anders, A. Anders, J.W. Ager III, I.G. Brown, K. Komvopoulos and D.B. Bogy, *Diamond Relat. Mater.* **5** (1996) 1080
[104] U.Kim, R. Pcionek, D.M. Aslam and D. Tomanek, *Diamond Relat. Mater.* **10** (2001) 1947
[105] S. Seraphin, D. Zhou, J. Jiao, M.A. Minke, S. Wang, T. Yaday and J.C. Withers, *Chem. Phys. Lett.* **217**(3) (1994) 191
[106] L. Ley, R. Graupner, J.B. Cui and J. Ristein, *Carbon* **37** (1999) 793
[107] M. Hiramatsu, C.H. Lau, A.M. Bennett and J.S. Foord, *Thin Solid Films* **407** (2002) 18
[108] A. Heiman, I. Gouzman, S.H. Christiansen, H.P. Strunk, G. Comtet, L. Hellner, G. Dujardin, R. Edrei and A. Hoffman, *J. Appl. Phys.* **89** (2001) 2622
[109] L.C. Chen, P.D. Kichambare, K.H. Chen, J.-J. Wu, J.R. Yang and S.T. Lin, *J. Appl. Phys.* **89** (2001) 753
[110] C.Z. Gu and X. Jiang, *J. Appl. Phys.* **88** (2000) 1788
[111] T. Sharda, T. Soga, T. Jimbo and M. Umeno, *Diamond Relat. Mater.* **9** (2000) 331

Chapter 3

Diamond surface conductivity

3.1 Introduction
3.2 Gaseous Environment Studies
  3.2.1 Experimental
  3.2.2 Results
    3.2.2.1 Gas Adsorbates
    3.2.2.2 Thermal Stability
  3.2.3 Discussion
    3.2.3.1 Surface Adsorbates
    3.2.3.2 Temperature
  3.2.4 Conclusion
3.3 Solution Phase Effect and Electrochemical Studies
  3.3.1 Experimental
  3.3.2 Results
    3.3.2.1 pH and Temperature
    3.3.2.2 Electrochemistry
    3.3.2.3 Metal Deposition and Stripping
    3.3.2.4 SEM Investigation
    3.3.2.5 Potential Pretreatment Modification
    3.3.2.6 Conductance *vs* Metal Deposition
  3.3.3 Discussion
    3.3.3.1 Changes of Conductivity
    3.3.3.2 Electrochemical Properties
  3.3.4 Conclusion

3.1 Introduction

The surfaces of as-prepared polycrystalline CVD, single crystal and natural diamond films show an exceptionally high conductivity as recognized for the first time ten years ago [1,2,3]. Earlier publications have reported that the conductivity of diamond thin films can be decreased by several orders of magnitude by thermal annealing and the subsequent hydrogen plasma treatment could cause an increase in the conductivity toward the initial value. Ever since then, this *p*-type H-conductive surface has allowed the fabrication of a range of diamond electronic devices after the addition of appropriate metallic contacts. The fabricated surface conductive diamond can even display much higher levels of performance than those based on boron-doped diamond material.

This diamond surface related conductivity has now been exploited for electronic applications, such as the manipulation of diamond-based Schottky diodes [4,5,6] and diamond-based field effect transistor (FET) for metal-semiconductor (MES), metal-insulator-semiconductor (MIS) and metal-oxide-semiconductor (MOS) structures [7,8,9,10,11,12]. Recently, the nanofabrication for metal-insulator-metal (MIM) diode-like material has also been explored [13]. The fabrication of diamond FET in electrolyte was also made possible, which was called as ion sensitive FETs (ISFET) [14,15,16].

However, there is an increasing interest in investigating diamond surface conductivity since it contributes to the bulk conductivity which in turn influences the performance negatively, such as in many electronic applications [17]. Moreover, the exact chemical nature of the surface conductive layer is still the subject of some controversy, with the various explanations encompassing adsorbed-hydrogen induced upward band bending [15], hydrogen defects in the near surface region [18], and the presence of electronegative adsorbates [19].

Stallcup *et al.* [20] observed that approximately 20% of the CVD diamond surface was covered with non-diamond carbon and they speculated that such non-diamond carbon might contribute to the surface electrical conducivity. The idea was supported by Muto *et al.* [21] suggesting that the surface conductive layer was due to the existence of graphite-like low resistivity layer, generated by hydrogen plasma. Landstrass and Ravi [1,2] however, proposed that the reduction of resistivity was the result of the passivation of deep levels due to hydrogen termination. This was postulated following their observation of trap-limited behavior with steeply rising current in I-V curves. Based on the results of the XPS and contact potential difference measurements by Kelvin probe analysis, Shirafuji and Sugino [22] proposed a band-bending model to explain the surface conductivity, suggesting that the treatments with hydrogen plasma and with oxygen plasma will lead to downward and upward shifting, respectively, of the surface Fermi level. However,

Hayashi *et al.* [23] believed that the layer with high conductivity was due to the holes generated by shallow acceptor levels related to incorporated hydrogen in the subsurface region, which was in agreement with that proposed previously by Maki *et al.* [24]. Kawarada [25] has proposed a similar surface band-bending model suggesting that holes compensation of the net charge was required to satisfy the surface charge neutrality, thus upward band bending is induced. Ley *et al.* [18] however, suggested the occurrence of downward band bending for hydrogenated diamond from their ample spectroscopic evidences, and showed that the surface could only be conductive after the exposure to atmospheric air. They [18] claimed the atmospheric adsorbates were responsible for the acceptor states that could induce upward band bending for hole accumulation.

The literature reports of surface conductivity are complex and conflicting, however some agreements have been made in common: (i) the conductivity is due to positive charge carriers with mobilities of between 30 and 70 $cm^2V^{-1}S^{-1}$ at 300 K, indicating band transport holes within the crystalline solid, (ii) the surface concentration of charge carriers is weakly temperature dependent with value found between 10^{12} and 10^{13} cm^{-2} at 300 K, (iii) and the surface conductivity can be varied by orders of magnitude by exposing the surfaces to different ambients [8-10,19, 22-26,27].

Experimentally, it appears to be the case that the hydrogenated diamond does not display a high surface conductivity until it is exposed to atmosphere, but the processes occurring in this air-exposure are not well defined since the first air-exposure after hydrogenation is frequently carried out in an uncontrolled manner. Therefore, the aim of this chapter is to investigate the critical chemical components of the adsorbed layer that are required to maximize the surface conductivity observed. The changes of conductivity due to temperature and pH in both gaseous and solution (or electrolyte) medium have also been investigated. Novel examination on the electrochemical properties of the surface conductive layer has been performed.

3.2 Gaseous Environment Studies

3.2.1 Experimental

Optical grade CVD diamond thin films (as shown in figure 1), grown by microwave-assisted CVD were used throughout. The films are ~100 microns thick with a grain size of 10-20 microns and a random grain orientation. Prior to the measurements, all the samples were immersed in a boiling $(NH_4)_2S_2O_8/H_2SO_4$ solution, saturated at 200 °C for 2 hours, which is known to result in a contaminant free oxidized surface.

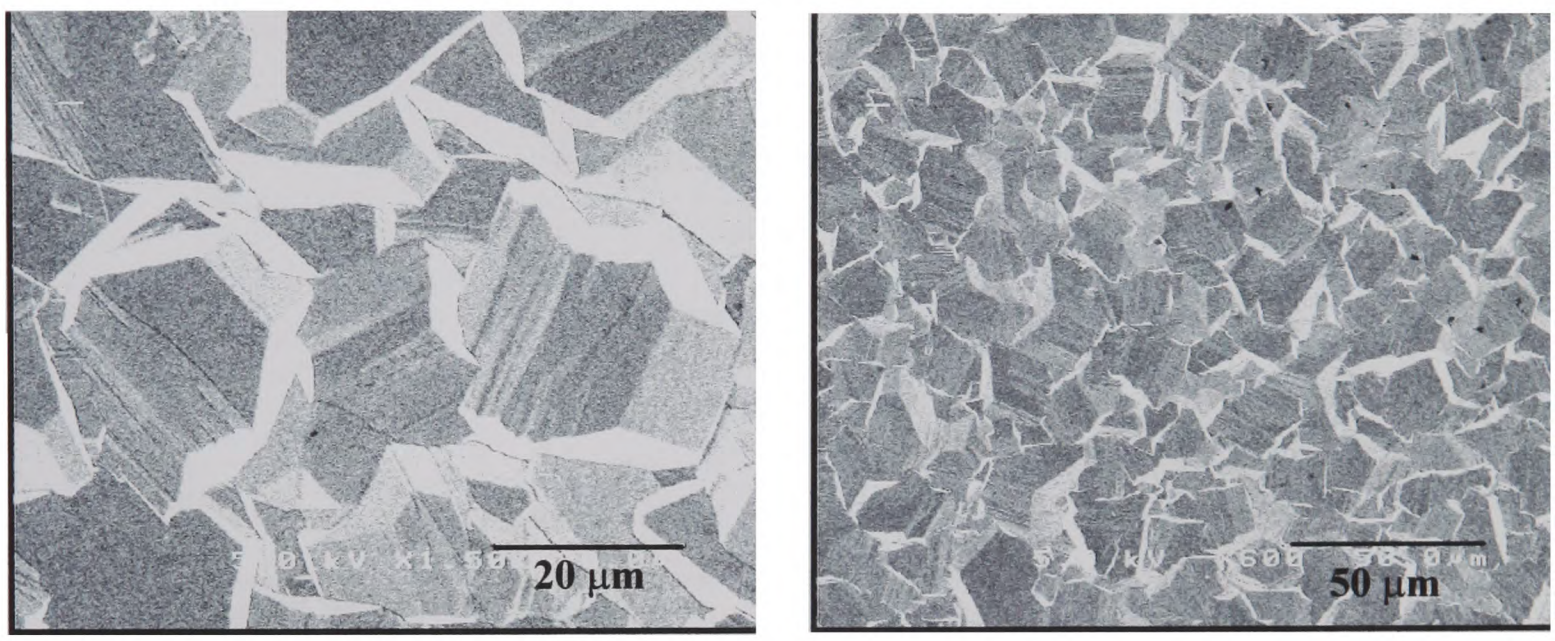


Figure 1. SEM images of diamond used in surface conductivity measurements

The measurements of surface conductivity have been carried out *in-situ* in a microwave plasma chamber (Penta Science & Technology Ltd PD01A; 2.45 GHz; 2kW). The films were hydrogenated under a total gas pressure of 45 Torr with a flow rate of 200 sccm, operating at a microwave power of 1.5 kW and at a nominal substrate platen temperature of 600 °C. Two point of gold coated probes with ~ 5 mm distance in between, was used to make ohmic contacts on the diamond. This ohmic behaviour was tested from the linearity of I-V plots. The temperature on the diamond surface was calibrated prior to the conductivity measurements, using alumel-calomel thermocouple spot-welded to the sample holder. A clean diamond surface (free of adsorbates) was prepared by annealing it at 800 °C in 45 Torr of N_2, whereas diamond was oxidized by annealing the surface up to 600 °C at a pressure of 45 Torr in O_2 ambient condition.

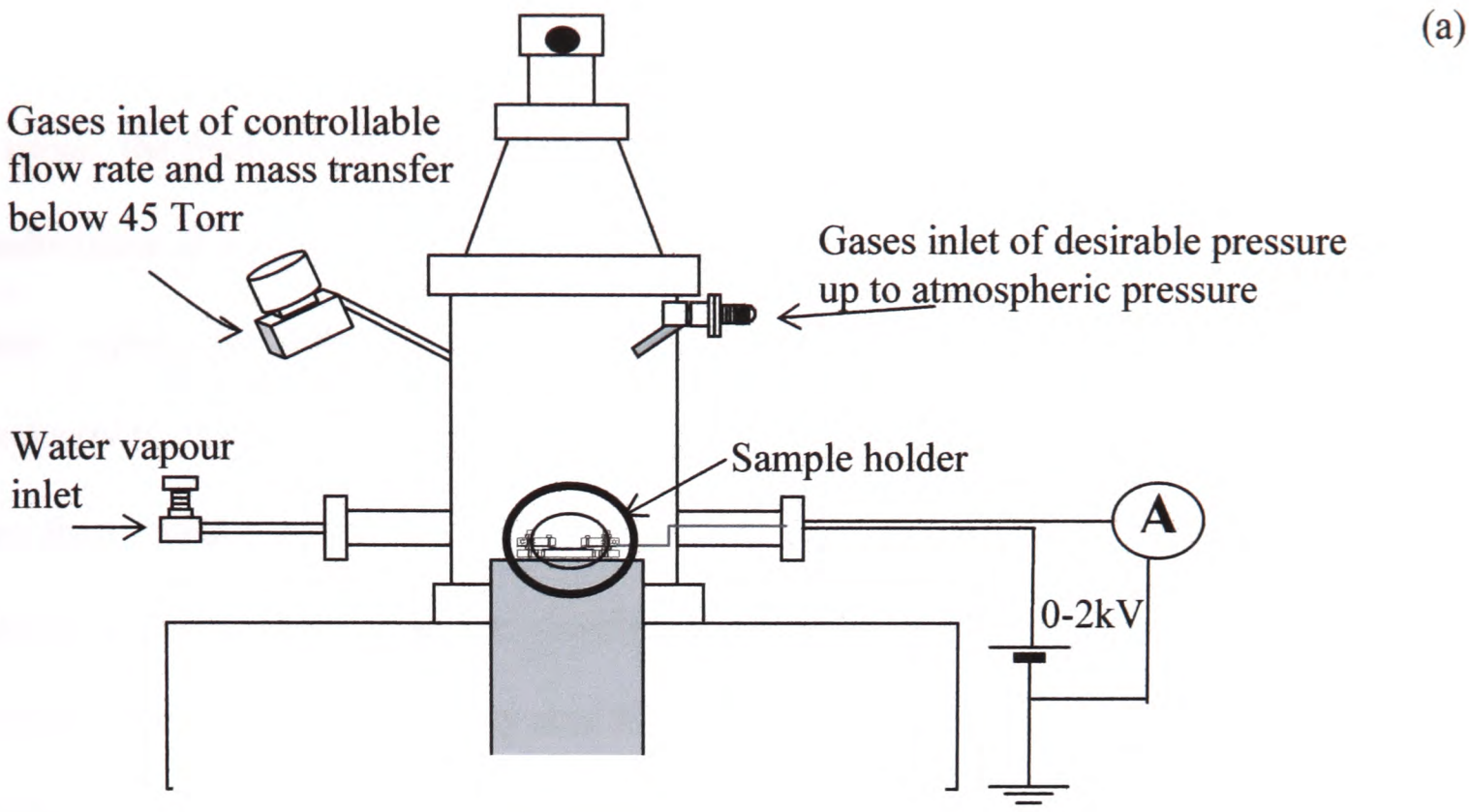


Figure 2. The design of surface conductivity measurements in microwave plasma chamber (a), the side view of sample holder (b) and from the top view (c)

Changes were reported in surface conductivity, which arose when freshly hydrogenated CVD diamond was exposed to a range of pure gases, immediately after the hydrogen plasma was extinguished, and before "uncontrolled" exposure to atmosphere took place. The gaseous exposures carried out encompassed pure water vapour, synthetic dry air, nitrogen, oxygen, carbon dioxide and hydrogen environments, and simultaneous or sequential exposures based on these components at varying substrate temperatures. The pH of water vapour in the microwave plasma chamber was altered by the admittance of formic acid.

3.2.2 Results

3.2.2.1 Gas Adsorbates

In *vacuo*, the freshly hydrogenated diamond shows very low surface conductivity with the conductance of $10^{-12} - 10^{-11}$ S. The sample was then exposed to 15 Torr of de-oxygenated water vapour for 600 s at room temperature, which produced a small increase in conductivity close to 10^{-10} S, as illustrated in the inset in figure 3 (iv). The water vapour was then rapidly evacuated, and dry synthetic air (comprising 21% O_2, 0.05% CO_2, balance N_2) was admitted to the chamber at a leak rate corresponding to 22.5 Torr per minute. The sample conductivity was found to rise significantly over a period of several minutes. As the pressure rose above ~150 Torr, a much slower change was observed.

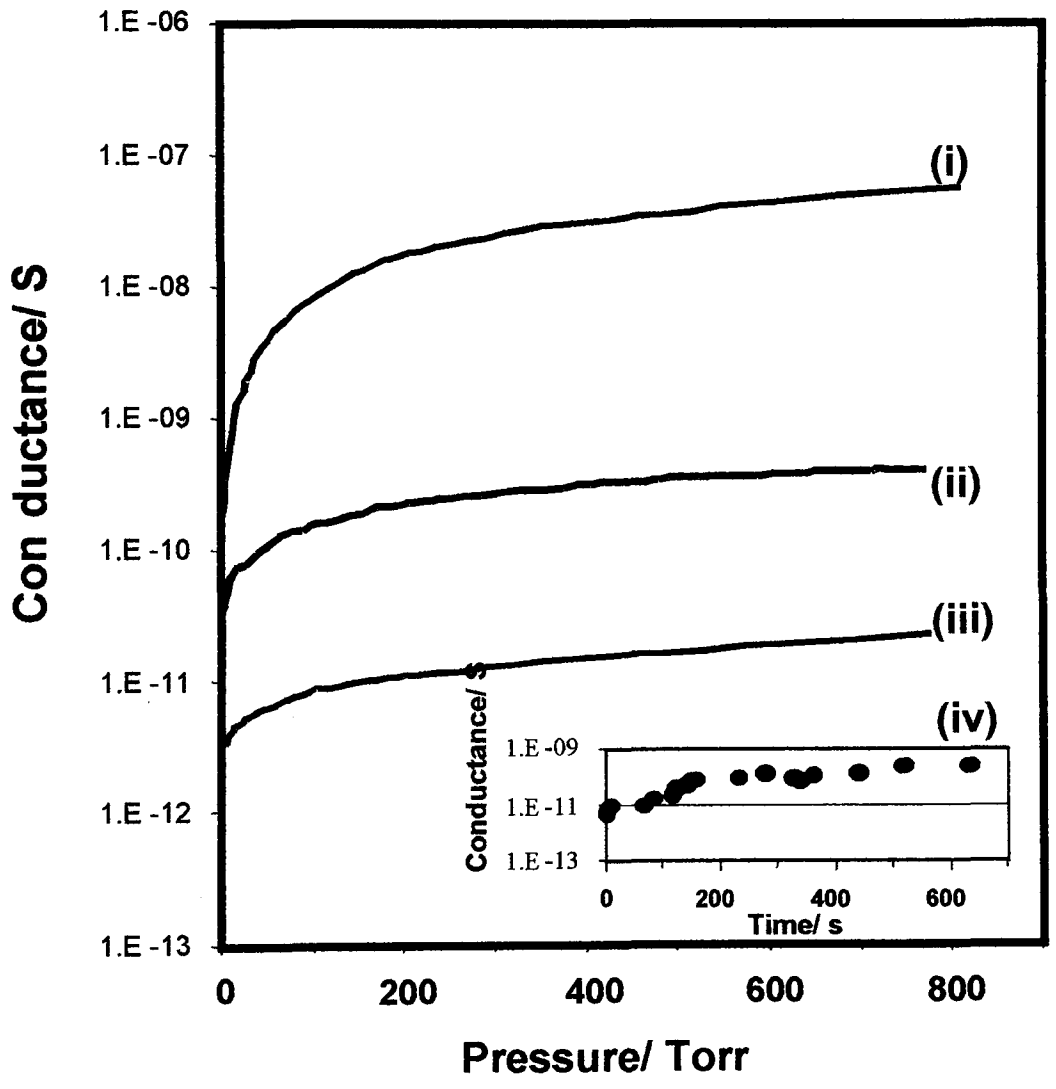


Figure 3. The changes of conductance on different treated surfaces after the exposure to dry air at a wide range of pressure (~ 22.5 Torr min^{-1}) at room temperature; (i) on moist H-surface, (ii) on dry H-surface, and (iii) on free of adsorbate surface; inset (iv) showing the change of conductance on the admission of water vapor

The results plotted in figure 3 illustrates that the surface conductivity arises approximately four orders of magnitude higher than the initially hydrogenated surface in

this experiment. It can also be seen in figure 3 that this is approximately three orders of magnitude higher than if the exposure to dry air is carried out without prior exposure to water vapour. This result reveals the importance of the moist surface of diamond after hydrogenation. However, no great change of SC was observed for clean (free of adsorbates) diamond surface.

This result was investigated further by changing the pH of the water vapour *via* the admittance of formic acid at 300 K. Figure 4 shows the sharp increase of conductivity, which indicates that low pH can enhance the SC more efficiently on the diamond surface.

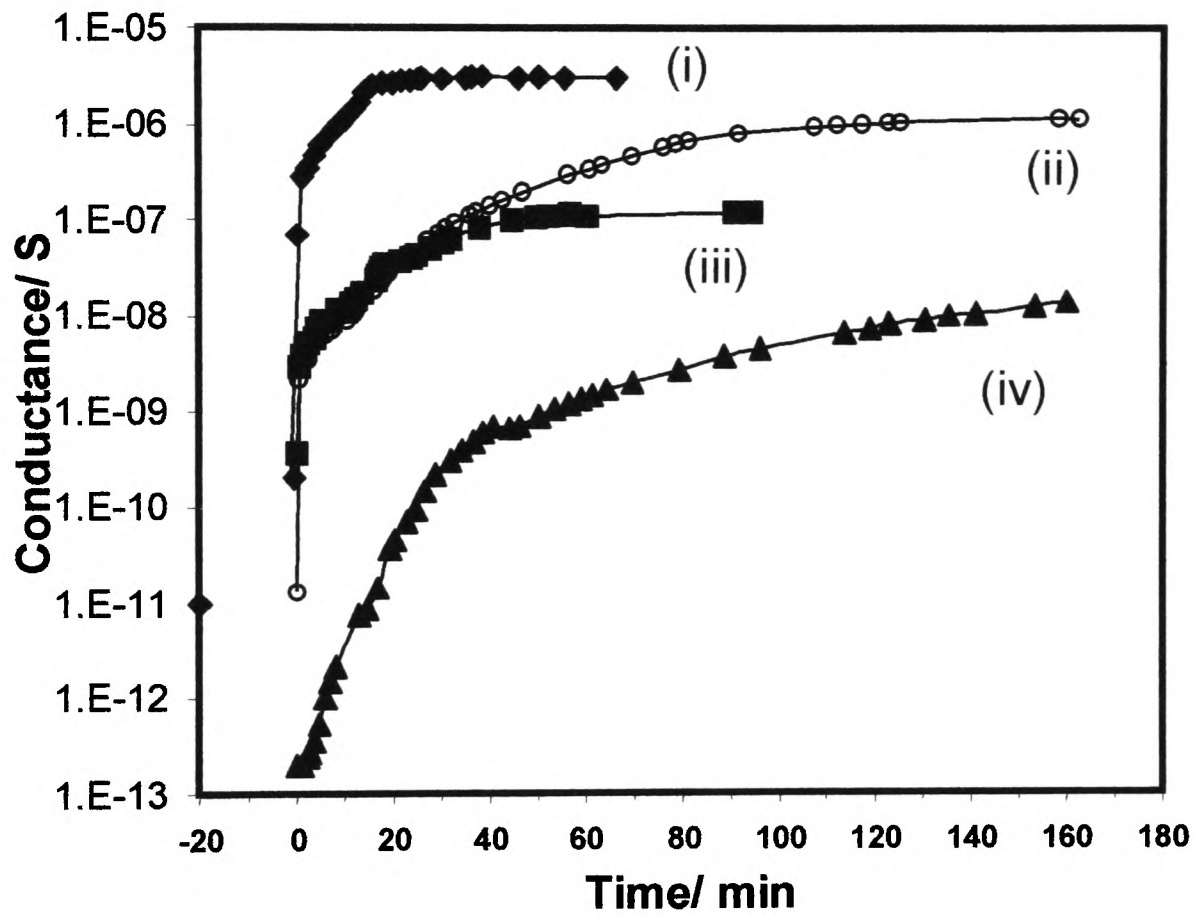


Figure 4. The changes of surface conductivity after being exposed to formic acid in various pre-treated surfaces (i) moist H-surface, (ii) dry H-surface, (iii) free of adsorbate surface, and (iv) dry oxidized surface; the rate of increase in pressure was ~ 0.15 Torr min^{-1}

The moist hydrogenated surface provides very efficient condition for the dissolution of formic acid in watery medium as referring to the sharp increase of SC from 3 x 10^{-10} S to 5 x 10^{-6} S and the SC value was saturated in just 10 min (figure 4i). The surface conductivity of formic acid dosed on hydrogenated diamond (4ii), however arouse at a slower rate than 4(i) surface and the saturation level was about 1 x 10^{-6} S after 3 hours

measurements. The adsorbate-free surface showed low conductance and was saturated at a value of 1 x 10^{-7} S whereas the oxidized diamond surface (4 iv) showed the least effect on SC.

Major atmospheric gases were introduced in the chamber in order to investigate the influences of the specific atmospheric adsorbates on the surface conductive diamond. Figure 5(a) shows the dependence of conductivity on gas pressure, as various gases were admitted through a calibrated leak rate at high flow rate, corresponding to 50 Torr per minute. The admittance of oxygen (i) onto the moist hydrogenated diamond surface induced a drastic increase of conductance up to 5 x 10^{-9} S when the pressure was increased to 765 T. This trend was followed by the effect of carbon dioxide dosages on moist H-diamond at an order of 10^{-9} S (ii), and lower conductance was obtained on dry diamond surface at a value of 5 x 10^{-10} S (iii). The introduction of gas O_2 (figure 5 iv) on "dry" hydrogenated surface showed no remarkable increase of conductivity, whereas N_2 has shown very little effect on conductivity for either hydrogenated or wet H-surfaces.

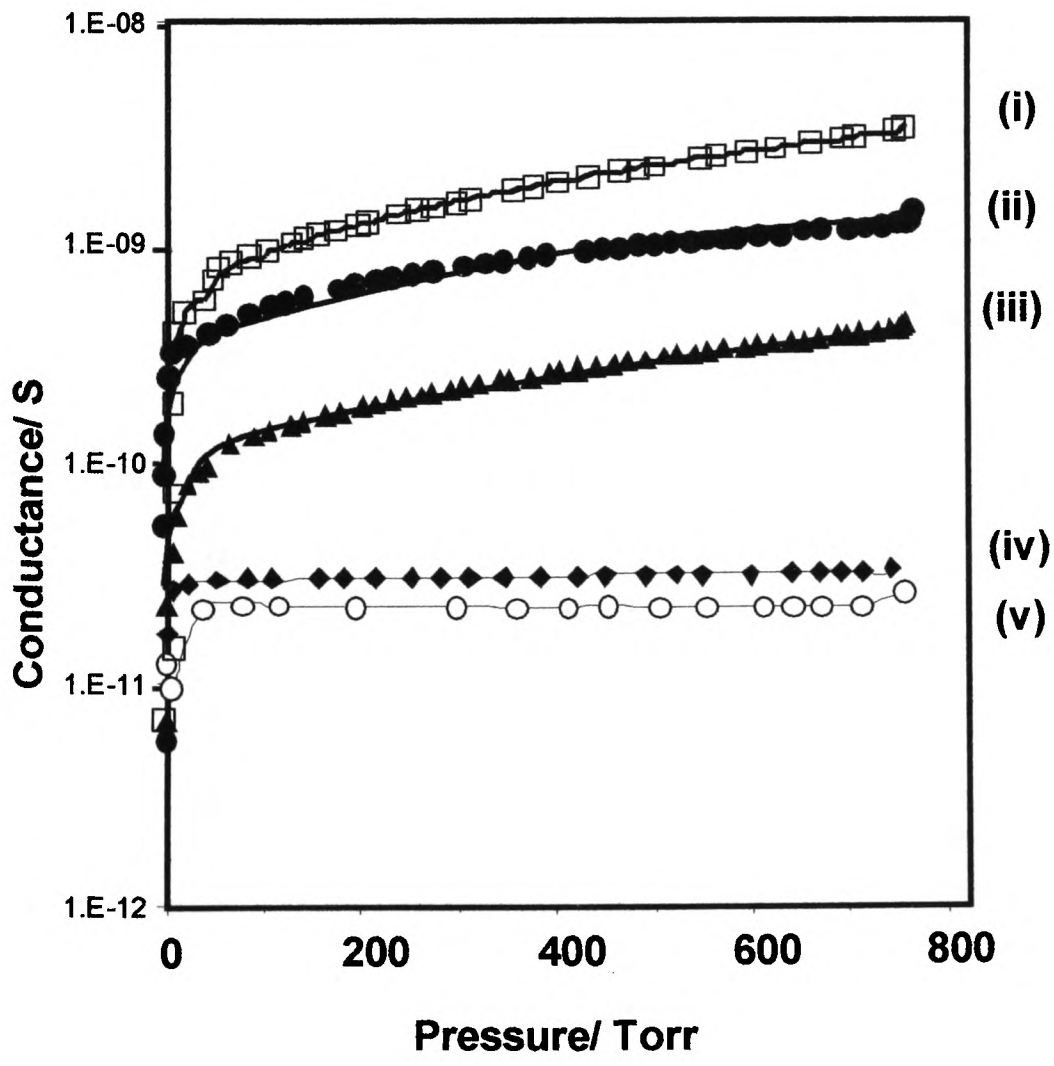


Figure 5(a). The dependence of surface conductivity on the systems of (i) O_2/moist H-surface, (ii) CO_2/moist H- surface, (iii) CO_2/dry H-surface, (iv) O_2/dry H-surface, (v) N_2/moist H-surface The rate of increase in pressure was 50 Torr min^{-1}

The change of surface conductivity varied in time was investigated in response to the mixtures of water vapour and different gases at a total pressure of 40 Torr. The results, as presented in figure 5(b), show the rise in surface conductivity with the admission of nitrogen to the chamber is significantly less than that seen in figure 3, where dry air (79% N_2) was used, suggesting nitrogen is not the active component of the gas responsible for the main conductivity change.

However, greater changes in conductivity are seen if pure gases corresponding to the other components such as oxygen or carbon dioxide are employed, suggesting these are the active chemical species responsible. Carbon dioxide with high moisture results in rapid increase in surface conductivity at the initial stage, but the enhanced conductivity was mostly prominent under the mixture of oxygen and water vapour after the period of 3 hours. Dry air (with water content < 5 vpm) with similar composition of atmospheric air results in lower conductivity than the other two.

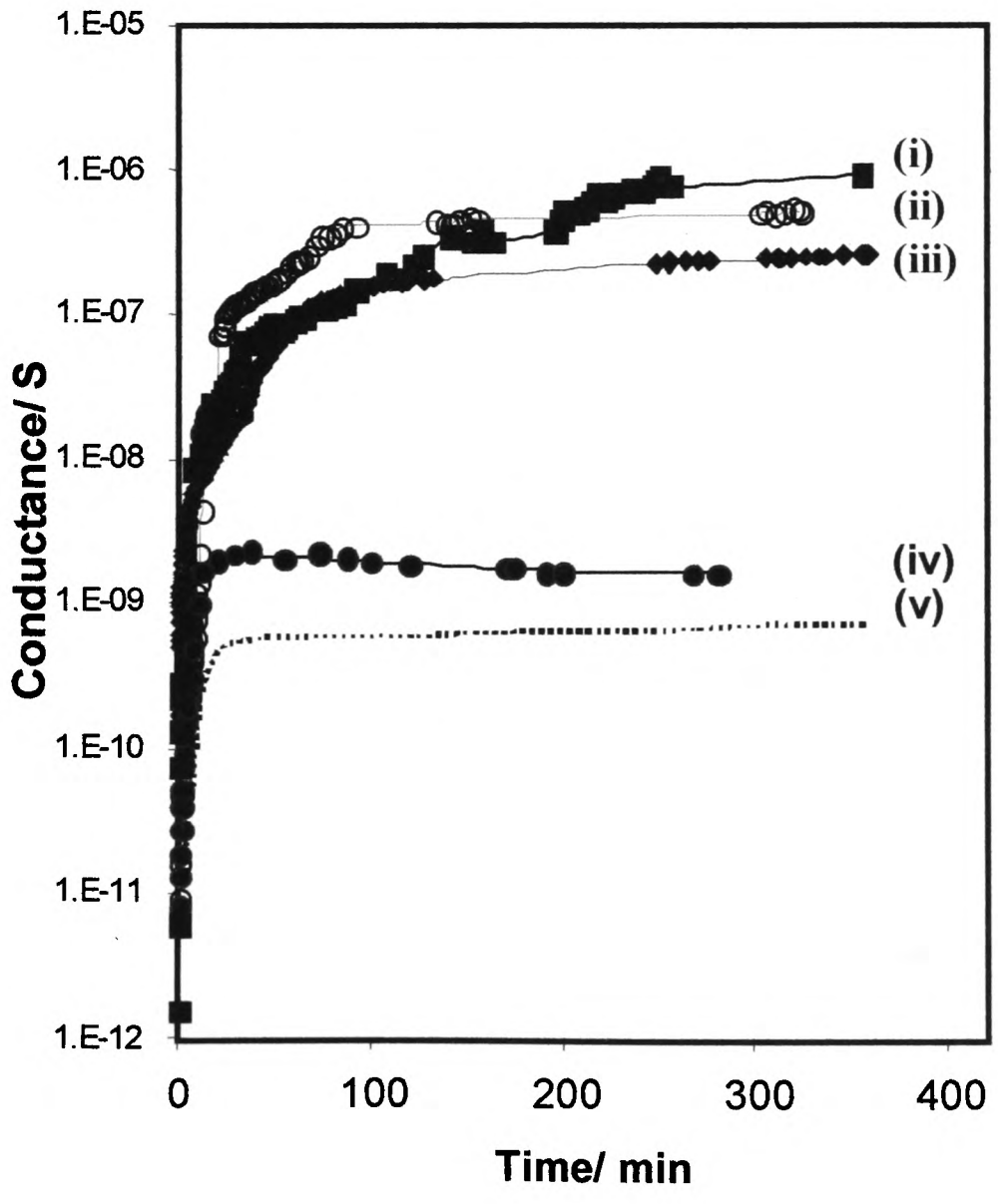


Figure 5(b). The dependence of surface conductivity of hydrogenated surface on the systems of

(i) $O_2 + H_2O$,
(ii) $CO_2 + H_2O$,
(iii) *dry air* + H_2O,
(iv) $N_2 + H_2O$,
(v) *dry air only*

Water was admitted for the first 20 min to 20 T, followed by the admittance of gas to 40 T

Physisorption of water from humid atmospheres enables subsequent dissolution of the gas concerned in the "wetting phase" and thus the sequence in which the differing gas exposures is carried out is crucial. For this aspect, different gases were admitted continually inside the chamber in the mixture of other gases, as indicated in figure 6. The result shows very similar trend for the increases of conductivity, corresponding to the original exposure of "dry" hydrogenated surface to wet air.

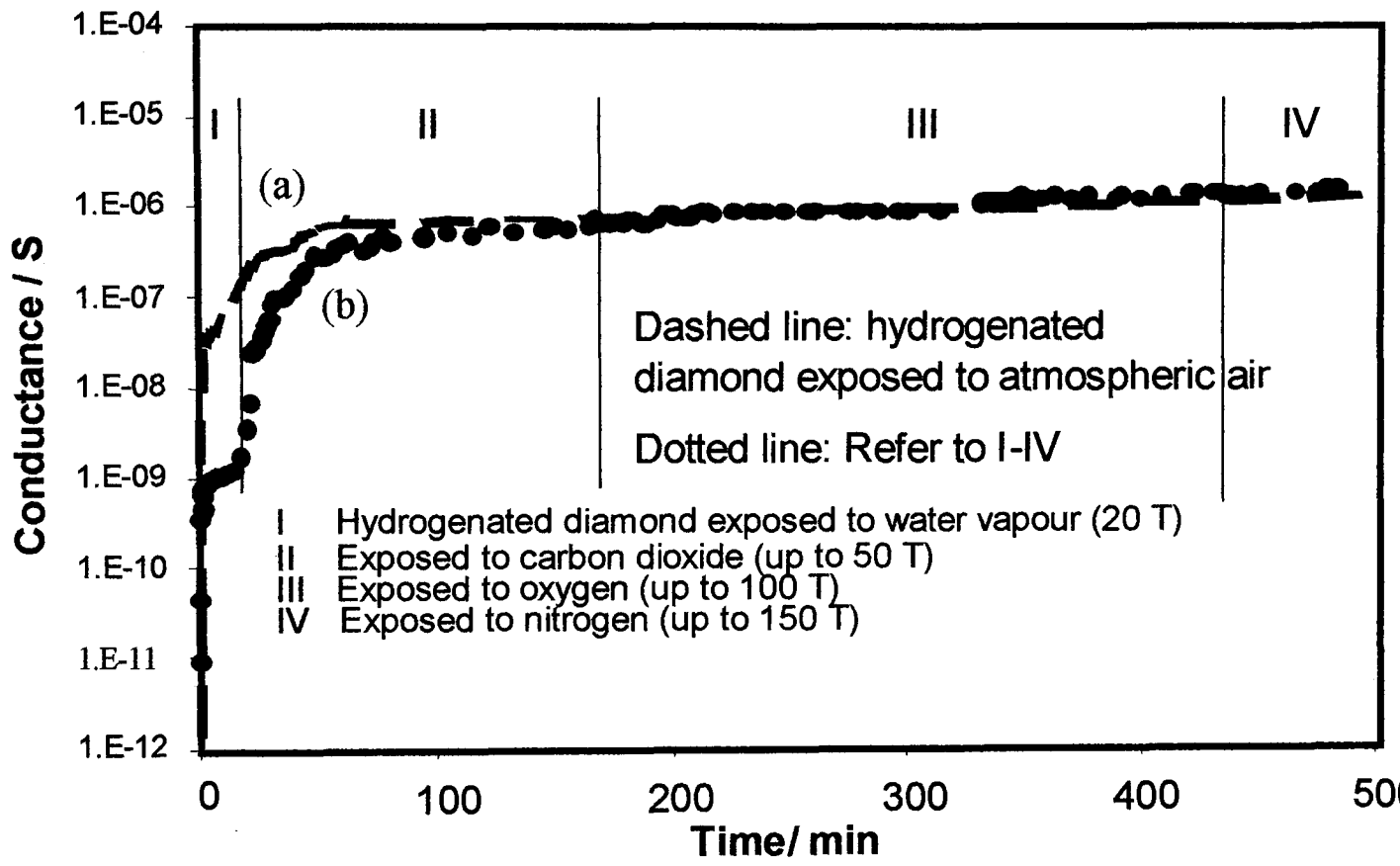


Figure 6. The increase of diamond surface conductivity for (a) H-surface being exposed to wet air; (b) successive exposure of H-surface to various gases under low pressure

Water vapour has increased the surface conductance up to 10^{-9} S within the period of 20 min. Upon the admittance of CO_2 for 50 T (see figure 6b II), the conductance has increased sharply up to approximately 8 x 10^{-7} S in 160 min, and the following introduction of O_2 to a total chamber pressure of 100 T, the conductance has leveled off at the value of an order between 10^{-6} and 10^{-7} S. This result was surprisingly consistent with the result obtained in the real life situation when a hydrogenated diamond was exposed to atmospheric air (figure 6a). Within the period of III region, the surface conductivity of diamond remains unchanged at a saturated value of 1 x 10^{-6} S and the effect of the

presence of gaseous N_2 (IV) in the chamber would make no difference on the value. The result in figure 6 has clearly revealed that the conductivity is mostly time variance dependent, rather than the effect of the increase of partial gas pressures (as shown in figure 5a).

In brief, the main atmospheric gases responsible for inducing diamond surface conductivity are expected to be carbon dioxide and oxygen underlying on top of the watery interlayer medium (moisture from air).

The performance of white diamond (optical graded) and black diamond (thermal management graded) were compared on their surface conductivity. White diamond is being "white" in colour due to light scatter from the rough top surface of the film, whereas the black colour of black diamond is normally associated with high levels of graphite inclusion when higher percentages of hydrocarbon are used within the gas used to grow the film, which dramatically enhance the growth rate. In contrast to white diamond, black diamond shows a 1332 cm^{-1} peak imposed on a broad feature between 1100 and 1500 cm^{-1} (see Raman on the right of figure 7), implying significant non-diamond carbon content within the films. Prior to hydrogenation, the diamonds were boiled in ammonium persulfate/sulfuric acid. The diamonds were then hydrogenated under the conventional parameter, and were later exposed to atmospheric air. The surface conductance for both diamonds increased in an identical rate and saturated at 1×10^{-6} S in a day (results not shown).

Both of the white and black diamonds were annealed for 10 minutes at different temperature inside a programmable furnace in the atmospheric ambient condition. The sharp falls of conductance were observed soon after 300 °C. At annealing temperature above 400 °C, both of the diamonds became very insulating with surface conductances of $\sim 5 \times 10^{-11}$ S. As shown in figure 7, white and black diamonds show insignificant difference in thermal stability on surface conductivity.

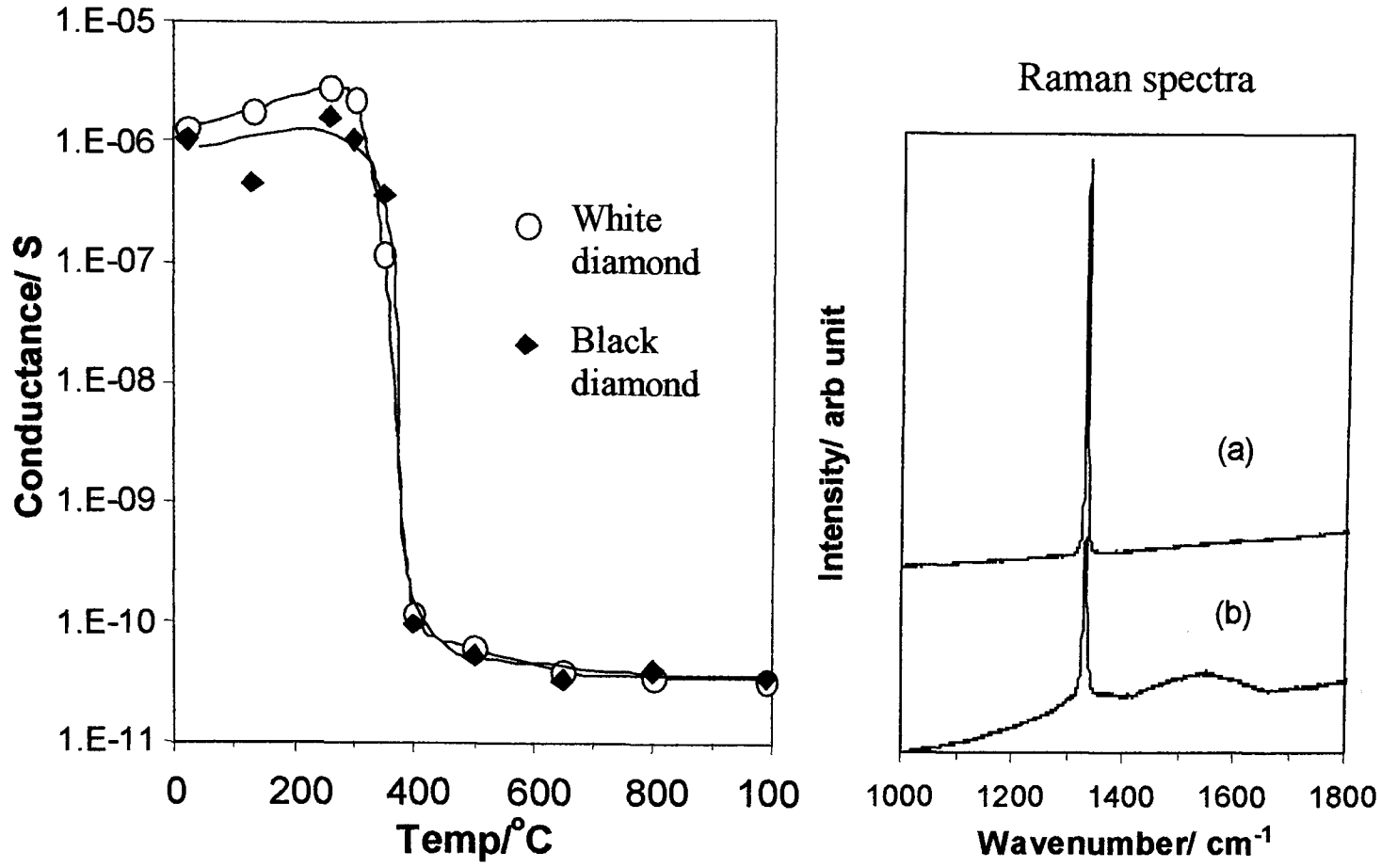


Figure 7. The conductance of surface conductive diamond versus annealing temperature (10 minutes furnace in ambient atmosphere); spectra on the right showing the Raman of (a) white diamond and (b) black diamond

3.2.2.2 Thermal Stability

The thermal stability of the surface conductive layer is subjected to various investigations. Due to the ceramic (insulator) lying beneath the diamond film, the actual temperature is far less than the temperature settings in the microwave chamber. The surface temperature was calibrated by fitting alumel-calomel thermocouples attached to diamond, and subsequent temperature was annealed and was calibrated to the reading of a digital voltmeter. The calibration plot is shown in figure 8 and was used throughout as the reference for the rest of the experiments.

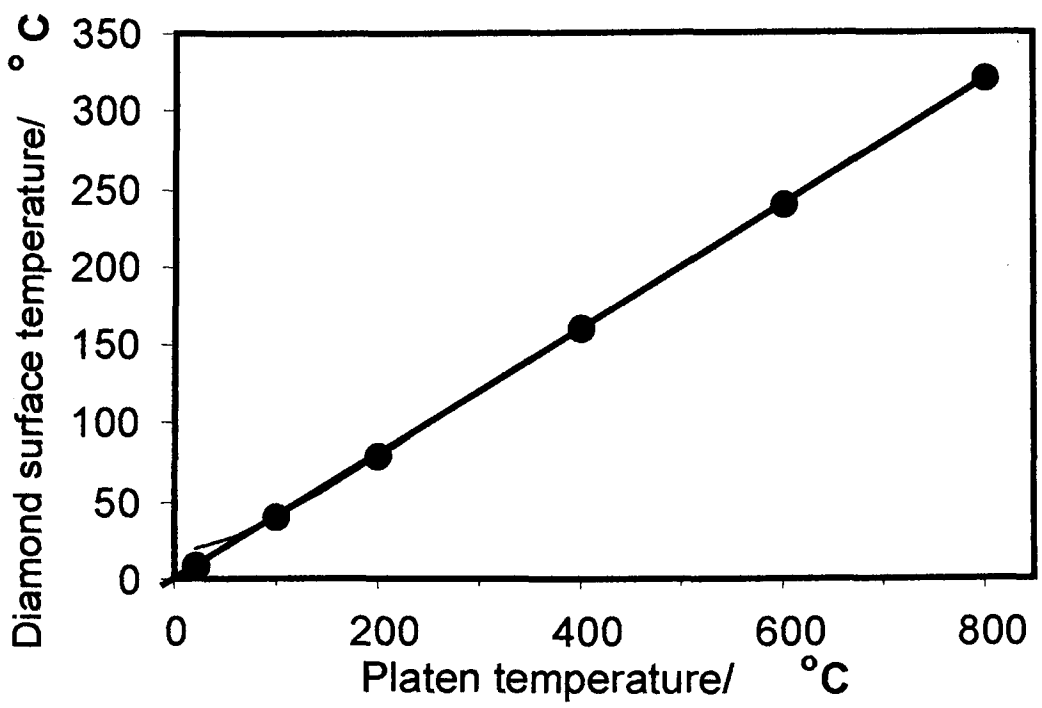


Figure 8. The calibration curve of diamond surface temperature to platen temperature

To test the effect of thermal stability on the surface conductive layer, two series (a and b) of experiments were carried out.

(a) The first experiment is to test the thermal stability of the surface conductive layer. Initially insulating diamond was hydrogenated, and was later exposed to atmospheric air. The surface conductance reached 10^{-7}-10^{-6} S after the exposure to air in two hours. The conductive diamond was later mounted back in the chamber, and was annealed up to a particular temperature for 60 min in vacuum (figure 9(i)) or in wet air at 765 T (figure 9(ii)), and was then allowed to cool down to room temperature in vacuum. The effect of these annealing cycles on conductivity was later measured. The procedure was repeated for other annealing temperatures after the diamond was re-hydrogenated and exposed to air. Both of the annealing environments show the rapid falls of surface conductivity when the surface temperature reached 200 °C. However, the surface conductance for the annealed surface conductive diamond under *vacuo* (9i) is at a magnitude of two orders higher than the SC upon the annealing under wet air condition (9ii).

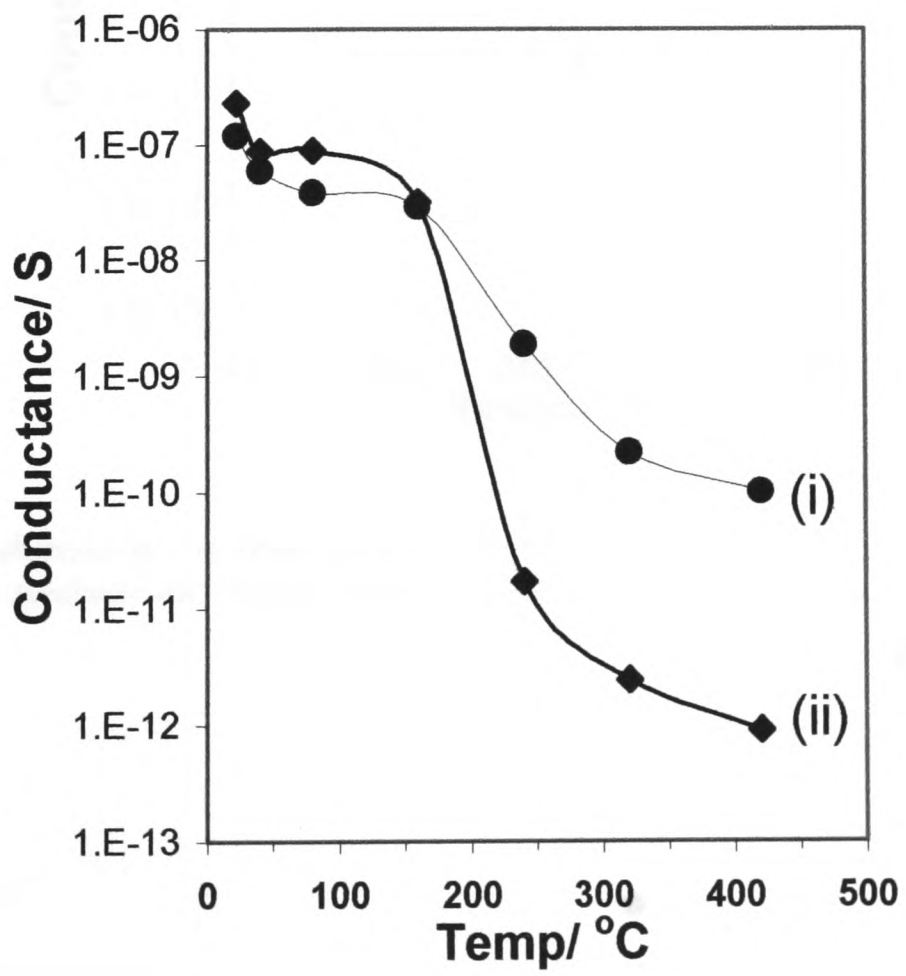


Figure 9. The change of conductance for surface conductive diamond versus annealing temperature (60 min) in (i) vacuo and (ii) wet air at 765 Torr

(b) The second test is to anneal the freshly hydrogenated diamond inside the chamber for 60 min before they are exposed to atmospheric air. Results presented in figure 10, shows the annealed hydrogenated surface sustains high conductance even after the annealing temperature has risen up to more than 300 °C for 2 hours. This result is different from the case if the hydrogenated diamond was annealed under dry air (45 Torr) for 20 min prior to the exposure to air, which showed the rapid drop of conductance after 200 °C. As has been noted previously [26], the surface conductivity is irreversibly lost if the sample is annealed at temperatures in the range 200 - 300 °C in air.

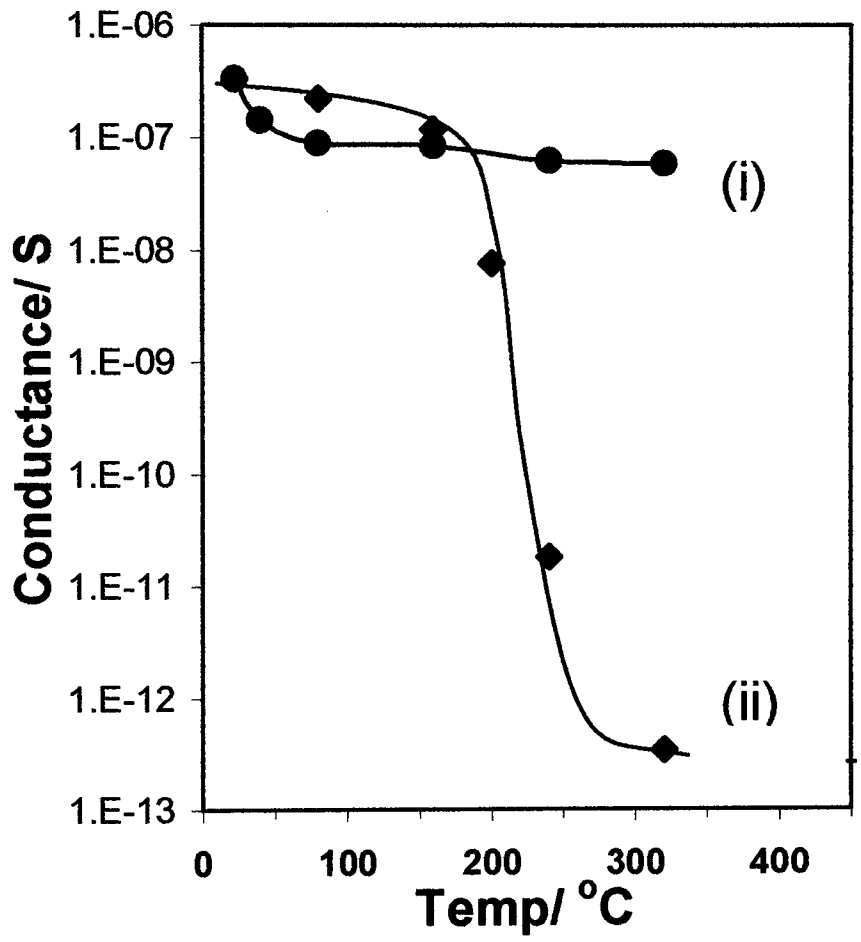


Figure 10. The dependence of hydrogenated diamond on annealing temperature (60 minutes) in (i) vacuo and (ii) synthetic air, before being exposed to atmospheric air

3.2.3 Discussion

Hydrogen-terminated undoped diamond surfaces display *p*-type characteristic semiconductor due to hole accumulation, which form a conducting surface layer in the subsurface region, rather than the top surface monolayer [2,24,28]. The acceptors are completely activated at room temperature with activation energy less than 50 meV [15]. Recently, the acceptor energy of hydrogen-induced conductivity is reported due to the localized states of traps holes in the range of 6 meV at very low temperature ($T < 70$ K) [29]. In contrast, boron-doped diamond exhibits a deep acceptor level of 0.38 eV in the extrinsic region at room temperature with only 0.01 % of the acceptors are activated [15]. This will make the boron-doped layers display high temperature-dependent resistivity, making the devices hard to operate at room temperature.

3.2.3.1 Surface Adsorbates

Previous work has been done showing the rise of surface conductivity on hydrogenated diamond in the exposure to atmospheric air [26]. Though the influence of the environment is known, the specific adsorbates is still yet being explored due to the uncontrolled exposure of gases. Present work is aimed at controlling the adsorbates *via* the selective exposure to individual gases in order to clarify the mechanism involved on the conductive layers.

The results reported here show that the electron transfer to chemical acceptors in a "wetting layer" is responsible for the formation of the *p*-type conductive layer. Small changes in conductivity occur when the hydrogenated surface is exposed to most vapours (figure 3), but this is likely to be attributable to trace contaminants in the gases used, since surface coverages of the order of monolayers can be formed from such species, when present even in the parts per million range, or well below, in experiments where exposure to pressures up to atmospheric are concerned. The highly surface conductive state is

however only obtained in the results in figure 3 and 5(b) when the freshly hydrogenated surface is exposed *in situ* to first water vapour, and then particular atmospheric gases or other species. In particular exposure to moisture or the individual gaseous components alone is ineffective in producing the high surface conductive state. The sticking probability for chemisorption of the common atmospheric constituents on diamond is negligible and their saturated vapour pressures are too high for significant physisorption to take place. Apart from nitrogen and inert noble gases, the natural gases species in air that would take part in inducing surface conductivity would be CO_2 and O_2, as both are found in synthetic air and wet air. Therefore, the physisorption of water is clearly responsible for the subsequent dissolution of the gas concerned, followed by the electron exchange between diamond and gas adsorbates.

The model proposed [30] suggests that the reduction of protons incorporated as hydroxonium ions in the surface layers is the chemical reduction process driven by injection of electrons from the underlying diamond lattice (see figure 11). Under standard atmospheric conditions, chemical potential μ_e of a water layer lies just below the valence band maximum (VBM), which is below the Fermi level E_F of *p*-type diamond. Electrons would thus be transferred from the diamond to the $H_3O^+/ (H_2O + H_2)$ redox couple (equation 3) and leave a hole accumulation layer, which in return provides the charge carriers (holes) responsible for high conductivity. The equilibrium is reached when the diamond-surface Fermi level is pinned at μ_e.

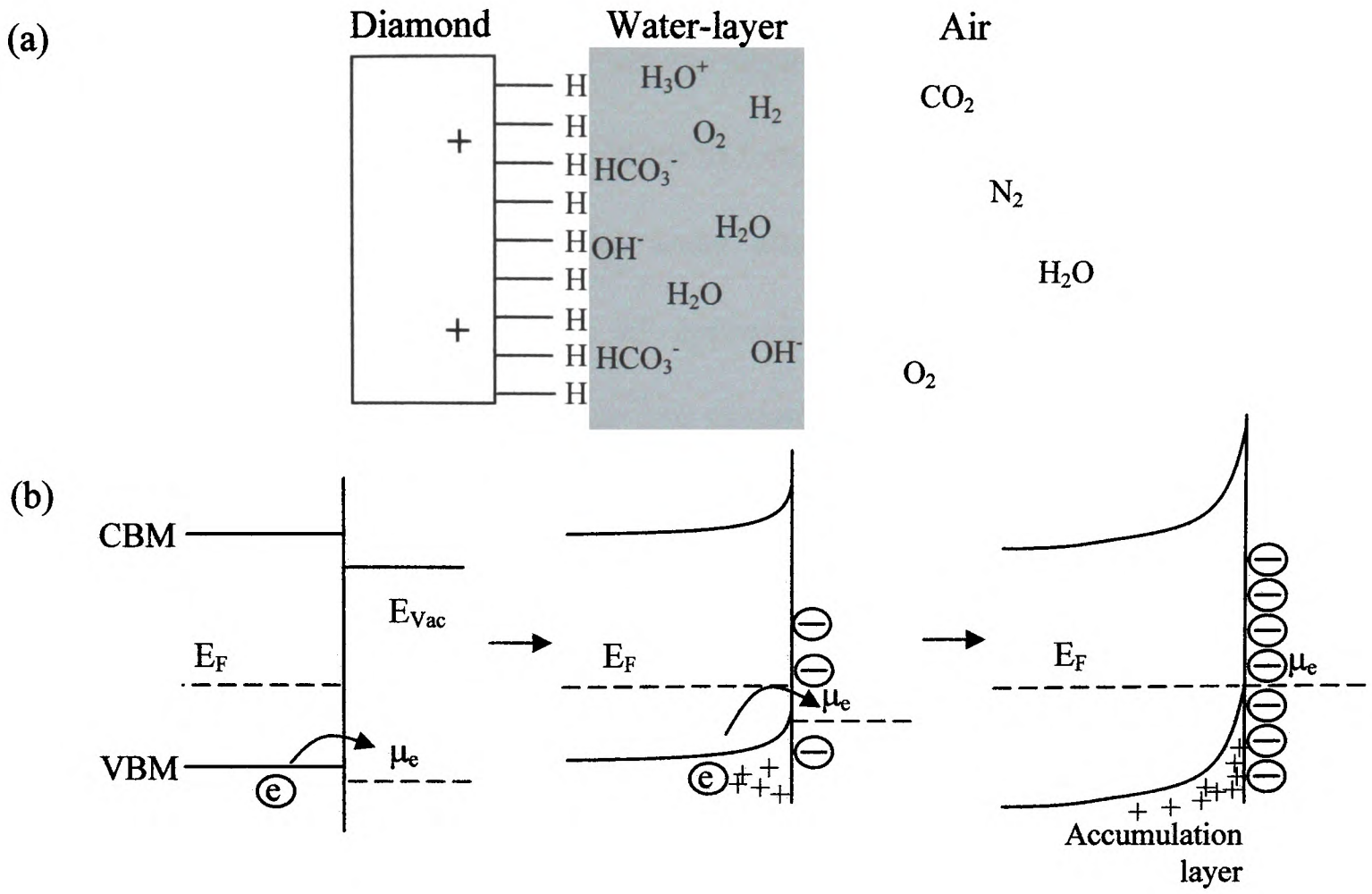


Figure 11. (a) Schematic picture of the hydrogenated diamond surface in contact with a water layer as it forms ***in air****; (b) evolution of band bending during the electron transfer process at the interface between diamond and the water layer*

Vapour phase species dissolved in the wetting layer which promote surface conductivity are likely to be acidic species which show the greatest free energies of dissolution and dissociation to form hydroxonium ions, unless kinetic factors are operative. The results again lend some qualitative support to this since both pure CO_2 (pKa 6.10, figure 5, eqn 1) and formic acid vapour (pKa 3.75, figure 4, eqn 2) are found to be effective in promoting surface conductivity, with the latter particularly so in line with its greater solubility and acidity in water compared to CO_2.

$$CO_2\,(g) + 2\,H_2O\ (\lambda) \leftrightarrow H_2CO_3\,(g) + H_2O\,(\lambda) \leftrightarrow H_3O^+\,(aq) + HCO_3^-\,(aq) \quad \text{(eqn 1)}$$

$$HCOOH\ (g) + H_2O\ (\lambda) \leftrightarrow H_3O^+\ (aq) + HCOO^-\,(aq) \quad \text{(eqn 2)}$$

$$2\,H_3O^+\,(aq) + 2\,e^- \leftrightarrow H_2\,(g) + 2H_2O\,(\lambda) \quad \text{(eqn 3)}$$

Screened protons, *i.e.* oxonium ions H_3O^+ will form as a consequence of the dissociation of carbonic acid and formic acid in both cases (eqn 1, 2 respectively). In nature, the CO_2 will dissolve in thin water layer to form carbonic acid, H_2CO_3 (pKa 6.10) through a proteolysis process and under usual atmospheric conditions an oxonium concentration according to a pH-value of approximately 6 will result. Thus, the electrolytic system at the diamond surface can exchange electrons with the diamond as soon as the hydrogenated diamond is being exposed to wet air.

As shown in figures 3 and 5, pure oxygen/moisture is effective at promoting surface conductivity when exposed to the moist diamond surface. In contrast, nitrogen is not effective for enhancing surface conductivity. This is because there are no nitrogen reduction couples with sufficiently positive electrochemical potentials (*i.e.* sufficiently negative reduction free energies) to be driven by electron injection from the valence band in diamond [30]. However for oxygen, direct reduction to water/hydroxide or peroxo species is energetically more favourable under standard thermodynamic conditions than the H^+/H_2 couple [31] (see equation 4 - 6), and so this can provide an equally viable route to the reduction of protons for electron acceptance from the diamond valence band.

$$O_2\,(g) + 4\,H^+\,(aq) + 4\,e^- \leftrightarrow 2\,H_2O\,(\lambda) \qquad E^{\varnothing} = 1.229\ V\ vs\ SHE \qquad \text{(eqn 4)}$$

$$O_2\,(g) + 2\,H_2O\,(\lambda) + 4\,e^- \leftrightarrow 4\,OH^-\,(aq) \qquad E^{\varnothing} = 0.401\ V\ vs\ SHE \qquad \text{(eqn 5)}$$

$$O_2\,(g) + 2\,H^+\,(aq) + 2\,e^- \leftrightarrow H_2O_2\,(aq) \qquad E^{\varnothing} = 0.682\ V\ vs\ SHE \qquad \text{(eqn 6)}$$

Dissolved oxygen is expected to physisorb instead of chemisorbing on the H-terminated surface at room temperature, as the oxygen chemisorption can paralyze the surface conductivity. The presence of oxygen on surface conductive diamond was probed from gas evolution spectra [17,32], showing predominantly CO_2 and CO were desorbed. The results were also in agreement with the discussion in Chapter 5, showing that more O_2

adsorption on H-terminated diamond occurs than on clean surface due to kinetic factor, though their surface coverage is low.

By employing equation 3 (derived from CO_2 dissolution in water) into Nernst equation 7, a solution with pH 6 will be generated with hydrogen partial pressure (pH_2) = 10^{-3} mbar. μ_0 = - 4.44 eV is the chemical potential for electrons under standard hydrogen electrode (SHE) conditions.

$$\mu_e = \mu_0 - \frac{kT}{2}\ln\left[\frac{\left([H_3O^+]/[H_3O^+]_{SHE}\right)^2}{\left([H_2]/[H_2]_{SHE}\right)}\right]$$

$$= -4.44eV + \frac{0.05915}{2}eV\left[2pH + \log\left(\frac{pH_2}{bar}\right)\right]$$

$$= -4.44eV + \frac{0.05915}{2}eV\left[2(6) + \log\left(10^{-6}bar\right)\right]$$

$$= -4.44eV + 0.18eV$$

$$= -4.26eV \qquad \text{(eqn 7)}$$

The calculated value for initial chemical potential μ_e (before band bending to occur) of an aqueous wetting layer is - 4.26 eV. Using the same equation, with pH = 1, the initial value of μ_e will be pinned at - 4.56 eV. Whereas for O_2, by employing equation 4 with pH solution equivalent to 7 and oxygen partial pressure (pO_2) is 205 mbar at 1 atm into the Nernst equation (equation 8), the chemical potential of electrons in the liquid phase, μ_e is calculated as – 5.25 eV.

$$\mu_e = \mu_0 + \mu_{O_2/H_2O} - \frac{kT}{4}\ln\left(\left[H^+\right]^4.\left(\frac{pO_2}{bar}\right)\right)$$

$$= \mu_0 + (-1.23eV) + \frac{0.05915}{4}eV\left(4pH - \log\left(\frac{pO_2}{bar}\right)\right)$$

$$= -5.67eV + \frac{0.05915}{4}eV\left(4(7) - \log\left(205x10^{-3}\right)\right)$$

$$= -5.67eV + 0.42eV$$

$$= -5.25eV \qquad \text{(eqn 8)}$$

According to the hypothesis proposed by Ri *et al.* [19], the electron transfer will occur from diamond to gas adsorbates when the adsorbates have larger negative electron affinity, χ or chemical potential, μ_e than the work function, ϕ of the diamond. Considering the electron affinity of - 1.3 eV for the hydrogenated diamond [15], the work function of moist hydrogenated diamond is approximately 4.2 eV relative to the vacuum level and the pinning position of E_F at the water/diamond interface lies just 50 meV below VBM. As both of $\mu_{e,O2}$ and $\mu_{e,CO2}$ are more negative than $\phi_{diamond}$, electrons will be transferred from the semiconductor to the mediated surface states, which will in turn create holes in the subsurface region. The accumulation of holes charge will further bring upward band bending, which increases the acceptor levels of hydrogen-related states near the surface and create high surface conductivity of hydrogenated diamond.

As normal atmospheric air contains both CO_2 (a source of hydroxonium ions in water) and O_2, albeit at much lower pressures than O_2, it is clearly possible that both species can provide sources of electron acceptors during exposure of freshly hydrogenated diamond to atmosphere to produce the surface conductive film.

Black diamond is generally used as a *passive application* in thermal management in regard to its low quality and low cost. The surface conductivity at varying annealing temperature (see figure 7) for *thermal management* graded black diamond is not much different from the *optical grade* white diamond of higher quality. The air exposed of H-surfaces for both diamond reaches the high conductive level at almost identically rates within the same exposure period to atmospheric air. Even though the black diamond is of low quality material, a hydrogen plasma can clean the non-diamond impurities to the state that the surface conductive is dependent on the H-subsurface layer, instead of carbonaceous impurities. Similar carrier concentration and mobility values were reported for black, white or even single crystal diamond [33] by mean of Hall measurements

results. Therefore, black diamond could perform as well as high quality of optical grade diamond when hydrogenated to generate *p*-type characteristics.

3.2.3.2 Temperature

The above work indicates two crucial components that are responsible for surface conductive layers on diamond, (a) chemisorbed hydrogen to reduce the work function of diamond, and (b) the wetting layer with acceptors in it, to enable electrons to be transferred from the diamond valence band. Therefore, the disruption of either of these layers will destroy the surface conductivity.

Results in figure 9 show if the surface conductive diamond is heated and then cooled in vacuum, the conductivity is lost at 200 °C. Results in figure 7 shows if the surface conductive diamond is heated for a short period and cooled in air, the conductivity is stable up to 400 °C. Results in figure 10 shows a long period of heating in air before the exposure to adsorbates, the conductivity is stable up to 250 °C; whereas in vacuo the SC is stable above 400 °C. This arises since

(a) The hydrogen layer is stable in vacuum above 400 °C. Therefore, pre-annealing above such temperature will not desorb the hydrogen layer because the chemisorbed hydrogen requires much higher temperature, up to 800 – 1000 °C [34] to desorb efficiently in *vacuo*. Once the H-surface is exposed to wet air, the adsorption of air adsorbates will induce high surface conductivity. This result is shown in figure 10, revealing that the surface conductance decreases insignificantly from the initial conductive value. The well-known thermal stability of hydrogen is evidenced with the RHEED analysis [35], showing that the surface structure is remain in the form of visible (001)-2 x 1, which is well terminated with hydrogen at such temperatures. Thermal desorption results [36] has actually suggested that the presence of bonded hydrogen (up to 70 %) can be related to the

water adsorption while the diamond is exposed to atmospheric air. Thus, the moisture in air could possibly mediate the small amount of vacancies due to the loss of hydrogen during the annealing process.

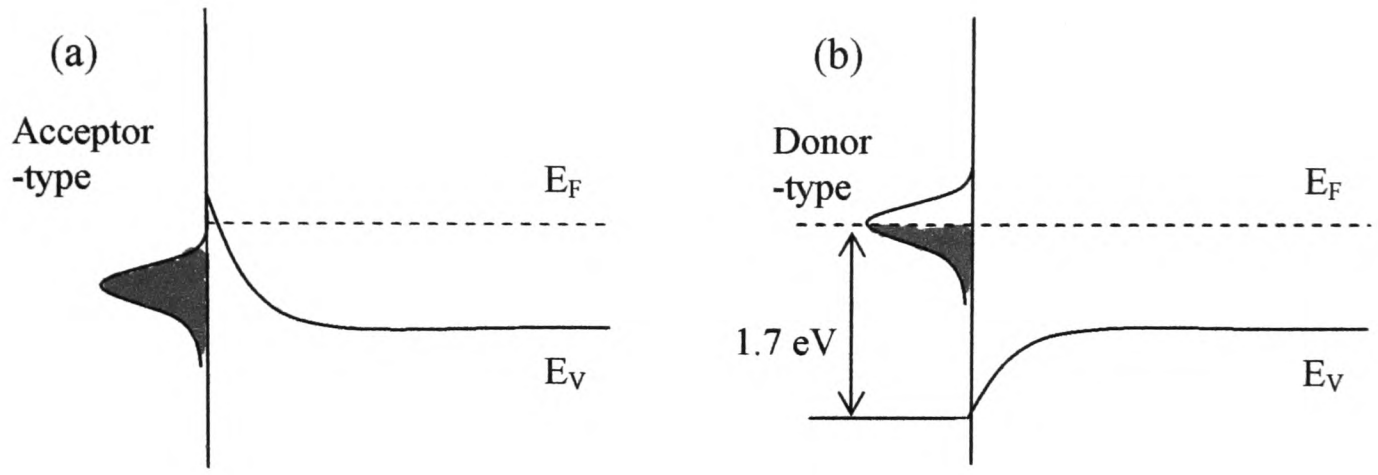


*Figure 12. Proposed energy band diagrams for undoped diamond of (a) **conductive** hydrogenated and (b) oxygenated surfaces*

(b) Hydrogen layer in air is unstable at 250 – 400 °C. Annealing the hydrogen-terminated surface under such condition disrupts the hydrogen phase, including the surface hydrogen and the out-diffusion of hydrogen incorporated in the film [35]. The surface conductivity collapses to an insulating state [37,38] due to the participation of oxygen or water vapour in the hydrogen desorption process. This phenomenon is regarded similar to the oxygen plasma treated surface or the chemically etched surfaces in a hot CrO_3-H_2SO_4 aqueous solution [21,22]. The Fermi level of the oxygenated diamond in this case is proposed to be pinned at 1.7 eV above the valence band edge [22] (figure 12,b) and the energy band bends downwards to give depletion layer for holes, as compared to surface conductive layer (a). This will provoke the loss of carriers from the surface or the generation of more scattering centers [8]. Therefore, no conductivity can be observed due to the loss of hydrogen layer.

(c) Air adsorbates are unstable above 200 °C. Any heating of a surface above this temperature will desorb the adsorbates to some extent. For example, the annealing of the surface conductive diamond in *vacuo* (see figure 9i) shows higher SC, with two orders of

magnitude larger than that being annealed in wet air (9 ii). This is because some amount of the negatively charged air adsorbates within the wetting layer, such as HCO_3^- and OH^- remains on the sufficiently hydrogenated surface, thus inducing the minimal amount of surface conductance. Whereas, annealing in air removes the hydrogen, which acts as the bonding sites for the air adsorbates, thus disrupting the SC completely.

Therefore, this lack of stability of surface conductivity is a problem for the diamond-based electronic application, such as field effect transistor and Schottky diodes.

3.2.4 Conclusion

Freshly hydrogenated CVD diamond surfaces under microwave plasma are insulating, even with *in situ* exposures to water vapour and other common atmospheric gases in individual exposures. However exposure to water vapour (moist) followed by the exposure to gases, such as formic acid, oxygen or carbon dioxide produces a large increase in conductivity, although nitrogen is ineffective in this regard.

The results are qualitatively consistent with previous suggestions that the conductivity at exposed hydrogenated diamond surfaces arises through electron transfer to adsorbates, which is mediated by the presence of a "wetting layer".

Black diamond is as good as white diamond, showing the similar characteristics of surface conductivity.

Changes in atmospheric conditions are regarded to affect the density of the negatively charge radicals adsorbed to the C-H surface bonds, correspondingly to the changes of acidity and gaseous solubility.

Surface conductive layers are not thermally stable due to its stability depends exactly on the environment in which the heating is done. This would be a problem for the potential electronic application.

3.3 Solution Phase Effect and Electrochemical Studies

3.3.1 Experimental

High quality MWPECVD undoped freestanding diamond samples (see SEM figure 1) were used for surface conductivity measurements in solution. Prior to the hydrogenation, all samples were boiled in concentrated $H_2SO_4/(NH_4)_2S_2O_8$ solution at 200 °C for 2 hours to obtain contaminant free oxidized diamond surface. Similar to Section 3.2.1, hydrogenation was carried out on the undoped diamond surface inside a microwave plasma chamber under the same parameters. Diamonds were placed on a molybdenum substrate holder. After cooling down to room temperature, the diamonds were exposed to atmospheric air for 1 - 3 days to bring the surface conductance up to the maximum level of 1 – 2 μS. Home grown boron-doped diamonds (1 mm in diameter) using hot filament method (HFACVD) were used for comparison.

Diamond was mounted on top of a layer of insulator (plastic) to avoid measuring the current passing through from the backside of the diamond (see figure 13c). Two brass holders with gold foil layered clips were used to clamp the on-top diamond surface. With the conductive surface left exposed to gas or solution media (standardized area of working electrode = 0.04 cm^2, stated otherwise), the rest of the diamond was covered by insulating putty (Bostik Blu® Tack) to prevent any leakage current during CV measurement.

To ascertain no leakage of solution through the diamond | insulator contact, the surface conductance was measured *via* two-probe holders before and after dipping the diamond inside the solution. The conductivity for freshly hydrogenated sample was expected to be similar in both media. Currents were recorded *in-situ* while applying 2 volts through the diamond surface (see experimental setup in figure 13a, b). During the CV measurement, the wires were disconnected from the external circuit, and later clipped to the working electrode. Platinum wire was used as counter electrode and saturated

calomel electrode (SCE) as reference electrode. Electrochemical experiments were conducted with an Autolab PGSTAT20 system (EcoChemie, Netherlands).

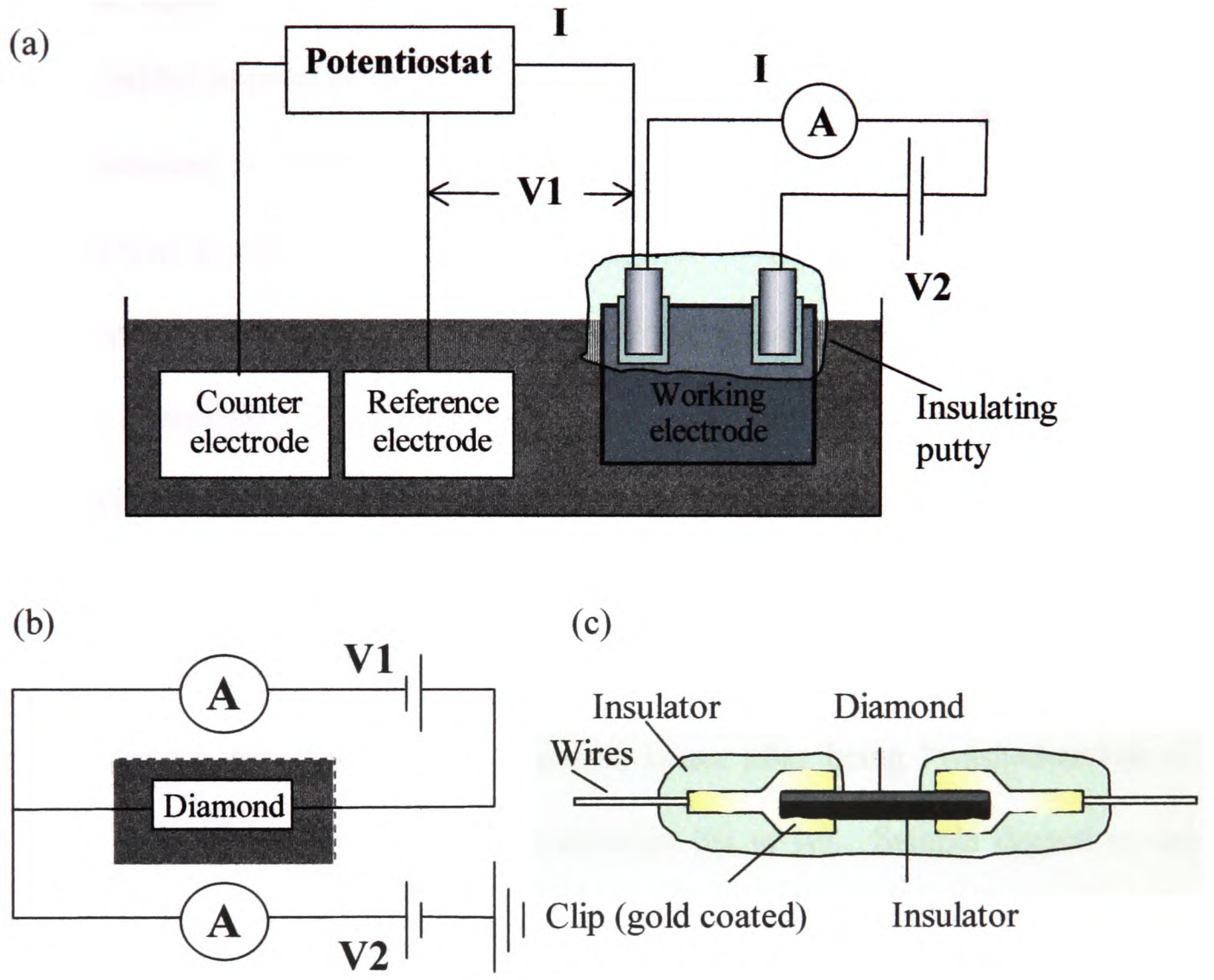


Figure 13. The schematic diagram for the setting of diamond as the working electrode in solution (a) with the circuit assignment in connection to potentiostat; (b) the schematic circuit, with the circuit grounded at external wires connection via V2; and (c) the side view of sample mounting

Chemical reagents used were of analytical grade. $CuCl_2$ (JMC, 99+ %), $CuSO_4.5H_2O$ (Aldrich, 98+ %), $Ru(NH_3)_6Cl_3$ (Alfa Aesar, assay), KCl (Aldrich, 99+ %), $NaHCO_3$ (BDH, 99.5 %) were used directly without further purification. Demineralised water was taken from an Elgastat filter system with resistivity of not less than 18 MΩ cm. Experiments were conducted after de-aerating with high purity argon (BOC) for at least 15 minutes. The temperature was 22 ± 2 °C.

3.3.2 Results

3.3.2.1 pH and Temperature

The changes of conductance in different pH environments were tested. Conductive diamond was dipped into solutions comprising 0.1 M KCl (pH 7), or with 0.1 M HCl or 0.1 M KOH added to produce pH 1 or pH 13 acidities respectively at 300K. Conductivity was both measured in solution, or after the substrate was withdrawn from solution and allowed to dry by argon in the laboratory atmosphere. Results are illustrated in figure 14, where the variation in conductance compared to the initial conductive state is plotted for the differing treatments. The conductance in solution under pH 1 condition is comparable to that observed from the sample prior to insertion; the conductivity falls for the solutions of higher pH. This shows that for lower pH, an approximately four times the conductance is obtained in air than in solution (i *vs* vi); whereas the diamond that was dipped inside solution of pH 13, the conductance measured in air after being "washed-and-dried" is much lower than that measured in basic solution (iii *vs* iv). Sample dipped in neutral solution shows intermediary conductive behaviour between the solutions of different pH (ii *vs* v).

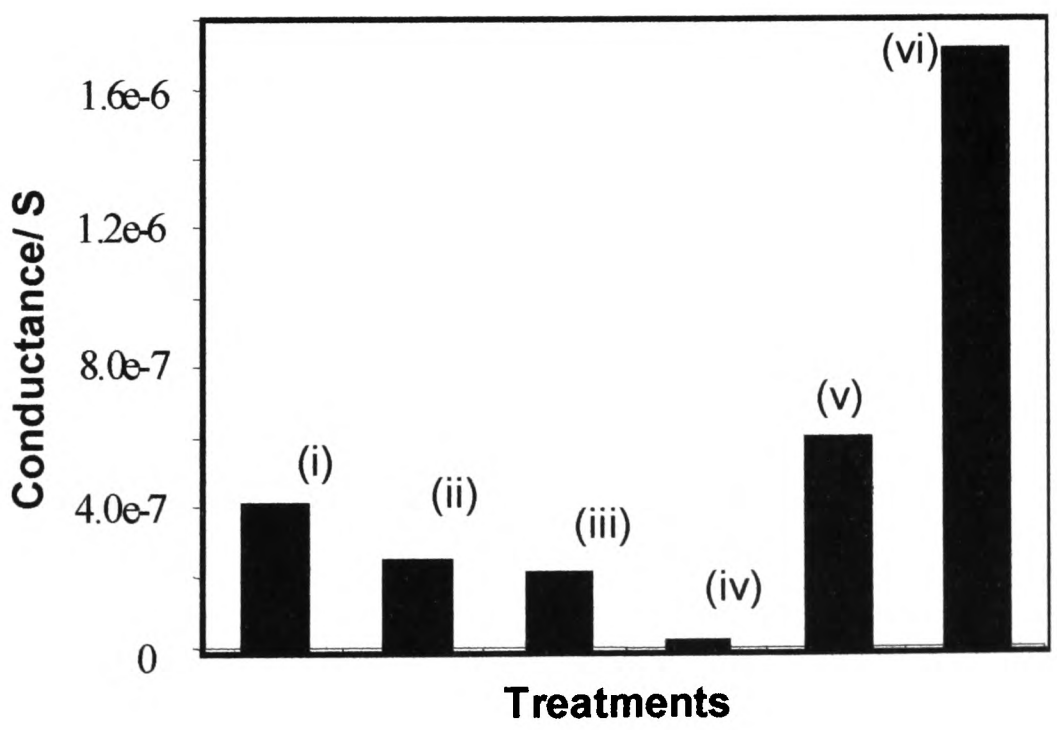


Figure 14. Conductance observed in solution at (i) pH 1, (ii) pH 7, (iii) pH 13 and after sample was withdrawn and dried from solutions of (iv) pH 13, (v) pH 7 and (vi) pH 1

By simply washing the diamond pieces with pure water, the initial SC value of 1 x 10^{-6} S can be restored. The measured changes in conductivity were also found to be insensitive to the KCl concentration as it was varied in the range 0.5-0.05 M (results not shown), suggesting that it is the concentration of hydroxide and hydroxonium ions which are primarily responsible for the changes occurring.

The thermal effect on surface conductive diamond in the exposure to different chemical environments (*i.e.* pH) was investigated. Experiments were conducted by increasing the temperature in the solutions of pH 1 or pH 13, while the *in-situ* changes of diamond surface conductance was recorded. The result presented in figure 15 shows the diamond in alkaline solution which suffered sharp fall of conductance soon after 50 °C and irreversible change of surface conductivity was observed, even the solution was later cooled down to the room temperature. The diamond under SEM (not shown) reveals low intensity of image as compared to surface conductive region with high hydrogen content, suggesting that the surface has suffered from oxidization. As compared to acidic medium, the surface conductance remains at high conductive state in solution even if the temperature of the solution was brought up to boiling point.

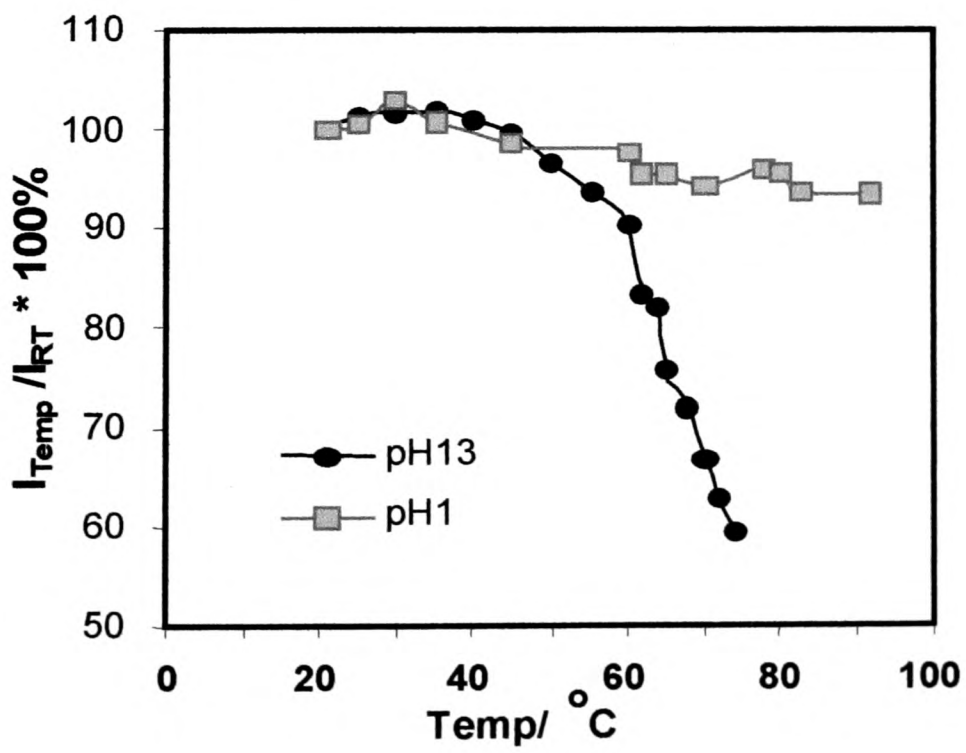


Figure 15. Conductivity at temperatures indicated in acidic solution (0.1 M KCl solution, pH 1), and alkaline solution (0.1 M KCl solution, pH 13)

The *in-situ* change of conductance relative to the changes of pH environment was carried as follow (see the experiment setup in figure 16, illustrated on the right). Diamond was mounted as before and the SC was measured with two probe contacts. The sample was dipped in $NaHCO_3$ solution (0.1 M, pH 8.45), and HCl (0.1 M, pH 1.00) was titrated gradually inside the solution. The solution was stirred well with a magnetic stirrer for 5 min to induce homogeneity for each HCl addition. With the addition of acid, the conductance increased at nearly 3.6×10^{-8} S/ pH from the initial value of 2.5×10^{-7} S. The SC was saturated at 3.2×10^{-7} S in the pH range of 6.5 – 2.5, which was the equivalent point of $V_{HCl}/V_{NaHCO_3} \sim 1.0$. With the increase of acidity in the medium, the conductance has started to increase drastically at approximately 7.0×10^{-8} S/ pH.

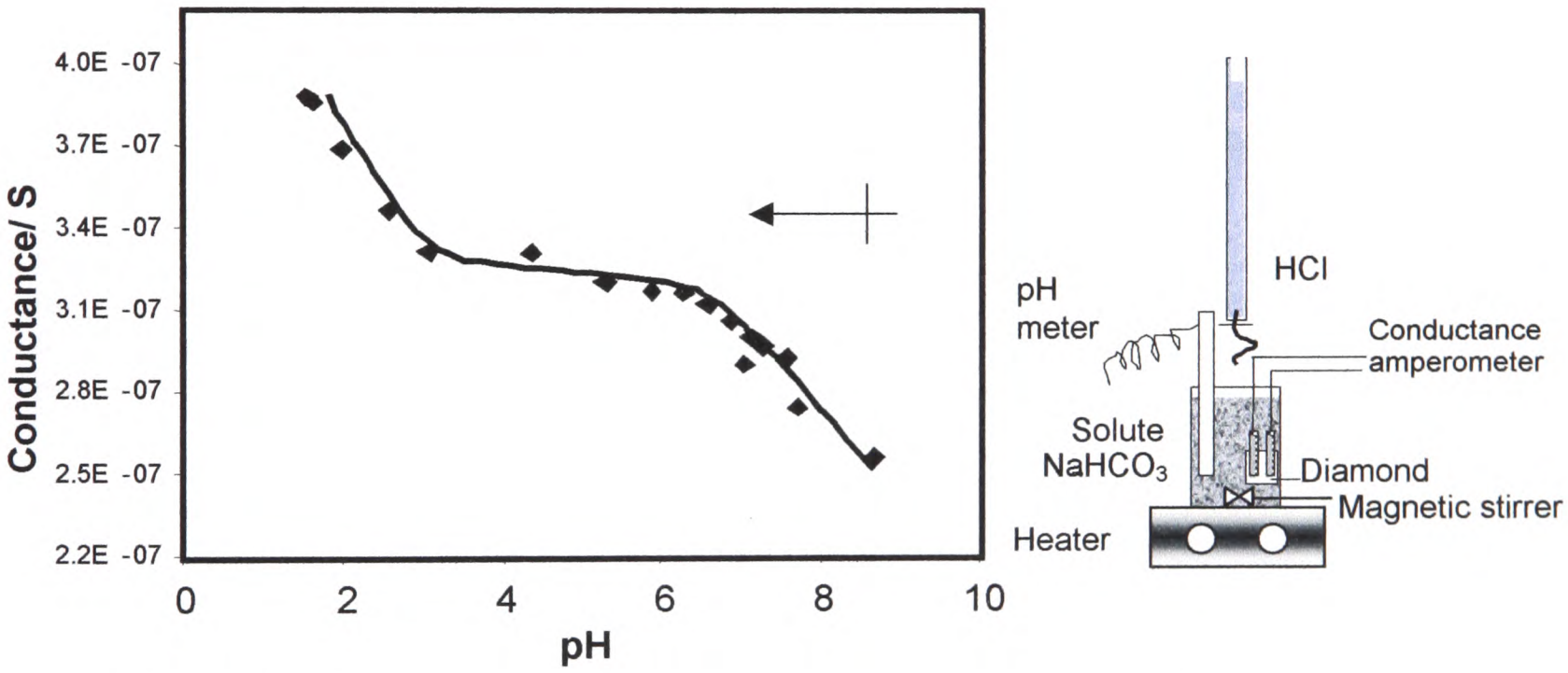


Figure 16. Variation of conductance in solution as HCl is titrated into a weakly basic bicarbonate solution; schematic drawing on the right showing the experiment setup

Briefly, the change of surface conductivity on surface conductive (undoped) diamond has shown much significant effect in air than in solution. With the magnitude changes of conductance in air of 5 - 6 orders between two extreme chemical environments (*i.e.* pH), the changes of SC in solution would merely be observed in less than 1 order of magnitude.

3.3.2.2 Electrochemistry

The surface conductive diamond was tested for one-electron reduction of $Ru(NH_3)_6^{3+}$ to probe the basic electrochemical behavior. CVs were recorded at different scan rates for the reduction of 3 mM $Ru(NH_3)_6^{3+}$ in 0.1 M KCl .

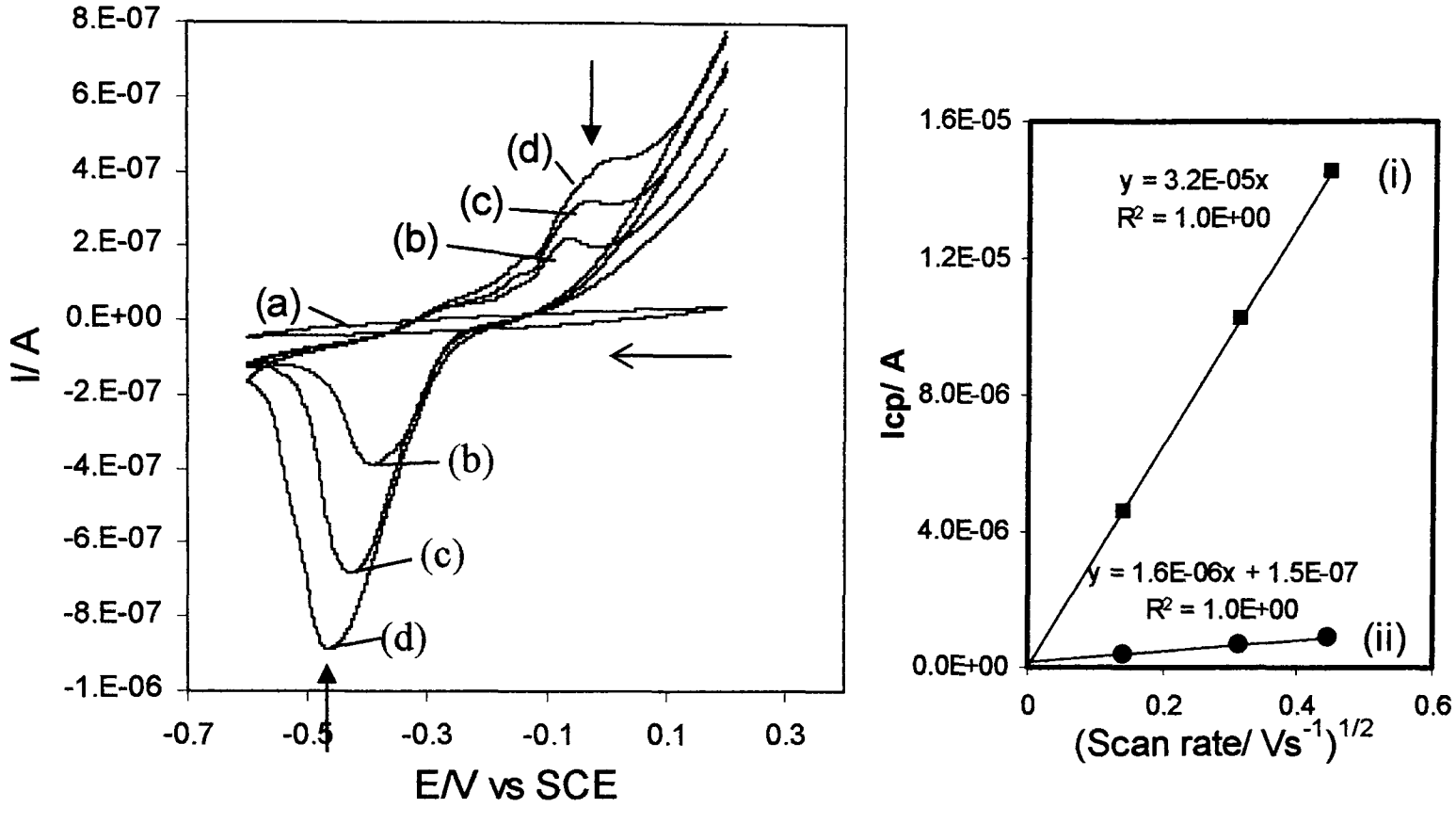


Figure 17. CVs for surface conductive diamond in 0.1 M KCl at a potential scan rate of 0.1 Vs^{-1} (a), and the reduction of 3 mM $Ru(NH_3)_6^{3+/2+}$ in 0.1 M KCl at different potential scan rates (b = 0.02 Vs^{-1}, c = 0.1 Vs^{-1}, d = 0.2 Vs^{-1}). Figure on the right shows the correlation plot of cathodic peak current, Icp vs $v^{1/2}$ for (i) theoretically expected current and (ii) experimental current

The potential ramp was initiated at 200 mV and scanned in the negative direction. On the forward sweep, cathodic peaks are observed at - 410 mV, which are associated with one-electron reduction of $Ru(NH_3)_6^{3+}$ to $Ru(NH_3)_6^{2+}$. On the reverse sweep, anodic peaks of oxidation current are observed at approximately - 51 mV, which are associated with one-electron oxidation of $Ru(NH_3)_6^{2+}$ generated at the electrode surface back to $Ru(NH_3)_6^{3+}$. The average difference between oxidation and reduction peak potentials (ΔEp) is 359 mV and asymmetrical feature of CV was observed, with cathodic current higher than anodic current. The cathodic peak currents for this redox analyte varied linearly with $v^{1/2}$ ($r^2 \sim 0.99$), however does not pass exactly through the zero intercept. According to *Randles-Sevcik* equation, a reversible electron transfer reaction shows the

direct proportionality between the peak current and square root of scan rates, crossing the zero origin. Therefore, the process involved here is not fully diffusion controlled. The magnitude of the cathodic peak current 17(ii) is about 1 - 2 orders smaller than the theoretically predicted current, (i).

3.3.2.3 Metal Deposition and Stripping

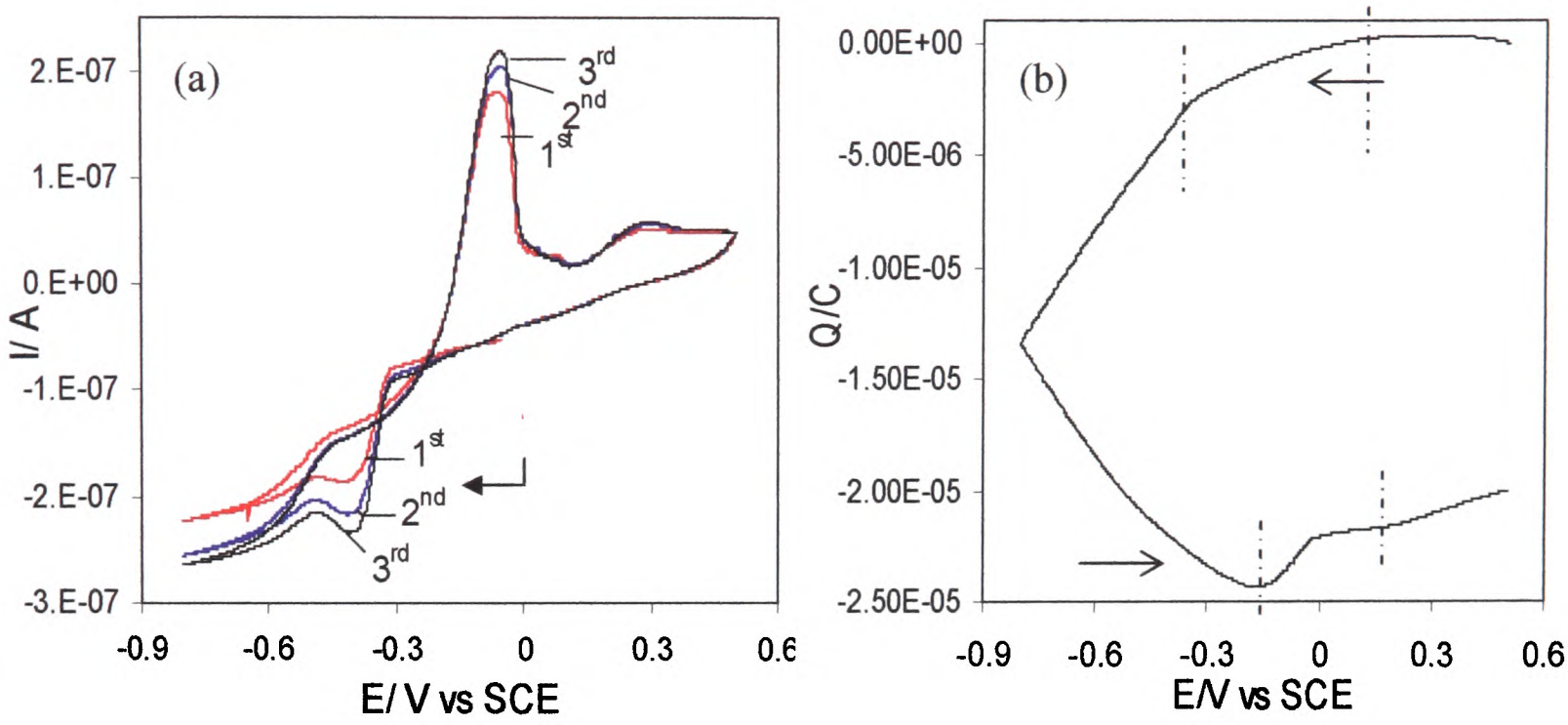


Figure 18. (a) CVs for three consecutive scans obtained on surface conductive diamond with a potential scan rate of 20 mV s^{-1} for the reduction of 1 mM $CuCl_2$ in aqueous 0.1 M HCl and (b) the corresponding integrated current response of the third potential cycle.

The metal deposition onto surface conductive diamond was performed electrochemically in aqueous solution of 1 mM $CuCl_2$ dissolved in 0.1 M HCl. The scan was initiated at 0 V in the negative direction, and continues to flow at less negative potentials on reversal of the scan direction as two *potential crossovers* were found within the potential of - 0.20 and -0.4 V *vs* SCE, indicating the mechanism of growth and deposition initiated on the reduced copper as nucleation sites. The copper reduction and deposition is observed with the maximum cathodic peak at – 0.43 V. The continued scanning in the positive direction yielded a very well-defined metal stripping (*i.e.*, oxidation) peak at – 0.05 V, followed by a second stripping peak at 0.28 V *vs* SCE. The integrated current response, as revealed in

figure 18b, showed the possible occurrences of two reductions (linear slopes upon cathodic direction) and two metal stripping processes (marked curvatures on reverse scan).

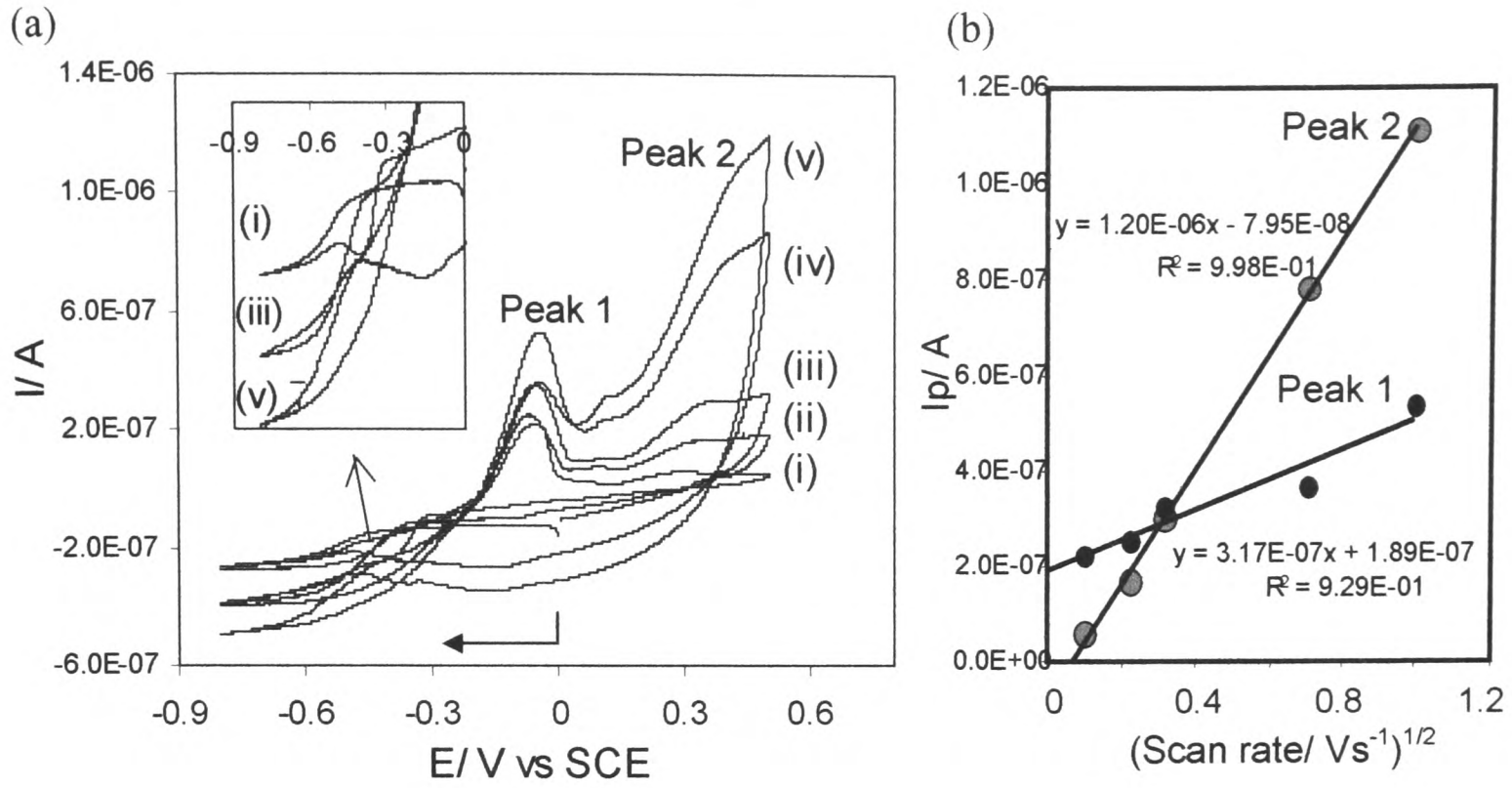


Figure 19. (a) CVs of copper electrodeposition and stripping process on surface conductive diamond in response to $CuCl_2$ (1 mM, pH 1) in 0.1 M HCl at different potential scan rates (i = 0.01 Vs^{-1}, ii = 0.05 Vs^{-1}, iii = 0.10 Vs^{-1}, iv = 0.50 Vs^{-1}, v = 1.00 Vs^{-1}) with the magnified region in inset for - 0.9 ≤ E ≤ 0 V vs SCE; (b) The correlation plot of stripping peak currents, Peak 1 and Peak 2 vs square root of scan rates, $v^{1/2}$

Figure 19a shows the CVs at different potential scan rates, ranging from 0.01 Vs^{-1} to 1.00 Vs^{-1}, with the inset showing the potential crossover curves within – 0.8 and 0 V *vs* SCE regions at different scan rates. With increasing of potential scan rates, the cathodic reduction curves were shifted down to more negative current, while peak 2 that was observed at 0.28 V increased drastically as compared to peak 1 at – 0.05 V *vs* SCE. Figure 19b shows the correlation of copper stripping peaks, peak 1 and peak 2 to the square root of the scan rates, $v^{1/2}$, revealing the linear correlations for their stripping current to $v^{1/2}$ though the plots do not pass through the zero origin, signifying fairly *less* diffusion controlled process have taken places.

The stripping efficiency, $Q_{stripping}$ (or Q+/Q-) is defined here as the charge accumulated under the anodic stripping peak divided by the charge counted under the cathodic deposition peak for the copper deposition and stripping process. The stripping

efficiency as a function of potential scan rates is plotted in figure 20. The stripping efficiency increased from 0.2 at a scan rate of 0.01 Vs^{-1} to 0.85 at 1.0 Vs^{-1}. The increase of the ratio shows that the deposited copper particulates could more easily be stripped off when higher potential scan rates were applied.

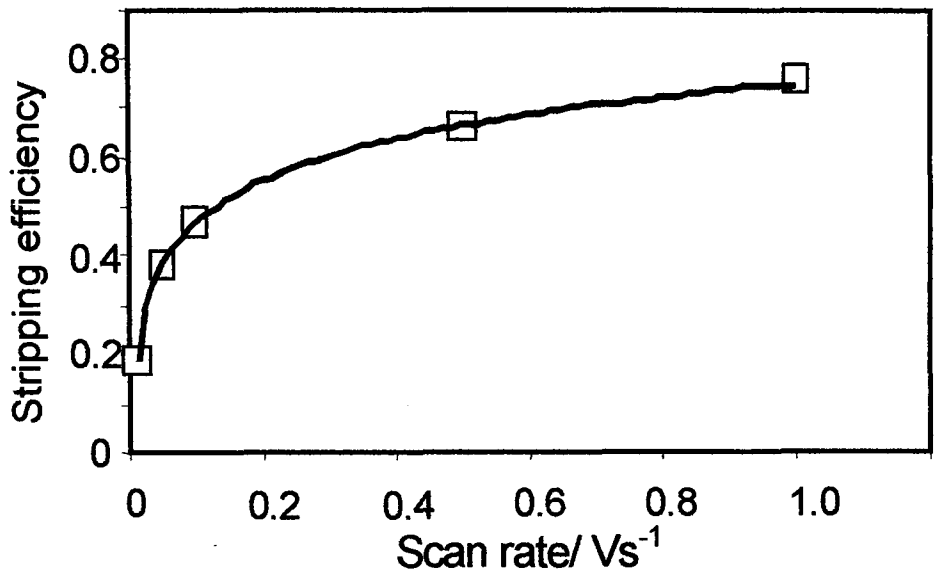


Figure 20. The correlation plot of stripping efficiency (Q+/Q-) versus the scan rates on surface conductive diamond in response to $CuCl_2$ (1 mM, pH 1) in 0.1 M HCl

The electrochemical behaviour of surface conductive diamond was compared to boron-doped diamond in response to $CuCl_2$ solution (1 mM, pH 1). For boron-doped diamond, two copper stripping peaks were observed at – 0.11 V and 0.30 V *vs* SCE, and the metal reduction and stripping peaks increased accordingly to the increase of respective square root of the scan rates, $v^{1/2}$ (not shown). Unlike surface conductive diamond, the stripping peak that was observed at 0.30 V on boron-doped diamond did not show the drastic increase of stripping current at high potential scan rate.

The comparison of electrochemical response of surface conductive diamond (a) and boron-doped diamond (b) to $CuCl_2$ is revealed in figure 21. The corresponding current signal for the surface conductive (order of 10^{-7} A) is nearly an order of current magnitude smaller than boron-doped diamond (order of 10^{-6} A). Furthermore, the copper deposition and stripping peaks occurs at a wider potential for surface conductive diamond ($-0.8 \leq V \leq 0.5$) than boron-doped diamond ($-0.5 \leq V \leq 0.5$), signifying a type of sluggish kinetics process has taken place electrochemically on the surface conductive diamond electrode.

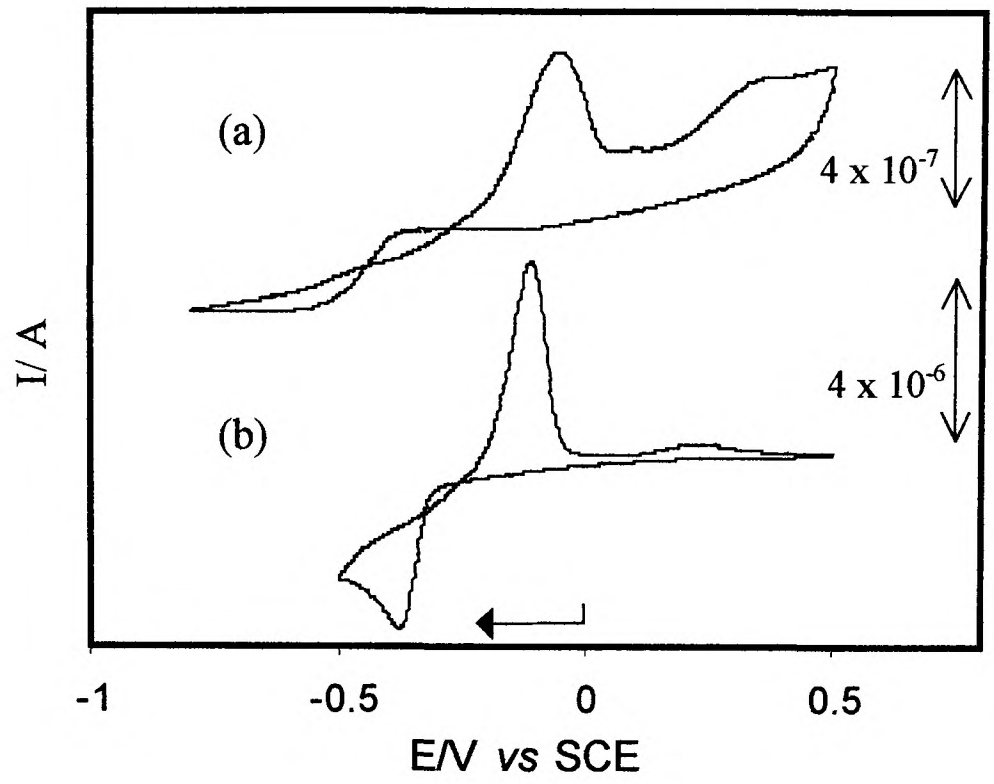


Figure 21. The comparison of CVs responses to $CuCl_2$ (1 mM, pH 1) in 0.1 M HCl at a potential scan rate of 0.1 Vs^{-1}, on (a) surface conductive diamond (0.04 cm^2), and (b) boron-doped diamond (0.0079 cm^2)

In order to study the condition of a chloride free environment, acidified $CuSO_4$ solution in 0.1 M HCl and neutral $CuSO_4$ (pH 7) in 0.1 M Na_2SO_4 were conducted for the comparison to the previous experiments. CVs in figure 22 show the response of surface conductive diamond to $CuSO_4$ (pH 1) at different concentration, ranging from 0.5 mM – 10 mM.

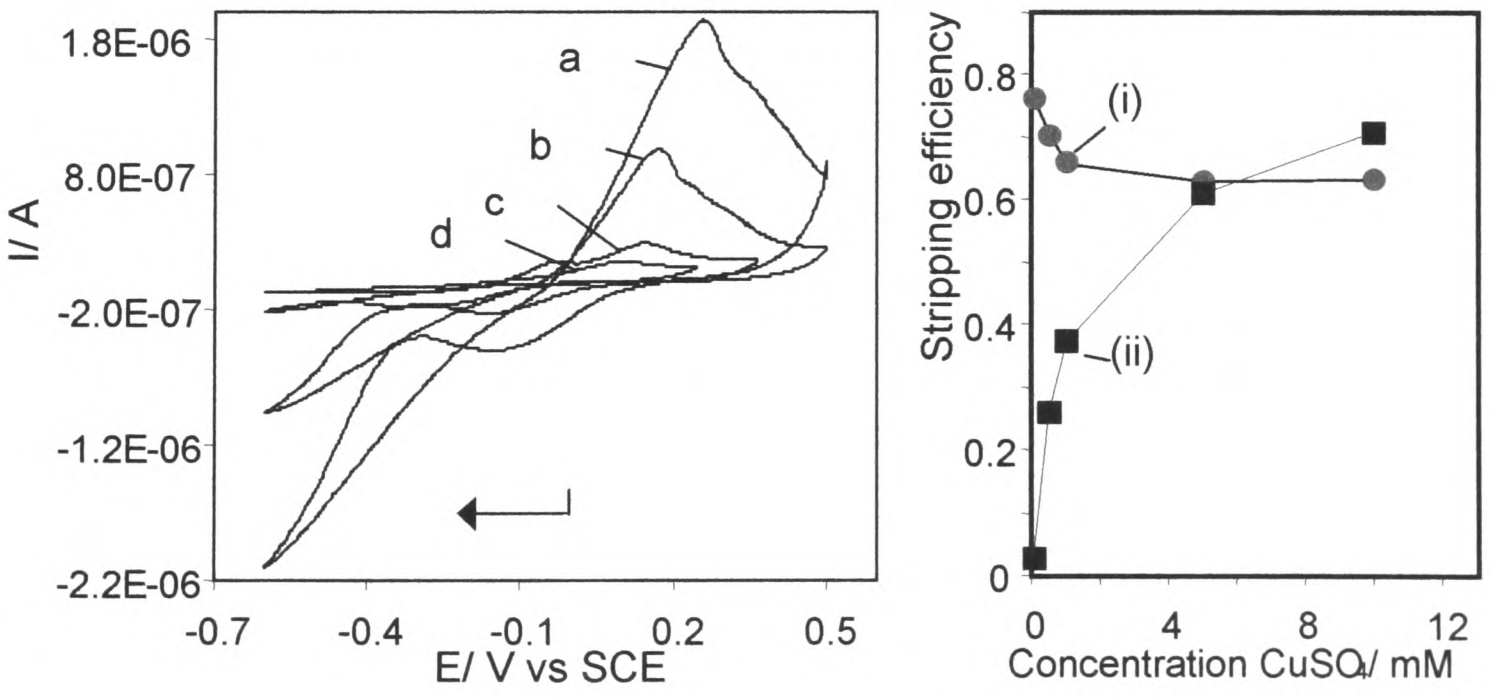


Figure 22. CVs response of surface conductive diamond on different concentration of $CuSO_4$ (pH 1) in 0.1 M H_2SO_4 (a = 10 mM, b = 5.0 mM, c = 1.0 mM, d = 0.5 mM). Figure on the right showing the stripping efficiency vs $CuSO_4$ (pH 1) concentration of (i) surface conductive diamond and (ii) boron-doped diamond

In figure 22, the intersecting of forward and reverse current *vs* E curves on cathodic sweeps were also observed due to the metal nucleation and growth mechanism. The reduction peak was observed at – 0.1 V in response to different concentration whereas the oxidation peak shifted to higher stripping potential from 0.02 V (for 0.5 mM $CuSO_4$) to 0.20 V (for 10 mM $CuSO_4$).

The stripping efficiency of copper on surface conductive diamond (see figure 22i) was found to be independent on the concentration of $CuSO_4$ solution, with an averaged Q+/Q- ratio of 0.68 within the range of concentration. This was in contrast to the boron-doped diamond (22ii) as the stripping efficiency increased exponentially with the increasing concentrations of $CuSO_4$ solution.

The surface conductive diamond was also compared electrochemically to boron-doped diamond in response to $CuSO_4$ solution, as the result is shown in figure 23. The CV for the conductive diamond was extended to a larger potential range (- 0.6 ≤ V ≤ 0.5) and the redox current signal was nearly an order of magnitude smaller than boron-doped diamond. The copper dissolution peak for boron-doped (23b) diamond was observed at 0.02 V *vs* SCE, as compared to 0.20 V for surface conductive diamond (23a).

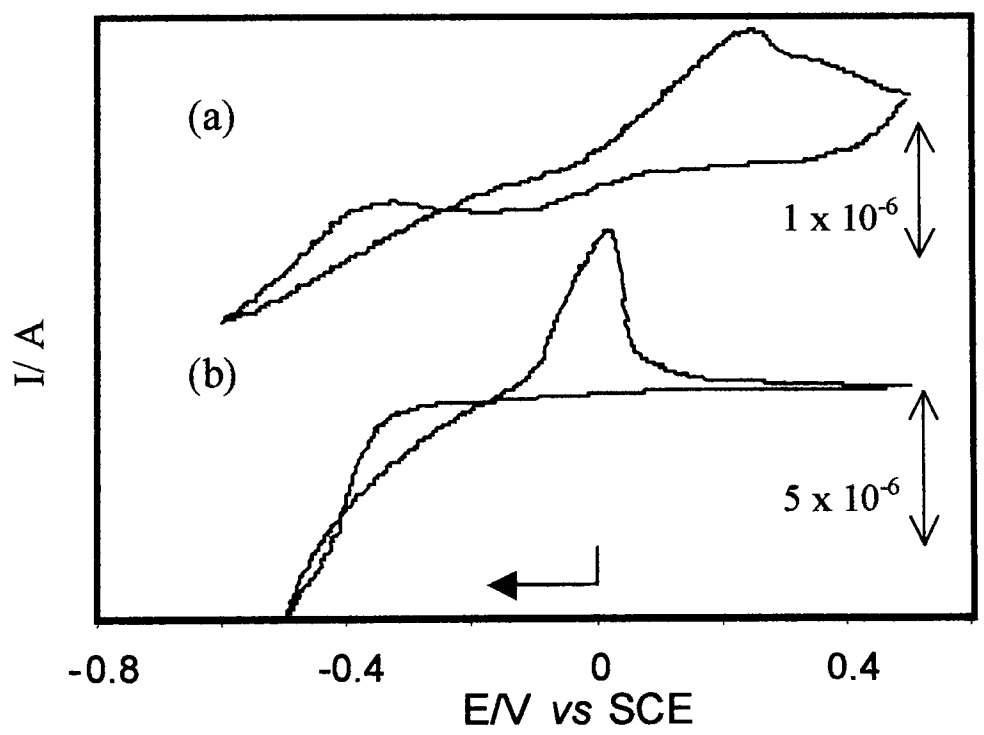


Figure 23. The comparison of CV responses to $CuSO_4$ (5 mM, pH 1) in 0.1 M H_2SO_4 at a potential scan rate of 0.1 Vs^{-1}, on (a) surface conductive diamond (0.04 cm^2), and (b) boron-doped diamond (0.0079 cm^2)

The pH sensitivity of surface conductive diamond was investigated by changing the acidic environment to neutral solution of $CuSO_4$ in 0.1 M Na_2SO_4. The first few scans have shown the gradual decreases in faradaic signals upon the potential scanning, followed by the subsequent loss in signal (i – iii). As revealed in figure 24 (A), the CV shows high resistive feature of electrochemical process with insignificant response of copper deposition on negative potential scans. Upon positive potential sweeping, no copper dissolution peak was observed at different potential scan rates. Figure 24 (B) presents the comparison of CV signals towards $CuSO_4$ solution of pH 1 and pH 7, as referenced to the non-conductive diamond with a surface conductance of ~ 1 x 10^{-11} S.

Thus, the electrochemistry of the surface conductive layer is very pH dependent.

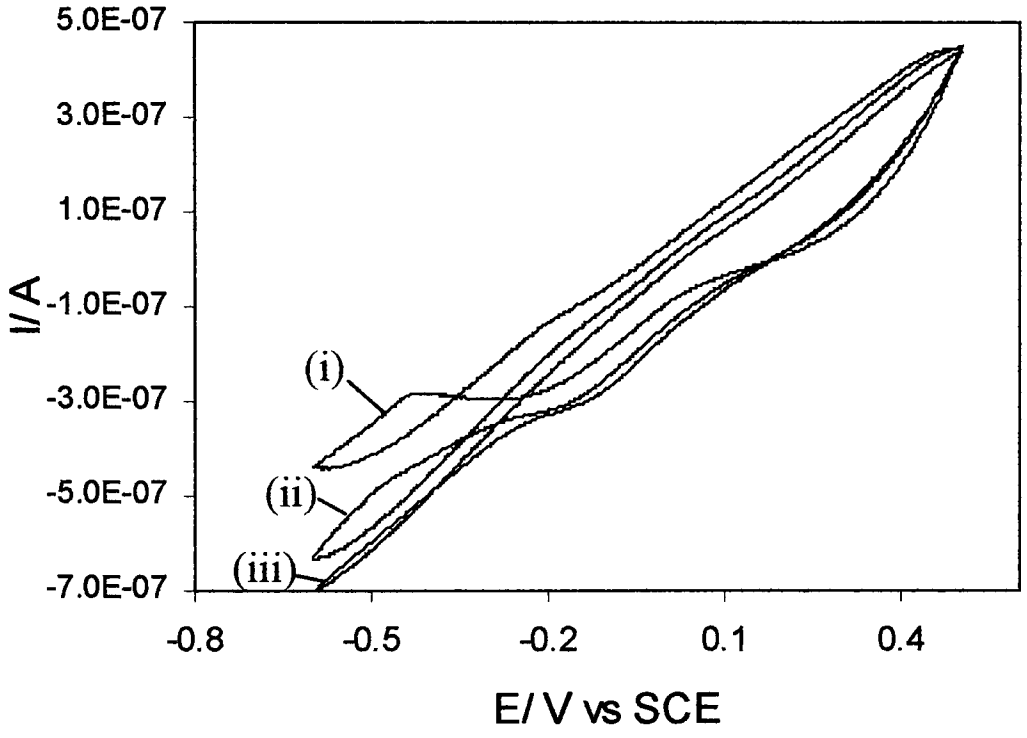


Figure 24 (A). CVs response of surface conductive diamond to $CuSO_4$ (1 mM, pH 7) in 0.1 M Na_2SO_4 at different potential scan rates (i = 0.05 Vs^{-1}, ii = 0.1 Vs^{-1}, iii = 0.2 Vs^{-1})

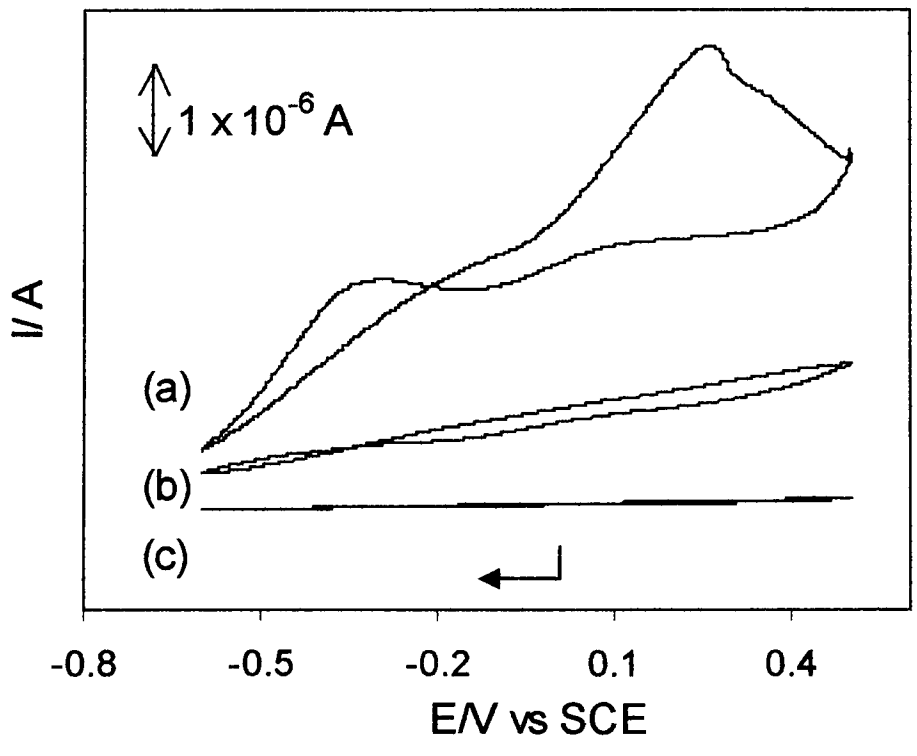


Figure 24 (B). CVs response of surface conductive diamond to 10 mM $CuSO_4$ at a potential scan rate of 0.1 Vs^{-1} (a = in pH 1, b = in pH 7) as being compared to non-conductive diamond (c, in either pH 1 or 7)

3.3.2.4 SEM Investigation

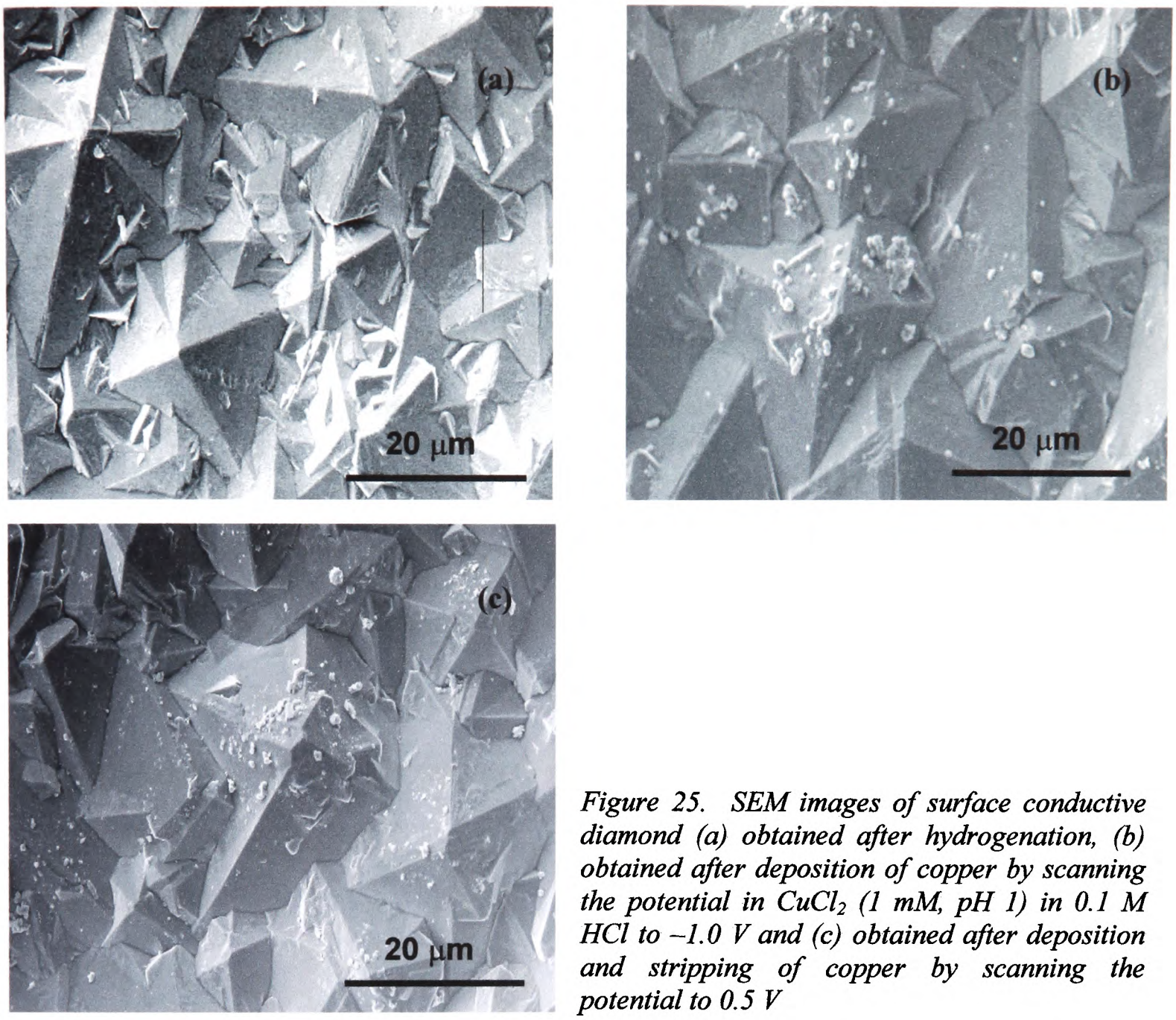


Figure 25. SEM images of surface conductive diamond (a) obtained after hydrogenation, (b) obtained after deposition of copper by scanning the potential in $CuCl_2$ (1 mM, pH 1) in 0.1 M HCl to –1.0 V and (c) obtained after deposition and stripping of copper by scanning the potential to 0.5 V

The surface morphology of the surface conductive diamond was examined using SEM. The nature of the copper deposits formed under different conditions could also be investigated. As-grown and after hydrogenated diamond shows a very clean, and well faceted surface, with (111) structures of approximately 20 μm dominating the surface structure.

The possibility of electroless metal deposition on the surface conductive diamond was performed by dipping the conductive diamond in 1 mM $CuCl_2$ (pH 1) and the diamond was left in the solution for a day. The result showed no copper being deposited under the examination of EDX (result not shown) and exhibited similar image to (a). After sweeping the diamond to negative potential of – 1.0 V and keeping hold for 1

minute, the SEM shows ball-shaped copper clusters with diameter 1.0 - 2.0 μm (figure b) deposited randomly on surface edges, and some were found on grain boundaries. The same procedure was carried out, by holding the potential for a minute at – 1.0 V, and then continued scanning to anodic potential, and later keeping hold at 0.5 V for 1 minute. The diamond was brought out and later washed-dried (SEM in figure c). There was only a small amount of copper remains on diamond surface under the investigation of SEM and EDX, signifying an incomplete metal stripping has taken place.

3.3.2.5 Potential Pretreatment Modification

The effect of pretreating the electrode surface before deposition and stripping of copper was investigated. Polarization at anodic and cathodic potentials is known to change the nature of surface functionalities such as O-groups, on boron-doped diamond electrodes.

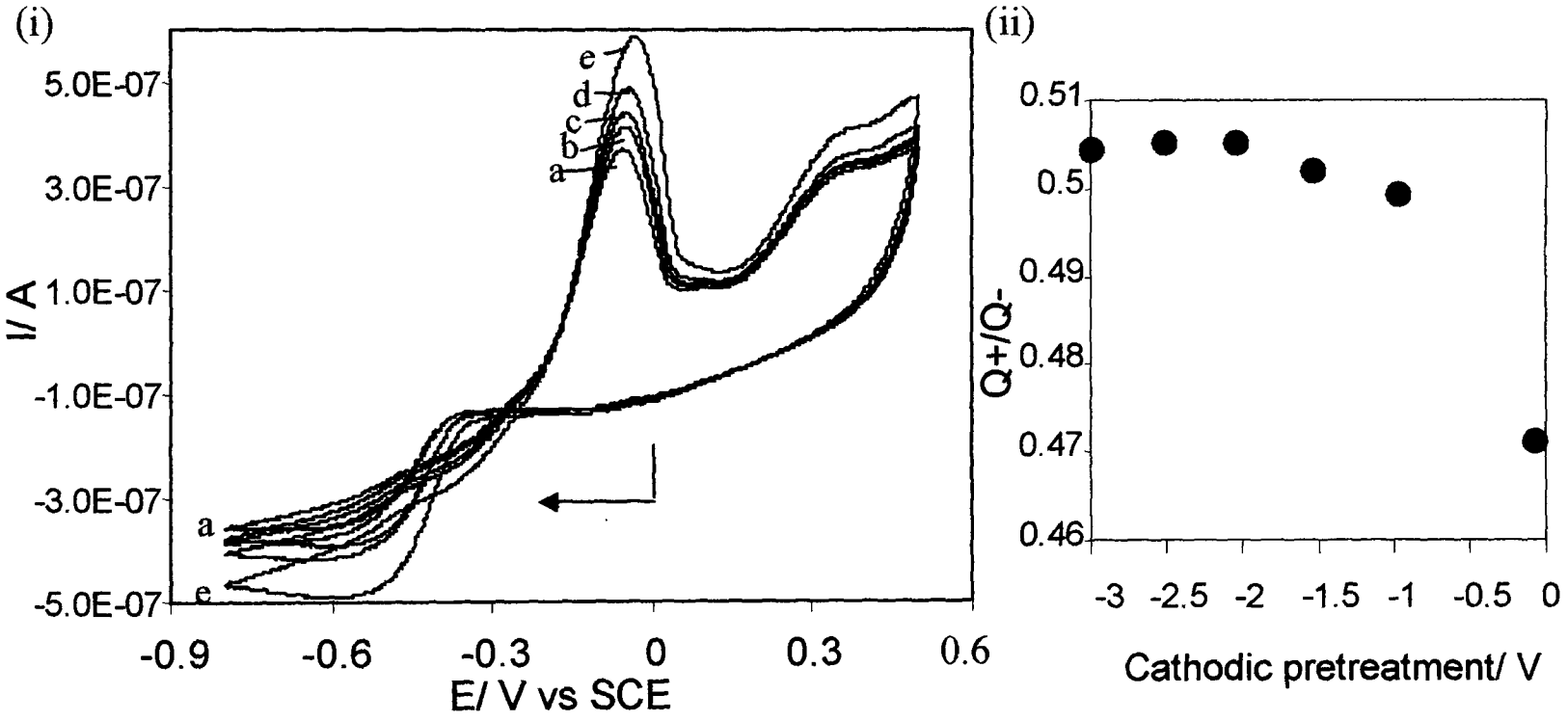


Figure 26. (i) The third CV scans after the subsequent cathodic pretreatments for 30 s in $CuCl_2$ (1 mM, pH 1) at a potential scan rates of 0.1 Vs^{-1}(a = – 1.0 V, b = –1.5 V, c = –2.0 V, d = –2.5 V, e = –3.0 V vs SCE); (ii) The correlation plot of the dependence of stripping efficiency, Q+/Q- on applied cathodic pretreated potentials

The surface conductive diamond was pre-polarized to cathodic potentials for 30 s in the range of – 1 to – 3 V *vs* SCE before the start of the CV scans, and the third voltammograms of each respective applied potentials are shown in figure 26 (i). The

figure shows no feature of potential crossovers that indicates the growth and deposition mechanism for the first scan (not shown). This is simply due to the massive amount of deposited copper upon cathodic polarization. However, the feature re-appeared for the second and the third scan. The amount of deposited copper increased at higher cathodic polarization, followed by higher stripping peaks at anodic potential of – 0.05 V *vs* SCE. Figure 26 (ii) is a plot of stripping efficiency, Q+/Q- *vs* the cathodic potentials, revealing that higher Q+/Q- (≥ 0.5) can be achieved at a potential above – 1.0 V. Further polarization at more negative potentials shows insignificant change on the ratio.

Figure 27 shows the CVs of the cathodically treated diamond, with somewhat enhanced reduction signal after the pretreatments. However, the stripping signals before and after the cathodic polarization remain unchanged at – 0.05 V *vs* SCE.

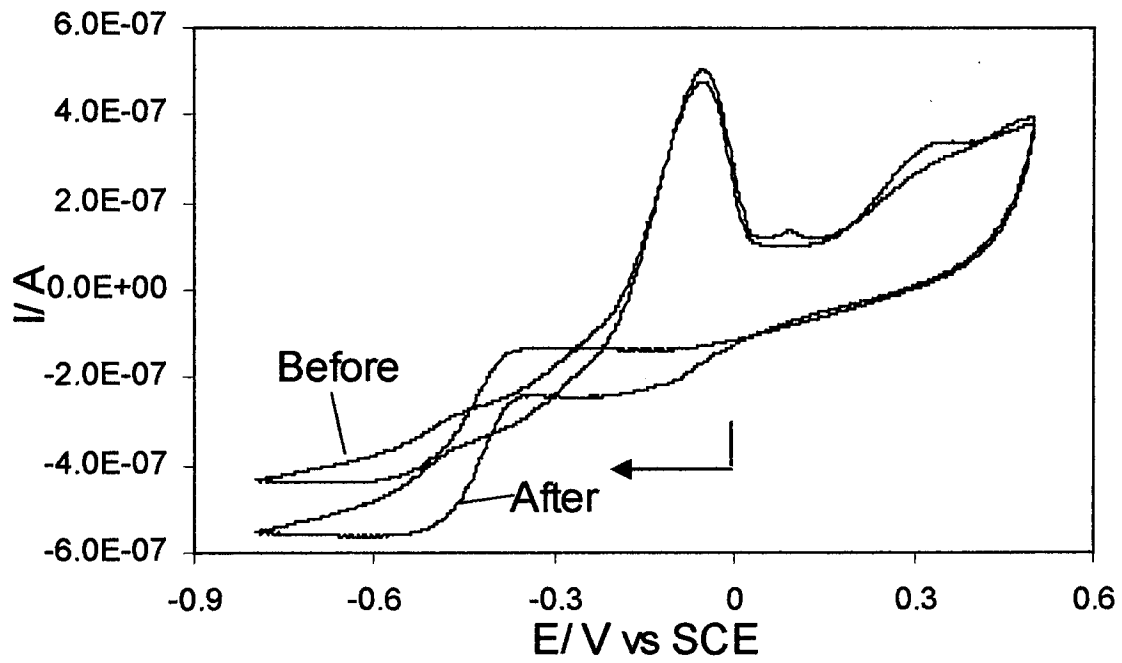


Figure 27. The CV responses of surface conductive diamond to $CuCl_2$ (1 mM, pH 1) at a potential scan rate of 0.1 Vs^{-1} before and after cathodic treatment.

Anodic pretreatments were performed on the surface conductive diamond by applying a certain positive potential for 30 s before the start of CV scans. Figure 28 shows the CVs response of the diamond to 1 mM $CuCl_2$ (pH 1), ranging from the pre-applied potentials of 0.5 V to 2.0 V. Drastic decrease of copper stripping peak was observed from figure 28c to 28d, revealing that an anodic potential of 1.5 V can diminish the

electrochemical response. By continuing the pretreatment to higher positive potential, both of the current signals for copper reduction and stripping disappeared (e).

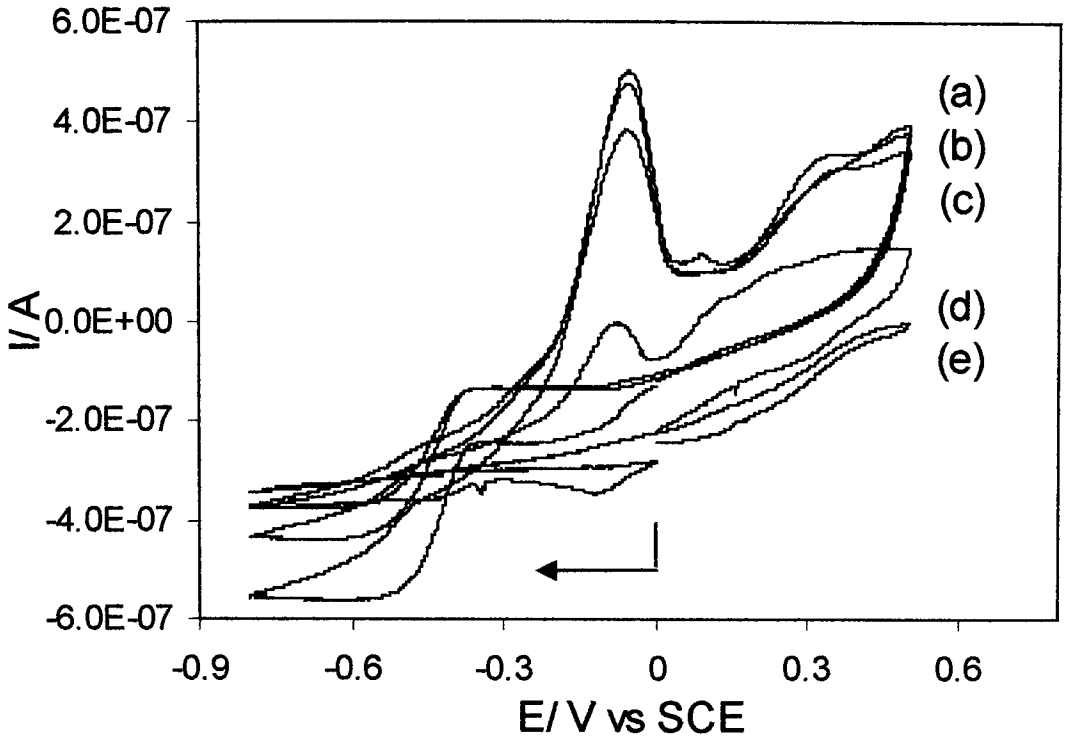


Figure 28. The CV responses of surface conductive diamond to anodic polarization for 30 s in $CuCl_2$ (1 mM, pH 1) at a potential scan rateof 0.1 Vs^{-1}; (a = 0 V, b = 0.5 V, c = 1.0 V, d = 1.5 V, e = 2.0 V vs SCE)

Attempts were made to restore the anodized surface to initial conductive state, either by re-applying cathodic pretreatments or by just exposing the diamond to the air. In figure 29, the faradaic signal for copper reduction and stripping increased from (a) to (b) after being applied at – 2.0 V for 2 mins. The diamond was later polarized cathodically to longer period up to 4 min at the same potential, as presented in (c). The response was barely increased at orders less than two after vigorous cathodic pretreatment; however, by purposely exposing the surface to atmospheric air for a day, the CV response was enhanced more than fourfold (figure 29d).

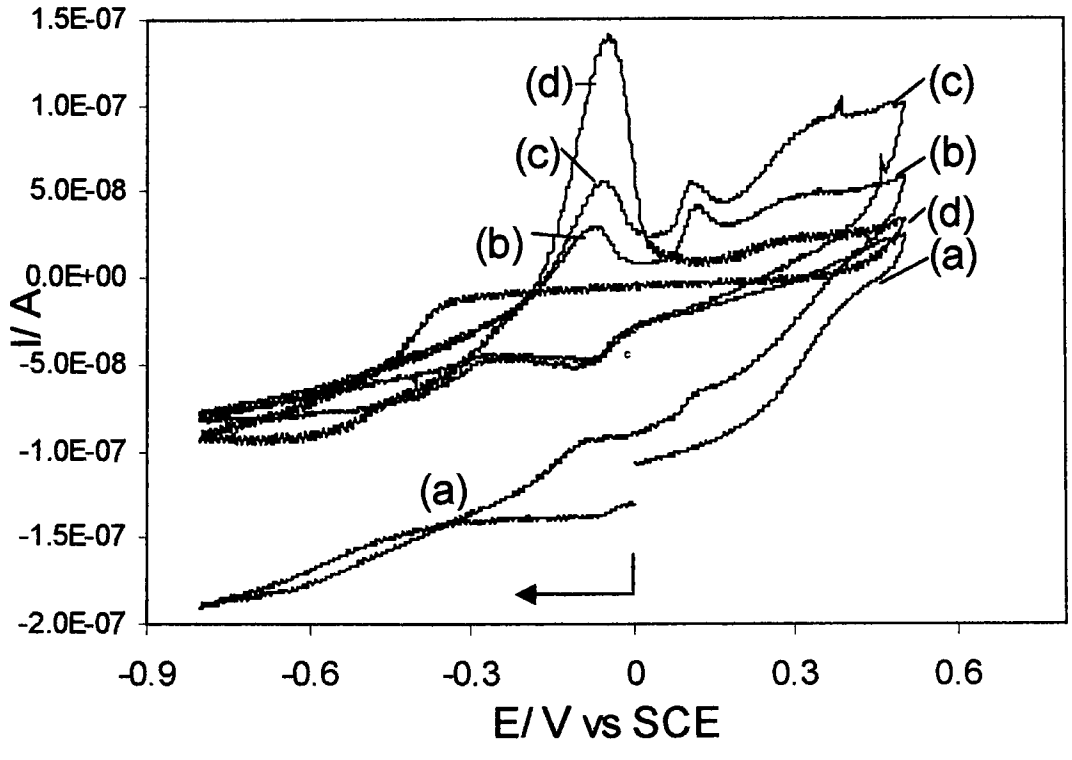


Figure 29. The CV response of surface conductive diamond to $CuCl_2$ (1 mM, pH 1) at a potential scan rate of 0.1 Vs^{-1};
(a) anodically polarized (b) cathodically polarized at -2.0 V for 2 mins (c) cathodically polarised at -2.0 V for 4 min (d) exposed to air for a day

Stripping efficiency for each surface treatment under anodic plarization was compared, as presented in the figure 30. As similar to the case that was shown earlier in CV of figure 28, the stripping ratio, Q+/Q- decreased significantly after the anodic pretreatment was performed up to 1.0 V for 30 s. By applying the cathodic pre-treatment and the exposure to atmospheric air (for a day), the Q+/Q- ratio increased.

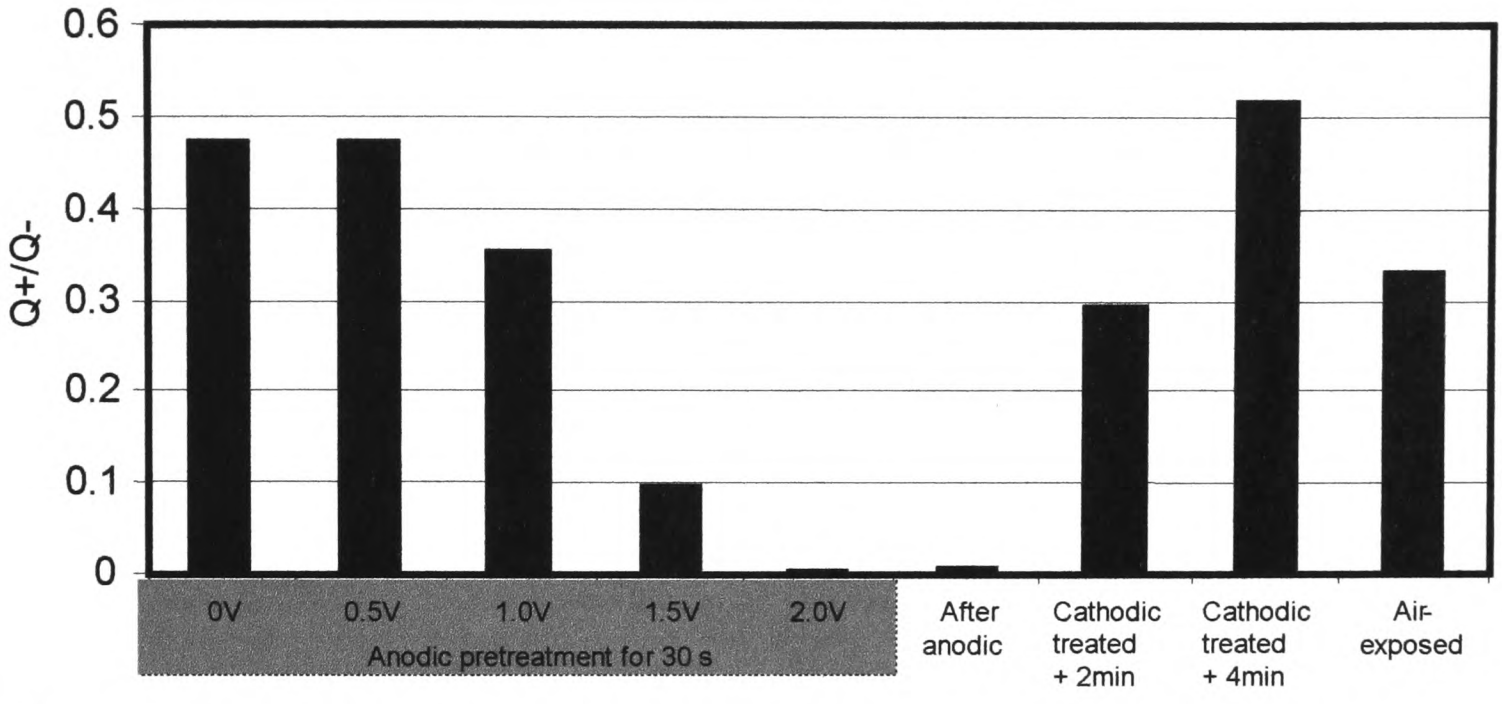


Figure 30. The stripping efficiency, Q+/Q- after each subsequent pretreatments

The distinctive comparison for the electrochemical effect by anodic polarization on surface conductive diamond is shown in the CVs of figure 31. The CVs in the response to $CuCl_2$ for the initial condition of surface conductive diamond (a) is compared to the CVs obtained after the diamond was anodically pretreated (b) and after being exposed to air (c).

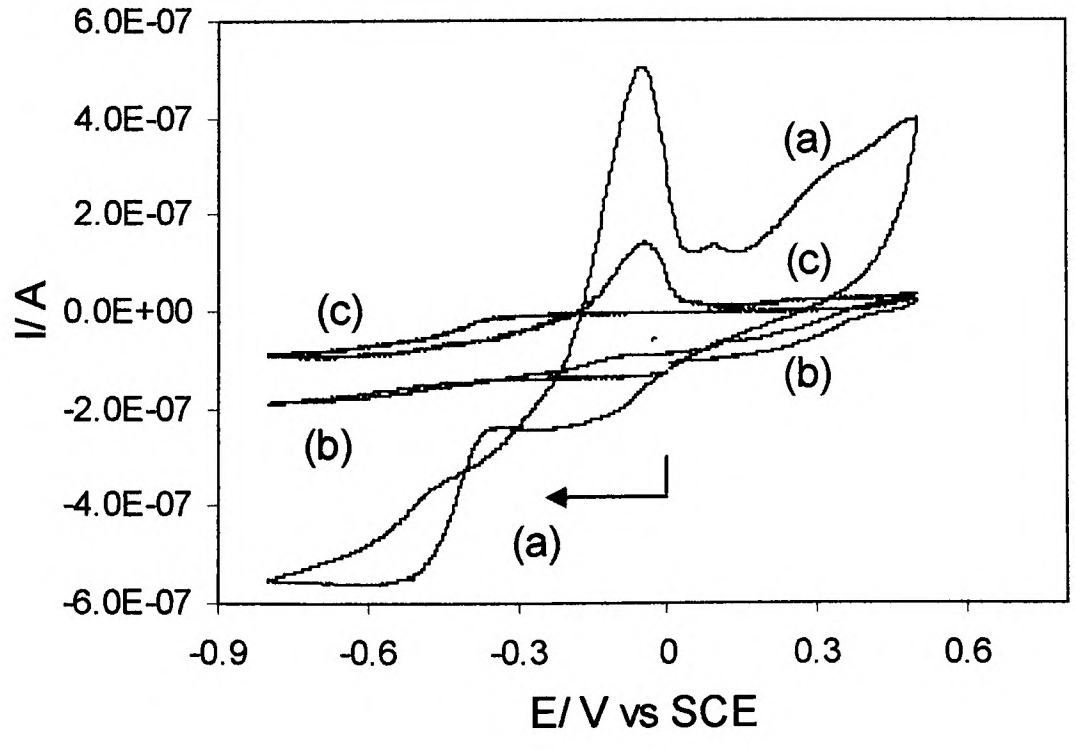


Figure 31. The CVs of the response to 1 mM $CuCl_2$ (pH 1) in 0.1 M HCl at a potential scan rate of 0.1 Vs^{-1};
(a) initial surface conductive signal,
(b) after sequential anodic pretreatments,
(c) after exposed to air

3.3.2.6 Conductance *vs* Metal Deposition

Experiments were performed to measure the changes of surface conductivity during metal deposition *via* two probing contacts on both end sides of diamond, inside the $CuCl_2$ (1 mM, pH 1) solution. The *in-situ* conductance is measured under the applied voltage of 2 V around the external circuit. One of the contacts on diamond is connected to a potentiostat, as shown in experimental setup in figure 13 (a) and a cathodic potential of -3.0 V *vs* SCE is applied for 10 minutes in a typical chronoamperometric method. Only a specified small area (4 mm x 3 mm) in the centre of the diamond was exposed to solution, with insulating putty covering the rest.

The figure 32 (a) shows the decrease of surface conductance in solution while cathodic potential is applied. Within the period of 10 min, the conductance I_t at time t of the exposed area decreased linearly for 30 % from the initial value, I_0. The diamond was later taken out to air and rinsed with pure water. After the diamond was let dried, the conductance of different regions was tested with two-probe measurement. One of the probes was fixed at position A (as presented in figure 32 (b)) and probe B was adjusted at a position perpendicular to the piece of diamond. The surface remains conductive at the optimal level at 5×10^{-6} S on un-exposed diamond area, which is still well hydrogen-terminated. When the conductance was measured in between the position around 4 and 8 mm from probe A, the surface conductance dropped to a value of 5×10^{-8} S. The measurement for probe B in the center of copper deposited area showed a significant decrease of surface conductivity, down to 1×10^{-11} S. The related figures are shown in the next page.

The exposed area in the middle of the diamond has shown to be more hydrophilic as compared to the covered area by insulating putty. This phenomenon was simply evidenced by observing the water droplets tend to stay on the surface with much smaller contact angle, signifying the occurrence of higher surface wettability. However, the

region on the else parts exhibited the water-repulsive behaviour of hydrophobic characteristics, due to the presence of high surface hydrogen content.

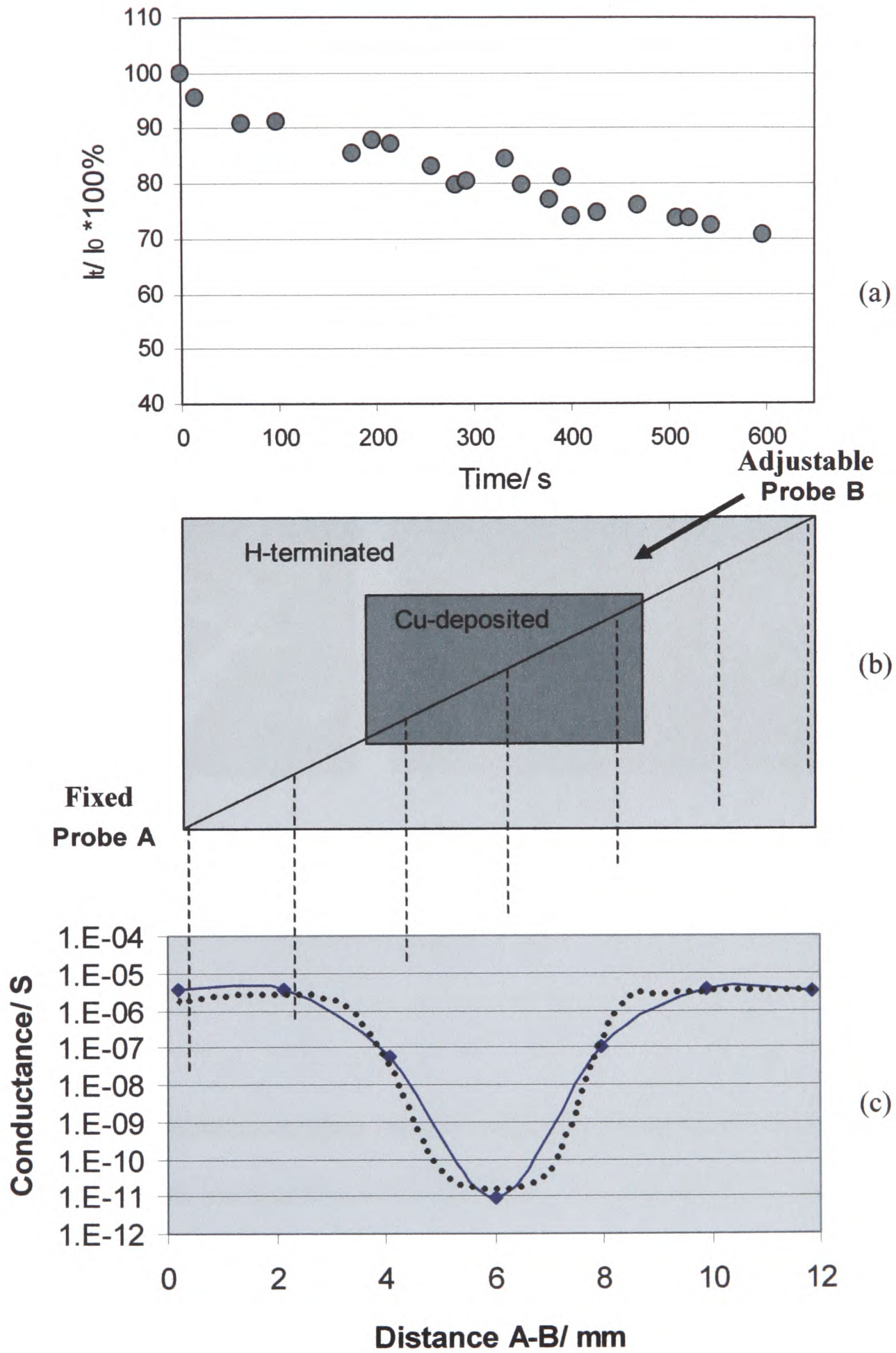


Figure 32. (a) The decrease of conductance at time t in $CuCl_2$ (1 mM, pH 1) in 0.1 M HCl solution vs the deposition period of copper; (b) the exposed area of diamond in the solution medium with deposited copper, as compared to the remains conductive hydrogen-terminated region and (c) the corresponding conductance between two-probe contact measurements, A and B

The exposed area of the surface conductive diamond in $CuCl_2$ solution was further examined under SEM, as presented in figure 33. The image shows the presence of copper particulates scattering randomly on the exposed area, with the observed metal cluster sizes of approximately 1 μm. Under the electron bombardment in SEM, the image for the unexposed area of the conductive surface was much brighter than the metal deposited region (which was in the dark side), suggesting the exposed surface has suffered from the electrochemical oxidation and the loss of conductive layer.

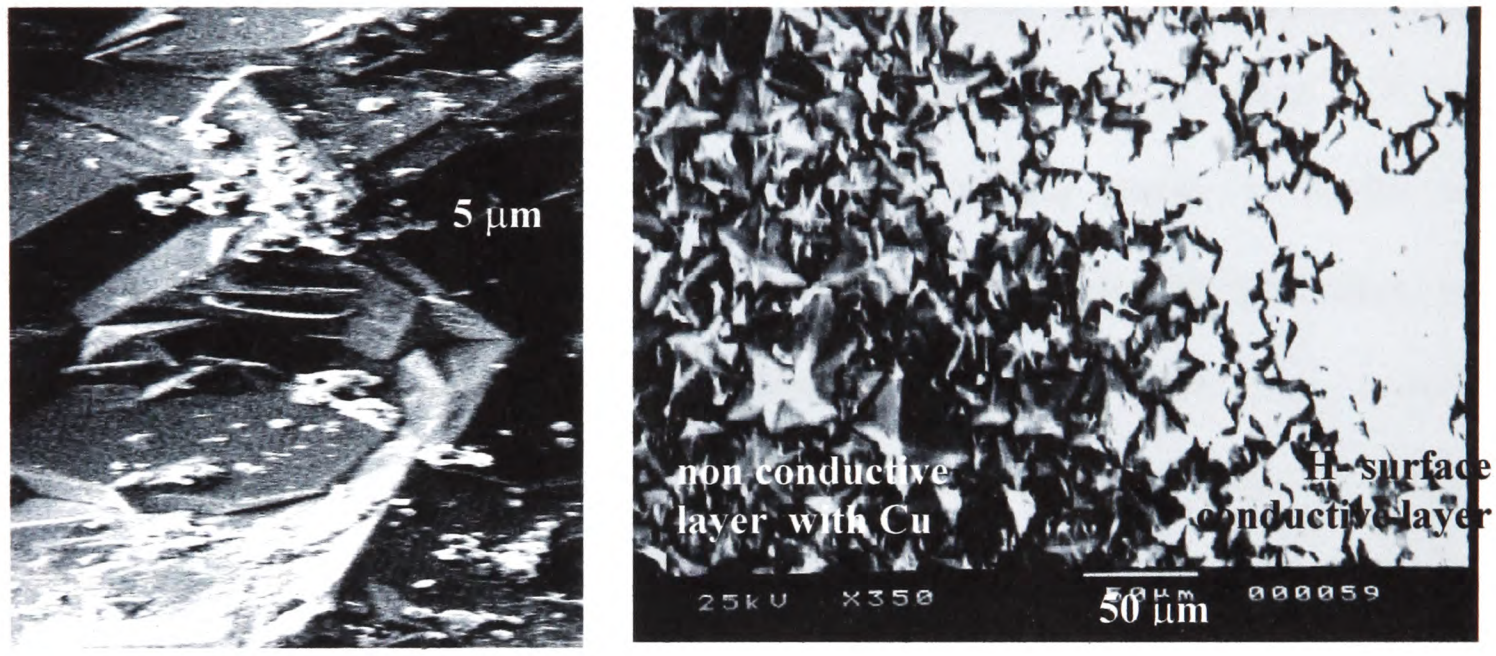


Figure 33. SEM (on the right) shows the two distinctive regions of conductive and non-conductive layers. The expanded SEM on the left showing the darker region with copper deposits

3.3.3 Discussion

There is a growing interests in using surface conductive diamond as a liquid sensor [14-16] in devices, such as ion sensitive FETs (ISFETs). There is also an interest in realizing the electrochemical sensors based on the surface conductive diamond. In both cases, the attraction is the application for high quality electronic devices, which can be made from surface conductive diamond, either as the sensor itself or as "on-board" electronics, in comparison to boron-doped diamond material. These are the two main reasons that provide the motivation for our present studies.

3.3.3.1 Changes of Conductivity

According to models of SC in previous section, the adsorption of ions should change the band bending, thus subsequently resulting in the change of SC. This is what we observe in solution, where for example the surface conductivity falls as the pH is raised. This pH dependence is qualitatively similar to that predicted from the gas phase observations so it is possible that the surface chemistry occurring in the two situations is similar.

Works shown in figure 14 and 16 suggest that the diamond surface conductivity in solution is greatly dependent on the presence of ionic species. This is in agreement with previous work [16,39], which indicates the effect is arising from the proposed change in the band bending accordingly to the ad-species in the surface conductive model (see mechanism in figure 34a). The increased pH sensitivity of the H-terminated channel can result from an increased density of the ionic radicals attached to the surface C-H. In acidic solution, electron densities are accepted by oxoniums from the surface hydrogen. Hydrogen atoms on diamond surface would thus be positively charged, causing the attraction of valence electrons (from valence bonds), which will directly correspond to the presence of holes. Reports [16,25] suggested that the surface dipole formed within the C-H bonds will in turn induce the surface-potential pinning at the valence band edge, thus a lower activation energy of Fermi level is generated, equivalent to the chemical potential in the solution (figure 34 b). The process is described as in equation 9, although it is probably too simplistic to discuss this in terms of integral electron transfer;

$$\text{C-H} + \text{H}_3\text{O}^+ \rightarrow \text{C-H}^+ + \text{H}_3\text{O} \rightarrow \boldsymbol{h} + \text{C-H} + \text{H}_3\text{O} \qquad \text{(eqn 9)}$$

where C-H is the hydrogen terminated surface and $\boldsymbol{h}$ is the hole in acceptor layer. The existence of hole accumulation would cause the upward band bending corresponding to the appearance of the *p*-type layer (figure 34b).

With the increases of pH, the negatively charge ionic radicals from basic solutions, such as ^{-}OH (from KOH, see figure 14) and HCO_3^- (from $NaHCO_3$, figure 16) would adsorb on the H-terminated diamond surface, weakening the polarization of the C-H bond and shifting the energy level of the bond-related electronic state to higher energy. The surface Fermi level would then be shifted up accordingly (figure 34 c), resulting in the depletion or downward band bending of the *p*-type channel [16] and compensating (neutralizing) the hole charge. The process of surface neutralization by KOH will form water (H_2O) and salt (KCl), with the disappearance of holes, as described in equation 10;

$$H_3O + \boldsymbol{h} + OH^- + K^+ + Cl^- \rightarrow 2H_2O + KCl \qquad \text{(eqn 10)}$$

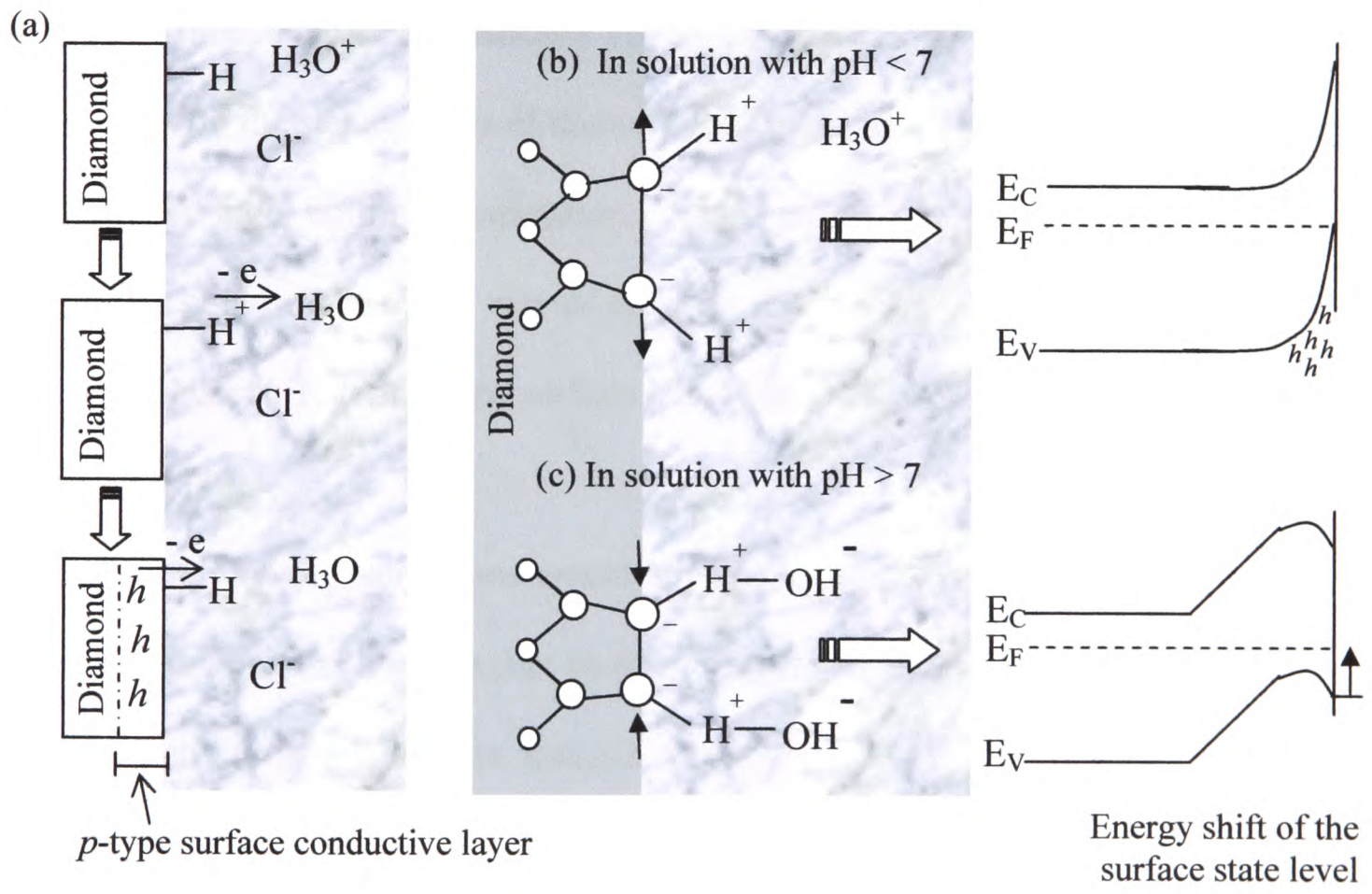


*Figure 34. Schematic model for the pH sensing mechanism on diamond surface in **solution**; (a) the process of hole creation in diamond film, (b) surface pinning by hydrogen in solution with pH < 7, (c) effect of basic ion adsorption in solution with pH > 7*

Changes in conductivity can be observed after the surface conductive diamond is taken out from solution and dried (as shown in figure 14), and the conductance becomes even more amplified. Evidently although the solution phase is necessary to mediate the

electron transfer from the diamond valence band, once this has occurred the charge transfer can be maintained even when the solution is removed. The remaining ions, such as H_3O^+ would stay on the H-terminated surface for inducing hole accumulation whereas the OH^- would induce the opposite effect, by neutralizing the hole charges. Without the presence of non-specifically adsorbed species within the double charge layer found in the solution phase, the ions would dominate the charge transfer in air and enhance the effect of the hole manipulation in acceptor layers. Normal conductivity can be regained by rinsing with water, which can wash off the ions.

With the increase of temperature in the solution, the adsorption rate for OH^- (in alkaline solution) would be accelerated through thermal enhanced diffusion process, thus the conductance is reduced drastically due to massive formation of depletion layer. This is in contrast to the steady states of diamond surface conductivity in acidic solution (figure 15), even at high boiling temperature. This would suggest that the ionic oxonium compounds could mediate the rate of electron transfer and the substitution of hydrogen radical in between H-terminated surface and oxonium is not impossible at high solution temperature [40].

These above observations would suggest that there is 'mileage' in using surface conductive diamond as a sensor, but they are likely to be problems of two important issues (i) the selectivity in response to specific ion species, and (ii) the chemical stability, for example the result in figure 14 shows that the SC is stable in acid, but not in alkali media. This is a major problem for the applications of surface conductive diamond.

3.3.3.2 Electrochemical Properties

Virtually, all electrochemical works on diamond have been done with boron-doped diamond. This is the first work to investigate the electrochemical properties of surface conductive diamond since it would be very useful to combine diamond electrochemical sensing properties with "high quality" electronics based on such *p*-surface conductive layer.

(i) Electrode kinetics

From the electrochemical point of view, surface conductive diamond has shown well-behaved electrochemical properties, similar to boron-doped diamond and other carbon materials. From the *Randles-Sevcik* equation (Section 2.10.2, Chapter 2),

$$\text{Peak current, } I_p = (2.69 \times 10^5)\, n^{3/2}\, A D^{1/2}\, C \nu^{1/2} \qquad \text{(eqn 11)}$$

the effective electrochemically active area for the surface conductive diamond can be estimated. From the reduction of 3 mM $Ru(NH_3)_6^{3+}$ shown in figure 17, at a scan rate (ν = 0.02 Vs^{-1}), diffusion coefficient of $Ru(NH_3)_6^{3+}$ ($D_{Ru(NH_3)_6^{3+}}$ = 9.1 x 10^{-6} cm^2s^{-1}) [31] with one electron transfer involved, the active area, A is estimated as 0.12 mm^2. With the same equation applied to $CuCl_2$ (from figure 18), by employing D_{CuCl_2} = 5.7 x 10^{-6} cm^2s^{-1} [31], ν = 0.02 Vs^{-1}, C = 1 mM, n = 2 electrons transferred during deposition, the estimated active area, A = 0.10 mm^2. Both of the theoretically predicted areas are nearly 1-2 orders of magnitude smaller than the standardized geometrical area in these experiments, A_{real} = 4.00 mm^2. The small magnitude of currents is due to the fact that not all exposed surface (geometrical area) are electroactive, and more likely that the electroactivity is strongly dependent on the (a) density of the surface conductivity and (b) coverage of the sub-surface H-conductive thin layer. However, the calculated area for boron doped diamond is in good agreement with the geometric area in the response to $Ru(NH_3)_6^{3+}$ and $CuCl_2$ which suggests that the geometric electrode area of boron-doped diamond is similar to the

electroactive area upon the experimental time scale. For example, for the redox system involving $CuCl_2$ in figure 21(b), the estimated area from the reduction peak current of 4.2 μA is 0.73 mm^2 which represents well the geometrical area of boron-doped diamond electrode of 1 mm in diameter.

For the peak separation, ΔEp = 359 mV of surface conductive diamond in figure 17, and correspondingly ψ = 0.015 [41] (calculated from equation 52, Chapter 2), the heterogeneous constant, k was estimated to be 7.08 x 10^{-5} cms^{-1}. The low k in comparison to boron-doped diamond is an indicator of very slow/sluggish kinetic process or due to alternative potential drop across the diamond surface. The correlation plots between the peak current for $Ru(NH_3)_6^{3+}$ and $CuCl_2$ to the square root of scan rates (Ip *vs* $v^{1/2}$) have shown a linear correlation, though the plots do not cross the origin. This suggests a not fully diffusion-like controlled process to have occurred on the surface conductive diamond, which can be due to some inhibited electrode kinetics or even surface roughness, causing inhibited kinetic factor (slower in response to the potential change at certain period) particularly at high scan rates.

The possibility of interfacial adsorption of the analytes on surface conductive diamond can be ruled out from occurring, as the plot of peak currents to scan rate (Ip *vs* v) is nonlinear. Therefore, the electrochemistry involving electron transfer has shown to take place on surface conductive diamond, rather than just adsorption-desorption process on the surface.

(ii) Metal deposition and stripping features

The deposition of copper on the surface conductive diamond shows the behaviour of a typical nucleation and deposition mechanism, which is similar to the type of behavior that has been observed for Pt, Pb and Hg on boron-doped diamond [42] (figure 18, and comparison in figure 21). The initial nucleated sites on surface conductive diamond

would serve for sequential growth and deposition; thus the cathodic current flows at less negative potentials than that required to initiate the deposition. This explains why the copper was deposited randomly as small clusters with 1 – 2 μm in diameter, instead of forming a copper layer.

The copper clusters are randomly distributed on the surface. This SEM observation is in contrast to the reports [43,44], which have shown that the copper [43] and silver [44] preferably covered the grain boundaries under their high potential electroplating method. According to their reports, the conductive pathway [43] has been suggested to be contributed both by the grain boundaries on the surface (lateral measurement) and within the bulk (vertical measurement), whereas hopping transport within grain boundaries [44]. However, these results would be doubtful as the generation of non-diamond properties would be favourable under high applied potential (~ - 15 V). This is because under high electrical supply (voltage breakdown), more defective areas would be created preferably on the grain boundaries due to low surface energy, and thus became the suitable deposition area. The insignificant amount of grain boundaries exist on surface conductive single crystal can easily rule out the arguments about surface conductivity is only saturated on grain boundaries pathways. In surface conductive diamond, the conductivity arises laterally due to adsorbates on the surfaces; hence any effects due to grain boundary conduction are negligible.

According to the model postulated [45], it is likely that a part of the metal phase adhering to poor conducting sites of the electrode cannot be stripped at the anodic polarization. In contrast, when the electrode surface is electrically and chemically uniform, the crystallization process may start from different randomly located sites and any deposited metal on the surface can be completely removed upon anodization. After an anodic potential is applied, SEM (see figure 25c) shows a small remaining amount of copper clusters on the diamond with the stripping efficiency less than unity (figure 22i),

suggesting an incomplete stripping process occurs on the *less* conducting sites. It is probable that the deposited metal disrupts the surface conductivity underneath, hence the metal particles have poor electrical contact to the underlying diamond surface, and thus not all of the deposits can successfully be stripped off. The high potential inertness of the deposit can also be attributed to the unusual stability of thermodynamic factor, by which a higher overpotential is required to strip the deposited metals.

In figure 22, the stripping efficiency of surface conductive diamond is fairly independent on the copper concentration. For undoped diamond, the acceptors are completely activated at room temperature, though the surface electroactive sites are comparatively low in uniformity and density. Thus, the interaction of copper on surface conductive diamond would be specific, involving the H-conductive layer. The deposition-stripping was suggested to follow the hole injection mechanism involving the electron transfer from the valence band of surface conductive diamond to copper redox couple in the solution, regardless of the concentration of copper solution. This phenomenon was reported similar to the case of metals deposition onto *p*-type semiconductors, by which a stripping peak is usually observed due to the transfer of valence band holes (majority carriers) to the metal at sufficiently positive potentials [46,47]. In contrast, boron-doped diamond shows great dependence of stripping efficiency on copper concentration. This may due to the acceptor level of boron-doped diamond lies deep in extrinsic region at room temperature [15]. The amount of activated acceptors is *much* less, causing weak adhesion and small electrostatic interaction effects between the reduced particles and diamond surface, particularly at low concentration. Subsequently, the small copper particles will dissolve into the solution phase before they can be successfully stripped off. Report [48] has shown the same trend of stripping efficiency to copper concentration, suggesting the formation of colloidal copper could have taken place at low concentration.

(iii) Redox system

From the CV shown in figure 18, the possible copper reduction from $CuCl_2$ may proceed according to the reaction in equation 12 and 13 by considering the individual reduction potential standards. However, the equation 12 is more thermodynamically favourable as the deposited metallic coppers were found under our SEM investigation (shown in figure 25).

$$Cu^{2+}(aq) + 2e^- \rightarrow Cu(s) \qquad E^{\varnothing} = 0.337 \text{ V } vs \text{ SHE} \qquad \text{(eqn 12)}$$

$$Cu^{2+}(aq) + 2Cl^-(aq) + e^- \rightarrow CuCl^-_2(aq) \qquad E^{\varnothing} = 0.485 \text{ V } vs \text{ SHE} \qquad \text{(eqn 13)}$$

Upon scanning to positive potential, copper was stripped at – 0.05 V *vs* SCE (peak 1), which is attributed to the conversion of Cu (s) to Cu^+ in the form of dichlorocuprate ion, $CuCl^-_2$ [49] as given in equation 14;

$$Cu(s) + 2Cl^-(aq) \rightarrow CuCl^-_2(aq) + e^- \qquad E^{\varnothing} = 0.189 \text{ V } vs \text{ SHE} \qquad \text{(eqn 14)}$$

This is followed by a second stripping peak occurred at 0.28 V (peak 2), which denotes the transformation of Cu^+ to Cu^{2+} [47,50], in equation 15;

$$CuCl^-_2(aq) \rightarrow Cu^{2+}(aq) + 2Cl^-(aq) + e^- \qquad E^{\varnothing} = 0.485 \text{ V } vs \text{ SHE} \qquad \text{(eqn 15)}$$

The direct copper dissolution from metallic copper to Cu^{2+} is also considered possible

$$Cu(s) \rightarrow Cu^{2+}(aq) + 2e^- \qquad E^{\varnothing} = 0.337 \text{ V } vs \text{ SHE} \qquad \text{(eqn 16)}$$

As shown in figure 19, the stripping current of Peak 2 increased drastically at high scan rate as compared to Peak 1 on surface conductive diamond. In contrast, this abnormal increase of Peak 2 at high scan rate was not observed on boron-doped diamond. The explanation for this is the slow kinetic behaviour of surface conductive diamond. At Peak 1, the stripping process for metallic copper was unsuccessful, particularly at higher

potential scan rates, which is due to the slow kinetics/ poor contact between metal on surface conductive diamond. This would therefore increase the amount of copper to dissolve into Cu^{2+} *via* the second stripping Peak 2, following the equation 16. Due to much higher electrode kinetic for boron-doped diamond, the amount of metallic copper that can dissolve into the solution at Peak 1 is obviously much higher, thus the stripping current for Peak 2 remains at small magnitude.

For the electrochemistry of surface conductive diamond in acidified $CuSO_4$ medium, the stripping peak observed at 0.25 V *vs* SCE is corresponding to the dissolution of deposited copper, following the simple reaction as shown in equation 16.

Not surprisingly, the performance of surface conductive diamond is dependent on the solution, by which the diamond shows selective response to analyte at different pH, thus pH dependent. In figure 24, CVs show ohmic behaviors and the absence of metal stripping peak in response to neutral solution. This is in great contrast to boron-doped diamond, which shows well-behaved electrochemical response even at high alkaline solution. Two reasons for these are (a) in the absence of hydrosonium ions, the surface conductivity drops due to the suppression of hole and the weakening of C-H diamond bonding. Therefore, there would be no effective conducting layer to serve as a nucleation site for metal deposition, though the surface is still well H-terminated. (b) the presence of the unbuffered solution creates electrostatic interaction between the copper cluster and the surface conductive diamond. The passage of the cathodic current may increase the local pH near the electrode, which lead to the possible formation of copper hydroxide on the surfaces of the copper particles. Since the cluster is negatively charged by the hydroxide absorption, it would be electrostatically repelled from the negatively charged diamond electrode surface upon scanning to negative potential.

(iv) Effects of potential polarization

As expected [51], polarization can oxidize the diamond surface. This is evidenced by the wettability of a surface by water, which is generally regarded as a measure of the concentration for polarizable groups, which can interact with water by hydrogen bonding [52]. The initial hydrophobic H-surface is observed to be more hydrophilic after polarization, which can be due to the formation of oxygen functionalities and the partial loss of the hydrogen termination.

Anodic polarization has greater effect on modifying the surface conductive layer (figure 28) than under the cathodic pretreatment (figure 26). Under anodic polarization, the onset of oxygen evolution (equation 17) would likely to be generated above 1.0 V *vs* SCE as compared to the hydrogen evolution which is initiated only below – 2.0 V *vs* SCE, suggesting a potential window of 3.0 V for surface conductive diamond. The solvent window for the surface conductive diamond is higher than that observed for a glassy carbon electrode, spanning ca. 2.3 V [53] and a nanodiamond electrode, spanning ca. 2.5 V [54], but is smaller compared to the solvent window at a boron-doped diamond electrode, spanning ca. 3.5 V [55];

$$2\,H_2O\,(\lambda) \rightarrow O_2\,(aq) + 4\,H^+\,(aq) + 4\,e^- \quad E^{\varnothing} = 1.229\ V\ vs\ SHE \qquad \text{(eqn 17)}$$

The peroxy-like intermediates such as HO_2^- and C-O-O• (equation 18,19) [56,57] and dissolved oxygen (equation 20) are reactive to hydrolyze H-terminated or polyhydride compounds [58,59] into the formation of different oxygen functionalities, such as carbonyl, hydroxyl and carboxylate.

$$H_2O\,(\lambda) + O_2\,(aq) + 2\,e^- \leftrightarrow HO_2^-\,(ads) + OH^-\,(aq) \quad E^{\varnothing} = -0.076\ V\ vs\ SHE \qquad \text{(eqn 18)}$$

$$C\text{—}H\,(s) + HO_2^-\,(ads) \rightarrow [C\text{-}O\text{-}O\bullet]\,(s) + 2\,H^+\,(aq) + 2\,e^- \qquad \text{(eqn 19)}$$

$$C\text{—}H\,(s) + O_2\,(aq) \rightarrow [C\text{-}O\text{-}O\bullet]\,(s) + H^+\,(aq) + e^- \qquad \text{(eqn 20)}$$

The XPS C 1*s* at boron-doped diamond has shown the surface is much more highly oxidized upon anodic polarization rather than cathodic treatment [51]. Oxidation is known to destroy surface conductivity hence it is unsurprising that anodic polarization has the greater effect. Subsequently, the carrier density of the conductive site is greatly reduced, thus decreasing the surface conduction in response to electrochemical signals. However, these effects seem somewhat reversible, since standing in air allows the recovery. Oxidation of the diamond surface is irreversible in air so this is somewhat unexpected. Presumably disruption of the crucial surface adsorbates instead of break up of the surface conductive layer due to loss of H-termination must therefore be implicated. This must display the re-adsorption of air adsorbates on the surface.

The cathodic pretreatment on surface conductive diamond in copper solution would enhance both copper deposition and abstraction/evolution of H on the reactive surface. Hydrogen evolution is believed to interact with the hydrogen-terminated surface. A mechanism analogous to the gas phase atomic hydrogen abstraction on surface hydrogen during growth was suggested [60], given in equation 21;

$$C\text{—}H\,(s) + H^{+}\,(aq) + e^{-} \rightarrow C\bullet\,(s) + H_2\,(g) \qquad \text{(eqn 21)}$$

The exposed free radical sites, C• will react with dissolved oxygen or water to form oxygen functionalities on the surface. The copper ions might also be reduced on the reactive dangling bonds.

The other possible hydrogen evolution might involve the weakly adsorbed H on the hydrogen-terminated diamond surface, rather than the chemically bound hydrogen [61], which follows the equation 22;

$$C\text{—}H\,(s) \ldots H\,(ads) + H^{+}\,(aq) + e^{-} \rightarrow C\text{—}H\,(s) + H_2\,(g) \qquad \text{(eqn 22)}$$

The corresponding CV (figure 27) and stripping efficiency (figure 26 ii) were remains unaffected at high negative potential. This would mean that the H radicals could possibly re-attach again onto the carbon radical and maintain the C-H bonding without distorting the surface band bending, thus the surface remains conductive. The simple mechanism involved is an H regeneration process, shown in equation 23;

$$C\bullet\,(s) + 3\,H^{+}\,(aq) + 3\,e^{-} \rightarrow C\text{—}H\,(s) + H_2\,(g) \qquad \text{(eqn 23)}$$

However, the experiment was carried at short period, which is just before the surface can be destroyed by both copper deposition and rigorous cathodic polarization.

Under the negative polarization for long period, the surface condition is different. As shown in figure 32, diamond was pretreated at a potential of – 3.0 V *vs* SCE in $CuCl_2$, and the changes of surface conduction in solution *versus* cathodic treated period was monitored. The regeneration of H^{+} on free carbon radical is severely suppressed and at the same time, the copper concentration is greatly increased in the vicinity of the electrode surface. Dangling bonds due to the loss of hydrogen was *irreversibly* substituted by reduced copper under high and prolonged cathodic polarization. In turn, the eliminated hydrogen radicals will stay within the diffusion layer and create artificial remaining conductivity of diamond in the solution. However, after the surface was allowed to dry, the effect of the cathodic manipulation was amplified with the observation of very low surface conductivity. Since the negative electron affinity of diamond surfaces is due to a dipole layer induced by the heteropolar carbon-hydrogen bonds of the surface atoms, the loss of hydrogen will in turn increase the electron affinity (more positive) of the diamond surface, which produces low electron emission under SEM image in figure 33.

3.3.4 Conclusion

Conductivity of surface conductive diamond can be changed by aqueous environment. Changes persist if the diamond is withdrawn from the solution and can be reversed by washing. This is consistent with the ideas that the surface conductivity in diamond arises from the charge transfer/ adsorption process at the interface layer. This would suggest the possibility for sensor applications if (i) selectivity and (ii) chemical stability are satisfactory.

Surface conductive diamond can be used for diamond electrochemistry. Electrochemical signals on surface conductive diamond can be obtained and the work was demonstrated on $Ru(NH_3)_6^{3+/2+}$, $CuCl_2$ and $CuSO_4$.

Surface conductive diamond shows similar chemical behavior with boron-doped diamond, *e.g.* metal/metal stripping. The randomly distributed metal deposits and incomplete metal stripping are attributed to low uniformity and low density of the electroactive sites.

Electrochemical process on surface conductive diamond involves less electroactive area and sluggish kinetics, thus contributing respectively to the phenomena of small peak current and wider potential window.

Electrochemical behaviour of surface conductive diamond is very sensitive to (i) solution *e.g.* pH, and (ii) polarization effects. The stripping efficiency of surface conductive diamond is independent on the metal concentration due to highly activated acceptor level at room temperature.

Electrochemistry gradually degrades surface conductive layer. The potential window of surface conductive diamond is ~ 3.0 V between – 2.0 and 1.0 V *vs* SCE.

3.4 References for Chapter 3

[1] M.I. Landstrass and K.V. Ravi, *Appl. Phys. Lett.* **55** (1989) 975
[2] M.I. Landstrass and K.V. Ravi, *Appl. Phys. Lett.* **55** (1989) 1391
[3] S. Albin and L. Watkins, *Appl. Phys. Lett.* **56** (1990) 1454
[4] H. Kawarada, M. Aoki, H. Sasaki and K. Tsugawa, *Diamond Relat. Mater.* **3** (1994) 961
[5] M.C. Hicks, C.R. Wronski, S.A. Grot, G.Sh. Gildenblat, A.R. Badzian, T. Badzian and M. Messier, *J. Appl. Phys.* **65** (1989) 2139
[6] Y. Mori, H. Kawarada and A. Hiraki, *Appl. Phys. Lett.* **58** (1991) 940
[7] M. Itoh and H. Kawarada, *Jpn. J. Appl. Phys.* **34** (1995) 4677
[8] R.B. Jackman, H.J. Looi, L.Y.S. Pang, M.D. Whitfield and J.S. Foord, *Carbon* **37** (1999) 817
[9] H. Shiomi, Y. Nishibayashi and N. Fujimori, *Jpn. J. Appl. Phys.* **18** (1989) L2153
[10] K. Tsugawa, K. Kitatani, H. Noda, A. Hokazono, K. Hirose, M. Tajima and H. Kawarada, *Diamond Relat. Mater.* **8** (1999) 927
[11] K. Tsugawa, H. Umezawa and H. Kawarada, *Jpn. J. Appl. Phys.* **40** (2001) 3101
[12] Y. Yun, T. Maki and T. Kobayashi, *J. Appl. Phys.* **82** (1997) 3422
[13] M. Tachiki, T. Fukuda, K. Sugata, H. Seo, H. Umezawa and H. Kawarada, *Appl. Surf. Sci.* **159-160** (2000) 578
[14] H. Kawarada, Y. Araki, T. Sakai, T. Ogawa and H. Umezawa, *Phys. Stat. Sol. (a)* **185**(1) (2001) 79
[15] A. Denisenko, A. Aleksov, A. Pribil, P. Gluche, W. Ebert and E. Kohn, *Diamond Relat. Mater.* **9** (2000) 1138
[16] A. Denisenko, A. Aleksov and E. Kohn, *Diamond Relat. Mater.* **10** (2001) 667
[17] M. Szameitat, X. Jiang and W. Beyer, *Appl. Phys. Lett.* **77**(10) (2000) 1554
[18] J. Ristein, F. Maier, M. Riedel, J.B. Cui and L. Ley, *Phys. Stat. Sol. (a)* **181** (2000) 65
[19] S.G. Ri, K. Tashiro, S. Tanaka, T. Fujisawa, H. Kimura, T. Kurosu and M. Ida, *Jpn. J. Appl. Phys.* **38** (1999) 3492
[20] R.E. Stallcup, A. F. Aviles and J.M. Perez, *Appl. Phys. Lett.* **66** (1995) 2331
[21] Y. Muto, T. Sugino, J. Shirafuji and K. Kobashi, *Appl. Phys. Lett.* **59** (1991) 843
[22] J. Shirafuji and T. Sugino, *Diamond Relat. Mater.* **5** (1996) 706
[23] K. Hayashi, S. Yamanaka, H. Watanabe, T. Sekiguchi, *et al.*, *J. Appl. Phys.* **81** (2) (1997) 744
[24] T. Maki, S. Shikama, M. Komori, Y. Sakaguchi, K. Sakuta and T. Kobayashi, *Jpn. J. Appl. Phys.* **31** (1992) L1446
[25] H. Kawarada, *Surf. Sci. Report* **26**(7) (1999) 205
[26] F. Maier, M. Riedel, J. Ristein and L. Ley, *Diamond Relat. Mater.* **10** (2001) 506
[27] B. Koslowski, S. Strobel and P. Ziemann, *Appl. Phys. A* **72** (2001) 311
[28] K. Hayashi, S. Yamanda, H. Okushi and K. Kajimura, *Appl. Phys. Lett.* **68** (1996) 376
[29] S. Sauerer, F. Ertl, C.E. Nebel, M. Stutzmann, P. Bergonzo, O.A. Williams and R.B. Jackman, *Phys. Stat. Sol. (a)* **186**(2) (2001) 241
[30] F. Maier, M. Riedel, B. Mantel, J. Ristein and L. Ley, *Phys. Rev. Lett.* **87**(16) (2000) 3472
[31] CRC Handbook of Chemistry and Physics, R.C. Weast and M.J. Astle (*eds.*), CRC Press, Boca Raton, 1981

[32] T. Ando, M. Ishii, M. Kamo and Y. Sato, *J. Chem. Soc. Faraday Trans.* **89**(11) (1993) 1783
[33] O.A. Williams, R.B. Jackman, C. Nebel and J.S. Foord, *Diamond Relat. Mater.* **11**(3-6) (2002) 396
[34] D. Ballutaud, F. Jomard, B. Theys, C. Mer, D. Tromson and P. Bergonzo, *Diamond Relat. Mater.* **10** (2001) 405
[35] S. Yamanaka, D. Takeuchi, H. Watanabe, H. Okushi and K. Kajimura, *Appl. Surf. Sci.* **159-160** (2000) 567
[36] I.I. Arkhipov, B.V. Spitsyn, A.E. Gorodetsky, A.P. Zakharov, G. Popovici, T. Sung, M.A. Prelas and S. Khasawinah, *Diamond Relat. Mater.* **5** (1996) 121
[37] B.F. Mantel, M. Stammler, J. Ristein and L. Ley, *Diamond Relat. Mater.* **10** (2001) 429
[38] B.F. Mantel, M. Stammler, J. Ristein and L. Ley, *Diamond Relat. Mater.* **9** (2000) 1032
[39] S.G. Ri, T. Mizumasa, Y. Akiba and Y. Hirose, *Jpn. J. Appl. Phys.* **34** (1995) 5550
[40] J.S. Foord, C.H. Lau, M. Hiramatsu, R.B. Jackman, C.E. Nebel and P. Bergonzo, *Diamond Relat. Mater.* **11** (2002) 856
[41] R.S. Nicholson, *Anal. Chem.* **37** (1965) 1351
[42] M. Awada, J.W. Strojek and G.M. Swain, *J. Electrochem. Soc.* **142**(3) (1995) L42
[43] B.J. Lee, B.T. Ahn. J.K. Lee and Y.J. Baik, *Diamond Relat. Mater.* **10** (2001) 2174
[44] B. Fiegi, R. Kuhnert, M. Ben-Chorin and F. Koch, *Appl. Phys. Lett.* **65**(3) (1994) 371
[45] J. Zak and M. Kolodziej-Sadlok, *Electrochim. Acta* **45** (2000) 2803
[46] G. Oskam, J.G. Long, A. Natarajan and P.C. Searson, *J. Phys. D* **31** (1998) 1927
[47] H. Gerischer, *Electrochim. Acta* **35**(11/12) (1990) 1677
[48] S. Nakabayashi, D.A. Tryk, A. Fujishima and N. Ohta, *Chem. Phys. Lett.* **300** (1999) 409
[49] P.M. Vereecken, F. Vanden Kerchove and W.P. Gomes, *Electrochim. Acta* **41**(1) (1996) 95
[50] M.B. Davies, R.J. Mortimer and T.R. Vine, *Inorg. Chim. Acta* **146** (1998) 59
[51] C.H. Goeting, F. Marken, A. Gutierrez-Sosa, R.G. Compton and J.S. Foord, *Diamond Relat. Mater.* **9** (2000) 390
[52] J. Laskowski and J.A. Kitchener, *J. Colloid Interface Sci.* **29** (1969) 670
[53] J. Wang, U.A. Kirgoz, J.W. Mo, J.M. Lu, A.N. Kawde and A. Muck, *Electrochem. Comm.* **3** (2001) 203
[54] C.H. Lau, K.J. Grehan, R.G. Compton, J.S. Foord and F. Marken, to be published (2002) *J. Electrochem. Soc.*
[55] B. Fausett, M.C. Granger, M.L. Hupert, J. Wang, G.M. Swain and D.M. Gruen, *Electroanalysis* **12**(1) (2000) 7
[56] H.H. Yang and R.L. McCreery, *J. Electrochem. Soc.* **147**(9) (2000) 3420
[57] J. Xu, W.H. Huang and R.L. McCreery, *J. Electroanal. Chem.* **410** (1996) 235
[58] H. Notsu, I. Yagi, T. Tatsuma, D.A. Tryk and A. Fujishima, *J. Electroanal. Chem.* **492**(1) (2000) 31
[59] H. Notsu, T. Fukazawa, T. Tatsuma, D.A. Tryk and A. Fujishima, *Electrochem. Sol. State Lett.* **4**(3) (2001) H1-H3
[60] H.B. Martin, A. Argoitia, J.C. Angus and U. Landau, *J. Electrochem. Soc.* **146**(8) (1999) 2959
[61] J.C. Angus, H.B. Martin, U. Landau, Y.E. Evstefeeva, B. Miller and N. Vinokur, *New Diamond Front. Carbon Tech.* **9**(3) (1999) 175

Chapter 4

Nanodiamond and Electrochemistry

4.1 Introduction
4.2 Experimental
4.3 Characterization
4.4 Results and Discussion
  4.4.1 Growth
  4.4.2 Solvent Window and Stability in Aqueous Media
  4.4.3 Electrochemical Characterization
    4.4.3.1 The Reduction of $Ru(NH_3)_6^{3+}$
    4.4.3.2 The Oxidation of $Fe(CN)_6^{4-}$
  4.4.4 The Redox System of Organic Compounds
    4.4.4.1 Ascorbic Acid
    4.4.4.2 Hydroquinone
    4.4.4.3 NADH
    4.4.4.4 Cytochrome *c*
    4.4.4.5 Deactivation Test
  4.4.5 $Ce^{4+/3+}$ Redox System
  4.4.6 The Deposition and Stripping of Metals
    4.4.6.1 Gold
    4.4.6.2 Copper
  4.4.7 Surface Modification
    4.4.7.1 Surface Treatments
    4.4.7.2 Effect of Thermal Annealing
    4.4.7.3 Abrasive and Adhesiveness Test
    4.4.7.4 Solvent Test
4.5 Conclusion

4.1 Introduction

Conventionally, CVD diamond that has been grown by using a mixture of hydrocarbon in excessive hydrogen gas to produce polycrystalline diamond film consists of crystallites with size ranges 1 - 50 μm. Hydrogen is expected to react with hydrocarbon precursor radicals, such as CH_3 and C_2H_2, which are dissociated from carbon-containing gases by high temperature plasma. The radicals are responsible for forming fundamental sp^3 bonding spreading upon the nucleated diamond seeds and their addition results in the growth of the crystal lattices. Hydrogen suppresses the further secondary nucleation by

etching away non-diamond properties, and thus sp^2 content is decreased and higher quality of diamond can be obtained.

With the decreases of hydrogen content and the subsequent additions or the increases of noble gases (such as Ar and He), the transition of crystalline size from micro- to nano-scaled is observed. However, reports by Matsumoto *et al.* [1,2] and Zhu *et al.* [3] suggested that the mixture of noble gases with hydrocarbon would favour the growth of non-diamond, as the role of hydrogen as an active etchant has been removed. In such condition, the C_2 would react with the freshly produced CH_4 and C_2H_2 to form propyne and cyclobutyne, respectively. The subsequent reaction of C_2 with those products would further create a series of larger compounds in *gas phase*, which is regarded as a process of homogeneous nucleation. Non-diamond deposition, mainly graphite, amorphous carbon and diamond-like carbon are favoured in this process.

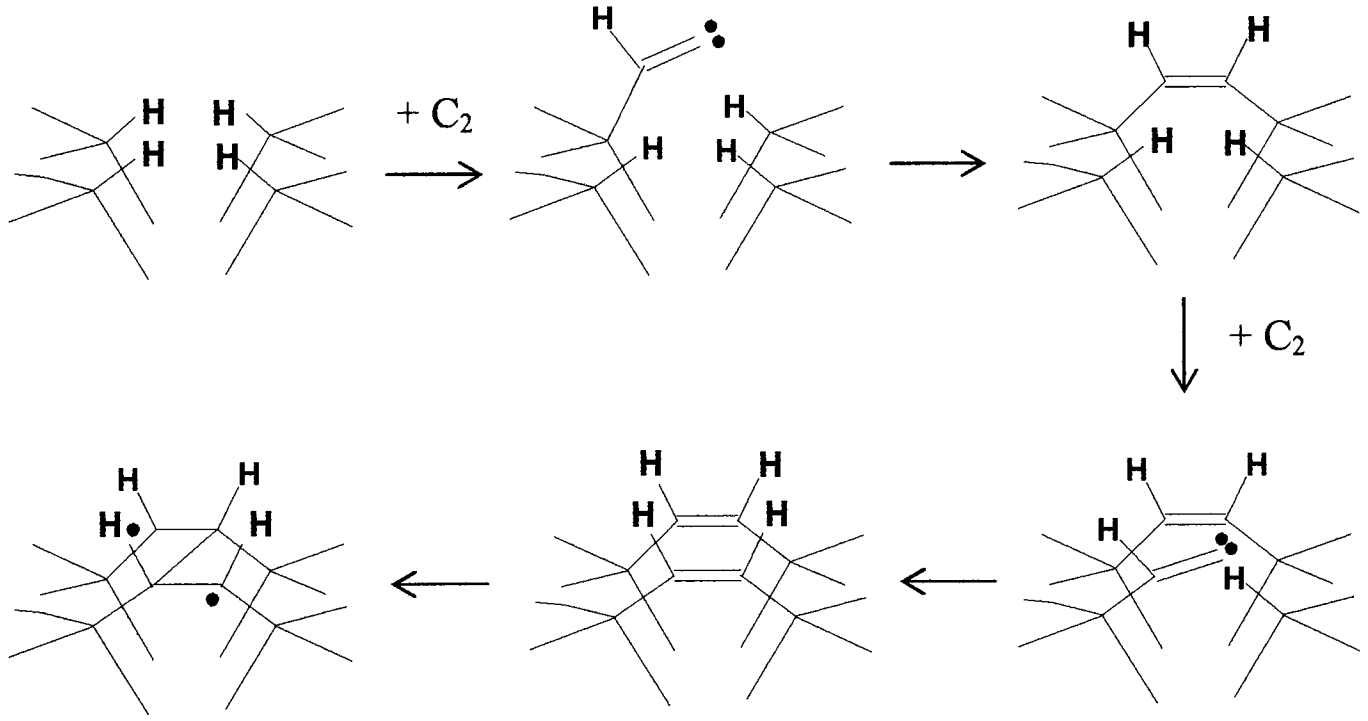


Figure 1. Mechanism of the direct two-step C_2 addition to the (110)-(1 x 1):H diamond surface

In contrary to the process, by scratching the substrate with small diamond particles (~ 0.1 micron) and later treated ultrasonically in solvent, a nucleation density of 10^{10} cm^{-2} is normally achievable [4] and hence heterogeneous nucleation is favoured upon proper diamond seeding on a substrate (*solid*). At low hydrogen content, the C_2 concentration

would increase drastically by two to three orders of magnitude. The insertion of C_2 into CH-bonding occurs to form ethylene-like adsorbate [5] (see figure 1), and further formation of single bonds between adjacent adsorbed C_2 units can occur directly without the initiation by hydrogen additions. The linking of three or more C_2 units creates a series of carbon dimers formed on the seeds, which are the dominant growth species.

Due to the reductions in crystallite size to nanometer scale, the amount of grain boundaries that rich with sp^2 π-bonding carbons will increase. Such boundaries are responsible for a high conducting pathway, which can increase the surface conductivity [6]. Conventional polycrystalline diamond film has shown great prospects in a wide range of applications, but due to its surface roughness, it would hinder the immediate use for optical and tribological application. Nanodiamond films appear to be promising in such aspects. With low surface roughness for nanodiamond film, the effect of light scattering could be reduced and will increase the optical transparency substantially [4]. When used in sliding-wear applications, such smooth films cause very low friction and wear losses on mating surfaces, which make nanometric diamonds better candidates as coating material for mechanical tools. Therefore, nanodiamond film meets the consensus of maintaining the crucial diamond sp^3 content, and at the same time have good surface smoothness.

However, diamond nanocrystallites are always embedded in a matrix of amorphous or diamond-like carbon. Depending on the conditions during a particular growth process, the nondiamond phases form a lesser or greater fraction of the film volume. Seminal work by Gruen [7], as reported in 1994, has proposed the standard evaluation in grading the quality nanocrystalline diamond films, include

- absence of nondiamond phases (< 5%) (phase purity)
- specification of crystallite size ranges (3-15 nm, low – "ultrananocrystalline diamond"; 17-75 nm, medium; 75-375 nm, high) (crystal size)

- maintenance of nanocrystallinity to thicknesses greater than 3 μm, preferably to at least 30 μm (film thickness)
- random grain orientation to maximize π-bonding across grain boundaries (orientation)

Since the large number of defects and grain boundaries are likely contributing to the surface electronic states, the nanodiamond may be considered as another important electrochemical material. The potential advantages of using nanodiamond films in electrochemistry [8], compared to the more common microcrystalline films, include

(a) the ability to deposit continuous films at nanometer thicknesses rather than micrometer thicknesses leading to time and cost savings,

(b) easier coating of irregular geometry substrates like fibers and high surface area meshes, and

(c) the different film morphology and characteristic electronic properties might lead to unique electrochemical and photoelectrochemical behavior.

In this report a novel approach for the formation of diamond films is introduced based on a microwave plasma deposition process employing only dihydrogen and methane as reactive gases in a helium atmosphere. Nanodiamond films with small grain sizes are grown on titanium substrates in this way, which display significant electrical conductivity due to the graphitic content and high concentration of grain boundaries in the material. These diamond film electrodes are mechanically strong (in abrasion test experiments) and to some extent resistant to anodic processes. The use of titanium as a substrate material is attractive for commercial applications. The nanodiamond electrodes are employed in stationary and rotating disc voltammetry experiments. A survey of important aqueous redox systems shows that these nanodiamond films display interesting and advantageous electrochemical properties in comparison to the more conventional boron-doped diamond materials.

4.2 Experimental

Nanodiamonds were grown on Ti substrates (2 mm diameter, 12 mm height) on a Mo substrate holder in a MWPECVD (2.45 GHz) reactor with a 2 kW microwave generator (Penta Science & Technology Ltd). Samples were scratched with 0.1 μm diamond paste (1/10–KD-C1 Kemet) on carborundum paper (first with 600 graded and later 1000 graded) and agitated in ethanol under ultrasonic bath for 30 min. The samples were stood vertically and shielded from the intense plasma ball. Prior to the generation of microwave plasma, the samples were annealed up to 750 °C for 30 min. The growth was initiated with the simultaneous admittance of three gases, He (200 cm^3 min^{-1}), H_2 (4 cm^3 min^{-1}) and CH_4 (1.5 cm^3 min^{-1}), at a total pressure of 80 Torr and a substrate temperature of 600 °C. The input (forwarded) microwave power was 400 W, with the reflected power less than 5 %. The growth period was typically 4 hours and nanodiamonds are approximately 2 μm in thickness. The freshly grown diamond will later be cooled in a flow of He gas.

The as-grown films were characterized by using Raman spectroscopy (Dilor Labram spectrometer fitted with a Ar 20 mW laser (514.2 nm)), scanning electron microscopy (SEM Cambridge Stereoscan 360 system) and atomic force microscopy (AFM Digital Instruments Multimode Scanning Probe Microscope). The field electron emission characteristics of the fabricated diamond films is measured with a spherical stainless steel anode of 2 mm diameter in a vacuum chamber of a pressure of 10^{-6} Torr. The anode-cathode (diamond film) spacing was kept at 75 μm.

Reagents as KCl, HNO_3, H_2SO_4, $Ru(NH_3)_6Cl_3$ (Aldrich), $K_4Fe(CN)_6$, K_2PO_4 and KH_2PO_4, $CuSO_4.5H_2O$, *L*-ascorbic acid (BDH), hydroquinone and NADH (Agros) were obtained commercially and used without further purification. $HAuCl_4.3H_2O$ (Aldrich) was dissolved in dilute aqua regia solution (0.1 M HCl, 0.3 M HNO_3). Horse heart cytochrome *c* (type VI, Sigma, molecular weight 12384 $gmol^{-1}$) was purified by size eclusion chromatography (prepacked Sephadex G-25 M columns, Amersham Pharmacia

Biotech AB, Uppsala, Sweden). Aqueous electrolyte solutions contained 0.1 M phosphate buffer (pH 7) or 0.1 M KCl. Cu foil (99.99 % purity, Goodfellow) was used as the abraded target material for abrasive stripping voltammetry (AbSV).

Demineralised and filtered water was taken from an Elgastat water purification system (Elga, High Wycombe, Bucks) with a resistivity of not less than 18 MΩ-cm. For voltammetric studies an Autolab PGSTAT 30 potentiostat system (EcoChemie, Netherlands) was employed with a Pt wire counter electrode and a saturated Calomel (SCE) reference electrode (Radiometer, Copenhagen). Nanodiamond working electrodes (2 mm diameter, on titanium) were mounted in Torr Seal™ (Varian) with a silver epoxy back contact. For experiments with polycrystalline boron-doped diamond, 2 mm diameter electrodes deposited using HFACVD on tungsten were employed. Experiments were conducted after de-aerating with high purity argon (BOC) for at least 15 min. The temperature for voltammetric experiments was 22 ± 2 °C.

4.3 Characterization

Nanodiamond films were characterized by scanning electron microscopy, atomic force microscopy, Raman spectroscopy and field emission measurement. Nanodiamond deposits are formed on titanium substrates in a microwave plasma process in approximately 2 μm thickness. Figure 2 (a) and (b) shows the scanning electron micrographs (SEM) of the nanodiamond films deposited on well scratched (with diamond paste) Ti substrates placed on the Mo holder. The diamond films revealed in figure (a) consist of small and fine structures unresolved by SEM, grown on different stages of diamond plates. An assembly of thin crystal platelets with sharp edges in about micron size can be observed. Larger topographic features on the nanodiamond electrode surface (see figure 2b) are due to scratch lines and reflect the underlying titanium substrate.

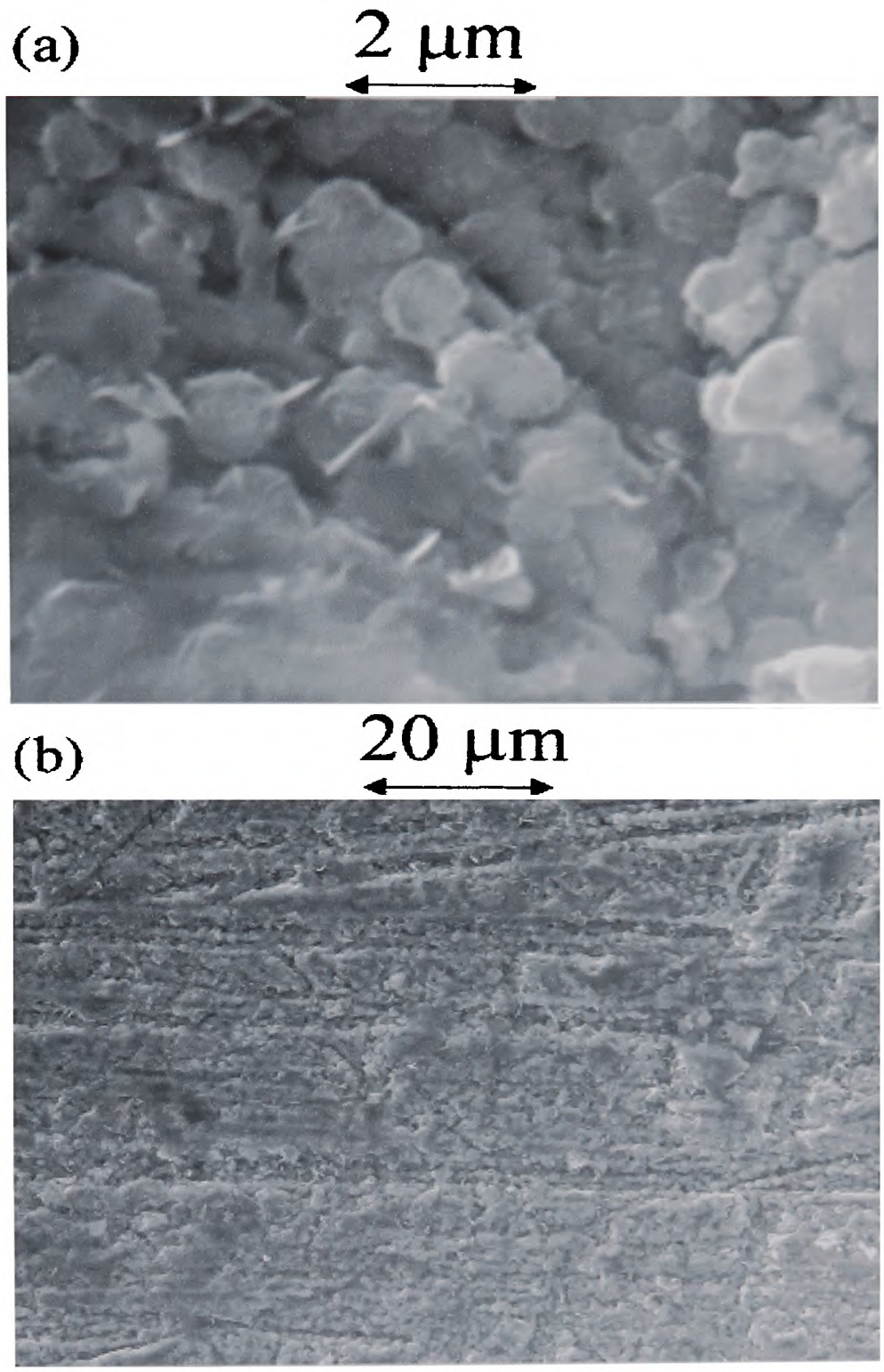
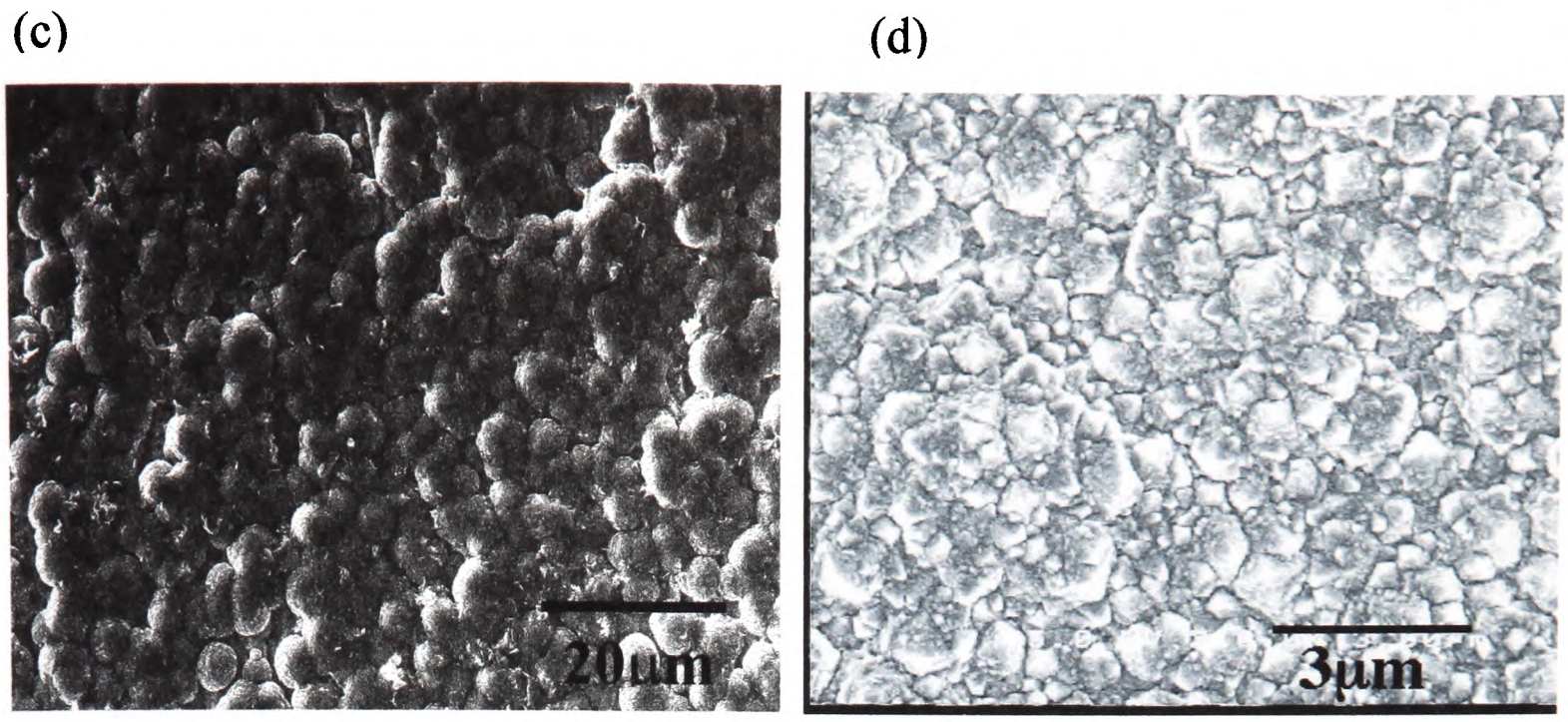


Figure 2. SEM images of a nanodiamond film deposit on a titanium substrate in low and high magnification, grown on Mo substrate holder (He/CH_4) ... cont. ...

In contrast, microcrystalline diamond exhibits well faceted morphology (see SEMs in figure 16a-c, Chapter 2), comprising almost exclusively diamond crystallites with smooth crystalline facets and smaller grain boundaries. SEM 2c shows the image of diamond grown on scratched (without diamond paste) Ti substrate, revealing the "cauliflower" clusters with diameter ranging ~ 1 - 5 μm. SEM 2d is the image of nanodiamond grown on silicon substrate upon a graphite substrate holder (refer to Section 2.15.3, Chapter 2), showing the meso to nano-scaled surface morphology with average grain size about 400 nm (is denoted as NCD 2).



cont... figure 2 (c) SEM image of a diamond film deposit on scratched titanium substrate without diamond paste and (d) SEM image of a nanodiamond/Silicon (NCD 2) deposited on graphite substrate holder (H_2/CH_4)

The surface roughness of nanodiamond/Ti was further measured by AFM images (air, contact mode) (as shown in figure 3). The image reveals the nano-scaled crystalline structures of diamond over 100 x 100 nm^2 area with the size distribution of averagely 20 - 70 nm. The nominal feature size is about 100 nm in diameter with a height of 50 nm. The roughness over the area of 5 x 5 μm^2 as measured under roughness analysis is 103.48 nm (RMS). The images show continuous coverage of film grown over the entire Ti substrate.

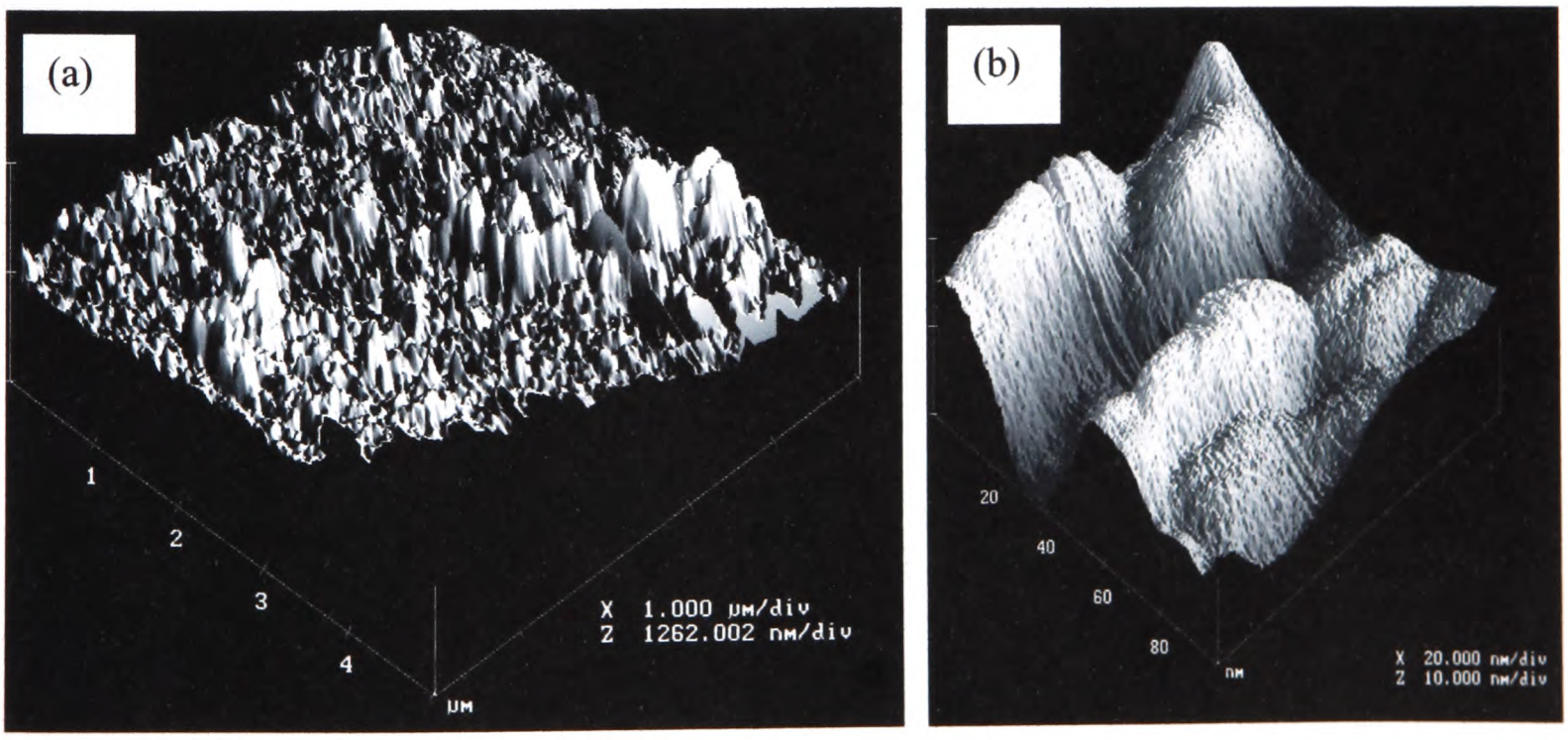


Figure 3. AFM of nanodiamond/Ti (Mo substrate holder, He/CH_4), over (a) 5 x 5 μm^2 area, and (b) 100 x 100 nm^2 area

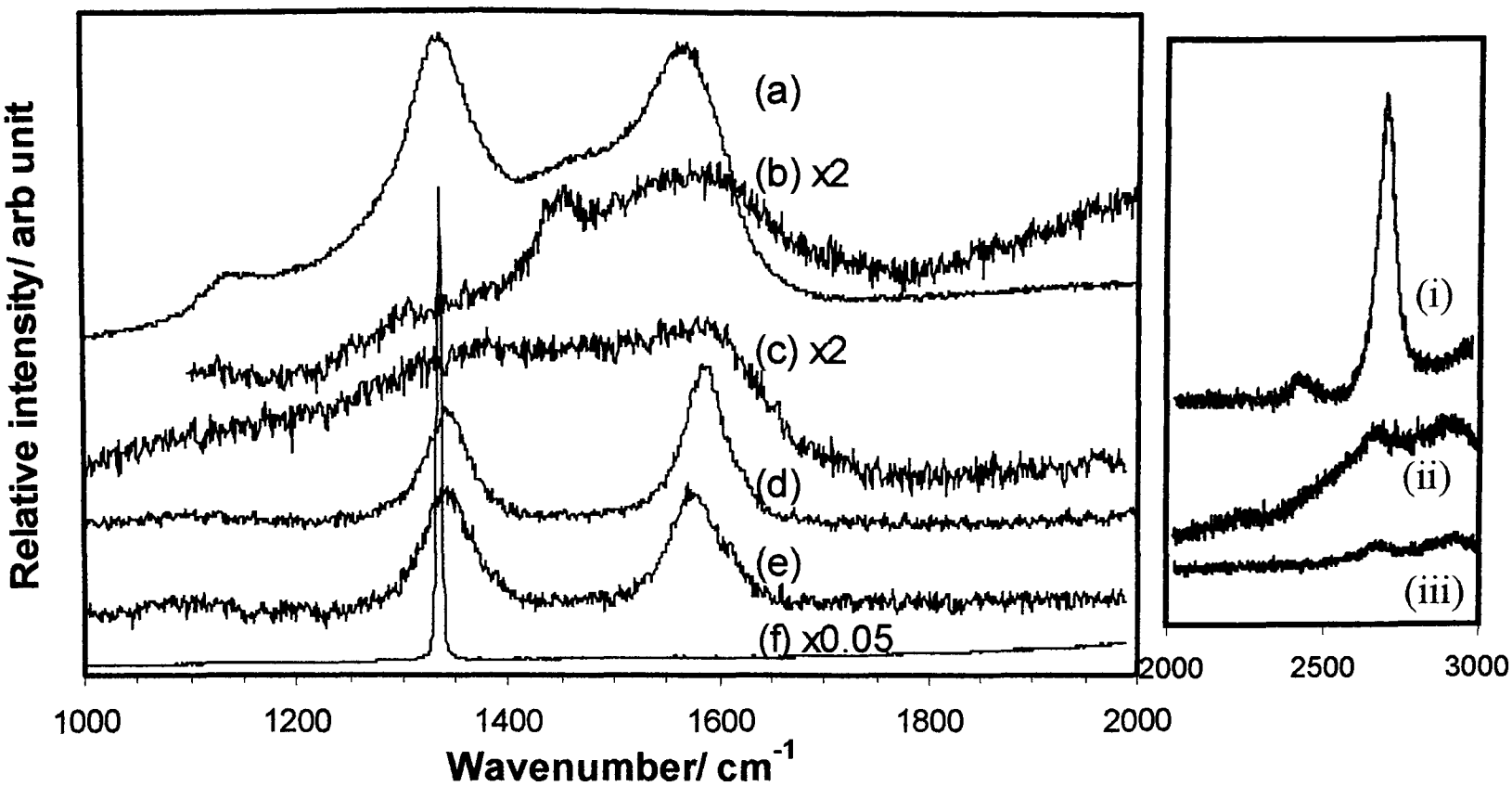


Figure 4. Raman spectra of (a) nanodiamond/Ti, (b) diamond-like carbon, (c) amorphous carbon, (d) nanotube, (e) glassy carbon, and (f) CVD diamond; with the extended Raman region on the right (i = nanotube, ii = nanodiamond, iii = Ti substrate)

The Raman spectra of as-deposited nanodiamond film shown in figure 4 (a) exhibits three main features, as compared to CVD diamond and other carbon materials. (a) A broad Raman band centered approximately at 1335 cm^{-1}, which is the characteristic vibrational mode of crystalline diamond. Broadening of the diamond band is generally attributed to a decrease in the grain size to a nanometer-scale, and also to an increasing concentration of a variety of growth defects, including point defects, twins, internal stresses and sp^2 admixtures [9]. (b) The Raman bands in the region of 1450 - 1560 cm^{-1} are associated with π-bonded carbon at grain boundaries in the nanodiamond film [7]. And (c) a Raman band at approximately 1140 cm^{-1} has been attributed to nanodiamond, or to disorder in a tetrahedral (sp^3) carbon network [7]. However, the peak was examined critically [10], suggesting that the peak should be assigned to transpolyacetylene segments of sp^2-bonded configurations at grain boundaries and surfaces. In principle, the sp^3 bonds (diamond) should be excited more strongly with increasing the excitation energy, but they found the peak at 1140 cm^{-1} decreased in intensity and its peak wave number dispersed by 50-100 cm^{-1}, which act similarly to the peak near 1450 cm^{-1} (the tail of the G peak). This

suggests that the peaks are most likely sp^2 sites, which can more easily be excited by visible light due to their small band gap.

Raman spectra for diamond-like carbon (figure 4b) and amorphous carbon (4c) differ particularly in the absence of the main diamond 1330 cm^{-1} signal (4a,f). Nanotube and glassy carbon differ from nanodiamond with the presence of 1347 cm^{-1} (D line) and their intense second-order peaks at 2700 cm^{-1} (shown on the right, figure 4), by which both peaks are attributed to the defects in the curved graphene sheets and disordered sp^2 carbons [11,12,13]. The existence of G band peaks at 1580 cm^{-1} (4b-e) is due to the different degrees of developed graphitisation in size effect [14,15].

Figure 5 shows the characteristic emission current versus the applied field for the nanodiamond/titanium (with He/CH_4 in this Chapter), as compared to films grown with H_2/CH_4 (see section 2.15.3 of Chapter 2) on graphite substrate holder (producing nanodiamond/silicon, denoted previously as NCD 2) and molybdenum substrate holder (producing microcrystalline diamond). Both of the nanodiamond films were shown to present better field emission properties with good reproducibility than microcrystalline diamond films. The threshold (turn-on) electrical fields for nanodiamonds (figure 5i) are only about 5 V/μm (nanodiamond/titanium) and 7 V/μm (NCD 2), which are smaller than that of the microcrystalline diamond films (18 V/ μm). The well-fitted Fowler-Nordheim plots (5ii) of the films indicate that the field emission property can be explained by tunnelling mechanism. The maximum current carrying abilities for nanodiamond/titanium is 10 mA/cm^2 and the time ageing test (5iii) shows the reduction of 15 % for an hour measurements. It is therefore confirmed that our nanodiamond comprises small-grained film, which exhibits a low emission threshold with high in stability and emission.

Three crucial elements in improving the field emission properties of nanodiamond films are the small grain size, a high density of grain boundaries and the graphite content in the film. In contrasts to large grain size of microscopic diamond, electrons can

effectively tunnel through the nearby tiny diamond edges and can be emitted from a larger surface area of small grain size for nanodiamond. This will lead to the larger field enhancement geometry factor and facilitate electrons to escape easily into vacuum, thus the emission site density would be increased greatly [16].

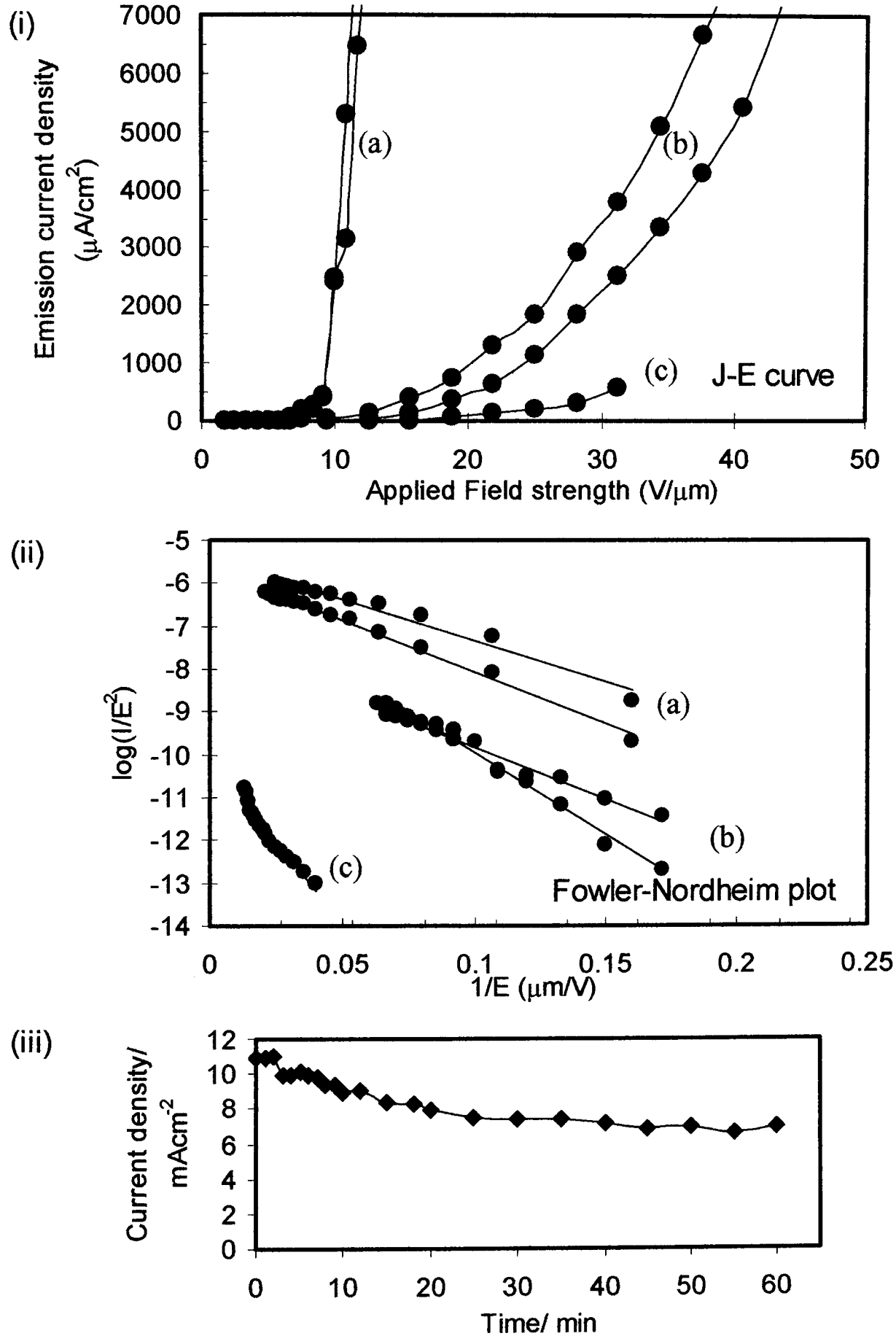


Figure 5. (i) J-E curve and (ii) Fowler-Nordheim plot of (a) nanodiamond/Ti (Mo substrate holder, He/CH_4), (b) nanodiamond/Si, NCD 2 (graphite substrate holder, H_2/CH_4) and (c) microdiamond/Si (Mo substrate holder, H_2/CH_4), (iii) long-time current stability of nanodiamond/Ti at an applied field strength of 10 V/μm

The large amount of grain boundaries can enhance the film conductivity, thus favouring the electron emission. Moreover, the high-density crystalline defects concentrated in the grain boundaries are believed to induce the defect states or sub-bands within the band gap [17]. This forms the conducting medium of the interface structure for grain boundary-diamond-vacuum [18], which will reduce the energy barrier thus eases the electrons tunnelling. The emission could also be due to the diamond/graphite interface. The optimal graphite content should crucially be just enough to fill the gaps between the densely agglomerated diamond grains [19]. Any decrease of graphite content would decrease the interface area and the field emission will drop. Insufficient content of graphite could further eliminate the conducting channels, and thus the emission properties will rapidly be degraded.

4.4 Results and Discussion

4.4.1 Growth

Under the optimal growth condition for nanodiamond on a well-scratched substrate with diamond powders/pastes, the enlargement of individual diamond crystallites is strongly confined by the frequent generation of the secondary nuclei, particularly the C_2 dimer, as the etching role played by hydrogen is removed. The diamond-paste scratches will act as the nucleation sites to promote the subsequent diamond growth. Unlike CH_3, C_2 dimer growth surface is rich of vacant sites and dangling carbon bonds. This will enhance the second and higher order nucleation, resulting in the increase of the total number of the diamond crystallites rather than the increase in grain sizes, and this therefore leads to the formation of nanodiamond films (see SEM, figure 2a,b).

In the case of scratched substrates without the presence of diamond particles (SEM, figure 2c), the scratches formed play the crucial role in nucleation sequence, but the procedure is less efficient than the effect of scratching with diamond powder/paste.

This treatment in turn tends to produce ball-shaped diamond crystallites with larger spatial space to ensure that each cluster has the lowest surface energy, and under such conditions, the non-diamond properties matter is preferentially formed due to the lack of effective nucleation sites. The carbon clusters were made of either tiny diamond crystallites or DLC [20]. For NCD 2, the SEM (figure 2d) and Raman shown in section 2.15.3 (Figure 17 of Chapter 2) indicate that the behaviour of diamond precursors would be influenced by the substrate holder materials and the deposits on the chamber wall, even if the external parameters for diamond growth (process gases, substrate temperature, input power, bias, and so on) were unchanged. Secondary products such as C_2 and CH_n radicals from the graphite surface (substrate holder) possibly influence on the diamond growth. However, the C_2 Swan band was not observed under our optical emission measurement within the visible wavelength range [21], thus detailed investigation using spectroscopic technique is essential to make clear the influences of radical/surface interactions on the diamond growth.

Ti rods have been chosen as substrates for this project, due to its low price coupled with its properties of stability, inertness and adherence [22]. Titanium based materials have been widely utilized into aerospace, electrochemical and biomedical application due to their low density, high mechanical strength and good wet corrosion resistance [23]. However, the materials show low resistance against wear, fretting fatigue and erosion. Provided with a well-adhered diamond film coating, Ti based materials would prevent these damages. These factors would make Ti as an alternative coating material to improve the industrial and technological feasibility besides the widely used materials, such as Si [24], W [25], Mo [26] or more recently Zr, Ta and Nb [27].

Ti-based systems reveal a multi-layer structure. With the original very thin TiO_2-film on Ti, the layer is expected to be substituted by a titanium carbide (TiC) interlayer of rhambrabaevite during diamond growth, forming a strong interfacial bonding between

diamond and Ti substrate [22]. Titanium is also sensitive to temperature and light elements, especially hydrogen. Prior to the generation of microwave plasma, the annealing of Ti substrates at 750 °C is crucial in order to transform the initial large β-titanium grain boundaries (~ 300 μm) on the surface to acicular primary α-titanium grains with a fine eutectoid mixture of secondary α-titanium grains. This step is performed to reduce the thermal expansion mismatch between diamond and titanium, which would create high residual stresses in the diamond coatings and is very detrimental to their adhesion [28]. The growth of nanodiamond was initiated with the plasma of all gaseous reactants (rather than just hydrogen) in order to avoid the formation of titanium hydrides, which can cause severe embrittlement of titanium-based materials at high temperature.

Therefore, the coating of nanodiamond on Ti, modified within carefully tuned parameters leads to pronounced changes and coarsening in the grain structure, which will in turn induce better quality of diamond growth.

4.4.2 Solvent Window and Stability in Aqueous Media

Initially, the electrochemical characteristics of nanodiamond electrodes that immersed in aqueous electrolyte solution without redox-active reagents were explored.

Figure 6 shows the first and second cycle of cyclic voltammograms obtained with 'as grown' nanodiamond electrodes. Voltammograms in figure 6a and b are recorded in 0.1 M KCl. During the course of the first potential cycle, a pronounced oxidation response at approximately 1.1 V *vs* SCE is detected. This oxidation response is tentatively attributed to graphitic (sp^2) and pristine non-diamond material present on the diamond surface after synthesis. In the second and following potential cycles this response is not detected. The solvent window for the nanodiamond electrode is similar to that observed for a glassy carbon electrode, spanning ca. 2.3 V, and is smaller compared to the solvent window at boron-doped diamond electrodes, spanning ca. 3.5 V [8].

When immersed in aqueous 1.0 M H_2SO_4 (see figure 6c and d) the potential window becomes limited at negative potentials by the earlier onset of the hydrogen evolution process. However, the positive potential window is expanded accordingly and a range from ca. – 0.8 to + 1.7 V is accessible. The anodic response during the first potential cycle is detected at E_p = 0.8 V *vs* SCE. During the second and following potential cycles this peak is absent. Analogous results were obtained in other aqueous media such as phosphate buffer solution at pH 2.

The slightly higher background current in aqueous KCl and H_2SO_4 for nanodiamond film (~ 5 - 10 μA) as compared to the generally background current of 1 μA for boron-doped diamond [5] is likely due to the increased amount of grain boundary carbon. The increased density of states (DOS) most likely results from the grain boundary carbon, which can lead to a larger surface charge density and a larger capacitive background current.

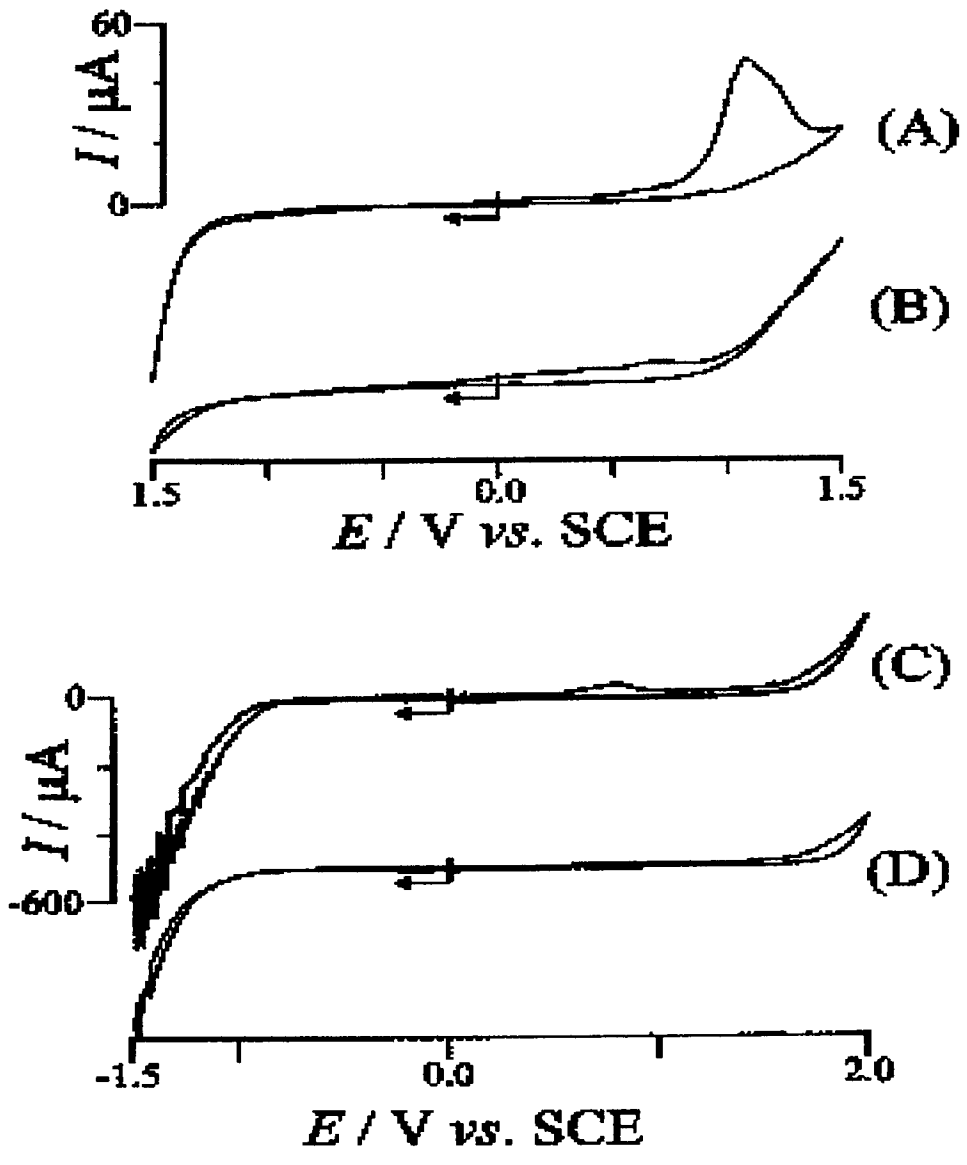


Figure 6. CVs (scan rate 20 mV s^{-1}) for 'as-grown' nanodiamond immersed in (A= 1st scan, B= 2nd scan) aqueous 0.1 M KCl and (C= 1st scan, D=2nd scan) aqueous 1 M H_2SO_4

After cycling the potential for 10 cycles between 0 and 3 V *vs* SCE the electrode remains active (see figure 7c). However, the capacitive background current is considerably enhanced. Cycling the potential for 10 cycles between 0 and 5 V *vs* SCE shows the similar CV feature to Ti (a), probably due to the passivation by TiO_2 formation. It is believed that at highly applied anodic potentials, the generated O_2 etches away sp^2 at grain boundaries and creates holes tunnelling through the diamond layer. This would lead to the interaction of O_2 with the substrate and subsequent passivation is expected.

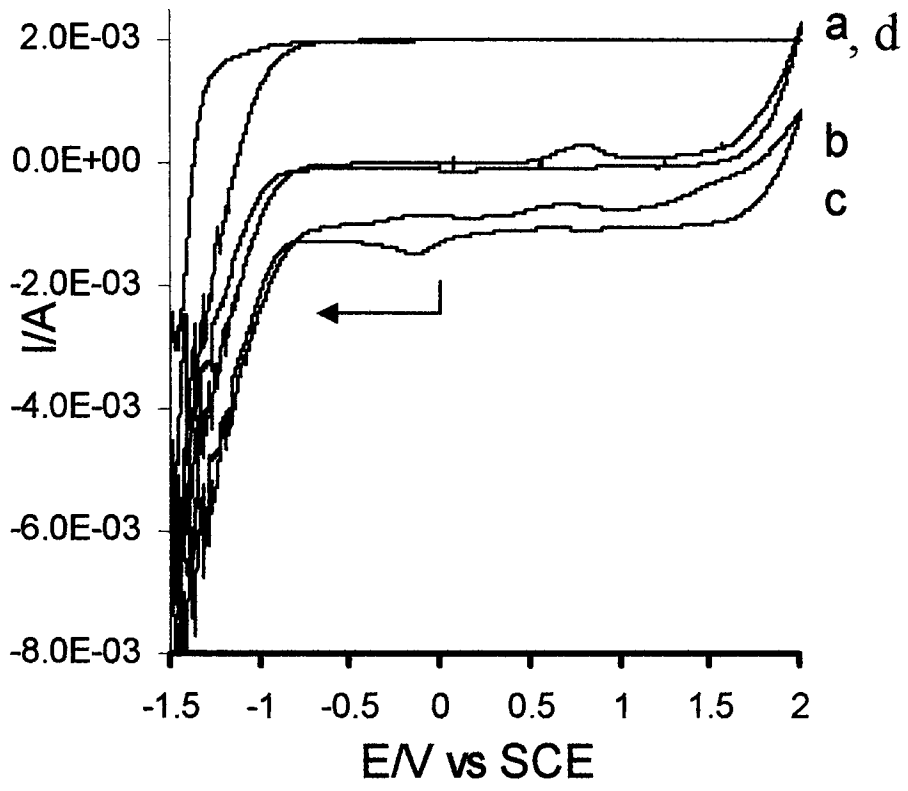


Figure 7. CVs (scan rate 20 mV s^{-1}) obtained for (a) Ti substrate, (b) 'as-grown' nanodiamond/Ti, (c) nanodiamond/Ti after 10 scans to + 3V vs SCE, (d) nanodiamond/Ti after 10 scans to + 5 V vs SCE. All of the electrodes were immersed in aqueous 1 M H_2SO_4

The specific capacitance of electrochemical double capacitive layer is usually linked to the physical area, the pore size, the chemical changes at the interface, the electrolyte properties and the changes of internal density of states (DOS) [28]. For an ideal double-layer capacitor where the time constant is zero, the CVs are characterized by a perfectly rectangular-shaped profile [29]. Though electrochemical impedance measurements are usually employed to determine the capacitance of the diamond|aqueous electrolyte interface, a simple but crude capacitance test can be carried out by applying high potential scan rates, and the calculation is based on equation 1

$$\Delta j/v = \Delta I/\{(dV/dt) \text{ x electrode area}\} \qquad \text{(eqn 1)}$$

where Δj = current density, $v = dV/dt$ = potential scan rate.

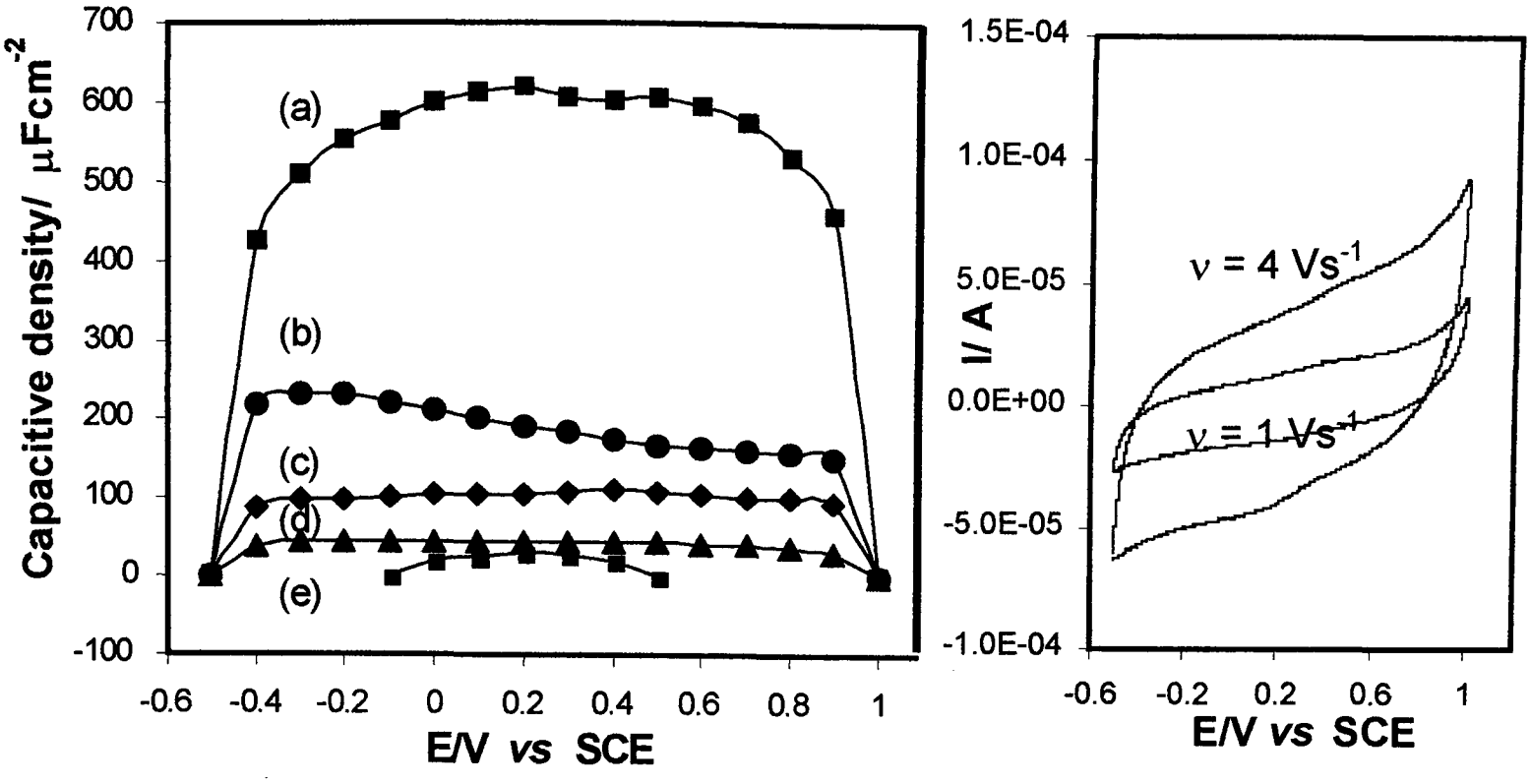


Figure 8. Capacitive density (figure left) calculated from ΔI/{(dV/dt) x electrode area} from CVs in 0.1 M KCl for (a) nanodiamond/Ti, (b) glassy carbon, (c) boron-doped diamond, (d) Ti substrate, and (e) surface conductive diamond. Figure on the right shows the CVs of nanodiamond/Ti at the potential scan rates of 1 and 4 Vs^{-1}

As shown in figure 8, nanodiamond/Ti shows very high capacitive density of 600 $\mu F/cm^2$ (as compared to 30 $\mu F/cm^2$ for Ti substrate) within the solvent window from – 0.5 to 1.0 V *vs* SCE and an appreciably rectangular-shaped profile is observed in CV. The high interfacial capacitance could be attributed to (i) the high surface area of nanodiamond (ii) the defective DOS contents exposed to the solution phase, which allows more charges to be stored within the double layer and allows the layer structure to change upon applied potential. Glassy carbon material shows reasonably good capacitive behaviour of 200 $\mu F/cm^2$ owing to the high surface area derived from its open-pore structure of reticulated vitreous carbon in cross-linked graphite-like sheets [30]. Boron-doped diamond and undoped surface conductive diamond shows comparatively low capacitive density, which can be attributed to the low surface area, well faceted morphology and small amount of grain boundaries.

4.4.3 Electrochemical Characterization

4.4.3.1 The Reduction of $Ru(NH_3)_6^{3+}$

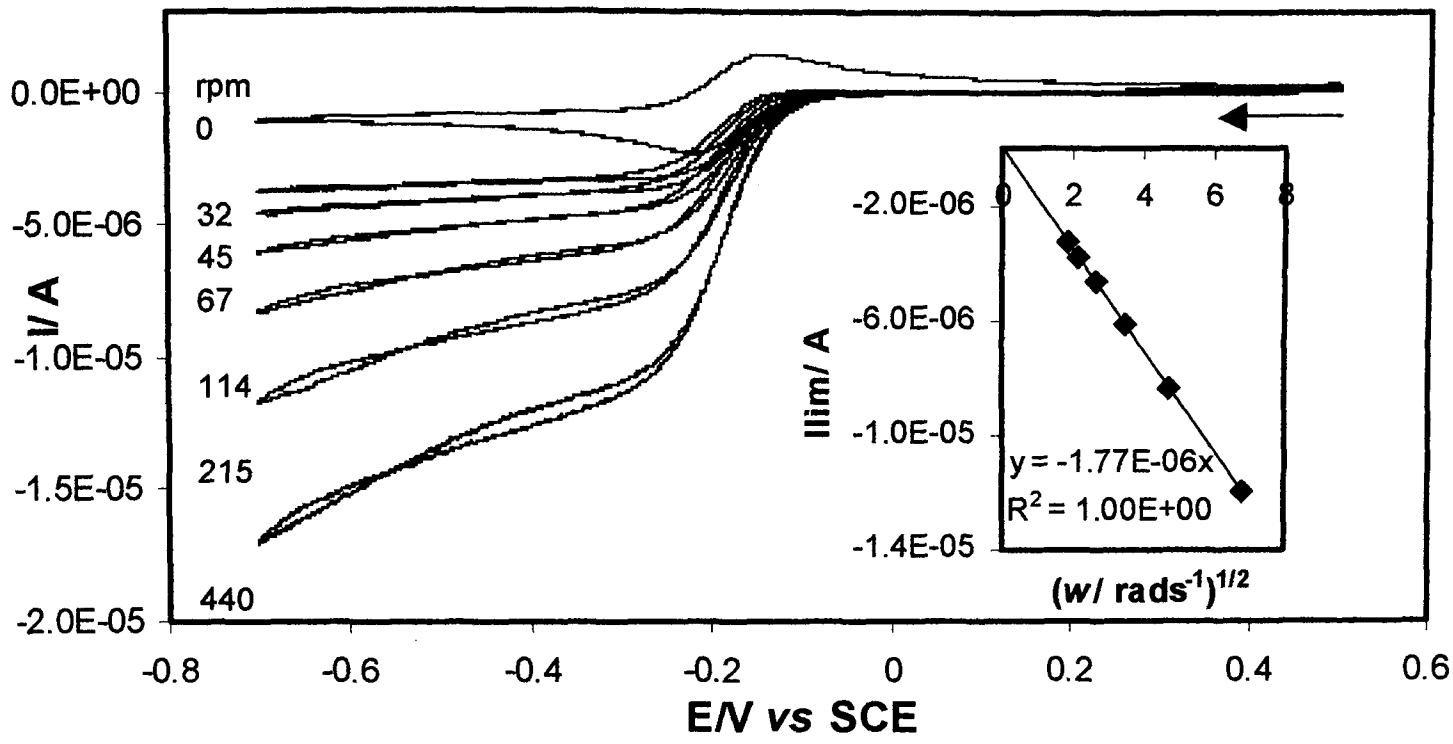


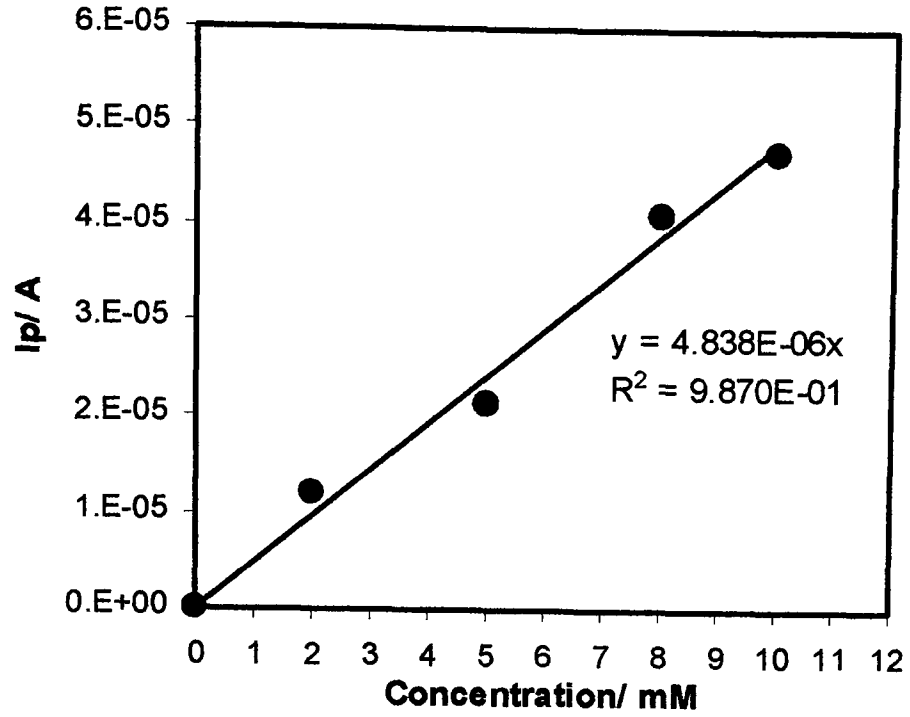
Figure 9. CV (scan rate 20 mVs^{-1}) of reduction of 1 mM $Ru(NH_3)_6^{3+}$ in 0.1 M KCl at different rotation speed at nanodiamond; with inset showing the Levich plot of limiting current, I_{lim} versus $\omega^{1/2}$

The electrochemical reduction of $Ru(NH_3)_6^{3+}$ proceeds *via* one electron transfer according to the reaction below (equation 2);

$$Ru(NH_3)_6^{3+}(aq) + e \leftrightarrow Ru(NH_3)_6^{2+}(aq) \qquad \text{(eqn 2)}$$

Figure 9 shows the CV of reduction of 1 mM $Ru(NH_3)_6^{3+}$ at a potential scan rate of 20 mVs^{-1} at 0 rpm and is compared to a series of limiting current responses as a function of rotation speed. Under rotating disc voltammetry conditions, the shape of the voltammogram becomes sigmoidal and the mass transport controlled limiting current increases consistent with the Levich equation (equation 54, Chapter 2) [31], with $D_{Ru(NH_3)_6^{3+}}$ (9.1×10^{-10} m^2s^{-1}), *vkinematic* (1.0×10^{-6} m^2s^{-1}). The zero-intercept ($r^2 = 1$) indicates the perfect diffusion-controlled process on nanodiamond. At high scan rates and at high concentration of $Ru(NH_3)_6^{3+}$ under stationary CVs, the cathodic current response remained well behaved, but the response on the reverse scan became asymmetric (data not shown). This electrochemical behaviour could be attributed to the surface oxidized layers or even the finite electron transfer kinetics.

(a)



(b)

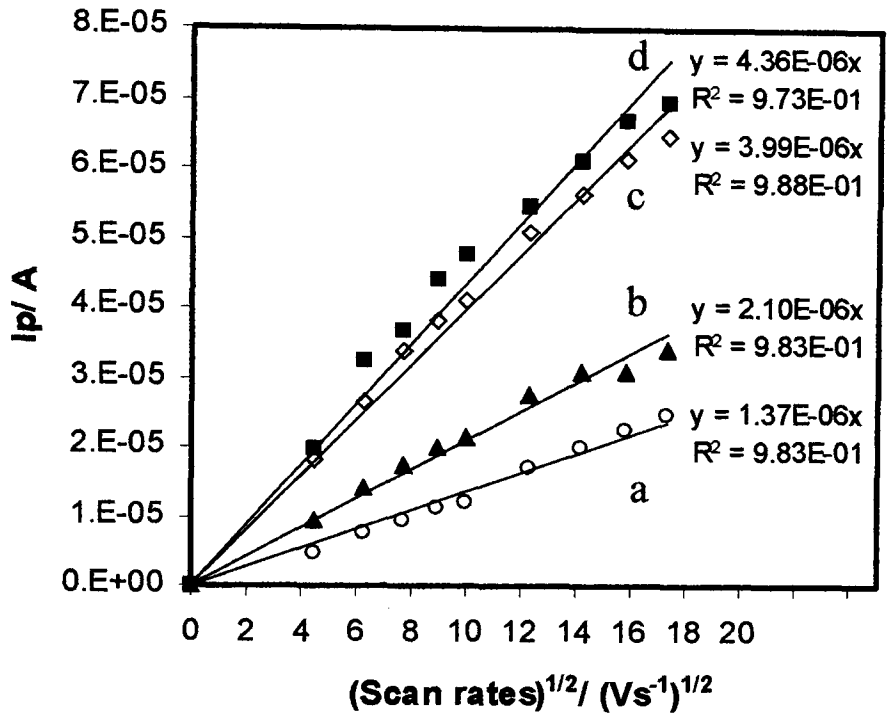


Figure 10. The response of reduction peak current, Ip^{red} of nanodiamond to $Ru(NH_3)_6^{3+}$ in 0.1 M KCl at (a) different concentration and (b) square root of scan rates (a = 2 mM, b = 5 mM, c = 8 mM, d = 10 mM)

Figure 10 shows the current response for $Ru(NH_3)_6^{3+}$ to different concentration (10 a) and *vs* square root of scan rate (10 b). The I_p^{red} values varied linearly with $v^{1/2}$ at various concentrations, range from 2 mM to 10 mM with linear regression yielding near-zero intercept and an r^2 value of 0.982. The I_p^{red} values also varied linearly with the concentration from 2 mM to 10 mM with a near-zero intercept and an r^2 value of 0.990. Voltammetric data are summarized in Table 1. The calculated values for $k°$ are around 10^{-3} cms^{-1}, ranging from 1.6 to 5.1 x 10^{-3}, indicative of a quasi-reversible response. Within our experimental parameters, the averaged value for ΔEp is 129 mV and I_p^{ox}/I_p^{red} ratio is

of 1.70. The values are in good agreement with the reported results of Swain [8]. The rate of electron transfer for $Ru(NH_3)_6^{3+}$ is relatively insensitive to the surface microstructure, surface oxides, and adsorbed monolayers on sp^2 carbon electrodes [32]. However, the density of electronic states near the formal potential of the redox system and the fraction of edge plane exposed on grain boundaries are crucial factors affecting the rate of the reaction [33]. This would suggest that the quasi-reversible electron transfer kinetics in the electrochemical reduction system of $Ru(NH_3)_6^{3+}$ is strongly supported by the density of states and surface charge carrier concentration of nanodiamond.

Table 1. Data obtained from CV for the reduction of $Ru(NH_3)_6^{3+}$ in 0.1 M KCl

Conc. (mM)	Scan rate (Vs^{-1})	$E_{1/2}$ (*vs.* SCE)	ΔEp (mV)	Ip-red (μA)	Ip-red/ Ip-ox	$k°$ ($10^{-2}cms^{-1}$)
2	0.02	-0.18	107.4	-9.37	1.97	0.22
	0.06	-0.18	108.0	-15.1	1.56	0.40
	0.1	-0.18	109.9	-18.9	1.56	0.51
	0.2	-0.18	125.3	-34.6	1.71	0.49
5	0.02	-0.18	112.1	-17.7	1.88	0.20
	0.06	-0.19	127.1	-28.3	1.62	0.29
	0.1	-0.19	131.8	-34.6	1.62	0.29
	0.2	-0.19	153.8	-47.8	1.51	0.33
10	0.02	-0.19	122.0	-41.6	2.10	0.16
	0.06	-0.20	133.2	-66.5	1.81	0.22
	0.1	-0.20	139.1	-84.6	1.78	0.27
	0.2	-0.20	188.4	-97.7	1.60	0.22

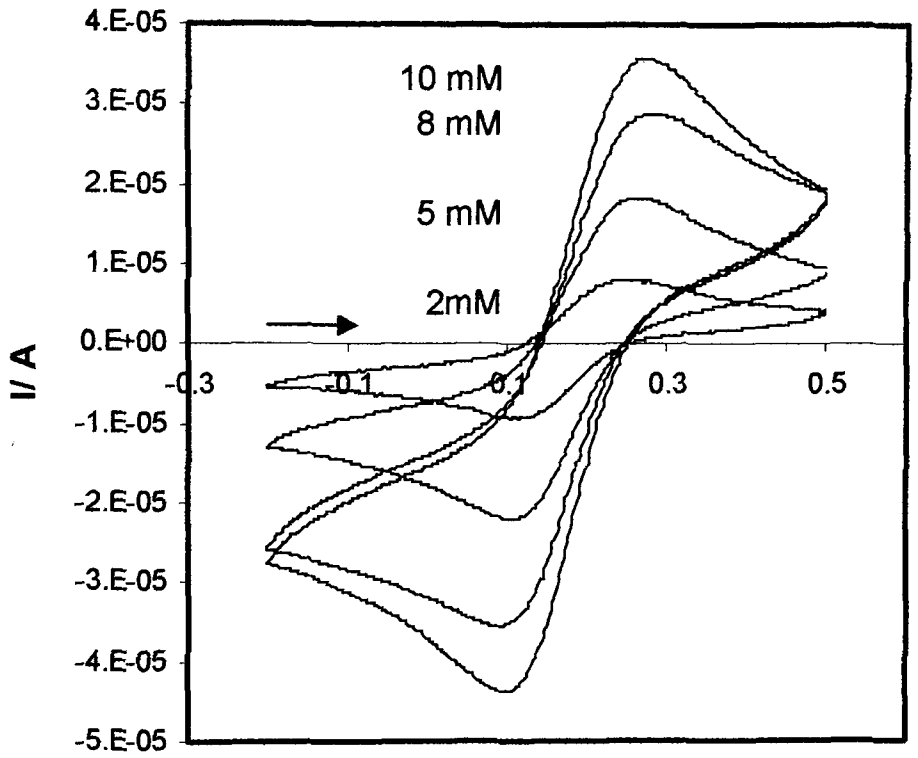
For a concentration of 2 mM $Ru(NH_3)_6^{3+}$ at potential scan rate 0.1 Vs^{-1}, the calculated area is 3.7 ± 0.2 mm^2, for 5 mM 2.7 ± 0.2 mm^2, and for 10 mM the area is 3.3 ± 0.2 mm^2. This shows that the electrochemical active area (calculated) is consistent with the geometrical area of 2 mm nanodiamond electrodes (3.1 ± 0.2 mm^2).

4.4.3.2 The Oxidation of $Fe(CN)_6^{4-}$

The interfacial kinetics for the electron transfer for the oxidation of $Fe(CN)_6^{4-}$ in aqueous media is sensitive to the state of carbon surfaces and has been employed extensively to characterize diamond electrodes. The electrochemical oxidation of $Fe(CN)_6^{4-}$ proceeds *via* one-electron transfer as in equation 3

$$Fe(CN)_6^{4-}(aq) \leftrightarrow Fe(CN)_6^{3-}(aq) + e^- \qquad \text{(eqn 3)}$$

(a)



(b)

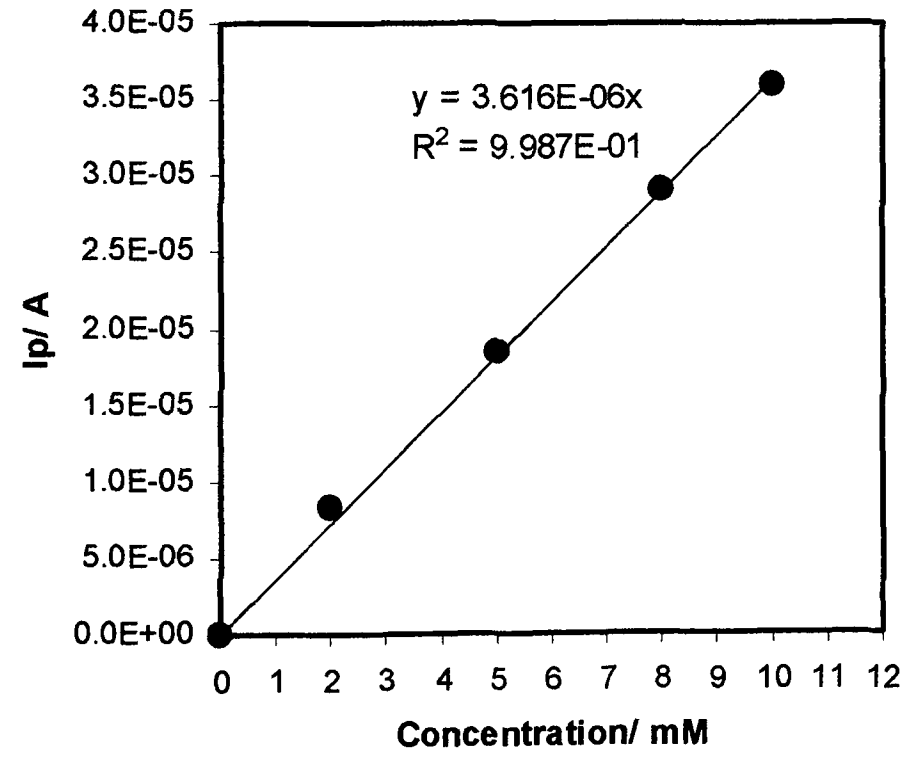
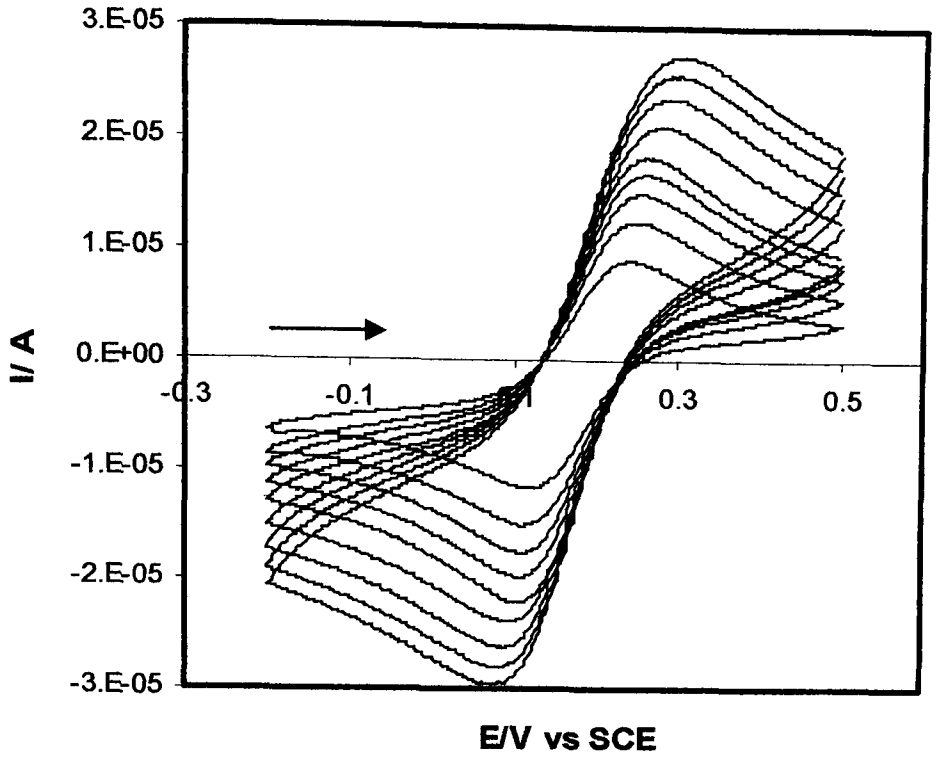


Figure 11. (a) The CVs of nanodiamond in response to $Fe(CN)_6^{4-}$ in 0.1 M KCl at different concentration; and (b) the correlation plot of oxidation peak current, Ip^{ox} of nanodiamond to $Fe(CN)_6^{4-}$ at concentrations of 2 mM, 5 mM, 8 mM and 10 mM

(a)



(b)

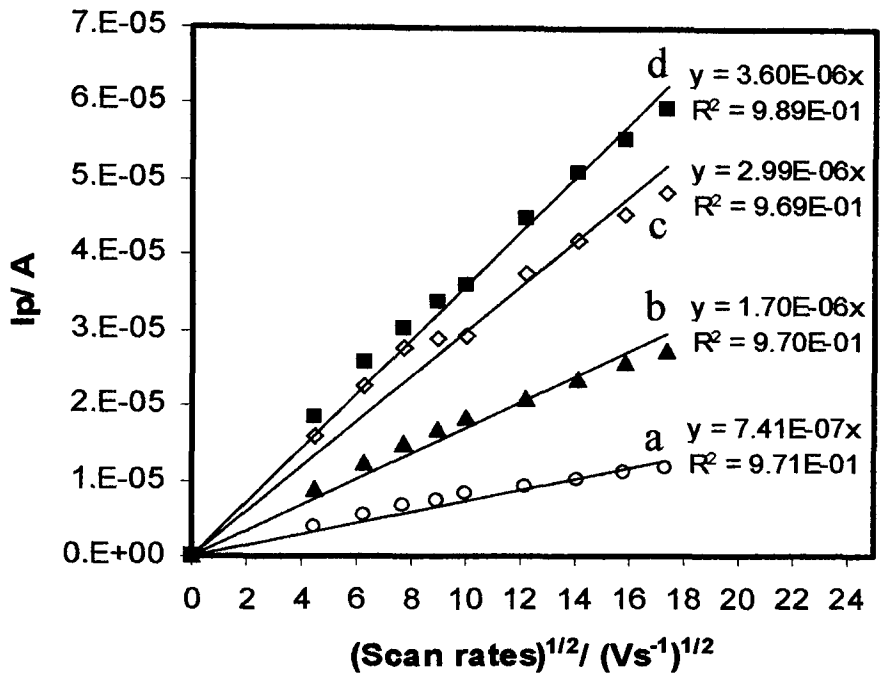


Figure 12. (a) The CVs of nanodiamond in 5 mM $Fe(CN)_6^{4-}$ in 0.1 M KCl at different scan rates, ranging from 0.02 to 0.30 Vs^{-1} and (b) Ip^{ox} responses to square root of scan rates at different concentration (a = 2 mM, b = 5 mM, c = 8 mM, d = 10 mM)

The quasireversible current response of nanodiamond to $Fe(CN)_6^{4-}$ at different concentration and scan rates are shown in figure 11 and figure 12 respectively. Well-defined voltammetric responses are detected, indicating that the nanodiamond surface is very active. Similar observations have been reported for 'as grown' boron-doped diamond electrodes with sufficiently high boron doping level [34,35]. Three possible reasons for this observation are (i) the high surface area of nanodiamond, (ii) many electrochemically active sites *e.g.* at edges of the nanodiamond deposit and (iii) sp^2 content along grain boundaries. Voltammetric data are summarized in Table 2, by employing diffusion coefficient of ferrocyanide, $D_{Fe(CN)_6^{4-}}$ (6.3×10^{-10} m^2s^{-1}). Experiments with concentrations

of 2 mM, 5 mM, and 10 mM $Fe(CN)_6^{4-}$ gave essentially the same results indicating that indeed the electron transfer kinetics are probed. The standard rate constant for electron transfer for the ferrocyanide oxidation process can be determined from the peak-to-peak separation [36] as approximately $k^0 = 1.5 \pm 0.5 \times 10^{-3}$ cm s^{-1}. In contrast to $Ru(NH_3)_6^{3+/2+}$ system, the kinetics for $Fe(CN)_6^{4-/3-}$ is very sensitive to the surface carbon-oxygen functionalities. The high content of nano-scaled edge plane surfaces could contribute to the increased of ΔEp values significantly for this redox analyte, as compared to the microcrystalline diamond with $\Delta Ep \sim 65$ mV [8].

Table 2. Data obtained from CV for the oxidation of $Fe(CN)_6^{4-}$ in 0.1 M KCl

Conc. (mM)	Scan rate (Vs^{-1})	$E_{1/2}$ (*vs.* SCE)	ΔEp (mV)	Ip-ox (μA)	Ip-red/ Ip-ox	$k°$ ($10^{-2}cms^{-1}$)
2	0.02	0.18	129.4	3.74	1.24	0.11
	0.06	0.18	148.9	6.56	1.10	0.16
	0.1	0.18	146.4	8.18	1.14	0.21
	0.2	0.18	188.0	10.4	1.11	0.19
5	0.02	0.18	134.3	9.03	1.28	0.11
	0.06	0.18	148.9	15.1	1.16	0.16
	0.1	0.18	163.6	18.4	1.20	0.18
	0.2	0.19	195.6	23.6	1.11	0.17
10	0.02	0.18	131.9	15.9	1.22	0.11
	0.06	0.18	144.1	27.2	1.18	0.17
	0.1	0.18	188.0	29.0	1.22	0.13
	0.2	0.19	202.7	42.2	1.12	0.15

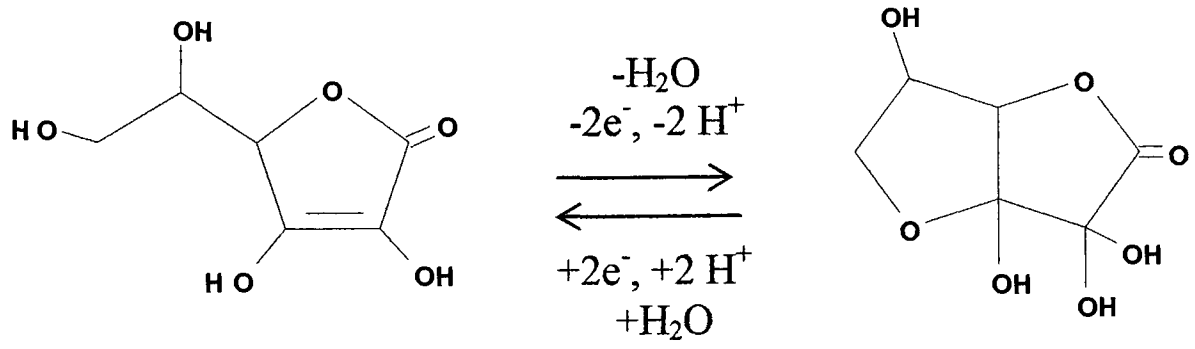
At potential scan rate at 0.1 Vs^{-1}, the concentration of 2 mM yielded the calculated area of 1.9 ± 0.2 mm^2, for 5 mM is 1.7 ± 0.2 mm^2 and for 10 mM is 1.4 ± 0.2 mm^2. These values are around 50 % less than the geometrical area of the electrode (assumed to be flat and circular) of 3.1 mm^2, which implies it is likely that the entire surface may not be active for electron transfer, due to some oxygen functionalities as the electrode was previously used for a series of experiments in Section 4.4.2 and 4.4.3.1.

4.4.4 The Redox System of Organic Compounds

Electron transfer reactions between electrodes and organic redox systems dissolved in aqueous media have been studied extensively often with the aim of selective analytical detection. Here, the electrochemical characteristics at nanodiamond electrodes are surveyed for a range of important organic redox systems dissolved in aqueous media. It is demonstrated that 'as grown' nanodiamond electrodes are highly reactive for many redox processes.

4.4.4.1 Ascorbic Acid

Ascorbic acid/ascorbate is a vital component in the diet of humans. Humans lacking the active enzyme of *L*-gulonolactone oxidase in their livers (which is involved in the mammalian conversion of blood glucose to ascorbic acid) results in the mammalian genetic liver-enzyme disease (a true "inborn error of carbohydrate metabolism") called Hypoascorbemia. Ascorbic acid is a simple glucose-related carbohydrate material. The presence of the ene-diol group in the molecule confers electron lability, which makes it an electroactive species in redox system. The redox system for ascorbic acid is an irreversible electrooxidation process and is of an EC type (equation 4), by which the electrochemical oxidation involves a 2 electron 2 proton pathway (a **E**lectrochemical process), followed by its subsequent reaction with water and cyclization (a **C**hemical process) to yield electrochemically inactive dehydroascorbic acid.



Ascorbic acid Dehydroascorbic acid (eqn 4)

A selective amperometric determination of ascorbic acid has been a major target of electroanalytical research. The compound is considered to be very difficult to detect

electrochemically by direct oxidation on a conventional electrode due to its large overpotential and fouling by the oxidation products. Several studies have addressed the interaction between boron-doped diamond electrodes and ascorbic acid. The potential for oxidation process is indicative for the state of the diamond electrode surface [37,38].

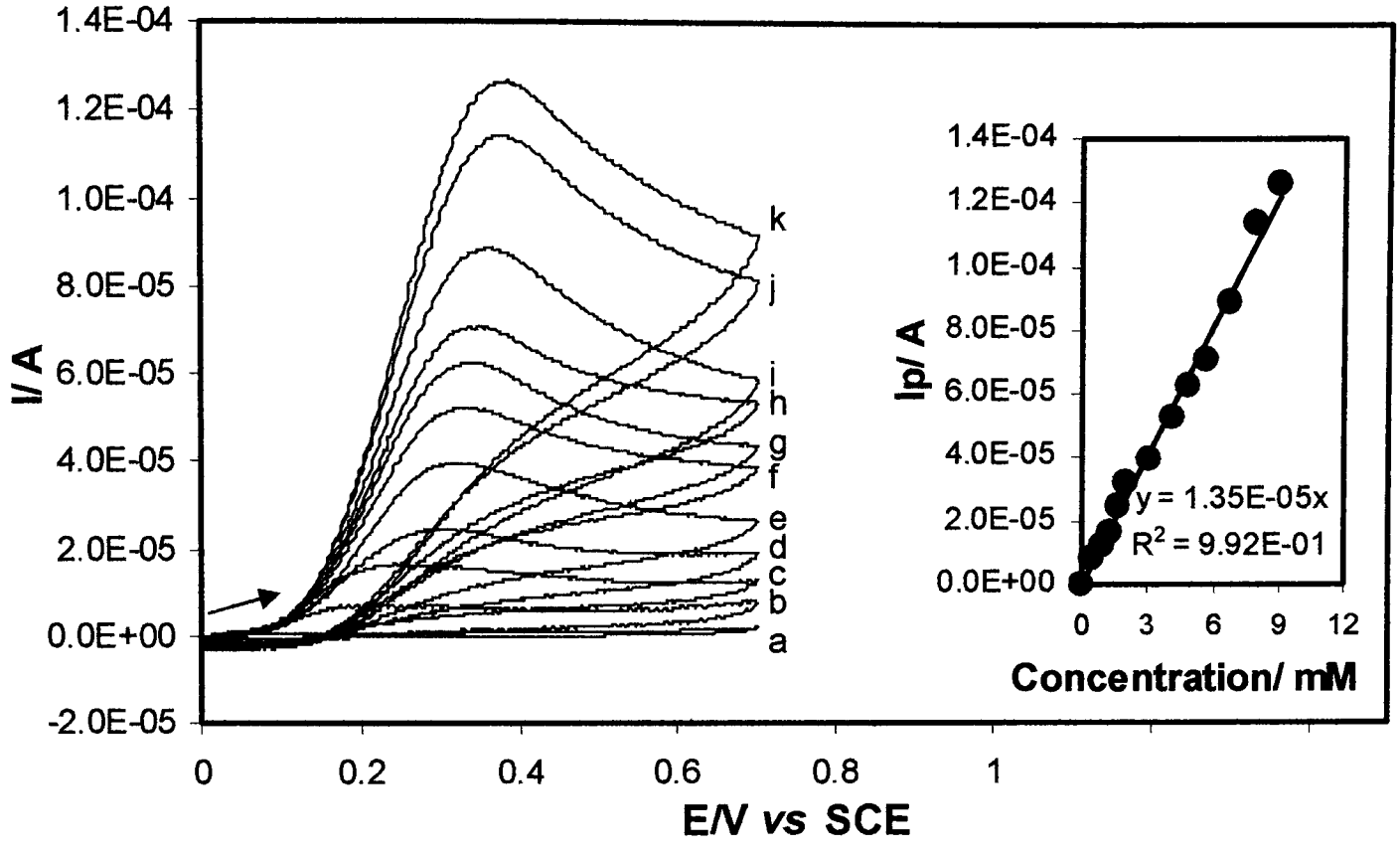
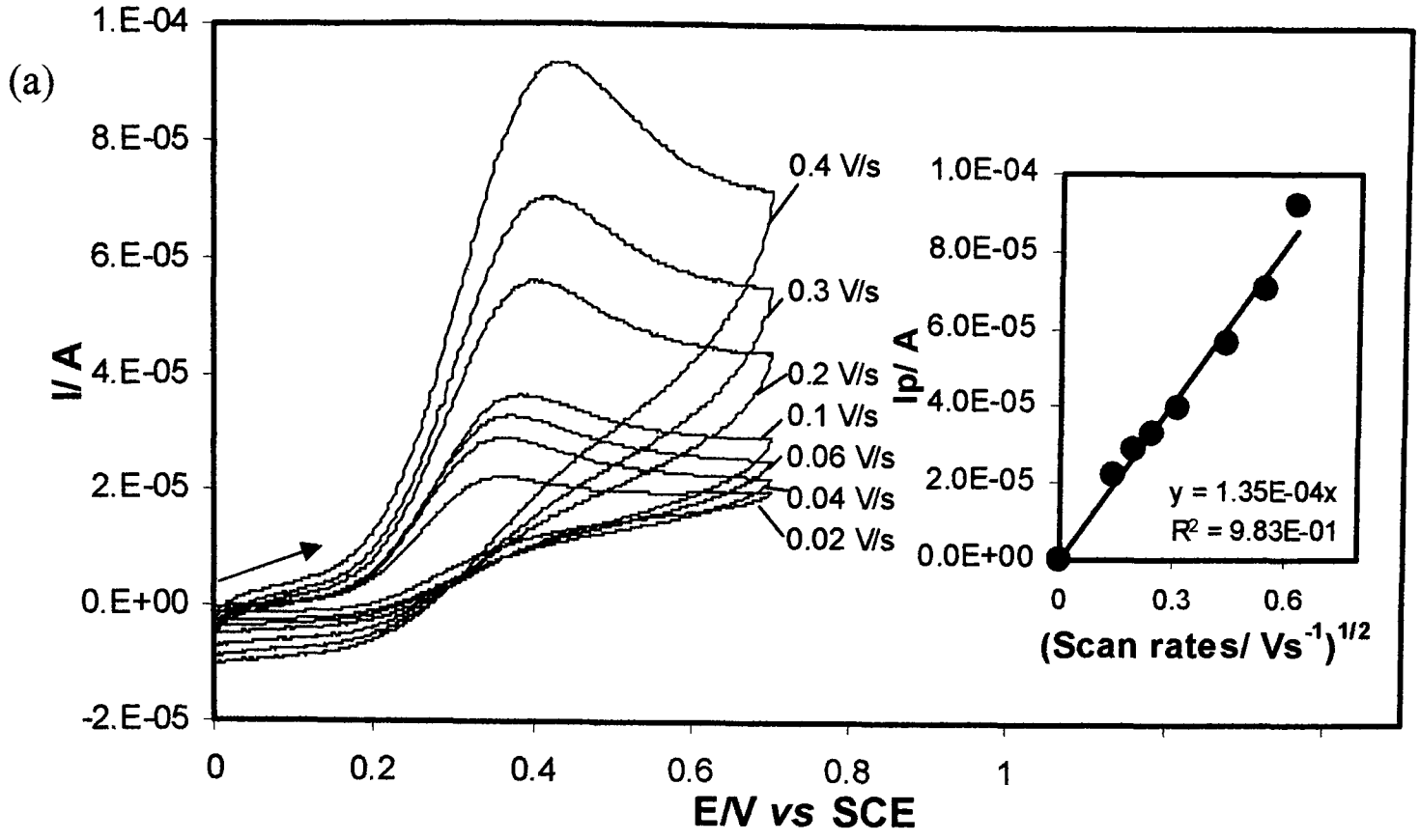


Figure 13. CVs (scan rate 0.1 Vs^{-1}) of the nanodiamond in the absence (a) and in the presence of ascorbic acid (b = 0.50 mM, c = 0.89 mM, d = 1.66 mM, e = 2.74 mM, f = 3.10 mM, g = 4.13 mM, h= 5.67 mM, i = 6.82 mM, j = 8.68 mM, k = 9.23 mM) in 0.1 M KCl; with inset showing the correlation plot of oxidation peak current, Ip^{ox} versus different concentration

Figure 13 shows the CV response of nanodiamond to the absence and the presence of ascorbic acid, in the concentration range of 0.5 - 9 mM. The well-defined anodic peak current is observed to increase with the increasing ascorbic acid concentration in the solution. The inset of figure shows that the anodic peak current is linearly dependent on the concentration of ascorbic acid, with a correlation coefficient of 0.992. The anodic peak at low concentration has shifted approximately 100 mV to positive potential at higher concentration and was later fixed at potential of 0.37 V.

The diffusion coefficient for ascorbic acid can further be determined by using *Randles-Sevcik* equation, yielding a value of 3.47 x 10^{-10} m^2s^{-1}, well in agreement with previous report [39], by employing $n = 2$ and $Ip^{ox} = 130$ μA for $c_0 = 9.23$ mM (figure 13*k*).



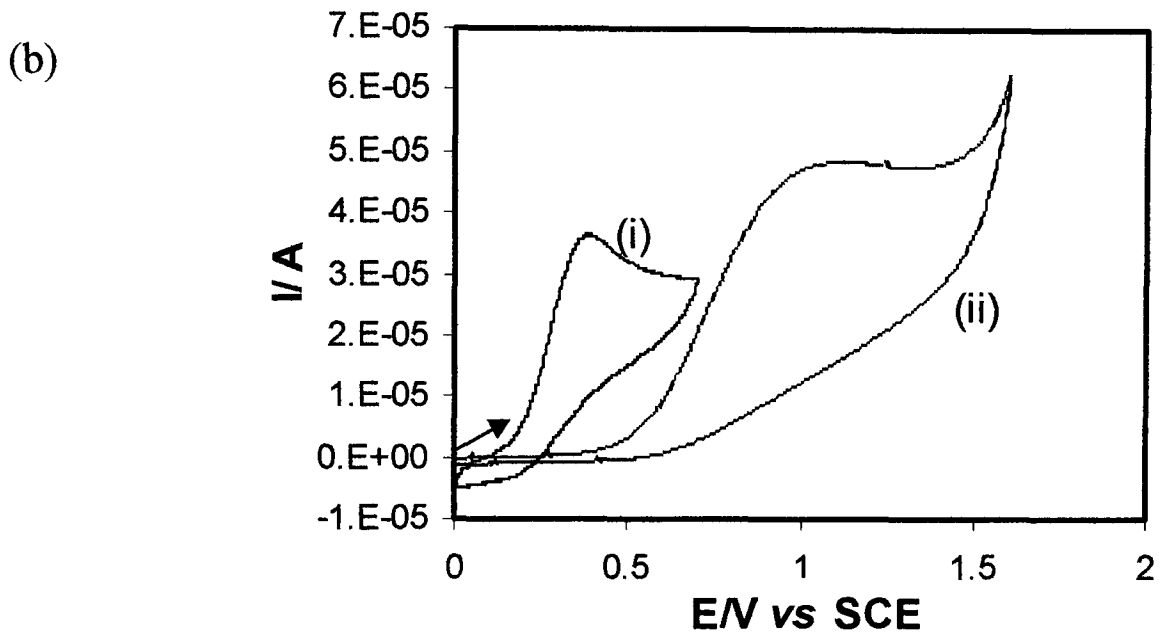


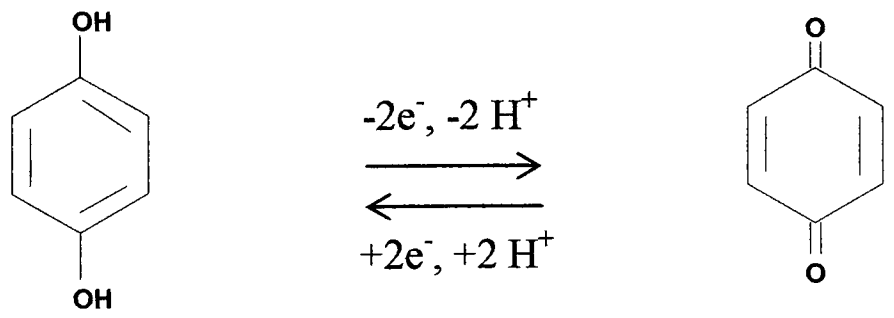
Figure 14. (a) CVs for the oxidation of ascorbic acid (2.0 mM) at nanodiamond as a function of different scan rates, with inset showing the correlation plot of oxidation peak current, Ip^{ox} versus square root of scan rate; and (b) the response to ascorbic acid (2.0 mM) of nanodiamond (i), compared to the boron-doped diamond (ii) at a potential scan rate of 0.1 Vs^{-1}

The CVs of nanodiamond at various scan rates in the presence of 2.0 mM is shown in figure 14, with inset showing the oxidation peak current, Ip^{ox} varies linearly to the square root of scan rates, suggesting a well diffusion controlled process. The defined voltammetric signal for the oxidation is detected at $E_{p,a}$ = 0.36 V *vs* SCE and is shifted to positive potential at higher scan rates, which is attributed to the kinetic limitation in the reaction between the redox sites of the nanodiamond and ascorbic acid, as was also reported by Pournaghi-Azar [39]. The response is also compared to boron-doped diamond electrode in figure 14b, which shows an anodic peak at much higher positive potential.

This would suggest that a higher overpotential is required for boron-doped diamond in order to oxidize ascorbic acid. However, for nanodiamond, a potential of approximately 0.5 V less positive is needed to drive the oxidation reaction from ascorbic acid to dehydroascorbic acid, indicating a very fast electrooxidation process.

4.4.4.2 Hydroquinone

Hydroquinone can usually be used as a biomarker found in human urinary metabolites, who suffer from the exposure to quinone compounds, such as heavy smokers and the workers in shoe or ink industries [40]. The is made possible due to the indolequinone or benzo[*a*]pyrene quinone compounds can readily be reduced to the hydroquinone by NADH-quinone oxidoreductase in human bodies without the intermediacy of radical-anions [41]. The oxidation of hydroquinone, in aqueous media proceeds *via* a two-electron transfer with de-protonation steps coupled to the electron transfer. In neutral or acidic media, overall two protons are released per molecule hydroquinone (HQ) and benzoquinone (Q) (equation 5) following ECEC pathway.



Hydroquinone Benzoquinone (eqn 5)

Figure 15 shows the cyclic voltammetric behaviour of nanodiamond electrode in response to hydroquinone in 0.1 M KCl at different concentration, ranges from 0 to 10 mM. Two redox systems are detected with $E_{1/2}$ = - 0.12 and $E_{1/2}$ = 0.35 V *vs* SCE. For redox system at higher potential, the currents that are corresponding to the oxidation (~ 0.09 V *vs* SCE) and reduction (~ 0.53 V *vs* SCE) processes increased as the concentration of the electroactive species in the solution increased. At lower potential, two smaller

peaks were observed at – 0.21 and – 0.06 V *vs* SCE, increasing at slow magnitude of current compared to the earlier mentioned peaks. A comparison with voltammograms obtained at glassy carbon electrodes (not shown) shows that a similar effect is observed and therefore this feature is not unique to nanodiamond electrodes, but typical for active electrode surface [42].

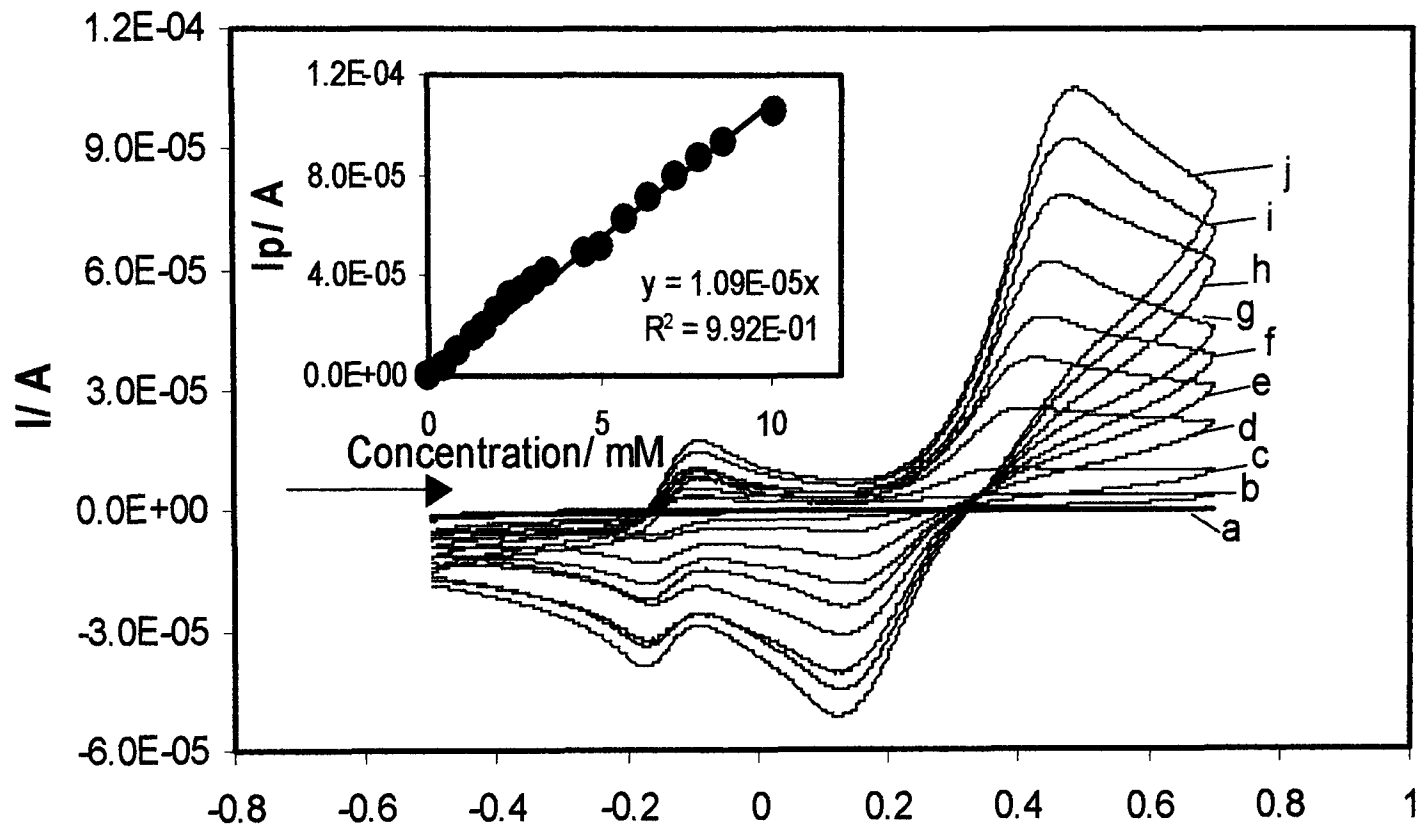


Figure 15. CVs (scan rate 0.1 Vs^{-1}) of nanodiamond in the absence (a) and in the presence of hydroquinone (b = 0.5 mM, c = 2.03 mM, d = 3.45 mM, e = 4.53 mM, f = 5.20 mM, g = 5.72 mM, h = 7.18 mM, i = 8.60 mM, j = 10.04 mM) in 0.1 M KCl; with inset showing the correlation plot of anodic peak current at 0.45 V, Ip^{ox} versus different concentration

The oxidation of HQ in 0.1 M KCl at different scan rates was shown in figure 16. With increasing of scan rates and HQ concentration, the peak at 0.5 V *vs* SCE increases to much higher order of current magnitude. Reversing the scan direction between the two responses allows the smaller signals to be detected independently.

Interestingly, when the supporting electrolyte was changed from KCl to phosphate buffer solution (PBS), the redox system at $E_{1/2}$ = - 0.12 V became featureless (as shown in figure 17) and the peak separation of the redox system at $E_{1/2}$ = 0.35 V *vs* SCE became much wider with the observed change from 250 mV to 480 mV.

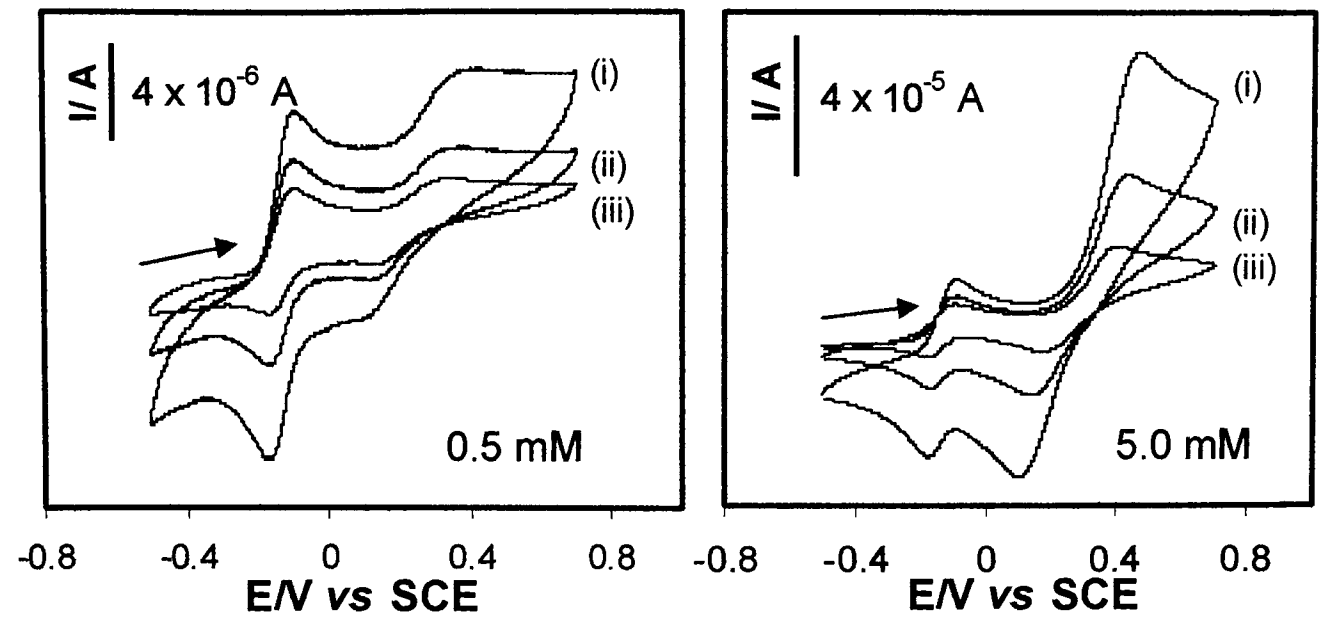
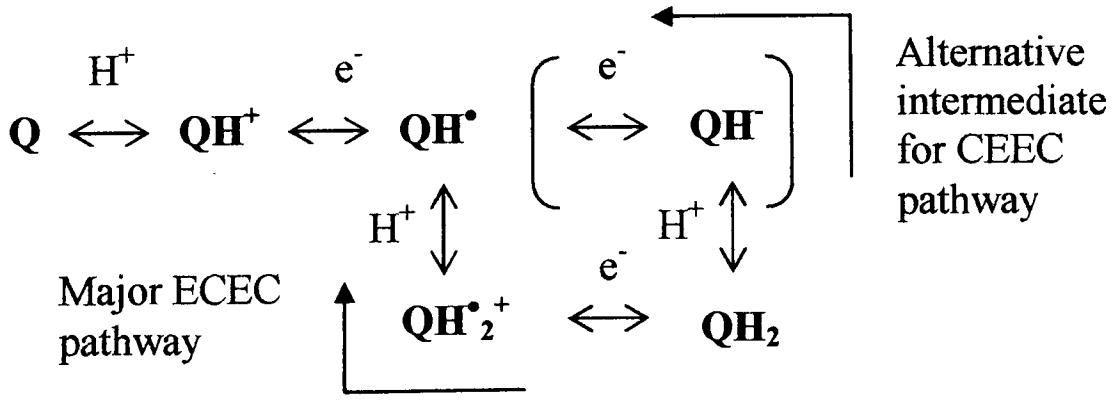


Figure 16. CVs for oxidation of 0.5 mM (left) and 5.0 mM (right) hydroquinone in 0.1 M KCl at nanodiamond at different potential scan rates (i = 0.3 Vs^{-1}, ii = 0.1 Vs^{-1}, iii = 0.02 Vs^{-1})

Therefore, the nanodiamond is sensitive to the drastic alteration of surface pH in an unbuffered solution, such as the case in KCl solution compared to PBS. The pH changes by the partially deprotonated form of hydroquinone (QH^-) were expected to adsorb on the nano-structure surface, which would further generate the surface state oxidation through the catalyzed reaction, occurs particularly at low potential [43]. This behaviour has shown that redox kinetics of HQ/Q is more facile in the presence of hydrogen ions in KCl rather than in the buffered solution of PBS. Jeftic and Manning [44] have proposed the possible mechanism for HQ/Q redox process; and this suggests that the prewaves are most likely resulted from the deprotonation of HQ at the electrode surface prior to the electron transfer (oxidation) of hydroquinone [45] *via* the intermediate pathway of CEEC (see equation 6). However, this behaviour of HQ is not detected separately at kinetically slow electrode surfaces, such as boron-doped diamond.



(eqn 6)

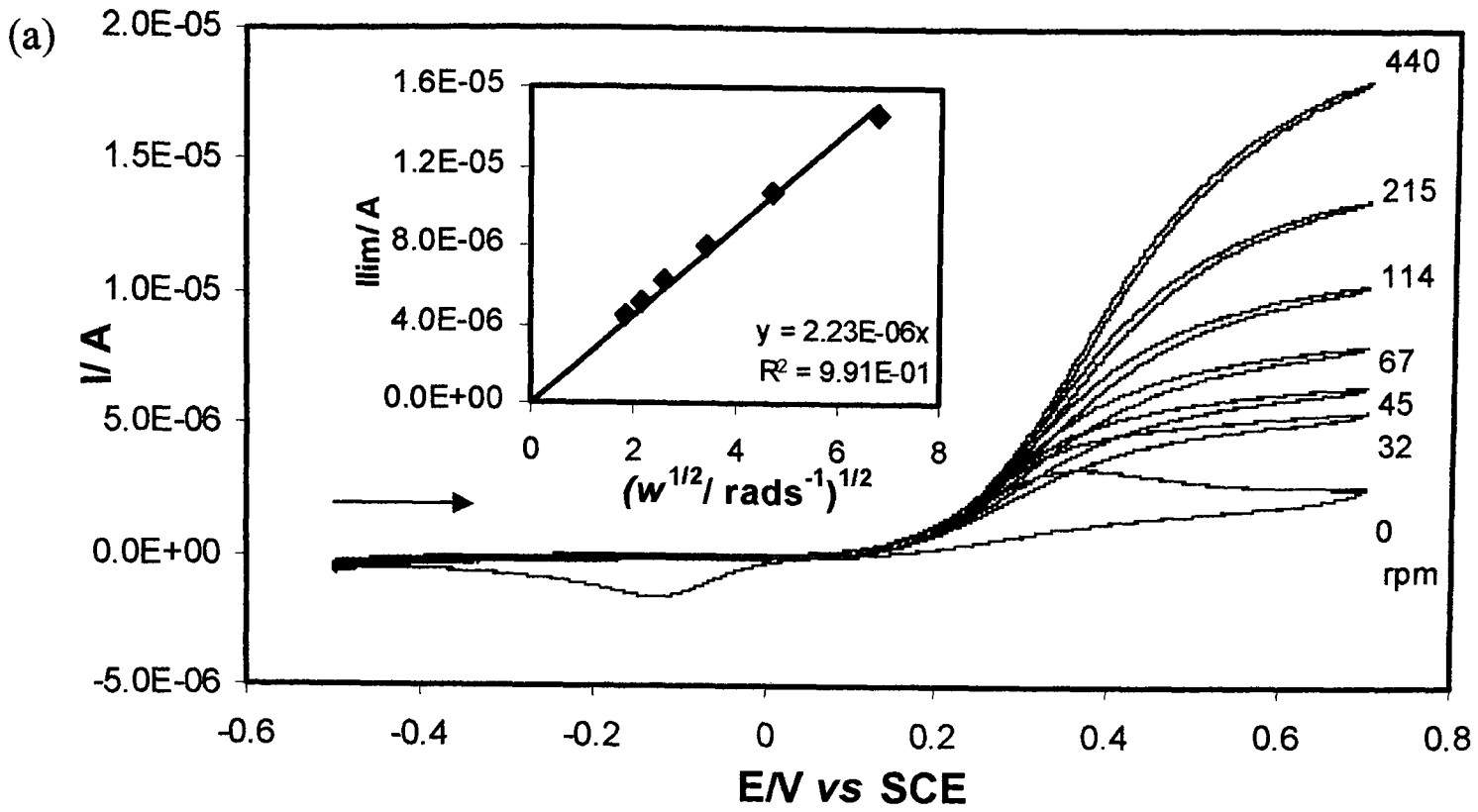


Figure 17. CV of the oxidation of hydroquinone at nanodiamond electrode. (a) In the oxidation of 1 mM hydroquinone in 0.1 M phosphate buffer solution at pH 7 is followed at a rotating disc electrode as a function of rotation speed (scan rate 20 mVs^{-1}); with inset showing the correlation plot of limiting current, I_{lim} versus square root of rotating speed, $\omega^{1/2}$. (b) In the behaviour of nanodiamond (i) and boron-doped diamond (ii) for the oxidation of 10 mM hydroquinone (scan rate 100 mVs^{-1}) are compared in 0.1 M phosphate buffer solution at pH 7

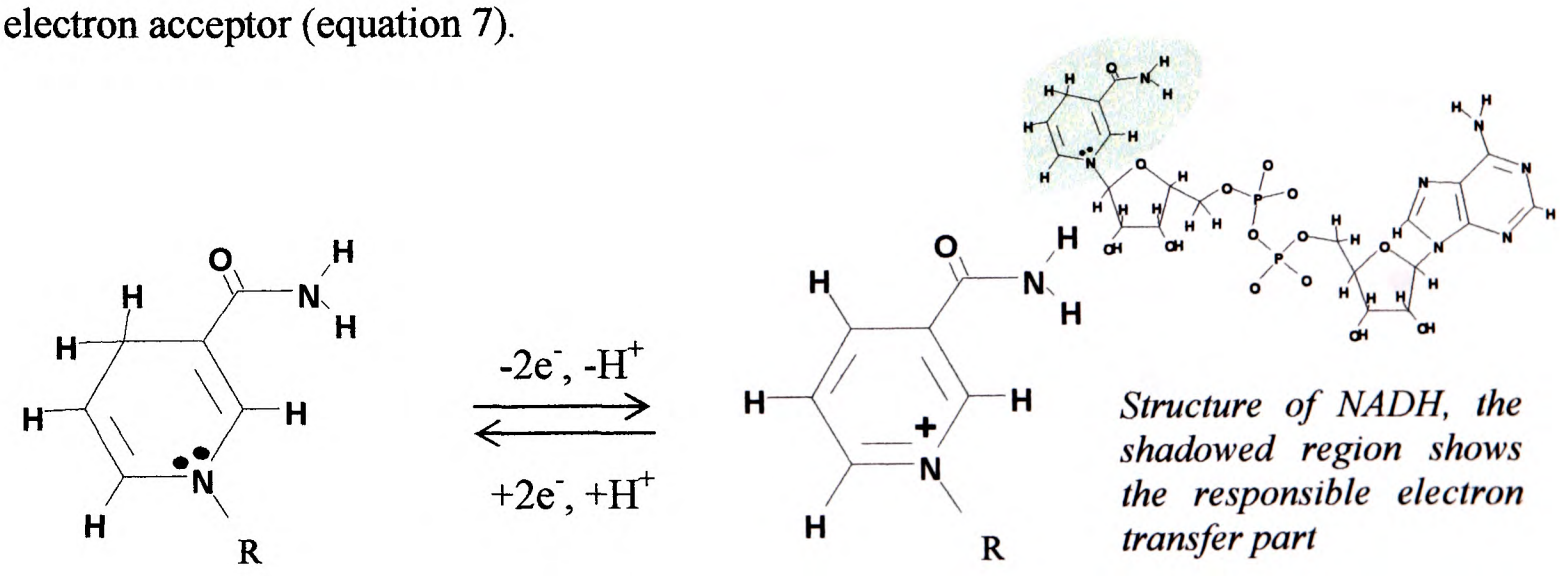
The hydrodynamic voltammetry has been used to extract precise quantitative information on the electrochemical kinetics. The oxidation of HQ as a function of rotation speed is shown in figure 17 (a). The Levich plot shows linear correlation (r^2 = 0.99) between limiting current, I_{lim} and square root of rotation rate, $\omega^{1/2}$. This would mean that the electrooxidation process for HQ at nanodiamond is purely diffusion-controlled electrochemical process. The peak separation for the boron-doped diamond (17 bii) is ~ 1400 mV, similar to the redox system of HQ in HCl [46], by which the value is

significantly wider than the peak separation for nanodiamond. Ramesham [47] has suggested the electrochemical irreversiblity of boron-doped diamond can be improved by providing chemical treatments, by eliminating some surface impurities and by reducing the electrical resistivity (higher conductivity). Interestingly, those are the characteristic behaviours that can be found naturally on nanodiamond without requiring any surface pre-treatment.

The number of electrons, n being transferred can be calculated from the *Levich* equation, yielding a value of 1.79 (~ 2 electrons) by employing $D_{HQ} = 5.90 \times 10^{-10}$ m^2s^{-1} [45,46], with reference to $I_{lim} = 11.2$ μA at a rotation speed of 215 rpm.

4.4.4.3 NADH

Due to its ubiquitous use as cofactor for over 300 enzymes, redox processes involving nicotinamide adenine dinucleotide (NAD^+) are employed in the fine chemical industry using NAD^+-dependent biocatalyst and in the development of dehydrogenase-based amperometric biosensor. Therefore, the NADH/NAD^+ redox process is important for the biosensor applications, electrochemically driven enzyme reactions and for applications of biocatalysis [47]. In redox process, the nicotinamide ring of NAD^+ functions as the electron acceptor (equation 7).



Structure of NADH, the shadowed region shows the responsible electron transfer part

NADH NAD^+ (eqn 7)

High overpotential for the NADH oxidation is always required at bare electrode and different attempts have been approached to decrease the overpotential, such as by

using mediators in homogeneous solution and by modifying the electrode surface. At boron-doped diamond electrodes, stable and reproducible voltammetric responses for the oxidation of NADH were reported [48].

The CVs obtained for the oxidation of 1 mM NADH in 0.1 M PBS pH 7 is shown in figure 18. The electrooxidation for NADH is observed at 0.45 V *vs* SCE for low scan rate and the anodic peak is shifted to more positive potential region with the increasing of sweeping rate, due to some kinetic limitation. However, the linear plot of *Ip* against (scan rate)$^{1/2}$ is linear with $r^2 \sim 0.97$, indicates that the electron transfer is diffusion-controlled.

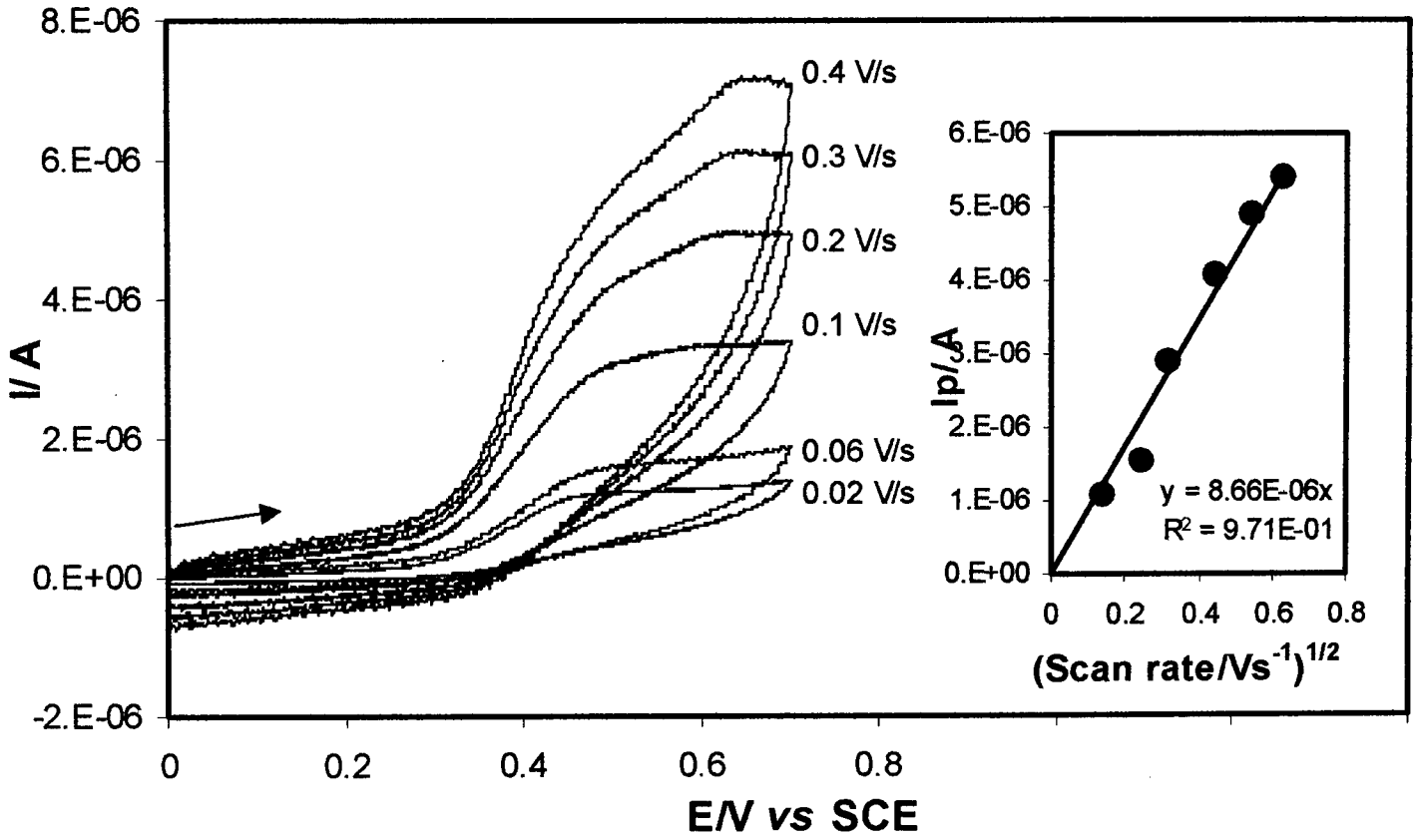


Figure 18. CVs for the oxidation of NADH (1.0 mM) in 0.1 M phosphate buffer solution at pH 7 as a function of different scan rates, ranging from 0.02 Vs^{-1} to 0.4 Vs^{-1}; with inset showing the correlation plot of oxidation peak current, Ip^{ox} versus square root of scan rate

The rotated-disk voltammograms obtained for the electrooxidation of NADH is shown in figure 19 (a). The anodic limiting current (*Ilim*) of the NADH oxidation increases with increasing of rotational speed (ω) and the linearity of *Ilim*-$\omega^{1/2}$ was observed, indicating that the oxidation process is diffusion controlled. A direct comparison of the oxidation response for 1 mM NADH at a nanodiamond electrode and at a boron-doped diamond electrode is shown in figure 19 (b).

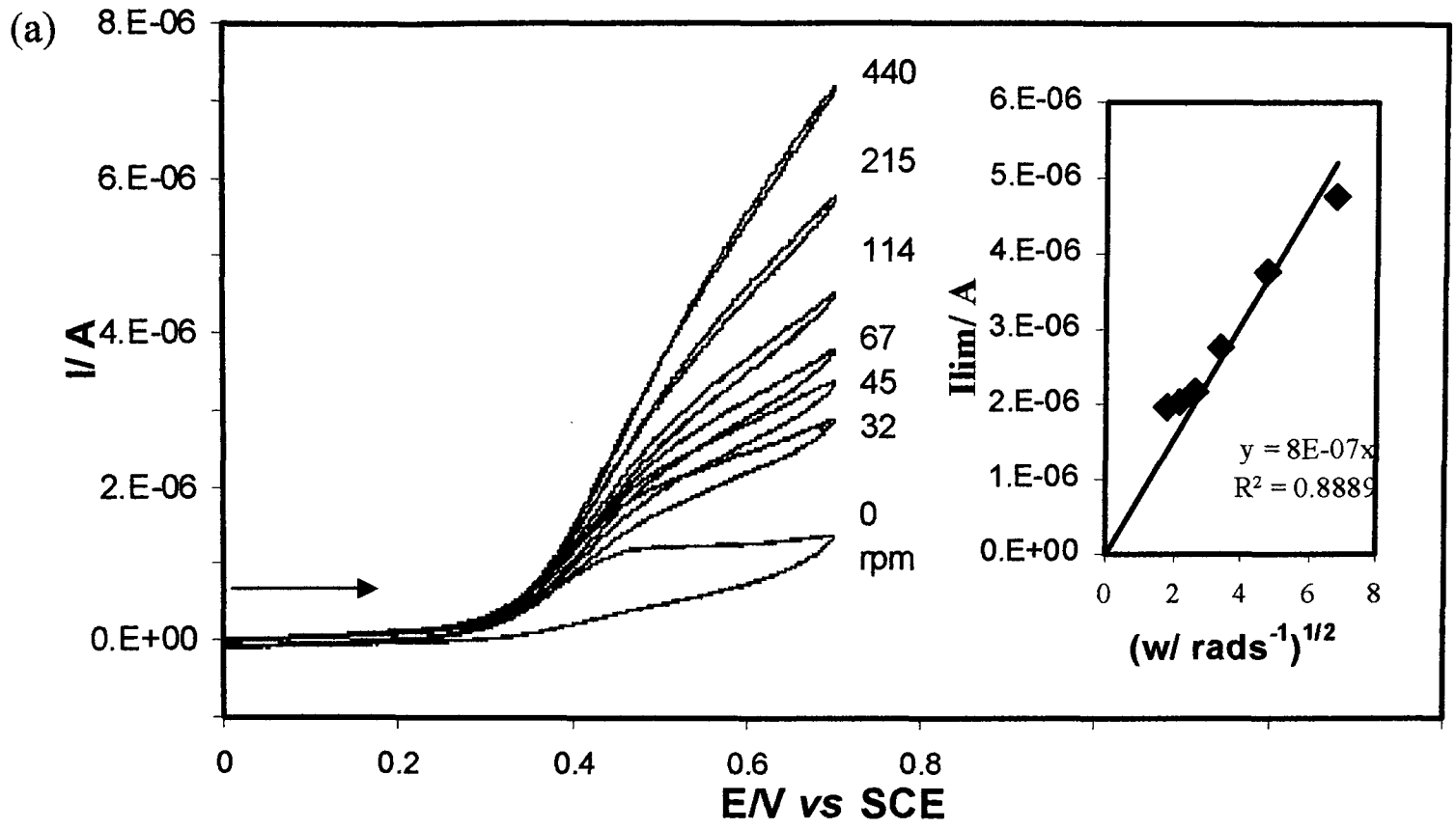


Figure 19. CV of the oxidation of NADH at nanodiamond electrode. (a) In the oxidation of 1 mM NADH in 0.1 M phosphate buffer solution at pH 7 is followed at a rotating disc electrode as a function of rotation speed (scan rate 10 mVs^{-1}); with inset showing the correlation Levich plot of limiting current, I_{lim} versus square root of rotating speed. (b) In the behaviour of nanodiamond (i) and boron-doped diamond (ii) for the oxidation of 1 mM NADH (scan rate 20 mVs^{-1}) are compared in 0.1 M phosphate buffer solution at pH 7

The oxidation potential for NADH at boron-doped diamond is observed at 0.56 V, or at 0.60 V *vs* SCE as reported by Fujishima *et al.*, even though the concentration used was 20 times more diluted [49]. This shows again the nanodiamond is very reversible controlled material by which the required overpotential is lower than boron-doped

diamond. The higher rate of electron transfer to the aqueous redox system may be attributed to the nanodiamond surface topography and the availability of active edge sites.

Referring to the Levich equation, the theoretical value obtained for *Ilim* is 6.88 μA at a radian speed of 215 rpm with the reported diffusion coefficient, $D_{NADH} = 2.4 \times 10^{-10}$ m^2s^{-1} [49]. Whereas, the experimental value of *Ilim* is relatively small ~ 3.73 μA, suggesting that only the limited active sites on nanodiamond are involved in the redox system, which might be due to the aggregation of NADH molecules – inducing small fouling effect on the surface.

4.4.4.4 Cytochrome *c*

The reduction of ferricytochrome *c* at nanodiamond was investigated. Cytochrome *c* is a water soluble hame protein, important in the biological respiratory chain, which function is to receive electrons from cytochrome *c* reductase and deliver them to cytochrome *c* oxidase. The structural unit responsible for the electron exchange is a haem *c* (see structure in figure 20) with a $Fe^{2+/3+}$ redox center, involving

$$Fe^{3+}\,(\text{Cyt } c) + e^- \rightarrow Fe^{2+}\,(\text{Cyt } c) \qquad \text{(eqn 8)}$$

The redox center is embedded in a rigid 3.4 nm diameter shell with overall +9 molecular charge at pH 7 (for ferricytochrome *c*) and with a considerable dipole moment [50]. The electrostatic interaction between the positive end of cytochrome *c* and the substrate is crucial for the reaction with the negatively charged (biological) partner.

Figure 20 shows the CV obtained for the reduction of 0.1 mM cytochrome *c* in aqueous 0.1 M PBS buffer solution at pH 7. The first scan of the CV shows the fairly visible redox peaks at – 211 mV (cathodic peak potential) and – 119 mV (anodic peak potential), with $\Delta Ep = 92$ mV and the peak current for the reduction is $I_p^{red} = 0.1$ μA, as compared to $I_p^{red} = 0.61$ μA for a boron-doped diamond electrode [51]. By employing the reported diffusion coefficient for the cytochrome *c* molecules, $D = 6.0 \times 10^{-11}$ m^2s^{-1} [52],

the theoretically expected peak current for the reversible reduction is I_p^{red} = 1.6 μA. The experimental peak current for both type of diamonds remained smaller than the theoretical peak current, suggesting only parts of the electrode surface appear to be active. This would be attributed to the possibility of cytochrome *c* molecules to form aggregates that hinders the direct electron transfer process, which bring subsequent loss in sensitivity. Such occurrence was also reported at activated carbon electrode [53].

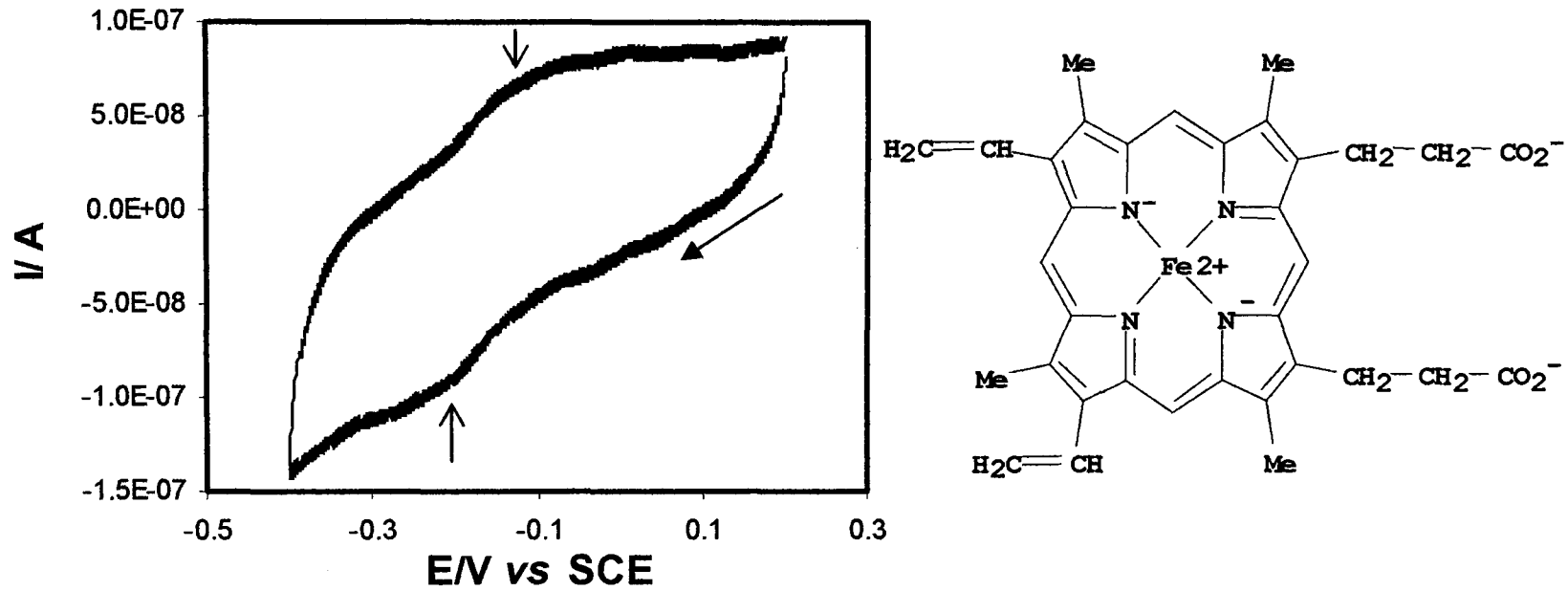


Figure 20. CVs (scan rate 0.1 Vs^{-1}) of 0.1 mM cytochrome c immersed in 0.1 M phosphate buffer solution (pH 7); Structure of haem c (on the right) is responsible for the electron exchange

However, soon after the first complete scan, the redox system disappeared. This would suggest that the nanodiamond had suffered from the passivation by the massive organic molecules, which blocked the surface electroactive sites. The concentration of cytochrome *c* could be too high which increase the competition amongst themselves for the active sites; therefore, the molar fraction of cytochrome *c* undergoing electron transfer decreases. The further denaturated of the metalloprotein [54] will be deposited onto the active sites, causing the fouling to occur with a consequent total loss in signal.

Therefore, further investigation of surface manipulation on nanodiamond is required, such as a more favorable interaction can be induced between the positively charged cytochrome *c* with a polished diamond surface [52].

4.4.4.5 Deactivation Test

Many of the carbon-based electrodes would suffer from the signal deactivation as a function of time due to the exposure to the laboratory atmosphere or working solution. The problem is more severe when biological sample solutions are used which cause serious fouling and organic passivation, and thus seriously requires further activation or reactivation of the electrode [54,55]. The reason for these could be attributed to high porosity, the presence of electroactive carbon-oxygen surface functional groups, and low degree of resistance to electrochemical and chemical oxidative attack.

Experiment was performed to measure the electrochemical stability of the used nanodiamond in response to electrooxidation of small organic molecules, after the electrodes were left for 2 weeks. Figure 21 (a) and (b) show the voltammetric responses for 'as-grown' and the used electrodes respectively to electrooxidation of ascorbic acid and hydroquinone. Reproducible results were obtained for both systems with the observation of small positive potential shifts (less than 50 mV). This suggests that the electrodes remains electrochemically stable to the oxidation of small organic compounds, without suffering from the organic contamination and adsorption onto the surface.

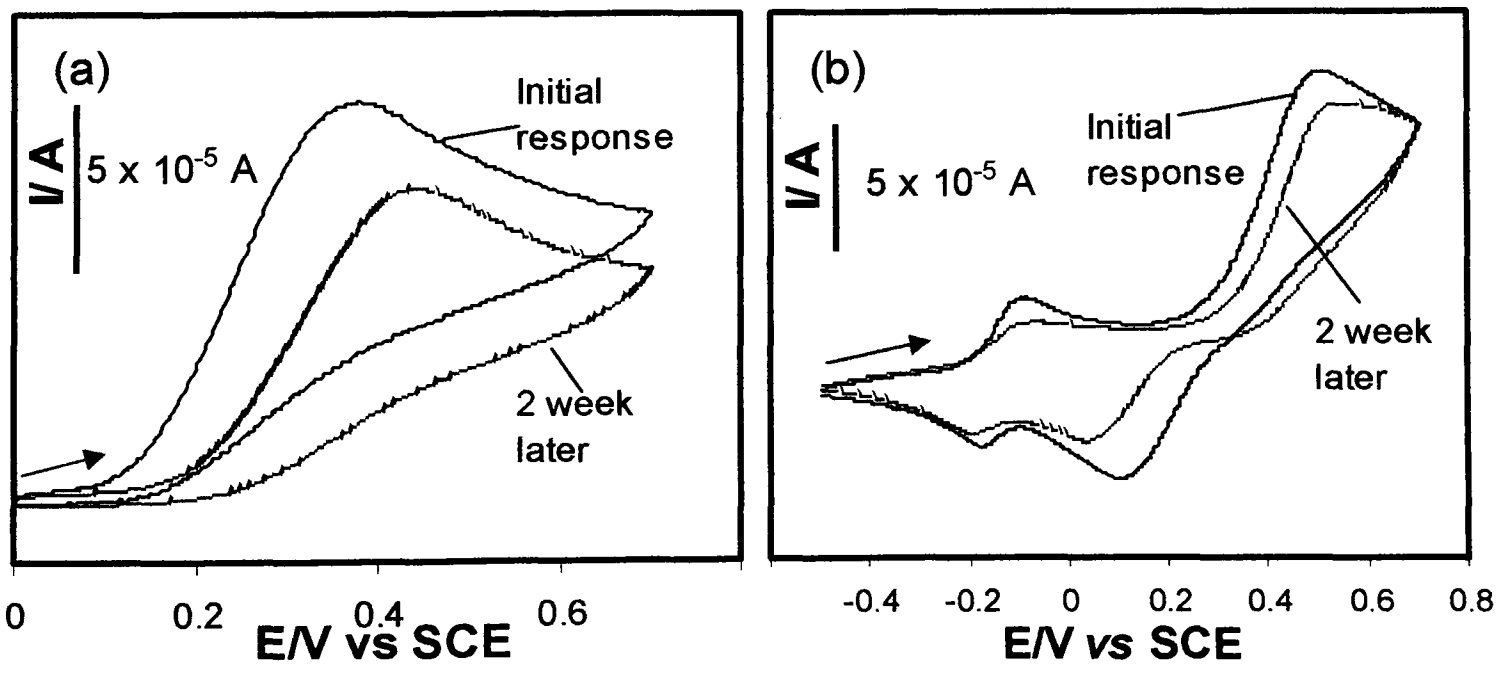


Figure 21. The comparison of CVs (scan rate 100 mVs^{-1}) of nanodiamond for 'as-grown' electrode and the "used" electrode after 2 weeks; (a) 10 mM ascorbic acid in 0.1 M KCl and (b) 10 mM hydroquinone in 0.1 M KCl

4.4.5 $Ce^{4+/3+}$ Redox System

It has been found difficult to observe the redox couple of $Ce^{4+/3+}$ (equation 9) species due to its very high oxidation at positive potential. This would mean that a comparatively high overpotential of an electrode is required before the oxygen evolution region; otherwise severe interferences of the effect would damage the electrochemical signals. An extensive study comparing the voltammetric characteristics for the $Ce^{4+/3+}$ system on different types of electrodes was reported recently by Fujishima and coworkers [56]. Boron-doped diamond had shown good performance for this couple, because it has a very high overpotential for oxygen evolution but of such broad voltammetric responses detected, the electron transfer appears to be rate limiting in stagnant solution.

$$Ce^{4+}(aq) + e^{-} \leftrightarrow Ce^{3+}(aq) \qquad E^{\varnothing} = 1.443\ \text{V } vs \text{ SHE} \quad \text{(eqn 9)}$$

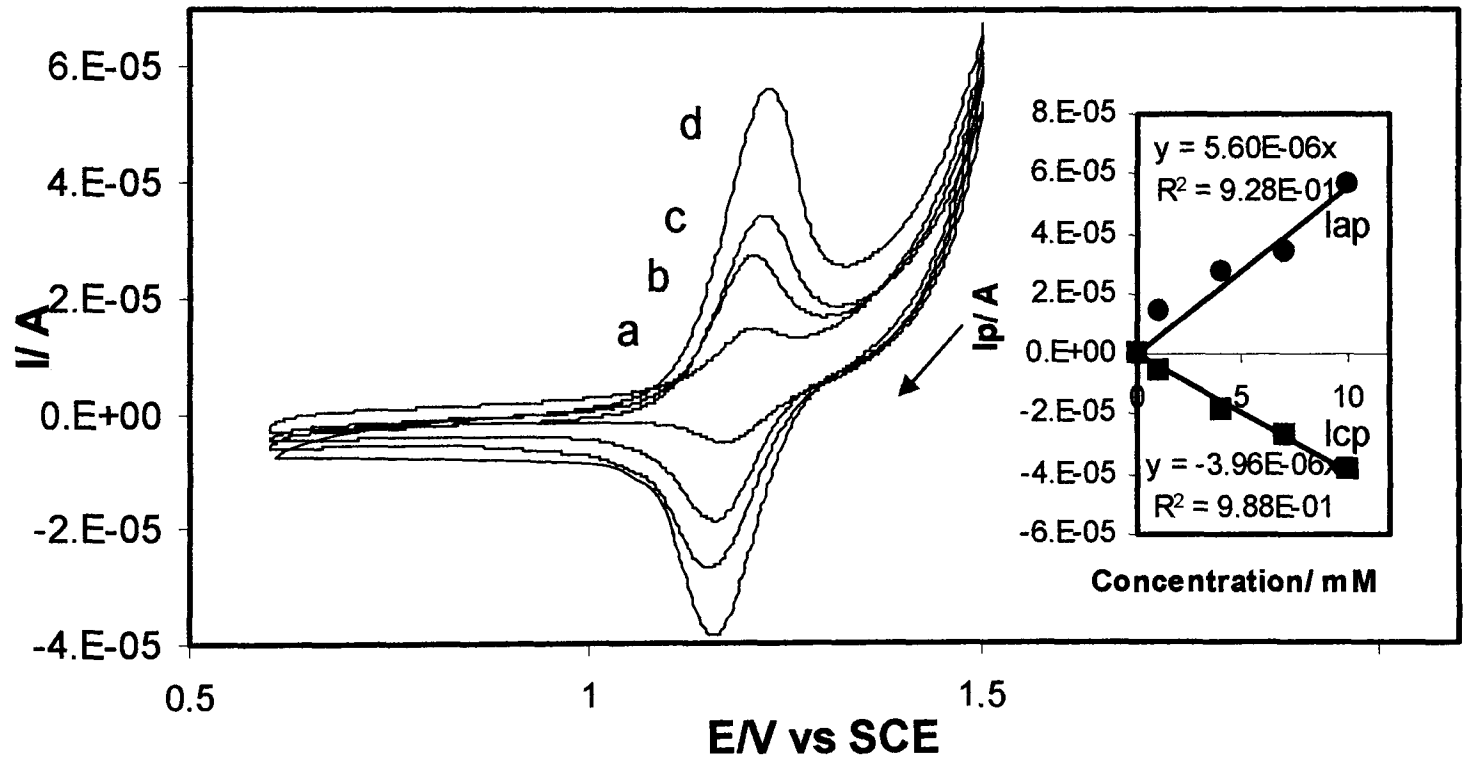


Figure 22. CVs (scan rate 10 mVs^{-1}) obtained at nanodiamond electrode for the $Ce^{4+}/^{3+}$ system in aqueous 0.1 M H_2SO_4. The concentration of Ce^{4+} was varied from 1 mM (a), 4 mM (b), 7 mM (c) to 10 mM (d); with the inset showing the correlation plot of anodic peaks, Iap and cathodic peaks, Icp to the concentration of Ce^{4+}

A set of CVs at nanodiamond for various Ce^{4+} concentrations in 0.1 M H_2SO_4 solution is shown in figure 22. The well-defined voltammetric responses of cathodic

reduction peak and anodic oxidation peak were observed respectively at the potentials of 1.15 V and 1.25 V *vs* SCE with approximately 100 mV peak-to-peak separation, and both peaks increase linearly with the increasing of the Ce^{4+} concentrations. The small peak separation for $Ce^{4+/3+}$ couple is due to the fast interfacial electron transfer kinetics that occurs on nanodiamond. The redox peaks are quite similar to the glassy carbon electrode with the observed E_{pc} and E_{pa} respectively at 1.05 V and 1.27 V *vs* SCE [57] in H_2SO_4 medium. In contrast, both of the redox couples potential at boron-doped diamond are far wider, with the observed reduction peak at 0.76 V and oxidation peak at 1.62 V [56], which is attributed to the irreversibility feature of the electrode.

It is found that the *Ipa* is significantly higher than *Ipc* (inset of figure 22). T. Vijayabarathi *et al.* [57] reported the same behaviour under the investigation on glassy carbon electrode and attributed this phenomena to the effect of weak adsorption of anionic Ce(III) complexes such as $Ce(HSO_4)^{2+}$ and $Ce(HSO_4)_2^{+}$ (equation 10), along with the diffusion current component at the anodic scan direction.

$$\begin{array}{ccccc} & \overset{HSO_4^-}{\longleftrightarrow} & & \overset{HSO_4^-}{\longleftrightarrow} & \\ Ce^{4+} & & [Ce(HSO_4)]^{3+} & & [Ce(HSO_4)_2]^{2+} \\ & & \updownarrow e^- & & \updownarrow e^- \\ & & [Ce(HSO_4)]^{2+} & & [Ce(HSO_4)_2]^{+} \end{array} \qquad \text{(eqn 10)}$$

Various scan rates of 1 mM Ce^{4+} reduction at nanodiamond were also performed in 0.1 M H_2SO_4 solution (not shown). (a) The proportional relationship of reduction peak current *vs* concentration and (b) the linear correlation of reduction peak current *vs* square root of scan rates show that the reduction of Ce^{4+} to Ce^{3+} can occur without the interference of oxygen evolution, indicating the diffusion controlled process.

These preliminary results show crudely that the nanodiamond is an alternative material for electrochemical analysis of species with highly positive redox potentials in aqueous solutions due to its lower required overpotential.

4.4.6 The Deposition and Stripping of Metals

The electrochemical deposition of metal on semiconductor depends crucially on charge transfer between a conducting substrate and ions in solution. The charge transfer involved may occur *via* the conduction band, the valence band (hole injection), or in some cases, *via* surface states [58]. For nanodiamond, the electron density of the surface states is induced by sp^2 species along the grain boundaries, which would greatly affect the properties of adhesion and texture of metal deposits.

The stripping efficiency, $Q_{stripping}$ is defined as the charge under the anodic stripping peak (Q+) divided by the charge under the cathodic deposition peak (Q-) for the metal deposition and stripping process on nanodiamond, as a function of metal concentration or potential scan rates.

4.4.6.1 Gold

Gold deposition on different types of carbon and metal electrodes has been studied for trace metal detection [59] and metal recovery [60] purposes. A recent study of the deposition and stripping of gold on boron-doped diamond electrodes [61] has shown that the state of the electrode surface has a considerable effect on the gold deposition and stripping process. In particular, on anodized boron-doped diamond electrodes gold appears to form very weakly adhering particles. A considerable loss of gold metal particles from the electrode surface into the solution phase occurs and the analytically important stripping process becomes inefficient in particular at low concentrations [61].

The gold deposition process in the presence of dilute *aqua regia* may be regarded as a one step multi electron process (equation 11), which has been shown to be sensitive to the type of electrode material employed [61].

$$AuCl_4^-\,(aq) + 3\,e^- \rightarrow Au^0\,(s) + 4\,Cl^-\,(aq) \quad E^{\varnothing} = 0.994\ V\ vs\ SHE \quad \text{(eqn 11)}$$

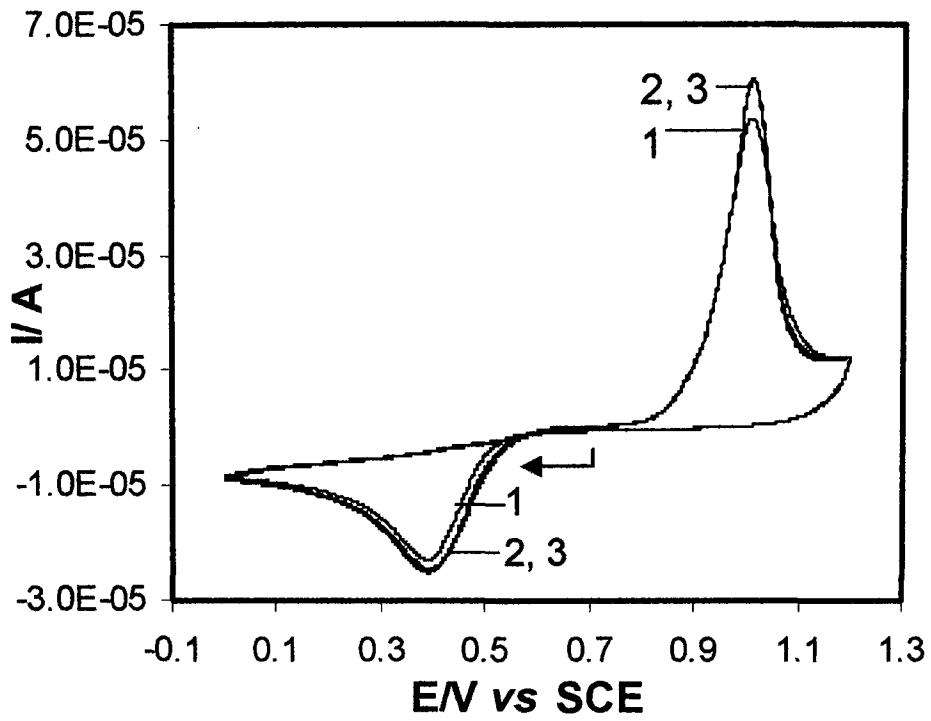


Figure 23. CVs (scan rate 20 mVs^{-1}) of three consecutive scans for the reduction and re-oxidation of 1.0 mM $AuCl_4^-$ in aqueous 0.3 M HNO_3/ 0.1 M HCl

Figure 23 shows the first three consecutive CVs for the reduction of 1 mM $AuCl_4^-$ onto a nanodiamond electrode immersed in dilute *aqua regia*. On the first scan to cathodic potential, the reduction of the gold complex has started at 0.55 V and the reduction peak was observed at 0.39 V *vs* SCE. The reduction continues on the reverse scanning on anodic potential until 0.7 V and a distinctive stripping peak was found at 1.01 V *vs* SCE. In contrast, on boron-doped diamond electrodes deposition and stripping were detected at $E_{p,c}$ = 0.32 V and $E_{p,a}$ = 1.13 V *vs* SCE, respectively [61]. The smaller gap between deposition and stripping peaks observed at nanodiamond electrodes indicates faster kinetics and more facile deposition and stripping on nanodiamond.

The subsequent second and third scans at nanodiamond have shown increases of reduction potential to 0.60 V and reduction occurs at higher negative current. Higher stripping currents were also observed for the two following scans. The behaviour was reported [61] as the consequence of gold deposition on pre-nucleated sites and 3-D growth nuclei was formed on stalking order, instead of forming gold layer.

The charge accumulated under anodic (Q+) and cathodic (Q-) for figure 23 are in good comparative ratio with stripping efficiency, $Q_{stripping} \sim 1$ (data not shown), which suggests that a reversible and complete metal stripping process has taken place.

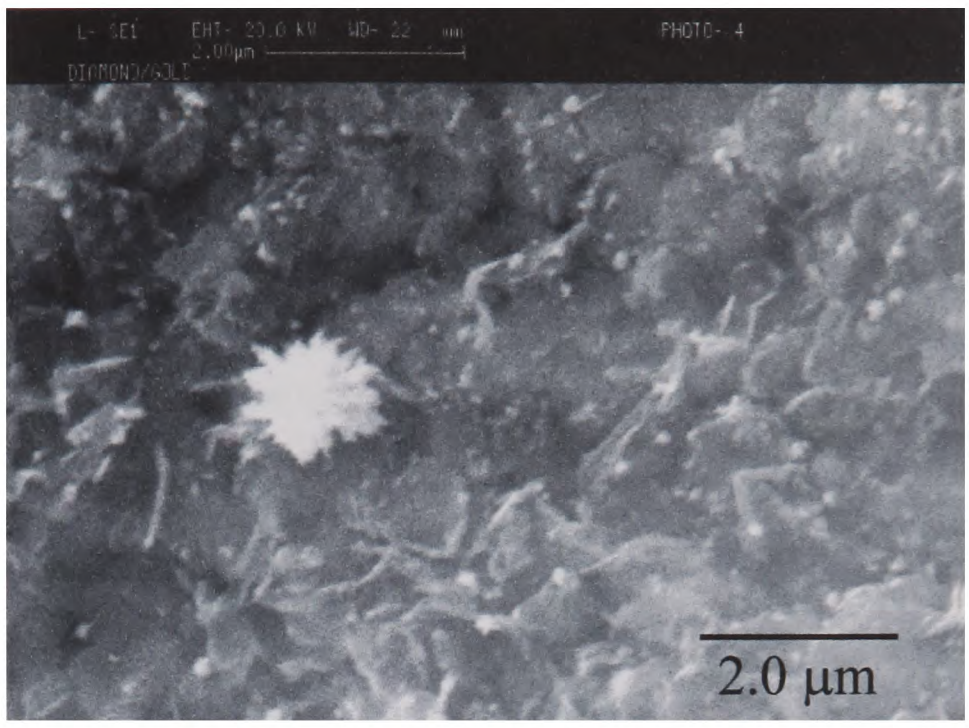


Figure 24. SEM image of nanodiamond, obtained after deposition of gold

SEM was carried out to investigate the morphology of gold deposits on nanodiamond. The scanning from 0.7 V to – 0.2 V *vs* SCE and was kept hold for a minute in 1 mM $AuCl_4^-$ solution will deposit gold on nanodiamond in relatively amount of quantities. Figure 24 shows the SEM of gold deposits under such condition and was confirmed by EDX. The deposit is formed predominantly at edge sites probably due to surface energy effects with the size of the gold particles in nanometer scale, ranging less than 100 nm. A few larger gold clusters ("gold flowers") were found in the diameter of 1 µm. In wide imaging scan (not shown), the gold deposit forms evenly over the nanodiamond surface. The uniform size distribution and the sub-micron distance between individual gold nuclei (which is much shorter than the diffusion length at this time scale) strongly supports the idea that nucleation of gold on nanodiamond is a facile process, which occurs with relatively low overpotential. The same procedure was repeated, but the CV was preceded to scan from 0.7 to 1.4 V and kept hold for another one minute in the same solution. The SEM (not shown) revealed no trace of gold on nanodiamond. This is in great agreement with the stripping efficiency of ~ 1, which concludes that the gold deposits are completely stripped off upon anodic stripping potential.

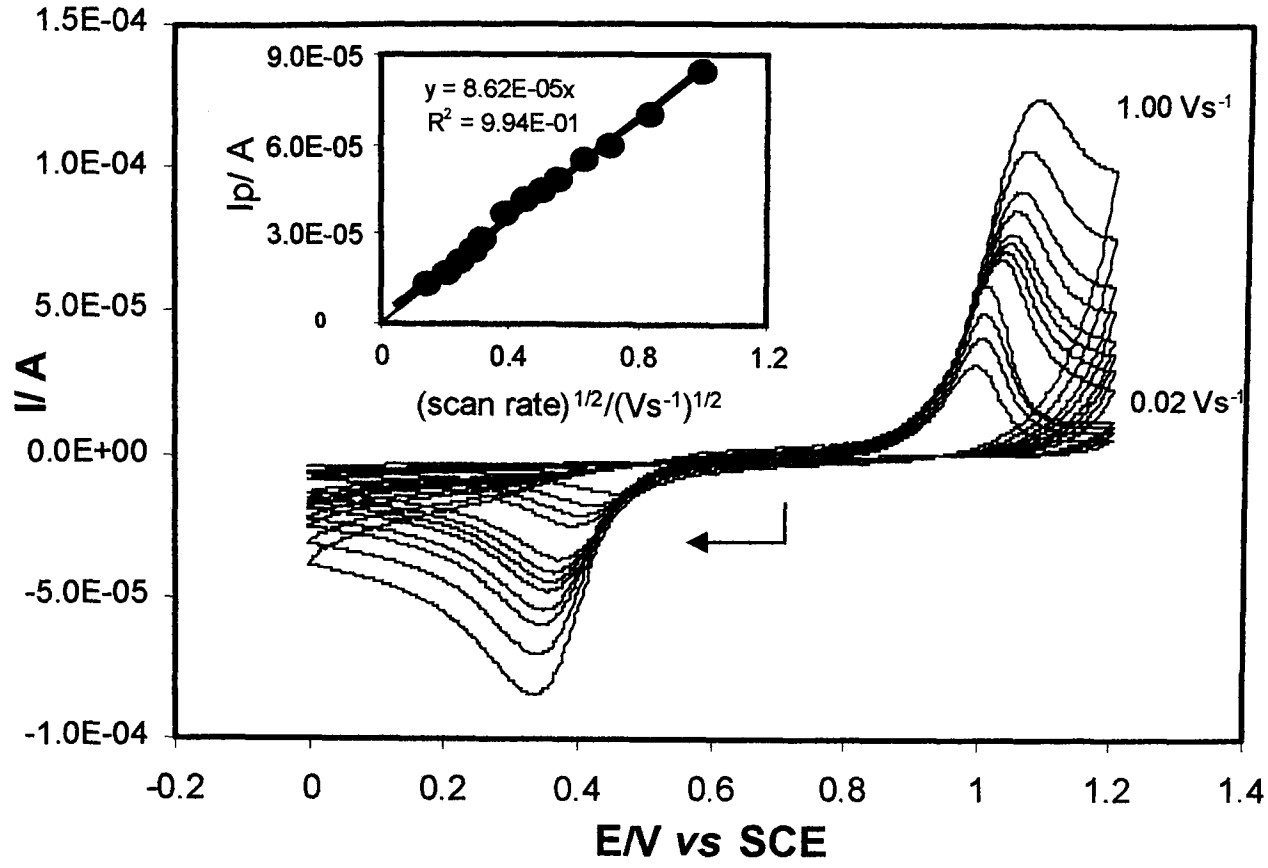


Figure 25. CVs of nanodiamond to 1 mM $AuCl_4^-$ in aqueous 0.3 M HNO_3/0.1 M HCl, with scan rates varied from 0.02 to 1.00 Vs^{-1}, with inset showing a plot of reduction peak current, Ip^{red} vs (scan rate)$^{1/2}$

Figure 25 shows the CV for the same system with the scan rates varied. The inset shows a linear relationship between Ip^{red} and square root of scan rate, with R^2 yielding a value of 0.994, implying diffusion-controlled process for electron transfer. Peak separation increases from 0.53 to around 0.75 V as the scan rate is increased up to 1.00 Vs^{-1}, suggesting the occurrence of some kinetic limitation. The stripping efficiency shows no significant dependency on the scan rate and remains at unity within experimental error.

The CVs of nanodiamond was performed over a wide range of $AuCl_4^-$ concentration, ranging from 10 μM up to 10 mM and the related data was shown as in figure 26. The peak separation remains constant as the concentration is increased, implying reversible electrode kinetics. The figure 26b confirms the approximately linear relationship between gold concentration and anodic stripping response. Deviations from linearity may likely be a consequence of kinetic effects, resulting from the fast scan rate.

As shown in figure 26c, the stripping efficiency of nanodiamond remains at unity within experimental error over the concentration range. This is contrary to the studies on boron-doped diamond, which have yielded the values of nearly 0.5 [61], suggesting either

the effect of the incomplete stripping or the weak adhesion of gold particles or colloid on diamond. Such colloidal formation was reported on BDD electrodes, partly based on the absence of stripping peaks at concentrations below 40 μM. This behaviour was not observed with the nanodiamond electrodes, which showed a stripping peak at all concentrations used, including 10 μM.

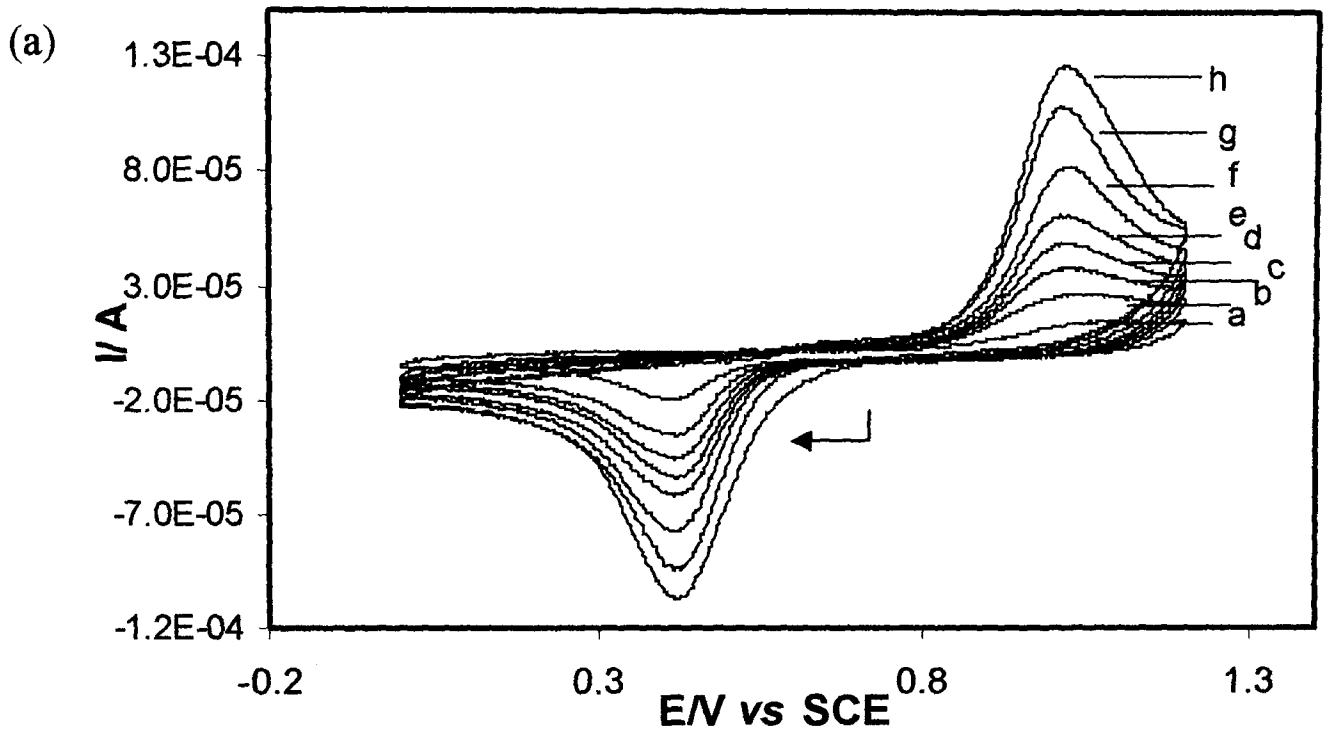


Figure 26.
(a) The CVs (scan rate 0.1 Vs^{-1}) responses of nanodiamond to different concentration of $AuCl_4^-$ in aqueous 0.3 M HNO_3/0.1 M HCl
(a = 10 μM, b = 206 μM, c = 320 μM, d = 376 μM, e = 485 μM, f = 593μM, g = 723μM, h = 935 μM)
(b) Plot of the anodic stripping peak versus the concentration of $AuCl_4^-$
(c) Plot of the stripping efficiency, $Q_{stripping}$ versus the concentration of $AuCl_4^-$

4.4.6.2 Copper

The deposition and stripping processes for copper on boron-doped diamond electrodes has been reported under some experimental conditions to lead to the formation of a copper sol rather than a copper metal deposit [62]. This striking observation was attributed to the weak adhesion of the copper metal deposit on diamond during the course of the electrochemical process. The overall process during copper deposition from aqueous dilute sulfuric acid solution is given in equation 12.

$$Cu^{2+}\ (aq) + 2\ e^- \rightarrow Cu^0(s) \qquad E^{\varnothing} = 0.337\ V\ vs\ SHE \qquad (eqn\ 12)$$

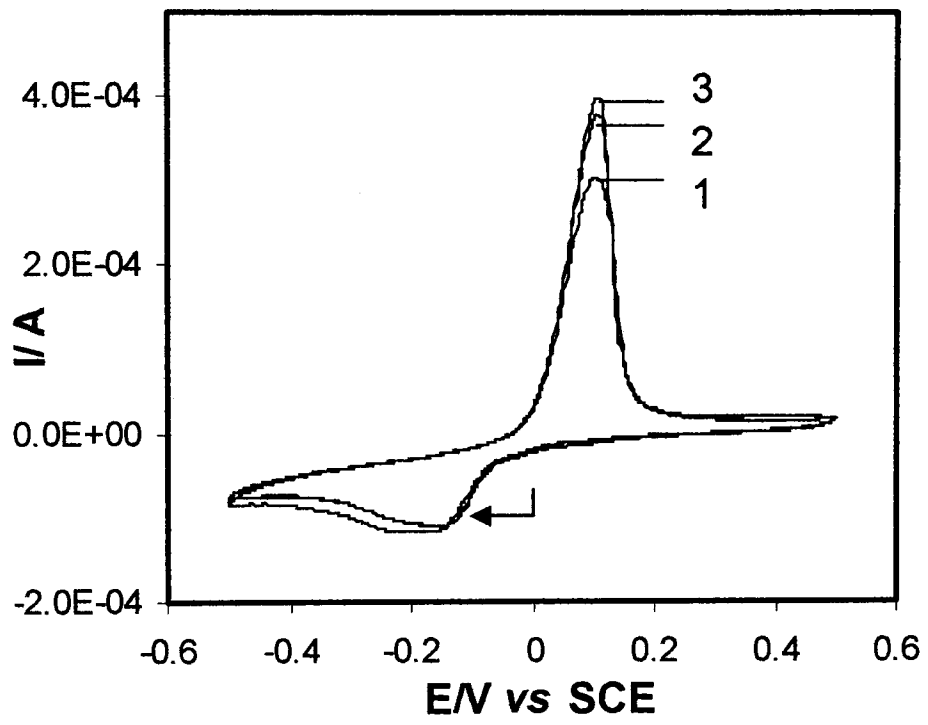
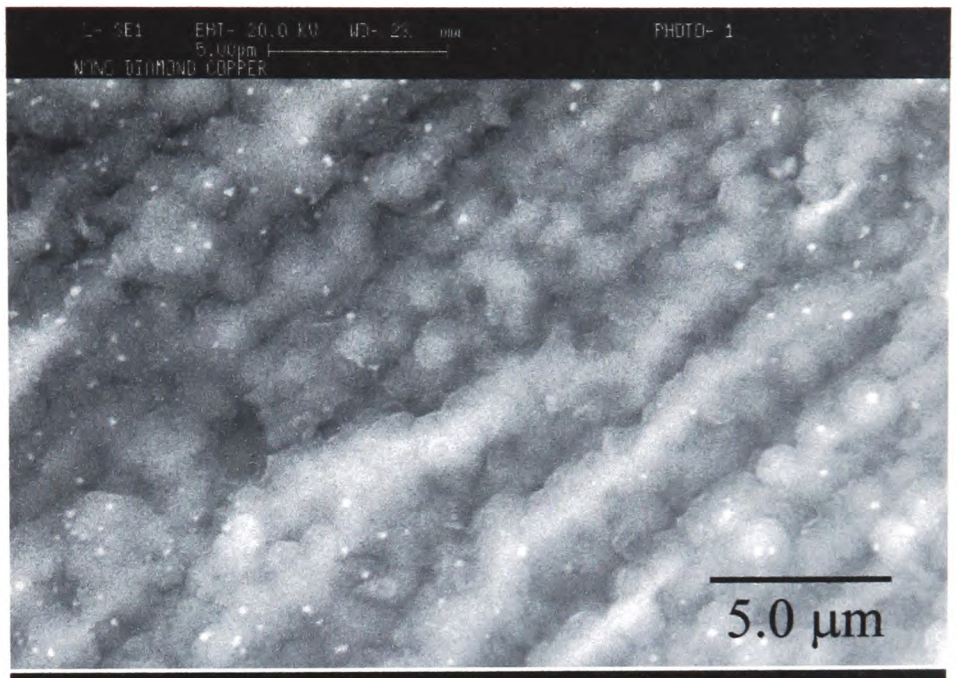


Figure 27. CVs (scan rate 0.1 Vs^{-1}) of three consecutive scans for the reduction and re-oxidation of 7.5 mM $CuSO_4$ in aqueous 0.1 M H_2SO_4

Figure 27 shows first three cycles for the deposition of copper from a solution of 7.5 mM Cu^{2+} in aqueous 0.1 M H_2SO_4 onto a 2 mm diameter nanodiamond electrode. Similar to the characteristics observed for the gold deposition process, highly reversible deposition and stripping processes are observed at $E_{p,c}$ = - 0.2 V *vs* SCE and $E_{p,a}$ = 0.1 V *vs* SCE, respectively. The following second and third scans have shown insignificant change from the start point of reduction potential, but reduction occurs at larger magnitude of current. The reductions were subsequently followed by higher stripping anodic currents at the same oxidation potential as for the first scan.

SEM was carried out to investigate the morphology of copper deposits on nanodiamond. The CV was scanned from 0 V to – 0.5 V and was kept hold for a minute in 1 mM Cu^{2+} solution. The nanodiamond was taken out, rinsed with pure water and let dried.

(a)



(b)

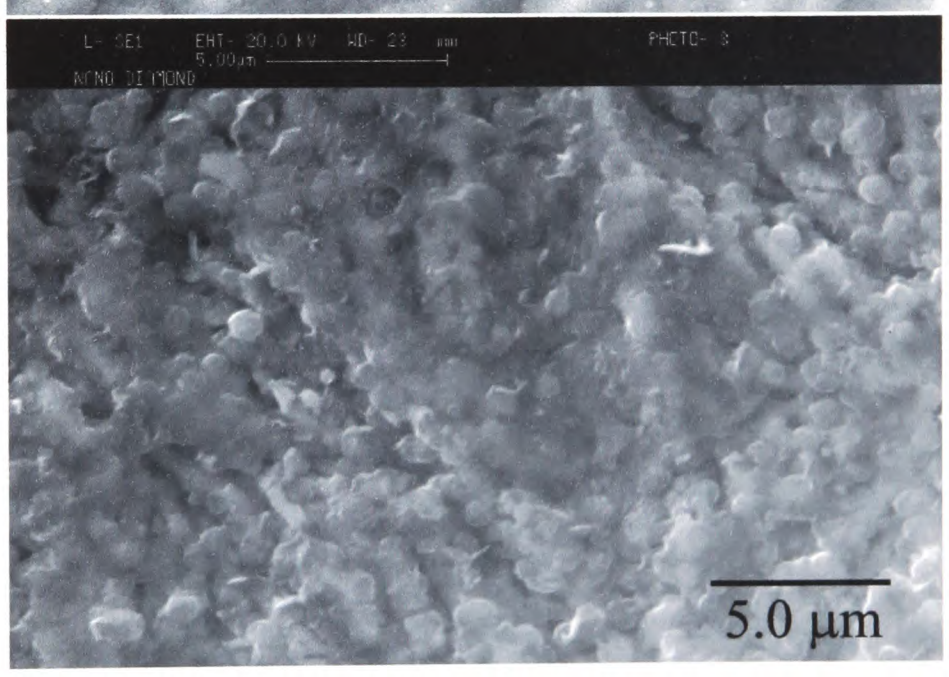


Figure 28. SEM images of nanodiamond, obtained (a) after the deposition of copper, immersed in 1 mM $CuSO_4$ in aqueous 0.1 M H_2SO_4 and (b) after stripping of copper

SEM (figure 28) shows the formation of copper nanoparticles deposited randomly on the nanodiamond surface similar to those observed for gold. The size distribution of copper particles range from 100 to 500 nm. No copper cluster in micro-scaled was found. Another SEM was recorded for nanodiamond after being deposited as before and was later scanned up to positive potential at 0.5 and was taken out immediately, and rinsed-dried.

No copper particles at any forms were found (figure 28b) and the results were proved with non-existence of copper under EDX examination.

The voltammetric behaviours of Cu^{2+} reduction and re-oxidation were enhanced under the hydrodynamic convection by rotating disc electrode. The Levich plot (inset of figure 29) shows the limiting currents increases linearly to square root of rotating radian speed. Stripping peaks were detected under such condition, which would prove that the deposition of reduced metallic copper, instead of colloidal copper has taken places on nanodiamond prior to the applied anodic potential. The results were also supported by sonovoltammograms (not shown) carried out for 0.1 mM and 1.0 mM of $CuSO_4$ dissolved in 0.1 M H_2SO_4, which have clearly shown the stripping of copper peaks. Due to the increase in mass transport, both the limiting current during deposition and the stripping peak increase. The shape of the rotating disc voltammograms during deposition at more negative potentials is unusual (non steady state, see Figure 29) and is indicative of a mechanistic complication [63].

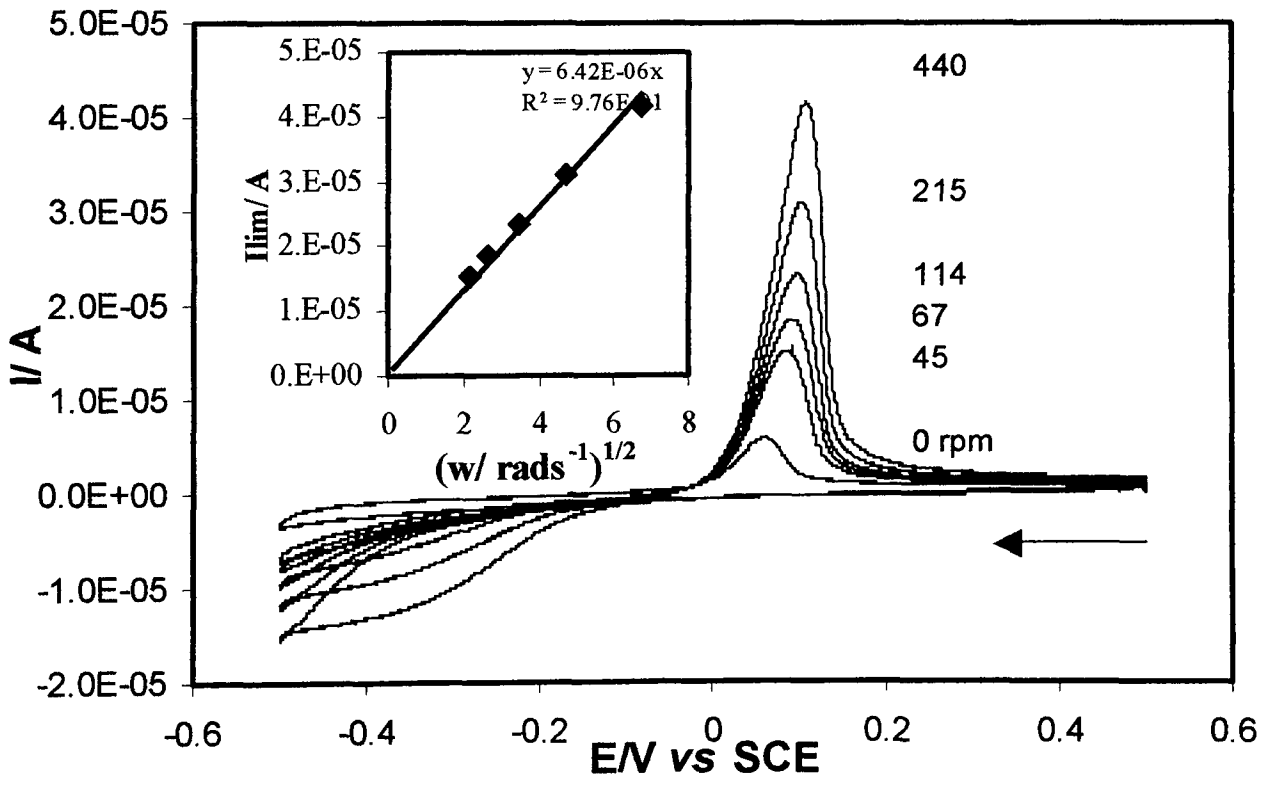


Figure 29. The CVs (scan rate 20 mVs^{-1}) responses of nanodiamond to 1 mM $CuSO_4$ in 0.1 M H_2SO_4 at 0 rpm, followed by a series of rotating disc voltammograms with radian speed ranging from 45 to 440 rpm; with inset showing the Levich correlation plot of limiting current, I_{lim} versus square root of rotating speed, $\omega^{1/2}$

Voltammetric experiments were conducted with the response of nanodiamond to different concentration of Cu^{2+}, ranges from 10 μM to 10 mM (see figure 30). Stripping response was detected from the concentration as low as 10 μM. Linear dependency of currents for both cathodic and anodic peak on the increasing concentration of Cu^{2+} was observed (as shown in inset of figure 30), suggesting diffusion controlled electron transfer and reversible electrode kinetics. A plot of the calculated stripping efficiency (Qstripping) as a function of concentration for copper stripping was found independent of the concentration of Cu^{2+} (figure 30g), implying occurrence of facile, reversible and complete stripping process. This is in agreement with the previous result of gold in Section 4.4.6.1.

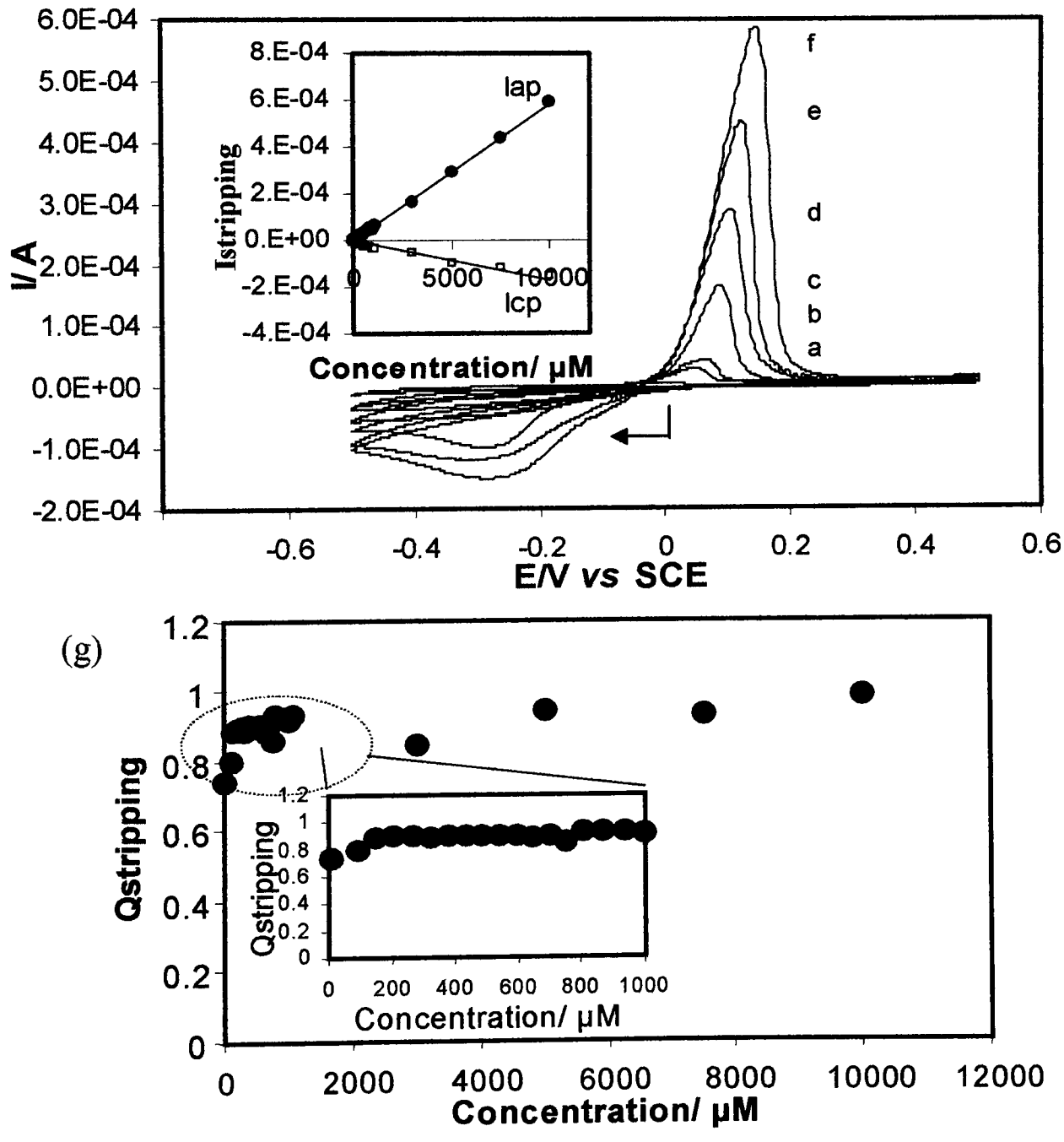


Figure 30. The CVs (scan rate 0.1 Vs^{-1}) response of nanodiamond to different concentration of $CuSO_4$ in 0.1 M H_2SO_4; (a) 500 μM, (b) 1000 μM, (c) 3000 μM, (d) 5000 μM, (e) 7500 μM and (f) 10000 μM, with inset showing the peak currents of anodic oxidation, Iap and cathodic reduction, Icp vs the concentration; (g) shows the correlation of stripping efficiency, Qstripping vs concentration, with inset showing the expanded area of concentration less than 1000 μM

4.4.7 Summary

The redox systems involving organic compounds and metal stripping-deposition processes may be attributed to the high electron density of states (DOS) on nanodiamond surface. Surface states that are distributed in energy throughout the bandgap will mediate electron exchange between the valence band of diamond and the redox system. The existence of the disordered carbon layer particularly as nanometer-sized crystallites along grain boundaries could disperse the band gap of crystalline diamond (5.5 eV) into a multiple DOS for a magnitude of 3.3 eV (as shown in figure 31) [64,65]. The decrease in inner spectra of conduction band (CB) could ease the electron transfer of surface states (SS) from oxidant species (Ox) to reduced species (Red). The surface states exchange holes with the valence band by multiple electron hopping through the captures (schematically shown figure 32i) or de-trapping (ii), and then is followed by transfer of electrons to the solution (iii) (as shown in equation 13-15) [59].

$$SS^0 + e^-(CB) \rightarrow SS^- \qquad \text{(eqn 13)}$$

$$SS^- \rightarrow SS^0 + e^-(CB) \qquad \text{(eqn 14)}$$

$$SS^- + Ox \rightarrow SS^0 + Red \qquad \text{(eqn 15)}$$

where equation 13 and 14 represent the processes of filling and emptying the surface states respectively, and equation 15 is the process of electron transfer to the solution.

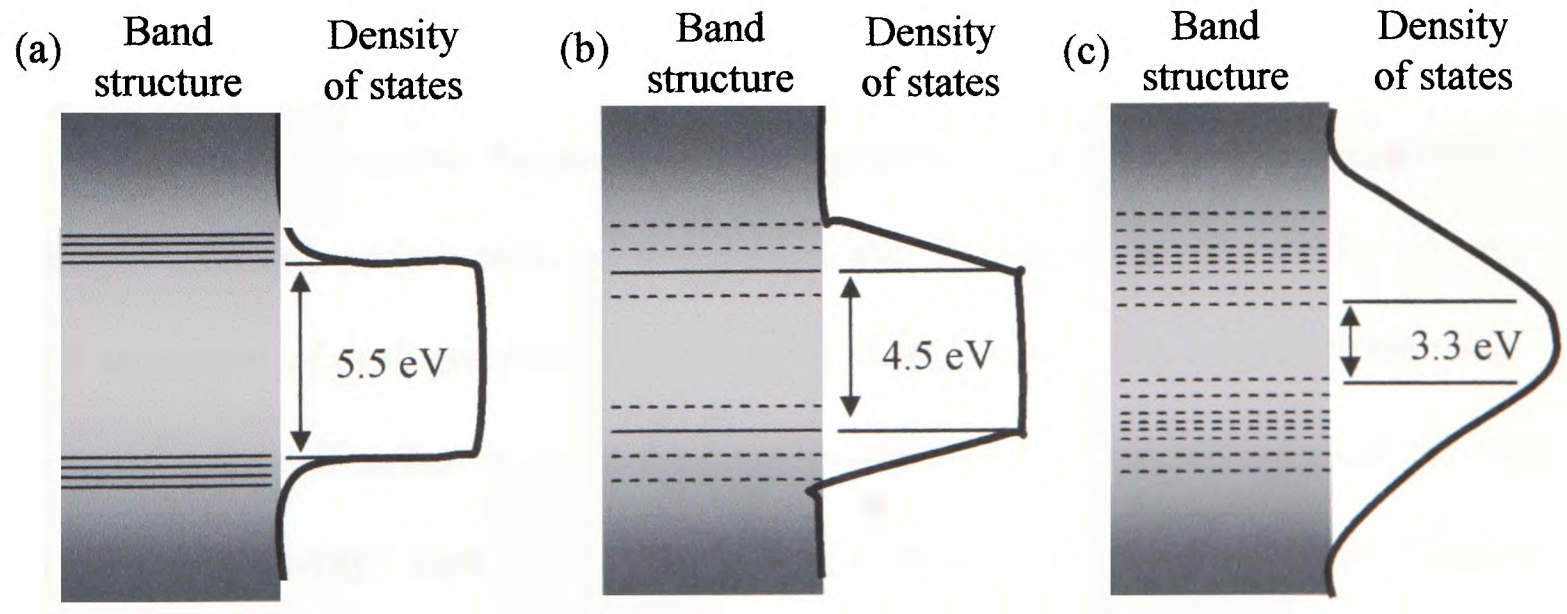


Figure 31. Schematic illustration of magnitude of band gap and density of states for (a) crystalline diamond, (b) amorphous diamond, and (c) nanodiamond [66]

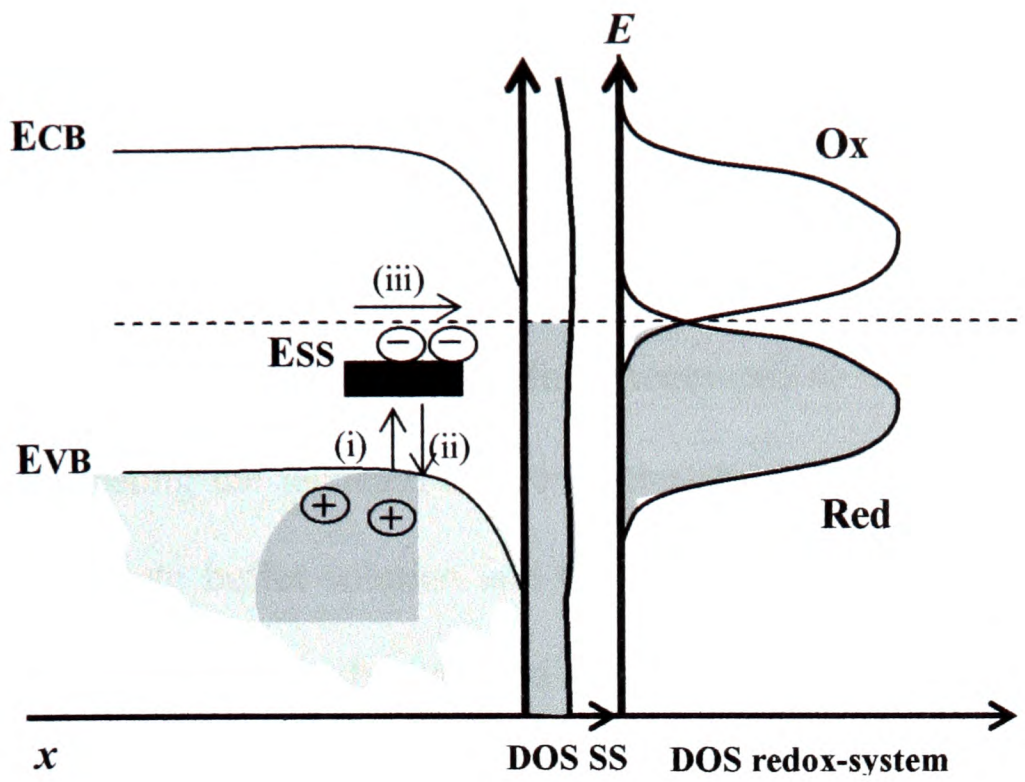


Figure 32. Energy band diagrams illustrating the possible mechanism of metal deposition onto an nanodiamond (p-type semiconductor) with the electron transfer from surface states; (i) represents the excitation of electrons from the valence band to the surface states (SS), (ii) recombination of electrons in the surface states with holes in the valence band and (iii) transfer of electrons from the surface states to an electron acceptor in the solution

4.4.8 Surface Modification

4.4.8.1 Surface Treatments

The modification of surface functionalities was conducted as follows

a) hydrogenation of 'as-grown' diamond under a total pressure of 35 Torr, at a flow rate of 100 sccm, with a forwarded power of 700 W, a surface platen of 600 °C for 10 min

b) electrochemical anodization in 0.1 M phosphate buffer solution of pH 2, with five continuous scans within the potential of 0 – 1.5 V *vs* SCE

c) electrochemical oxidation in 10 mM Ce^{4+} in the 0.1 M H_2SO_4 medium, with 10 continuous scans within the potential of 0.6 – 1.5 V *vs* SCE

The microcrystalline diamond after hydrogenation would normally produce highly hydrogen-saturated surface with sp^3 termination and the surface usually results in very small separation of peak potential (ΔEp) in CV [35,66]. In contrast, nanodiamond relies on the sp^2 π-bonded carbon atoms in the grain boundaries to act as the charge carriers for electrical conductivity. Upon the hydrogenation, hydrogen chemisorbs at the sp^2-bonded carbon sites and would change the bonding to sp^3. The conductive pathway will therefore

be destroyed and subsurface resistance increased. Similar occurrence has been reported earlier [33]. This is consistent with the electrochemical signal in response to the oxidation of 1 mM $Fe(CN)_6^{4-/3-}$, with (i) the increase of the ΔEp (from 114.8 mV to 249.2 mV), suggesting the sluggish kinetic process, and (ii) the decrease of oxidation peak current from 3.76 μA (as-grown, before treatment) to 2.66 μA after treatment (figure 33 b), suggesting the decrease of the electroactive sites. The anodic polarization in acidified phosphate buffer solution and Ce^{4+} (0.1 M H_2SO_4) shows the enhancement signals for both faradaic and background currents. The possible reason for this is the oxidized nanodiamond surface has become hydrophilic, and thus aqueous solution can penetrate into the small nano-structures with higher surface reactive sites (as calculated by using Randles-Sevcik equation). The somewhat increased of ΔEp (166.4 mV for (c) and 180.7 mV for (d)) shows that the loss of some reactive sp^2 π-bonded carbon sites, which in turn inhibits the heterogeneous electron transfer. Effects from the underlying titanium substrate seem to be insignificant. In a control experiment under identical conditions with just a 2 mm diameter titanium electrode, surface passivation due to oxidation was detected.

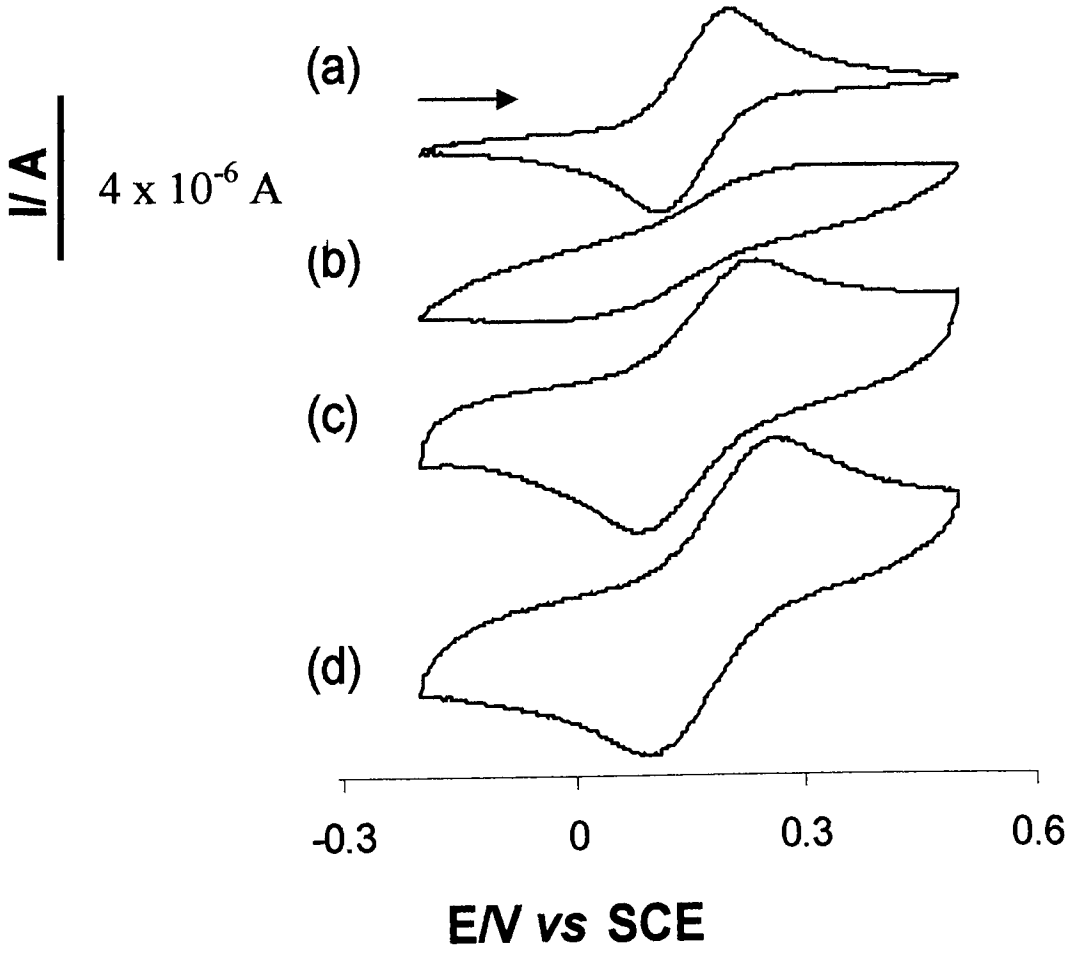


Figure 33. CVs (scan rate 0.1 Vs^{-1}) of different surface treated nanodiamond in response to 1 mM $Fe(CN)_6^{4-}$ in 0.1 M KCl; (a) as-grown nanodiamond, (b) hydrogen-plasma treated, (c) anodic polarization in 0.1 M PBS, and (d) anodic polarization in $Ce^{4+/3+}$ redox system

4.4.8.2 Effect of Thermal Annealing

In order to explore the effect of thermal annealing on the properties of nanodiamond films on titanium substrates, a series of experiments with annealing treatments was conducted. Figure 34 shows the effect of the treatment on the stripping efficiency (a) and on the voltammetric responses (b) to 1 mM $CuSO_4$ in 0.1 M H_2SO_4 solution. Nanodiamond was annealed in furnace (air medium) at specific temperature for 10 minutes, and was later cooled down to room temperature (RT). CV measurement will then be performed. The stripping efficiency ($Q_{stripping}$) was used as an indicator for surface electrochemical activity, and has clearly shown the existence of two decaying ratio regions, ranging from the RT ($Q_{stripping}$ at a ratio of 1.0) to 450 °C (0.60), and the other region ranges above 450 °C with stripping efficiency decreased drastically to 0.18.

Annealing at lower temperature than 450 °C in air will increase the conversion rate of metastable sp^3 diamond bonds to graphitic (sp^2) bonds. This decreasing slope signifies the incomplete stripping of deposited copper, which could be possibly attributed to the tendency of oxidized graphite to coordinate or to intercalate with copper [67]. With the increasing of temperature, the low surface electrical resistivity will increase with the formation of oxygen functionalities on the interfacial sp^2 carbon, which would mean that the surface is becoming less electrochemically reversible or becoming semiconducting. The shape of the stripping responses indicated ohmic distortions probably due to reduced (or rectified) electron transfer rates between the diamond surface and the copper deposit.

The CV done at nanodiamond after being annealed more than 450 °C has clearly indicated the high cathodic current with very low stripping current, which is due to some solution permeated through the graphitised layers and react with Ti substrate. At this point, conductivity measurements indicate a dramatic drop in nanodiamond conductivity, which is also likely to be due to the loss of conducting sp^2 carbon at surfaces and in grain boundaries.

The readily graphitised nanodiamond around 600 °C [68,69] is believed to have drastically combusted to carbonaceous gases. The high resistive background current of annealing at temperature higher than 700 °C is the signal given by the TiC or TiO_2 mixture layers.

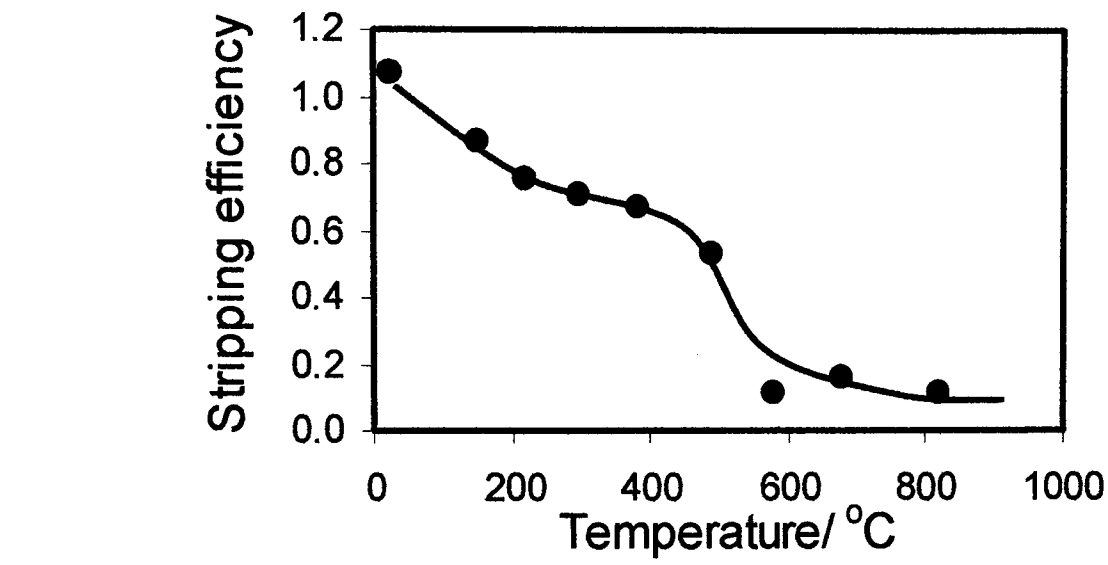


Figure 34. (a) Plot of the stripping efficiency, $Q_{stripping}$, for the anodic copper stripping process (cyclic voltammograms, scan rate 0.1 V s^{-1}) versus the annealing temperature (10 minutes furnace in ambient atmosphere). (b) Cyclic voltammograms (scan rate 0.1 V s^{-1}) for the reduction of 3 mM Cu^{2+} in aqueous 0.1 M H_2SO_4 at a 2 mm diameter nanodiamond electrode as a function of annealing temperature

4.4.8.3 Abrasive and Adhesiveness Test

Abrasive stripping voltammetry (AbSV) [70,71] involves the mechanical transfer of small amounts of a targeted solid material onto the surface of an electrode in order to be analysed by voltammetric methods, particularly anodic stripping voltammetry (ASV). The electrode will generally be subjected to an anodic potential to investigate the manner in which the material was stripped off and the effect of the process on the electrode. The method is an easy and time saving way to fingerprint the adsorbed metal both qualitatively and quantitatively, but the range of materials studied has greatly been limited by the hardness and friction of the electrodes.

Nanodiamond was fixed into a brass connector as a holder, and is held at the base of a rod whilst a copper foil moves beneath it at standardized scratching rate of 2 mm s^{-1}. Different vertical forces (weights) were applied gradually on top of the rod, and every run was comprised of 5 scratches. Copper was chosen as the solid material in this case because of its considerably low hardness (2.5 - 3 of Moh's Value or 369 MPa of Vicker's hardness). Nanodiamond has very smooth surface with Moh's value scaled of 10 (88 - 92 GPa of Vicker's hardness [72]), implying the occurrence of less surface damages which is due to the expected lower friction and less abrasiveness forces at the contact layer between the two materials. The abraded nanodiamond was later anodically stripped by employing ASV method in 0.1 M KCl solution at a potential scan rate of 0.05 Vs^{-1}.

As shown in figure 35, a distinctive anodic stripping peak was observed at 0.06 V *vs* SCE, which can be attributed to the stripping of abraded copper to ion Cu^{2+} (equation 16), as being reported in [73]

$$Cu\ (s) \rightarrow Cu^{2+}\ (aq) + 2\ e^{-} \qquad E^{\varnothing} = 0.337\ V\ vs\ SHE \quad (eqn\ 16)$$

The magnitude of this current peak signal is comparable to the AbSV of copper on boron-doped polycrystalline diamond [74] with a stripping peak positioned at 0.11 V *vs* SCE.

The increase of current signals is proportional to the applied vertical forces (r^2 = 0.999), suggesting that the contact of nanodiamond on copper during the abrading process is much better than on microcrystalline diamond. This could be due to the low surface morphological index for nanodiamond that make better interlayer contact, thus reducing the friction. The other possible reason is that the abraded copper on nanodiamond is weakly bonded. This could be attributed to the presence of high electronic conductivity on the nanodiamond surface, enabling the electrode reaction to proceed at the copper (solid reactant) – KCl (electrolyte interface) which induces direct dissolution of copper into the electrolyte solution with simultaneously ion transfer between the abraded copper and the electrolyte solution.

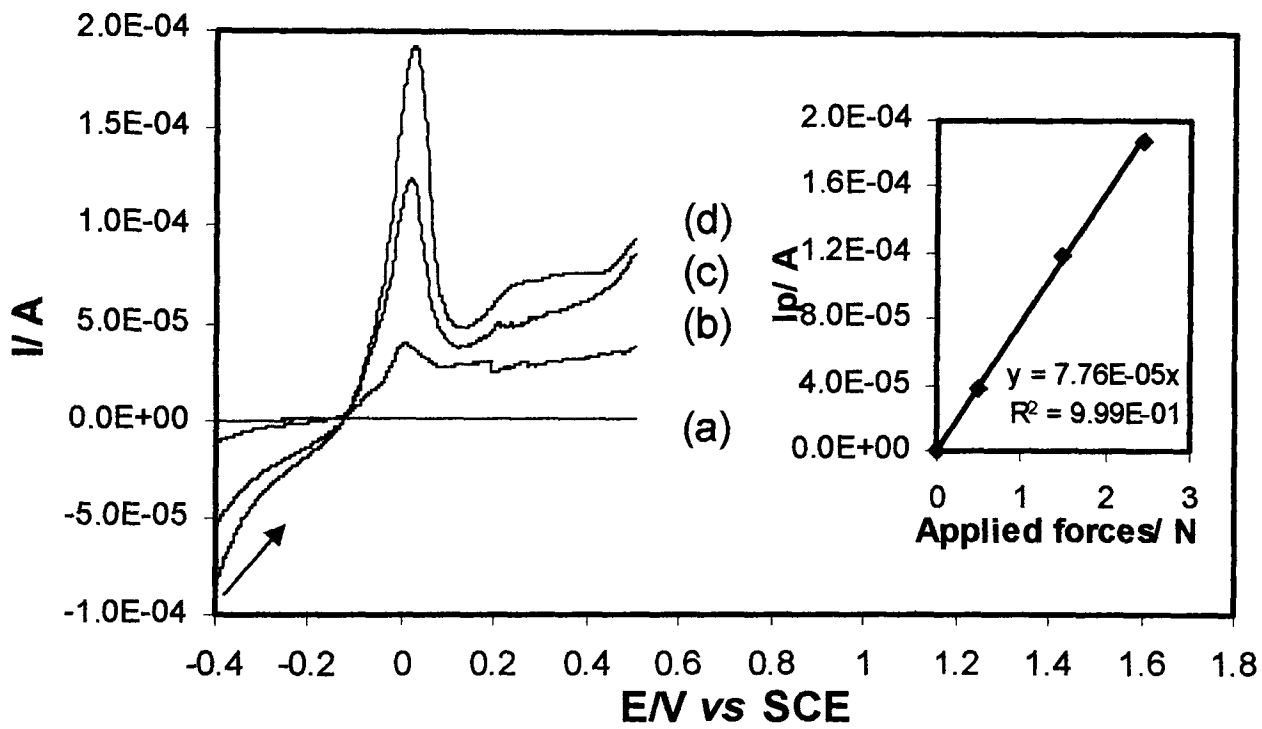


Figure 35. AbSV (scan rate 0.05 Vs^{-1}) for copper abraded nanodiamond in 0.1 M KCl with calibrated applied forces (i.e. plus the weight of Al holder = 0.49 N); no Cu abraded nanodiamond (a), applied forces of 0 N (b), 0.98 N (c) and 1.96 N (d); with inset showing the correlation plot of stripping peak current, Ip at 0.03 V vs SCE versus applied forces

After AbSV, our nanodiamond exhibits similar features to the original surface (under SEM examination), suggesting that the home-grown nanodiamond is of highly packed density structure and is bonded strongly to Ti substrate under the measurements up to 1.98 N. From the simple adhesion test with adhesive tape (3 M Magic tape), all of the

nanodiamond electrodes can survive without peeling off from the Ti substrate. Due to the nano-scaled grain size of nanodiamond, excellent mechanical properties were expected.

From these results, it can be concluded that the 'as grown' nanodiamond possesses high mechanical and hardness properties and is suitable for AbSV.

4.4.8.4 Solvent Test

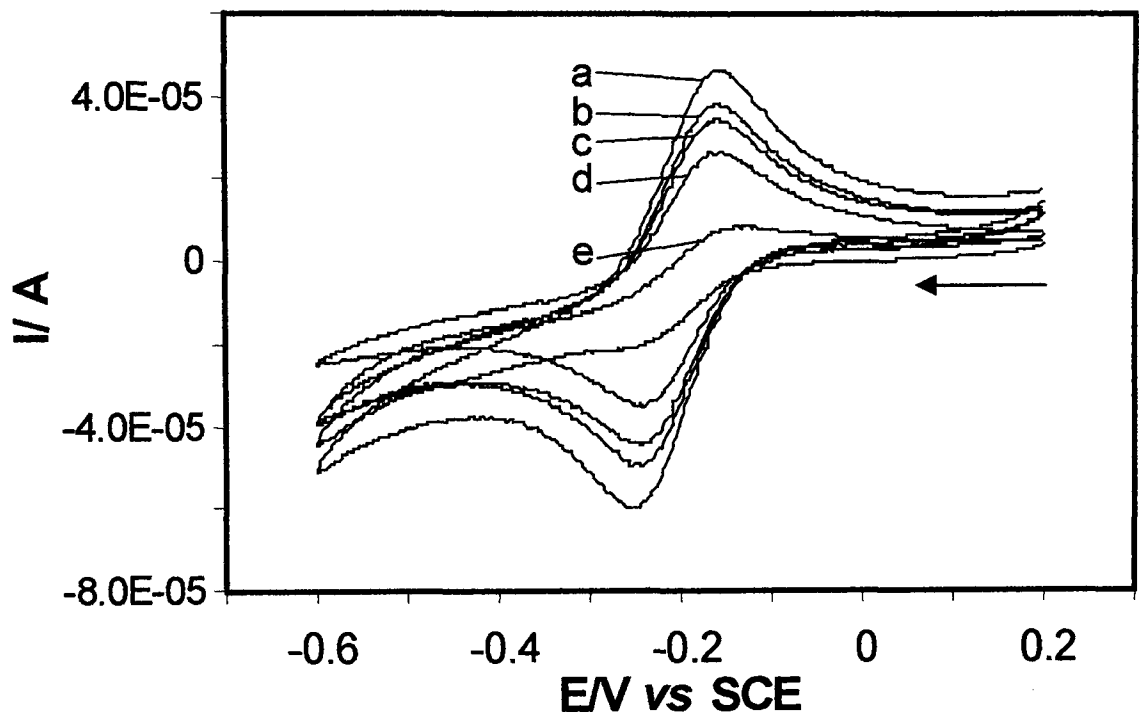


Figure 36. The CVs (scan rate 0.1 Vs^{-1}) response of nanodiamond to 5 mM $Ru(NH_3)_6^{3+}$ in 0.1 M KCl after the as-grown nanodiamond was dipped in a solvent and let dried (a = ethanol, b = chloroform, c = acetone, d = as-grown, e = paraffin oil)

An easy test on nanodiamond reactivity towards solvent polarity has been performed. This was done by dipping the nanodiamond in a solvent for 30 s and was then dried in air before a CV was carried out in 5 mM $Ru(NH_3)_6^{3+}$. The nanodiamond was later rinsed with nanopure water, before the test was repeated for the second time and then for the other solvent.

Figure 36 shows the increased faradaic current by the solvent effects of ethanol, chloroform and acetone on nanodiamond, as compared to the as-grown signal. The possible explanation for these is that the solvents would chemisorb onto the conductive sites of nanodiamond surface due to similar polarity in between solvent and nanodiamond surface. The functional groups, such as hydroxyl (-OH), carbonyl (C=O) or highly dipole

moment of $CHCl_3$ could act as the reactive adsorbates on the conductive pathway of nanodiamond. In contrast, the nanodiamond can severely be passivated by paraffin oil, which clearly indicates the reactive sites have been blocked by highly non-polar polyhydride compounds.

These results reveal the dependence of nanodiamond on the polarity of media/ environment to exhibit its conductive signal in response to any redox system.

4.5 Conclusion

It has been shown that nanodiamond thin film electrodes offer an interesting alternative to conventional carbon electrodes. Nanodiamond appears to offer advantages over boron-doped diamond in terms of enhanced reactivity and over glassy carbon in terms of mechanical and chemical robustness. This suggests that the nanodiamond films studied here may have advantages in particular applications, and provides evidence that the performance of diamond electrodes can be "tuned" by careful manipulation of the grain size and sp^2 content.

Nanodiamond is formed on titanium substrate from methane (as carbon source) and dihydrogen (as etchant), without intentional addition of doping reagents. Nanodiamond shows complete grown surface with averagely crystal sizes of 20-70 nm and with thickness of 2 μm. Raman spectroscopy, SEM, AFM, field emission and electrochemical measurement have been performed to characterize the quality of as-grown nanodiamond.

Solution phase electron transfer processes involving simple one-electron redox couples, organic compounds and metal deposition-stripping processes are fast and efficient at nanodiamond compared to processes at boron-doped diamond. The redox systems show well-defined and reproducible voltammetric responses, low overpotentials required by organic compounds and high metal stripping efficiency. These behaviours

may be attributed to the nanodiamond surface topography, the availability of active edge sites and sp^2 content on grain boundaries.

The nanodiamond is fairly unstable in H_2 and O_2 evolution regions with the possible window potential of 2.5 V range within – 0.8 to 1.7 V *vs* SCE as compared to the 2.3 V for glassy carbon and 3.5 V for boron-doped diamond. Nanodiamond can easily be deactivated by hydrogen plasma treatment, which converts the sp^2 to sp^3 termination. Nanodiamond has shown good adhesive properties on titanium substrate, well-behaved abrasive stripping voltammetry and the dependence on solvent polarity for giving optimal responses.

4.6 References for Chapter 4

[1] O. Matsumoto, H. Toshima and Y. Kamazaki, *Thin Solid Films* **128** (1985) 341

[2] O. Matsumoto and T. Katagiri, *Thin Solid Films* **146** (1987) 283

[3] W. Zhu, A. Inspektor, A.R. Badzian, T. McKenna and R. Messier, *J. Appl. Phys.* **68** (1990) 1489

[4] L.C. Chen, P.D. Kichambare, K.H. Chen, J.J. Wu, J.R. Yang and S.T Lin, *J. Appl. Phys.* **89**(1) (2001) 753

[5] D. Zhou, T.G. McCauley, L.C. Qin, A.R. Krauss and D.M. Gruen, *J. Appl. Phys.* **83** (1998) 540

[6] S.S. Proffitt, S.J. Probert, M.D. Whitfield, J.S. Foord and R.B. Jackman, *Diamond Relat. Mater.* **8** (1999) 771

[7] D.M. Gruen, *Annu. Rev. Mater. Sci.* **29** (1999) 211

[8] B. Fausett, M.C. Granger, M.L. Hupert, J. Wang, G.M. Swain and D.M. Gruen, *Electroanalysis* **12**(1) (2000) 7

[9] K. Fabisiak, M. Maar-Stumm and E. Blank, *Diamond Relat. Mater.* **2** (1993) 722

[10] A.C. Ferrari and J. Robertson, *Phys. Rev. B* **63** (2001) 121405-1

[11] H. Hiura, T.W. Ebbesen, K. Tanigaki and H. Takahashi, *Chem. Phys. Lett.* **202** (1993) 509

[12] W.Z. Li, H. Zhang, C.Y. Wang, Y. Zhang, L.W. Xu and K. Zhu, *Appl. Phys. Lett.* **70**(20) (1997) 2684

[13] A.V. Baranov, Y. S. Bobovich and V.I. Petrov, *Opt. Spektrosk.* **63**(5) (1987) 1026

[14] A.A. Ogwu, R.W. lamberton, S. Morley, P. Maguire and J. McLaughlin, *Physica B* **269** (1999) 335

[15] Q. Zhang, S.F. Yoon, J. Ahn, B. Gan, R. Rusli and M.B. Yu, *J. Phys. Chem. Sol.* **61** (2000) 1179

[16] N. Jiang, K. Sugimoto, K. Eguchi, T. Inaoka, Y. Shintani, H. Makita, A. Hatta and A. Hiraki, *J. Crys. Growth* **222** (2001) 591
[17] W. Zhu, G.P. Kochanski and S. Jin, *Mat. Res. Soc. Symp. Proc.* **416** (1996) 443
[18] J.Y. Shim, H.K. Baik and K.M. Song, *J. Vac. Sci. Technol. A* **18**(4) 2000 1977
[19] W. Kehui, E.G. Wang, Z.X. Cao, Z.L. Wang and X. Jiang, *J. Appl. Phys.* **88**(5) (2000) 2967
[20] N. Jiang, S. Kujime, I. Ota, T. Inaoka, T. Inaoka, Y. Shintani, H. Makita, A. Hatta and A. Hiraki, *J. Crys. Growth* **218** (2000) 265
[21] M. Hiramatsu, C.H. Lau, A.M. Bennett and J.S. Foord, *Thin Solid Films* **407** (2002) 18
[22] F. Beck, W. Kaiser and H. Krohn, *Electrochim. Acta* **45** (2000) 4691
[23] T. Grogler, E. Zeiler, A. Horner, S.M. Rosiwal and R.F. Singer, *Surf. Coat. Tech.* **98** (1998) 1079
[24] A.Y. Sakharova, V. Pleskov, F. Di Quarto, S. Piazza, C. Sunseri, I. G. Teremetskaya and V. P. Varnin, *J. Electrochem. Soc.* **142** (1995) 2704
[25] H.B. Martin, A. Argoitia, U. Landau, A.B. Anderson and J.C. Angus, *J. Electrochem. Soc.* **143** (1996) L133
[26] R. Ramesham and M.F. Rose, *Diamond Relat. Mater.* **6** (1997) 17
[27] M. Fryda, D. Herrmann, L. Schafer, C.P. Klages, A. Perret, W. Haenni, C. Comninellis and D. Gandini, *New Diamond Frontier Carbon Technol.* **9** (1999) 229
[28] E. Endo, Y.J. Kim, T. Maeda, K. Koshiba, K. Katayam and M.S. Dresselhaus, *J. Mater. Res.* **16**(12) (2001) 3402
[29] L.G. Austin and E.G. Gagnon, *J. Electrochem. Soc.* **120** (1973) 1052
[30] J. Wong, Analytical Electrochemistry,2nd edition, Wiley-VcH, 2000, pg. 114
[31] C.M.A. Brett and A.M.O. Brett, Electrochemistry: Principles, Methods and Applications, Oxford University Press, Oxford, 1993
[32] Q.Y. Chen, D.M. Gruen, A.R. Krauss, T.D. Corrigan, M. Witek and G.M. Swain, *J. Electrochem. Soc.* **148**(1) (2001) E44
[33] M.C. Granger, M. Witek, J. Xu, J. Wang, M. Hupert, A. Hanks, M.D. Koppang, J.E. Butler, G. Lucazeau, M. Mermoux, J.W. Strojek and G.M Swain, *Anal. Chem.* **72** (2000) 3793
[34] D.A. Tryk, K. Tsunozaki, T.N. Rao and A. Fujishima, *Diamond Relat. Mater.* **10** (2001) 1804
[35] M.C. Granger and G.M. Swain, *J. Electrochem. Soc.* **146** (1999) 4551
[36] F. Marken, A. Neudeck and A.M. Bond, in Electroanalytical Methods Guide to Experiments and Applications, F. Scholz (*ed*), Springer, Berlin, 2002
[37] M.A. Kutnik, W.C. Hawkes, E.E. Schaus and S.T. Omage, *Anal. Biochem.* **66** (1982) 424
[38] L.A. Pachla, D.L. Reynolds and P.T. Kissinger, *J. Assoc. Off. Anal. Chem.* **68** (1985) 1
[39] M.H. Pournaghi-Azar, H. Razmi-Nerbin, *J. Electroanal. Chem.* **488** (2000) 17
[40] A.M. Medeiros, M.G. Bird and G. Witz, *J. Toxicol. Environ. Health* **51**(6) (1997) 519
[41] B. Simone, V. Anu, B. Christine, M. Katja, D. Pierre and H. Ari, *Biomarkers* **6**(6) (2001) 440
[42] C.H. Lau, K.J. Grehan, R.G. Compton, J.S. Foord and F. Marken, to be published (2002) *J. Electrochem. Soc.*
[43] L.A. Kamel, A.M. Shams and E. Din, *J. Electroanal. Chem.* **24** (1970) 230
[44] L. Jeftic and G. Manning, *J. Electroanal. Chem.* **26** (1970) 195

[45] K. Takamura and Y. Hayakawa, *J. Electroanal. Chem. Inter. Electrochem.* **31** (1971) 225
[46] R. Ramesham and M.F. Rose, *J. Mater. Sci. Lett.* **16** (1997) 1693
[47] H.O. Finklea, in: A.J. Bard, I. Rubinstein (*eds.*), Electroanalytical Chemistry Vol. 19 Marcel Dekker, New York, 1996, pg. 109
[48] A. Fujishima, T.N. Rao, E. Popa, B.V. Sarada, I. Yagi and D.A. Tryk, *J. Electroanal. Chem.* **473** (1999) 179
[49] J.J. Sun, J.J. Xu, H.Q. Fang and H.Y. Chen, *Bioelectrochemistry and Bioenergetics* **44**(1) (1997) 45
[50] L. Stryer, in: Biochemistry, Freeman, New York, 1995, pg. 541
[51] F. Marken, C.A. Paddon and D. Asogan, *Electrochem. Comm.* **4**(1) (2002) 62
[52] H.A. Hill, Y. Nakagawa, F. Marken and R.G. Compton, *J. Phys. Chem.* **100** (1996) 17395
[53] A.K. Abass and J.P. Hart, *Electrochim. Acta* **46** (2001) 829
[54] I.F. Hu, D.H. Karweik and T. Kuwana, *J. Electroanal. Chem.* **188** (1985) 59
[55] J.B. Baur, E.W. Kristensen, L.J. May, D.J. Wiedemann and R.M. Wightman, *Anal. Chem.* **60** (1988) 1268
[56] Y. Maeda, K. Sato, R. Ramaraj, T.N. Rao, D.A. Tryk and A. Fujishima, *Electrochim. Acta* **44** (1999) 3441
[57] T. Vijayabarathi, D. Velayutham and M. Noel, *J. Appl. Electrochem.* **31** (2001) 979
[58] G. Oskam, J.G. Long, A. Natarajan and P.C. Searson, *J. Phys. D* **31** (1998) 1927
[59] A.M. Bond, S. Kratsis, S. Mitchell and J. Mocak, *Analyst* **122** (1997) 1147
[60] R.R. Barefoot and J.C. Van Loon, *Talanta* **49** (1999) 1
[61] K.B. Holt, G. Sabin, R.G. Compton, J.S. Foord and F. Marken, *Electroanalysis* **14**(12) (2002) 797
[62] S. Nakabayashi, D.A. Tryk, A. Fujishima and N. Ohta, *Chem. Phys. Lett.* **300** (1999) 409
[63] C.H. Lau, K.J. Grehan, C.H. Goeting, R.G. Compton, J.S. Foord and F. Marken, accepted for publication in *Electroanalysis*, 2002
[64] O. Groning, O.M. Kuttel, P. Groning and L. Schlapbach, *J. Vac. Sci Technol. B* **17**(5) (1999) 1970
[65] H. Hirai, M. Terauchi, M. Tanaka and K. Kondo, *Diamond Relat. Mater.* **8** (1999) 1703
[66] I. Yagi, H. Notsu, T. Kondo, D.A. Tryk and A. Fujishima, *J. Electroanal. Chem.* **473** (1999) 173
[67] J.W. Peckett, P. Trens, R.D. Gougeon, A. Poppl and R.K. Harris, J. Michael, *Carbon* **38**(3) (2000) 345
[68] A. Reznik, V. Richter and R. Kalish, *Diamond Relat. Mater.* **7** (1998) 317
[69] H.O. Pierson, Handbook of Carbon, Graphite, Diamond and Fullerenes, Noyes Publications, United States, 1993, pg. 274
[70] F. Scholz, L. Nischke and G. Henrion, *Naturwissenschaften* **76** (1989) 71
[71] F. Scholz and B. Lange, *Trends Anal. Chem.* **11**(10) (1992) 359
[72] H. Yoshikawa, C. Morel and Y. Koga, *Diamond Relat. Mater.* **10** (2001) 1588
[73] S. Scheurell, F. Scholz, T. Olesch and E. Kemnitz, *Supercond. Sci. Technol.* **5** (1992) 303
[74] C. Arnab, Part 2 Thesis, "Abrasive Stripping Voltammetry of Boron-doped CVD Diamond", Oxford, 2000

Chapter 5

Diamond Adsorption Chemistry

5.1 Introduction
5.2 Experimental
5.3 Oxygen Adsorption Chemistry
  5.3.1 Previous Work
  5.3.2 Results
    5.3.2.1 Effect of pre-Hydrogenation on Oxygen Adsorption
    5.3.2.2 Effect of Substrate Temperatures on Oxygen Adsorption
    5.3.2.3 Hydrogen Etching on Oxygenated Surfaces
    5.3.2.4 Effect of Thermal Annealing on Oxygenated Surfaces
  5.3.3 Discussion
  5.3.4 Conclusion
5.4 Lithium Adsorption Chemistry
  5.4.1 Previous Work
  5.4.2 Results
    5.4.2.1 Adsorption of Li on Diamond Surface
    5.4.2.2 Depth Profiling of Li Adsorption
    5.4.2.3 XPS Investigation
    5.4.2.4 Lithium and Hydrogen
    5.4.2.5 Lithium and Oxygen
    5.4.2.6 Lithium and Ammonia
  5.4.3 Discussion
  5.4.4 Conclusion

5.1 Introduction

The main motivation for studying the oxygen adsorption chemistry onto diamond surfaces comes from its potential effects on the characteristics of diamond growth and its influence on electronic properties of diamond surfaces. Oxygen figures prominently in the chemistry of diamond growth by controlling the quality and the defect density of diamond grown by chemical vapour deposition (CVD) [1,2] by combining with hydrogen and hydrocarbons. Oxygen can reduce the amount of unsaturated species in the gas phase and increase the concentration of methyl radicals [3], which are the essential factors for the diamond growth. Oxygen could also etch away the non-diamond carbon and the sp^2 defects from the deposited diamond films, thus enabling higher purity of diamond to be obtained [1,4]. The effectiveness of this etching is known to be better than that of H

alone. Oxygen or oxygen-containing molecules (H_2O, CO, CO_2, *etc*) [5,6,7,8,9,10] can also be introduced into the growth process at much higher concentrations, suggesting, according to Bachmann *et al.* [11] that diamond can be successfully grown with carbon and oxygen alone. The adsorption of oxygen has profound technological influences on diamond surfaces properties, such as electron emission [12,13,14,15,16], electrical conductivity [17], and the Schottky barrier height of metal contacts [18,19]. The impact due to the oxygen uptake on photocathode is significant, which in turn raises the electron affinity [15]. The oxygen concentration that brings this about is often limited to very low values, suggesting that reaction at defect sites is implicated. Thus, it is crucial to understand the nature of the oxygen chemisorption.

The electronic structure associated with the chemisorption of a single alkali-metal atom on a surface is controversial because under all the circumstances that an alkali-metal atom adsorbs, its description as an ion on the surface is much too simplistic. The presence of adsorbed ion results in a decrease in work function of the diamond and charge transfer of the metal-diamond layer, which requires the presence of an electric dipole. The explanation for this ranges from the most extreme picture of an ion inducing a mirror charge in the substrate to very complex hybridizations of adsorbate and substrate derived states [20]. Li adatoms have considerably smaller dipole moments (2.3 D) and smaller atomic size (3.04 Å) than the other alkalis. This character results in anomalous properties of Li, which lead to the greatest polarization power amongst the alkali metal ions and singularly great tendency toward solubility and covalent bond formation. Hence, a full Li monolayer is expected to occupy all active adsorption sites at the surface. For the other alkalis such as K and Cs, due to their larger atomic size, the monolayer film is of significantly lower density. Therefore, the aim of this work is to study Li adsorption on diamond surface and to investigate the extent of how Li follows the properties expected for other alkali metal.

5.2 Experimental

The experiments were performed in an ultrahigh vacuum (UHV) system with a base pressure of < 5 x 10^{-10} mbar. The system (see Chapter 2; figure 2) was equipped with a Hiden Analytical HAL EPIC quadrupole mass spectrometer (QMS) for the temperature programmed desorption (TPD) studies and a PSP X-ray source with a Mg anode (1253.6 eV) for X-ray photoelectron spectroscopy (XPS). The XPS spectra were fitted with asymmetric mixed Gaussian-Lorentzian sum functions using the XPS peak fitting programme XPSpeak (version 4.0). Energies in the core-level spectra are quoted as the binding energies relative to the C 1*s* bulk component.

All pure dosing gases, H_2, O_2 and NH_3 (all standard BOC gases) were used without further purification. Molecular gas dosage was delivered *via* an *ex situ* leak valve and stainless steel dosing line, with the tip of which was 10 mm from the sample. An iridium (Ir) filament was present in the system, which electronically excites the molecular O_2 dosing gas or thermally dissociates the NH_3 when desired. This was done over the optimal Ir temperatures in the range 1650 – 2000 K at an applied current of 5.0 A, which should not impose any Ir-related contamination on the surface [21]. The system was also equipped with an atomic beam source (Sairem), for O or H atom dosing [22]. All of the gases dosages were performed at a pressure of 5 x 10^{-6} mbar.

The high-quality boron-doped CVD diamond sample used was grown by MWPECVD on Si, and displayed a well-faceted, random grain orientation with a grain size in the 5 – 10 μm range. The B-doped sample was mounted as shown in Section 2.4 of Chapter 2. Undoped single crystal diamond (4 x 4 x 1 mm^3) was used to make comparison with the polycrystalline diamond, and the mounting of sample was shown in the figure 1. A Ta filament was used to heat the backside of the diamond up to 500 °C by thermal emission and "black body" radiation.

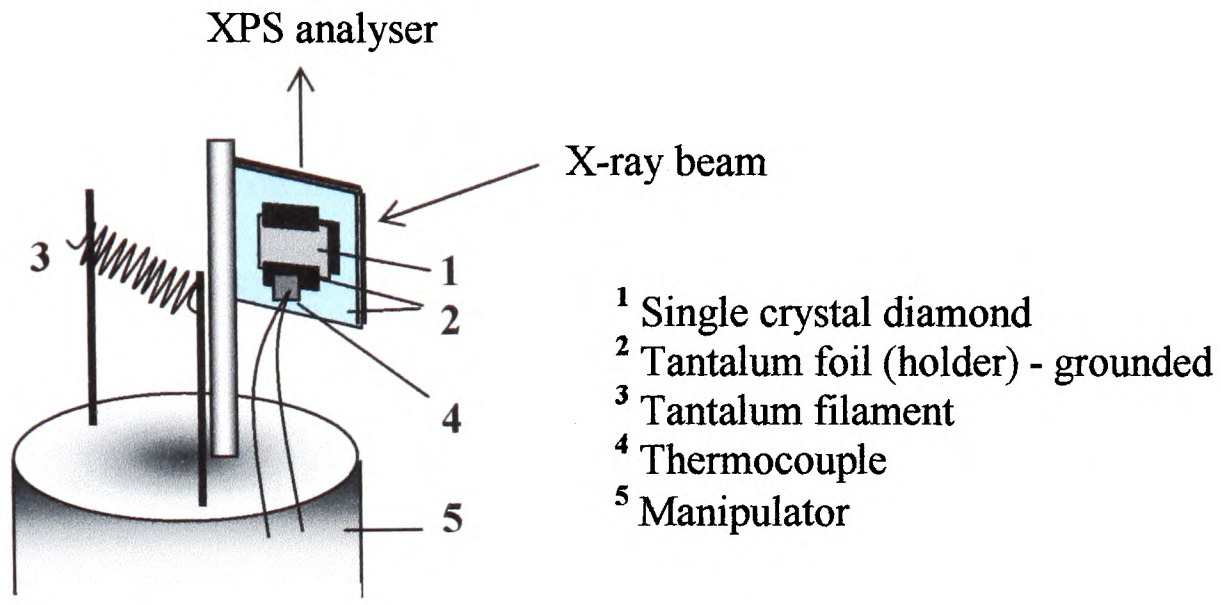


Figure 1. The mounting of undoped homoepitaxial single crystal diamond

Li depositions were carried out with a Li dispenser (SAES Getters) at 300 K, at a pressure below 1 x 10^{-9} mbar and at a distance 25 mm from the sample. The operation current of the Li getter source was 7.3 A, but higher currents (even up to 9 A) were required to open the source slit. When the source emitted Li, the current can later be reduced to a certain value depending on the dosage determination.

The diffusion profile of Li was acquired on the Atomika 4500 SIMS instrument at University of Warwick. The profiling conditions used were with an incident beam of 1 keV O_2^+ at an angle of 30 ° from the normal. The charge compensation used during profiling of these particular profiles was conducted with a floating low energy electron gun (FLEG).

Note: a shorthand notation is used in this chapter - A/B/diamond denotes the interface formed by adsorbate A dosed on pre-adsorbed B on the diamond surface. The forms of adsorbate could either be from gas dosing or metal evaporation.

5.3 Oxygen Adsorption Chemistry

5.3.1 Previous Work

Research on the interaction of oxygen with diamond surfaces started as early as 1918, with the investigation carried out on the surface oxides of diamond powder [23]. Lambert [24] suggested that molecular oxygen would chemisorb onto the surface of a clean diamond powder as a carbon dioxide complex and that carbon monoxide could only be formed in the presence of catalysts, while Barrer [25] reported oxygen physisorption on diamond powder surfaces can only occur below 0 °C. Lander and Morrison [26] showed that the adsorption of water and oxygen on the C(111) surface produced the LEED patterns with the characteristic of disordered surfaces, even the high oxygen doses failed to produce patterns on both the C(100) and C(111) surfaces. In 1968, Sappok and Boehm [27] investigated diamond powder and suggested an ether-like O bridge-bonding on the C(111) and C(110) faces, whereas carbonyl groups were bounded to the (100) face.

Thomas *et al.* [28] investigated the interaction of oxygen with the C(100)-(2 x 1) surface using thermal desorption spectroscopy (TDS) and low-energy electron diffraction (LEED), revealing that the adsorbed oxygen was desorbed as CO (major) and CO_2 (minor). They also showed that Ir-excited molecular oxygen, O_2* was able to convert the (2 x 1) structure to (1 x 1), by which this type of surface reconstruction was proved theoretically later [29]. By using diffuse reflectance infrared (IR) study on diamond powders combined with the TDS and thermogravimetric analysis, Ando *et al.* [30] attributed IR peaks that were observed from the oxygenated polycrystalline diamond powder to ether, ketone, lactone, carboxylic acid and carboxylic anhydride species. Similar multiple internal reflection infrared analysis was used to analyze the reaction of a diamond prism with water [31] or with oxygen [32].

Oxygen adsorption on diamond was also studied by using ultra-violet photoemission spectroscopy (UPS) with RHEED [33], suggesting that the observed

emission state at ~ 3 eV following O adsorption was assigned to the O-induced surface state; and after annealing to 800 °C, the reconstructed surface with the emission at 2.5 eV was attributed to the π-bond reconstruction of the sub-surface carbon layers, following the desorption of the first layer CO from the surface. Other techniques that have been used for investigating oxygen adsorption were high-resolution electron energy loss spectroscopy (HREELS) [34,35,36], electron stimulated desorption studies [37], elastic recoil detection analysis (ERDA), Rutherford backscattering spectrometry (RBS) and time-of-flight secondary ion mass spectrometry (TOF-SIMS) [38].

Theoretical studies were also employed to understand the oxygenated diamond surfaces and the origin of the O-induced emissions state, by mean of *ab initio* total energy calculation [29], first principles linear muffin-tin orbital (LMTO) method [33], SLAB-MNDO molecular orbital methods [39] and the density functional methods [40].

For the first part of this chapter, the discussion will be focused on the results of the oxygen adsorption chemistry on diamond with regard to the differing oxygen dosage methods, such as molecular, excited and atomic oxygen. The effect of hydrogen pre-adsorption and substrate temperature platen are also examined on oxygen adsorbability.

The interaction of oxygen and diamond is considered crucial to gain insight the performance of the diamond photocathodes, particularly due to the effect of photoyield degradation induced by oxygen (analysed and discussed in Chapter 6) and also its electrical influences on diamond surface conductivity (analysed in Chapter 3).

Abbreviated terms of surface treatment were used: O_2 (molecular oxygen); O_2* (thermally excited oxygen by the incandescent iridium filament); O (atomic oxygen or dissociated oxygen, generated *via* microwave plasma source); H (atomic hydrogen or dissociated hydrogen, generated *via* microwave plasma source).

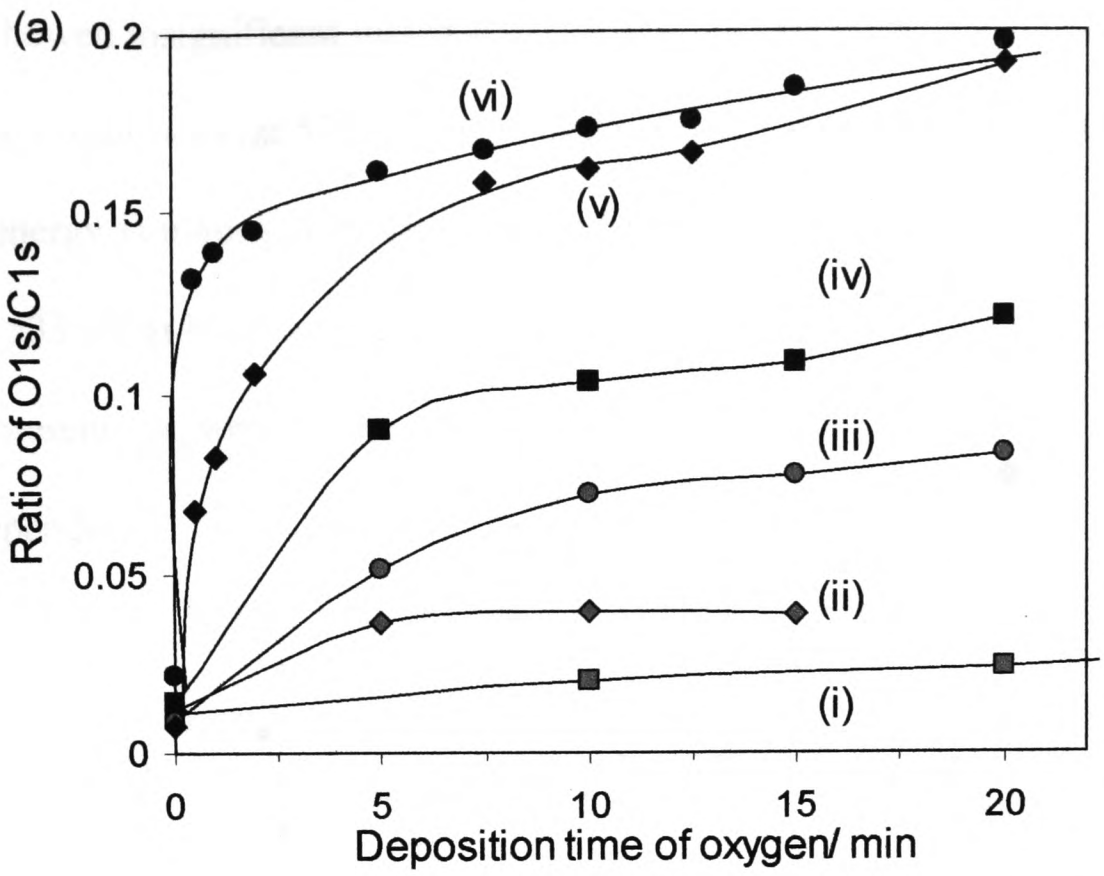
5.3.2 Results

5.3.2.1 Effect of pre-Hydrogenation on Oxygen Adsorption

XPS studies

The kinetics of oxygen adsorption on the diamond sample were studied by measuring XPS spectra after the exposure to oxygen of an atomically clean surface, prepared by desorbing all residual hydrogen from the surface by heating to approximately 1200 K. A surface was dosed with atomic hydrogen close to 300 K using the atomic microwave beam source to achieve saturation surface coverage, as measured by thermal desorption spectrometry. Experiments were carried out with molecular O_2, with electronically excited O_2* *via* interaction with the iridium filament, or with atomic O obtained from the O beam source. Results showing the resultant of relative O coverage *versus* oxygen dose for these differing conditions are illustrated in figure 2a. A barely perceptible rise in O coverage with gas dose is seen when the hydrogen-free surface is exposed to molecular O_2. If the dosing gas is electronically excited, or atomised, then the rate of oxygen uptake increases enormously, as does the 'saturation' oxygen coverage observed in this dosing pressure regime. An equally notable effect is that the hydrogen-saturated surface measured in terms of saturation coverage and the initial rate of oxygen uptake is at least as reactive as the hydrogen-free surface. Using XPS sensitivity factors and photon attenuation down to 5 carbon monolayers (in eqn 31, Chapter 2), the O1*s*/ C1*s* signal intensities can be converted to approximate surface coverages. Such calculations indicate that the oxygen coverages observed vary from ~ 0.08 monolayers for molecular oxygen adsorption on H-free diamond up to ~ 0.8 monolayers for a similar gas exposure using the O atom source.

XPS spectra of the O 1*s* region for the oxygen-dosed surfaces are illustrated in figure 2b. Some of the recorded spectra exhibit peaks with an appreciable energy spread, suggesting that they comprise of several chemically shifted components, indicating the presence of differing oxygen species on the surface.



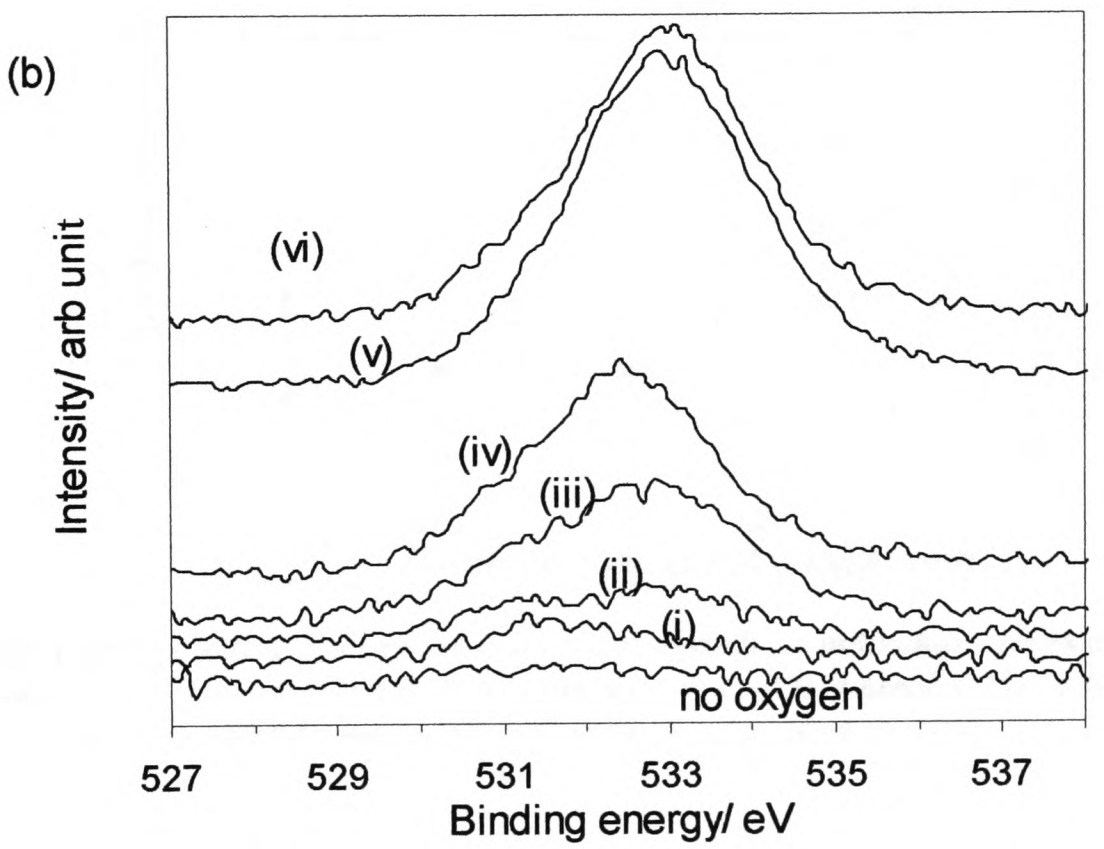


Figure 2. (a) Plot of O 1s/ C 1s ratio intensity versus gas exposure time (5 x 10^{-6} mbar) and (b) O1s spectra after 4500 L oxygen exposure at 300 K; (i) O_2/diamond, (ii) O_2/H/diamond, (iii) O_2 /diamond, (iv) O_2* /H/diamond, (v) O/diamond and (vi) O/H/diamond*

Figure 3 shows the shifts of O 1*s* binding energy in regard to the individual treatment on diamond surface. Atomic oxygen produces the chemisorbed oxygen with the highest binding energy at 533.1 eV (v, vi). The electronically excited O_2* on both clean (iii) and H-saturated diamond (iv) have shown linear increases of O 1*s* binding energy shifts to 532.7 eV within the dosing period of O_2* for 20 min. Molecular oxygen

adsorption showed insignificant increase of the binding energy shift for both H-treated (ii) and untreated (i) surfaces (at 532.0 eV). A likely interpretation of these data are that the O 1*s* binding energy is mainly dependent on surface coverage, rising from ~ 532 eV at low coverage to 533 eV at high coverage. This is probably due to changes in the nature of the O species present, as well as the charges in bond polarity, which are expected to be coverage dependent.

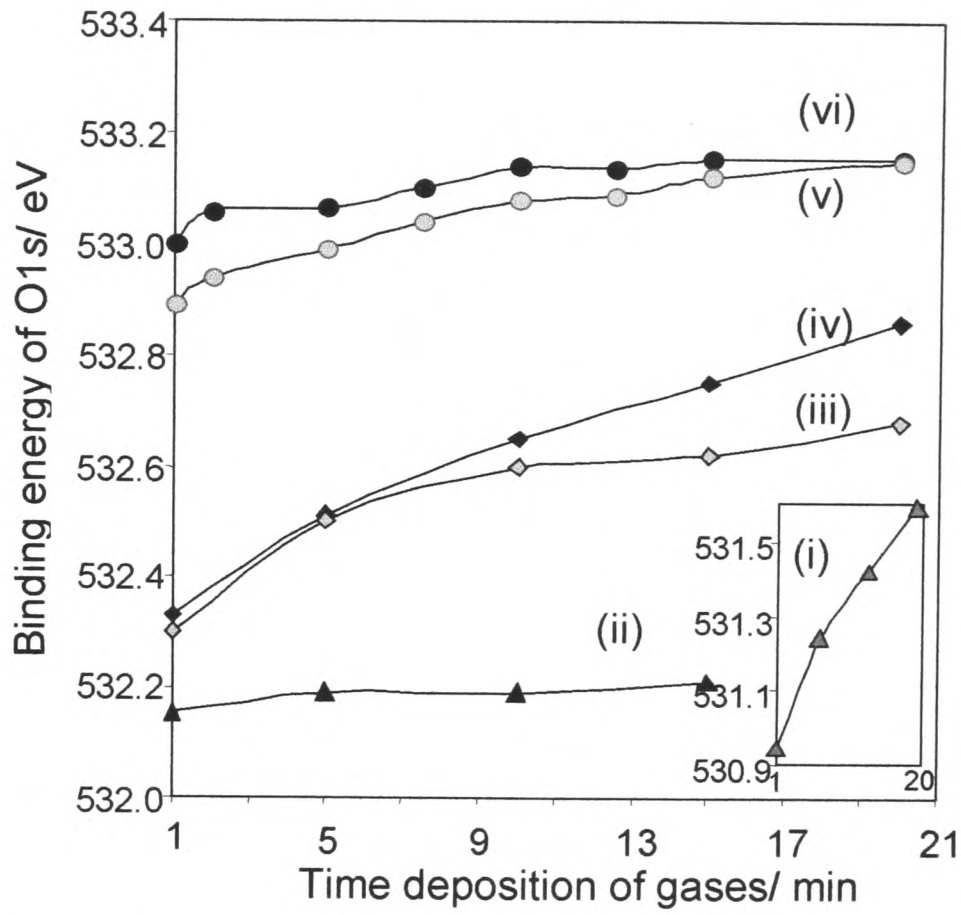


Figure 3. The shift of binding energy for O 1s with regards to individual treatment on diamond, (i) O_2/diamond, (ii) O_2/H/diamond, (iii) O_2/diamond, (iv) O_2*/H/diamond, (v) O/diamond and (vi) O/H/diamond (Note: a dose of 20 min at 5 x 10^{-6} mbar is equivalent to 4500 L)*

Peak fitted C 1*s* spectra are shown in figure 4. The peak at approximately + 1.0 eV can be ascribed to carbon atoms bonded in polyhydride (CH_x, $x \geq 2$) configurations adsorbed on the surface [41]. The peaks with shifts between 2.0 and 2.5 eV can be attributed to hydroxyl and ether functional groups on the surface, whereas the peak at + 3.6 – 4.8 eV is assigned to carbonyl and carboxyl groups or multiple ether linkages [42,43]. As compared to the C 1*s* of hydrogenated diamond (figure 4 v), the arising peaks at binding energies > + 2.0 eV (as referenced to the bulk carbon peak) were observed for the oxygenated diamond systems (i - iv). After the exposure to iridium filament activated

O_2*, a deconvoluted peak was observed at a binding energy of + 2 eV (~ 286.0 eV), resulting in a full width at half maximum (FWHM) ~ 1.5 eV (see figure 4 i, ii). Whereas, after the exposure to atomic O beam, there was a significant increase of the compositional peak at a binding energy of + 4.5 eV (~ 288.5 eV) for 4 (iii) and 4 (iv), with the increase of FWHM up to 2.2 - 2.4 eV.

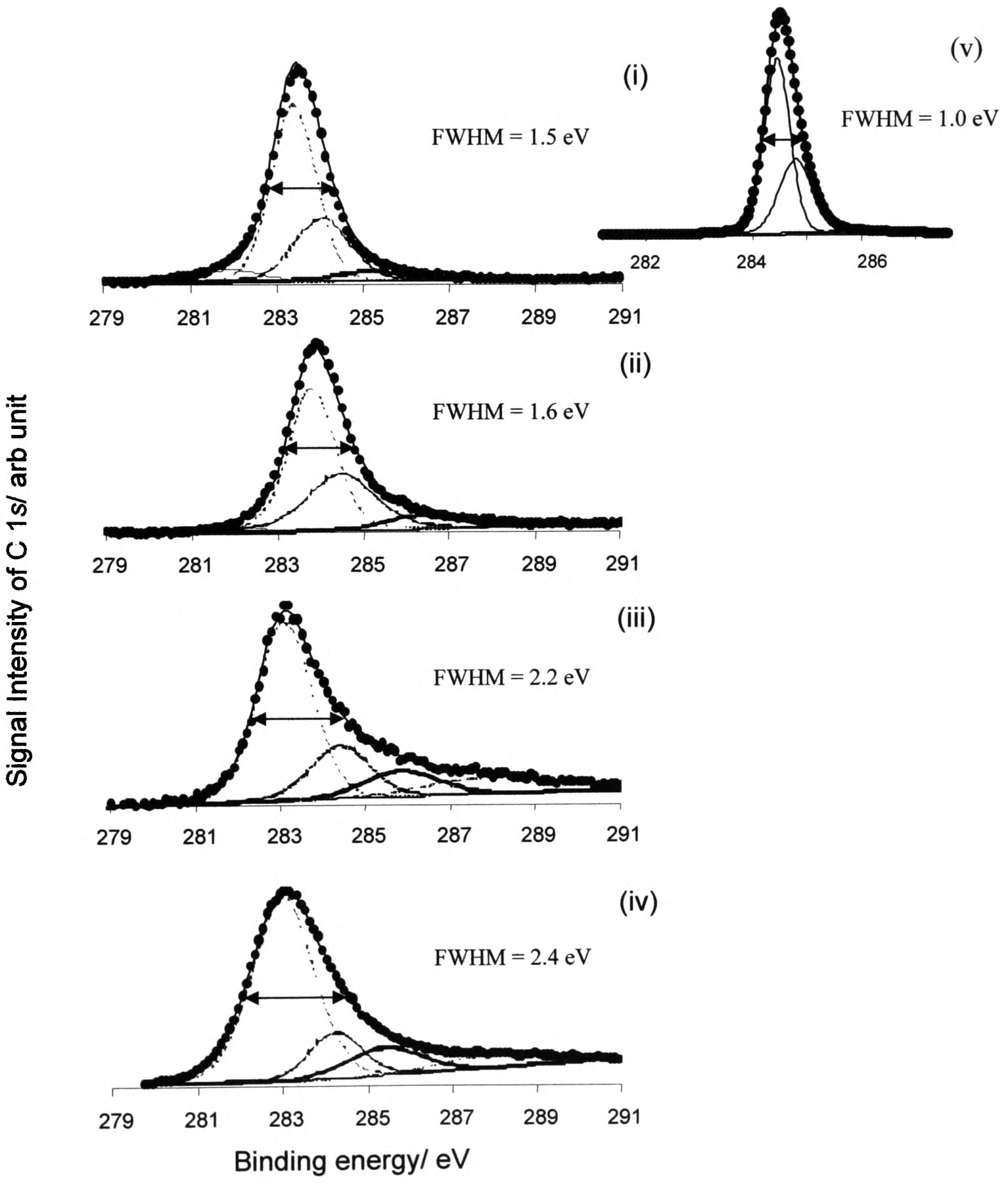


Figure 4. XPS C1s spectra for different treated diamond samples at oxygen saturation dosed, giving the binding energy with individual functional component: (i) O_2/diamond, (ii) O_2*/H/diamond, (iii) O/diamond and (iv) O/H/diamond with reference to (v) fully hydrogenated diamond, H/diamond centred at 284.4 eV*

Accordingly, the polyhydride content (+ 1.0 eV from the carbon bulk) had clearly declined after higher degree of oxygenation was carried out. Note that the binding energies for C 1*s* of differing condition are different, 284.4 eV for H/diamond, 283.4 eV for O_2*/diamond, 283.8 eV for O_2*/H/diamond and 283.1 eV for both O and O/H- treated diamond.

The comparison of the functional components after each chemical surface treatment carried out on diamond surface is shown in figure 5. Atomic oxygen treated diamond samples have higher amount of carbonyl and carboxylate related species at higher binding energy with relative decreases in polyhydride content, whereas the sample exposed to iridium activated oxygen, O_2* (ii, iii) has shown less C=O/COO species than (iv), (v) with higher polyhydride content. Hydrogenated diamond (i) has shown no significant amount of oxygen containing functionalities.

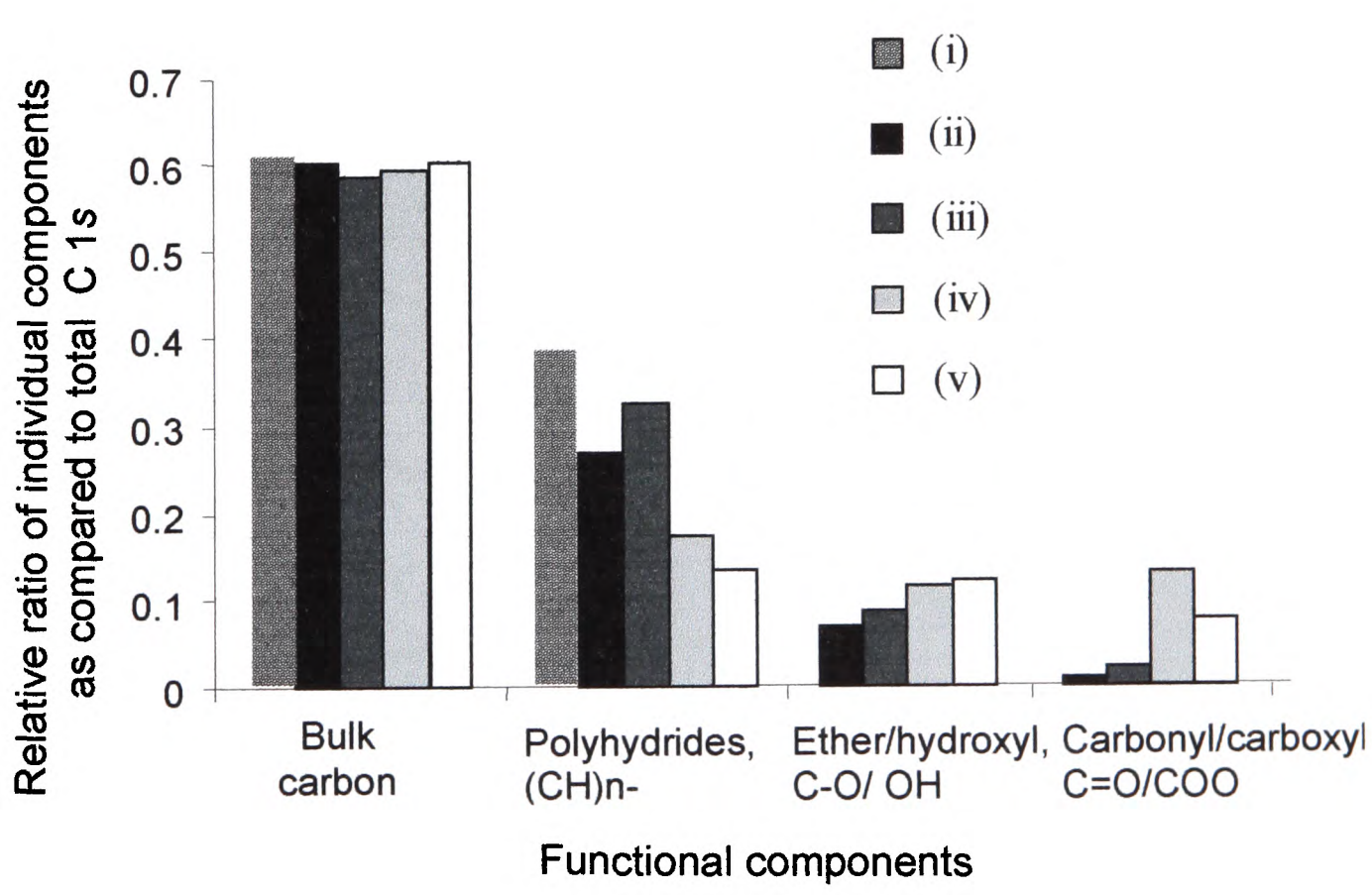


Figure 5. The comparison of functional components on each chemical surface treatment on diamond; (i) H/diamond, (ii) O_2/diamond, (iii) O_2*/H/diamond, (iv) O/C and (v) O/H/C; Note that oxygen containing groups is insignificant for (i)*

Thermal desorption studies

Thermal desorption spectra (TDS) were monitored to examine the thermal stability of the adsorbed layers. The main desorbing species were found to be CO and CO_2 and the representative desorption spectra at 3600 *L* exposure are illustrated in figure 6. No O_2 desorption was detected for any treatments. When Ir-excited O_2* was dosed onto the clean diamond surface, TDS (see 6a) showed the adsorbed oxygen was removed from the surface over a broad temperature range 300 - 800 °C, and a corresponding CO desorption peak was evident in this temperature range. Small amounts of CO_2 desorption was observed. Pre-hydrogenation of the surface tended to shift the temperature range in which CO and CO_2 started to desorb to somewhat lower temperatures, a shift of nearly 200 °C for O_2* on H/diamond surface (b, f) and a shift of 100 °C for atomic O on H/diamond (d, h) as compared to clean diamond surfaces (c, g).

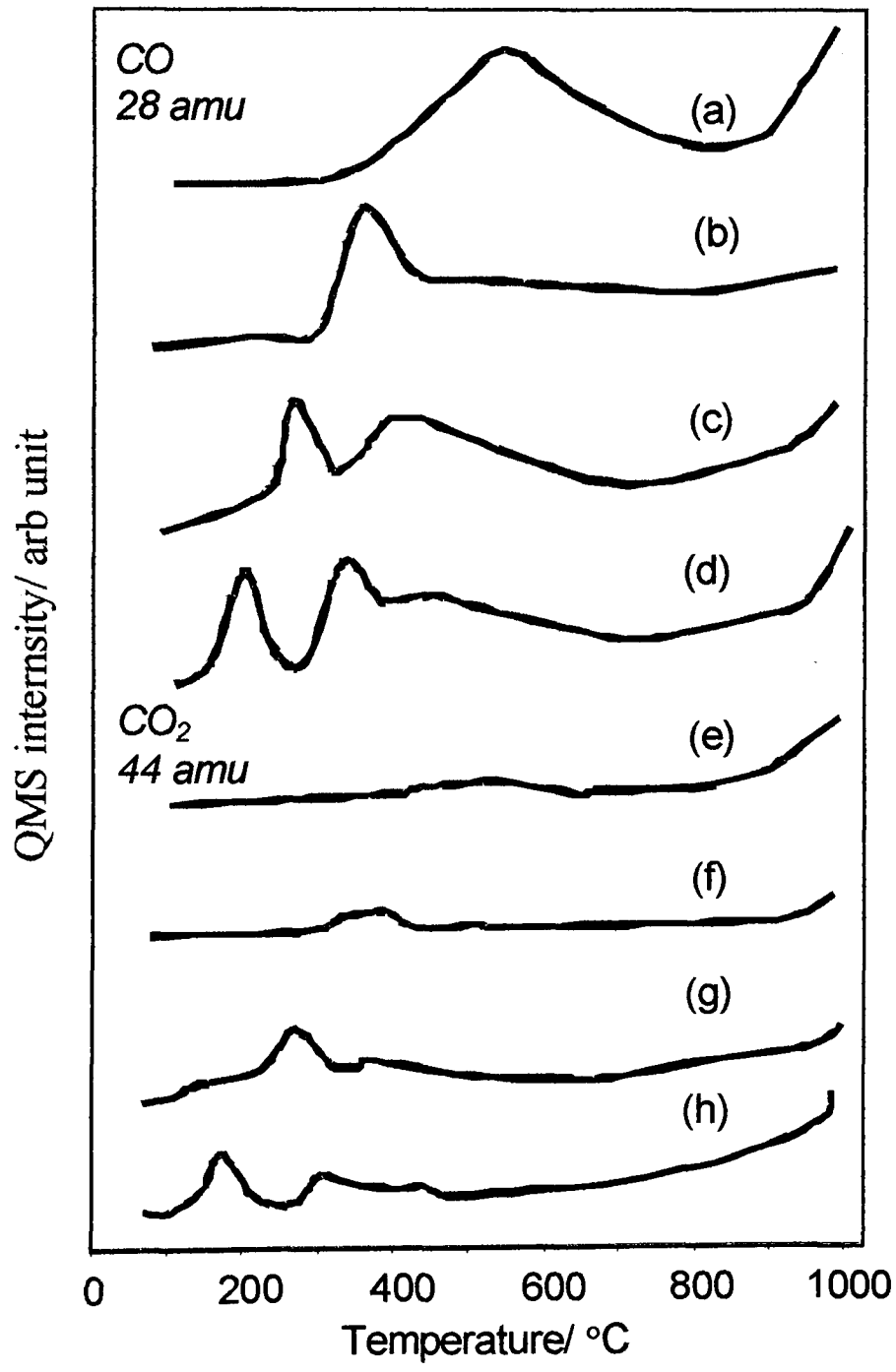


Figure 6. Thermal desorption spectra monitoring for CO (28 amu, a-d) and CO_2 (44 amu, e-h) following the exposure to 3600 L oxygen at 300 K;
(a),(e) O_2/diamond,*
(b),(f) O_2/H/diamond,*
(c),(g) O/diamond and
(d),(h) O/H/diamond

When dosed with the atomic oxygen beam, some oxygen loss was also evident at much lower temperatures (ca. 250 °C) for the H-free surface, in the form of CO and CO_2, with this shifting down to 150 °C for adsorption on the hydrogenated surface. TPD spectra monitoring H_2 indicated that the total amount of hydrogen desorbing was significantly reduced, compared to the oxygen-free surface, by exposure to Ir-excited O_2* or atomic oxygen O. The following figures (7-9) show the series of thermal desorption spectra monitored as the amount of oxygen dosage increases.

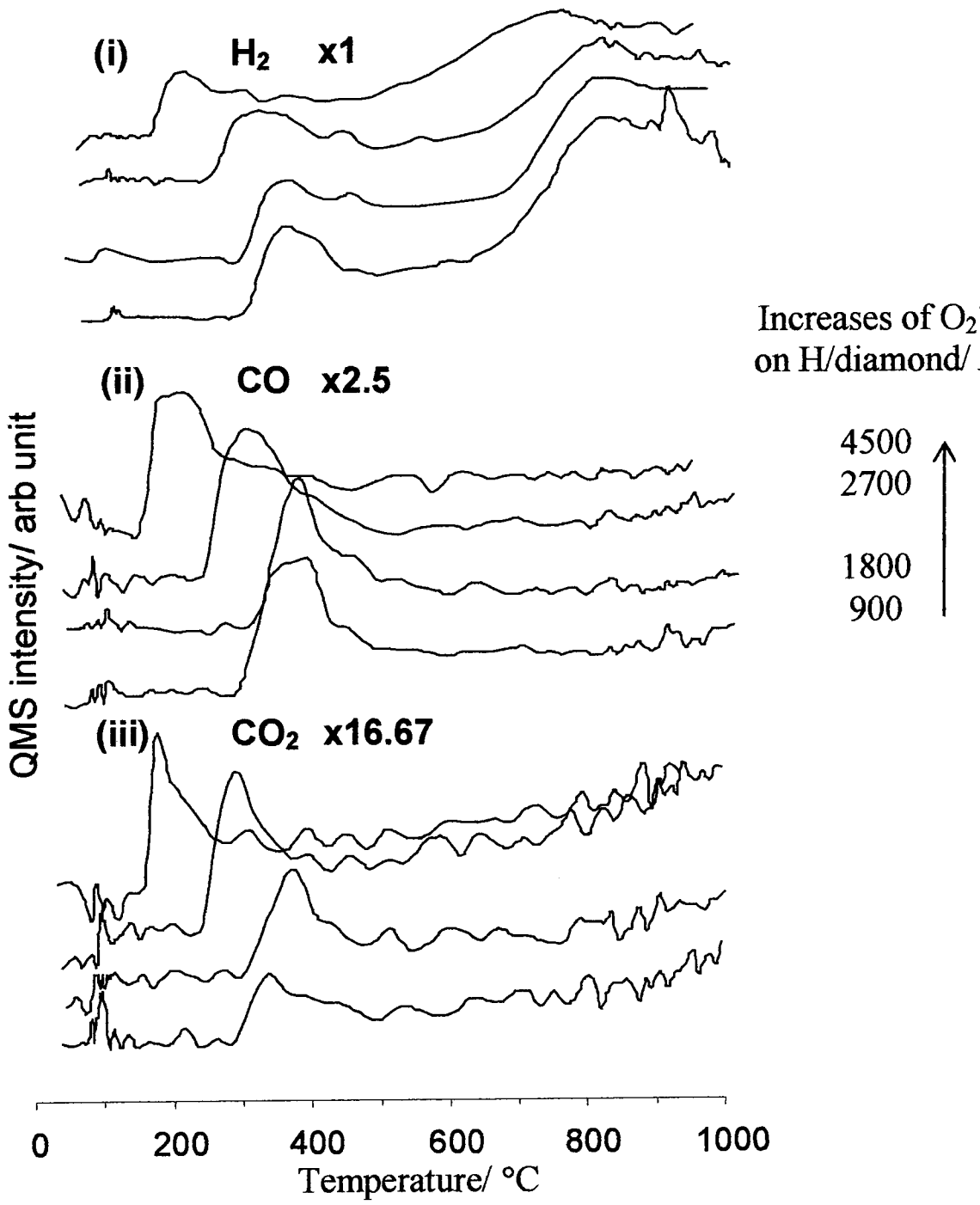


Figure 7. TD spectra recorded for (i) H_2 (2 amu), (ii) CO (28 amu) and (iii) CO_2 (44 amu) of O_2/H/diamond, following the exposure of fully pre-hydrogenated diamond to the increase doses of iridium filament activated oxygen, O_2* at 300 K (900 - 4500 L)*

TDS of activated O_2* dosed on pre-hydrogenated diamond is shown in figure 7, revealing the desorption of CO (ii) and CO_2 (iii) peaks centred at a temperature of 380 °C,

which grew in intensity and shifted to lower desorption temperature with the increasing O_2* exposure. This indicates a second order of desorption has taken in place. This trend was followed by the small decrease of amount for the desorbed hydrogen at 800 °C (i) at a saturation dose of 4500 *L*.

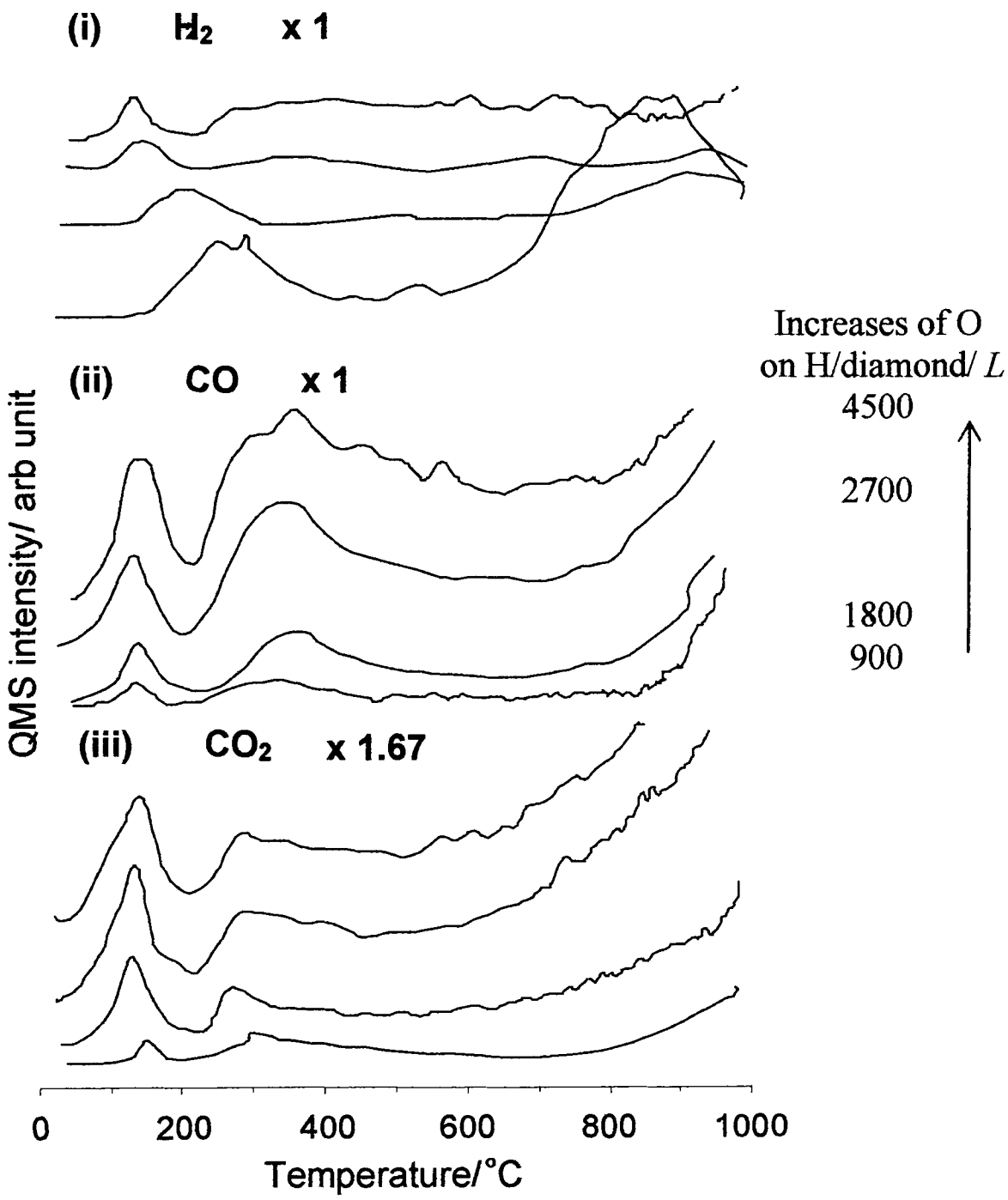


Figure 8. TD spectra recorded for (i) H_2 (2 amu), (ii) CO (28 amu) and (iii) CO_2 (44 amu) of O/H/diamond, following the exposure of fully pre-hydrogenated diamond to the increase doses of atomic oxygen at 300 K (900 - 4500 L)

Atomic oxygen dosed on H-saturated diamond surface has shown distinctively different TD spectra in figure 8 with two apparent desorption peaks, positioned at 170 °C and 300 °C independent on the increases of O doses, which is the first order desorption behaviour. The amount of desorbed hydrogen has decreased remarkably with the increases of O dosages, with the disappearing H_2 peak at 850 °C. It is noticeable that the

QMS intensity ratio for the desorbed CO and CO_2 are relatively similar (x 1.67/1.0) for O/H/diamond, if compared to the case for O_2*/H/diamond (with x 16.67/2.5).

Figure 9 shows the TD spectra for the exposure of clean diamond to the increasing dosages of atomic oxygen. Maximum desorption peaks were located at 180 °C for both desorbed gases, with the observed second arising broad peak around 400 °C.

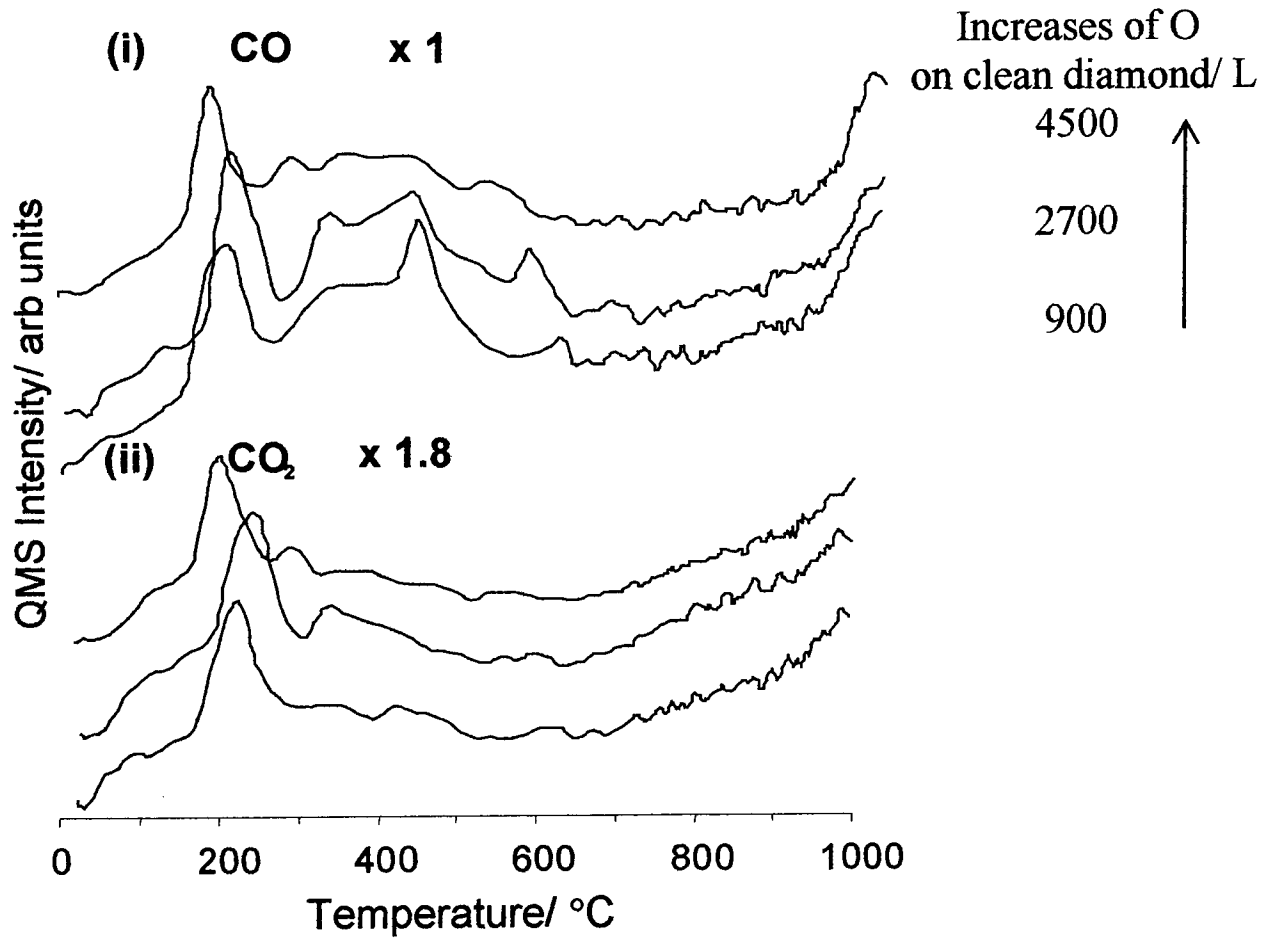


Figure 9. TD spectra recorded for (i) CO (28 amu) and (ii) CO_2 (44 amu) of O/diamond, following the exposure of clean diamond to the increase doses of atomic oxygen, O at 300 K (900 – 4500 L)

5.3.2.2 Effect of Substrate Temperatures on Oxygen Adsorption

A number of experiments were performed at higher dosing temperatures and data is shown in figure 10. In figure 10a, the saturation coverage achievable from molecular oxygen (v) and excited oxygen (iii) show a gradual increase with temperature above 300 °C, suggesting an increase in reaction probability, though the coverage decreased later after 450 °C. In contrast, the surface coverage evident after dosing with atomic O (i) decreased somewhat, which is as expected, given the thermal stability exhibited for these adlayers, indicating that some decomposition of the adsorbed layer occurs in this temperature range.

It is worth noting that the H-pretreated surfaces showed the maximum coverage of oxygen at ~150 °C for both molecular (O_2/H/diamond, iv) and excited oxygen (O_2*/H/diamond, ii), and the coverage decreased later with further increases of the substrate temperature.

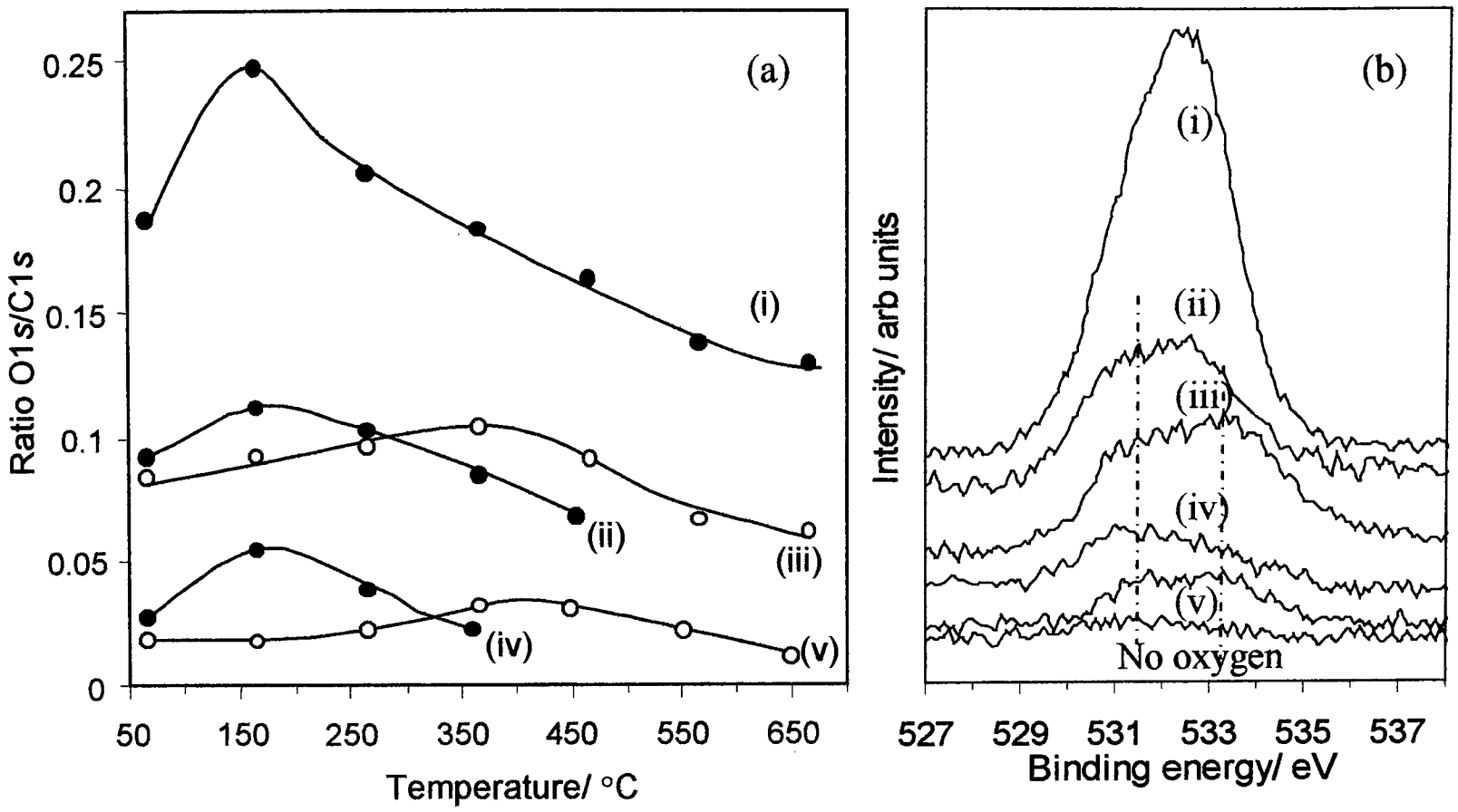


Figure 10. O 1s/C 1s ratios against substrate temperature (a) and XPS of O 1s at substrate temperature of ~ 350 °C (b) for the doses of 2250 L by different oxygen states; (i) O/diamond, (ii) O_2/H/diamond, (iii) O_2*/diamond, (iv) O_2/H/diamond and (v) O_2/diamond*

From figure 10b, two underlying chemical positions for O 1*s* were observed at c*a.* 531.4 eV and 533.2 eV and the peaks were further fitted carefully by mean of XPS Gaussian-Lorentzian peak fittings. The ratios of the compositional area for the lower binding energy peak (denoted A) to the higher binding energy peak (B) are shown in figure 11. At perhaps 275 °C, these two peaks interchanged their area ratios for the surfaces treated by O_2 and O_2*, except for the atomic O exposed surface, which has a low A/B ratio even from the exposure at 300 K. Figure 12 shows the fitted XPS spectra for a clean diamond after being exposed to Ir-activated molecular oxygen, O_2*. At low substrate temperature, the underlying dominant peak in O 1*s* was observed at lower binding energy, but the peak was later decreased with the increases of the substrate temperature, by which the O 1*s* at higher binding energy became more prominent.

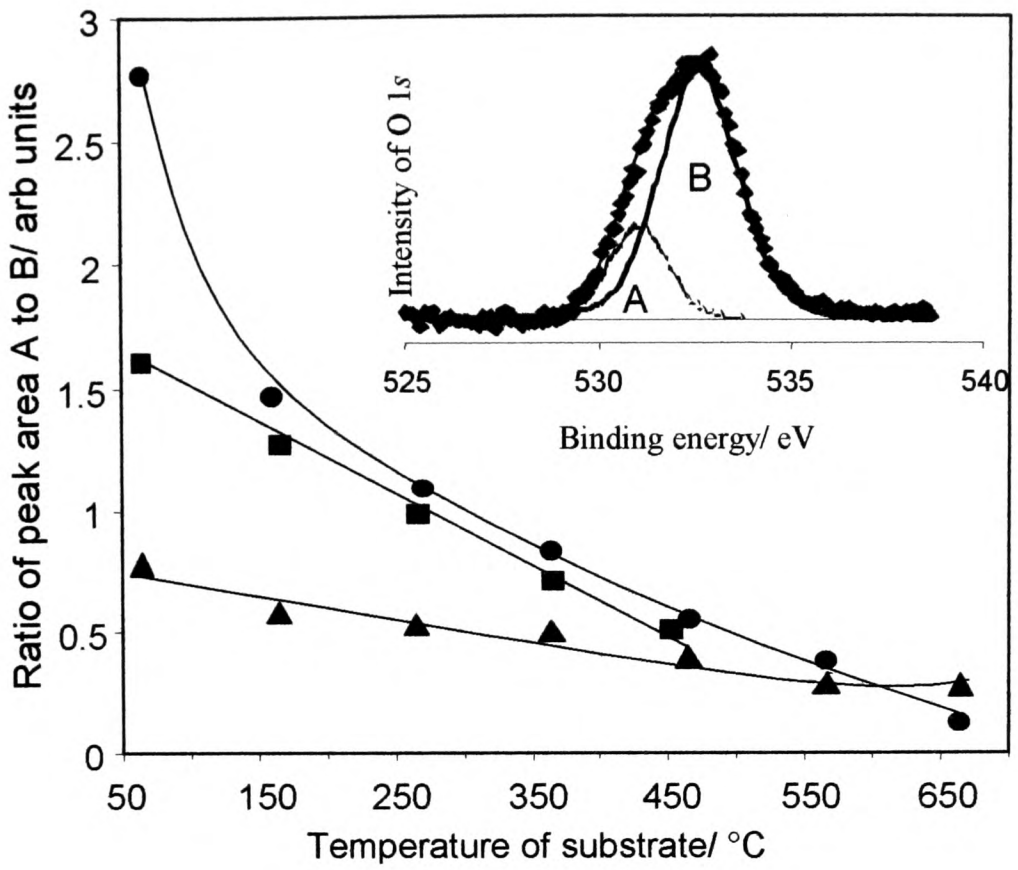


Figure 11. Ratio for O 1s compositional peaks A to B at the elevated temperatures;
(i) O_2/diamond (●)*
(ii) O_2/H/diamond (■)*
(iii) O/diamond (▲)

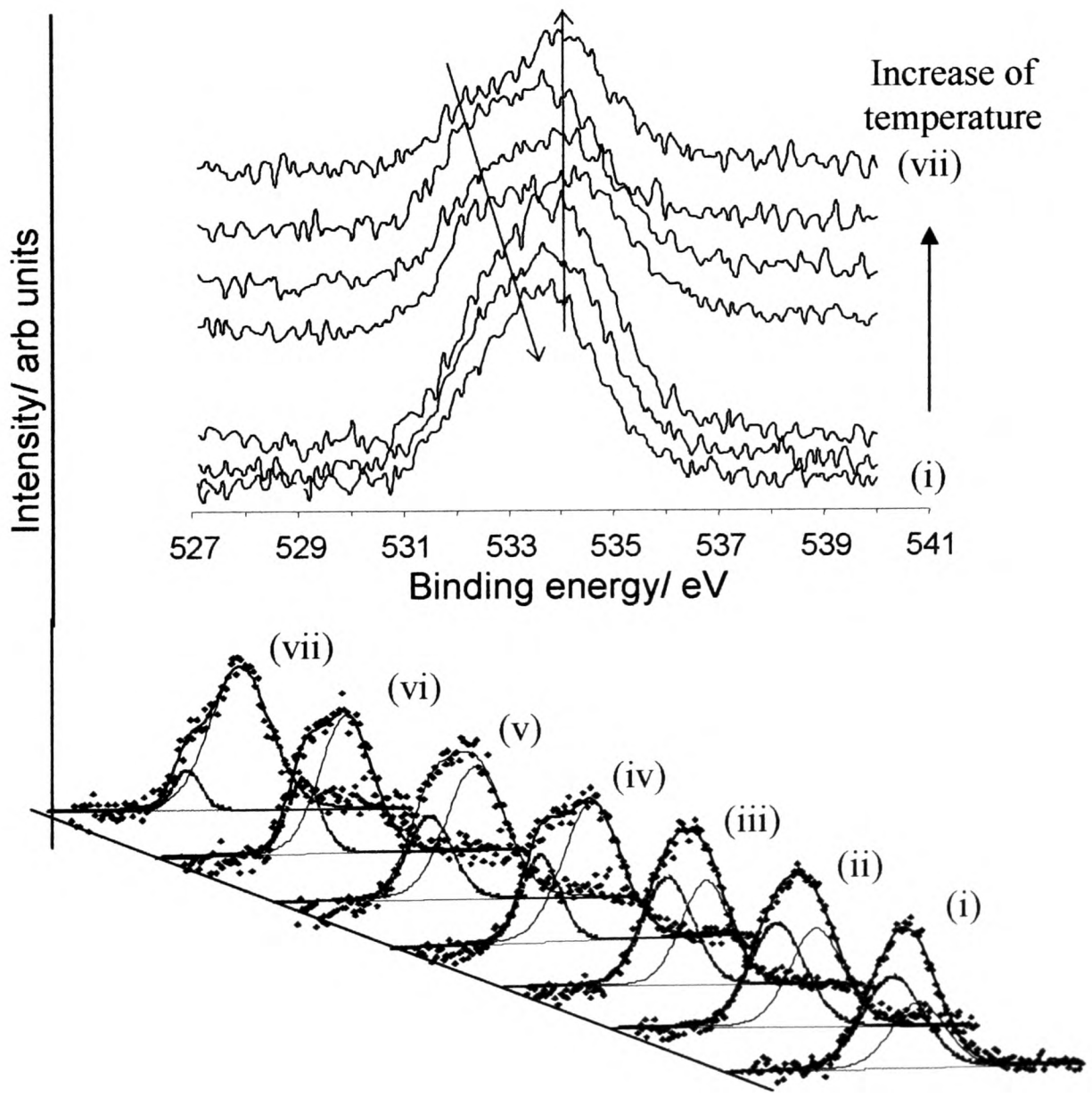


Figure 12. The 2250 L doses of activated oxygen, O_2 on the elevated substrate temperatures; (i) room temperature, ≤ 65 °C, (ii) 165 °C, (iii) 265 °C, (iv) 365 °C, (v) 465 °C, (vi) 565 °C, (vii) 665 °C*

TPD had also been performed with masses tuned at H_2, CO and CO_2 for surfaces dosed with oxygen at the elevated substrate temperatures. Figure 13 shows the TD comparison of the surface dosed for (a) O_2/H/diamond and (b) O_2*/H/diamond at different temperature, revealing the drastic decreases of H_2 desorption at 365 °C for (b), and more CO and CO_2 were desorbed from diamond surface dosed at lower temperatures. For O_2*/H/diamond, the desorbed CO peak (b ii) became broader as the substrate temperature was increased up to 365 °C, by which the desorbed CO peak feature is similar to O_2*/diamond (refer figure 6a). Comparatively, a much higher amount of CO_2 was being desorbed in (b) than (a) along with the oxygen dosing process.

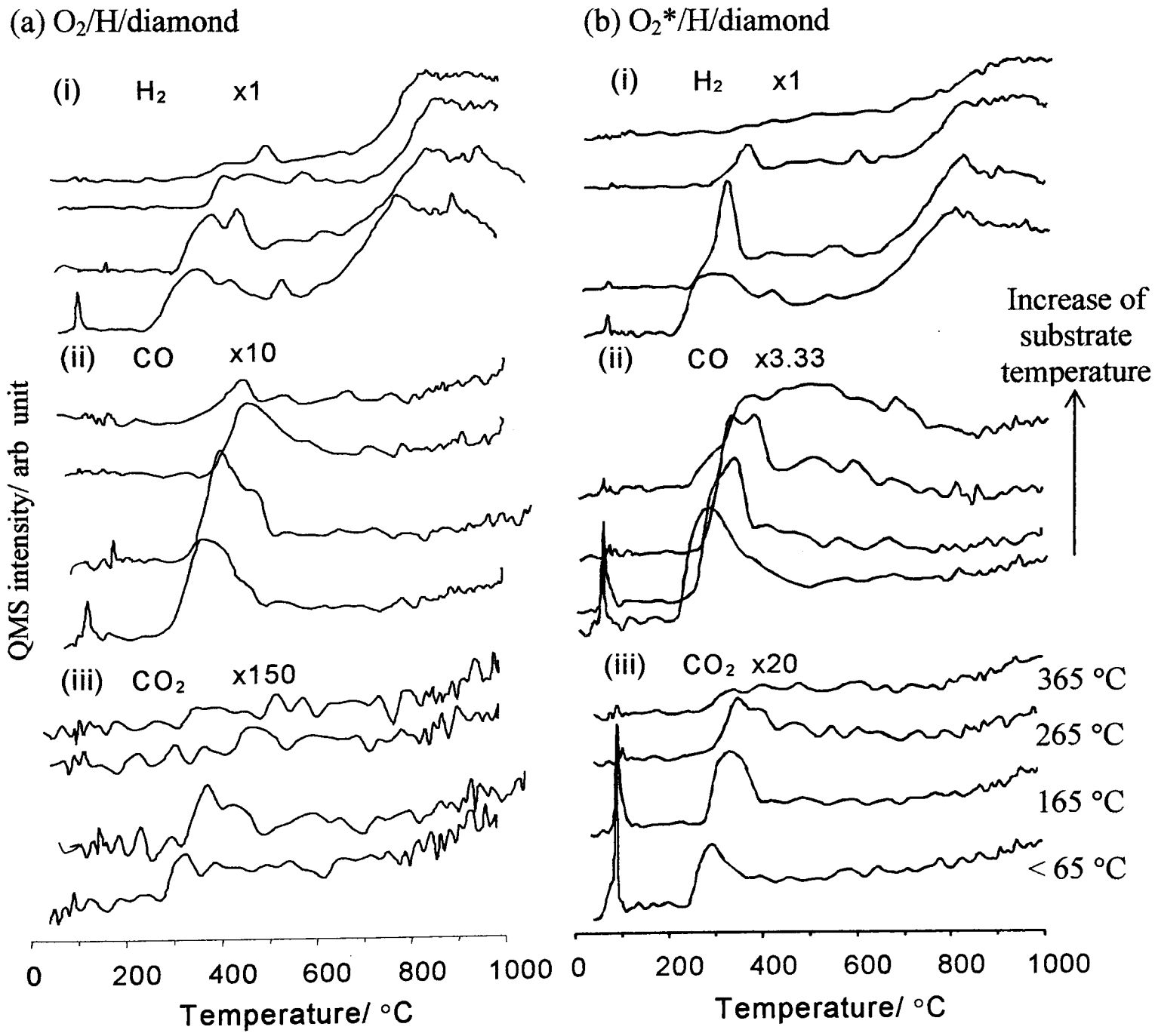


Figure 13. TD spectra recorded for (i) H_2 (2 amu), (ii) CO (28 amu) and (iii) CO_2 (44 amu) for the exposure of fully pre-hydrogenated diamond to 2250 L of (a) O_2 and (b) O_2, at the elevated substrate temperatures of ≤65 ℃, 165 ℃, 265 ℃ and 365 ℃*

The effect of substrate temperature on the thermal distribution of desorbed CO and CO_2 from the O exposed diamond is shown in figure 14. Interestingly, the desorbed CO and CO_2 peaks have shown different peak features after dosed at the elevated substrate temperatures. The products were desorbed at much higher desorption temperature with the increases of the substrate temperature while the dosing of atomic oxygen was carried out, suggesting different type of compositional oxygen were involved with the formation of a wide variety of oxygen functionalities. The desorption spectra is much different from the oxygen dosages at 300 K (was shown previously in figure 9).

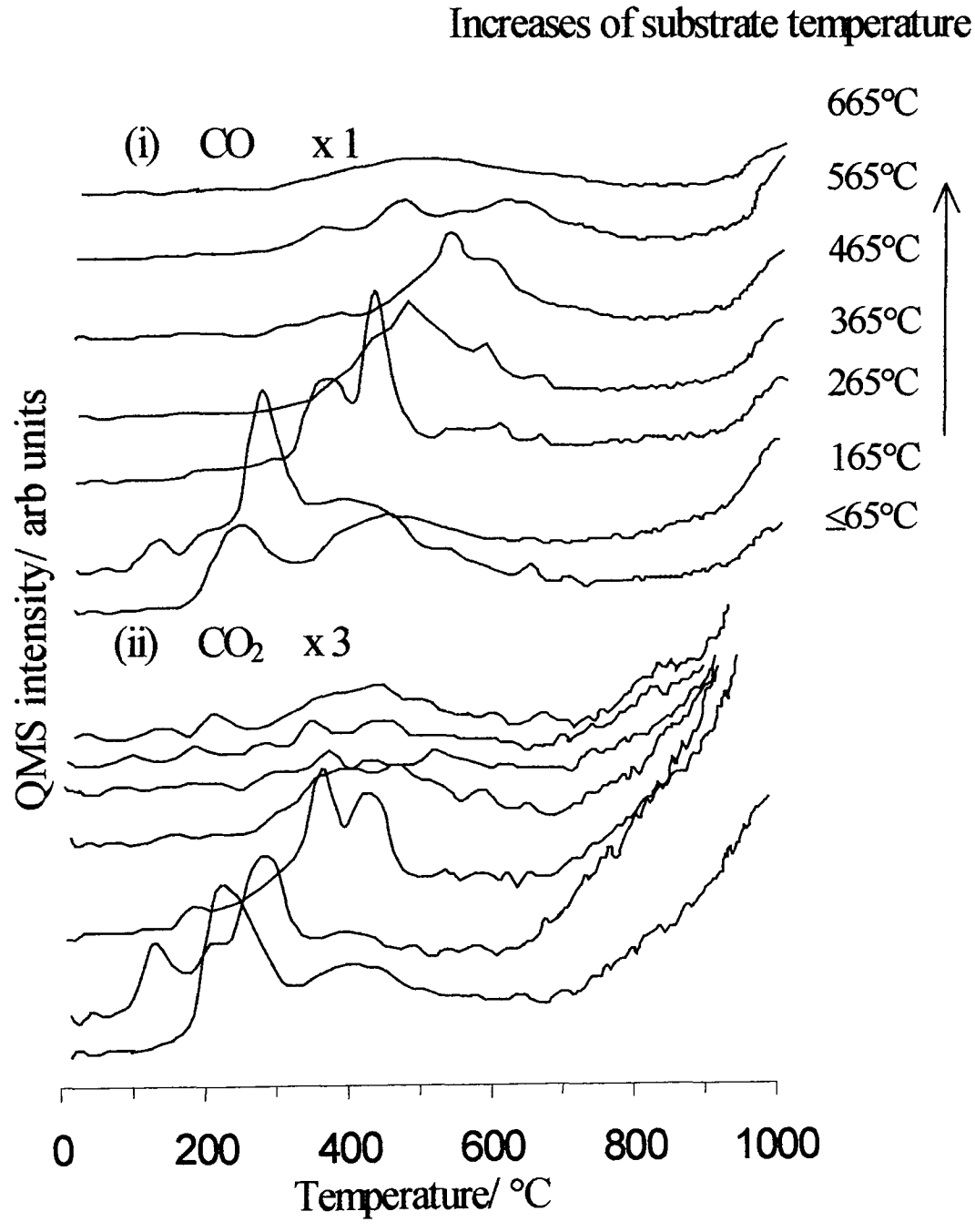


Figure 14. TD spectra recorded for (i) CO (28 amu) and (ii) CO_2 (44 amu) of O/diamond, following the exposure of clean diamond surface to atomic oxygen (2250 L) at the elevated substrate temperatures (from ≤ 65 °C to 665 °C)

5.3.2.3 Hydrogen Etching on Oxygenated Surfaces

Two types of oxygenated diamonds, O_2*/diamond (figure 15a) and O/diamond (b) were treated with atomic hydrogen at a pressure of 5 x 10^{-6} mbar. With increasing exposure to atomic hydrogen, both of the O 1*s* peaks positioned initially at 532 eV have shifted to 533.6 eV with their XPS intensities in decline. At the same time, C 1*s* peaks have shifted from ~ 283.1 – 283.5 eV to higher binding energy at ~ 284.5 eV.

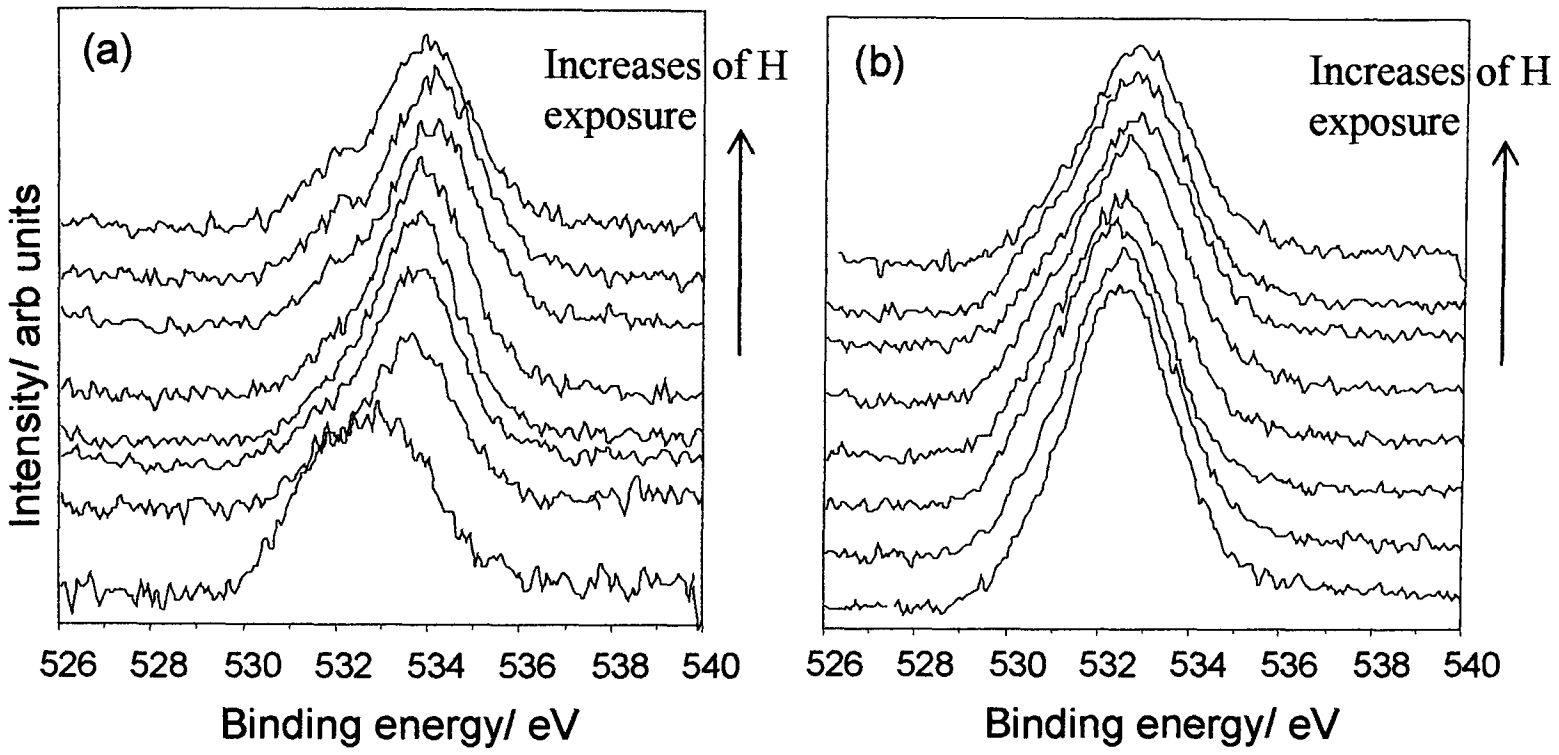


Figure 15. XPS of O 1s spectra as a result of atomic hydrogen (5 x 10^{-6} mbar) etching on (a) Ir-excited oxygen, O_2- terminated, and (b) dissociated atomic oxygen, O- terminated surfaces*

Figure 16 shows the declines of O 1*s*/C1*s* ratio after the oxygenated surface was etched by atomic hydrogen, with the decreases of nearly 30 % for O_2*/diamond and 22 % for O/diamond surfaces after the exposures to 3375 L of atomic hydrogen.

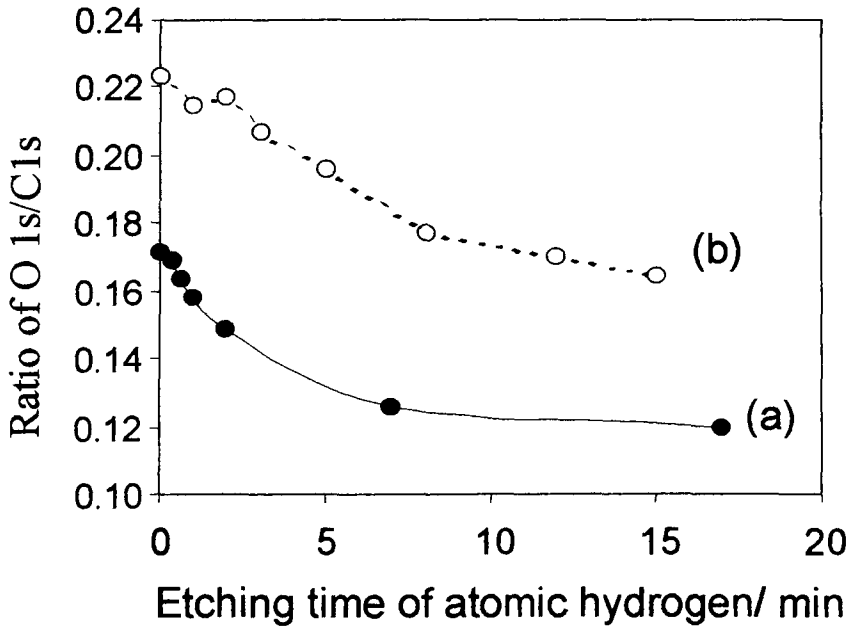


Figure 16. Plot of O 1s/C 1s ratios against the length of atomic hydrogen etching on oxygenated diamond surface, with
(a) O_2/diamond, and*
(b) O/diamond

The QMS was also tuned to record signals corresponding to the etching of atomic H on surface oxygen, arising from the spontaneous desorption from the diamond surface at 300 K. Figure 17 shows that the time evolution of the main scattered resultants includes water, CO, CO_2 and OH signals while the diamond was faced to the atomic hydrogen beam. At short hydrogen pretreatment time (for $t < 40$ s), the surface yielded predominantly CO and CO_2. For longer etching period ($t \geq 40$ s), the yield of water and OH increased until it reached the saturation level at $t \sim 300$ s. During the same period, the amount of CO and CO_2 decreased. The cracking pattern (in inset) suggests the possibility of OH being derived from the fragmented H_2O, as the experimental intensity is similar to the theoretical value.

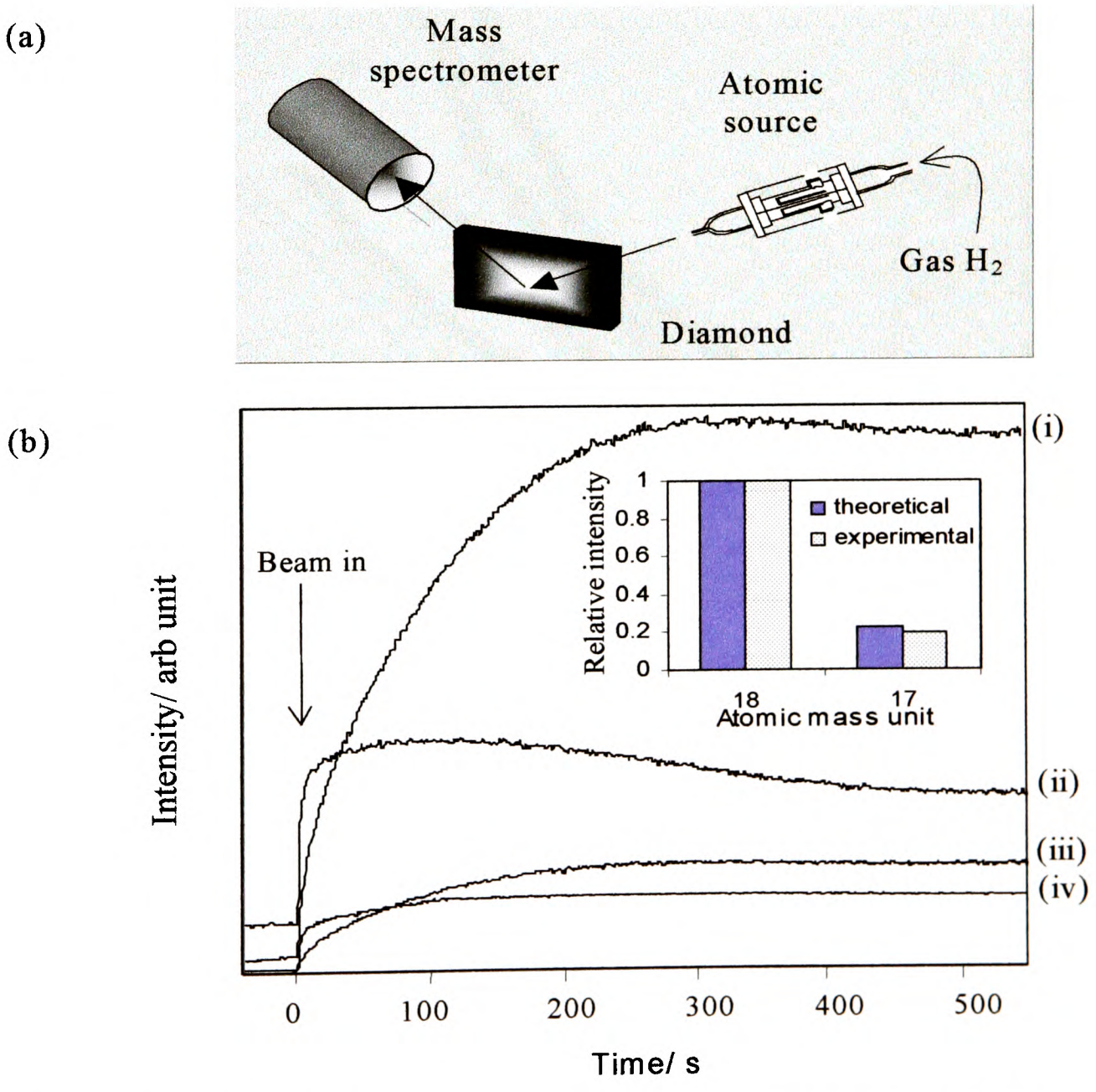


Figure 17. (a) The schematic diagram showing the on-spot measurement of the desorbants by QMS spectrometer, and (b) the QMS time evolution signals acquired from the exposure of oxygenated diamond surface to atomic hydrogen (with the admittance of atomic beam at 0 s) at 300 K; (i) H_2O^+ (18 amu), (ii) CO^+ (28 amu), (iii) OH^+ (17 amu) and (iv) CO_2^+ (44 amu); inset of figure (b) shows the comparison of theoretical and experimental data for water cracking patterns

5.3.2.4 Effect of Thermal Annealing on Oxygenated Surfaces

The thermal stability of the different oxygenated surfaces was examined. Samples were prepared as before by exposing both hydrogen-saturated and hydrogen-free surfaces to the saturation dose of oxygen at 300 K. The sample was heated rapidly to the successive increases of temperatures, and was later cooled down to room temperature before the coverage was monitored by XPS. The data is illustrated in figure 18 as a function of the maximum annealing temperature. The trends of the desorption curves were consistent with the TPD spectra as presented in figure 6.

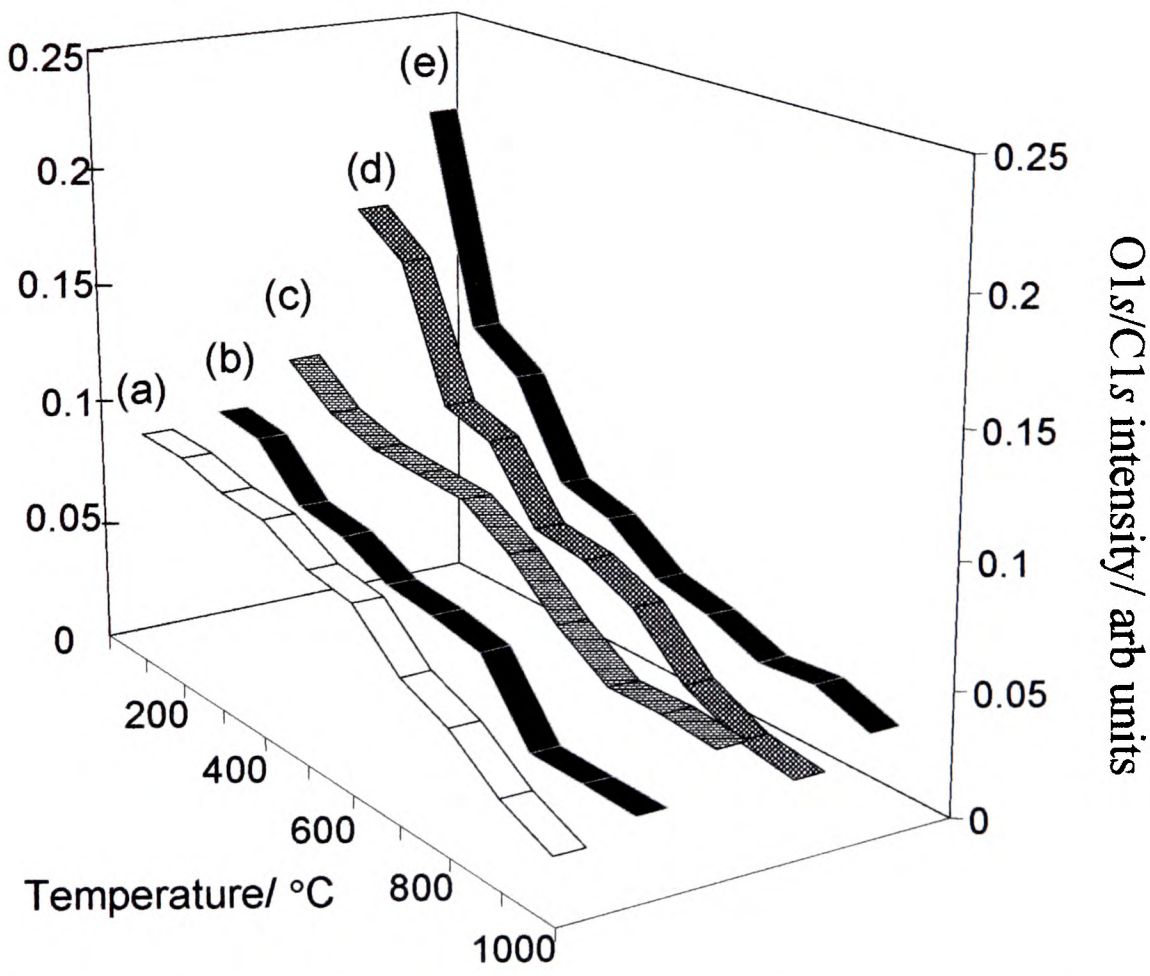


Figure 18. XPS signal intensity of O 1s/C 1s ratio versus annealing temperature for the surfaces of (a) O_2/diamond, (b) O_2*/H/diamond, (c) H/O/diamond, (d) O/diamond and (e) O/H/diamond*

The O/H/diamond (e) surface shows a drastic decrease for oxygen coverage below 200 °C, which was more apparent than the decrease for the O/diamond surface (d). Similarly, an earlier decrease in O1*s*/C1*s* was observed for the O_2*/H/diamond (b), as compared to O_2*/diamond surface (a). The H/O/diamond (c) however, shows greater thermal stability up to 500 °C by which the other oxygenated systems have already suffered from the sharp declines in O1*s*/C1*s* ratio down to 0.05.

5.3.3 Discussion

Despite the interest in the interaction of oxygen with diamond surfaces, the number of detailed studies on diamond materials other than powders are relatively few. Thomas *et al.* [28] studied the interaction of Ir-excited oxygen with a hydrogen-free diamond (100) single crystal, and observed rather broad thermal desorption traces due to CO evolution in the temperature range 400-800 °C. Hossain *et al.* [34] have also studied a similar system, and observed the formation of ether and carbonyl species, which desorb as CO near 800 °C. In the sense that the reaction probability of thermal O_2 is very low, that the reaction probability of Ir-excited O_2 is significantly higher and that the adlayers formed are relatively stable thermally, it seems clear from the present work that the reactivity of CVD diamond to O_2 is fairly similar to that seen for well-ordered single crystals.

It is notable that a much higher surface coverage can be achieved by using atomic oxygen compared to that obtained using the Ir filament, showing that more sites become reactive to atomic species compared to the electronically excited molecular entities produced by the Ir filament. Much of the oxygen accommodated on the surface is significantly less thermally stable, however, desorbing below 200 °C. It is also notable from figure 6 that, whereas CO is the main thermal desorption product at high temperature for low O surface concentrations, the product switches to CO_2 at these high oxygen coverages obtained using the atomic O beam. The three feasible desorption products expected for adsorbed oxygen are O_2, CO, and CO_2, with a thermodynamic stability ascending in this order. However, in high vacuum desorption experiments, it is the kinetic product which is formed. Spectroscopic data suggests that the main O species which dominate at low coverage are bridge-bonded C-O-C ether linkages and 'on-top' C=O carbonyl forms [44] where essentially no C atom is likely to be bonded to more than one O atom. Surface migration is thus needed to form the intermediate local structural forms leading to CO_2 desorption. At high surface oxygen coverage, C atoms are much more

likely to be bonded to two O species, such as carboxylate and carbonate compounds, so the switch to the thermodynamically more stable desorption product is not unexpected.

(i) "Bound forms of oxygen"

Different spectra in O 1*s* were observed as the coverage and the dosing temperature are changed. This is attributed to the complicated distribution of differing chemical forms of oxygen on diamond surface. XPS studies on well-defined polymer systems [45,46] show that isolated carbonyl and ether linkages display very similar chemical shifts to our results, where as significantly wider binding-energy ranges are expected if functional groups, such as ester, anhydride and carbonate groups, are also present.

Our data on O 1*s* shows a deconvoluted peak is apparent at higher binding energy at high dosing temperature or at high oxygen dosages. XPS O1*s* peak at higher binding energy (denoted as B in figure 11) begins to dominate the peak area around 270 °C for both environments of O_2*- or O_2*/H/diamond. The related O 1*s* peaks for O dosing also show the oxygen species at higher binding energy (figure 11, 12) dominates the surface throughout. XPS chemical shifts [42] shows that O 1*s* for ether-like (*i.e.* O=C-**O**R or C-**O**-C-**O**-C) is located at high binding energy ~ 533.4 eV whereas carbonyl compounds (*i.e.* C=O) is positioned at 531.7 eV, so the implication is that high temperature dosing or dosing using the atomic O source tends to produce ether type rather than carbonyl type species. This is similar to the previous reports [34], revealing the presence of carbonyl, ether and hydroxyl groups on the surface, with carboxylate and multiple ether linkages dominating at higher coverage. However, theoretical studies suggested that on-top carbonyl groups are more thermodynamically stable and favourable at temperature higher than 600 K due to an increase in entropy [35,47]. There is thus clearly some discrepancy between results and theory, possibly due to the involvement of kinetic factors.

The sticking coefficient for molecular oxygen, O_2 is very low, even with longer exposure period. There is small amount of CO and insignificant CO_2 detected in TPD signal (see figure 13a), which is concurrent with the published results [48]. This would suggest that the chemisorption of molecular oxygen on diamond surface does occur, probably involving dissociative adsorption, in view of the failure to observe molecular oxygen desorption. Two different mechanisms that could possibly be expected for molecular oxygen adsorption on the π carbon bonded chains of the freshly annealed un-reconstructed diamond surface [39] are through direct dissociative adsorption (eqn 1) and molecular precursor-mediated adsorption (eqn 2) (see figure 19). Equation 1 shows that an oxygen molecule dissociates on the diamond surface, and the oxygen adatoms occupy available adsorption sites. For the equation 2, the peroxylike O-O bridge bonding could be formed in three ways [49]; either on-top sites (oxygen molecules are positioned above dimers with O-O bonds parallel to the dimer C-C bonds), in-between sites (oxygen molecules are positioned between dimers of adjacent rows with O-O bonds parallel to the dimer C-C bonds) or perpendicular sites (oxygen molecules are positioned between dimers of the same row with O-O bonds perpendicular to the dimer C-C bonds).

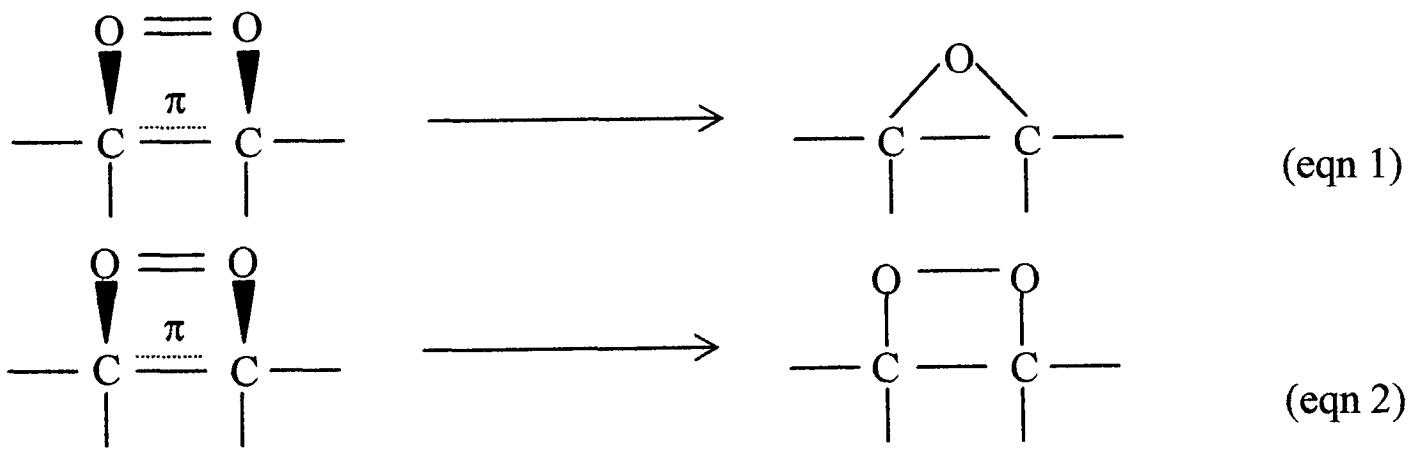


Figure 19. Chemisorption mechanism of molecular oxygen on π carbon

This type of molecular precursor bonding has widely been observed for Si(111) surface using STM and photoelectron spectroscopies [50,51,52] and HREELS and XPS [53].

However, these molecular oxygen precursors on diamond surface are unstable even at 300 K, and would rapidly convert to on-top configuration, which are more thermodynamically stable within hundreds or even tens of femtoseconds [47].

Excited oxygen, O_2* is expected to etch and break through the top layer of C-C dimers, which then form the relatively larger amount of oxygen related groups, such as carbonyl and ether groups on the surface. These two major functional groups are reported to co-exist under typical room temperature with the reference to theoretical studies [39,47], and the disordered configuration of LEED pattern [34,54]. On-top oxygen is reported to have lower desorption barrier than the bridge form [28], suggesting that the desorption pattern will cover a wide range of temperature. This can explain why the temperature coverage for CO desorption is wide (figure 6a,e), with the slow decline of O1*s*/ C1*s* ratio in temperature flashing spectra (see figure 18).

The increased amount of the desorbed CO_2 in TPD results when dosed with O suggests that atomic oxygen, O would penetrate into sub-surface carbon layer at the diamond surface and incorporates into back-bonds of the π-bonded carbon chains. With the combination of dangling bond oxidation, this would further lead to the formation of carboxylic (-(CO)O-) and lactone (CO(O)CO) species on the diamond surface, which thermally decompose producing CO_2 [30,44]. A high degree of oxygenation, as reported [35] can also roughen the diamond surface by creating reactive new sites at edges or defects by which carbon atoms with unsatisfied or strained bonds can more easily double-bonded to oxygen, again producing very oxidised centres. Lower desorption in TPD for atomically oxygenated diamond is due to the decrease in chemisorption energy on the high oxygen-saturated surface by repulsion between on-top oxygen atoms and by the stretching C-O bonds. As shown in figure 14, there is a series of CO and CO_2 desorbed peaks shift to higher temperature desorption with the increasing dosing temperature. This suggests

that higher temperature deposition allows the formation of higher form of oxidation species with higher activation energy, which desorb at higher temperature.

(ii) Effect of prehydrogenation

The exact nature of the oxygen reactive sites on diamond remains unclear. One obvious potential explanation, in view of the analogous situation seen with Si, is that the hydrogenated surface is inert, and that reaction occurs at sites where vacancies exist in the hydrogen adlayer. However, this does not appear to be correct, since we actually observe that the uptake of oxygen on the hydrogen-free surface is slower than on the hydrogenated surface, as has also been noted previously for other electronegative adsorbates [55,56]. Theoretical studies have also predicted that adsorbed hydrogen is capable of promoting O uptake [39,47]. One aspect to consider here is that it is well known that hydrogenation treatments can change the morphology of diamond surface, so an explanation of the enhanced reactivity would be that the hydrogenation used here essentially roughened the surface, thus leading to more surface sites on which oxygen can adsorb. This is, however, unlikely to apply in the present instance, since we used hydrogen exposures of the order of single monolayers, very much less than those needed for morphology changes, and the sample seemed to have a time-independent morphology, in that reproducible results would be obtained by alternating oxygen dosing on the hydrogen-free or hydrogenated surface. Attempts to inhibit the slow adsorption of oxygen by improving the level of hydrogenation are therefore unlikely to be successful, especially as we note that hydrogen is actually removed from diamond when exposed to 'excited' oxygen.

TPD in figure 7 and 8 show that when the diamond is dosed with O_2* or O, the hydrogen concentration drops. This would suggest that the main underlying mechanism for oxygen adsorption is through the abstraction by H rather than coadsorption. The rate of oxygen adsorption on hydrogen terminated diamond surface is higher than on clean

surface. This can deduct that pre-hydrogenation on freshly annealed π-bonded clean surface creates more readily active sites for the impinging of oxygen. The clean surface is probably more "inert" to oxygen adsorption due to the stabilisation of the surface by the π-bond reconstruction. Hydrogen preadsorption on clean diamond will disrupt the π-bonding and, when oxygen is dosed on this hydrogen-terminated surface, hydrogen will be abstracted with the emergence of dangling bonds, where by the adsorption rate on such sites is much faster than on the reconstructed π-bonded surface.

We observed lower temperature desorption from oxygen on H/diamond than on clean diamond. The result is surprising since the hydrogen should be removed. Therefore, the presence of hydrogen must either modify the surface or inducing different adsorption mechanism, which will produce slightly different adsorbed layer.

(iii) Hydrogen etching on adsorbed oxygen

Surface oxygen on diamond surface can be etched away by hydrogen, though only a small amount of oxygen can be removed. With regard to the time evolution QMS spectra in figure 17, different gases are desorbed as the major species at different periods, which would suggest different reaction channels are involved. The surface reaction was most probably initiated with the direct etching *via* decomposition of carbonyl or ether group to give CO as the major product and of the carboxylic (or lactone) group to give CO_2 (minor product), followed by the adsorption of hydrogen on the unstable surface carbon atoms (in eqn 3). When the amount of weakly oxygenated bonds was decreased, this etching process was then replaced by indirect conversion of hydroxyl groups (as the reaction intermediate) to water (eqn 4 and 5).

$$C_x\text{—}O\,(ads) + H\,(g) \longrightarrow C_{x-1}\text{—}H\,(ads) + CO\,(g)\ (\text{or } CO_2\,(g)) \qquad \text{(eqn 3)}$$

$$C_x\text{—}O\,(ads) + H\,(g) \longrightarrow C_x\text{—}OH\,(ads) \qquad \text{(eqn 4)}$$

$$C_x\text{—}OH\ (ads) + H\ (g) \longrightarrow C_x\bullet\ (ads) + H_2O\ (g) \qquad \text{(eqn 5)}$$

$$C_x\bullet\ (ads) + H\ (g) \longrightarrow C_x\text{—}H\ (ads) \qquad \text{(eqn 6)}$$

These possible pathways are supported with the results of EELS [34] and FTIR-DRIFT [30]. The appearance of the 104, 152 and 362 meV losses in EELS accompanied by the disappearance of the 215 meV loss suggested that O in the carbonyl was replaced by the atomic H. From the IR investigation [30], the increase of peak intensity for C-H stretching vibrations (2875-2895 cm^{-1}) paralleled the decrease of that of C=O stretching vibrations (1600-1800 cm^{-1}), suggesting that the adsorption of hydrogen proceeded simultaneously with the elimination of oxygen on diamond. Another possible mechanism involved is the reduction of carbonyl by hydrogen molecules or atoms to aldehyde group (-CHO) and further reduction would produce an alcoholic OH group (-CHOH).

After atomic H bombardments, the XPS O 1*s* binding energy has increased and broadened up to 533.6 eV (figure 15), suggesting that the surface is comprised of such different O-surface groups by comparing to the reported XPS data of O-containing polymers [45]. The unsaturated dangling bonds created *via* the elimination of the OH group would further be substituted with C-H groups (eqn 6).

As compared to other O-terminated surface, the H/O/diamond has shown relatively better thermal stability over 500 °C, as revealed in figure 18c. This would be attributed to the consequence of polarization of adspecies between hydrogen and oxygen atoms, forming the weak attraction, rather than repulsion interaction, which exists among carbonyl/hydroxyl or ether/hydroxyl groups [47,49].

(iv) Implications on photocathode

When operated in imperfect vacuum conditions, oxygen adsorption through interaction with dissociated or electronically excited oxygen produced during *uv* radiation must also be taken into account. The rate of uptake of oxygen by the surface increases massively when the dosing gas is electronically excited by an Ir filament, or dissociated to produce atomic O. Simple estimates of the apparent reactive sticking probability can be made from the uptake curves plotted by correlating the gas exposures used with the surface concentration of oxygen achieved. This indicates the sticking probability arises from approximately 10^{-5} for thermal O_2 adsorption on the hydrogenated surface, up to approximately 10^{-3} for the interaction with the atomic beam, although the degree of dissociation in the beam is significantly less than 100 %, so this is likely to be an underestimation. These reaction probabilities are still significantly less than unity, but nonetheless indicate that some care needs to be taken to keep the gas phase concentration of 'excited' oxygen species low, if stable photocathode operation is to be observed over an extended period. High concentrations of surface oxygen are relatively thermally unstable on the diamond surface, as illustrated in figure 18, suggesting that some other alternative strategies to prevent surface build-up of bound oxygen forms could be to operate the photocathode at higher temperature.

5.3.4 Conclusion

The surface reactivity of CVD diamond films with molecular (O_2), electronically excited (O_2*) and atomic (O) oxygen has been explored. The surface reaction probability with oxygen on CVD diamond films is proportional to the maximum extent of adsorption, showing low, but measurable reactivity with O_2; which increases markedly with electronically excited O_2* to form dilute oxygen adlayers; and rises to a maximum for atomic O. CO is the major desorbed species at low oxygen coverage, and more CO_2 is

evolved with increasing oxygen coverage. The desorption temperature shift from 800 K for low oxygen coverage to below 500 K for highly oxygenated surface.

The adsorption pattern for oxygen on CVD diamond thin films is similar to single crystal diamond. XPS shows a mixture of carbonyl and ether compounds at low oxygen coverage and at 300 K, but reveals more carboxylate and multiple ether linkages at high oxygen coverage and high temperature dosing, evidenced by the broad tailing features of C 1*s* at high binding energy.

The exact properties of the oxygen diamond adlayer changes with the adsorption temperature or pre-hydrogenation, probably due to the formation of a complex distribution of differing surface species. Greater surface reaction probabilities are observed if the diamond surface is pre-hydrogenated before the interaction with oxygen, probably through the hydrogen abstraction by oxygen, followed by the rapid adsorption on the dangling bonds, which would facilitate the oxidation of diamond surface.

Hydrogenation on an oxygenated diamond surface induces direct decomposition of O-containing groups and the formation of OH radicals, forming H_2O at 300 K. Only some of surface oxygen can be removed by hydrogen etching, producing mainly CO (short term period) or H_2O (long term period), which suggests different reaction channels are involved.

The performance of diamond photocathodes (and other diamond electron emission devices) is generally degraded by adsorbed oxygen, which raises the electron affinity. The present work shows that adsorption of molecular oxygen to produce such an effect is slow, but such processes will occur in the presence of excited molecular or atomic oxygen. Furthermore that prehydrogenation of the diamond surface is very ineffective at inhibiting such processes.

5.4 Lithium Adsorption Chemistry

5.4.1 Previous Work

The previous research carried out on lithium adsorption on diamond surfaces is relatively few compared to the other elements in alkali metal group. Most of the research, practically or theoretically, has focused on the incorporation of lithium in order to form n-type diamond [57,58]. However, the studies on Li have widely been reported for other III-V semiconductors, such as Si, GaAs, GaP, InP and InSb for emission, channeling and blocking purposes [59]. These results showed that the Li can interact strongly with additional defects in semiconductors due to its positive charge, leading to a tendency to be preferentially embedded with negative defects or even with neutral defects such as oxygen. Other studies of Li adsorption have also been performed on various substrates, such as Ru [60], Al [61,62], graphite [63] and chitosan-based film [64].

The alkali-induced promotion of subsequent adsorption of gases on diamond is usually attributed to an increase in the rate of dissociative gaseous adsorption, which can be characterized by a rapid increase in the initial sticking coefficient as the alkali coverage increases [65]. It is commonly recognized that the dissociation of the molecules such as O_2 near a metal surface is affected by filling the antibonding $2\pi^*$ orbital. Local electrostatic fields in the vicinity of partly ionized alkali adatoms can facilitate the proper positioning of the affinity level below the Fermi energy. Whereas, Li adatoms on diamond surface are expected to have noticeably smaller dipole moments in comparison with other alkali adsorbates due to the relatively small size and effective charge.

Salts of Li^+ are exceptionally stable owing to their very high lattice energies. LiH is stable to approximately 900 °C. Li is uniquely reactive to N_2 give a stable ruby-red crystalline nitride, Li_3N. When heated with carbon, Li can react to form the acetylides Li_2C_2. Li reacts with O_2 to form the oxide, Li_2O, with only a trace of Li_2O_2 and LiO_2, whereas the other alkali oxides, M_2O, react further giving as principal products the

peroxides, M_2O_2, and (from K, Rb and Cs) the superoxides, MO_2. Li can react with NH_3 to form $LiNH_2$ and Li_2NH_2.

Li is expected to have shallow donor level with an activation energy of 0.1 eV [66] or to be fully ionized when incorporated interstitially in diamond [67]. Experimentally, three different techniques have been applied to incorporate lithium in diamond; (i) ion implantation, (ii) *in-situ* doping during chemical vapour deposition, and (iii) in-diffusion.

The purpose of this section is to investigate the interaction of lithium with diamond to establish how its behaviour compared with that of other alkali metals. The interaction of the adsorbed Li with other gases, such as H_2, O_2 and NH_3 is also examined. Comparison was made between Li adsorption on boron-doped polycrystalline and undoped homoepitaxial diamond.

5.4.2 Results

5.4.2.1 Adsorption of Li on Diamond Surface

Figure 20 shows the comparison of TPD spectra for Li dosed (20 min) onto (i) clean, (ii) H-covered, (iii) oxidised and (iv) aminated diamond surfaces. The clean diamond surface was prepared by annealing the surface gradually up to 1000 °C for 20 min in order to remove residual carbon, hydrogen and oxygen species from the sample. Diamond was hydrogenated and oxygenated by using the atomic beam source or was aminated by dosing the surface over the incandescent Ir filament in NH_3 ambient. All of these gaseous treatments were performed under the pressure of 5×10^{-6} mbar for 10 min. The diamond surface that pretreated with hydrogen, shifted the thermal desorption of Li to much lower temperature around 350 °C and a minor peak was observed at 1000 °C. Li desorbed from the oxidised surface at a wide range of temperature around 500 °C. The desorption of Li from the aminated diamond occurred at 700 °C. For Li dosed on clean diamond surface, Li desorbed mostly at high temperature ~ 950 °C, with a minor desorption peak at 700 °C.

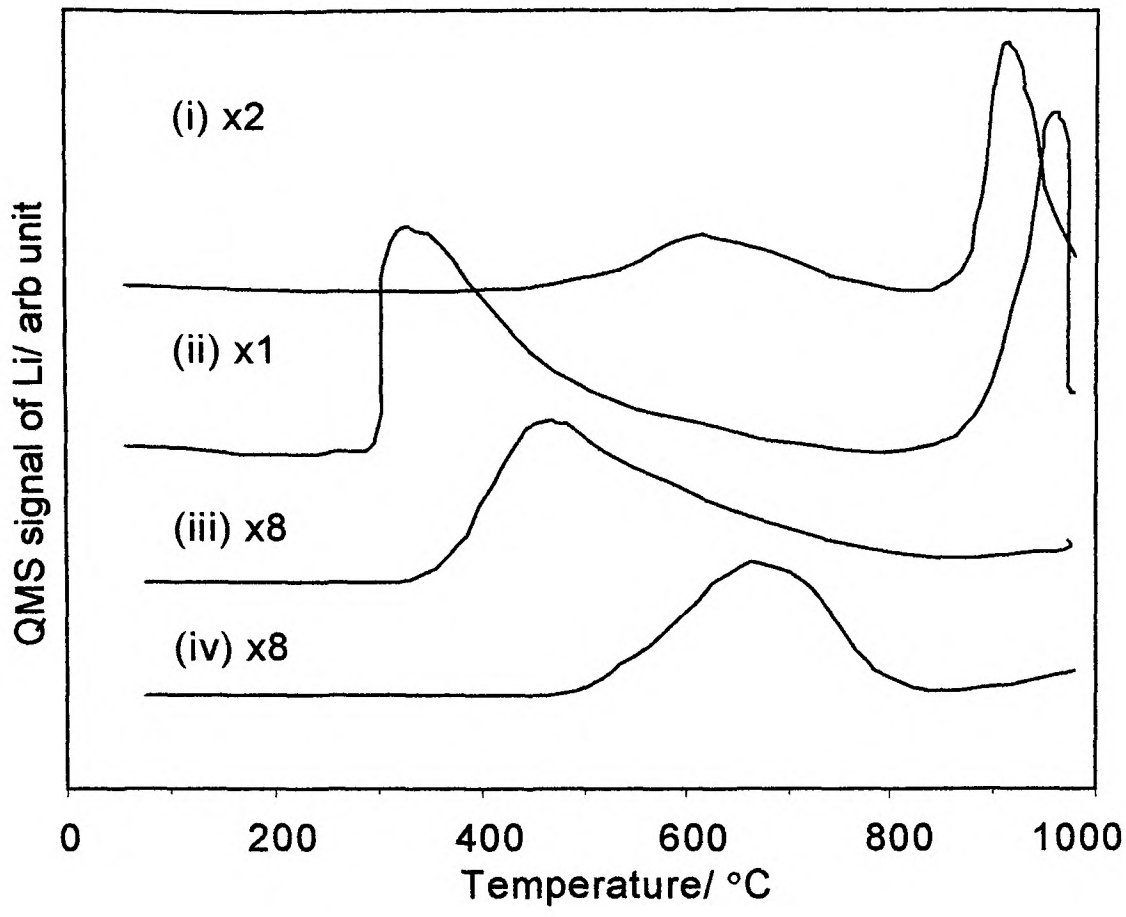


Figure 20. TD spectra of Li^+ (7 amu) from the Li dosed (20 min) onto pretreated polycrystalline diamond surfaces; of (i) clean, (ii) hydrogenated, (iii) oxygenated and (iv) aminated

From a plot of area *versus* the period of Li dosage shown in figure 21, Li tends to deposit most quickly at the hydrogenated surface, as measured by the desorption signal. This is followed by the linear increase of Li uptake on the clean diamond surface (b). Both of the pretreated diamond surfaces with oxygen plasma (c) and dissociated NH_3 (d) do not show as rapid increases of Li uptake as compared to the others.

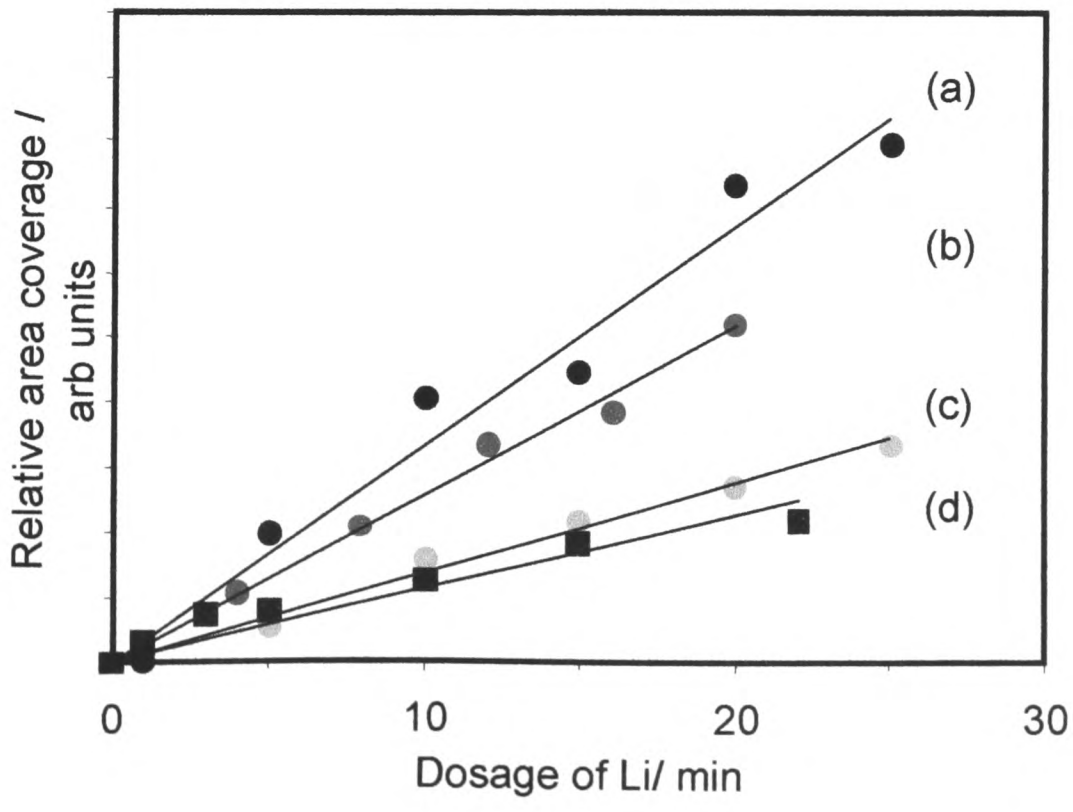


Figure 21. The Li uptake plots on different pretreated diamond surfaces, measured by using QMS-TPD method;
(a) hydrogen plasma
(b) clean diamond
(c) dissociated ammonia over Ir filament
(d) oxygen plasma treated

5.4.2.2 Depth Profiling of Li Adsorption

The polycrystalline diamond shows no changes of the surface morphology after the experimental procedures were conducted in the UHV chamber. However, the sample shows deep greyish region in the centre of the sample. To investigate further, SIMS depth profiling was carried out and the result is shown in figure 22. Due to no possible reference available, it is difficult to convert the ion yield into the term of concentration, atom cm^{-1}. Therefore, the concentration used here is represented by the ion yield as the received data. It appears that a high concentration of lithium has been embedded in the diamond sub surface (up to ion yield of $10^3/^7$Li as compared to 5 x $10^5/^{12}$C). The concentration of lithium is gradually decreasing to an ion yield of 10 at a depth of 0.2 μm, and is leveled off at a depth of 0.4 μm with the nearly non-existence of Li, which is comparable to the reported Li diffusion depth of ~ 0.5 μm by Popovici *et al.* [68] and Enckevort *et al.* [57]. From the profile, however there appears to be a significant increase in the ^{7}Li signal at the silicon substrate/CVD diamond interface at a depth of 1.0 μm. After profiling the sample with another form of charge compensation, this amount varied slightly between the techniques. Therefore, probably Li was pushed back into the sample while profiling by some means of charge-induced migration. This behaviour was reported for the migration of Na in SiO_2 film at increasing sample temperature during SIMS depth profiling [69,70], which was proposed due to the defects in the film. Although there may well be an increased amount of Li at the diamond/Si interface, this charge induced migration will in turn lead to some over estimation as to the amount of Li really present at the interface.

Theoretically, a very low solubility of lithium is predicted in the diamond [71,72] due to the high rigidity of the bulk lattice. Therefore, high temperature annealing is required for effective lithium diffusion [73]. Due to the ramping to high temperature for numerous TPD measurements, lithium is expected to diffuse into the diamond *via* an *in-diffusion* process.

From the concentration profiles, the diffusion coefficient for lithium in polycrystalline diamond can be obtained using the penetration theory [74], which is described by Fick's second law of diffusion;

$$\frac{\partial [Li]}{\partial t} = D\left(\frac{\partial^2 [Li]}{\partial x^2}\right) \qquad \text{(eqn 7)}$$

where $[Li]$ is the concentration of the diffused lithium atoms, t is the diffusion time, D is the diffusion coefficient and x is the depth below the surface. The solution of this equation for a surface source of impurities, which diffuse into a semi-infinite crystal is;

$$[Li] = [Li]_0 \times \left(erfc\left(\frac{x}{(4Dt)^{1/2}}\right)\right) \qquad \text{(eqn 8)}$$

where $[Li]_0$ is the concentration at the surface and *erfc* stands for the complementary error function. From this solution, the diffusion coefficient can be obtained by considering the tangent at $x = 0$ (at the surface). This tangent intersects the x-axis (*i.e.* [Li] = 0) at $x = (\pi Dt)^{1/2}$, the so-called penetration depth.

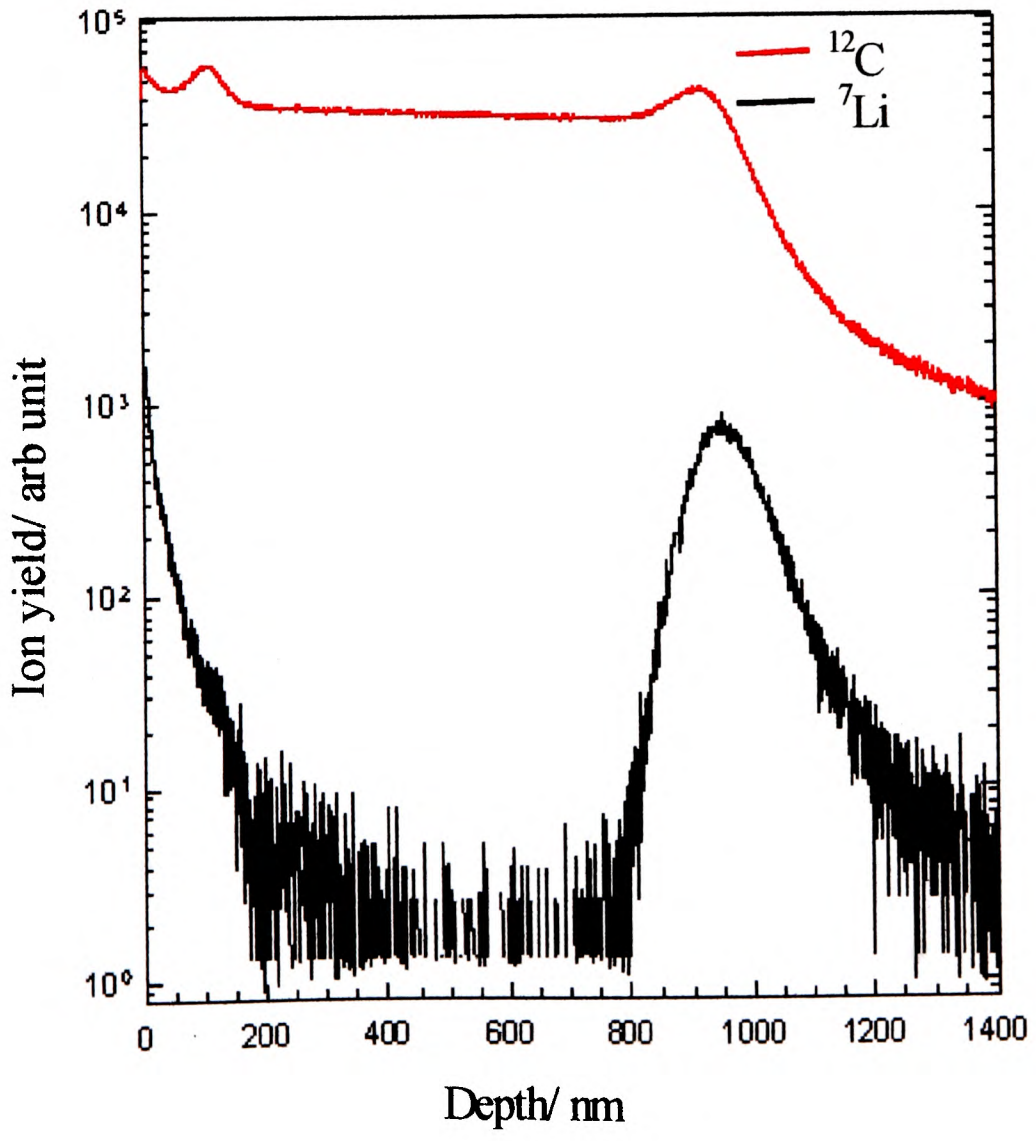


Figure 22. SIMS (1 keV) profile of Li on polycrystalline diamond with electron gun charge-compensation

From the Arrhenius plot of the lithium diffusion coefficient in diamond [57], the D_{Li} at 800 °C is nearly 5 x 10^{-14} cm^2 s^{-1} and with a total diffusion period of 2 hours, the predicted x depth profile is ~ 336 nm, which is quite in good agreement with the experimental data.

5.4.2.3 XPS Investigation

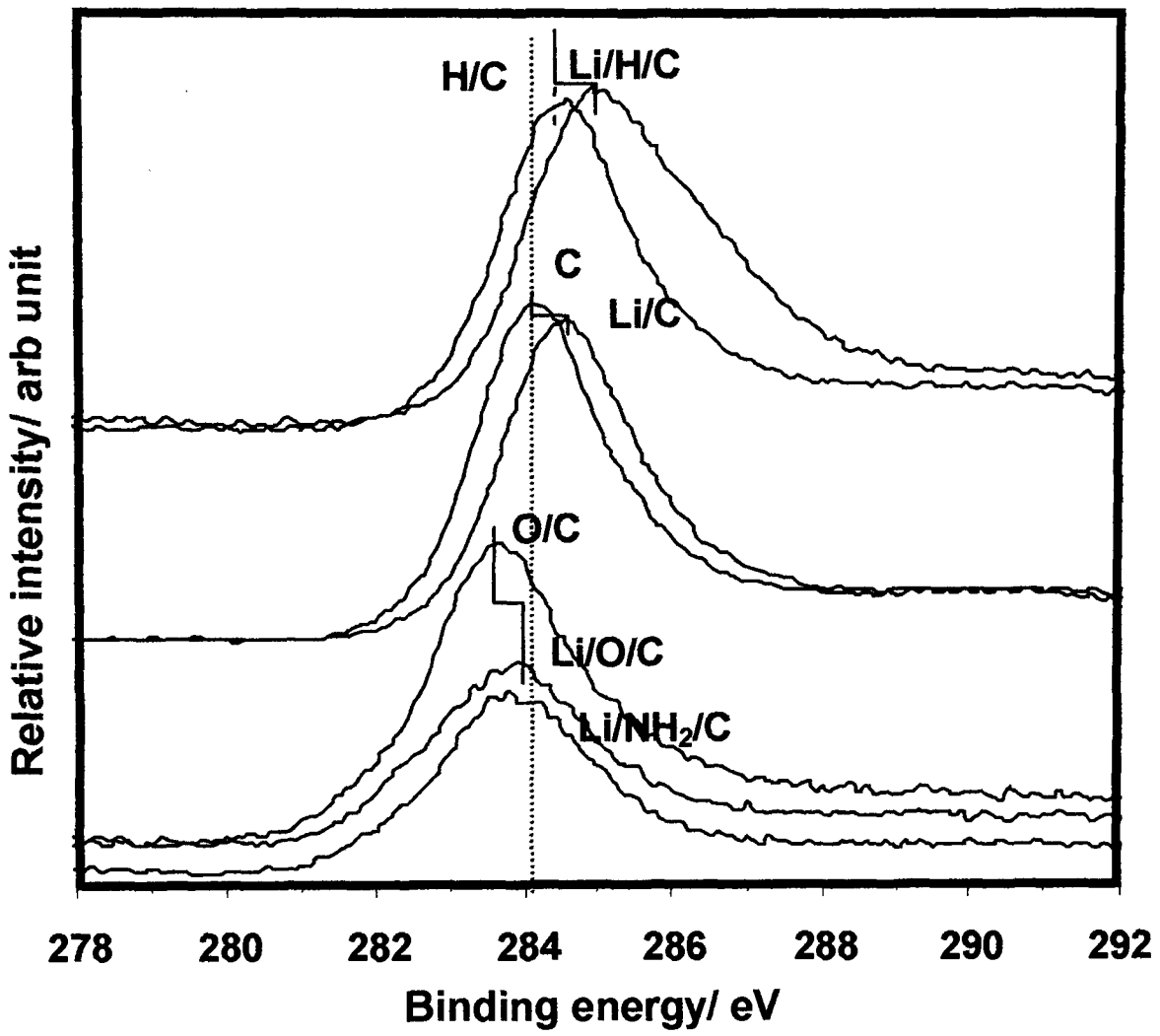


Figure 23. XPS C1s peak for different treated surfaces of polycrystalline diamond; the line positioned at 284.1 eV is for C 1s of the clean diamond, C (H = hydrogen plasma treated, O = oxygen plasma treated, NH_2 = treated with dissociated NH_3 or aminated)

XPS was measured after different pretreatment on diamond surfaces were performed at 300 K. From the figure 23, significant increase in binding energy of the diamond C 1*s* peak was observed (shifted to 285.2 eV) after the high Li doses on the hydrogenated surface (Li/H/C), with the appearing of peak tailing feature at higher binding energy. This C 1*s* shift could be due to the induced downward band bending and an additional chemical shift contributed by the chemical interaction of Li-H. C1*s* peak shifted approximately 0.5 eV to higher binding energy, following the Li adsorption on clean diamond surface. For

Li dosed onto an oxygenated surface, chemical shifts of about + 0.4 eV from 283.5 eV is observed, and lithium dosed at aminated surface shows insignificant change in binding energy.

Li was very hard to detect under XPS measurement due to its small X-ray ionization cross section. Moreover, Li with small radius could possibly diffuse into the polycrystalline diamond. Figure 24 shows the XPS Li 1*s* peak after high Li doses for 20 min on different pretreated surfaces. The Li peak can be detected at 55.0 eV for Li/H/diamond (a) with an estimated concentration ratio of 0.23 for Li to C. The Li peak can barely be seen at 55.5 eV for Li/O/diamond (d) or Li/NH_2/diamond (c) with a Li/C ratio of 0.03.

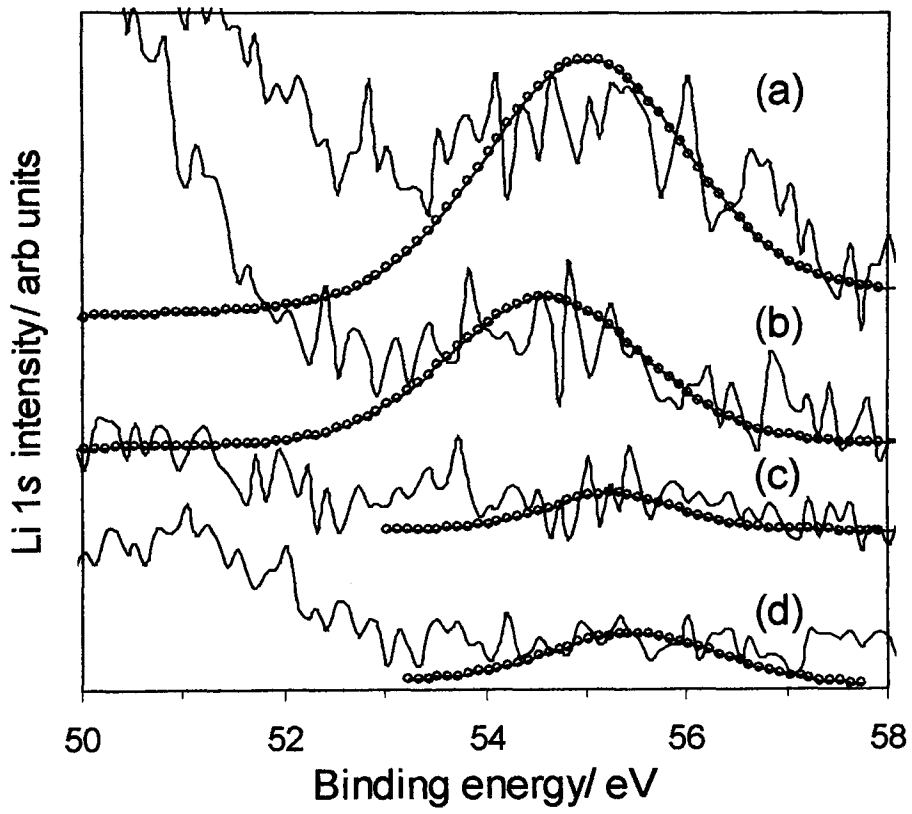


Figure 24. XPS Li 1s of Li dosed (20 min) on (a) hydrogenated, (b) clean, (c) aminated and (d) oxygenated polycrystalline diamond surfaces at 300 K

The unsuccessful detection of Li on polycrystalline surface leads to the comparison with a homoepitaxial (undoped) single crystal. Though the Li 1*s* peak was much easier to detect under XPS, it was found that the heating procedure was unsuccessful to anneal or even by mean of electron-bombarding the surface in order to resolve the clean surface. Electron bombardment up to 400 V could barely bring the surface temperature up to 500 °C, which was still inefficient to eliminate the atmospheric adsorbates thoroughly.

Therefore, the surface contains high oxygen concentration, and we have to treat the surface condition same as the oxygenated diamond surface. Figure 25 reveals the wide scan of XPS after the high Li dosages for 20 min. The Li 1*s* peak is clearly evidenced at 55.7 eV and the related gradual increase of Li peak is plotted in figure 26. The Li/C ratio is nearly 4.39 at a period of 20 min doses, which is much higher than the surface concentration of Li dosed on polycrystalline diamond surface.

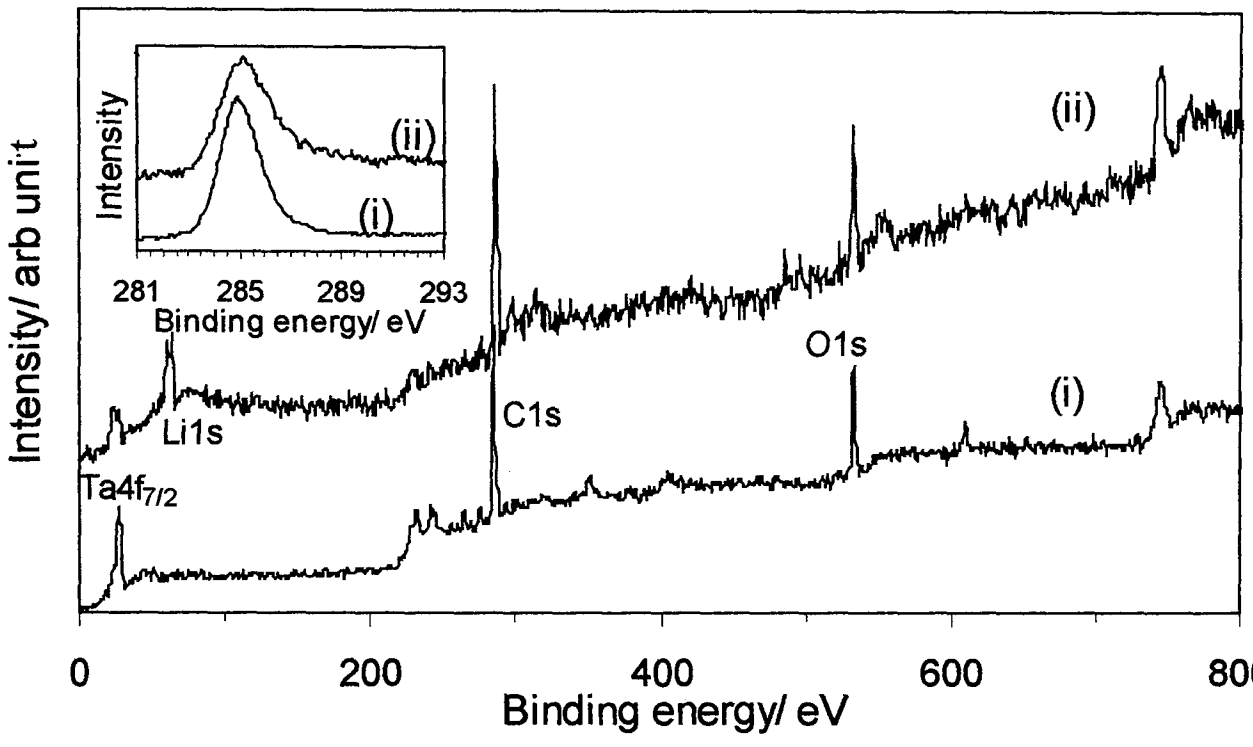


Figure 25. XPS wide scan of single crystal diamond (i) before and (ii) after the high doses of Li (20 min) at 300 K, with inset revealing the C1s peak; referenced to Ta $4_{f7/2}$ (diamond holder)

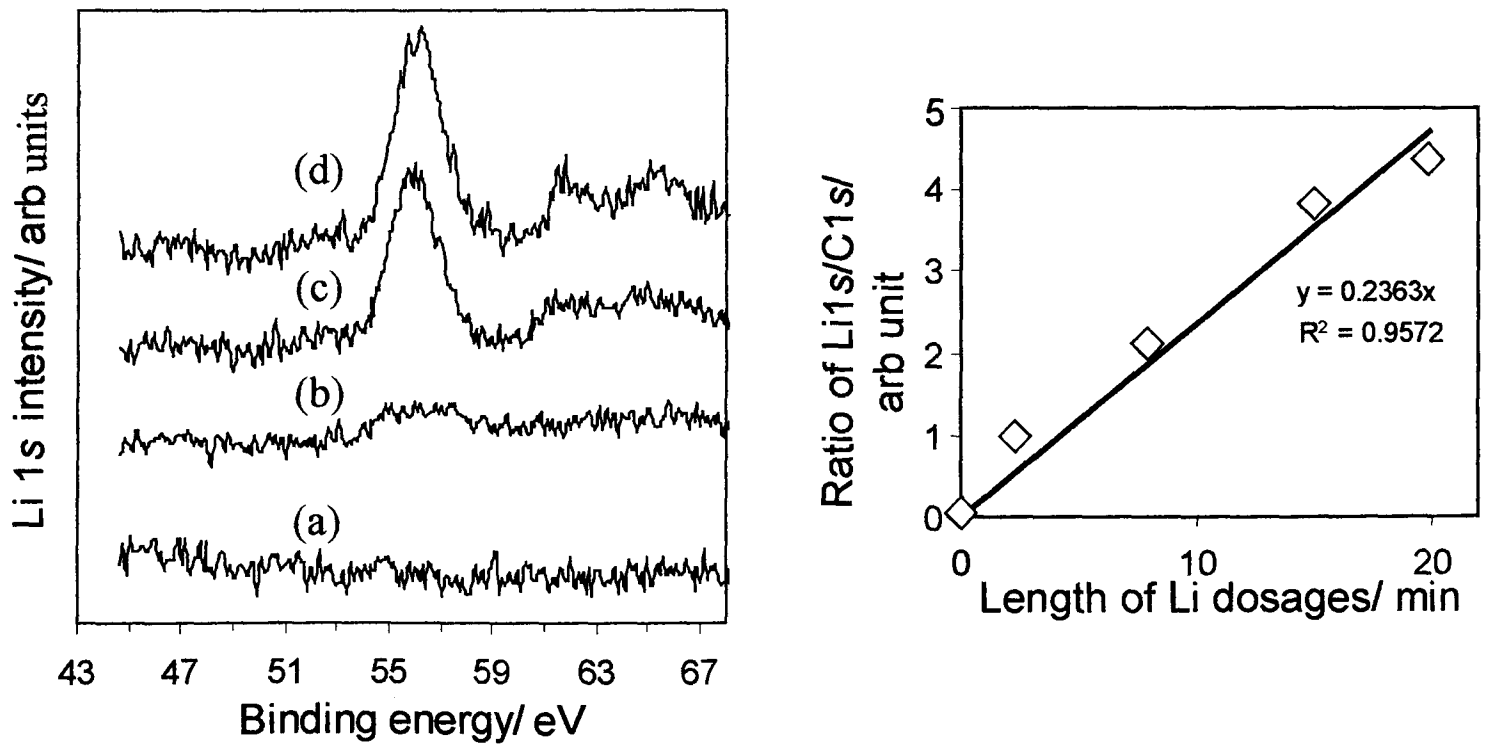


Figure 26. XPS Li 1s peak with the increasing Li dosages on single crystal diamond at 300 K; (a) no Li, (b) 2 min, (c) 16 min, (d) 20 min; figure on the right showing the Li1s/C1s ratios versus Li dosing period

5.4.2.4 Lithium and Hydrogen

The thermal desorption chemistry of different gases have been investigated using temperature-programmed desorption (TPD).

Figure 28(a) shows hydrogen desorbed from hydrogenated polycrystalline diamond surfaces in two temperature regions, with a desorption peak predominantly observed at ~ 850 °C, and the other at 350 °C.

Figure 28(b) reveals the increasing amount of desorbed hydrogen (and Li, as shown previously in figure 20ii) at 350 °C when more Li was dosed on the hydrogenated surface.

On the other hand, diamond was pre-dosed with Li for 10 min prior the exposure to hydrogen plasma and the related TPD spectra is shown in figure 28(c). The QMS signal of the desorbed H_2 peak at 800 °C was intensified with the increases of hydrogen plasma treatments, though there was insignificant change for the desorbed peak at 350 °C.

Interestingly, the increasing treatment of hydrogen plasma on the lithiated diamond surface could somehow enhance the Li desorption with the concurrent desorption of H_2 as shown in figure 27. Upon the same length of time for the exposure to hydrogen plasma, the amount of hydrogen was found to desorb less from the lithiated diamond (figure 27 b) as compared to the clean diamond surface (a).

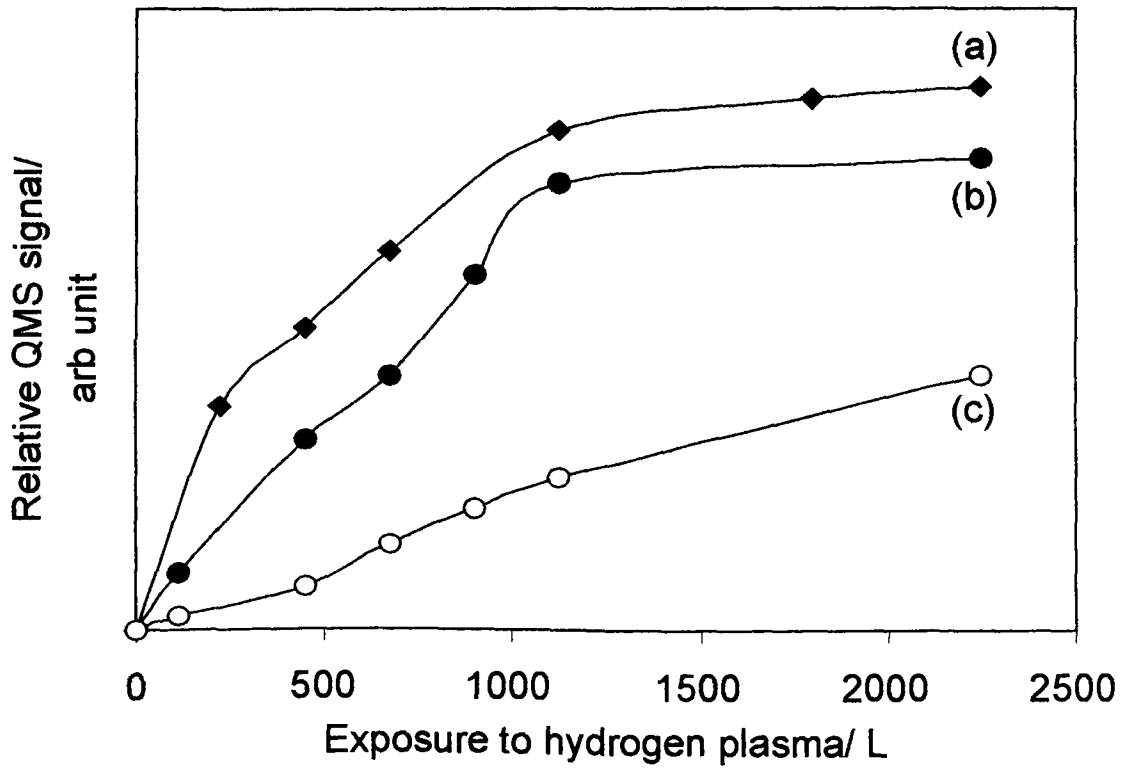


Figure 27. Thermal desorption yields for (a) H_2 (2 amu) of H/diamond; (b),(c) H_2 (2 amu) and Li^+ (7 amu) of H/Li/diamond

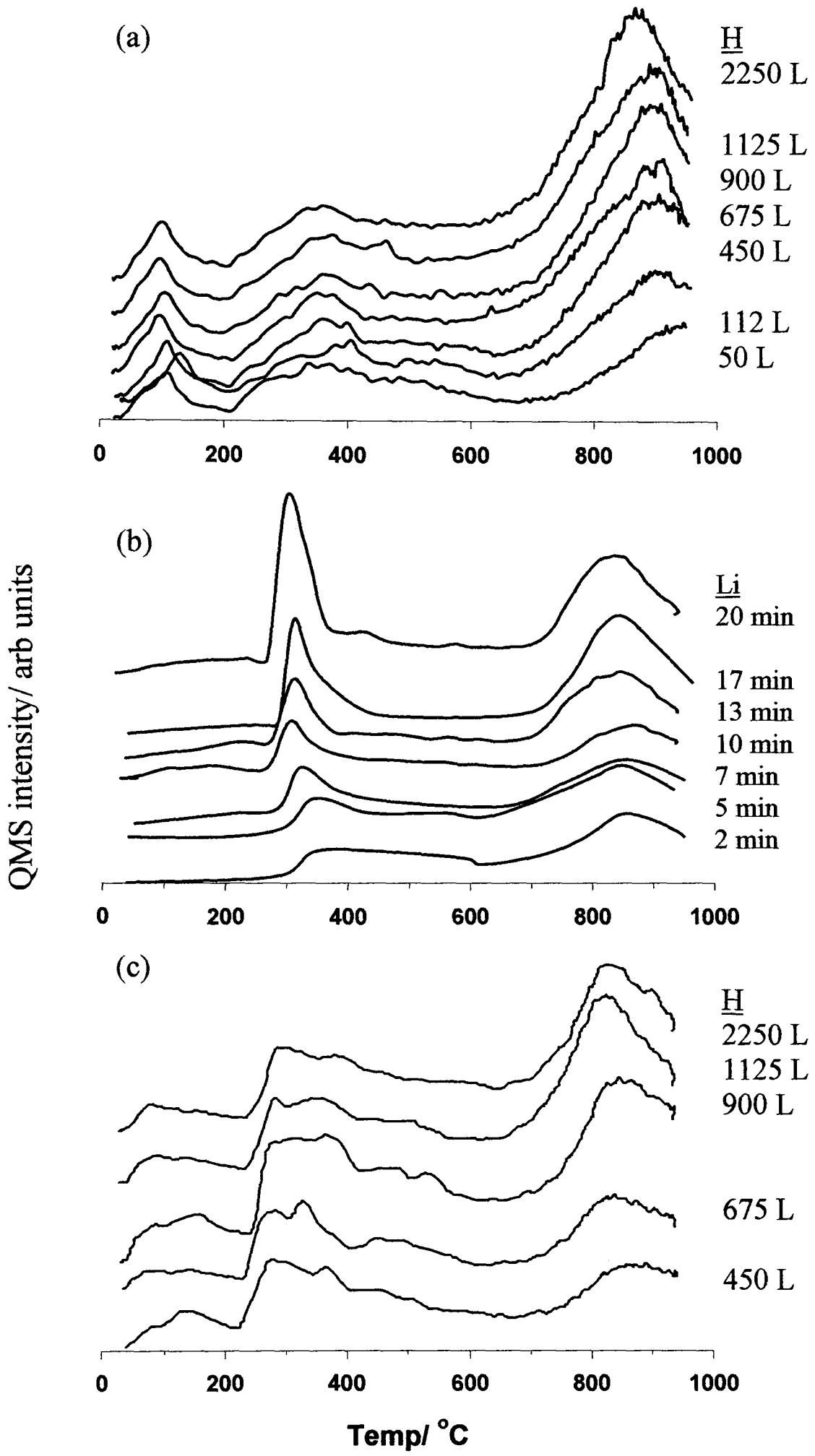


Figure 28. TPD spectra for H_2 (2 amu) of (a) H/diamond, (b) Li/H/diamond and (c) H/Li/diamond surfaces

The stability of adsorbed Li on H/diamond surface was examined by treating the surface with atomic hydrogen. The desorbed H_2 is shown in figure 29. This desorption H_2 pattern is similar to that from the barely hydrogenated clean diamond surface, as the result has been shown previously in figure 28(a). The molecular H_2 mainly desorbed at 800 °C, with a smaller desorbed signal being observed at 300 °C. The amount of Li that desorbed at 800 °C (not shown) was significantly in decrease after being exposed to the increasing amounts of atomic hydrogen.

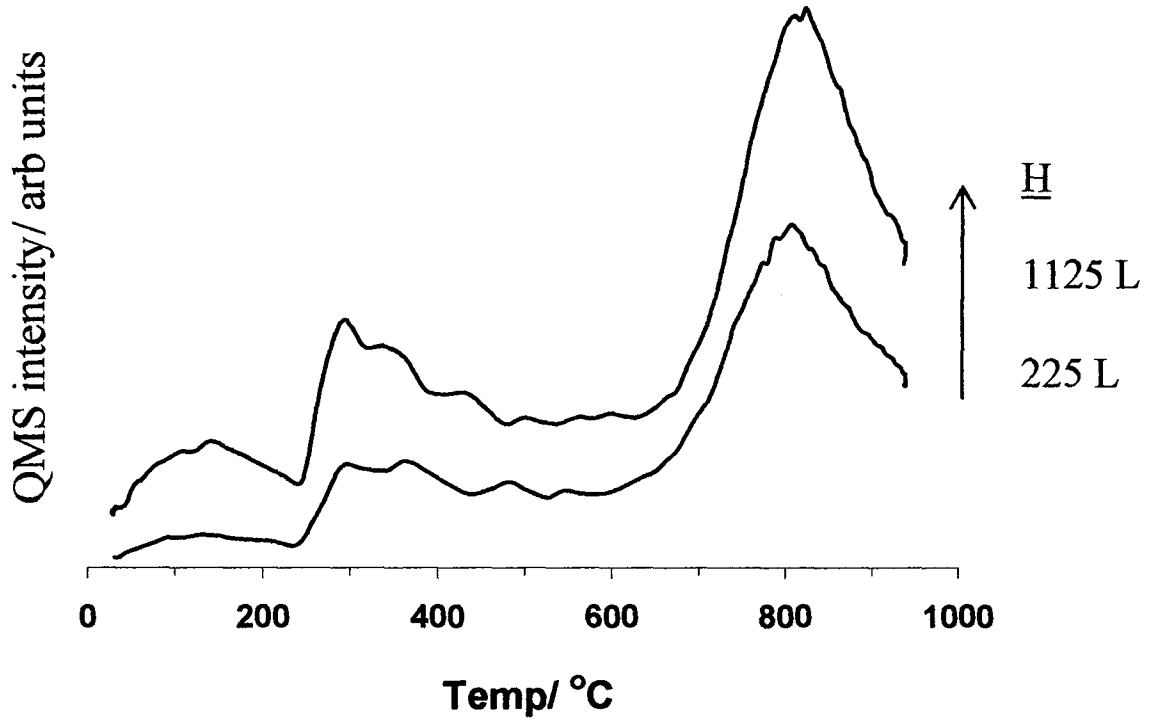


Figure 29. TPD spectra for H_2 (2 amu) of H/Li/H/diamond surface, following the exposure to 225 and 1125 L atomic hydrogen

Figure 30 shows the desorbed products while the lithiated surface (10 min) was bombarded by atomic hydrogen at 300 K. Immediately following the striking of the atomic hydrogen *via* microwave plasma, a significant rise in the signals corresponding to m/s = 7 amu (Li), m/s = 8 amu (LiH) and m/s = 9 amu (LiH_2) were observed. All of the spontaneous desorption of Li derivatives displayed monotonic increases with time. This simple experiment employing QMS-time evolution method proved the existence of highly reactive interaction between Li and atomic hydrogen that subsequently formed the intermediate compounds, such as LiH_2 and LiH. A significant point worth noting is the relative time-scale where the signal degenerates to the background level soon after the plasma was switched off.

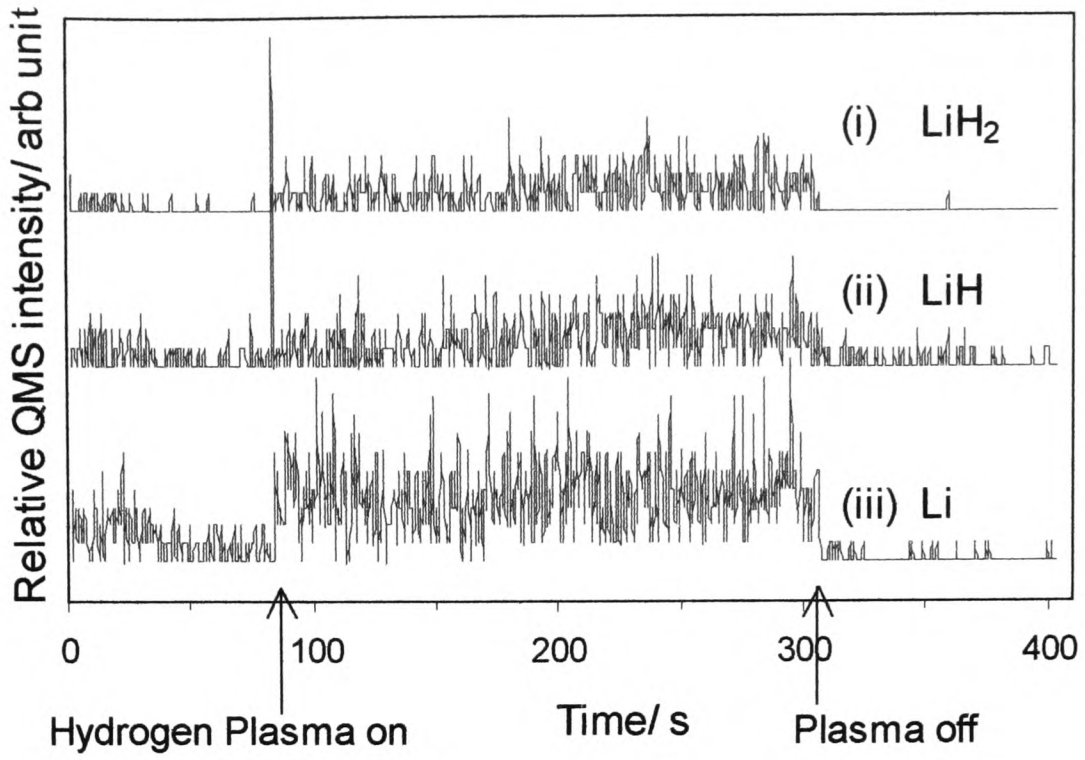


Figure 30. The on-beam products (i) LiH_2^+ (9 amu), (ii) LiH^+ (8 amu) and (iii) Li^+ (7 amu) by atomic hydrogen on lithiated (10 min) diamond surface

5.4.2.5 Lithium and Oxygen

Alkali metals are known to be reactive to both molecular and atomic states of oxygen. This property leads the interest of our research to investigate the chemical reactivity of Li with oxygen on diamond surface. Experiment was carried out by flowing the molecular oxygen, O_2 inside the chamber, in front of the lithiated (10 min) diamond surfaces. TPD spectra were later recorded (figure not shown). Very low desorption signals of CO and CO_2 were observed around 180 °C, though Li remains desorbed at high temperature of 800 °C. This result was similar to the desorption pattern for molecular oxygen dosed on clean diamond surface. Thus, it can be deducted that there is no chemical interaction between Li and molecular oxygen on the diamond surface.

CO and CO_2 are the main desorbed products for Li/O/diamond and O/Li/diamond, similar to the case for the plasma-induced oxygenated diamond surface, O/diamond. Both of the products desorbed from O/diamond at 300 °C. In contrast, as the amount of Li dosed on oxygenated diamond was increased (see figure 31), a new desorbed CO peak

appeared at much higher desorption temperature ~ 700 °C, followed by the decrease of the desorbed amount at 300 °C. For CO_2 however, the desorbed peak has shifted for only 50 °C up to 400 °C with no appearance of new arising desorption peak. The intensity for desorbed CO_2 was nearly unchanged with the increases of Li dosages. No desorption of molecular O_2 (32 amu) was observed.

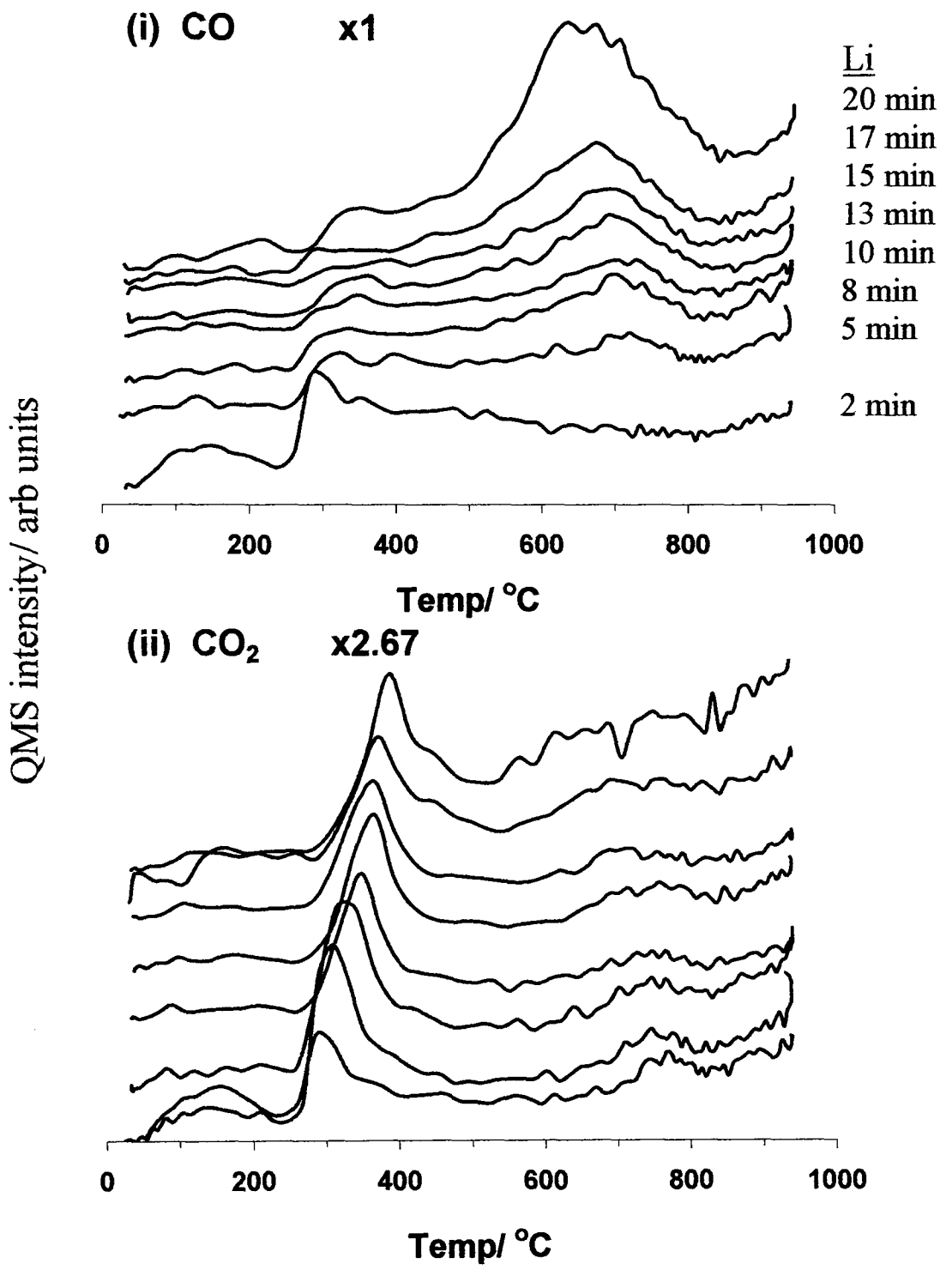


Figure 31. TPD spectra for (i) CO (28 amu) and (ii) CO_2 (44 amu) of Li/O/diamond surface, following the increasing doses of Li (up to 20 min) on oxygenated surface

To investigate the effect of further oxidation on Li-O bonding, Li/O/diamond was treated by atomic oxygen and the result is shown in figure 32. The desorption pattern shifted completely, by which the CO_2 became the major desorbed product when the

exposure to atomic oxygen was increased up to 1125 *L*. The desorbed CO peak covered a wide range of undefined desorption temperature from 300 to 800 °C, whereas CO_2 was desorbed distinctively at 350 °C. The desorption pattern is very much different from the result as presented in figure 31, signifying the notable difference in decomposition chemistry between the two. The chemical structure of O/Li/O/diamond due to the layered surface coverage of Li and O might also cause the differences in the oxidation chemistry.

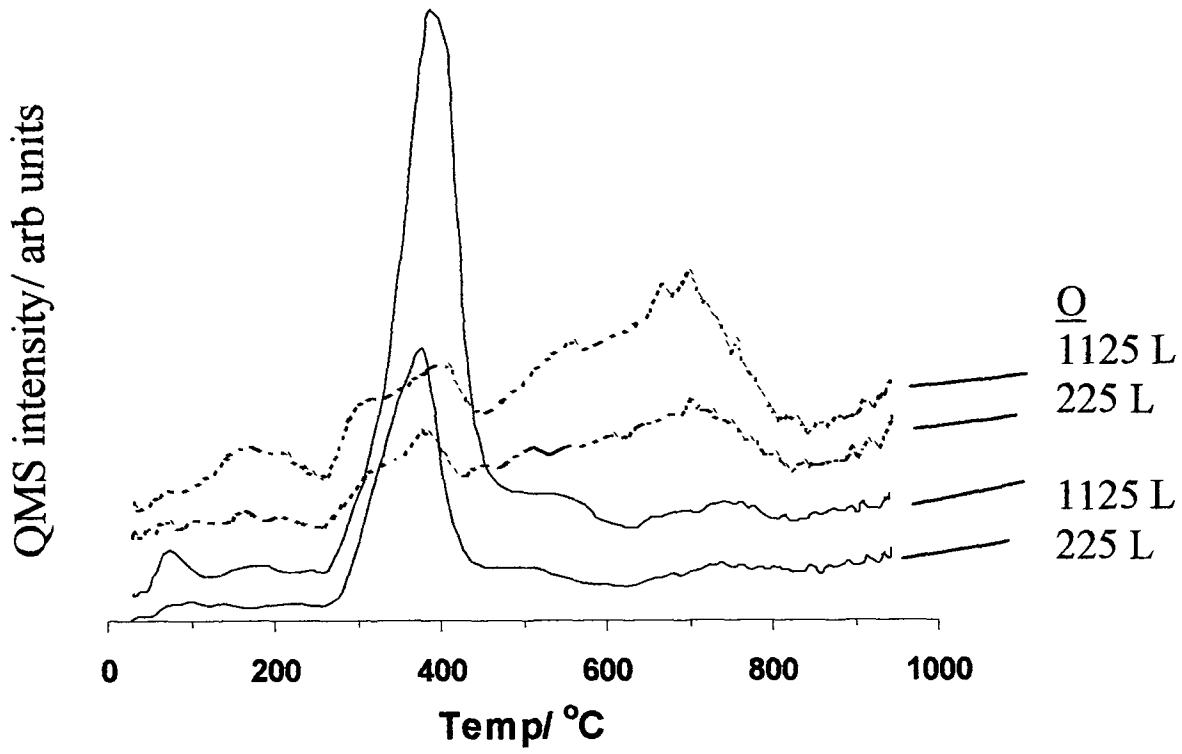


Figure 32. TPD spectra for CO (dashed line, 28 amu) and CO_2 (solid line, 44 amu) of O/Li/O/diamond surface, following the exposure to 225 or 1125 L of atomic oxygen

On the other hand, the lithiated surface was treated with atomic oxygen to probe the chemical decomposition pattern. As shown in TPD of figure 33, the desorbed CO peak at 700 °C was observed to dominate the desorption pattern, as compared to the peak at 350 °C. In contrast, the desorption patterns for CO_2 have changed. Besides the original desorption peak found at 350 °C, an arising peak has become apparently detected at 600 °C. Both of these desorbed CO_2 peaks increased tremendously upon the high exposures to atomic oxygen. The amount of CO_2 being desorbed was found to be relatively similar to CO, as shown in figure 33 (iii). O_2 however, was not observed from the desorption spectra.

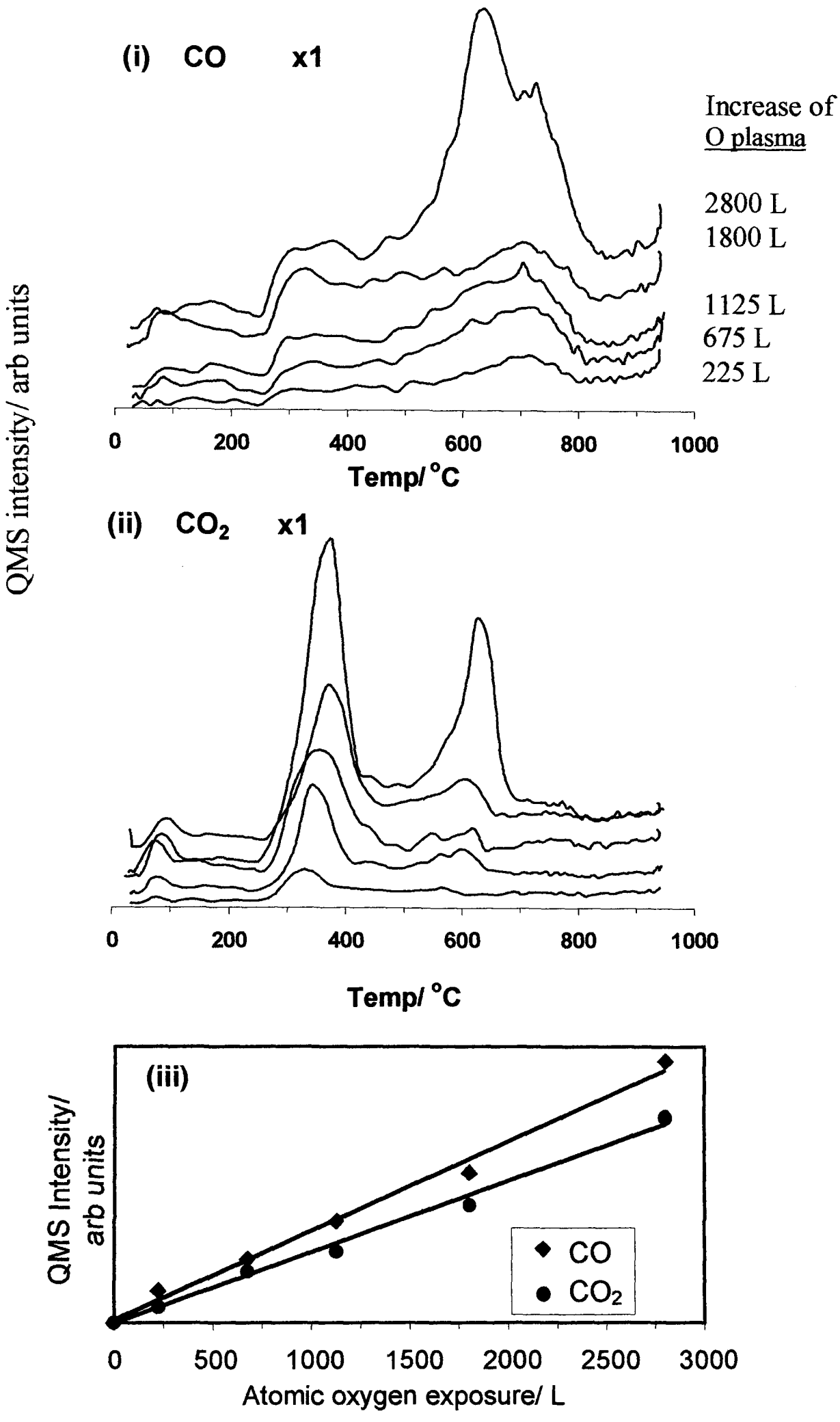


Figure 33. TPD spectra for (i) CO (28 amu) and (ii) CO_2 (44 amu) of O/Li/diamond surfaces, following the exposures of lithiated (10 min) diamond to the increasing oxygen plasma treatments; (iii) thermal desorption yields for the products of (i) and (ii) as a function of the exposure of Li/diamond surface to atomic oxygen

5.4.2.6 Lithium and Ammonia

Investigation on the interaction of molecular NH_3 with or without pre-dosed Li diamond was performed. The corresponding thermal desorption spectra (presented in figure 34) for H_2 and N_2 were monitored at 2 amu and 28 amu respectively as the exposure function of clean diamond surface to NH_3. Both of the gases desorbed at low temperature, with two H_2 desorption peaks appeared at 180 °C and 400 °C, whereas one desorption peak due to N_2 was observed at 180 °C. Desorbed N_2 was differentiated from CO by referring to their cracking fragmentation. No ammonia (17 amu), CN (26 amu) and HCN (27 amu) were observed in any desorption studies.

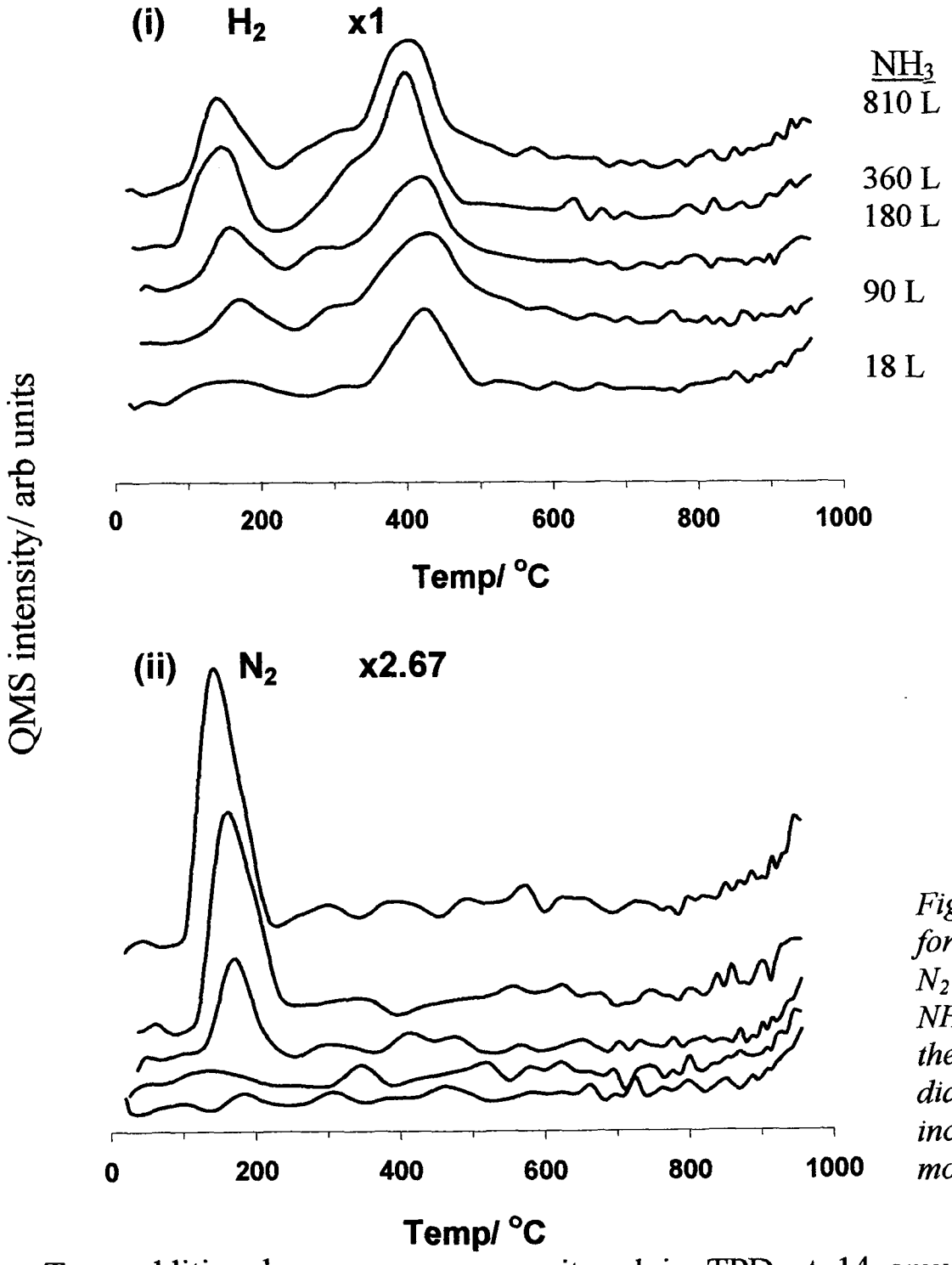


Figure 34. TPD spectra for (i) H_2 (2 amu) and (ii) N_2 (28 amu) of NH_3/diamond, following the exposures of the clean diamond surface to the increasing doses of molecular NH_3

Two additional masses were monitored in TPD at 14 amu and 16 amu. The QMS intensity tuned at 14 amu is equivalent to 7.2 % of the intensity for N_2, indicating the

presence of atomic nitrogen. There was no increase in intensity signal for the mass monitored at 16 amu, suggesting the desorbed signal at 28 amu is not due to CO.

The desorption pattern of the NH_3/diamond surface was compared to the exposure of lithium-covered surface to molecular ammonia (termed as NH_3/Li/diamond). Figure 35 shows the two main desorption products, *i.e.* H_2 and N_2. H_2 was found to desorb at 200 °C and 400 °C, similar to the desorption pattern of NH_3 dosed on clean diamond surface (figure 34). N_2, however desorbed at high desorption temperature of 650 °C, which was similar to the Li desorption range.

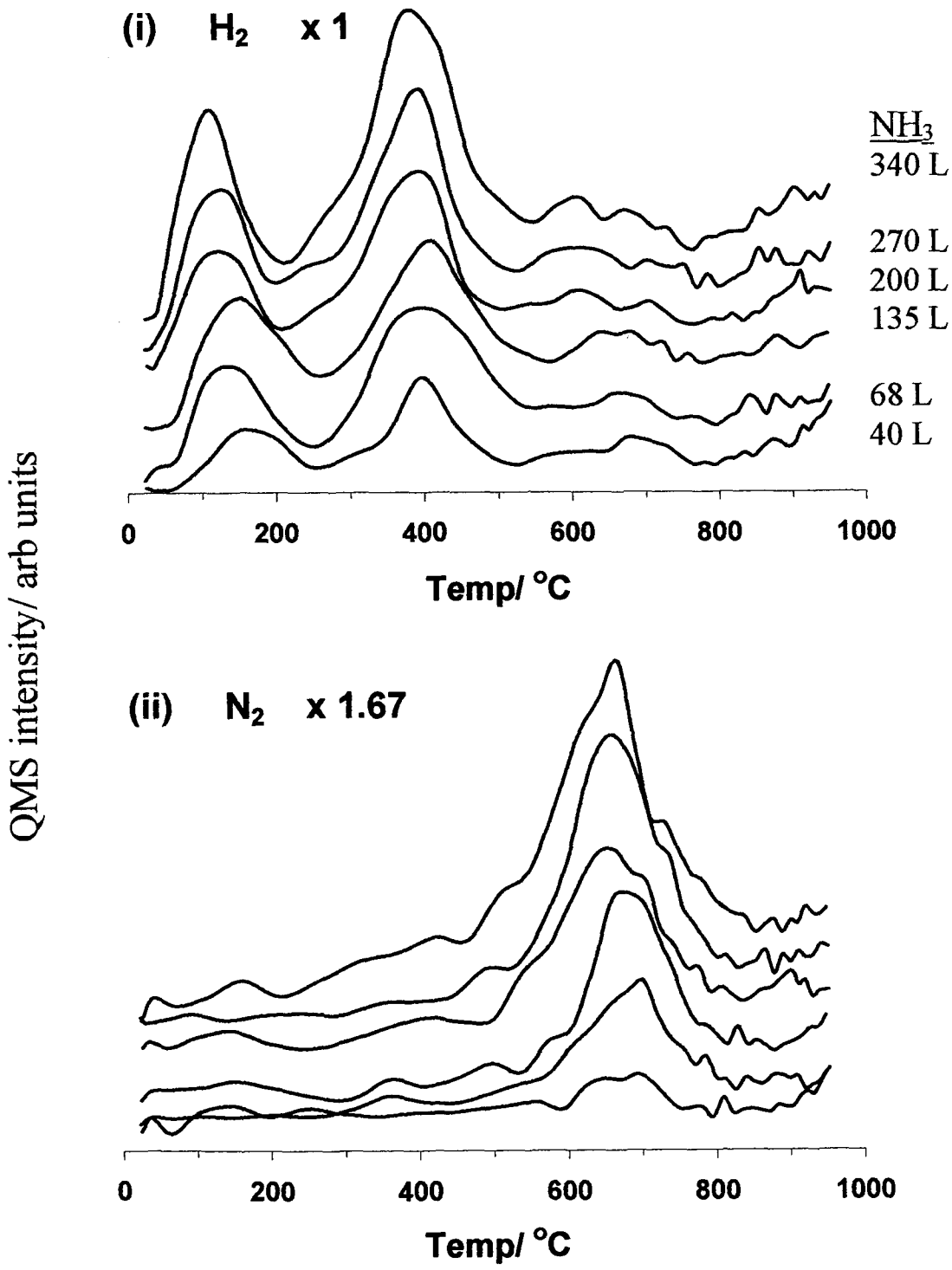


Figure 35. TPD spectra for (i) H_2 (2 amu) and (ii) N_2 (28 amu) of NH_3/Li/diamond, following the exposures of the lithiated (10 min) diamond surface to increasing doses of molecular NH_3

NH_3 was dissociated over the incandescent Ir filament by which a higher reaction of the gas on Li-covered diamond is expected. The system is termed as dissociated NH_3/Li/diamond, and the TPD result is shown in figure 36. H_2, which was originally desorbed at low desorption temperature has shifted to 350 °C when the exposure of the surface to NH_3 was increased. Desorbed N_2 has shifted from 650 °C to a wide coverage of desorption range from 300 to 800 °C, with a main peak being observed at 350 °C. Li showed the similar desorption pattern as N_2 (not shown).

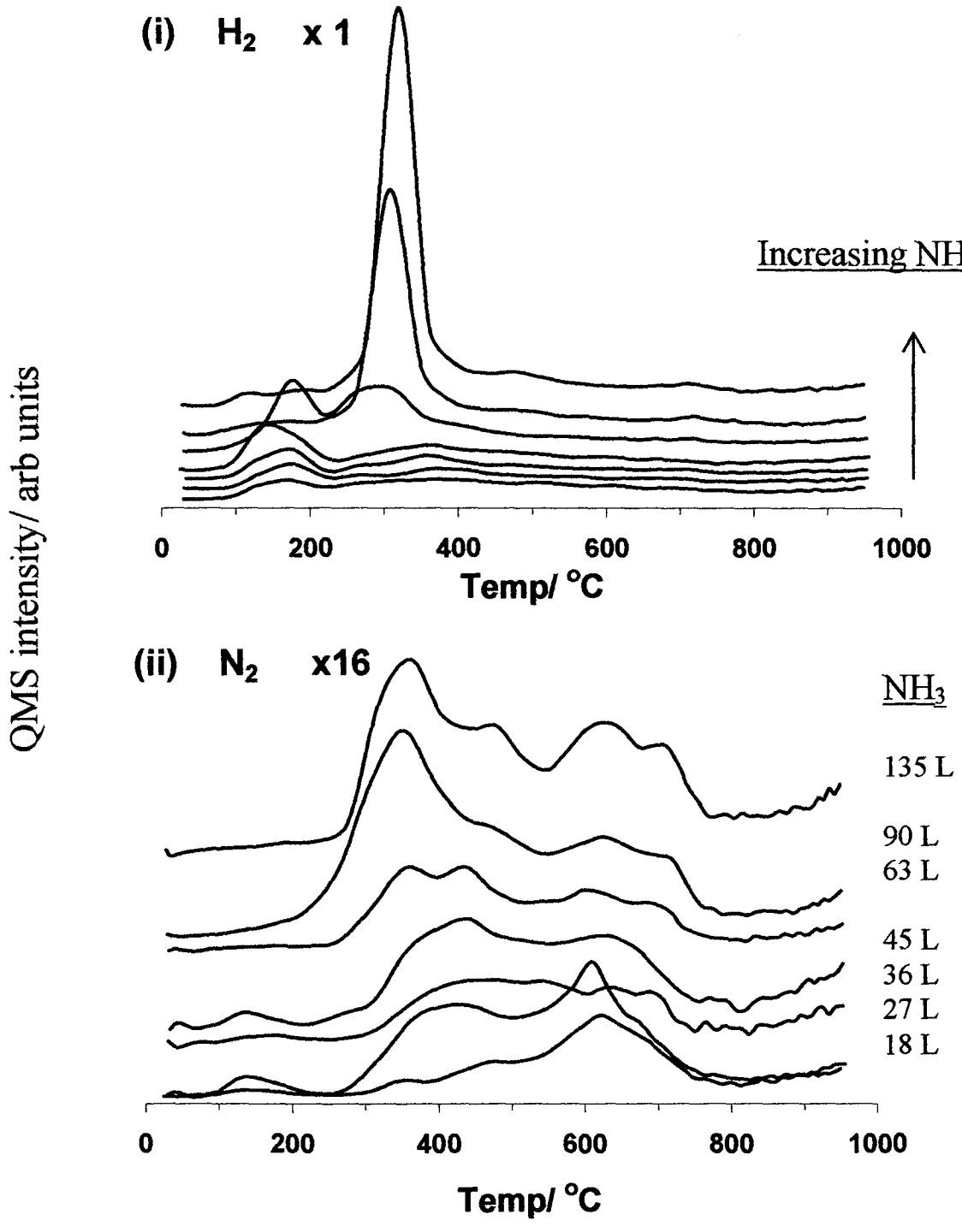


Figure 36. TPD spectra for (i) H_2 (2 amu) and (ii) N_2 (28 amu) of dissociated NH_3/Li/diamond, following the exposures of the lithiated (10 min) diamond surface to dissociated NH_3 dosages

The thermal desorption yields for the desorbed products are revealed in figure 37, showing significant increases of the desorbed amount for H_2 and N_2 from the aminated surface, particularly for the surface treated over the incandescent iridium filament in ammonia ambient. This could be attributed to the role of lithium on promoting more chemical interaction between the dissociated ammonia and the lithiated surface.

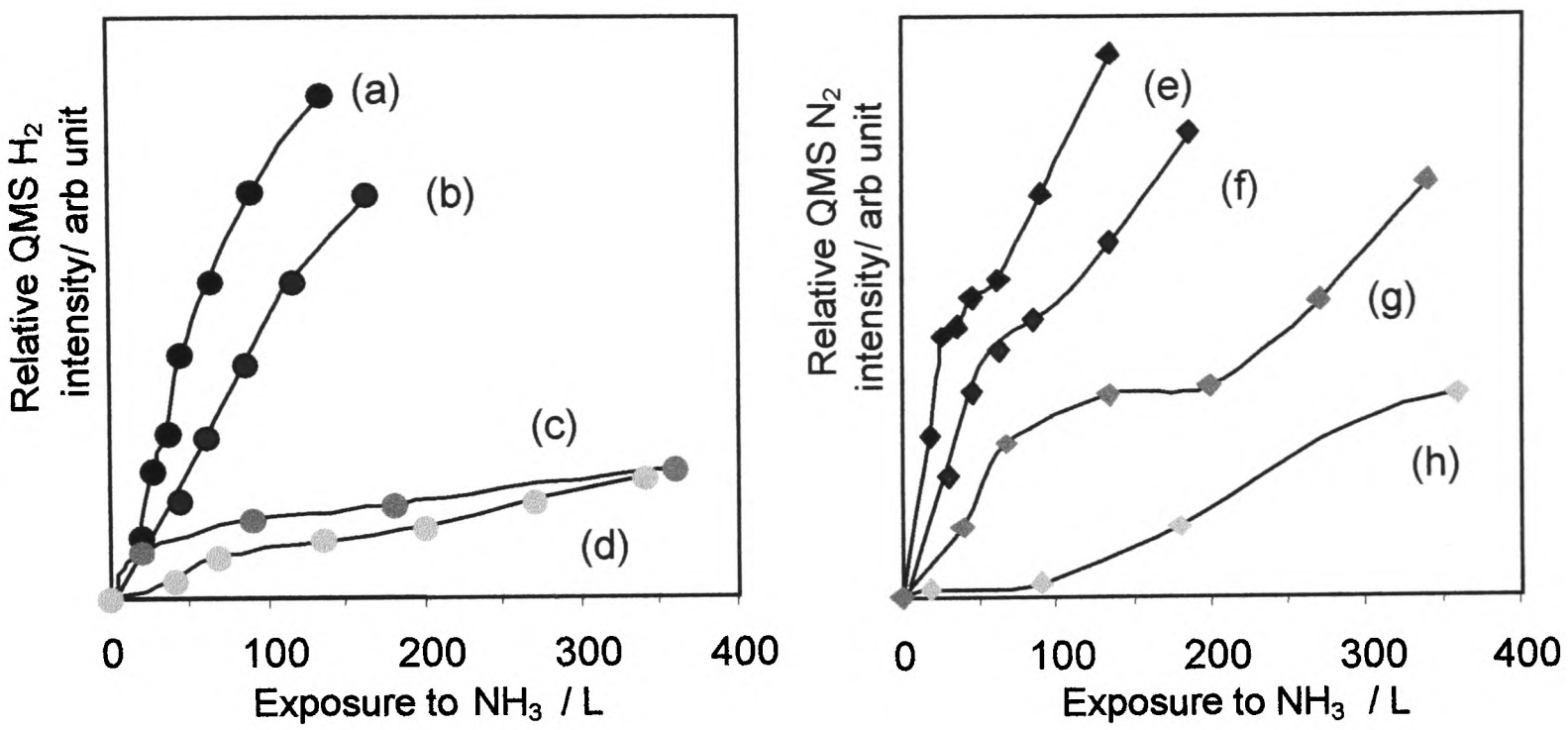


Figure 37. Thermal desorption yields of H_2 (a-d, 2 amu) and N_2 (e-h, 28 amu) for (i) dissociated NH_3/Li/diamond (a,e), (ii) dissociated NH_3/diamond (b,f), (iii) molecular NH_3/Li/diamond (c, g) and (iv) molecular NH_3 (d,h) on clean diamond surface

5.4.3 Discussion

Previous studies of K and Cs on diamond show a conventional chemistry as seen on other substrates in which the alkali metal forms chemisorbed overlayers, which massively increase the reactivity to gases, such as O_2, which otherwise show a very low sticking probability on the substrate is in question. Current data shows Li on CVD diamond appears to behave differently, including

(a) XPS shows only a very small concentration of Li present on the surface of the CVD film; even though a much larger surface concentration can be observed on the single crystal for an equivalent dose

(b) SIMS shows a lot of Li trapped in the bulk of the CVD film, clearly showing the onset of surface-to-bulk transport

(c) TPD shows mainly a high temperature desorption peak, which is unusual for alkali metals which normally desorb at low temperatures due to a low heat of chemisorption

(d) On the CVD film, Li does not promote reactivity to molecular oxygen

A consistent explanation for these observations is that the Li does not remain largely on the surface, when dosed onto an adsorbate-free polycrystalline CVD surface, but instead exhibits considerable surface mobility and migrates down into the bulk diamond *via* grain boundaries when dosed on a clean or bare surface. Data also shows that the surface chemistry of Li is quite affected by the nature of surface adsorbates present.

(i) Li Adsorption and Diffusion

The XPS data (figure 24) and the insignificant low temperature desorption signal of Li suggests that Li can hardly adsorb on the diamond surface layer. Due to its small size (d_{Li} = 3.04 Å), the adsorbed Li on the surface can rapidly diffuse through the grain boundaries of polycrystalline diamond down into the bulk lattice. The SIMS depth profiling in figure

22 has proved the occurrence of Li *in-diffusion* process, down ~ 3 μm into the bulk diamond. This phenomenon has well been reported for the case of Li passivation in polycrystalline silicon *via* their grain boundaries effect, showing that Li can diffuse at a magnitude of 3 orders more rapidly in the grain boundary than in the solid Si [75,76]. Considering the sensitivity of XPS down to only to 1 - 5 nm corresponding to 4 - 20 atomic or molecular monolayers (~ 2 x 10^{15} atoms cm^{-2} per monolayer) [77], the detection of the diffused Li in the bulk would be impossible. The origin of low photoelectric cross-section of Li has also made the XPS studies difficult. In contrast, Li can be easily detected by mean of XPS on single crystal diamond (see figure 25, 26). The possible reasons for the enhanced diffusion in polycrystalline diamond, rather than in single crystal diamond are due to the presence of grain boundaries on the polycrystalline surface and the presence of defects in the diamond bulk crystals, including vacancies, dislocations, vacancy complexes and microscopical voids. The presence of such defects can provide higher mobility routes for the atom migration and would increase the diffusion rates. Ion or atom can also be trapped in the bulk lattice, forming the complexes with the diffusing ion/ atom in the polycrystalline diamond [68].

(ii) Effect of Hydrogen on Li adsorption

Results show that the prehydrogenation causes

(a) low temperature desorption of Li

(b) concurrent low temperature desorption of H_2

(c) an increased desorption yield of Li

This would suggest the formation of a 2-D surface Li(H)ads compounds, which prevents the diffusion of Li down through the grain boundaries, by stabilizing the surface adsorbed form of Li. However, this Li(H)ads is relatively unstable thermally, and a reverse reaction tends to be favoured at a low desorption temperature when the substrate temperature is

increased. The presence of the desorbed Li and H_2 from Li(H)ads are respectively revealed in figure 20(ii) and figure 28(b), showing decomposition predominately at ~ 350 °C.

$$Li(H)\,(ads) \rightarrow Li\,(g) + \tfrac{1}{2}\,H_2\,(g) \qquad \text{(eqn 9)}$$

The desorbed Li at very high temperature ~ 900 °C is attributed to the embedded Li in the grain boundaries of the polycrystalline diamond, which is similar to that of the Li desorption peak from the clean diamond surface (figure 20i).

As shown in figure 27, more Li was found to desorb with the increasing of hydrogen plasma treatment on Li/diamond surfaces. The reasons for this unusual behaviour are (a) hydrogen can diffuse into the surface layers and "push" out the Li-occupied area. Li would migrate to shallow surface layers, and can desorb easily at high ramping temperature, (b) more Li(H)ads compounds are formed with the increasing hydrogen dosages. This would in return facilitate the desorption of Li *via* the disruption of Li(H)ads compounds. However, a full Li monolayer is expected to occupy all active adsorption sites at the surface, which will in turn block the adsorption sites for gases. This explains the reason why the desorbed yield for H/Li/diamond is lower than H/diamond surface (see figure 27 and 28c).

The spontaneous desorption during atomic hydrogen radiation (as shown in figure 30) suggests the presence of lithium dihydride (either LiH_2 or LiH_2^+) and lithium hydride, LiH. The suggested mechanisms are

$$Li\,(ads) + H\,(g) \rightarrow LiH\,(g) \qquad \text{(eqn 10)}$$

$$H\,(g) + LiH\ (ads) \rightarrow LiH_2\ (g) \qquad \text{(eqn 11)}$$

Atomic H is expected to excite Li adatom to its first excited state Li (^2P first excited state), as the reaction between Li (^2S ground state) is less favourable [78]. Thus, the singly

occupied molecular orbital in the excited LiH_2 complex will involve a *p* orbital on Li and the H_2 anti-bonding molecular orbital. The van der Waals minimum of Li...H_2 is reported to be small (< 2.09 kJ/mol) at a distance larger than 4.2 Å [79]. This molecule was previously analysed, by means of high temperature calorimetry, ionization potential measurements [80] and laser pump-probe approach [81]. Lithium hydride can be formed by the direct collision of H on adsorbed Li (equation 10) or *via* the breaking of LiH_2.

(iii) Effect of oxygen on Li adsorption

Li dosed on clean diamond surface shows no enhancement effect on the molecular oxygen adsorption, suggesting that Li suffers from the diffusion process into the diamond bulk lattice *via* the polycrystalline grain boundaries. Therefore, the chemical interaction is suppressed between diffused Li with the impinging O_2 on the surface. In contrast, bigger alkali metals such as K and Cs, which do not show the diffusion effect into the diamond bulk, are expectedly very reactive to dissociate O_2.

Figure 31 shows the TPD result for Li dosed on pre-oxygenated diamond surface, revealing the extensive desorption of CO_2 as well as CO. This indicates as for the other alkali metals that once Li is "anchored" on the surface, it enhances the oxidation of the diamond interface. The pre-oxygenated diamond surface provides excellent adsorption sites for Li and prevents the metal from diffusing inside the diamond bulk lattice. Therefore, the further Li adsorption would be stabilized by the O-terminated surface, producing high orders of O-containing compounds, such as carboxylate and polycarbonate, which would involve more likely Li-O-C bonding. Thus, the CO desorption would be favoured at higher temperature, with the CO_2 peaks correspond to the remaining high oxidized species, which are suggested due to the decomposition of Li_2CO_3 compounds. By dosing the atomic oxygen on such Li/O/diamond surface (see figure 32), the interaction of O to C is greatly enhanced with the presence of Li. Higher and more

complex oxidation states are expected to occur among the three elements, which can induce more CO_2 being desorbed.

Figure 33 shows the TPD result for predosed Li on a clean diamond surface prior the O treatment, revealing the significant thermal desorption yields for the desorbed products of CO and CO_2. This signifies that the bounded oxygen species on diamond surface would attract the embedded Li in the bulk lattice. This is followed by the strong reaction in between Li and O-surface, promoting a series of high order oxidation with the concurrent substrate etching process by atomic oxygen. The arising peak of CO_2 at 600 °C is attributed to the thermal decomposition of Li_2CO_3, by which the compound was reported to desorb from the Li-covered film of predeuterated propene carbonate in the range 477 – 587 °C [82]. In the view of surface electronic contribution, the mutual depolarization among the adsorbed Li and their denser packing on diamond surface would lower the potential distribution, resulting in the decrease of the work function. This would mean a lowering of the vacuum level relative to the Fermi level, which leads to the corresponding lowering of all energy levels for oxygen. The resonant tunnelling is thus enabled from diamond substrate to the oxygen *via* the deposited Li [65]. Therefore, the chemisorption of atomic oxygen on pre-dosed Li is greatly enhanced.

(iv) Effect of ammonia on Li adsorption

From the TPD spectra (see figure 34, 35) of the molecular NH_3 dosed on clean or lithiated diamond, the first desorption peak at 200 °C is attributed to the dissociative adsorption for ammonia on the diamond surface. This is evidenced with the absence of the ammonia desorption, where instead the dissociation products N_2 and H_2 are observed. With low dissociation energy of a NH_3 molecule (~ 4.8 eV) [83], this will lead to concerted hydrogen-abstraction reactions to take place, where H atoms are abstracted from NH_3 molecules to form NH_x (x = 1,2) moieties [84]. The simultaneous desorption of these two

gases at low temperature is expected to arise from the thermal decomposition of the adsorbed NH_x complex, which undergoes subsequent decomposition during TPD. The adsorbed hydrogen that saturates the dangling bonds, is expected to desorb at ~ 400 °C.

$$NH_x\,(ads) \rightarrow \tfrac{1}{2}\,N_2\,(g) + {}^{x}/_{2}\,H_2\,(g) \qquad \text{(eqn 12)}$$

The presence of Li on diamond shows more N_2 desorption at high temperature ~ 650 °C which is concurrent with the Li desorption, suggesting Li stabilises the adsorbed species with the formation of Li-N bonding.

The dissociated NH_3 over Ir filament dosed on lithiated diamond surface shows significant increases of desorption amount for N_2 and H_2 in TPD (figure 36) and thermal desorption yield (figure 37). This could probably due to the formation of lithium amine compounds, $LiNH_y$ (y = 1-3) on diamond surface in different chemical states with different bond enthalpies, thus they were desorbed at a wide coverage of temperature. These forms of highly aminated compounds have also been theoretically and experimentally reported [85,86,87]. By employing equation 10 in Chapter 2, assuming $\nu/\beta \sim 10^{12}\ K^{-1}$, the desorption of Li and N_2 from the temperature range in figure 36 will predict that the Li ... N bond energies are in the range of 170.67 - 263.02 $kJmol^{-1}$ due to different compositional lithium aminated compounds, and the range of temperature is comparable to the reported data of 167.44 kJ mol^{-1} [88] and 247.21 kJ mol^{-1} [89].

CN and HCN compounds were not observed in our desorption data, suggesting that the diamond is inert to promote the formation of unsaturated CN bonding (or the incorporation of nitrogen), such as C=N and C≡N. This result is consistent with the FTIR-DRIFT spectra for ammonia dosed on chlorinated diamond [90], showing no vibrational frequencies for these unsaturated CN bonds, but revealed the existence of frequency modes for N-H and C-N bonds.

5.4.4 Conclusion

On clean CVD diamond, Li adsorption behaves differently to most of the alkali metals – the main tendency seems to be for Li to diffuse down the grain boundaries, which occurs only on bare (or clean) polycrystalline surface.

This tendency is stopped if diamond surface is pretreated with H, O or NH_3 – which stabilities the adsorbed Li through the formation of surface compounds. Thus, no Li diffusion into the bulk is now seen.

Li shows the highest tendency for adsorption on hydrogenated diamond surface due to the formation of Li(H)ads compounds. Atomic hydrogen irradiation is also able to etch Li from the surface at room temperature, due to the formation of gaseous LiH and LiH_2.

As a consequence of grain boundaries diffusion, Li does not promote molecular O_2 adsorption, but if atomic O is pre-dosed to keep Li near surface, then subsequent O adsorption is promoted. Reactive O dosed on the pre-lithiated surface also seems able to attract Li from the bulk, forming highly oxidized compounds.

Dissociative adsorption of molecular NH_3 occurs on clean and lithiated diamond surface. Higher lithium amine compounds were formed with the interaction of dissociated NH_3 on diamond.

5.5 References for Chapter 5

[1] Y. Liou, A. Inspektor, R. Weimer, D. Knight and R. Messier, *J. Mater. Res.* **5** (1990) 2305

[2] M. Frenklach and K.E. Spear, *J. Mater. Res.* **3** (1988) 133

[3] L.S.G. Plano, in: Diamond – electronic properties and applications, L.S. Pan and D.R. Kania (*eds.*), Kluwer, Dordrecht, 1995, pg 61

[4] D.B. Rebuli, T.E. Derry, E. Sideras-Haddad, B.P. Doyle, R.D. Maclear, S.H. Connell and J.P.F. Sellschop, *Diamond Relat. Mater.* **8** (1999) 1620

[5] W.J. Zhang, C.Sun, I. Bello, C.S. Lee and S.T. Lee, *J. Vac. Sci. Technol. A* **17** (1999) 763

[6] J.A. Mucha, D.L. Flamm and D.E. Ibbotson, *J. Appl. Phys.* **65** (1989) 3448

[7] Y. Muranaka, H. Yamashita, K. Kato and H. Miyadra, *J. Appl. Phys.* **67** (1990) 6247

[8] R.A. Rudder, G.C. Dudson, J.B. Posthitt, R.E. Thomas, R.C. Hendry, D.P. Malta, R.J. Markunas, T.P. Humphreys and R.J. Nemanich, *Appl. Phys. Lett.* **60** (1992) 329

[9] C.F. Chen, T.M. Hong and S.H. Chen, *J. Appl. Phys.* **74** (1993) 4483

[10] C. Gomez-Aleixandre, M.M. Garcia, O. Sanchez and J.M. Albella, *Thin Solid Films* **303** (1997) 34

[11] P.K. Bachmann, D. Leers, and H. Lydin, *Diamond Relat. Mater.* **1** (1991) 1

[12] A. Shih, J. Yeter, P. Pehrsson, J. Butler, C. Hor and R. Abrams, *J. Appl. Phys.* **82** (1997) 1860

[13] T. Yamada, H. Ishihara, K. Okano, S. Koizumi and J. Itoh, *J. Vac. Sci. Technol. A* **15** (1997) 1678

[14] S.C. Lim, R.E. Stallcup II, I.A. Akwani and J.M. Perez, *Appl. Phys. Lett.* **75** (1999) 1179

[15] A. Laikhtman, A. Hoffman, R. Kalish, Y. Avigal, *et al.*, *Appl. Phys. Lett.* **73** (1998) 1433

[16] P.W. May, J.C. Stone, M.N.R. Ashfold, K.R. Hallam, W.N. Wang and N.A. Fox, *Diamond Relat. Mater.* **7** (1998) 671

[17] Y. Mori, H. Kawarada and A. Hiraki, *Appl. Phys. Lett.* **58** (1991) 940

[18] S.A. Grot, G.S. Gildenblatt, C.W. Hatfield, C.R. Wronski, A.R. Badzian, T. Badzian and R. Messier, *IEEE Electron Dev. Lett.* **11** (1990) 100

[19] H. Kiyota, E. Matsushima, K. Sato, H. Okushi, T. Ando, M. Kamo, Y. Sato and M. Iida, *Appl. Phys. Lett.* **67** (1995) 3596

[20] M. Kaack and D. Fick, *Phys. Rev. B.* **51**(24) (1995) 17902

[21] V.S. Smentkowski and J.T. Yates *Jr*, *J. Vac. Sci. Technol. A* **12**(1) (1994) 219

[22] D.P. Higgins, R.W. McCullough, J. Geddes, J.M. Woolsey, M. Schnapp and H.B. Gilbody, *Key Eng. Mater.* **99/100** (1995) 111

[23] A. Hofmann, *Anorganische Chemie* (1918) 287

[24] J.D. Lambert, *Trans. Faraday Soc.* **32** (1936) 542

[25] B.B. Pate, *Surf. Sci.* **165** (1986) 83, and references therein

[26] J.J. Lander and J. Morrison, *Surf. Sci.* **4** (1966) 241S

[27] R. Sappok and H.P. Boehm, *Carbon* **6** (1968) 573-588

[28] R.E. Thomas, R.A.Rudder and R.J.Markunas, *J. Vac. Sci. Technol. A* **10** (1992) 2451

[29] J.L. Whitten, P. Cremaschi, R.E. Thomas, R.A. Rudder and R.J. Markkunas, *Appl. Surf. Sci.* **75** (1994) 45

[30] T. Ando, M. Ishii, M. Kamo and Y. Sato, *J. Chem. Soc. Faraday Trans.* **89**(9) (1993) 1383
[31] L.M. Struck and M.P. D'Evelyn, *J. Vac. Sci. Technol. A* **11**(4) (1993) 1992
[32] B.L. Mackey, J.N. Russell, J.E. Crowell, P.E. Pehrsson, B.D. Thoms and J.E. Butler, *J. Phys. Chem. B* **105** (2001) 3803
[33] J.C. Zheng, X.N. Xie, A.T.S. Wee and K.P. Loh, *Diamond Relat. Mater.* **10** (2001) 500
[34] M.Z. Hossain, T. Kubo, T. Aruga, N. Takagi, T. Tsuno, N. Fujimori and M. Nishijima, *Surf. Sci.* **436** (1999) 63
[35] P.E. Pehrsson and T.W. Mercer, *Surf. Sci.* **460** (2000) 74
[36] P.E. Pehrsson and T.W. Mercer, *Surf. Sci.* **460** (2000) 49
[37] H.J. Hopman, J. Verhoeven and P.K. Bachmann, *Diamond Relat. Mater.* **9** (2000) 1238
[38] K.P. Loh, X.N. Xie, X. Zhang, E.J. Teo, T. Osipowicz, M.Y. Lai and N. Yakovlev, *Diamond Relat. Mater.* **11** (2002) 1385
[39] X.M. Zheng and P.W. Smith, *Surf. Sci.* **262** (1992) 219
[40] H. Tamura, H. Zhau, K. Sugisako, Y. Yokoi, S. Takami, M. Kubo, K. Teraishi, A. Miyamoto, A. Imamura, M.N. Gamo and T. Ando, *Phys. Rev. B* **61** (2000) 11025
[41] L. Ley, R. Graupner, J.B. Cui and J. Ristein, *Carbon* **37** (1999) 793
[42] G. Beamson and D. Briggs, High Resolution XPS of Organic Polymers, TheScienta ESCA00 Database, Wiley, Chichester, UK, 1992
[43] A.A. Haasz, S. Chiu and J.E. Pierre, *J. Vac. Sci. Technol. A* **14** (1996) 184
[44] T. Ando, K. Yamamoto, M. Ishii, M. Kamo and Y. Sato, *J. Chem. Soc. Faraday Trans.* **89** (1993) 3635
[45] D. Briggs and G. Beamson, *Anal. Chem.* **65** (1993) 1517
[46] C.H. Goeting, F. Marken, A. Gutierrez-Sosa, R.G. Compton and J.S. Foord, *New Diamond Front. Carbon Technol.* **9** (1999) 207
[47] S. Skokov, B. Weiner and M. Frenklach, *Phys. Rev. B* **49** (1994) 11374
[48] K. Bobrov, H. Schechter, A. Hoffman, M. Folman, To be published in *Appl. Surf. Sci.* (2002)
[49] S. Skokov, B. Weiner and M. Frenklach, *Phys. Rev. B* **55** (1997) 1895
[50] G. Dujardin, A. Mayne, G. Comtet, L. Hellner, M. Jamet, E. Le Goff and P. Millet, *Phys. Rev. Lett.* **76** (1996) 3782
[51] G. Comted, L. Hellner, G. Dujardin and M.J. Ramage, *Surf. Sci.* **352-354** (1996) 315
[52] G. Comted, G. Dujardin, L. Hellner, L. Philippe, M.J. Besnard-Ramage, T. Hirayama and M. Rose, *Surf. Sci.* **331-333** (1995) 370
[53] U. Hoffer, P. Morgen and W. Wurth, *Phys. Rev. B* **40** (1989) 1130
[54] J.J. Lander and J Morrison, *Surf. Sci.* **4** (1966) 241
[55] J.S. Foord, N.K. Singh, R.B. Jackman, A. Gutierrez-Sosa, S. Proffitt and K.B. Holt, *Surf. Sci.* **488**(3) (2001) 335-345
[56] S. Proffitt, C.H.B. Thompson, A. Gutierrez-Sosa, N. Paris, N.K. Singh, R.B. Jackman and J.S. Foord, *Diamond Relat. Mater.* **9**(3-6) (2000) 246-250
[57] J. te Nijenhuis, G.Z. Cao, P.C.H.J. Smits, W.J.P. van Enckevort, *et al.*, *Diamond Relat. Mater.* **6** (1997) 1726
[58] G. Gadiyak, *Nucl. Inst. Meth. Phys. Res. B* **127-128** (1997) 256
[59] U. Wahl, *Phys. Reports* **280** (1997) 145
[60] W. Preyss, H.D. Ebinger, D. Fick, C. Polenz, B. Polivka, *et al.*, *Surf. Sci.* **373** (1997) 33
[61] L.F. Li, Y. Luo, G.G. Totir, D.A. Totir, *et al.*, *J. Phys. Chem. B* **103** (1999) 164

[62] J.H. Petersen, C. Sondergard, S.V. Hoffmann and D.L. Adams, *Surf. Sci.* **461** (2000) 45
[63] R. Yazami, *Electrochim. Acta* **45** (1999) 87
[64] A.K. Arof, N.M. Morni and M.A. Yarmo, *Mater. Sci. Eng. B* **55** (1998) 130
[65] I.N. Yakovkin, V.I. Chernyi and A.G. Naumovets, *J. Phys. D: Appl. Phys.* **32** (1999) 841
[66] S.A. Kajihara, A. Antonelli, J. Bernholc and R. Car, *Phys. Rev. Lett.* **66** (1991) 2010
[67] A.B. Anderson and S.P. Mehandru, *Phys. Rev. B* **48** (1993) 4423
[68] G. Popovici, R.G. Wilson, T. Sung, M.A. Prelas and S. Khawasinah, *J. Appl. Phys.* **77**(10) (1995) 5103
[69] S. Reiko, H. Shun-ichi and K. Masahhiro, *Hyomen Kagaku* **21**(9) (2000) 584
[70] S.W. Novak, *J. Vac. Sci. Technol. A* **15**(3, Pt. 2) (1997) 1724
[71] J. Bernholc, S.A. Kajihara, A. Antonelli, MRS International Conference Proceedings, MRS, Pittsburgh, PA, 1991, pg 923
[72] S.A Kajihara, A. Antonelli and J. Bernholc, *Phys. B* **185** (1993) 144
[73] B.V. Spitsyn, G. Popovici and M.A. Prelas, 2nd International Conference on the Applications of Diamond Films and Related Materials, edited by M. Yoshikawa, M Murakawa, Y. Tzeng, W.A. Yarbrough, MY, Tokyo, 1993, pg 57
[74] R.B. Bird, W.E. Stewart and E.N. Lightfoot, Transport Phenomena, John Wiley and Sons, Inc., New York, 1960, Chapter 19
[75] F. Kai, G. Rajeswaran, M.A. Jackson, V.J. Rao and W.A. Anderson, 16th Conf. Rec. IEEE Photovoltaic Spec. Conf, 1982, pg 543
[76] R.T. Young, G.E. Jellison, *Jr.*, Y.K. Chang, M.C. Lu and G.A. Van der Leeden, 15th Conf. Rec. IEEE Photovoltaic Spec. Conf., 1981, pg 1316
[77] D. Briggs and M.P. Seah, Practical Surface Analysis 2nd *ed.* Vol. 1 – Auger and X-ray Photoelectron Spectroscopy, John Wiley and Sons, Inc., New York, 1994, pg 15
[78] P. Hobza and P.von Rague Schleyer, *Chem. Phys. Lett.* **105**(6) (1984) 630
[79] A.F. Wagner, A.C. Wahl, A.M. Karo and R. Krejci, *J. Chem. Phys.* **69** (1978) 3756
[80] C.H. Wu, *J. Chem. Phys.* **71**(2) (1979) 783
[81] A.F. Wagner, A.C. Wahl, A.M. Karo and R. Krejci, *J. Chem. Phys.* **69** (1978) 3756
[82] G.R. Zhuang, G. Chottiner, D.A. Scherson and E.B. Yeager, *J. Phys. Chem.* **99**(18) (1995) 7009
[83] I.N. Mihailescu, V. Craciun, L. C. Nistor, V. S. Teodorescu, E. D'Anna, G. Leggieri, A. Luches, M. Martino, A. Perrone, A. V. Drigo, S. Ganatsios, and J. Zemek, *J. Appl. Phys.* **70** (1991) 2123
[84] D. Chrysostomou, J. Flowers and F. Zaera, *Surf. Sci.* **439** (1999) 34
[85] I.T. Lentei and JK. Szaniszlo, *Acta Phys.Chim.Debrecina* **27** (1991) 61
[86] A. Hinchliffe, *Chem. Phys. Lett.* **45**(1) (1977) 88
[87] F.W. Dafert and R. Miklauz, *Monatsh* **33** (1912) 63
[88] A. Hinchliffe and J.C. Dobson, *Theoret. Chim. Acta* **39** (1975) 17
[89] S. Bhargava, S.P. Mehandru, R.C. Rastogi and N.K. Ray, *Indian J. Chem., Sect A* **16A**(2) (1978) 156
[90] T. Ando, M. Nishitani-Gamo, R.E. Rawles, K. Yamamoto, M. Kamo and Y. Sato, *Diamond Relat. Mater.* **5** (1996) 1136

Chapter 6

Diamond Photocathode

6.1 Introduction
6.2 Experimental
6.3 Results
  6.3.1 Growth and Quality Mode of Photoemission
  6.3.2 Reflective Photoemission Mode
    6.3.2.1 Photoyield Studies of Gas Hydrogen and Gas Oxygen On Diamond
    6.3.2.2 Photoyield Study of K on Diamond
    6.3.2.3 Photoyield Study of Cs on Diamond
    6.3.2.4 Photoyield Studies on Thermal Stability of Alkali Metals
  6.3.3 Transmissive Photoemission Mode
    6.3.3.1 Surface Characterization
    6.3.3.2 Photoyield Studies
  6.3.4 Analysis of the Filter
6.4 Discussion
  6.4.1 Growth and Comparison
  6.4.2 Reflective Mode
    6.4.2.1 Photoyield Studies
    6.4.2.2 X-ray Photoemission Studies
  6.4.3 Transmissive Mode
6.5 Conclusion

6.1 Introduction

Single crystal and CVD diamond films have a wide energy band gap of 5.47 eV which results in a very low dark current and selective absorption of light with wavelengths $\lambda <$ 225 nm. Some of them, like type IIb <111> diamond [1], the hydrogenated diamond surface [2], and the H-terminated CVD diamond films [3] have shown surface negative electron affinity (NEA), which is attributed to the hydrogen termination on diamond surfaces and thus, the subsequent enhancement of the photoyield (refer to Section 2.7 in Chapter 2).

With its high electron emission yields and stability under operational systems, CVD diamond films have been chosen for use as an advanced photoemitting material in

vacuum microelectronics and high frequency applications, such as photon detectors, high current-low power cold cathodes and electron emission devices. The high resistivity of diamond allows the fabrication of photoconductive devices, enabling light absorption directly into the diamond and avoiding the problem associated with light penetration through metallic contacts. The robustness and chemical stability of diamond films can also reduce the usual photocathode aging problems arising in the harsh environments by gas impurities, high-dose ionizing radiation and ion bombardment. The unique semiconducting properties of diamonds and the efficient charge transport in the bulk have led to the development of novel *uv* imagers and particle tracking detectors capable of withstanding very high radiation flux [4]. A number of other potential applications for diamond including satellite-borne astronomical observations, *uv* fluorescence from marked DNA, high-resolution photolithography and *uv* spectroscopy [5].

CVD diamond is capable of being used successfully for *uv* detection, and many successful photoconductive *uv* point source detectors have been fabricated. The realisation of *uv* imaging devices is more problematic since large-scale device integration is needed, using pixellated detectors. An alternative approach is to use a photocathode in combination with a luminescent screen to shift the *uv* image to the visible region of the spectrum, and CsI is a common material of choice in this *uv* imaging application. However, the CsI photocathodes are known to be highly unstable with respect to moisture, and can be strongly degraded by heat and intense radiation or suffer from ageing phenomena. Apart from CsI, silicon has also been used as a *uv* detector. However for wavelengths less than 400 nm, silicon becomes increasingly opaque making efficient detection more difficult. In many applications, it is essential that the *uv* detector remains 'blind' to visible light. Filtering has been employed in Si technology to achieve this purpose, but this will in turn reduce the performance levels. Moreover, Si devices and filters are quickly damaged if they are subjected to intense radiation. Though

photomultiplier tubes can be utilized, these are more expensive than semiconductor devices and are difficult to integrate with other devices. Therefore, interest has now begun to extend to the use of CVD diamond as a photocathode material, in view of its chemical stability, and optical and electronic properties.

The photoemission mechanism involved in the diamond photocathode design is the conventional three-step model [6], which involves bulk excitation by which absorption of light generates photoexcited carriers; transport of carriers to the surface region; and, emission/escape of electrons into the vacuum region, with more details discussed in Chapter 2 (Section 2.8.1). The QPY of the material can be approximately described by [7,8]:

$$QPY(h\nu) = \frac{(1-R)}{1+1/\alpha(h\nu)\,L} P \qquad \text{(eqn 1)}$$

where $\alpha(h\nu)$ and $R(h\nu)$ are the optical absorption coefficient and reflectivity of the material, respectively, and P is the surface escape probability for electrons. L is the electron diffusion length in the bulk and is a function of the kinetic energy of the photoexcited electrons, which in turn depends on the photon energy.

In this chapter, variations in photoyield at 186 nm and 252 nm have been measured from CVD diamond photocathode materials grown on silicon substrates, as the growth conditions and surface termination is changed. Two types of diamond photocathodes have been fabricated; reflective mode (photons and electrons interact with the same surface) and the more demanding transmissive mode (electrons emitted from the opposite surface to the incoming light). The efficiencies of these two designs are compared and discussed in terms of the fundamental optical and electronic properties of the diamond films that control them. The use of the alkali metals such as Cs and K in conjunction with various hydrogenation, oxidation and heat treatments is therefore explored, in order to lower the electron affinity in a stable manner.

6.2 Experimental

Two types of polycrystalline diamond grown by MWPECVD have been studied, namely undoped (Section 2.15.3) and boron-doped *p*-type (BDD) films. The former samples were used for the studies of growth-dependent photoyield (results in 6.3.1) and transmissive mode membranes (results in 6.3.3) in a home built UHV photocathode chamber (base pressure of 10^{-8} mbar) and the BDD was used for reflective mode (results in 6.3.2) studied in a UHV system (base pressure of 2 x 10^{-10} mbar) equipped with XPS. All of the photoyield measurements were carried out by measuring the total electron current emitted from the sample, with negative bias applied between 0 to 200 V (see figure 1). Both of the evacuated chambers were irradiated with a deuterium lamp (the *uv* light source) directly through a MgF_2 window, in place with the optional presence of a bandpass filter at 186 nm or 252 nm, above and below the diamond band gap (225 nm or 5.54 eV) respectively, and the photon flux is calibrated to a previously-characterised silicon *uv* photodiode (the reference detector). A Keithley 610 C electrometer with high sensitivity and accuracy was used for measuring the photoyield throughout.

For section 6.3.1, the surface treatments with the exception of hydrogenation were carried out *in situ* in the vacuum chamber using a Cs getter source or an Ir filament, over which oxygen was admitted. Molecular oxygen was activated over the hot glowing Ir filament, dosed at a pressure of approximately 1 x 10^{-5} mbar with an applied current of 4 A. The Cs getter was attached to a feed-through facing the sample with a dosing voltage of 7.0 V at varying lengths of time. Surface hydrogenation was carried out *ex situ* in the microwave reactor at a pressure of 45 Torr and a dissipated power of 1200 W for 30 minutes. The temperature of surface platen was held at 600 °C.

For the reflective mode studies (section 6.3.2), surface characterization was carried out *in situ* using XPS under UHV chamber as shown in figure 2 of Chapter 2, equipped with an atomic beam source for effective H and O dosing. All of these gaseous pre-

treatments were performed under the pressure of 5 x 10^{-6} mbar for 10 min. K and Cs were evaporated from well-outgassed SAES getter dispensers set at the flowing currents of 6.4 A and 7.6 A respectively for the maximum fluxes of dosages. During the deposition, the pressure was kept under 7 x 10^{-9} mbar. The purity of the deposited alkali metals layers as well as the coverage was monitored by XPS. The relative coverage of the deposited metals layers are calculated by comparing the intensities of K $2p_{3/2}$ and Cs $3d_{5/2}$ to diamond carbon C 1*s* core peaks, by taking consideration of the sensitivity and photoionization cross-section of the particular elements.

Diamond membranes were fabricated for the study of the transmission mode in photoemission (section 6.3.3). Diamond was pre-deposited on pre-scratched silicon substrate for the desired periods of time. After the complete growth on the face side, the silicon was flipped over, and a small piece of silicon was put to cover the centre of the bare substrate. The deposition of diamond will then be continued on the rest of the uncovered part of silicon for 8 hours in order to produce a diamond mask on the outer frames after being chemically etched away in $HF/HNO_3/CH_3COOH$ (3:5:3) solution.

The diamond membranes were placed in the photocurrent rig. The emitted or the transmitted photocurrent off the near and far faces (relative to the *uv* source) were recorded at a bias of 120 V. The experiment was then repeated for the comparison with a free standing black diamond of thermal management grade (of 200 μm) and a number of freestanding white diamonds of different thickness (4 to 100 μm). The position of the power supply and ammeter in the circuit can be changed to measure the total collected electrons (see figure 1b iii), the reflective photocurrent (1b i) and the transmissive photocurrent (1b ii). These connections were used to minimise the noise and emission from or to the chamber wall.

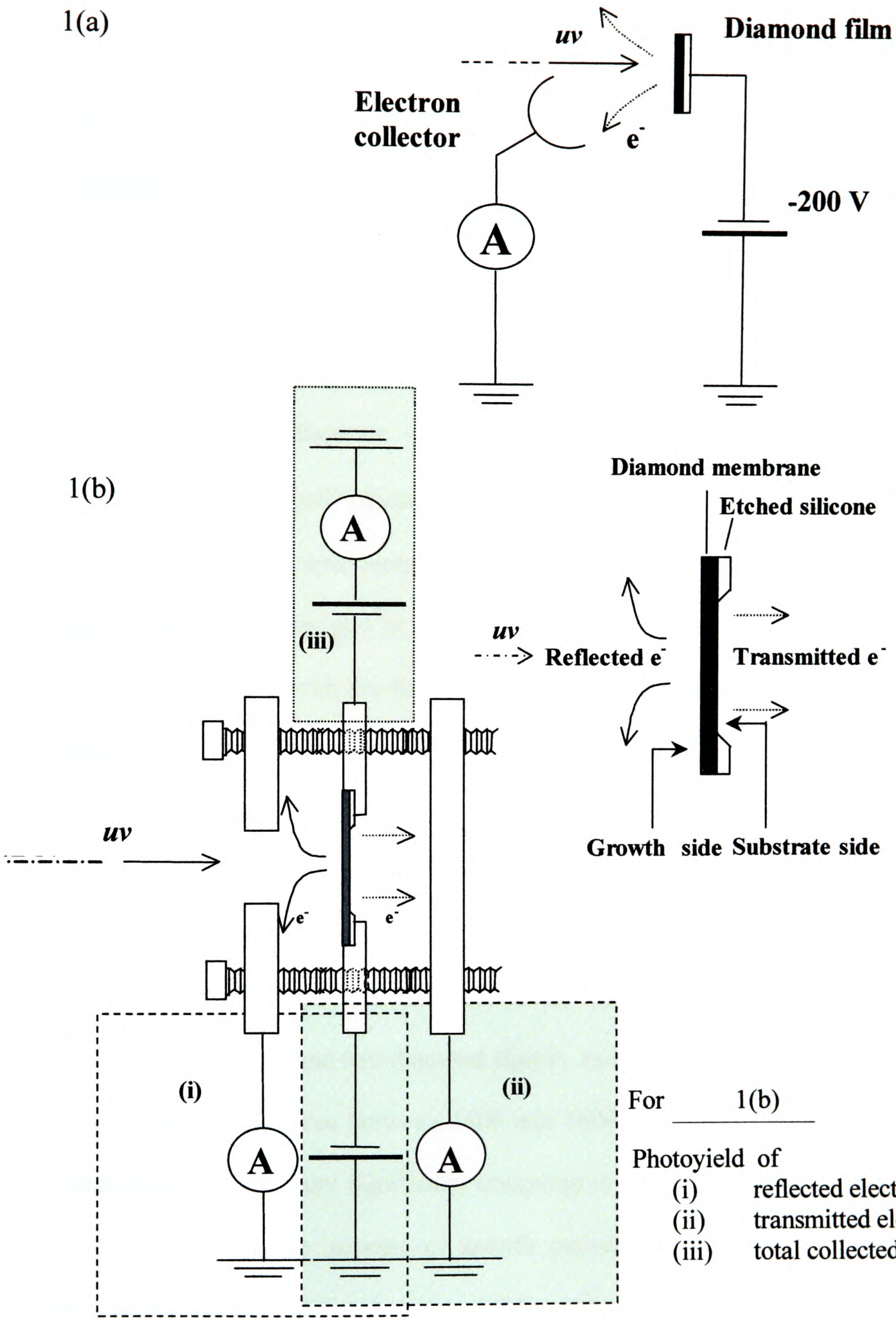


Figure 1. (a) The basic principle for quantum photoyield measurements in UHV chamber; (b) shows the QPY measurements in home-built chamber with diamond membrane and sample holder, revealing (i) – (iii) the different measured QPY targets with ceramic as insulators amongst the stainless steel holder

6.3 Results

6.3.1 Growth and Quality Mode of Photoemission

Attempts were made to correlate the different growth stages of the undoped diamond films to photoyield dependence. The surface was amply characterised with secondary electron microscopy (SEM), atomic force microscopy (AFM) and Raman spectroscopy, using 514 nm exciting radiation.

Figure 2 shows the SEM images of diamond growth under the periods of 6, 9, 15, 21 and 40 hours. At short growth times, the film consisted of randomly dispersed small-undefined crystallites (diameter ~ 6 μm) at 6 hours to very well (100) faceted discontinuous diamond "ball" (diameter ~ 10 μm) at 9 hours before coalescing together at 15 hours, displaying a continuous film with many grain boundaries. The surface morphology primarily consisted of exposed {100} crystallographic faces and the bigger faceted texture increases with the decrease of grain boundaries as observed with the longer growth times.

The difference between 9 hour and 40 hour samples is further shown under higher magnification of AFM in figure 3 with their root mean square roughness (RMS) 26.27 nm and 152.01 nm respectively.

Raman analysis has also been conducted to compare the growth quality with reference to the diamond and non-diamond signals, as shown in figure 4. At lower growth periods, the broad band area between 1400 and 1600 cm^{-1} due to sp^2 graphitic or non-diamond carbon phases were significant, compared to the broader diamond peak at 1331 cm^{-1}. However, with the increase of growth period, the diamond peak at 1331 cm^{-1} became more prominent with a decrease of full-width at half maximum (FWHM) to 6 cm^{-1} and the non-diamond broad band that centered at 1550 cm^{-1} has disappeared. This shows that a greater quality of diamond is obtained with the increase of deposition time.

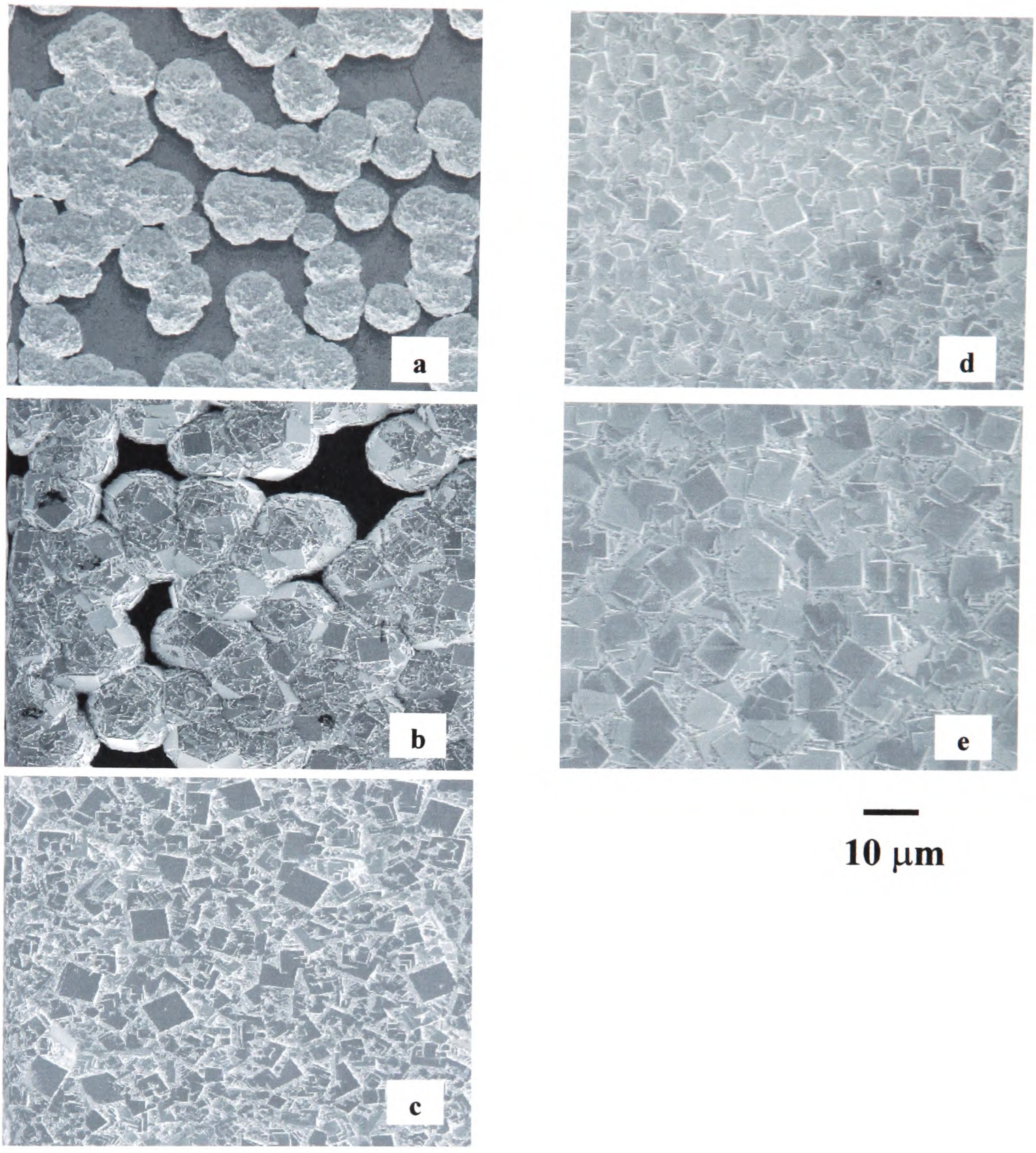


Figure 2. Secondary electron micrographs (SEM) of CVD samples for varying growth times: (a) 6 hours (b) 9 hours, (c) 15 hours, (d) 21 hours and (e) 40 hours

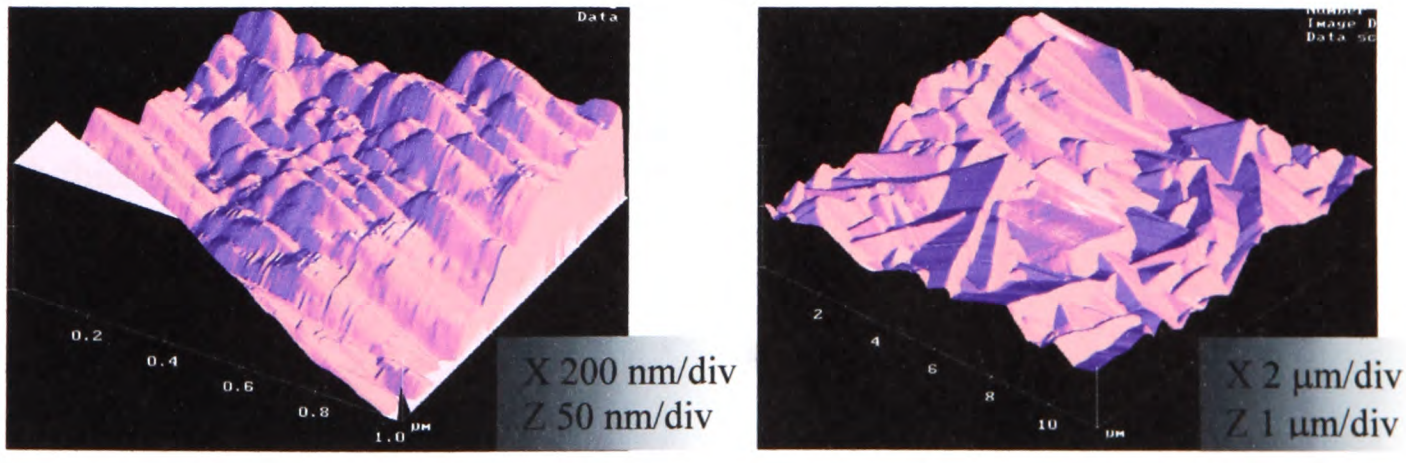


Figure 3. (a) AFM images of 9 hr sample (left) and 40 hr sample (right). Note the different scale

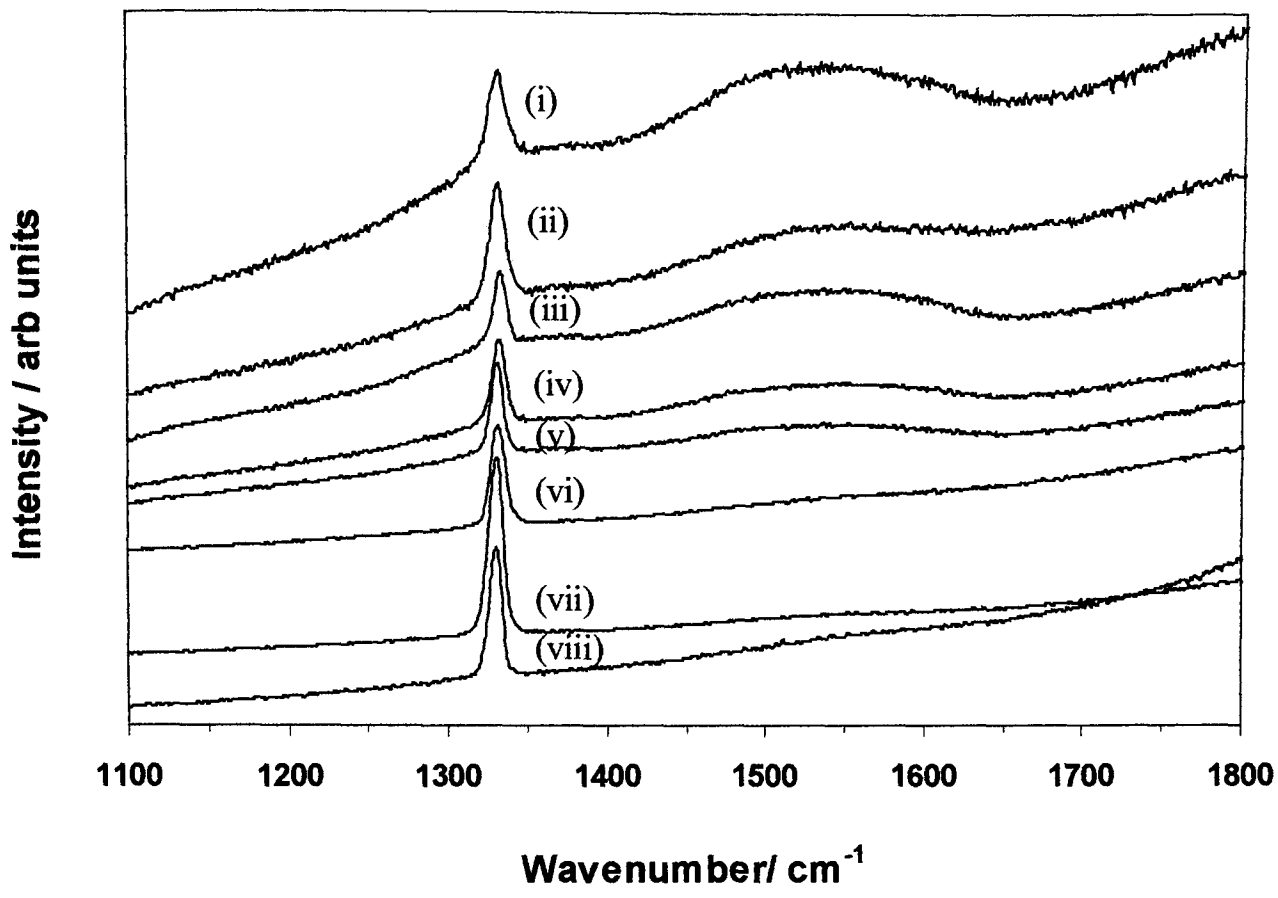
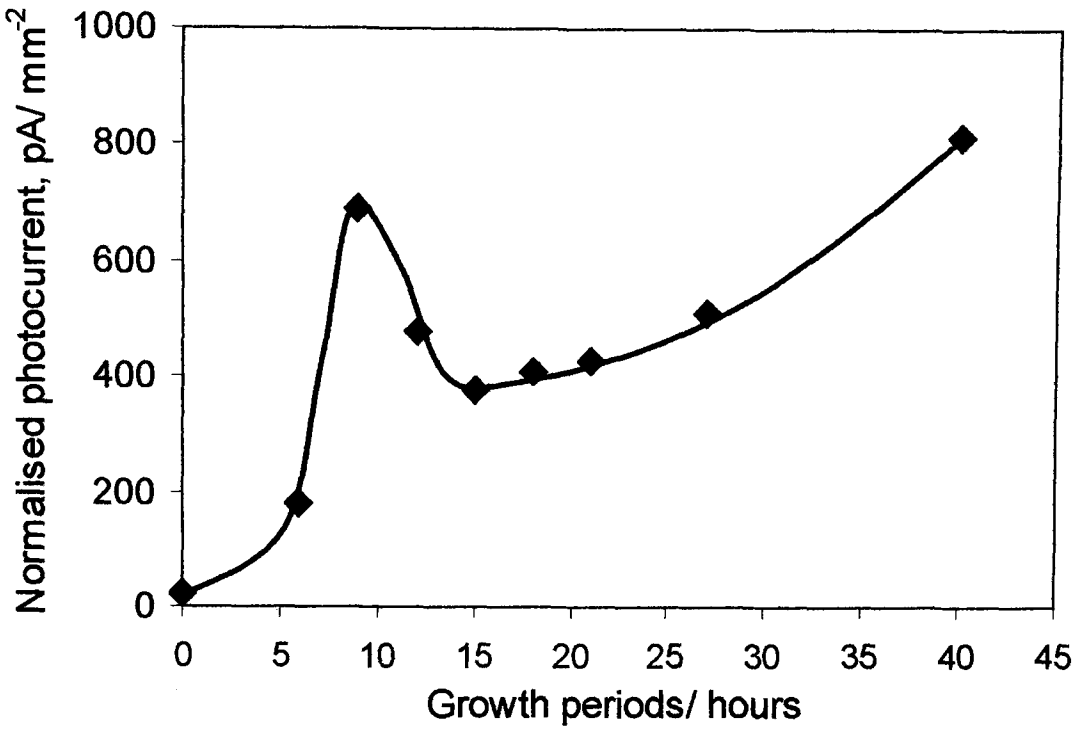


Figure 4. Raman spectra of CVD samples for varying growth times: (i) 6 hours, (ii) 9 hours, (iii) 12 hours, (iv) 15 hours, (v) 18 hours, (vi) 21 hours, (vii) 27 hours, (viii) 40 hours

The emitted photocurrents from the differing samples, recorded soon after growth, are shown in figure 5. It is apparent from this plot that short growth runs significantly increase the photoyield observed from the silicon substrate with an initial peak being observed in the yield plot at around 10 hours growth time, before a complete diamond film has formed on the surface. Subsequently the photoyield then declines before rising gradually at longer growth times. Reported measurements [9] shows that thick (> 200 μm) free standing CVD diamond typically displays photocurrents approximately 10 % greater than the thickest films explored here under the same conditions. It follows therefore that the short growth runs produce photoemitters, which are quite close in yield to such thick diamond layers. For short growth times (< 20 hrs) the photoyield at 252 nm showed a similar qualitative variation to that seen in figure 5 (a), but the yield declined at longer growth times. A plot of the relative photoyield at 186 nm and 252 nm is shown in figure 5 (b). The ratio of the photoyields at the two wavelengths shows little systematic

variation at short growth times, but a significant rise in the ratio is seen for the longer growth runs.

(a)



(b)

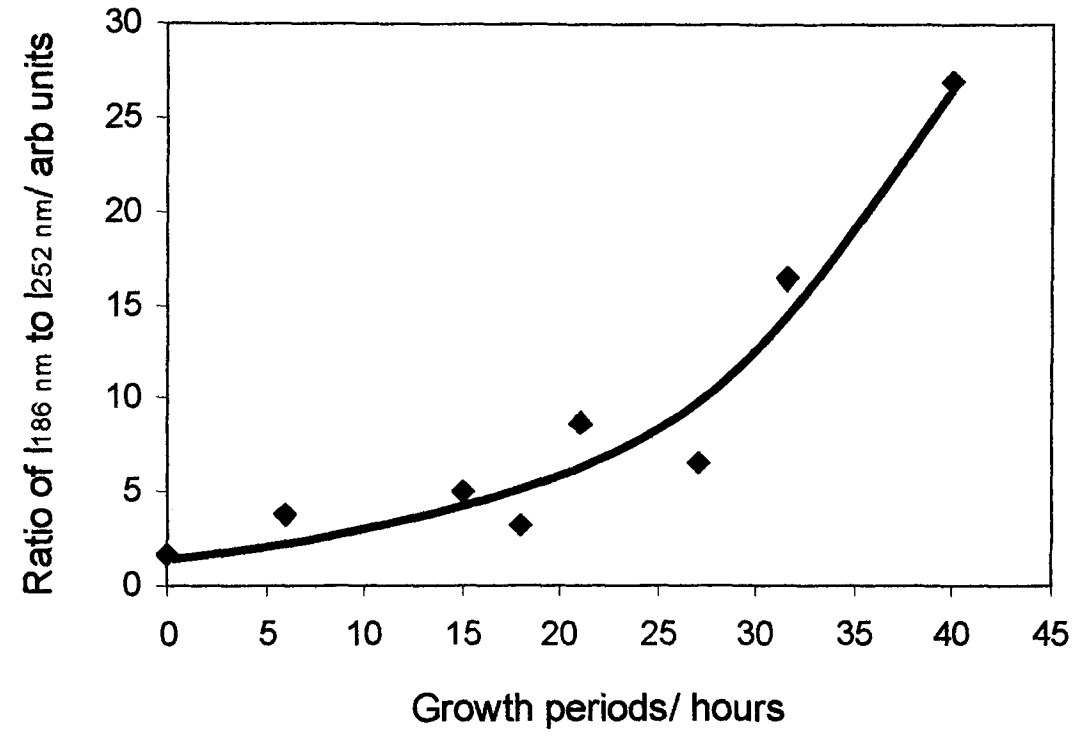


Figure 5. (a) Variation in photoemitted current without filter on growth time; (b) dependence of emitted photocurrent for the ratio of intensity after filteration by filters 186 nm to 252 nm on growth time

The as-grown samples studied in figure 5 have their surfaces largely terminated with hydrogen, which is present naturally on most CVD diamond samples because of the atomic hydrogen used during CVD growth and the stability of this layer in the atmosphere. The effects of differing surface treatments were examined to assess how the extent of growth influenced the photoresponse observed.

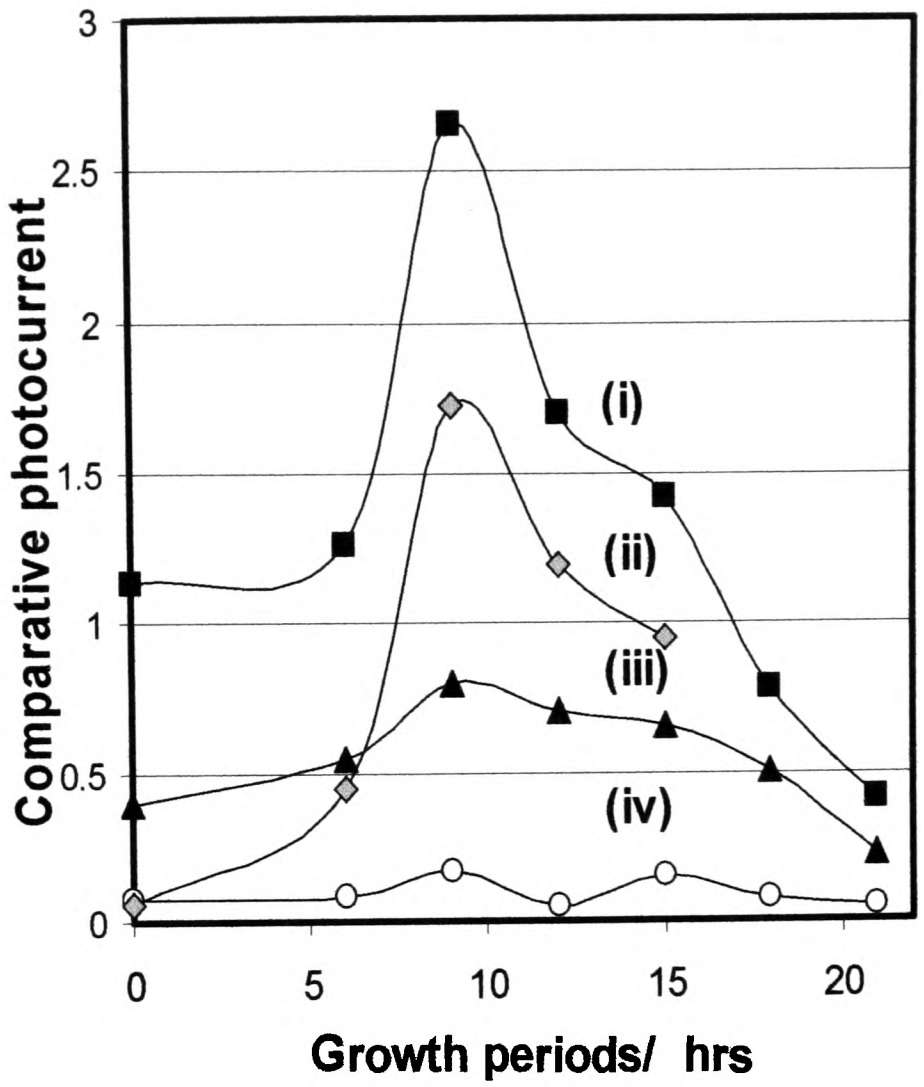
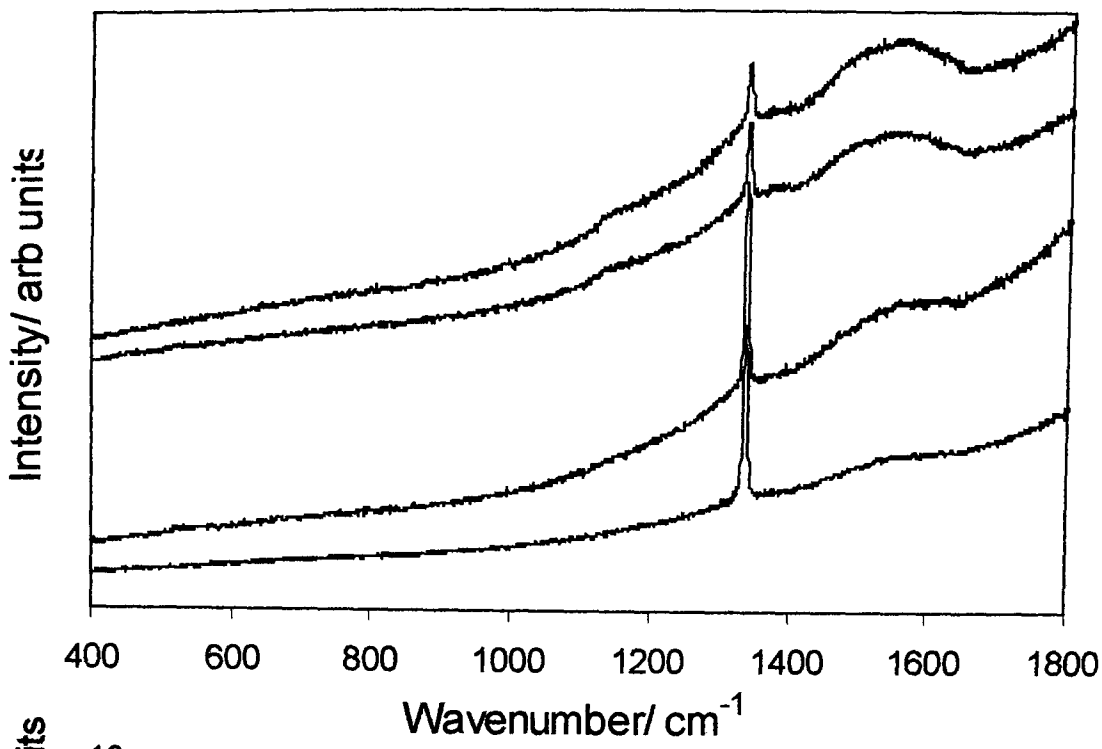


Figure 6. Influence of differing surface treatment on the photoyield at 186 nm for differing growth times: (i) caesiation, (ii) hydrogenated, (iii) annealed in vacuo at 500 °C, (iv) oxidized

The results are presented in figure 6 for as-grown samples which were then either caesiated by evaporating approximately a monolayer of Cs on the surface *in-situ*, oxidized by exposing the sample to 10^{-5} mbar of oxygen in the presence of the incandescent Ir filament, or annealed in vacuo at a temperature of ~ 500 °C. For the clean Si sample, the photoyield is very similar, whether the surface is pre-hydrogenated or oxidized, although vacuum annealing to desorb weakly bound surface contaminants or caesiation significantly increases the quantum yield. In the case of the samples with diamond deposited on them, the hydrogenated samples display a significantly higher photoyield than the oxidized surface, but caesiation again tends to increase the photoyield still further.

Experiments have been performed to compare the different quality of diamond on photoyield in order to gain the insight studies of responsible photoemitter zones on diamond. Four samples were grown in the CVD chamber for a period of 20 hours under

(a)



(b)

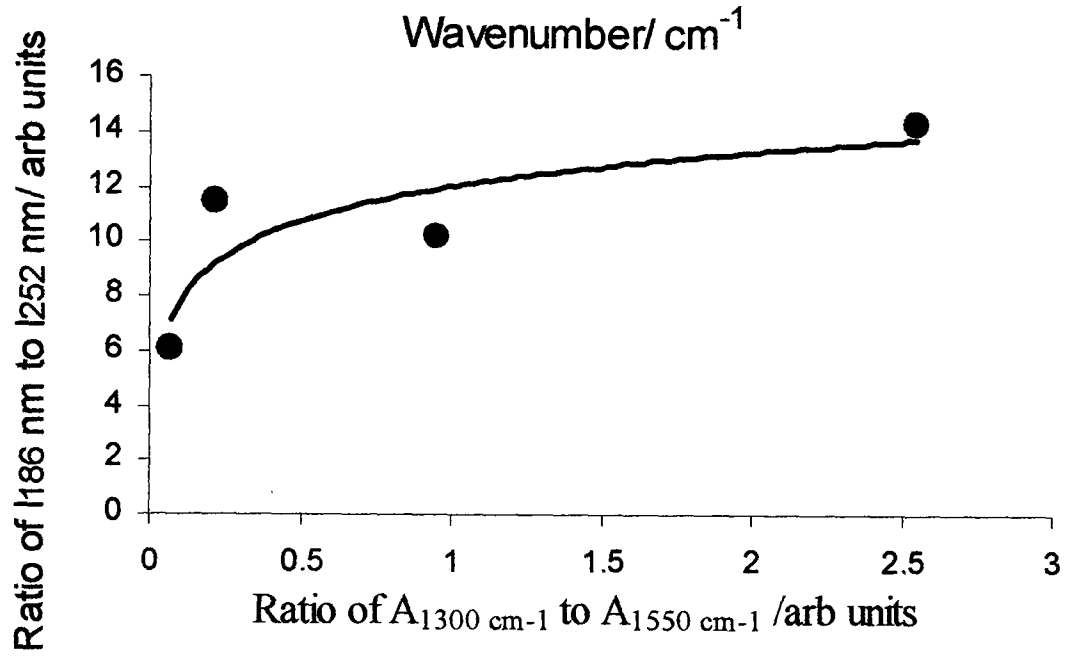


Figure 7. (a) Raman spectra of diamond samples at four different qualities; (b) The correlation in between the ratio of the emitted photocurrent after the filteration by 186 nm to 252 nm filters versus the films quality in term of ratio peaks at 1331 cm^{-1} (sp^3, diamond) to 1550 cm^{-1} (sp^2, non-diamond)

the same growth conditions, except for their different positioning on the platen from the plasma ball, so as to degrade the quality of the films produced. The further the distance from the concentrated plasma, the lower the quality of the diamond was obtained. The qualities of these samples were indicated through the Raman spectra in figure 7a. Individual plots of the variation in photocurrent with no filter and with 186 nm filter in place have shown a levelling off of photocurrent as film quality improves, while the plot for 252 nm filter shows a decrease in photocurrent at higher diamond quality (results not shown). Figure 7 b shows how the ratio of photocurrent of 186 nm to 252 nm filters in place changes with diamond quality. Overall, the ratio of the emission intensities

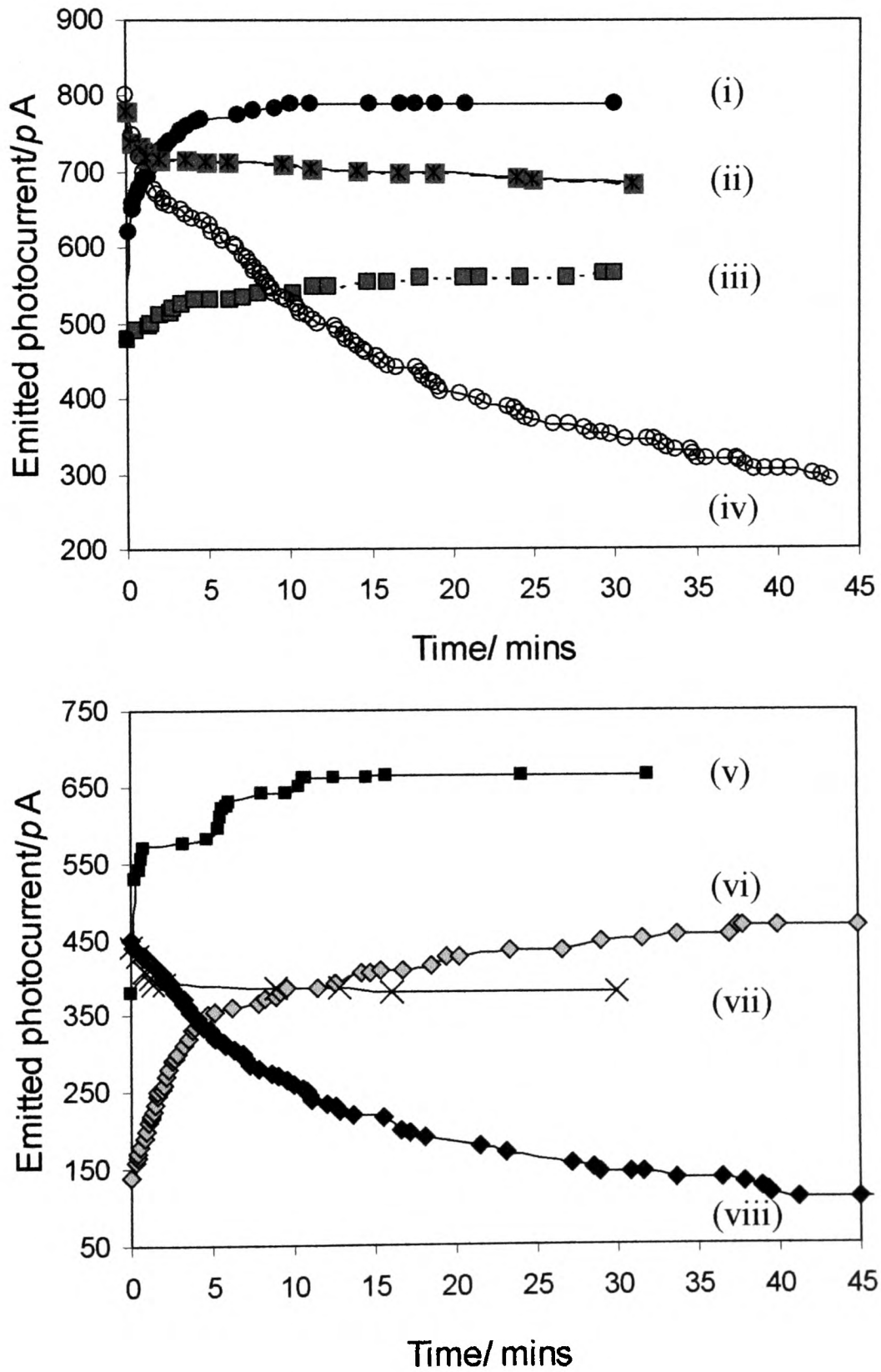
(I_{186}/I_{252}) was again found to increase (by a factor of 2-3) as the non-diamond content of the film reduced.

6.3.2 Reflective Photoemission Mode

6.3.2.1 Photoyield Studies of Gas Hydrogen and Gas Oxygen on Diamond

In-situ investigation of diamond thin film photoyield under UHV system was performed in conjunction with the surface coverage measurements by different gas treatments through XPS. Samples were initially annealed thoroughly at 950 °C to desorb impurities in order to restore the clean, reconstructed diamond surface. Thin films, which were annealed to high temperatures to desorb chemisorbed hydrogen, showed a quantum photoyield of 0.030 % with the emitted photocurrent of 480 *p*A. Gas hydrogen and oxygen were monitored to change the adsorbate termination of the clean diamond surface, which will directly probe the QPY. Each of the photocurrent data was recorded at the same time of the surface exposure to gases in the upper UHV chamber (refer Chapter 2, section 2.3.2), thus the dosing efficiency of gases would be 10-100 times less as the gases were admitted from the bottom chamber. Figure 8(a) reveals the emitted photocurrent as a result of exposure to hydrogen, and was later followed by oxygen dosages. Exposure of the clean diamond to molecular hydrogen (8 iii) has increased a small amount of photoyield to 550 *p*A, whereas the photoyield of clean diamond on the exposure to atomic hydrogen (8 i) has risen sharply to 800 *p*A in 5 min and become saturated. The surface hydrogenated with atomic hydrogen was later exposed to molecular oxygen (8 ii) or to atomic oxygen (8 iv), with the latter showing an exponential decrease in photoyield to 300 *p*A within 30 min. Molecular oxygen however showed merely a slight photoyield reduction to 700 *p*A. In contrast to 8(a), the emitted current in figure 8(b) are shown as a function of exposure to oxygen first, and the sample was later exposed to hydrogen. As soon as atomic oxygen was admitted, the emitted photocurrents decreased greatly in magnitude from the initial

photoyield of 460 *p*A to 130 *p*A within 30 min (8 viii). Re-exposure of the atomic oxygen terminated surface to atomic hydrogen (8 vi) has shown a very slow recovery in photoyield to the value of the clean diamond surface and even for long hydrogen doses the emitted photocurrent never recovers to the value seen without oxygen (atomic) dosing. Exposure of clean surface to molecular oxygen reduces a little photoemission (8 vii), but re-hydrogenation of the surface produces a good photoyield to 680 *p*A (8 v).



8 (a)

8 (b)

Figure 8. (a) The exposure of clean (after annealed and let cool) diamond to (i) atomic hydrogen, (iii) molecular hydrogen, and hydrogenated surface (i) was later treated by molecular oxygen to (ii), and atomic oxygen to (iv); (b) The exposure of clean diamond to (vii) molecular oxygen, and (viii) atomic oxygen, and both were later treated by atomic hydrogen to (v) and (vi) respectively

From the figure 8, it is clear that the photoyield is very sensitive to the amount of oxygen coverage (from the XPS O1*s*/C1*s* ratio) on the diamond surface, independently of how the oxygen was dosed onto the surface, be it prolonged exposure to an ambient atmosphere, exposure to the oxygen atom beam source, or even electrochemical oxidation [10]. The dependence of photoyield on the O:C surface coverage measured in XPS is shown in figure 9, where a near linear decrease in photoyield with the increase of oxygen coverage occurs up to O:C values of 0.1, at which point the photoyield has dropped to negligible values.

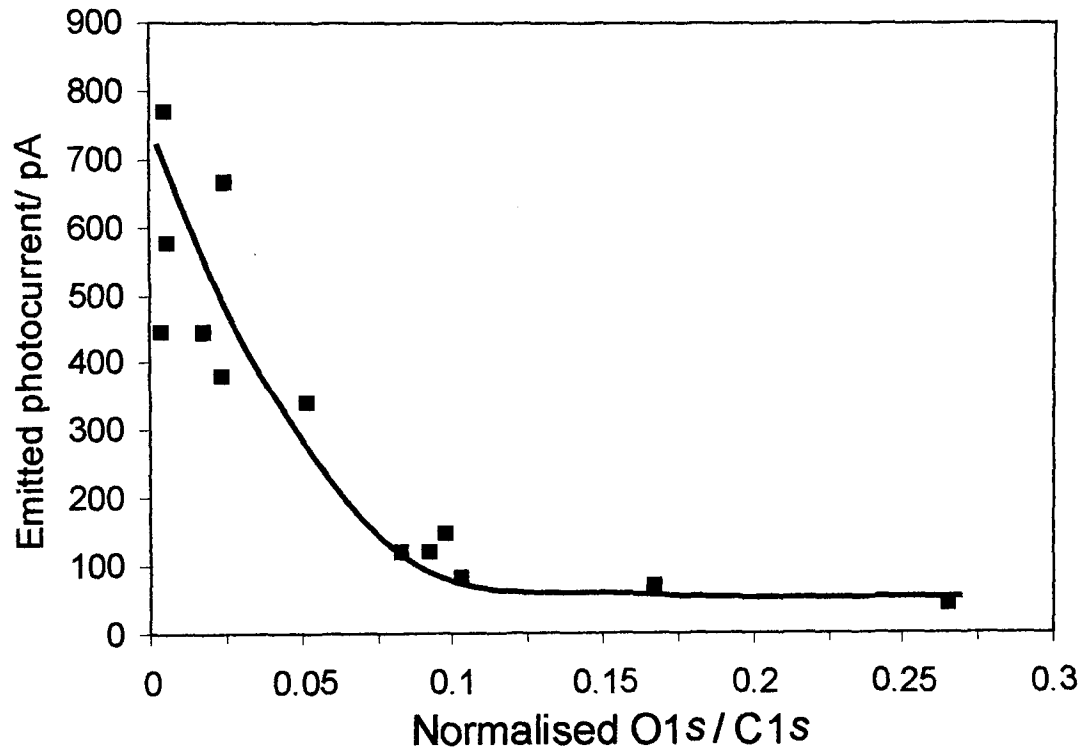


Figure 9. The emitted photocurrents of the hydrogenated diamond as a function of the surface oxygen coverage

The effects under various surface treatments on diamond were studied in order to know the surface compositional functionalities, individually induced by different gas dosages. The respective C1*s* XPS peaks at the end of each surface treatment are revealed in figure 10, where each deconvoluted peak has been fitted carefully using Gaussian Peak fitting. The bulk C1*s* peak for the as-grown sample is positioned at 284.0 eV in the XPS spectrum. Generally, the C1*s* will shift to higher binding energy to 284.4 eV with the

surface exposure to hydrogen, and will shift to lower binding energy at 283.1 - 283.5 eV at high oxygen dosages.

From the figure 10 (i) – (iv), the effect of oxygen dosed on the hydrogen surface is investigated. Under the dosage of atomic hydrogen, the diamond surface was contaminated with small amount of oxygen, which may due to the fact that the dosing was performed in the upper chamber, instead of being dosed in front of the microwave atomic beam source. The polyhydride region which is due to $-CH_x$, $x \geq 2$ species, positioned at + 0.5 eV relative to C 1*s* peak has clearly increased (ii), as compared to as grown (Chapter 2 - 2.13.2) or molecular hydrogen (i). After the exposure to atomic oxygen, the related area of oxygen functionalities increases within the + 2.0 – 3.5 eV (relative to bulk peak) for ether and hydroxyl, and + 4.0 eV for carboxylate related species (iii). This increase is followed concurrently with the decrease of polyhydride peak. Molecular oxygen has little effect on inducing carboxylate species, whether on pre-hydrogenated surface of (iv) or clean surface of (v).

The effect of hydrogen dosed on oxygen is shown as (v) – (viii) in figure 10. The atomic oxygen dosed on clean diamond surface is shown to be very effective in inducing carboxylate related species up to a much higher binding energy region, + 4.0 – 7.0 eV. The effect under the exposure of such oxygenated diamond to hydrogen was examined. Sharp decrease for the highly oxygenated functional group region in C1*s* peak was shown after the exposure to atomic hydrogen (vii).

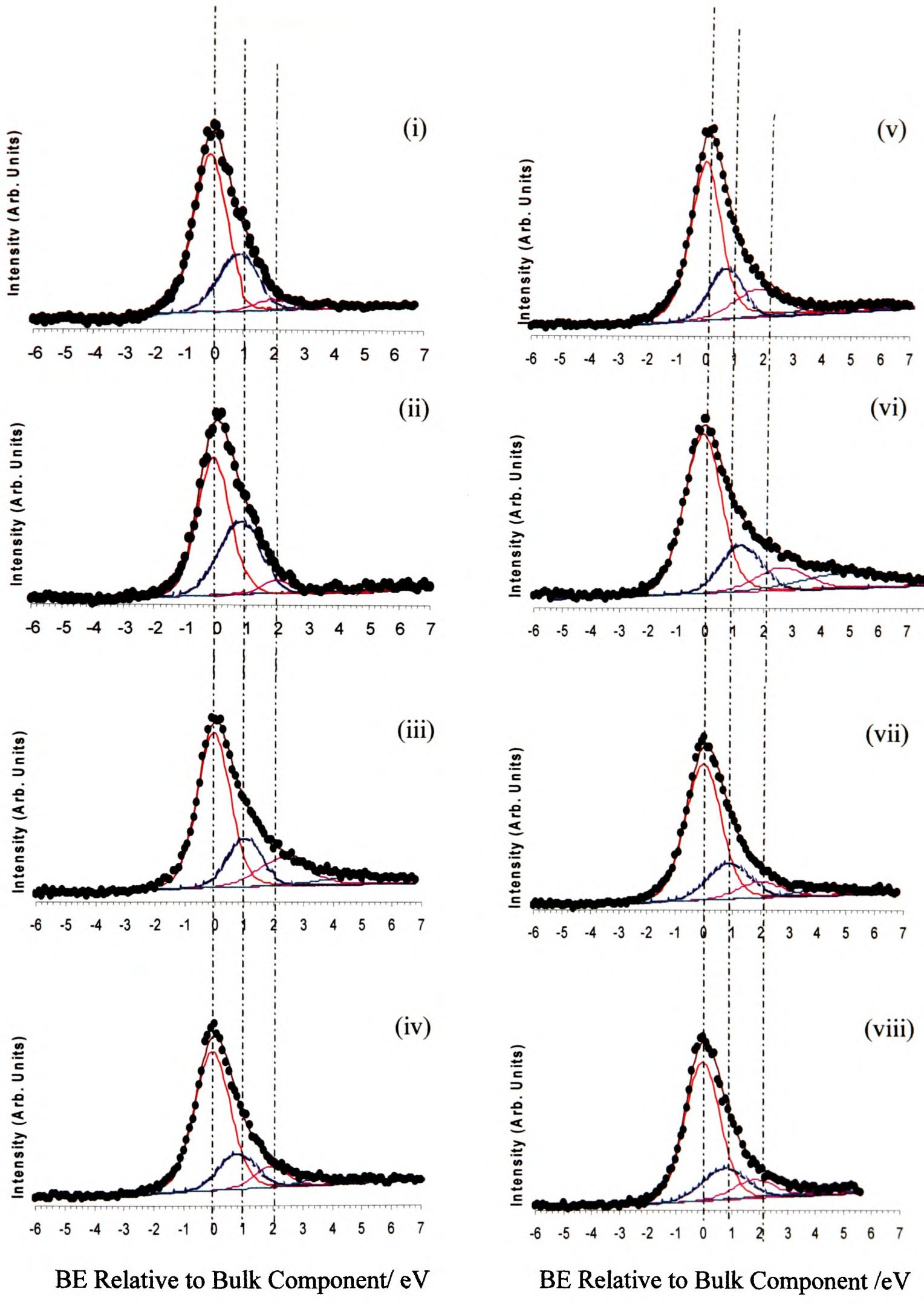


Figure 10. XPS C1s peaks for each surface treatments, as grown (clean) surface being exposed to (i) molecular hydrogen, (ii) atomic hydrogen, (iii) atomic oxygen on H-surface, (iv) molecular oxygen on H-surface; and, as grown surface being treated with (v) molecular oxygen, (vi) atomic oxygen, (vii) atomic hydrogenation on O plasma terminated, and (viii) atomic hydrogen on O_2 treated. Note the line passing 0 eV referred to bulk peak, the line passes 1 eV referred to polyhydride groups, and the line passes 2 eV is referred to ether/hydroxyl components, and the deconvoluted peak at highest energy (+ 4.0 eV) referred to carboxylated-related species

The oxygen coverage of each treated diamond under UHV (as revealed previously in figure 10) is calculated and the data is shown in figure 11, with the comparison made to as-grown and air-exposed surfaces. The diamond surface which is oxygenated under atomic oxygen source on clean (vi) or prehydrogenated (iii) have shown the highest oxygen coverage with nearly half a surface oxygen monolayer. Exposure of oxygenated surfaces to atomic hydrogen has decreased the oxygen coverage by a factor of 2-3, whereas the exposure of hydrogenated to atomic oxygen has shown a sharp increase by a factor of nearly 5-10.

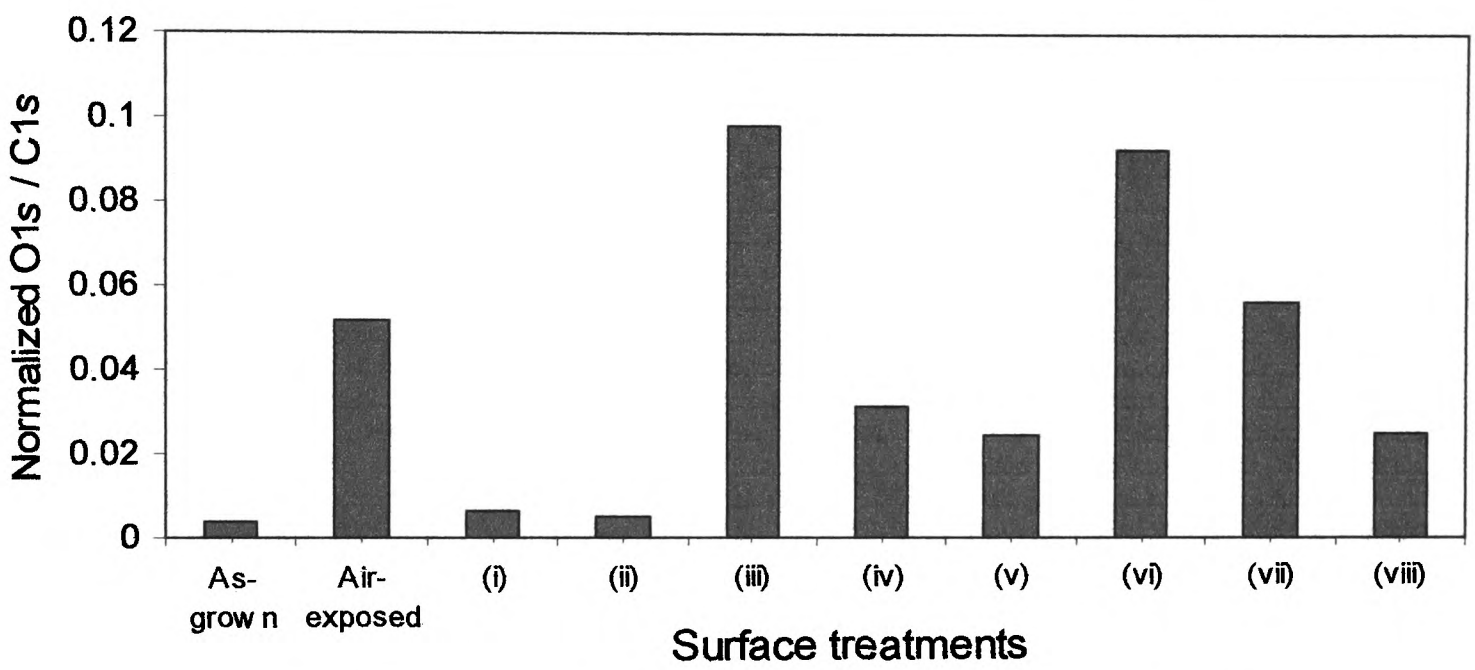


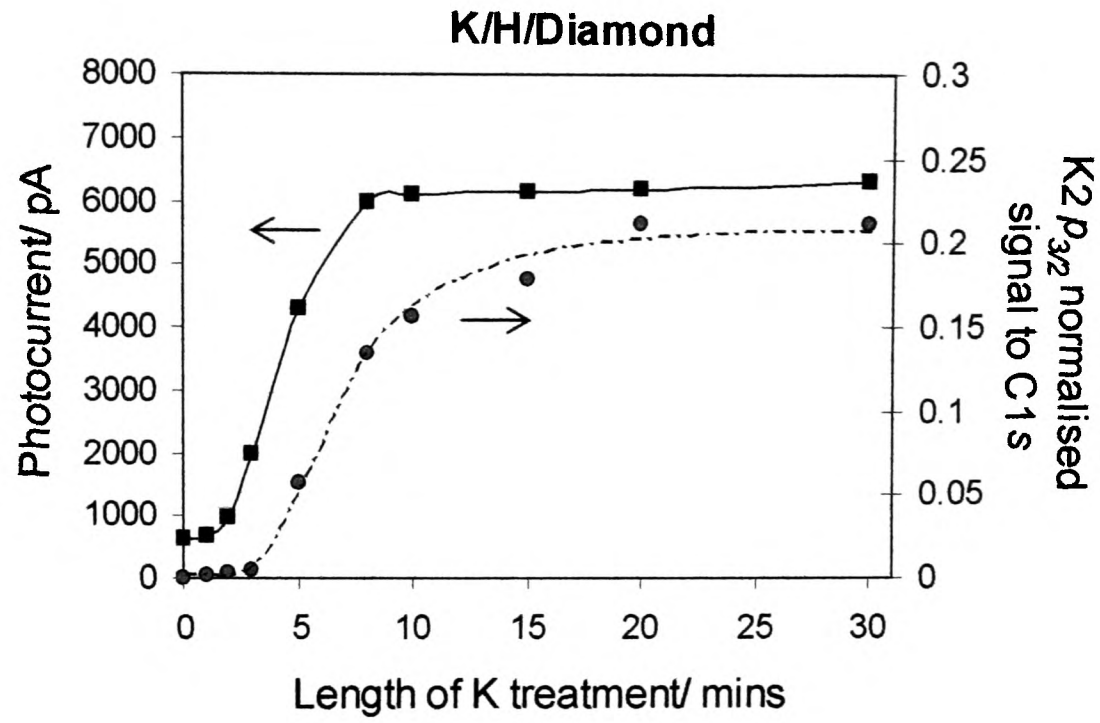
Figure 11. The normalised oxygen coverage of different treatments, compared to as-grown and air-exposed diamond. (i) molecular hydrogen on clean diamond, (ii) atomic hydrogen on clean diamond, (iii) atomic oxygen on (ii) surface, (iv) molecular oxygen on (ii) surface; (v) molecular oxygen on clean diamond, (vi) atomic oxygen on clean diamond, (vii) atomic hydrogen on (vi) surface, and (viii) molecular hydrogen on (vi) surface

6.3.2.2 Photoyield Study of K on Diamond

Adsorption of metals on photocathodes can usually enhance the photoyield in terms of surface fabrication into a more controllable manner. Alkali metals, K and Cs, have been chosen and deposited on both hydrogenated and oxygenated diamond surfaces. Figure 12 shows the K uptake on hydrogenated and oxygenated surfaces respectively, along with the emitted photocurrents when the length of deposition varies. For figure 12 (a), the initial photoyield of 800 *p*A for hydrogenated diamond has increased gradually with the

increases of K dosages and has reached saturation level at 6200 *p*A with a K:C ratio of 0.15. Further increases of K uptake to one monolayer of surface coverage will have no effect on the photoyield enhancement.

12 (a)



12 (b)

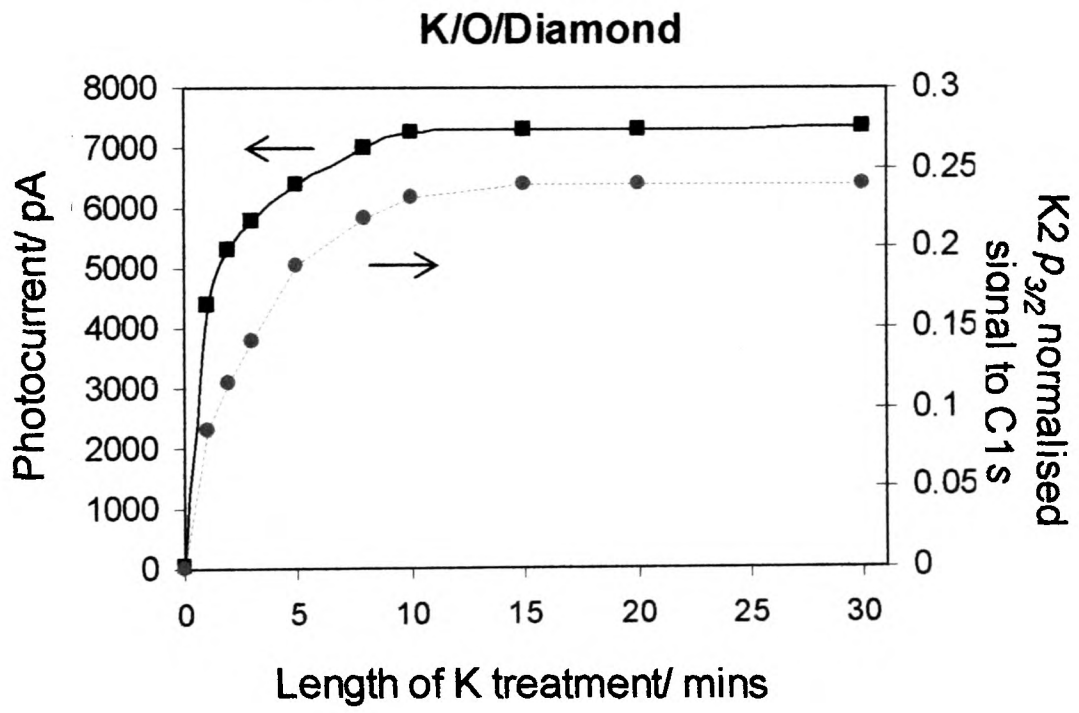


Figure 12. The dependence of photoyield (left vertical axis) and K uptake (right vertical axis) on the deposition of K on (i) H-surface, and (ii) O- surface at substrate temperature of 300 K at a supplied current of 6.4 A

The initially oxygenated diamond (figure 12 b) with very low photocurrent of 130 *p*A has increased drastically as soon as the K was deposited. The photoyield of K/O/diamond increased concurrently with the K uptake, as the length of K deposition period increased. The saturation level was reached with a photoyield of 7200 *p*A at a K:C ratio of 0.24 (of a K surface coverage of nearly one monolayer) after 10 min K deposition.

Figure 13 shows the photoyield of the surfaces after being exposed to molecular oxygen at a pressure of 2 x 10^{-6} mbar, resulting a rapid reduction in photocurrents of nearly 50 % for K/H and K/O surfaces, after 5 min. The photoyield was saturated at 30 min with photoyields of 1250 *p*A for K/H and 1510 *p*A for K/O surfaces at surfaces O: C of 0.21 and 0.35 respectively. .

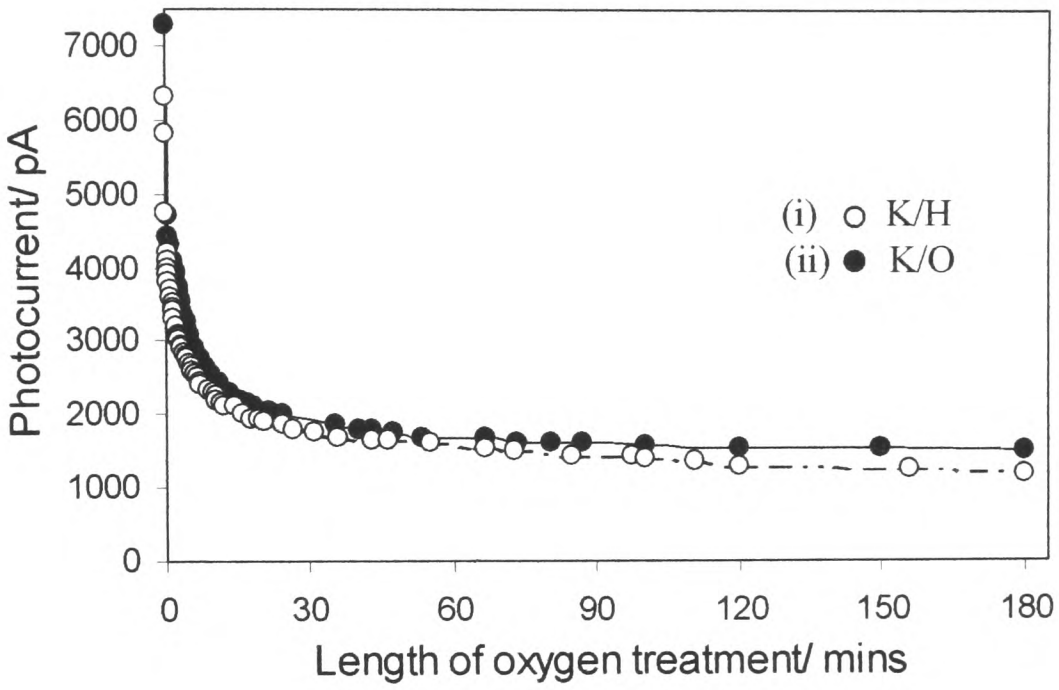


Figure 13. The time dependence of photoyield with the exposure of (i) K on H-surface, and (ii) K on O-surface to molecular oxygen

The possibilities of restoring the photoyield for the O_2 terminated surfaces was tested by re-exposing the surfaces to atomic hydrogen at a pressure of 2 x 10^{-6} mbar. Figure 14 shows sharp increases of photoyields to 2700 *p*A for both of the re-exposed surfaces, O_2/K/H and O_2/K/O to atomic hydrogen for the first 2 min. There is no difference between the two environments, O_2/K/H and O_2/K/O upon the treatment by atomic H.

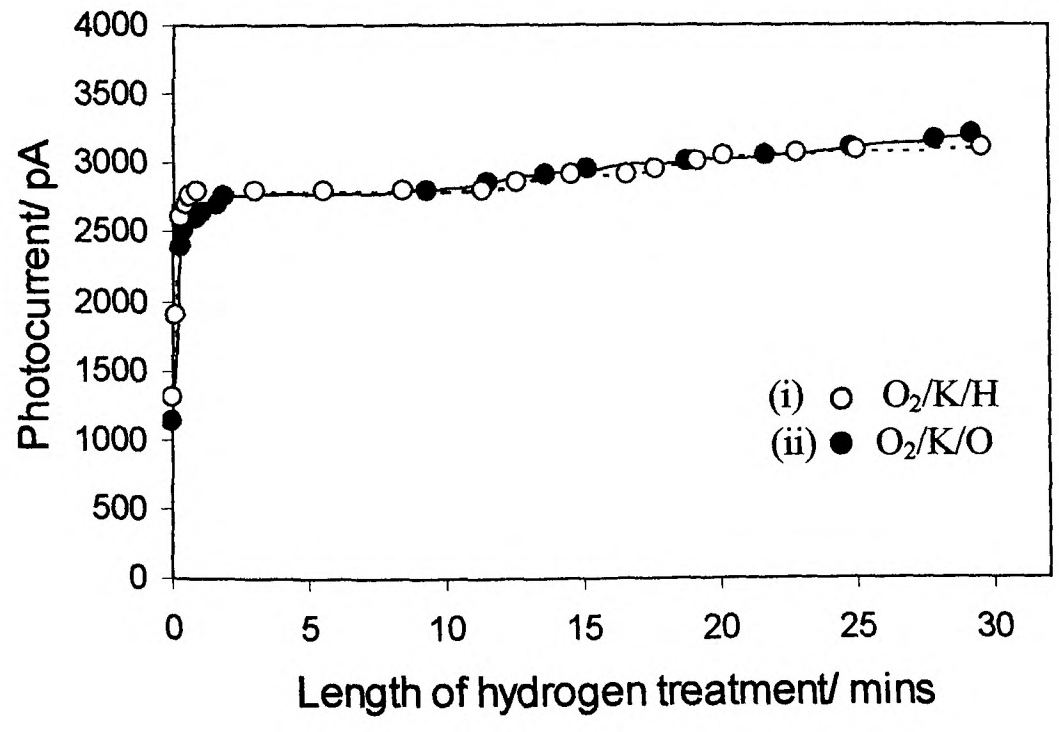
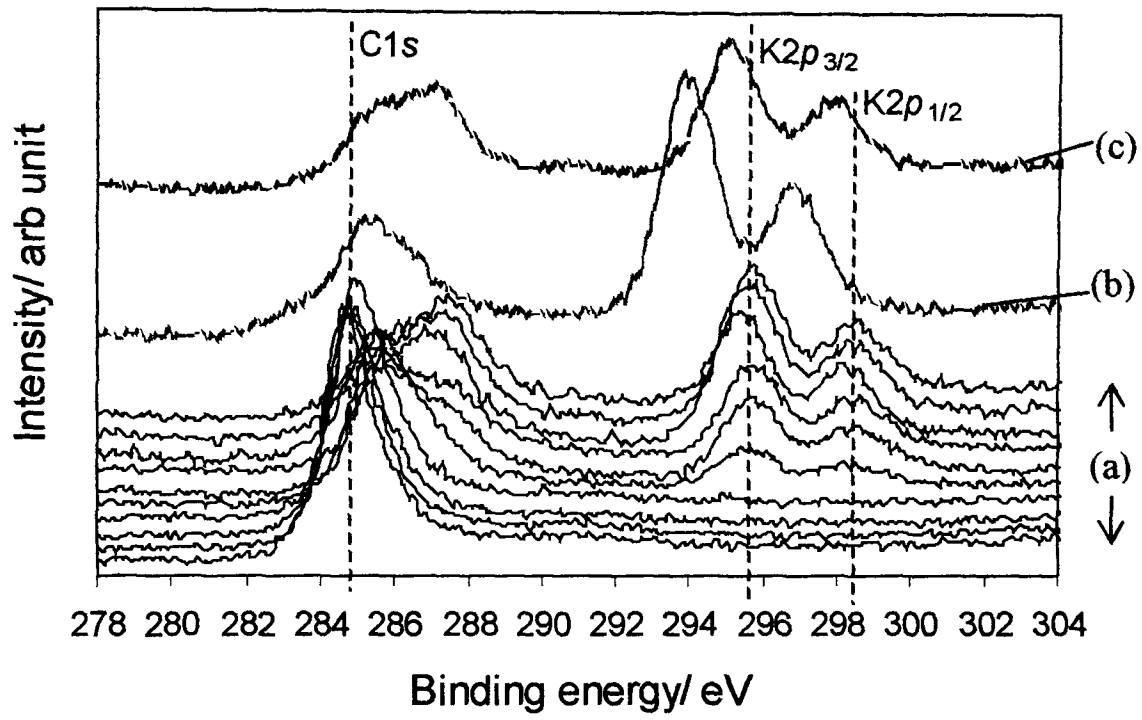


Figure 14. The time dependence of photoyield with the exposure of (i) O_2/K/H and (ii) O_2/K/O to atomic hydrogen

The surface compositional changes on K/H and K/O surfaces were monitored by XPS. The uptake of K on the hydrogenated surface is evidenced by the K 2*p* states (K $2p_{3/2}$ at 295.6 eV and K $2p_{1/2}$ at 298.4 eV) with insignificant chemical shift being observed during the K deposition. This is followed concurrently with the decreases of C 1*s* intensities. By dosing the K/H to the molecular oxygen (15 i b), both of the K 2*p* states have shifted to lower binding energy with a magnitude of ~ 1.8 eV and with the increases of K intensities. With the exposure to atomic hydrogen (15 i c), the individual chemical states of K 2*p* have shifted back to 294.9 eV and 297.7 eV.

15 (i)



15 (ii)

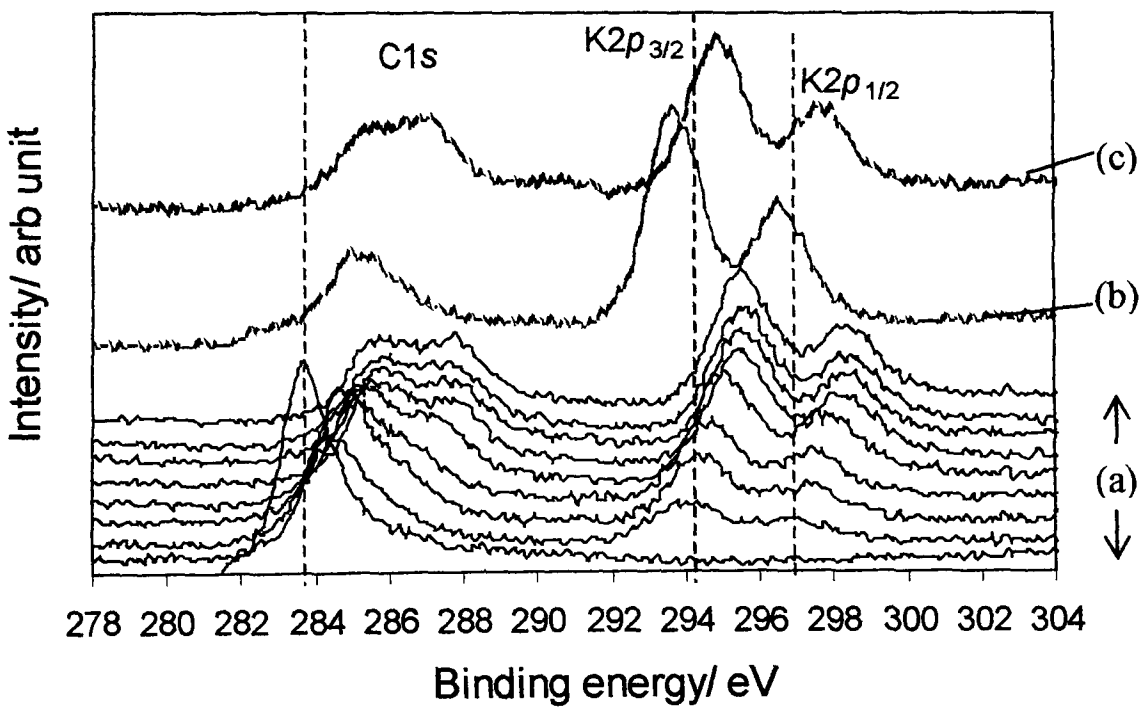


Figure 15. The XPS of K uptake (0 - 1 ML) on (i) hydrogenated, and (ii) oxygenated surface for "a region" with increases of time, later being exposed to 16200 Langmuirs molecular oxygen ("b") and "c" being re-exposed to atomic hydrogen; the lines are drawn as references relative to the initial respective binding energies

Oxygenated surfaces show C 1*s* binding energy at 283.6 eV (figure 15ii and 16), and the deposition of K had shifted both the C 1*s* and the chemical states of K 2*p* to higher binding energies (15ii a). The trend of chemical shifts of K 2*p* for K/O are similar to K/H after the surface were exposed to molecular oxygen, or later with atomic hydrogen. The C 1*s* peaks in XPS for K/O surface at different surface treatments were fitted, as shown in figure 16. A big increase of metal-carbon peak (~ +2.3 eV) arises clearly next to bulk peak along with the deposition of time.

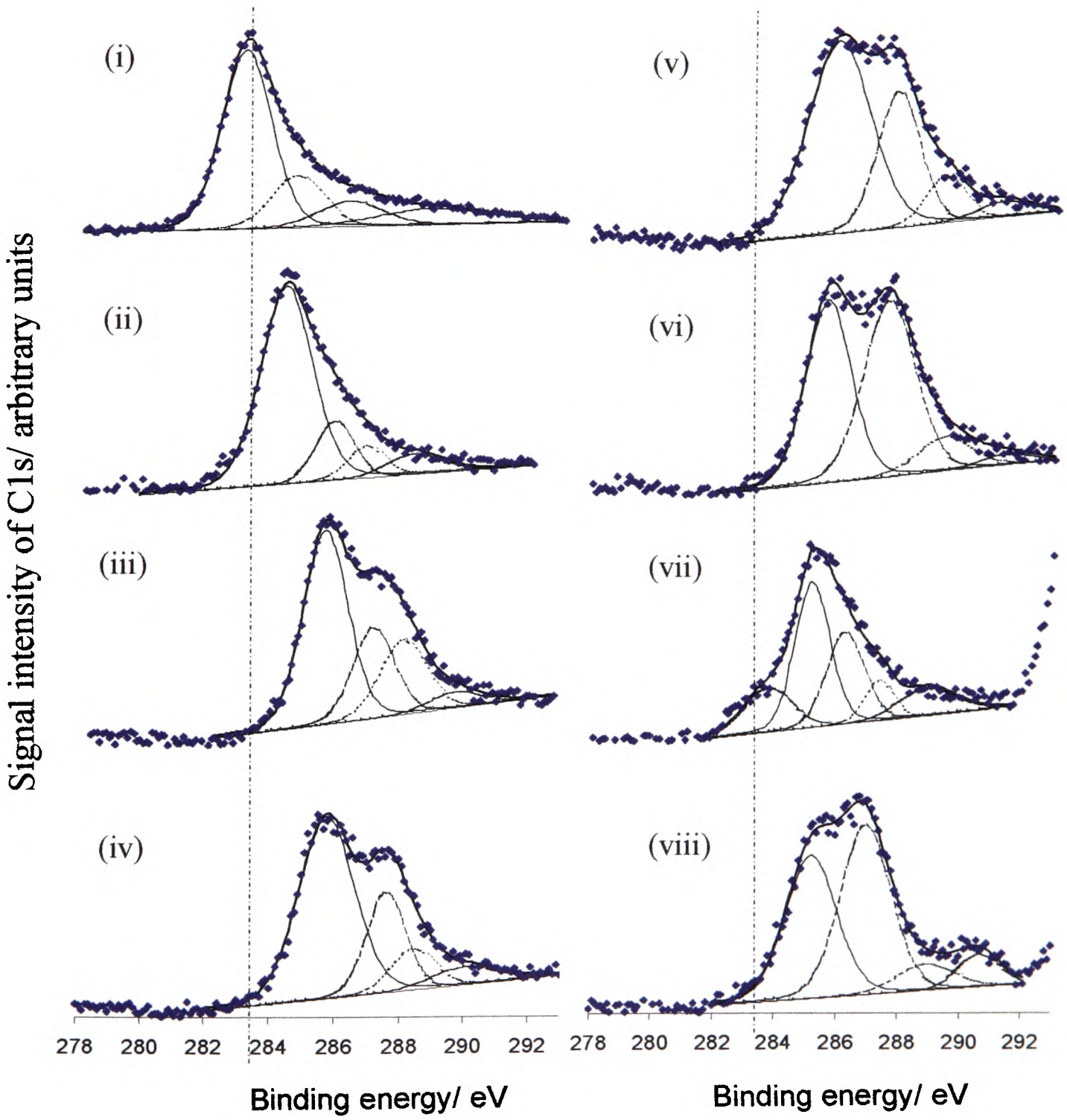
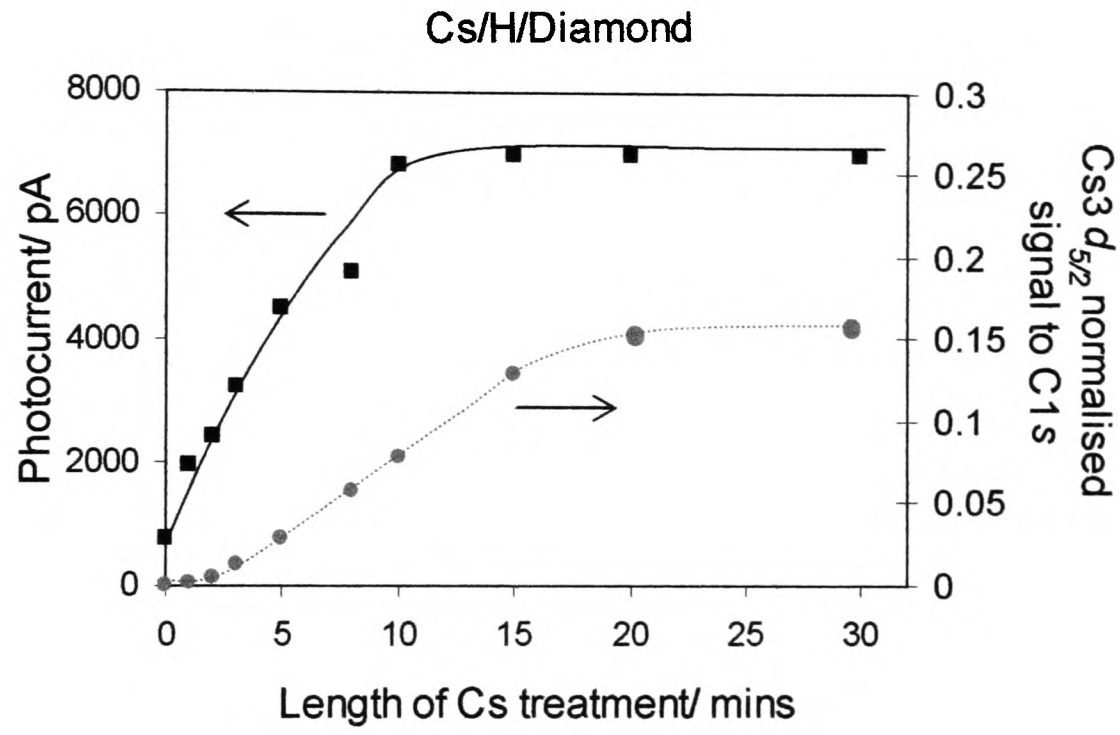


Figure 16. The changes of XPS peak fitted C1s peaks with the deposition of K on O-terminated surface (i)-(vi) with 0 ML K (i), 0.2 ML K (ii), 0.45 ML K (iii), 0.60 ML (iv), 0.80 ML (v) and 1.00 ML K (vi), later being exposed to 16200 Langmuirs molecular oxygen (vii), and re-exposed to atomic hydrogen (viii); the lines are drawn across 283.5 eV as a reference to the initial binding energy (O-surface)

6.3.2.3 Photoyield Study of Cs on Diamond

The same experiments have been repeated for Cs deposition. Figure 17(b) shows a significant increase in reflective mode photoyield for the Cs deposited surface, particularly on the pre-oxygen-terminated surface with an optimum photoyield of 10 *n*A, as compared to 7 *n*A for Cs/H-terminated surface (figure 17a). As a similar case to K/H, the emitted photocurrent from the Cs/H surface was saturated before the full Cs coverage, by which the Cs:C is observed at ~ 0.10. The photoyield for Cs dosed on an O-surface increases linearly with the increases of Cs:C ratio. The saturation dose is achieved at 0.15, which is equivalent to a monolayer of Cs on the surface.

17 (a)



17 (b)

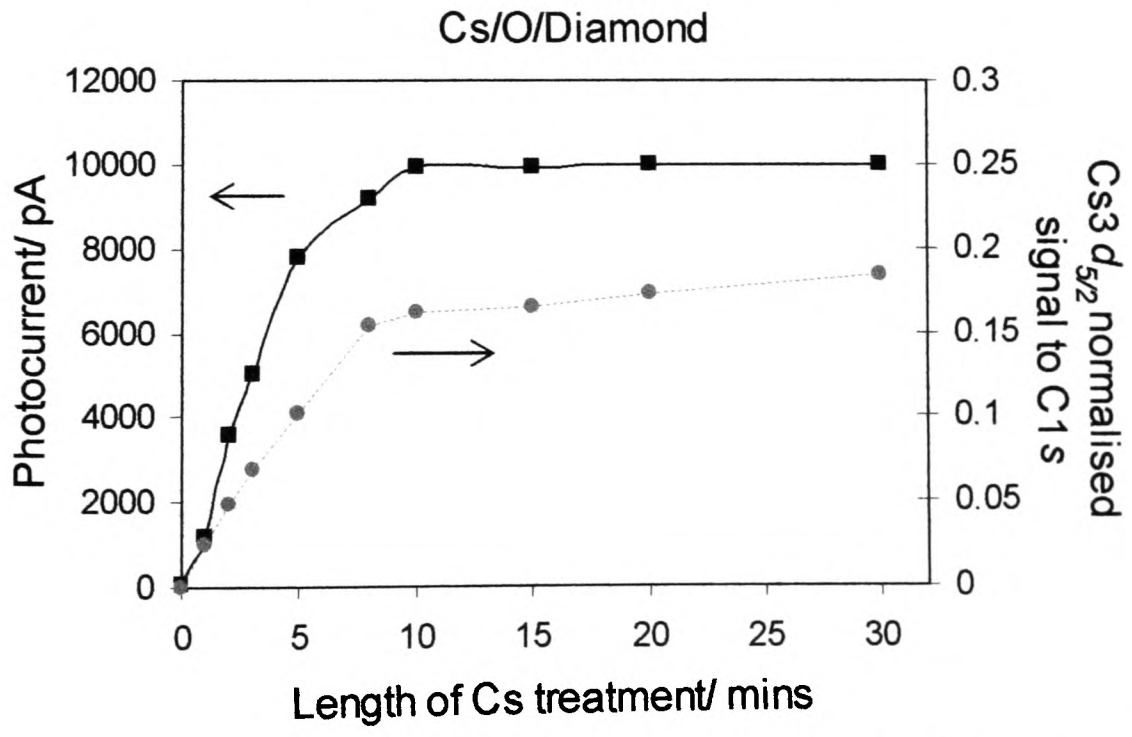


Figure 17. The dependence of photoyield (left vertical axis) and Cs uptake (right vertical axis) on the deposition of Cs on (i) H-surface, and (ii) O- surface at substrate temperature of 300 K at a supplied current of 7.6 A

Significant damages on photoyield performance were shown for both Cs/H and Cs/O surfaces as soon as with the admittance of molecular oxygen. The emitted photocurrent from the Cs/O surface decreased to nearly half of the initial value after the exposure to oxygen for 30 min at a pressure of 2 x 10^{-6} mbar. After 3 hours, the photocurrent was saturated at 2800 *p*A at a surface O: C ratio of 0.46. Cs/H surface shows a similar decrease rate and at the end of 3 hours exposure, the photoyield left was about 1400 *p*A at O: C ~ 0.36. Therefore, the Cs/O surface has shown the best photoyield emitter even with the corrosion of molecular oxygen, as compared to K/H, K/O or Cs/H surfaces.

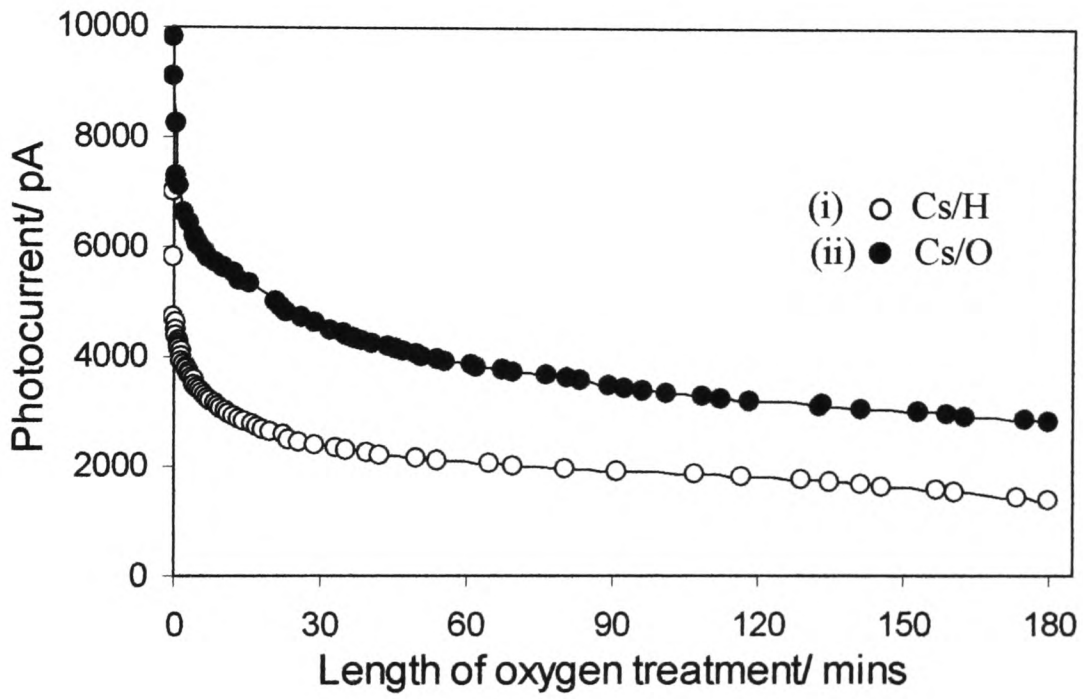


Figure 18. The time dependence of photoyield with the exposure of (i) Cs on H-surface, and (ii) Cs on O-surface to molecular oxygen

With the re-exposure of the treated surfaces in figure 18 to atomic hydrogen, the emitted photocurrents increased drastically up to 7550 *p*A for O_2/Cs/O and 3400 *p*A for O_2/Cs/H surfaces. This result is shown in figure 19. The restored photoemitting Cs surfaces show higher photoyields than the restored K surfaces (were shown earlier in figure 14).

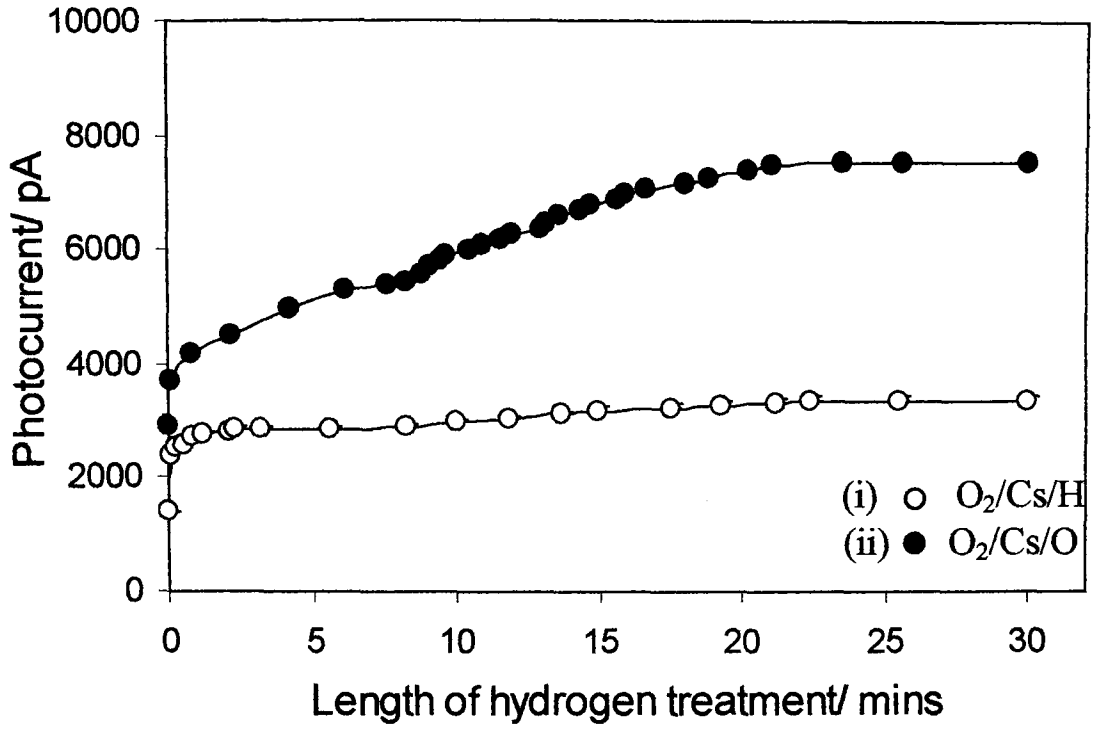
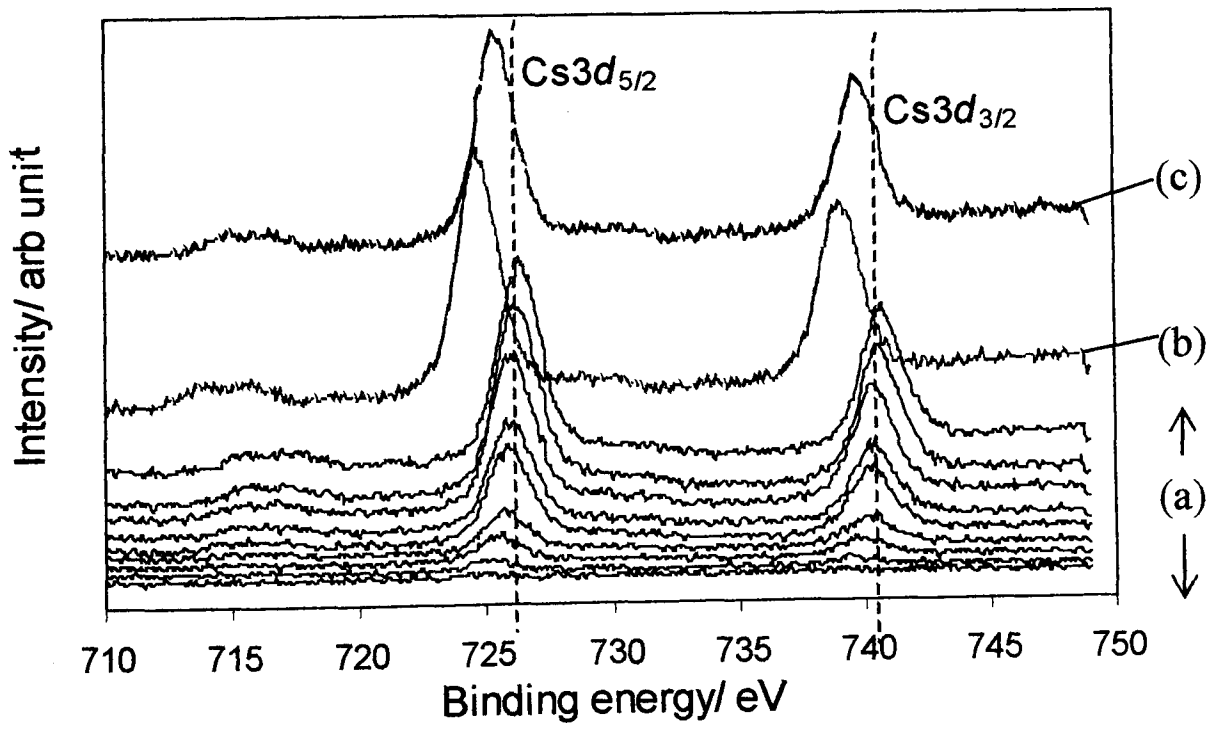


Figure 19. The time dependence of photoyield with the exposure of (i) O_2/Cs/H and (ii) O_2/Cs/O to atomic hydrogen

In figure 20 (i), the surface coverage by Cs deposition on the hydrogenated surface was monitored by XPS, showing the linear increase of both Cs 3*d* chemical states (Cs $3d_{5/2}$ at ~ 726.3 eV and Cs $3d_{3/2}$ at ~ 740.4 eV) for H-surface, without chemical shifts involved. However, with the exposure to molecular oxygen, figure 20 (i b), the chemical states of Cs 3*d* have shifted to lower binding energy of a factor of 1.8 eV, and recovered back to higher binding energy at 725.2 eV and 735.5 eV after being exposed to atomic hydrogen (c).

20 (i)



20 (ii)

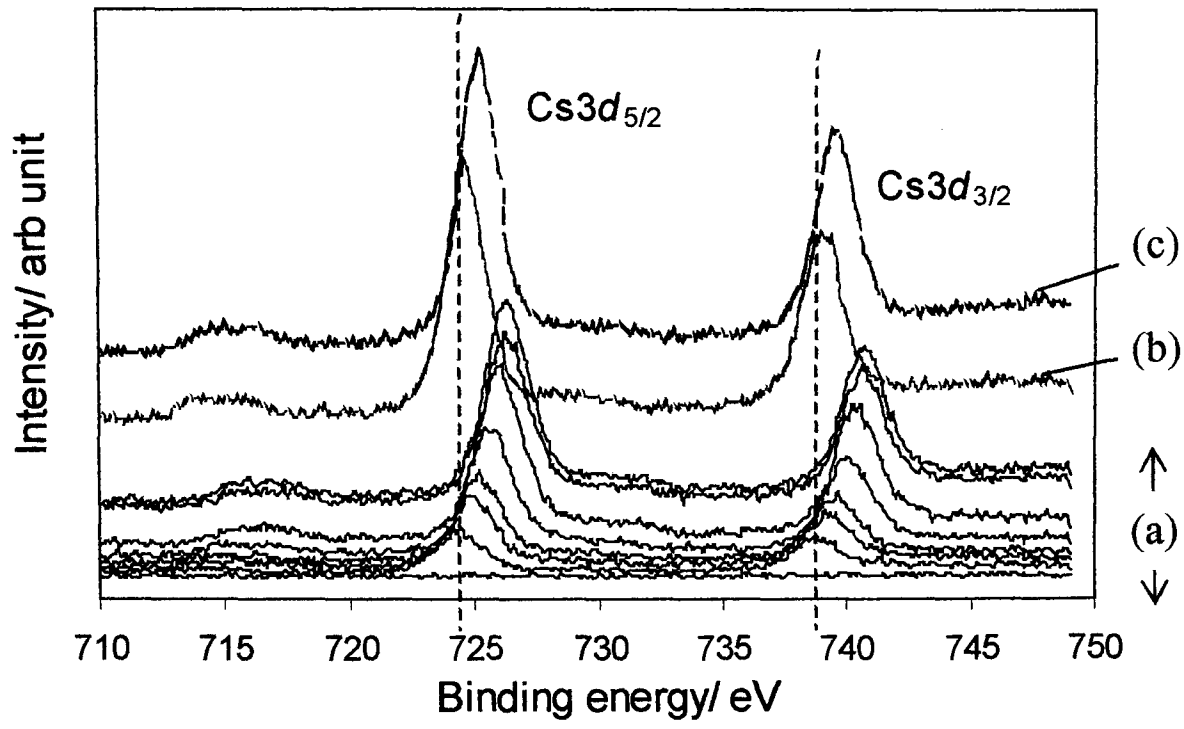


Figure 20. The XPS of Cs uptake (0 – 1 ML) on (i) hydrogenated, and (ii) oxygenated surface for "a region" with increases of time, later being exposed to 16200 Langmuirs molecular oxygen ("b") and "c" being re-exposed to atomic hydrogen; the lines are drawn as references relative to the initial respective binding energies

For the deposition of Cs on the oxygenated diamond surface, the binding energies for both Cs 3*d* chemical states have shifted from the initial 723.7 eV for Cs $3d_{5/2}$ and 738.7 eV for Cs $3d_{3/2}$ to higher binding energy of 726.0 eV and 740.5 eV respectively at a monolayer of Cs surface coverage. A similar trend to Cs/H is observed as the chemical states of Cs 3*d* were shifted to lower binding energy (- 1.4 eV) with the exposure to molecular oxygen (b) and were later shifted to higher binding energy (+ 0.8 eV) relative to (b) after the photoemitting surfaces were restored with atomic hydrogen (c).

With the increase in Cs deposition, the XPS intensities for C 1*s* peaks decreased with the emerging occurrence of chemical shifts towards higher binding energy accordingly to the increases of + 0.3 eV per 0.1 Cs monolayer formed on O-surface (figure 21). The deconvoluted peaks at + 0.5 eV relative to the bulk C 1*s* had arisen as a competitive major peak along with the increases of Cs dosage up to a Cs monolayer coverage (i) – (vi). The earlier assignment of this peak to polyhydrides should be ruled out, and thus should be attributed to diamond-metal bonding.

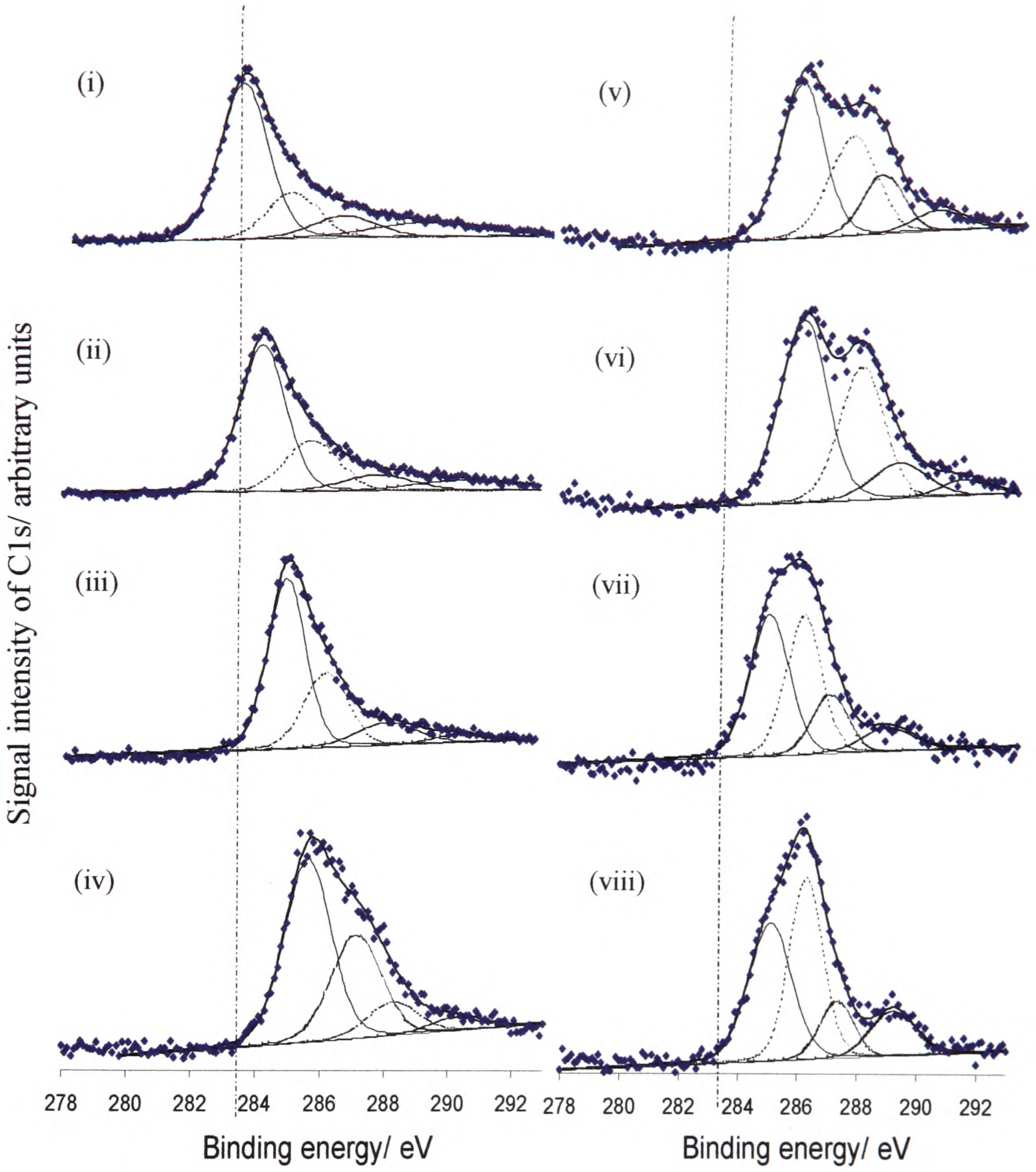


Figure 21. The changes of XPS fitted C1s peaks with the deposition of Cs on O-terminated surface (i)-(vi) with 0 ML Cs (i), 0.2 ML Cs (ii), 0.45 ML Cs (iii), 0.60 ML Cs (iv), 0.80 ML Cs (v) and 1.00 ML Cs (vi), and was later being exposed to 16200 L molecular oxygen (vii), and re-exposed to atomic hydrogen (viii); the lines are drawn across 283.5 eV as a reference to the initial binding energy O-surface

The relative change in O1*s* peaks for the series of Cs deposition on the oxygenated diamond surface (as shown in figure 22) demonstrates that the peak at 532.7 eV has split into three minor peaks with smaller intensities, whereas the peak at the lower binding energy of 531.6 eV increased simultaneously with increasing Cs deposition. The four

deconvoluted peaks remain in relatively similar ratios of intensity throughout the Cs dosages (i) - (v), at similar O 1*s* binding energy. With the admittance of molecular oxygen (vi), the O 1*s* shifted to 530.4 eV with the same remaining deconvoluted peaks. However, with the exposure to atomic hydrogen, only three major peaks under O 1*s* were visible, by which the peak at 531.6 eV in the middle of the three happened to have the highest intensity.

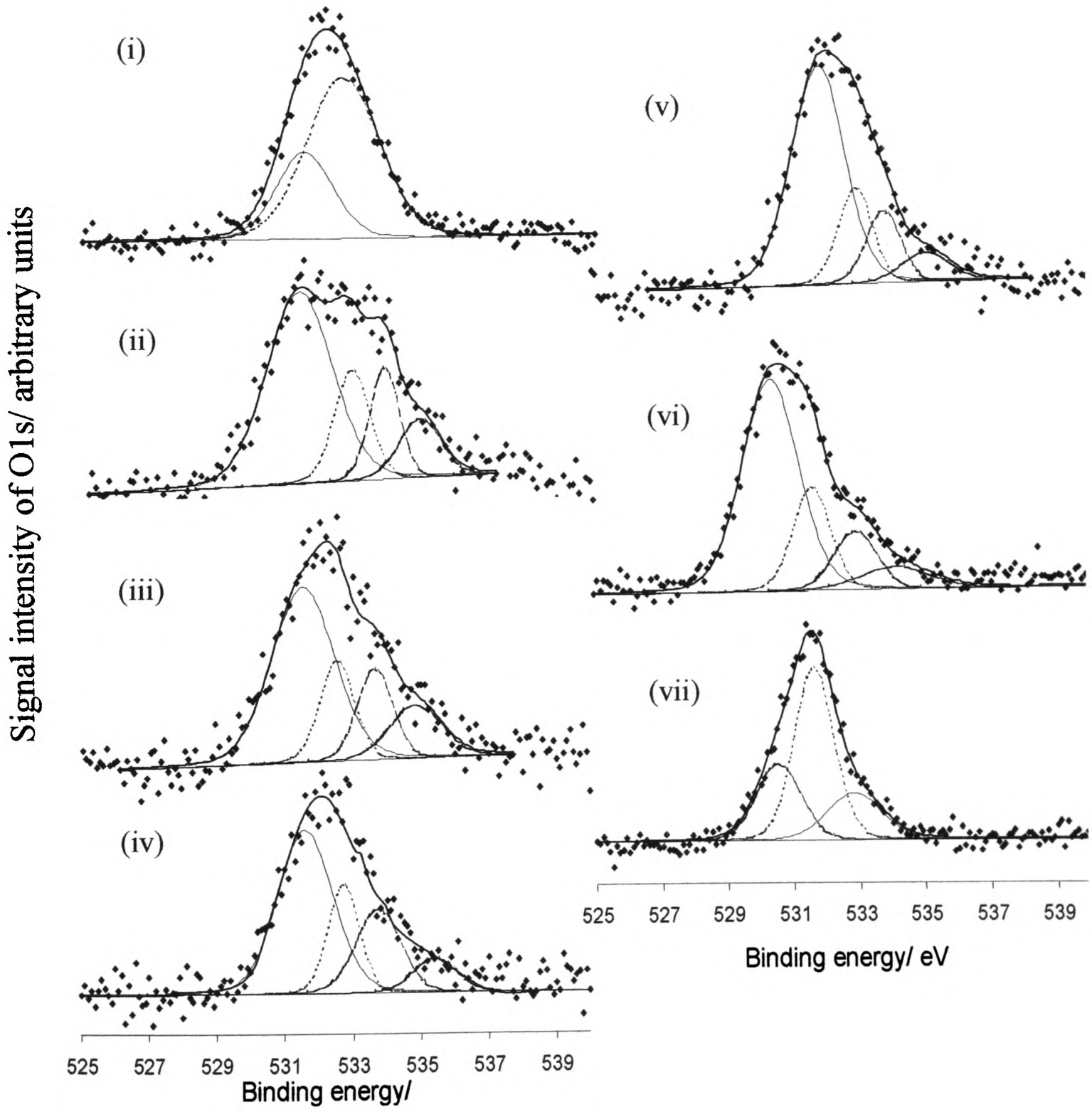


Figure 22. XPS of O1s peak with the deposition of Cs on O-terminated surface (i)-(v), with 0 ML Cs (i), 0.2 ML Cs (ii), 0.6 ML Cs (iii), 0.8 ML Cs (iv) and 1.0 ML Cs (v), and was later exposed to 16200 L molecular oxygen (vi), and later to atomic hydrogen (vii)

6.3.2.4 Photoyield Studies on Thermal Stability of Alkali Metals

An ideal photocathode should possess the properties of good photoemission, and at the same time the surface is required to withstand a high thermal stability for the application in harsh environments. The enhanced photoyields of diamond by alkali metals deposited on H- or O-surfaces have been investigated on such aspect, by subjecting the individual samples to a gradual increase of temperature for 10 min in UHV. The effects of annealing on the K deposited surface are shown in figure 23a. K/O shows higher photoyield than K/H as the annealing temperature increases. Both of the surfaces suffered from a sharp reduction (> 50 %) in emitted photocurrents as the temperature reached a cut-off point of 400 °C, with the occurrence of the rapid fall in K: C ratios shown in the inset. When this ratio dropped down to very low values, the photoyield became insignificant.

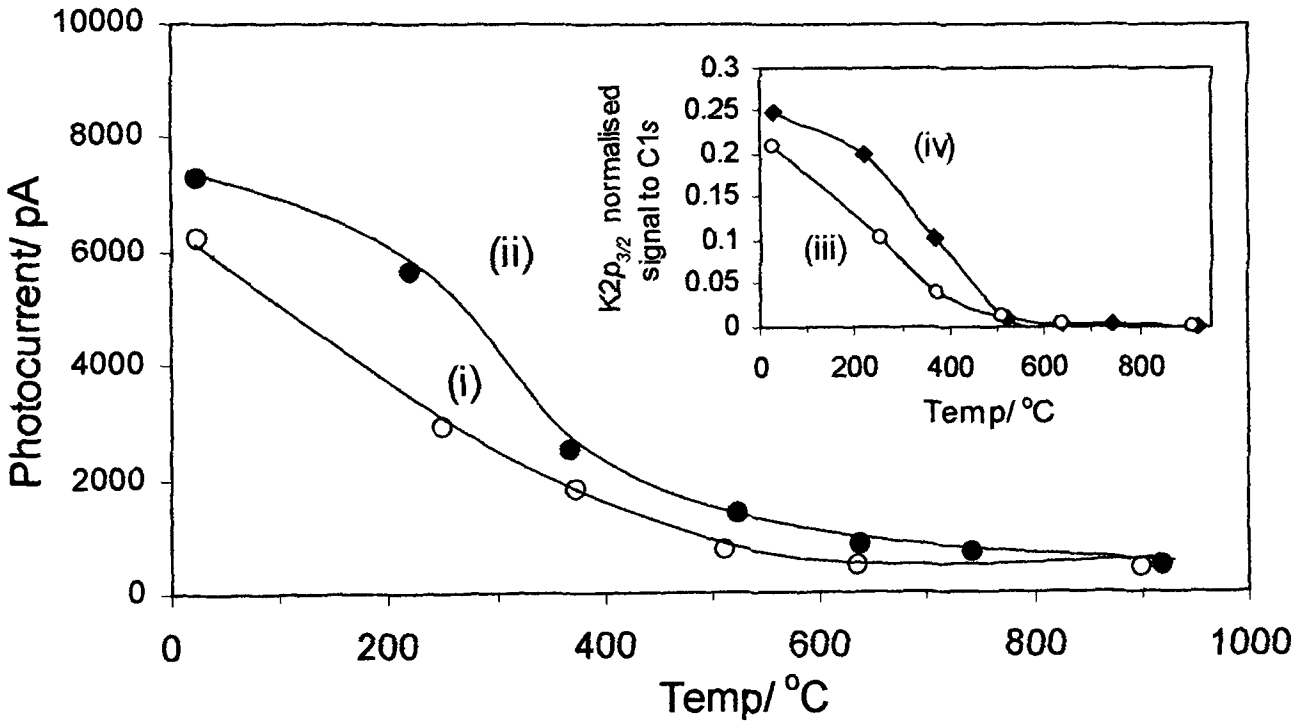


Figure 23a. The thermally dependence of photoyield for the K on (i) H-surface, and (ii) O-surface, with the inset showing the normalised $K2p_{3/2}$ intensities when the temperature increased for (iii) K/H and (iv) K/O surfaces

Caesiated surfaces were also annealed for similar purposes, and the result is shown in figure 23b. The trend of the decrease in photoyield by annealing temperature was quite similar to the K-surfaces, except for the comparatively higher photoyield obtained even with the temperature up to 400 °C. The photocurrents decreased as the Cs: C ratio declined.

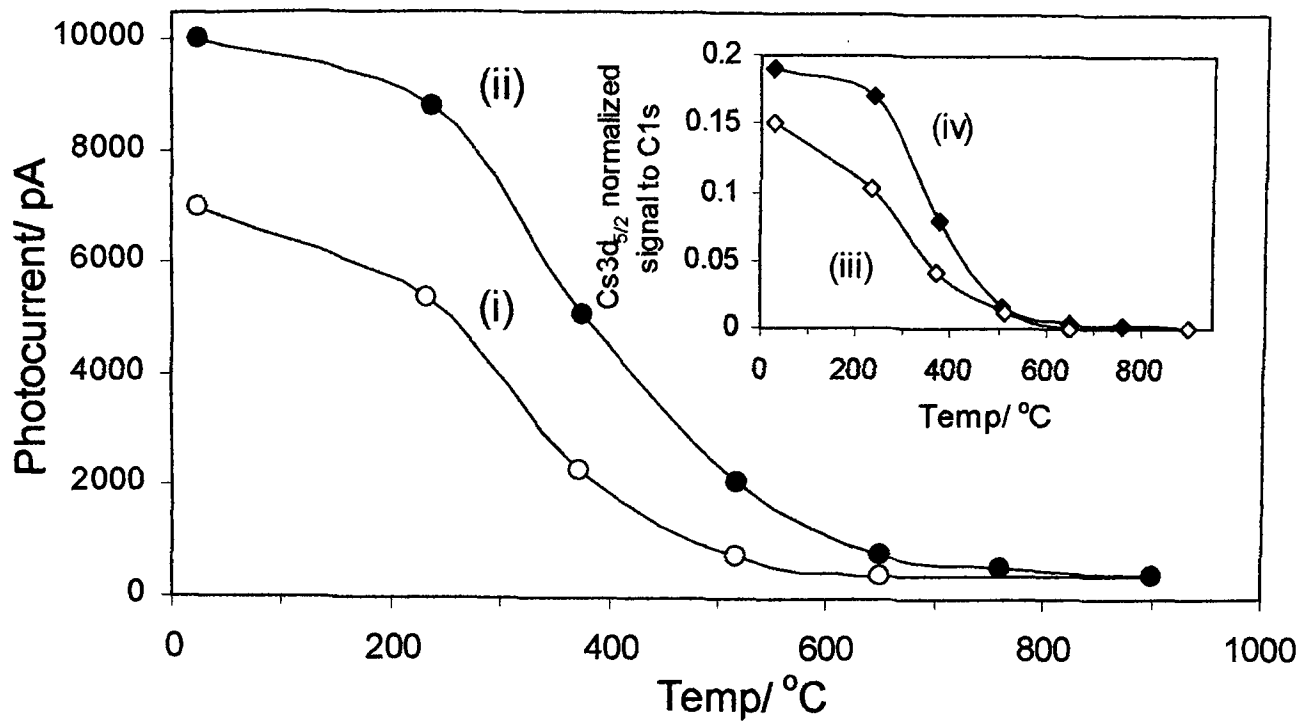


Figure 23b. The thermally dependence of photoyield for the Cs on (i) H-surface, and (ii) O-surface, with the inset showing the normalised $Cs3d_{5/2}$ intensities when the temperature increased for (iii) K/H and (iv) K/O surfaces

In brief, the oxygen-pretreated surfaces tend to provide better thermal stability than hydrogenated surfaces in the temperature region below 200 °C, and the Cs/O surface shows the best in thermal stability.

6.3.3 Transmissive Photoemission Mode

6.3.3.1 Surface Characterization

Three types of freestanding diamond were investigated for transmission mode photoemission studies, the home-grown diamond (30 hours, black in colour), the industrial black diamond (thermal management graded) and the industrial white diamond (optical graded). The diamonds were characterised for the front and backsides, by the means of AFM, SEM, XPS and Raman spectroscopy. The AFM in figure 24 reveals the much greater smoothness of the back (substrate, b) face over the front (growth) face, with the root mean square roughness of the substrate and growth faces being 33.87 nm and 145.89 nm respectively. The diamond paste scratching effect on silicon as substrate was reflected on the backside of the free standing diamond, showing the presence of horizontal marks

on the Si substrate. The height of the vertical extent of the front face is 1000 nm; while for the back face, it is 250 nm.

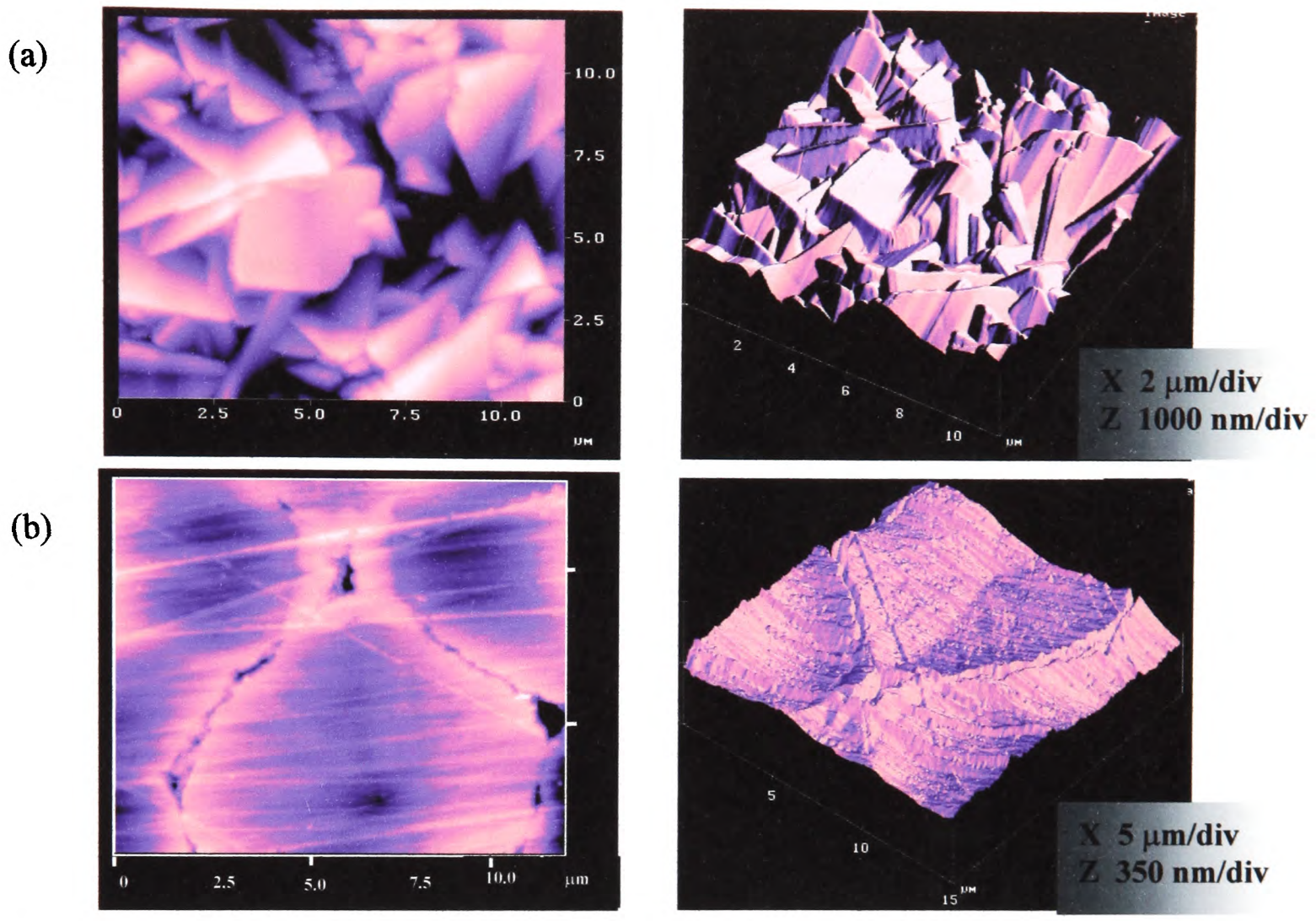


Figure 24. AFM of home-grown black diamond with 2-dimensional (left column) and 3-dimentional imaging; (a) growth side and (b) substrate side

Figure 25 shows the SEM images of the growth and back faces for optical graded white freestanding diamonds. The thermal management graded black diamond (not shown) has the same morphological surface features as figure 25.

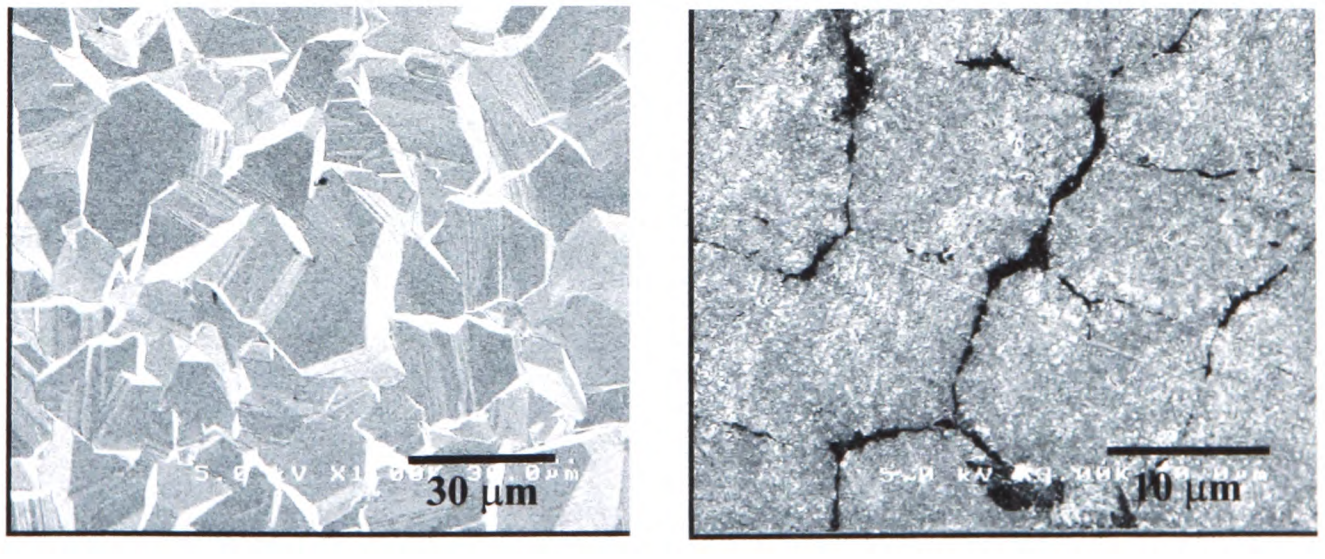


Figure 25. SEM of optical graded white diamond; showing front side (left) and back side

The surface composition of both sides of the home-grown etched diamond film from Si substrate was investigated through XPS. The front side (see figure 26a) has a typical diamond C 1*s* peak positioned at 284.3 eV with small contamination of O 1*s* and no visible Si $2p_{3/2}$ signal. The bulk C 1*s* peak is positioned at 283.9 eV for backside diamond (26b), revealing the existence of a large peak at lower binding energy, -1.6 eV relative to the bulk C 1*s* peak. This peak could be due to the large concentration of defective carbonaceous impurities, which may have formed together with Si-C bonding layers at the earliest nucleation and growth stage.

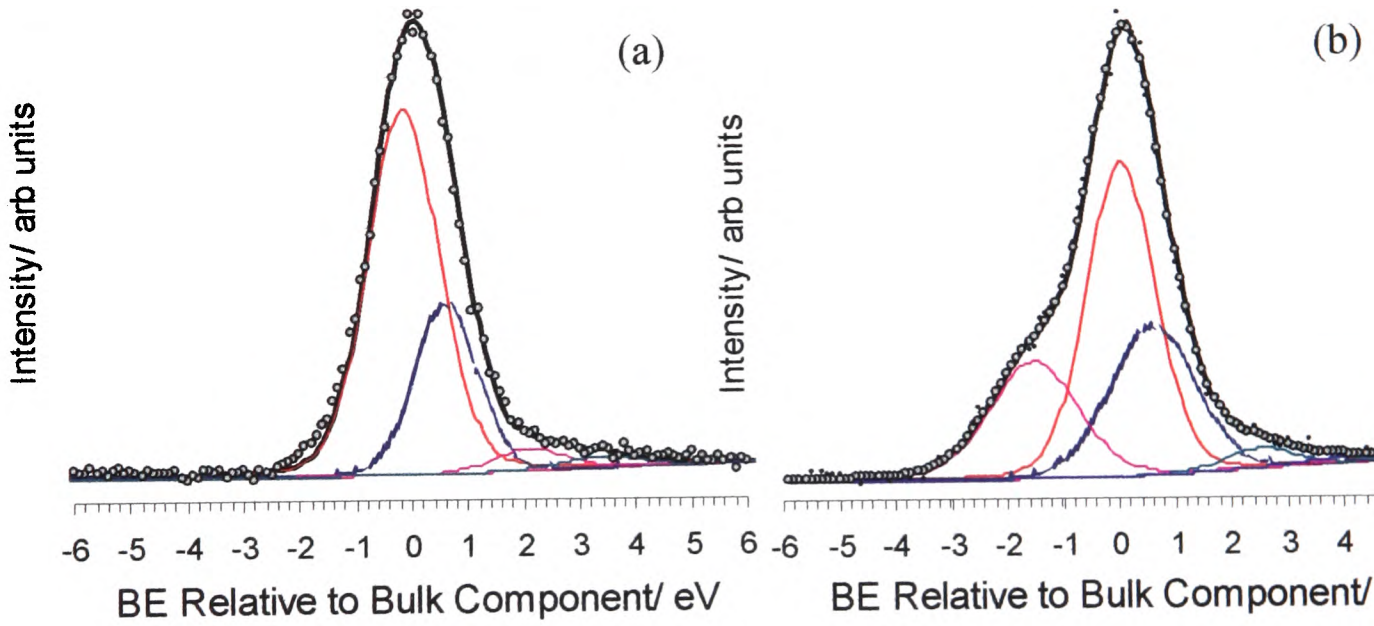


Figure 26. XPS fitted C 1s peaks of chemical etched free standing home-grown diamond membrane, for (a) front side and (b) back side

The Raman spectra of three different diamond samples are shown in figure 27, revealing that the optical grade white diamond (a) has the highest quality of diamond on both sides. This is followed by our home-grown black diamond (c), with an insignificant amount of the non-diamond broad peak centred at 1550 cm^{-1}, and an acceptable amount of impurities on the back side. The thermal management black diamond (b) is of the poorest quality, with profound graphitic and amorphous properties particularly for the backside of the diamond.

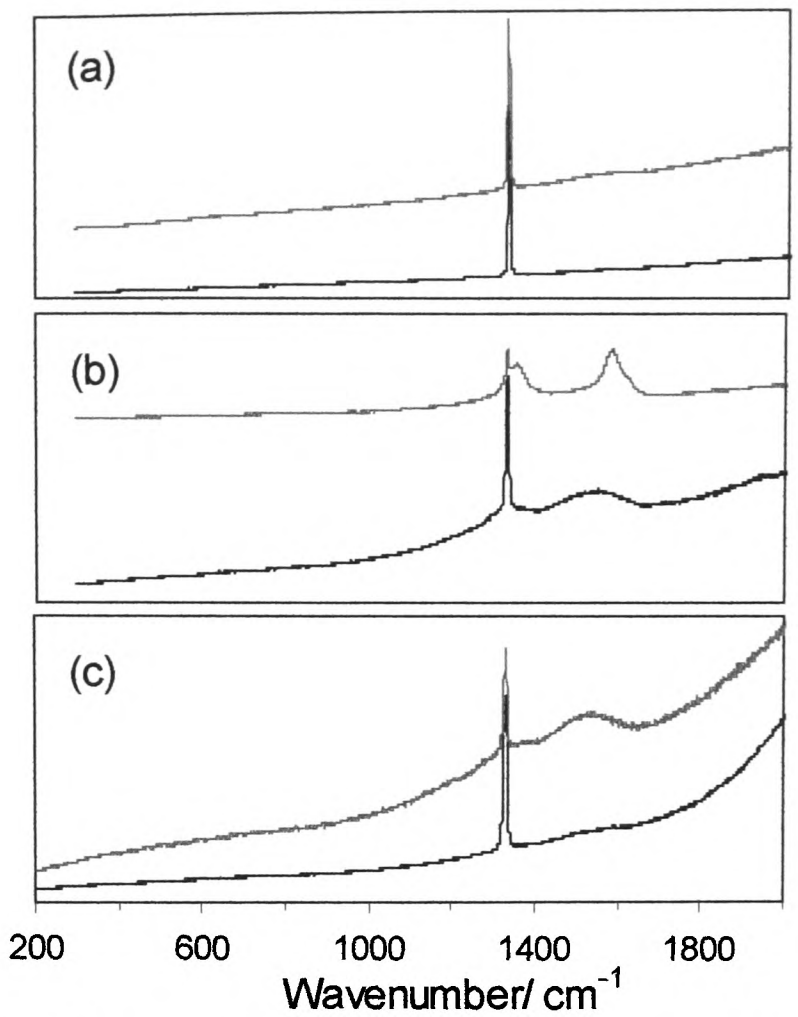


Figure 27. Raman spectra of growth side (dark black line) and substrate side (light grey line) for optical grade white diamond (a), thermal management grade black diamond (b), and home-grown black diamond (c)

6.3.3.2 Photoyield Studies

All types of freestanding diamond membranes were hydrogenated on both growth and substrate sides for an hour in the microwave chamber at a power of 1.2 kW, a platen temperature of 650 °C, with a total pressure of 45 Torr and a hydrogen flow rate of 200 sccm. The membranes were later placed in the set up (in figure 1 b), in order to measure the emitted photocurrents from front side (reflective mode) and backside (transmissive mode) for the respective growth or substrate faces (illustrated in details in figure 28).

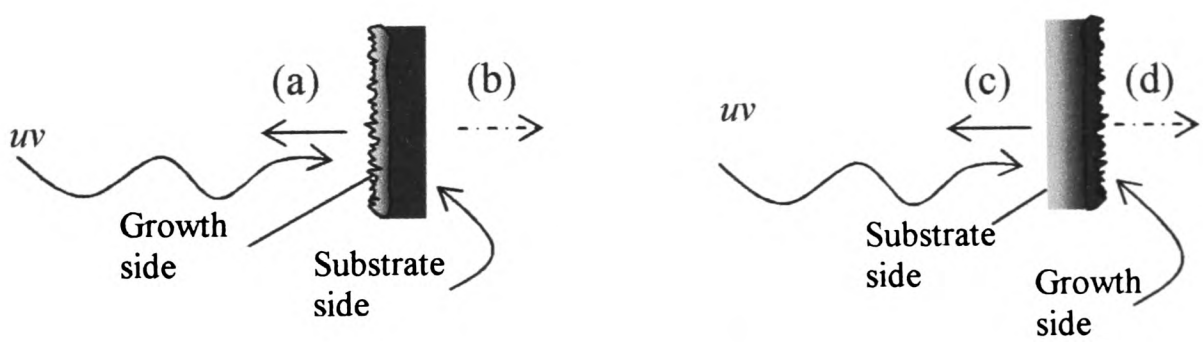


Figure 28. On facing the uv, the (a) reflected photocurrent from growth side, (b) transmitted photocurrent from substrate side, (c) reflected photocurrent from substrate side, (d) transmitted photocurrent from growth side

The photocurrent measured for a hydrogenated home-grown black diamond membrane (40 μm thick) is shown in figure 29, with reflective and transmission-mode of photoyield were made comparison to the growth or substrate faces of diamond. The results reveal that the reflective mode emission from the growth side has the highest photoemission at 720 *p*A, and levelled off after – 200 V. This trend is followed by the emission reflected from the substrate side for diamond with 350 *p*A, half of the emitted current from the growth side. The transmitted photocurrent from the substrate side is about 250 *p*A (c), which is higher than the 100 *p*A transmitted photocurrent from the growth side (d).

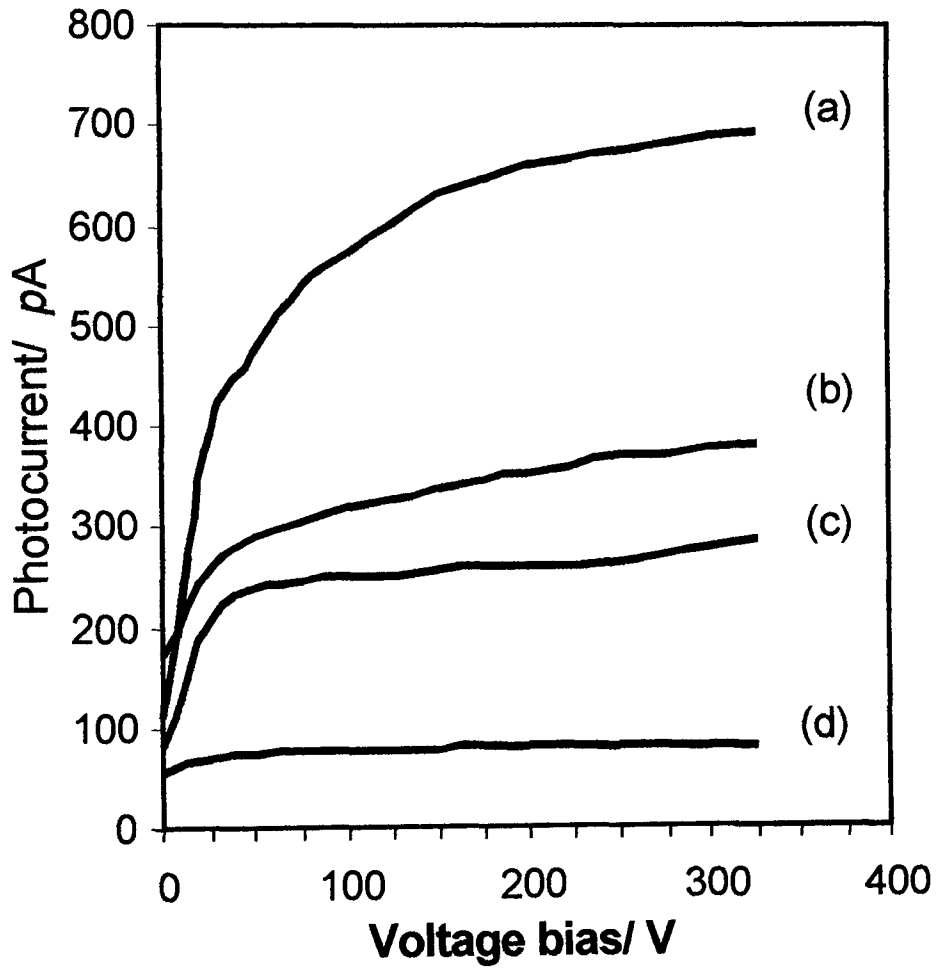


Figure 29. The photoyield of combined reflective and transmissive mode of photoemission study of home-grown black diamond for (a) reflected photocurrent from growth side, (b) reflected photocurrent from substrate side, (c) transmitted photocurrent from substrate side, and (d) transmitted photocurrent from growth side

For the industrial made optical graded white diamond, the order of photoemission efficiency is similar. Figure 30 shows the reflective and transmission mode of photocurrents measured from films with different thickness, ranging from 4 μm to 100 μm

presumably they are of the same high quality. The absolute current emitted from the near side (reflective mode of either growth or substrate) serves as the best emitter with a steady increase up to 1300 *p*A (a) or 440 *p*A (b) at a film thickness of 50 μm and levelled off at higher thickness, both for reflective mode of emitted current from growth side (a) and substrate side (b). In the transmission mode, the emitted current from substrate side as the far face from *uv* light (c), increased in the similar manner as such of the previous reflective mode, but decreased sharply (> 70 %) when the thickness of the diamond film was greater than 100 μm. However, the emitted current from growth side *via* diamond film (d) remains independent of the diamond thickness, as they emitted the lowest photocurrent - average 72 *p*A. In brief, diamond with a film thickness of 50 μm shows the highest reflective and transmission mode emission.

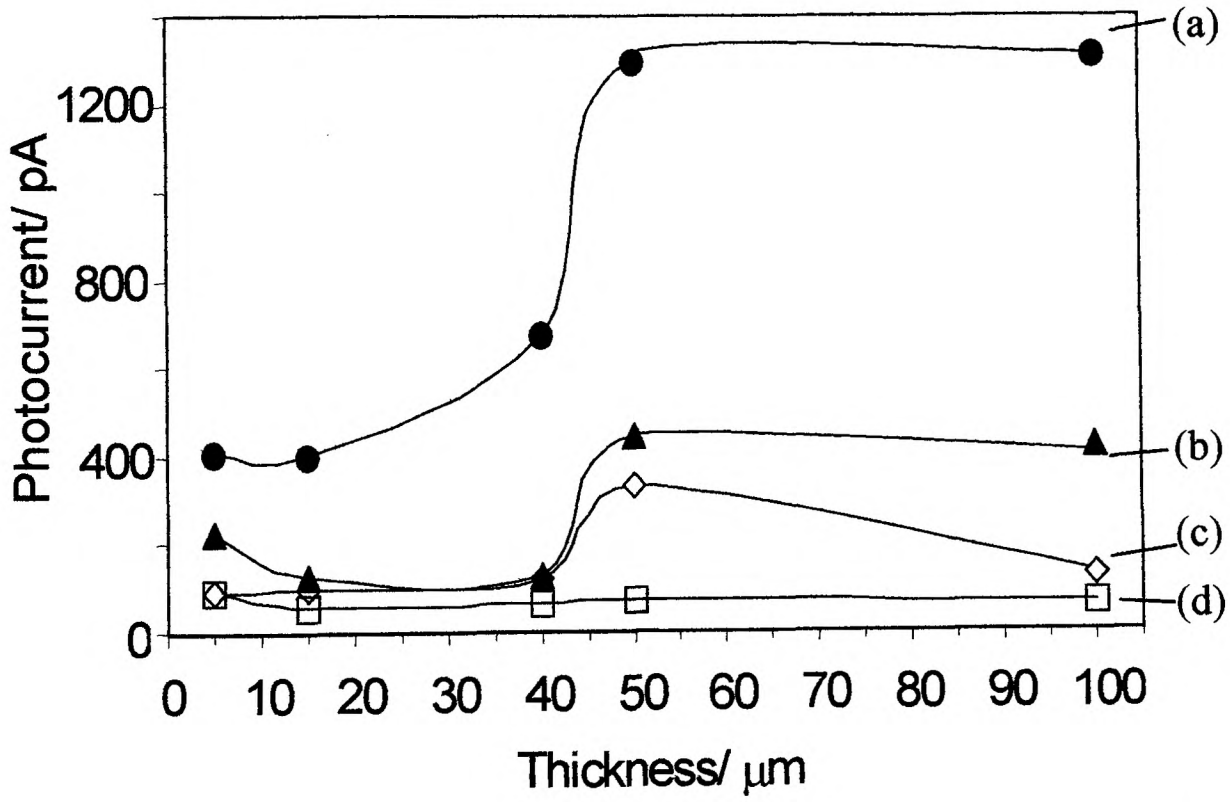


Figure 30. The photocurrent of optical grade white diamond, emitted from the reflective mode of (a) growth side, (b) substrate side, and the transmissive mode from (c) substrate side, (d) growth side

The wavelength selectivity of photocurrents for the white diamonds was further manipulated as a ratio of the photocurrent emitted from the back (or far) face, I_{trans} to the photocurrent reflected from the front (or near) side, I_{refl}, relative to the *uv* light direction.

Figure 31 (a) and (b) shows the ratio Itrans: Irefl for either growth or substrate as front side for two different filters, above and below diamond band gap respectively, revealing that the ratio remains unchanged when the film thickness is varied for growth as the near face to *uv* (i). However, when the substrate side of the diamond is the face nearer to *uv*, the ratio increases sharply at a film thickness of 15 μm when both 186 and 252 nm filters are in place, although the ratio magnitude of 252 nm is 4 times greater than the 186 nm filter. The Itrans: Irefl ratios with both filters in place were later decreased with the thicker films.

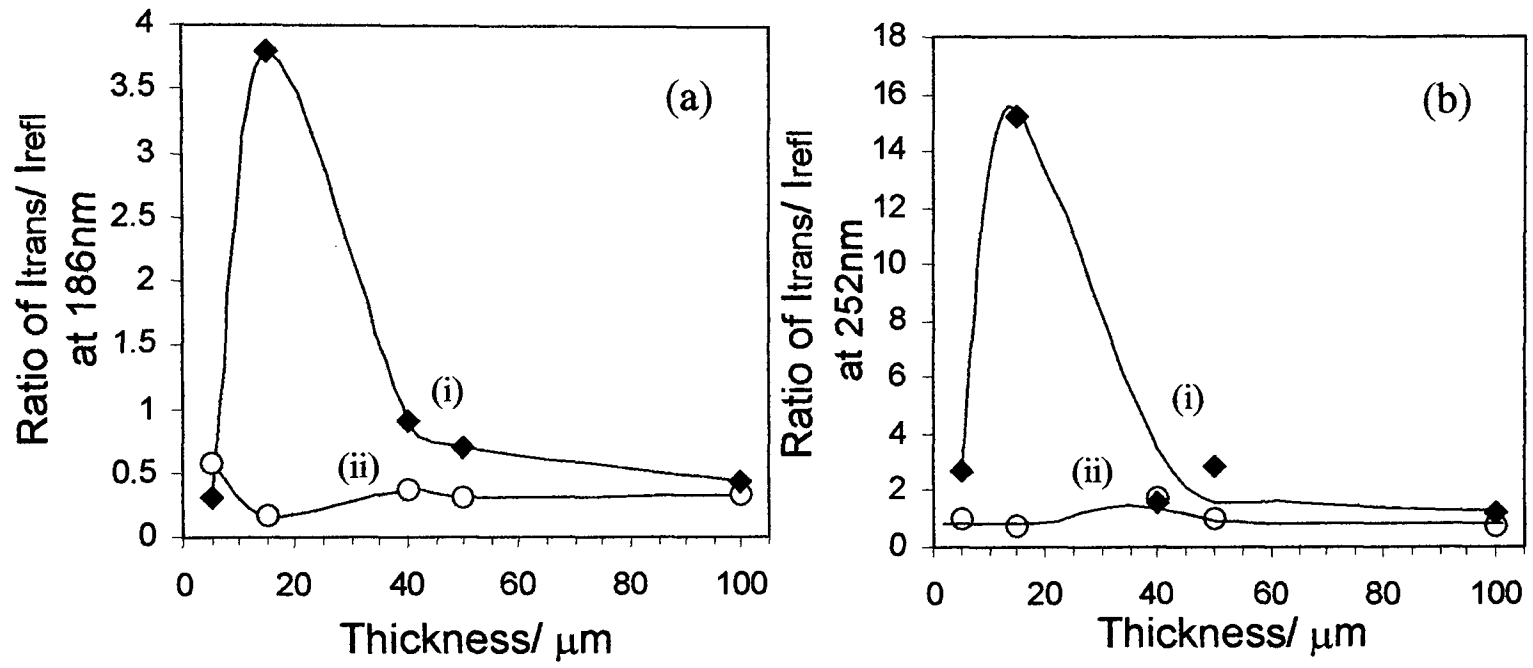
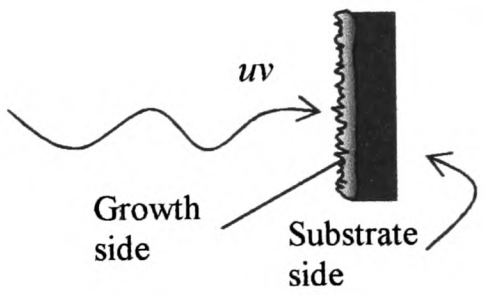
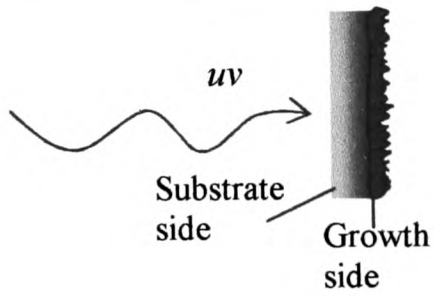


Figure 31. The Itrans/Irefl ratio of photoyield with filters (a) 186 nm in place, and (b) 252 nm in place for (i) substrate or (ii) growth as front sides facing to uv direction as a function of the thickness of optical graded white diamond

Thermal management graded black diamond (200 μm thick) has a very high collected total current for both sides of the diamond with a higher absorbed current for the substrate side than the grown side. In descending order of measured photocurrents we have, interestingly, reflective mode of substrate, reflective mode of grown side, transmission mode of substrate side, and lastly the transmission mode of grown side. However, with the 186 nm filter in place (data not shown), the order has changed to the similar trend as shown for the cases of optical grade white diamond and home-grown black diamond.

The comparison of the emitted photocurrents from both reflective and transmissive mode is shown in Table 1. Higher non-diamond properties of substrate side for thermal management graded black diamond and home-grown black diamond have shown to be the better total photocurrent collectors, with ~ 3000 *p*A being collected. However, by rationalizing the ratio of back side to total collected photoyield when growth side faces the *uv*, the optical graded white diamond produce the best transmissive mode photoemitter with a successive transmittance (Itrans/Irefl) of 20 %, compared to 14 % for thermal management grade black diamond, and 13 % for home grown black diamond. In contrast, the thermal management grade black diamond is a better phototransmitter of 15 % in the sense of transmitting electron when the substrate sides is faced to *uv*, as compared to ~ 6 % transmission for optical white diamond, and 4 % for home grown black diamond.

Table 1. The emitted photocurrents from growth or substrate side of diamond membranes toward uv direction

Type of Diamond						
	Emitted photocurrent from					
	Growth faces *uv*/ *p*A			Substrate faces *uv*/ *p*A		
	Total collected current	Reflected	Transmitted	Total collected current	Reflected	Transmitted
Optical graded white diamond[a)]	2150	1300	418	1290	440	72
Thermal graded black diamond[b)]	2450	1250	345	3100	1620	465
Home-grown black diamond[c)]	1650	704	217	3000	356	105

Notes; the cross-sectional thickness of a) 50 μm, b) 200 μm, c) 40 μm

6.3.4 Analysis of the Filters

The transmission of light through the filters should be similar (approximately 15 % of incident light is transmitted in the appropriate range for both filters used in experiment), though there are still different intensities of light at different wavelengths reaching the samples since the deuterium lamp emits different intensities of photons at different wavelengths.

The *uv* photodiode was used to work out the flux of photons reaching the samples for different filters in order to determine the quantum photoyields. It was placed in the same position as the diamond samples and a voltage was recorded, which was then converted into current (an order of 10^{-6} A). Using this value and the knowledge that the responsivity of the photodiode is 0.12 A/W at 190 nm, 0.14 A/W at 250 nm, and 0.15 A/W at 340 nm, the photon flux can be calculated for the various filters. The photodiode responsivity is the measure of sensitivity for optoelectronic, for the ratio of the photocurrent output in amperes to the radiant energy (in watt) incident on the photodiode. The responsivity is a function of the wavelength of the incident energy, reflections and internal resistance. Table 2 shows the different voltages given by the photodiode and the calculated photon flux from the equation 2 and 3,

$$Current = Voltage \; x \; 10^{-6} \qquad \text{(eqn 2)}$$

$$Power = \frac{Current}{\text{Re}sponsivity} = \frac{hc}{\lambda} \; x \; Photon \; flux \qquad \text{(eqn 3)}$$

Table 2. Photon flux with and without filters in use

Filter	Photodiode voltage/ V	Power/ W	Photon flux/ photon s^{-1}
None	12.9	9.21×10^{-5}	1.16×10^{14}
186 nm	0.123	1.02×10^{-6}	9.60×10^{11}
252 nm	0.150	1.07×10^{-6}	1.36×10^{12}

An average reduction in photocurrent from the photocurrent without filter when the two different filters are put in place is calculated from a selection of results. The

values are 11.18 % for 186 nm filter and 0.128 % for the 252 nm filter, showing the efficiency of 186 nm light in producing a photocurrent relative to 252 nm light. This is reflected in the absorption spectrum of diamond shown in figure 32. The absorption is related to the percentage of light absorbed by the sample using the Beer-Lambert law relationship,

$$I = I_0 e^{-Abs} \qquad \text{(eqn 4)}$$

where I is transmitted light, I_0 is incident light and Abs is absorbed intensity (absorption) as given by the *uv* spectrometer.

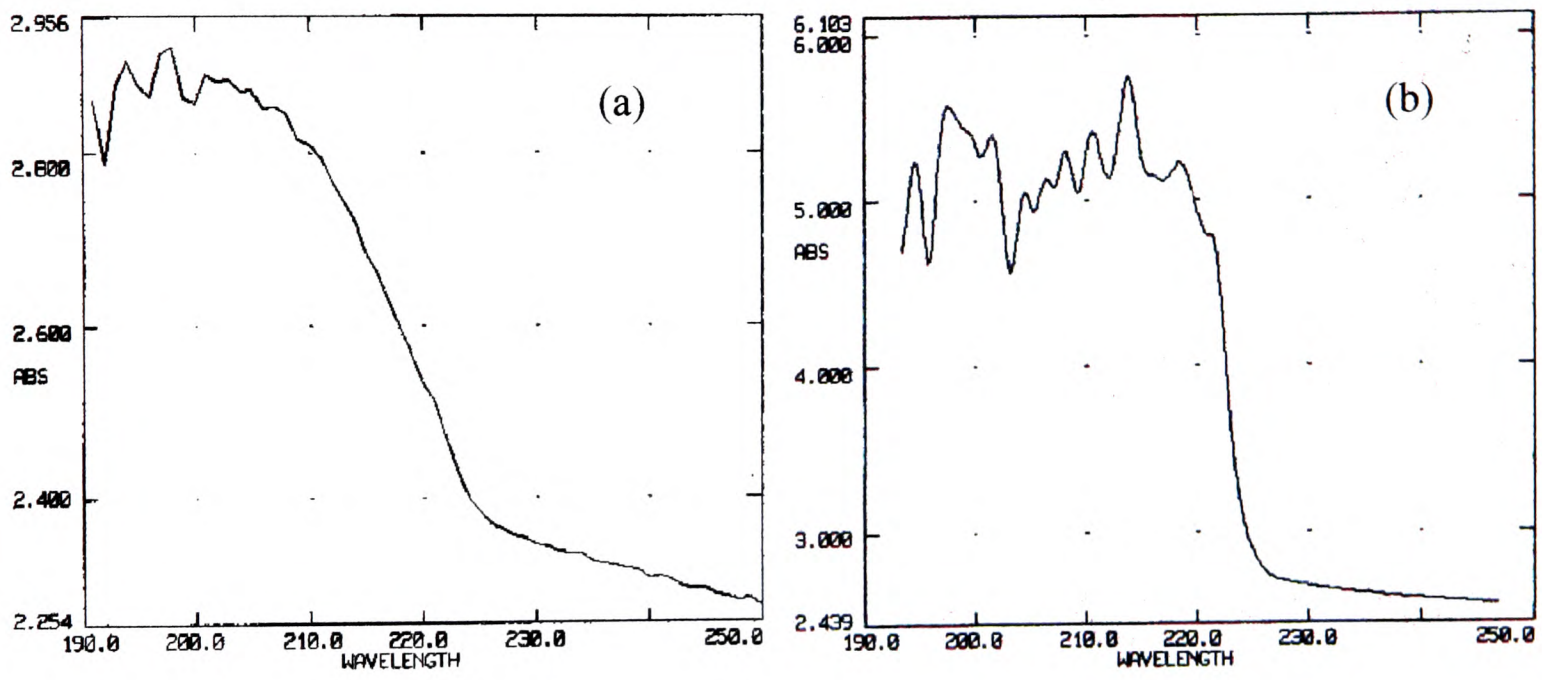


Figure 32. The uv spectra of optical graded white diamond with the thickness of (a) 4 μm, and (b) 50 μm

Figure 32 shows the cut off band gap for optical graded white diamond at 225 nm (5.5 eV). For above band gap absorption, more *uv* is absorbed for thicker diamond film of 50-μm with 99.3 % efficiency (Abs = 5.0), compared to 4-μm thin white diamond with 94.4 % absorbed light (Abs = 2.9). At sub band gap absorption, 90.6 % (Abs = 2.4) of light is absorbed for 4-μm diamond film whereas 93.4 % (Abs = 2.72) for 50-μm thick diamond.

The photon fluxes given above can be used in conjunction with the photocurrent to calculate the quantum photoyield (QPY) of the samples. This process involves calculating

the number of electrons emitted from the sample (each ampere is a coulomb/s and e = 1.602×10^{-19} C) and dividing by photons incident upon the sample. The tabulated data in Table 3 shows the summarised QPY for different treated surfaces.

$$QuantumPhotoyield,\ QPY = \frac{\dfrac{Photoyield\ (A)}{e\ (C)}}{Photon\ flux\ (photon\ s^{-1})} \qquad \text{(eqn 5)}$$

Table 3. Averaged Quantum Photoyield (QPY) of various treated surfaces

Treated surfaces	Without filter		With filters	
			186 nm	252 nm
	Photoyield/ *p*A	QPY/ arb units	QPY/ arb units	QPY/ arb units
As-grown	480	2.58×10^{-5}	3.49×10^{-4}	2.82×10^{-6}
H_2 molecular	550	2.96×10^{-5}	4.00×10^{-4}	3.23×10^{-6}
H plasma	800	4.31×10^{-5}	5.82×10^{-4}	4.70×10^{-6}
O_2 molecular	380	2.04×10^{-5}	2.76×10^{-4}	2.23×10^{-6}
O plasma	130	7.00×10^{-6}	9.45×10^{-5}	7.64×10^{-7}
K/H/C	6200	3.34×10^{-4}	4.51×10^{-3}	3.64×10^{-5}
K/O/C	7200	3.87×10^{-4}	5.23×10^{-3}	4.23×10^{-5}
Cs/H/C	7000	3.77×10^{-4}	5.09×10^{-3}	4.11×10^{-5}
Cs/O/C	10000	5.38×10^{-4}	7.27×10^{-3}	5.88×10^{-5}

Notes: I_{186} = 11.18 % x {Photoyield without filter}; I_{252} = 0.128 % x {Photoyield without filter}

Analysis of the results for the calculated absolute QPY at a wavelength of 186.8 nm, reveals a range from 4×10^{-4} to 6×10^{-4} for the hydrogenated diamond surface (whether the surface was dosed by means of H_2 or H), which is in good agreement with the results of absolute QPY measured by A. Breskin *et al.* [4] and A. Hoffman *et al.* [11] at this specific wavelength, with the range measured being between 10^{-3} to 10^{-5}. Whereas the QPY measured at 252 nm in place for H-surfaces shows a similar order of 10^{-6}.

6.4 Discussion

6.4.1 Growth and Comparison

(i) Growth phases of diamond

Highly oriented {100} with microcrystallites diamond thin films have been produced successfully on single-crystal silicon substrates. However, the early growth stages suffer from the presence of non-diamond carbon phases (Raman figure 4), possibly due to the deterioration of the crystallites by various bulk defects [12], such as twinning, dislocation and stacking faults, coupled with the presence of high lattice mismatch (52 %) for diamond-silicon interlayers, which would in turn result in the deposition of amorphous and graphitic layers. For the later growth stages, the nucleation and growth of diamond preferentially takes place on the stage where C and Si coexist [13,14] due to lower lattice mismatch (22 %) in between diamond and SiC. This interlayer would form the fundamental and strong adhesive layer for further diamond growth phases, and so the quality of diamond increases.

Previous studies of CVD diamond photocathodes have identified that the material exhibits significant quantum photoyields in the deep *uv* region, which is promising for device operation in "harsh" environments, and that hydrogenation increases the quantum yield, probably largely due to a lowering of the electron affinity of the sample [11,15,16]. It is also clear that the devices studied exhibit significant emission at energies below the diamond band gap, due to the presence of non-diamond carbon.

The two main issues concerning any photocathode material are the overall quantum yield of the devices involved, which determines overall sensitivity, and their wavelength variation upon which spectral response depends. The observations reported here demonstrate that the photoyield increases rapidly for short growth times (phase 1), then decays as the surface becomes covered in diamond (phase 2) before rising again as the diamond film gradually thickens (phase 3).

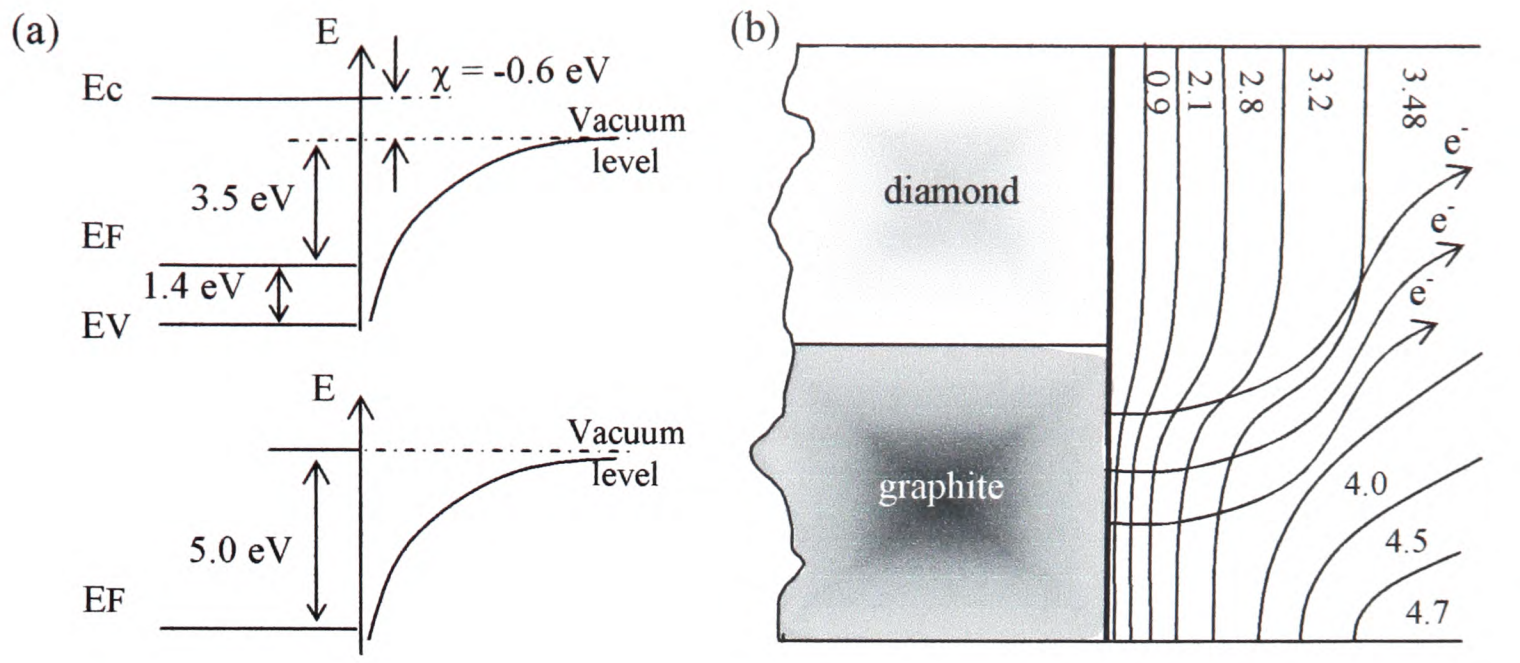


Figure 33. Schematic diagram of the potential distribution in front of the graphite-diamond junction for hydrogenated diamond; (a) top and bottom is the band diagrams of diamond and graphite respectively, (b) the image potential in front of the junction is given in the form of equipotential lines; a similar band diagram for silicon could be assigned with a work function of 4.67 eV

In phase 1 (from silicon to 10 hours growth), the NEA (hydrogenated) diamond surface is laid upon a positive electron affinity surface of the silicon. This can assist the emission from silicon, either by transport of electrons from silicon to diamond before emission, or perhaps electrons are more easily emitted from the silicon surface because of the nearby presence of an NEA diamond surface. Apart from the role played by Si, previous studies on diamond-graphite composites [9,17] prepared by mixing nanocrystalline powders have shown that the two phases in contact have a synergistic effect on each other in enhancing electron emission, since electrons emitted from graphite in a diamond matrix see an energy barrier corresponding to the work function of NEA diamond (see figure 33). It is possible that this effect is also responsible for the present observation since the phases present at short growth times certainly contain a mixture of carbon phases, of which diamond is dominant. The potential near a surface does not fall immediately to the vacuum potential but rather there is a potential gradient that varies inversely with the distance from the surface and asymptotically approaches the vacuum

level with the work functions for Si and graphite respectively of 4.67 eV and of 5.0 eV. Electrons emitted from Si or graphite near the Si/graphite–diamond junction can take advantage of the diamond potential gradient to be emitted more easily.

The diamond grown in this early stage of phase 1 is in the form of discontinuous nuclei crystals (see SEM a,b in figure 2), which would assist the transport of electrons *via* the conductive pathway along the isolated diamond-particle surface. These conductive layers are mostly derived from the non-diamond particles embedded in the grain boundaries or interfacial structure which is rich in defective and carbonaceous materials, forming good conduction channels and alleviating the photoemission to take place efficiently [18,19].

In phase 2 (around 15-20 hours growth), a complete diamond film has been formed on silicon. The decreasing amount of silicon no longer plays a role in photoemission. The thin and poor quality diamond film is a poor emitter compared to the semiconductor, so the photocurrents fall off. At a wavelength of 186 nm, light is absorbed within about 100-1000 nm of the surface [20] and the photoyield is roughly proportional to the reciprocal of the absorption length, suggesting that it is the comparatively inefficient diffusion of carriers to the surface which limits the photoyield.

In phase 3 (> 20 growth hours), the crystallographic quality of the diamond improves as the film thickens. Improvements in crystalline quality are expected to enhance the electron carrier diffusion, so an increase in photoyield is expected, although other changes such as in the morphology of the surface cannot be ruled out.

As the growth time increases, there is an increase in the selectivity for 186 nm light over 252 nm light. The indirect band gap of diamond falls in between the two wavelengths, so the 252 nm light cannot excite electrons all the way from the valence band to the conduction band. Therefore, the emission with the 252 nm filter in place is due to electrons excited to or from defect states situated in the band gap. These defect

levels are related to impurities, crystallographic defect such as dislocation, or defects occurring at grain boundaries [21], which are assigned to the defect levels at binding energies of 4.1 ± 0.1 eV (D_1) and 2.0 ± 0.1 eV (D_2) [22], with D_1 found in all diamond samples, and D_2 is thermally induced by annealing in vacuo. Acceptor-like defects located in the range (1.2 – 1.3) ± 0.1 eV were also reported to be responsible for sub-bandgap photocurrent emission [23]. As the quality of the diamond increases, the below band-gap emission drops off, while normal emission increases as defect states in the band gap (which can act as traps for electrons diffusing through the diamond) are removed.

(ii) Quality of diamond

Different qualities of diamond can be produced, which can be attributed to the different localised temperature and gas compositions in regard to the distances from the plasma density. The photocurrent without filter and with the 186 nm filter increase as with the increases of the diamond quality (see figure 7), simply due to the fact that the graphitic species has a higher work function (~ 5.0 eV) without NEA which does not ascertain good emission. Therefore, the low quality diamond emits little photocurrent due to the low diamond content; and *vice versa*. With the 252 nm filter in place, the initial increase in the emission as the quality of film increases is due to the introduction of NEA, but at higher film quality, the emission decreases as the defect levels necessary for sub-band gap emission disappear. This would explain the increase in selectivity of the films.

As illustrated in figure 6, the surface termination of the materials play a significant part in controlling the photoyield. Although hydrogenation has little effect on the silicon substrate, the other hydrogenated phases emit significantly better than surfaces, which are annealed to partially desorb hydrogen, or those that are oxidised. Caesiated surfaces do however appear to be the best photoemitters of all. Hydrogen is generally considered as the ideal adsorbate for termination of the diamond surface since it introduces NEA so that

barrier-less electron emission can occur from the bottom of the conduction band. Caesiation produces more downward band bending than adsorbed hydrogen, which increases the photoyield since it provides an enhanced field to transport the carriers to the surface. It is possible that the distribution of NEA and positive electron affinity surfaces on the crystallographically complex CVD interface is also dependent on the adsorbate (H *vs* Cs) and this can also be a factor [24]. It is notable that the surface treatments explored have the same qualitative influence on the photoemitter surfaces on the long and short growth time photoemitter surface. This again points to the energy barrier to electron emission for the latter samples being essentially determined by the diamond material present in the grown deposits, since for example hydrogenation of graphite makes no difference to the photoyield from this material, whilst having a strong effect on photoemission from diamond [25,26].

Though two different types of diamond, *i.e.* boron-doped and undoped have been used in this project, there is no difference in their performances of quantum photoyield being observed under the same condition of treatments. The only difference would be that the boron-doped diamond shows reduced dark current and faster response time in electrometer, which can be attributed to the presence of the higher conductivity of the samples [11] whereas, the charging effect induced on undoped diamond surface is due to low conductance.

6.4.2 Reflective Mode

6.4.2.1 Photoyield Studies

(i) Reflective Mode Behaviour of H and O Surfaces

The hydrogen terminated diamond surface is known to display an *effective* negative electron affinity and so unsurprisingly the hydrogenated surface shows good photoemission. The enhanced photoemission property is due to the surface dipole interaction arising from partially ionic C-H bonding and the reduced potential barrier at the surface. Subsequently, the accumulated electrons at the conduction band are eased for emission into the vacuum level, since the band is now lying above the vacuum level (figure 34 a). The C-H termination is also suggested to have lead to a breaking of the symmetry of the diamond structure, resulting in the formation of sub-bands, which will further increase the electron emission [27]. However, as discussed in previous Chapter 3, the potential of O contamination is significant to kill the photoyield.

Oxygen is more electronegative than carbon. Thus, a dipole opposite way to the C-H bond will be induced, raising the vacuum level above the conduction band minimum. Therefore, the electrons that are promoted to the conduction band cannot escape. Thus, NEA is destroyed and shifted to positive electron affinity with the low or the extinction of photoemitting properties. The transferred charge involved, ΔQ of 0.17 e is due to its high electronegativity as compared to 0.06 e for C-H bonding, by employing Pauling's electronegativity values (see equation 6 [28,29]) with $\chi_C = 2.55$, $\chi_O = 3.44$, $\chi_H = 2.20$ [30]

$$\Delta Q = e\,(0.16\,|\chi_X - \chi_Y| + 0.035\,|\chi_X - \chi_Y|^2) \qquad \text{(eqn 6)}$$

where X and Y are the participating elements. The resulting surface terminations can consist of various carbon-oxygen single, double and bridging bonds or OH attachments, which will form a surface dipole with estimated 1.10 D (1 D = 3.336×10^{-30} Cm) on average. From equation (7), the difference in emission barrier height due to adsorbed

atoms ($\Delta\phi$) can be estimated, where μ is the surface dipole, n is the adsorption sites per unit area, P is the surface coverage (%), and ε is the dielectric constant of the vacuum, 8.854×10^{-12} $J^{-1}C^2m^{-1}$.

$$\Delta\phi = \frac{\mu n P}{\varepsilon} \qquad \text{(eqn 7)}$$

The decrease of photoyield is rapid at lower coverage of chemisorbed oxygen and is saturated at an O: C ratio of 0.10 (see figure 9). At that ratio, the photoyield has degraded to an insignificant value, and equation 7 yields a $\Delta\phi$ equivalent to 0.64 – 0.91 eV at this coverage; assuming the number of adsorption sites per unit area is around 2×10^{15} atoms cm^{-2} (1.57×10^{15} atom cm^{-2} for {100} and 2.22×10^{15} atoms cm^{-2} for {111} surfaces).

One scenario to avoid oxygen poisoning of photocathodes would be to use photocathode in *in-situ* active hydrogen environment. Results (in figure 8) show that atomic hydrogen irradiation will remove O and restore the photoyield, although the effect is not completely. Therefore, this could be one way to avoid the problem with oxygen contamination.

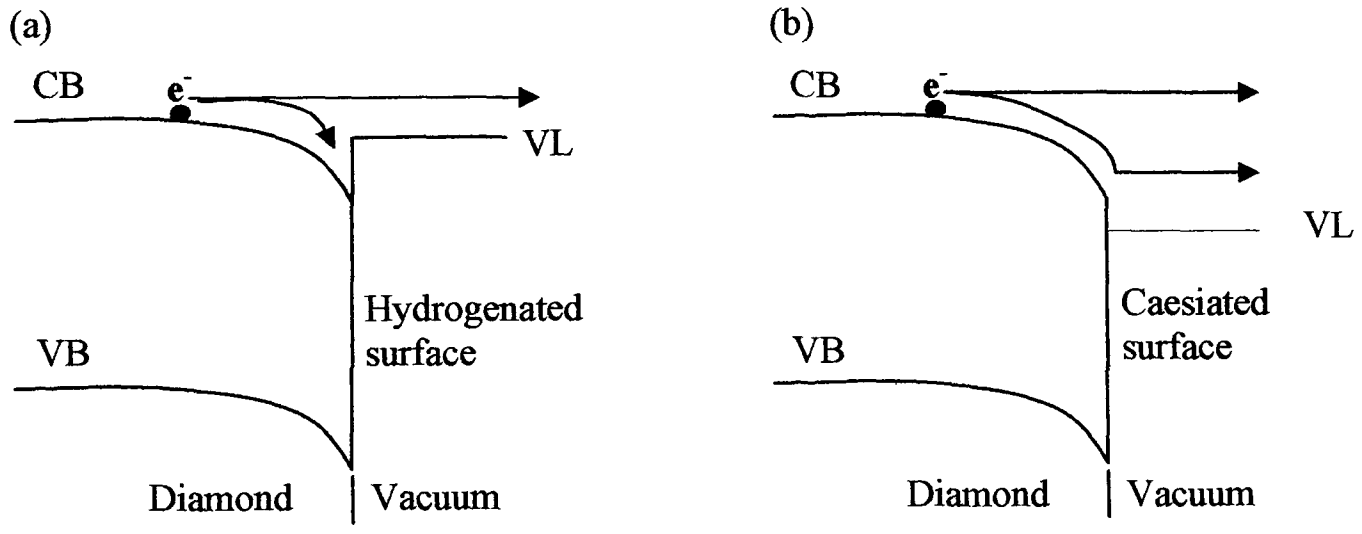


Figure 34. Schematic energy-band diagrams of hydrogenated and caesiated polycrystalline diamond photocathodes; (a) the hydrogenated surface exhibits effective NEA and (b) the caesiated surface exhibits true NEA (CB = conduction band, VB = valence band, VL = vacuum level)

(ii) Reflective Mode Behaviour of Alkali Metallized Surfaces

Although hydrogen terminated surface is a good emitter, the photoyield induced is not as good as the surfaces covered with alkali metals. The reasons are (i) perhaps not all crystallites are NEA – which might comprise of a mixture effect of positive electron affinity and effective NEA as the hydrogen density might vary on all the differing types of crystallite present in CVD films or from one crystallographic surface morphology to the other; (ii) little band bending involved at hydrogenated surfaces – which will cause no great field to drive the electrons to the surface and escape.

The deposition of alkali metals would enhance the *true* negative electron negative [31,32], by which the electron escape probability is exactly unity because the energy barrier between the surface and vacuum does not exist (see figure 34 b). The highly electropositive atoms are expected to induce greater surface polarity, which is more effective in producing much better emission characteristics over the whole surface. Therefore, the alkali metals deposited on diamond photocathode is a better photoemitter than the hydrogen-terminated surface, because (i) bigger dipole moment – with the bigger changes in the work function – and more likely all the surface can show the NEA properties; (ii) downward band bending is expected – the field which emits the electrons is much better (see figure 34b).

Surface spectroscopies show fairly complex behaviour in C 1*s* and O 1*s* XPS spectra, which depends on exactly how the layers are prepared with alkali metals. Thus, the chemistry of the interface varies with the exact procedure used to deposit the alkali metal, and the measured photoyield varies similarly, signifying the critical dependence of photoyield on the surface pre-treatment received by the diamond before metal deposition [33]. One simple correlation emerges is that the highest photoyield tends to occur if the alkali metal is adsorbed on top of the oxidized diamond surface. One reason for this is probably that the alkali metal is expected to show greater charge transfer when oxygen is

preadsorbed. Hence, the adlayer shows a greater dipole moment producing a greater lowering of the vacuum level.

The alkali metals are usually unreactive with the hydrogen-saturated surface compared to the O-terminated surface. The buffering zone of CH_x will prevent the direct reactive interaction for the alkali metal to diamond surface. The insignificant chemically shifted component in the Cs 3*d* or K 2*p* XPS spectra (see figure 15, 20) signifies a small change in an effective dipole [26,34,35], such as the calculated dipole moments for K-H (bond length 2.24 Å, electronegativity χ_K 0.82) and Cs-H (2.49 Å, χ_{Cs} 0.79) are respectively 3.12 D and 3.53 D.

Pre-treatment of the diamond surface with oxygen prior to the deposition of alkali metals would ideally generate approximate stoichiometric compounds of M_2O [36]. Oxygen is expected to draw the M ions close together, providing higher dipole moment per unit area and resulting in a lower work function. In comparison to the K and Cs, the latter is expected to have higher photoyield enhancement simply due to its stronger electropositive polarizability brought by its larger ionic radius. Cs on O terminated surface seems to be the best photoemitter, reflecting the presence of dipole layer between the very electropositive Cs and the electronegative oxygen. A stronger adsorptive capacity for Cs on O-surface is induced with greater oxygen-enhanced reactive charge transfer across the C-O-Cs hybrid interfaces [34]. This arises from primarily Cs *d* – O *p* hybridisation that contributes strongly to the net dipole, which subsequently lowers the work function of diamond. The calculated dipole moment for O-Cs (with bond length 2.40 Å) is ~ 7.70 D and O-K (bond length 2.21 Å) is ~ 5.43 D. The shift in XPS C 1*s* core-level peaks to higher binding energy is arising from downward band bending, which will enhance the NEA condition by placing the vacuum level farther away down from the bulk conduction band level.

(iii) Stability performance of photocathode

The observed oxygen-induced instability on alkali-metal deposited diamond surface can be understood as a long-term rearrangement of the oxygen atoms and/or their penetration into the activation layer. It has also been proposed that at high oxygen exposures, the oxygen atoms may position at the interstices between alkali metal atoms, shadowing the diamond sites severely [37]. This will result in enhancing the positive electron affinity of the surface on a larger time scale with the decreasing of the dipole moment [38].

As noted above, hydrogenated diamond photocathodes show a rapid degradation if oxygen has the possibility to adsorb on the surface, and even small quantities of oxygen show a significant degradation in performance. The results reveal that the alkali metal-treated surfaces show much higher photoyield with a lower corrosion rate even in the presence of oxygen. This is particularly true for the caesiated on O-terminated surface with a corrosion rate of 0.02 %/L O_2, presumably due to the fact that (a) oxygen can penetrate into the Cs-O activation layer with the involvement of a long-term reconstruction and (b) a whole range of caesium suboxides can exist, such as Cs_2O_3, Cs_3O, Cs_4O, $Cs_{11}O_3$ and Cs_7O which are known to possess low workfunctions [39,40] and thus are good vacuum emitters.

Due to the absence of the formation for such wide range of oxidation states, K-deposited surfaces suffer more degradation when oxygen adsorbs, with higher corrosion rate of 0.11 %/L O_2. Whereas, H-terminated surface provides more sites for dissociated oxygen to penetrate into the activation layer and possibly form the insulating oxides or even oxidize the diamond surface, thus decreasing the photoyield more rapidly.

The greater thermal stability (figure 23a, b) of the alkali metal-activated diamond when oxidised represents the stronger affinity of the alkali metal for the oxidised surface. However, with the surface being treated with hydrogen plasma, instead of O-pre

termination, the Cs or K-enhanced emission degrades with heat at a higher rate due to the alkali metal being more weakly bound to the hydrogenated surface.

It is also worth mentioning that the change in photoyield on different surface termination species is quite similar to the reported effect of surface treatments on diamond field emission [33,41,42], which would suggest that the two underlying mechanisms for the manipulation of their surface electron affinity are basically the same.

6.4.2.2 X-ray Photoemission Studies

(i) Adsorption alkali metal on H-terminated diamond surface

Our XPS work does in any case indicate that K and Cs readily adsorb onto H-terminated CVD diamond surface, as refer to figure 15 (i) and 20(i) respectively. This however, contradicts Benndorf *el al.* [43] who have reported the insignificant adsorption of K on the H-diamond surface. Hossain *et al.* [44] have suggested the possible bonding *via* the hybridization of K 4*s* to the adsorbate-free clean diamond (100) surface. This can be used to explain our case that the K 4*s* can bond more easily to the H $1s\sigma^*$ of the hydrogenated surface, which would further form a weakly-bound surface potassium hydride, KH(ads) compound. Such surface compound was previously reported [45] for the incoming K atoms on surface SiH species to form the surface complex, KH(ads). The same discussion can be addressed to the Cs/H/diamond surface.

The surface coverage of metallic alkali (M: C ratio) on diamond within the period of 20 min deposition is not much different for the H- and the O-terminated surfaces, as the surfaces were saturated with one monolayer alkali metal. However, the initial sticking probability for alkali metal (M) (see figure 12a & 15i, 17a & 20i) on H-terminated surface is smaller than that on O-terminated surface, which can be attributed to the effects of both induced dipole moment and depolarisation effect of these dipoles [46]. While the oxygen layer will mostly remain between the diamond and the metal overlayer, the alkali metal

atoms can replace the hydrogen as the electron acceptor at the surface. In this manner a dipole is induced at the diamond surface – depending upon the relative electronegativities of M and H, this may result in an increase in the magnitude of the dipole moment and hence lower the work function at the surface. This is the dominant mechanism at early stages of alkali metal deposition. With increasing of the M deposition, however, the hybridised M-H termination of diamond will become depolarised as the M-diamond covalent bond weakens due to the increasing electronic interaction among M adatoms. This will induce the inhomogeneous distributions of the dipoles with respect to the surface plane and more electronic charge from the M-diamond interface is shifted into the M overlayer [47,48], causing the M overlayer to metallise. Both of these conditions contribute to lowering the sticking coefficient for further metal adsorption.

(ii) Adsorption of alkali metal on O-terminated diamond surface

With the increase in metallic alkali deposition, the bulk C1*s* diamond peak is shifted to higher binding energy from 284.4 eV to 285.1 eV for H/diamond, and 283.3 eV to 285.7 eV for O/diamond, which confirms that stronger bonding occurs for metal-oxygen, M/O and the enhanced occurrence of downward band bending.

At the metal coverage more than 0.50 ML, the secondary peak at + 2 eV relative to bulk C 1*s* peak (which used to be assigned to polyhydride compounds) was shielded by metallic related species, including C to M and C-O-M compounds (see figure 16, 21). This is evidenced with the considerably reduction of the C 1*s* photoemission intensity. The peak at + 2.7 – 4.0 eV relative to the bulk C 1*s* peak is assigned to carboxylate and multiple ether linkages. The minor peak at + 5.0 eV is contributed by the alkali hydroxide on carbon bonding, possibly due to the contamination by moisture in the chamber. Such adsorption of OH was reported on GaAs photocathodes, due to the residual gas in an UHV condition [49].

Various O 1*s* binding energies are seen as small peaks in figure 22 (532.7 eV, 533.8 eV and 534.8 eV), which could arise from differing bonding mechanisms between O and C (ethers, carboxylate *etc*). However, comparing with the assigned O 1*s* peaks under very low temperatures [50,51,52], these three peaks can roughly be de-convoluted to give the complex metal oxide system of M_2O, M_2O_2 and MO_2 respectively, similar to some previous reports at 300 K condition [53,54]. Whereas, the O 1*s* peaks at lower binding energy at 531.5 eV will increase in intensity, suggesting the formation of more thermodynamically stable C-O-M groups, resulting from the conversion of those M-O complex.

(iii) Adsorption of O_2 on alkali-metal-deposited diamond

With the re-exposure of M/O/diamond or M/H/diamond to molecular oxygen (refer to figure 22,vi), the O 1*s* peaks were shifted to lower binding energy, which can be attributed to the effect of the induced upward band bending. The four de-convoluted peaks of O 1*s* remain the same, suggesting that all of the peaks are metal oxide related complexes and are still reactive to molecular oxygen, by either dissociating the gas into M-O species or facilitating the formation of the covalent state of adsorbed oxygen [55].

The state of O_2/M/O/diamond or O_2/M/H/diamond, however, is very unstable to atomic hydrogen, forming the major O 1*s* peak at 531.9 eV due to M-OH group, which will eliminate the M-O compounds of higher oxidation states. The minor peaks at 530.7 eV and 533.0 eV are respectively assigned to the remaining C-O-M and M_2O species.

6.4.3 Transmissive Mode

In general, the photocurrent generated by the reflective mode photoemission is nearly three-times greater than that of the transmission mode photocathodes, because in reflective mode, the electrons are emitted through the same surface the photons have entered. The majority of electron-hole pairs are created in the near vicinity of the photon entrance surface and therefore have a high chance of reaching the same surface and escaping through it into vacuum. For the transmission type design, however the photons enter the diamond layer from one side, the generated photoelectrons have to emerge into vacuum on the opposite side of the layer. Electrons have a relatively low chance to diffuse from the region close to the photon entry surface to the surface on the opposite side.

(a) For **high quality** diamond (white diamond, optical graded), it is clear that the adsolute photocurrents when the growth side faces to the illumination are always higher than the photocurrents when the substrate is the near face. If the substrate side of white diamond is facing the incoming radiation, it will absorb most of the light. Thus, photoelectrons cannot diffuse to the back surface, and the light does not penetrate there either. Hence a lower photoyield results. In contrast if the substrate diamond is at the back surface, light/photoelectrons from the front surface are free to travel to the back region, hence a good photoyield results. Figure 30 shows a higher transmission of photoelectrons is obtained for thicker diamond films but this will be limited by too thick diamond (such as up to 100 μm) as more internal inelastic scattering will hamper the phototransmission to take place. When the film is 4-μm thick, however it is too thin to induce sufficient photoelectrons.

Figure 31b shows the Itransmissive/Ireflective ratios with 252 nm filter in place are much higher than for the other plots probably because the light penetrates further towards the far face. The *uv* absorption spectrum for the 4 μm (figure 32a) thick film

shows absorption of over 90% of light above the diamond band gap suggesting that higher energy light is largely absorbed very near the near face of the diamond (certainly in the samples that are thicker than 4μm). This is why most emission occurs from the near face for high energy light. Back face emission is expected to be as much due to electrons diffusing through the diamond to the far face as it is due to light absorbed near the far face. With the sub-band gap light however the radiation can reach the far face and in fact needs greater thickness to be efficiently absorbed, and therefore far face emission is large and in some cases favoured. The above band gap radiation is rapidly absorbed and therefore there is a larger emission from the front face, while the sub band gap radiation penetrates further into the diamond and gives a larger proportion of far face emission.

(b) For **low quality diamond** (black diamond, thermal management graded), the photo-transmission is fairly orientation-independent, showing the similar transmittance ratio of ~ 14 %. This is because the defects are distributed homogeneously within grown or substrate sides, thus the extent of transmission is nearly independent on which side of the diamond faces the *uv* illumination. Since the black diamond (thermal management graded) is thicker and contains more graphitic than white diamond, thus more absorption of the light/photocurrent in the bulk is expected. Figure 35 illustrates the role played by higher graphitic content at the substrate side, which acts as a good *uv* adsorbing layer, thus higher photoelectron can be generated within bulk diamond, and most of them would be trapped in the defective zones. However, the photoemission under such condition is highly hindered by wavelength selectivity. This is because the graphitic contents are not good wavelength selectors, thus the device is not a *uv-vis* solar blind candidate.

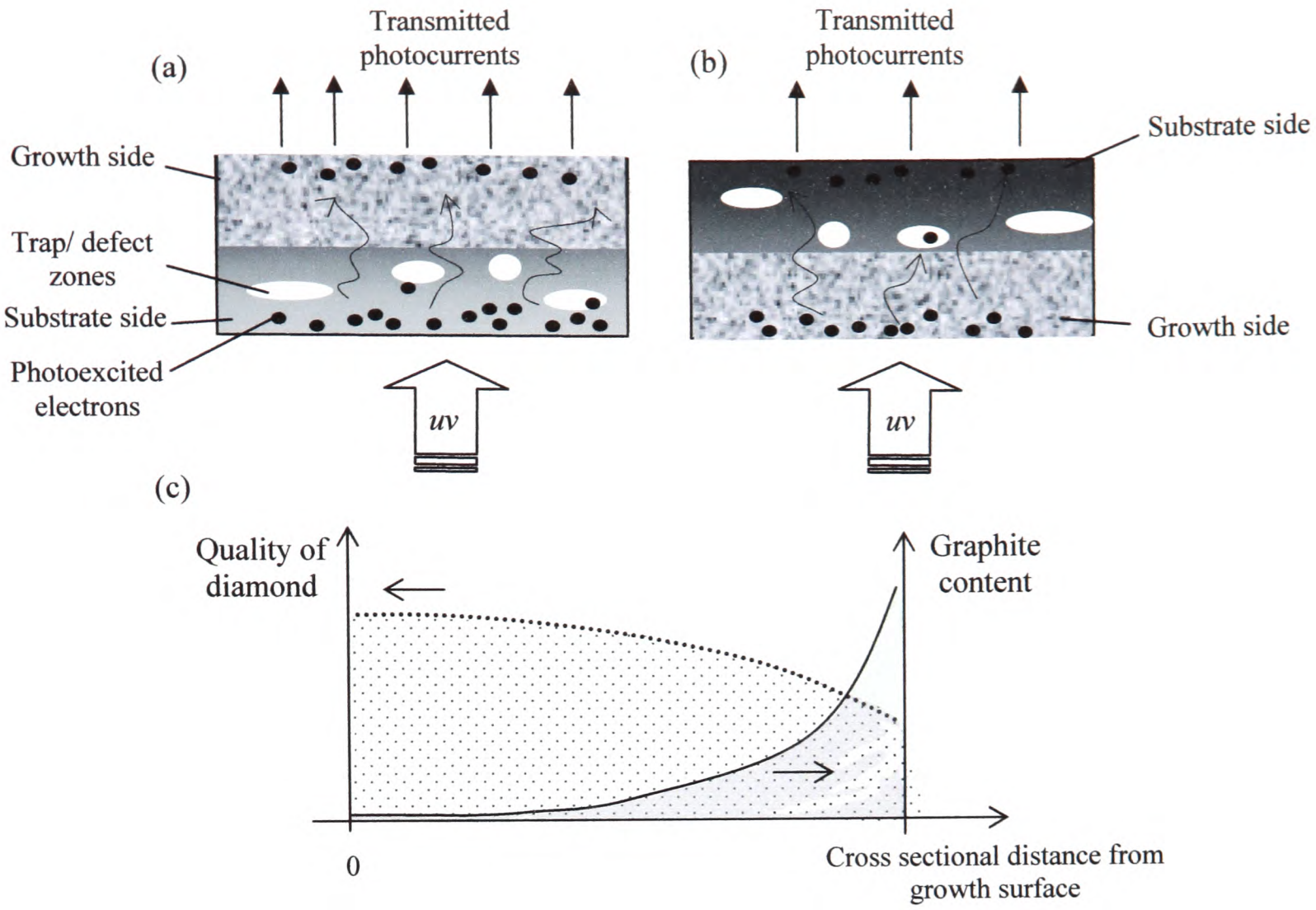


Figure 35. (a) The uv impinges on the substrate side and the accumulated electron diffused through the diamond thickness, and emitted from the growth side; (b) The uv impinges on the growth side and electron diffused through the diamond thickness, and emitted from the substrate side; and (c) the correlation of diamond and graphite content to the distance from growth side

(c) Comparing to the industrial white and black diamonds (as tabulated in Table 1), the **homegrown** black diamond shows the intermediary behaviour in the extent of photo-transmission, by which it shows dependence on

(i) the growth side to emit better on the back side, and

(ii) the substrate side to absorb more photo-excited electrons.

Therefore, a compromise clearly arises depending which way the diamond is oriented between high yield or/and high selectivity. An ideal photo-transmitter would be the light can penetrate as far as to the far face of the illumination, and excite directly the electrons that lie on the farther vicinity and emit from the back side. This will definitely guarantee a high photoemission in transmission mode.

The required diamond thickness for efficient transmission photoelectron is 2-3 times higher than required for GaAs and CsI photocathode [56,57,58,59]. This is due to the fact that the diamond is an indirect band gap semiconductor, in which the minimum in the conduction band and the maximum in the valence band occur at different locations in reciprocal space. The wide band gap 5.5 eV of diamond induces the indirect recombination of electron trapping *via* a gap state and enhances a longer electron transition path length than in the direct band gap semiconductors GaAs. Therefore, a longer mean free path of electron transition in bulk diamond is required for efficient transmission than direct band gap materials.

6.5 Conclusion

The performance of CVD diamond thin film as a photocathode material has been explored as a function of the growth conditions. Films that show a minimum content of non-diamond carbon demonstrate the best wavelength discrimination, as determined by responses at 186 and 252 nm. However, the total photoyield at 186 nm was found to be relatively insensitive to the quality of the film, and particulate layers present before film coalescence are particularly efficient photoemitters. This is attributed to effects that diamond and graphite in intimate contact exert on each, which influence the overall photoyield.

The photoyield observed is also very sensitive to surface termination, and it was found that caesiation enhances the photoyield compared to hydrogenated interfaces.

The hydrogenated diamond is readily contaminated by oxygen adsorption regardless of the type of treatments that takes place, leading to degradation in photoyield. The photoyield of hydrogenated surface drops to insignificant value at a surface O: C ratio of 0.1.

Adsorbing hydrogen onto an oxygenated surface is slow to restore the surface negative electron affinity. In contrast, adsorbing oxygen onto a hydrogenated surface can degrade the photoyield in a rapid manner, by inducing positive electron affinity.

The emitted photocurrent from metal-deposited diamond is saturated at a monolayer of alkali metals. Adding the alkali metal to an overoxidized surface with negative electron affinity compensates the presence of the electronegative oxygen atoms and restores the downward band bending.

The deposited Cs on oxygenated diamond has revealed to be an ideal photoemitter, showing higher photoyield, lower corrosion rate by oxygen, better NEA restoration by hydrogen and better thermal stability. K deposited on either pre-treated diamond surface by oxygen or hydrogen shows insignificant difference on photoyield in response to metal deposition and the corrosion by oxygen.

Diamond with high quality and large thickness can emit better as reflective and transmissive mode, though thinner diamond gives the highest ratio of transmissive/reflective photoyield. A phototransmitter with lower quality diamond facing to *uv* illumination can absorb more photo-excited electrons, but is less selective with respect to photon wavelength.

6.6 References for Chapter 6

[1] F.J. Himpsel, J.A. Knapp, J.A. Van Vechten and D.E. Eastman, *Phys. Rev. B* **20** (1979) 624

[2] J. van der Weide and R.J. Nemanich, *Phys. Rev. B* **49** (1994) 629

[3] N. Eimori, Y. Mori, A. Hatta, T. Ito and A. Hiraki, *Diamond Relat. Mater.* **4** (1995) 806

[4] A. Breskin, R. Chechik, E. Shefer, D. Bacon *et al.*, *Appl. Phys. Lett.* **70** (1997) 3446

[5] E. Pace, R. Di Benedetto and S. Scuderi, *Diamond Relat. Mater.* **9** (2000) 987

[6] W.E. Spicer, *Phys. Rev. B* **112** (1958) 114

[7] R.U. Martinelli and D.G. Fisher, *Proc. IEEE* **62** (1974) 1339

[8] V.B. Kvaskov and V.V. Gorbachev, *Sov. Phys. Semicond.* **22** (1988) 314

[9] J.B. Cui, M. Stammler, J. Ristein and L. Ley, *J. Appl. Phys.* **88** (2000) 3667

[10] C.H. Goeting, F. Marken, A. Gutierrez-Sosa, R.G. Compton and J.S. Foord, *New Diam. Front. Carbon Technol.* **9** (1999) 207

[11] A. Laikhtman, A. Hoffman, R. Kalish, Y. Avigal, A. Breskin, *et al.*, *Appl. Phys. Lett.* **73**(10) (1998) 1433

[12] G.Z. Cao, J.J. Schermer, W.J.P. van Enckevort, W.A.L.M. Elst and L.J. Giling, *J. Appl. Phys.* **79** (1996) 1357

[13] X.D. Zhu, H.Y. Zhou, R.J. Zhan, X.H. Wen and J.X. Wu, *Appl. Surf. Sci.* **136** (1998) 345

[14] M.J. Chiang and M.H. Hon, *J. Cryst. Growth* **211** (2000) 211

[15] A. Breskin, T. Boutbol, A. Buzulutskkov, R. Chechnik, G. Garty, E. Shefer and B.K. Singh, *Nucl. Inst. Meth. Phys. Res. A* **442** (2000) 58

[16] A. Breskin, R. Chechik, E. Shefer, D. Bacon, Y. Avigal, R. Kalish and Y. Lifshitz, *Appl. Phys. Lett.* **70** (1997) 3446

[17] J. Ristein, *Diamond Relat. Mater.* **9** (2000) 1129

[18] X.L. Peng, *Thin Solid Films* **370** (2000) 63

[19] J.Y. Shim, H.K. Baik and K.M. Song, *J. Appl. Phys.* **87**(10) (2000) 7508

[20] C.D. Clark, P.J. Dean and P.V. Harris, *Proc. R. Soc. Lond. A* **277** (1964) 312

[21] F. Foulon, P. Bergonzo, C. Borel, R.D. Marshall, C. Jany, L. Besombes, A. Brambilla, D. Riedel, L. Museur, M.C. Castex and A. Gicquel, *J. Appl. Phys.* **84** (1998) 5331

[22] J. Ristein, W. Stein and L. Ley, *Diamond Relat. Mater.* **7** (1998) 626

[23] M.C. Rossi, S. Salvatori, F. Scotti, G. Conte and E. Cappelli, *Phys. Stat. Sol. (a)* **181** (2000) 29

[24] J.S. Foord, C.H. Lau, M. Hiramatsu and A.M. Bennett, *Diamond Relat. Mater.* **11** (2002) 437

[25] J. Ristein, F. Maier, J.B. Cui and L. Ley, *Phys. Stat. Sol. (a)* **181** (2000) 65

[26] L. Diederich, O.M. Kuttel, P. Aebi, E. Maillard-Schaller, R. Fasel and L. Schlapbach, *Diamond Relat. Mater.* **7** (1998) 660

[27] J. Robertson, *Diamond Relat. Mater.* **5** (1996) 797

[28] L.N. Pauling, The Nature of the Chemical Bond, Cornell University Press, Ithaca, NY, 1939

[29] N.B. Hanney and C.P. Smith, *J. Am. Chem. Soc.* **68** (1946) 171

[30] N.N. Greenwood and A. Earnshow, Chemistry of the Elements, Pegamon, UK, 1984

[31] M. Niigaki, T. Hirohata, T. Mochizuki, S. Uchiyama, H. Kan and T. Hiruma, *Appl. Phys. Lett.* **75** (1999) 3533
[32] M. Niigaki, T. Hirohata, T. Mochizuki, S. Uchiyama, H. Kan and T. Hiruma, *Jpn. J. Appl. Phys.* **37** (1998) L 1531
[33] M.W. Geis, J.C. Twichell, J. Macaulay and K. Okano, *Appl. Phys. Lett.* **67** (9) (1995) 1328
[34] K.P. Loh, J.S. Foord, R.G. Egdell and R.B. Jackman, *Diamond Relat. Mater.* **6** (1997) 874
[35] F.H. Jones, A.B. Molloy, K.P. Loh, J.S. Foord and R.B. Jackman, *Diamond Relat. Mater.* **7** (1998) 651
[36] R.L Bell, Negative electron affinity devices, Oxford University Press, London, 1973
[37] Q.B. Lu, R. Souda, D.J. O'Connor and B.V. King, *Phys. Rev.* ***B*** **54**(24) (1996) R17347
[38] S. Pastuszka, A.S. Terekhov and A. Wolf, *Appl. Surf. Sci.* **99** (1996) 361
[39] C.W. Bates *Jr.*, *Appl. Phys. Lett.* **45**(10) (1984) 1058
[40] L. Soriano and L. Galan, *Jpn. J. Appl. Phys. Part 1* **32**(10) (1993) 4737
[41] P.W. May, J.C. Stone, M.N.R. Ashfold, K.R. Hallam, W.N. Wang and N.A. Fox, *Diamond Relat. Mater.* **7** (1998) 671
[42] J.B. Cui, J. Ristein, M. Stammler, K. Janischowsky, G. Kleber and L. Ley, *Diamond Relat. Mater.* **9** (2000) 1143
[43] S. Petrick and C. Benndorf, *Diamond Relat. Mater.* **10** (2001) 519
[44] M.Z. Hossain, T. Kubo, T. Aruga, *et al.*, *Diamond Relat. Mater.* **9** (2000) 162
[45] N. Minami, N. Takagi, M. Nishijima and T. Aruga, *Surf. Sci.* **325** (1995) 11
[46] C.A. Papageorgopoulos, *Phys. Rev. B* **40**(3) (1989) 1546
[47] J.P. Muscat and I. Batra, *Phys. Rev. B* **34** (1986) 2889
[48] E. Wimmer, A.I. Freeman, I.R. Hishes and A.M. Karo, *Phys. Rev. B* **28** (1983) 3074
[49] C.Y. Su, W.E. Spicer and I. Lindau, *J. Appl. Phys.* **54**(3) (1983) 1413
[50] J. Jupille, P. Dolle and H. Besancon, *Surf. Sci.* **260** (1992) 271
[51] S.L. Qiu, C.L. Lin, J. Chen and M. Strongin, *Phys. Rev. B* **41** (1990) 7467
[52] H. Shi and K. Jacobi, *Surf. Sci.* **276** (1992) 12
[53] K.P. Loh, D.Phil, "Growth Studies and Surface Modification of Thin Film Diamonds", Oxford, 1996
[54] A.R.H.F. Ettema, *Nucl. Inst. Meth. Phys. Res. A* **442** (2000) 342
[55] V.I. Bukhtiyarov, I.P. Prosvirin, R.I. Kvon, B.S. Bal'zhinimaev and E.A. Podgornov, *Appl. Surf. Sci.* **115** (1997) 135
[56] A. Sellai and P. Dawson, *Sol. State Elec.* **46** (2002) 29
[57] S. Pastuszka, M. Hoppe, D. Kratzmann, D. Schwalm and A. Wolf, *J. Appl. Phys.* **88**(11) (2000) 6788
[58] A.S. Tremsin and O.H.W. Siegmund, *Nucl. Inst. Meth. Phys. Res. A* **442** (2000) 337
[59] C. Lu and K.T. McDonald, *Nucl. Inst. Meth. Phys. Res. A* **343** (1994) 135